The joining of advanced high strength steels using resistance spot welding.

Miller, Christopher Carl Edward

The Joining of Advanced High Strength Steels using Resistance Spot Welding

Christopher Carl Edward Miller

Academic Supervisor

Dr George Fourlaris

Materials Research Centre
School of Engineering
Swansea University

2008

ProQuest LLC.
789 East Eisenhower Parkway
P.O. Box 1346
Ann Arbor, MI 48106 – 1346

ACKNOWLEDGEMENTS

The author wishes to acknowledge the financial support received from the Engineering and Physical Sciences Research Council and Corus Strip Products UK. I would like to thank my supervisors Dr G. Fourlaris and Mr T.B. Jones, for their technical and academic guidance during the course of this research programme. I would also like to thank the staff of Testing Solutions Wales, Swinden Technology Centre, TWI Port Talbot and the ECM^2 workshop, and in particular Mr M. Westacott, Mrs C. Aitchison, Mr W. Abbott and Mr S. Danks. I am especially grateful to Mr K. Chilvers for his invaluable help and advice in the field of resistance spot welding.

To my colleagues, thank you for making the past four years on the engineering doctorate scheme a truly enjoyable and memorable experience.

To my friends, especially Andy and Becky, thank you for your words of encouragement when times were tough.

Finally I would like to convey my deepest gratitude to my parents George and Merrill and my sister Stephanie for their continued support and patience. Thank you for having faith in me, I couldn't have done it without you.

ABSTRACT

Weight reduction of the automotive body-in-white structure is increasingly necessary to improve fuel efficiency and reduce the carbon emissions and environmental impact of motor vehicles. This must be achieved without compromising the strength of the body-in-white structure.

Steel manufacturers are continuing to develop advanced high strength steels (AHSS) which not only exhibit high strength and excellent energy absorbing characteristics but also retain a comparable degree of formability to low alloy grades. The specific properties of advanced high strength steels such as dual phase and TRIP are derived via the addition of specific alloying elements and careful control of thermomechanical processing routes in order to develop the required microstructures in the final product. The utilisation of such grades could yield significant reductions in the weight of body-in-white structures since they offer the automotive design engineer the opportunity to fabricate components out of thinner sheet whilst retaining or even improving on the structural strength and impact performance of components fabricated from thicker mild steel sheets.

A major barrier to the widespread acceptance and implementation of AHSS by the automotive industry is the perceived complexities associated with the joining of these materials using resistance spot welding, which remains the dominant joining process in modern automobile construction. The complex alloy chemistries of these grades coupled with the extremely high cooling rates generated by the resistance welding process can give rise to weld microstructures with properties differing greatly from the parent microstructure. Of particular concern for automotive manufacturers is the potential for the formation of martensite in the weld nugget and heat affected zones, since its high hardness and low ductility are thought to result in poor weld performance.

This research programme has investigated the weldability of six AHSS grades in comparison to low alloy grades typical of those currently used in the automotive industry, using a basic single pulse weld schedule. Simple modifications to welding parameters such as increasing electrode force and electrode tip diameter were investigated as well as the effects of advanced weld schedules on weld microstructures, microhardness and strength. The effect of joining selected advanced high strength steels to low carbon mild steel has also been studied.

LIST OF TABLES

LIST OF FIGURES

Figure 5.50b Micrograph illustrating the variation in microstructure from parent metal to weld nugget in DP1000 weld

Figure 5.50c Micrograph of DP1000 parent microstructure

Figure 5.50d Micrograph showing transition from parent material microstructure to heat affected zone microstructure in DP1000. Parent microstructure appears on left-hand side of image

Figure 5.50e Micrograph showing microstructure of the outer heat affected zone in DP1000

Figure 5.50f Micrograph showing microstructure of the inner heat affected zone in DP1000

Figure 5.50g Micrograph showing weld nugget microstructure in DP1000

Figure 5.51a Macro of $5\sqrt{t}$ spot weld formed in 1.0mm MS1400

Figure 5.51b Micrograph illustrating the variation in microstructure from parent metal to weld nugget in MS1400 weld

Figure 5.51c Micrograph of MS1400 parent microstructure

Figure 5.51d Micrograph showing transition from parent material microstructure to heat affected zone microstructure in MS1400. Parent microstructure appears on right-hand side of image

Figure 5.51e Micrograph showing microstructure of the outer heat affected zone in MS1400

Figure 5.51f Micrograph showing microstructure of the inner heat affected zone in MS1400

Figure 5.51g Micrograph showing weld nugget microstructure in MS1400

Figure 5.52a Macro of $5\sqrt{t}$ spot weld formed in 1.2mm TRIP800

Figure 5.52b Micrograph illustrating the variation in microstructure from parent metal to weld nugget in TRIP800 weld

Figure 5.52c Micrograph of TRIP800 parent microstructure

Figure 5.52d Micrograph showing transition from parent material microstructure to heat affected zone microstructure in TRIP800

Figure 5.52e Micrograph showing microstructure of the outer heat affected zone in TRIP800

Figure 5.52f Micrograph showing microstructure of the inner heat affected zone in TRIP800

Figure 5.52g Micrograph showing weld nugget microstructure in TRIP800

Figure 5.90a Macro of a $5\sqrt{t}$ TRIP800 spot weld treated with a 3.90kA secondary current pulse

Figure 5.90b Micrograph illustrating the variation in microstructure from parent metal to weld nugget in TRIP800 spot weld treated with a 3.90kA secondary current pulse

Figure 5.90c Micrograph showing microstructure in TRIP800 weld nugget treated with a 3.90kA secondary current pulse

Figure 5.91a Macro of a $5\sqrt{t}$ TRIP800 spot weld treated with a 4.05kA secondary current pulse

Figure 5.91b Micrograph illustrating the variation in microstructure from parent metal to weld nugget in TRIP800 spot weld treated with a 4.05kA secondary current pulse

Figure 5.91c Micrograph showing microstructure in TRIP800 weld nugget treated with a 4.05kA secondary current pulse

Figure 5.92a Macro of a $5\sqrt{t}$ TRIP800 spot weld treated with a 4.22kA secondary current pulse

Figure 5.92b Micrograph illustrating the variation in microstructure from parent metal to weld nugget in TRIP800 spot weld treated with a 4.22kA secondary current pulse

Figure 5.92c Micrograph showing microstructure in TRIP800 weld nugget treated with a 4.22kA secondary current pulse

Figure 5.93 Macro of $5\sqrt{t}$ TRIP800 spot weld treated with a 4.44kA secondary current pulse

Figure 5.94 Micrograph illustrating variations in microstructure in TRIP800 weld nugget treated with a 4.44kA secondary current pulse

Figure 5.95a Micrograph showing microstructure of weld at position (i) in figure 5.94

Figure 5.95b Micrograph showing microstructure of weld at position (ii) in figure 5.94

Figure 5.95c Micrograph showing microstructure of weld at position (iii) in figure 5.94

Figure 5.95d Micrograph showing microstructure of weld at position (iv) in figure 5.94

Figure 5.95e Micrograph showing microstructure of weld at position (v) in figure 5.94

CONTENTS

1. INTRODUCTION

With the current level of concern over carbon emissions and the perceived threat of man made global warming, automotive manufacturers face increasing pressure from both government and environmental groups to improve the fuel efficiency of the vehicles they produce. The recently published Stern report[1] highlighted the contribution of motor vehicles to the increasing concentration of CO_2 in the atmosphere. In an attempt to address this problem the European Automobile Manufacturers Association have committed to achieving an average CO_2 emission target of 140g/km in 2008 and 120g/km in 2012 for new cars sold in the EU, down from 186g/km in 1995[2]. Consumer demand for greater fuel efficiency has also been driven by steadily increasing fuel prices worldwide.

Various techniques have been employed by automotive manufacturers in order to tackle these demands. Advances in engine management, fuel delivery systems and the mechanical design of engine components have lead to the development of increasingly fuel efficient power plants. In addition a great deal of attention is now paid to vehicle design in terms of aerodynamics. Perhaps the most cost effective means of improving fuel efficiency is to reduce the total weight of the vehicle. However with an ever increasing number of weight-adding features such as electric windows and seats, climate control and in-car entertainment systems generally being regarded as standard equipment by consumers, automotive manufacturers have been forced to turn their attention to the body-in-white structure in order to achieve the desired weight reductions. It is vital that any weight reduction of the body-in-white structure is achieved without sacrificing the strength, rigidity or crash performance of the completed vehicle, particularly since consumer awareness of vehicle crash performance is greater than ever due to the introduction of schemes such as the European New Car Assessment Program (EuroNCAP)[3,4].

To date automotive manufacturers have been able to reduce the weight of the body-in-white structure by substituting thicker low strength grades with thinner high strength steels without sacrificing structural strength or crashworthiness. However the

strengthening mechanisms utilised in conventional high strength grades such as high strength low alloy steels tend to have a detrimental effect on formability and therefore their use has been limited to components that do not require a high degree of formability.

In response to the demand for high strength formable materials, steel manufacturers worldwide are continuing to develop a variety of advanced steel products such as dual phase (DP) and Transformation Induced Plasticity (TRIP) steels which offer superior tensile strengths and energy absorbing characteristics to mild steel grades whilst retaining a comparable degree of formability. These properties are derived from the unique multi-phase microstructures of these steels which are produced through the addition of selected alloying elements such as carbon, manganese and silicon and close control of thermal profiles during processing. The utilisation of such grades affords the automotive engineer a greater degree of freedom in component design and could potentially yield significant improvements in vehicle crashworthiness as well as further weight reductions.

Despite the potential benefits offered by advanced high strength steels, concerns persist regarding the ease with which these grades can be incorporated into body-in-white design using existing production facilities. In order for any potential grade to gain widespread acceptance within the automotive industry it must be readily weldable, specifically using resistance spot welding which remains the dominant joining process in the fabrication of body-in-white structures. The complex alloy chemistries of advanced high strength steels coupled with the extremely high cooling rates associated with the spot welding process can lead to the formation of martensite in the weld nugget and heat affected zones of joints formed in these grades. The primary method for assessing weld quality in most automobile assembly lines remains the chisel test, which as the name suggest involves manually forcing welds apart using a tapered chisel. The tendency of welds formed in some advanced high strength steels to fail interfacially when subjected to this basic shop-floor technique and the assumption that this represents poor weld quality is leading to reluctance on the part of the automotive industry in adopting these grades.

Various attempts have been made at controlling the final properties of spot welds formed in advanced high strength steels through the use of tailored welding parameters. These have included measures to reduce the cooling rate of the weld region in an attempt to suppress the martensite transformation and the introduction of in-process heat treatments in order to reduce the hardness and increase the toughness of the martensite once it has formed. However, such measures can significantly increase the amount of time required for the formation of a single spot weld with a corresponding loss of productivity.

Whilst there has been a significant amount of research focused on the behaviour of advanced high strength steels when joined to grades with the same or similar chemical composition, where high strength grades are currently used in body-in-white construction they are rarely joined to components formed from the same grade and are more likely to be welded to components fabricated from grades with significantly lower alloy contents. The effect of this on weld properties and joint performance remains largely un-investigated.

In order that the potential benefits offered by dual phase and TRIP steels in terms of light-weighting and crash performance are realised, a detailed investigation is required that addresses the issues described above. The present research program involved a critical review of the current knowledge in the field of resistance spot welding when applied to high strength steels. This included a discussion of the factors that influence weld quality in advanced high strength steels and the possible modifications to weld schedules that could yield improvements in weld performance. On the basis of this review a series of investigations were devised which sought to establish the weldability of a range of commercially available advanced high strength steels using basic weld schedules and to investigate the potential of modifications to standard welding practices for improving weld performance as well as the effect of alloying between advanced high strength grades and low carbon mild steel.

2. REVIEW OF LITERATURE

The following critical review of literature considers the various properties and strengthening mechanisms employed in the production of several advanced high strength steels that offer the potential for enhancing the crash performance of weight reduction of automotive body-in-white structures through down-gauging of components. Novel automotive joining processes which are finding applications in body-in-white construction are discussed as well as resistance spot welding which remains the dominant joining process. The main issues associated with the resistance spot welding of advanced high strength steels are defined along with potential solutions to these issues.

2.1 The metallurgy of low carbon steels

Despite the threat from lightweight materials such as aluminium and polymer based composites, low carbon strip steels remain the material of choice for automotive manufacturers due primarily to their comparatively low cost, excellent formability and the relative ease with which they can be joined.

One of the most important characteristics of steel alloys is the range of microstructures and subsequent mechanical properties that are available through heat treatment alone. A selection of the microstructures that can be found in low carbon steel at ambient temperatures are discussed in the following sections where they are split into two categories; microstructures resulting from equilibrium cooling conditions and microstructures resulting from non-equilibrium cooling conditions. Since resistance spot welding results in extremely rapid heating and cooling rates within the weld nugget and heat affected zone, it is the latter group of microstructures which are of greatest relevance to this investigation.

2.1.1The iron – iron carbide equilibrium phase diagram

In simplest terms steel is an alloy of iron and carbon. The microstructural constituents present in iron – carbon alloys at a given carbon concentration and temperature can be deduced from the iron – iron carbide equilibrium phase diagram shown in figure 2.1[6]. Due to the low solubility of carbon in ferrite at ambient temperatures, carbon is usually

present in low carbon steel in the form of cementite (Fe_3C). The morphology of this cementite depends largely on the cooling conditions experienced by the steel, however the phases typically found in low carbon steel microstructures formed under equilibrium conditions are described below.

Ferrite

Ferrite (α-iron) is an equilibrium phase, characterised by comparatively low strength and high ductility. Fully ferritic microstructures are only observed at ambient temperatures when the carbon content of the steel is extremely low. If the carbon content is greater than approximately 0.008wt%, the final microstructure will be comprised of ferrite with a volume fraction of iron carbide, typically cementite (Fe_3C). The mechanical properties of fully ferritic microstructures depend primarily on grain size. As the ferrite grain size decreases, the yield stress of the material increases. This is known as the Hall-Petch relationship and is commonly expressed by the following equation[9]:

$$\sigma_y = \sigma_i + k_y d^{-1/2}$$

Where:

σ_y = yield stress

σ_i = the friction stress opposing dislocation movement

d = ferrite grain size

k_y = constant

Consequently the strength of ferritic steel can be increased by refining the ferrite grain structure. A further advantage of a fine ferrite structure is improved formability and ductility. These characteristics make ferritic steels particularly useful for forming applications such as automotive panels.

Pearlite

Pearlite is a two-phase lamellar eutectoid consisting of alternate laths of ferrite and cementite (Fe_3C) and is the product of a diffusional solid state transformation. Pearlite begins to appear in steels with carbon contents greater than approximately 0.02%. Fully

pearlitic microstructures are only observed in steels which have a eutectoid composition (0.8%C), as can be seen from figure 2.1[6]. Low carbon steels have a hypo-eutectoid composition and will have microstructures that consist of pro-eutectoid ferrite with a percentage of pearlite second phase, assuming that the steel is cooled very slowly from the austenite region of the phase diagram.

Under equilibrium conditions, the transformation of austenite to pearlite should occur at 723°C according to the phase diagram. However, if the steel is being continuously cooled from the austenite region, the formation of pearlite is often depressed to lower temperatures due to the diffusional nature of the transformation. At some point below the eutectoid temperature, ferrite begins to nucleate at the austenite/pro-eutectoid ferrite grain boundaries and grows into the austenite grains. Due to the extremely low solubility of carbon in bcc ferrite, carbon is rejected into the adjacent fcc austenite which subsequently transforms to cementite. The pearlite forms as parallel lamellae of alternate ferrite and cementite, which grow co-operatively producing a two phase structure. An increase in the cooling rate or the degree of undercooling has the effect of increasing the driving force for the transformation and increasing the growth rate of the pearlite into the austenite. At a high growth rates, the carbon atoms not only have less time to diffuse away from the advancing ferrite but the mobility of the carbon atoms is reduced due to the undercooling thus the interlamellar spacing of the pearlite decreases. This is illustrated in figure 2.2[7]. A decrease in the interlamellar spacing has been shown to increase the strength and hardness of pearlite[10].

2.1.2 Non-equilibrium microstructures

The phases and microstructures predicted by the iron-iron carbide equilibrium phase diagram generally only occur if the steel is cooled very slowly from the austenite region. If the cooling rate is increased beyond a critical value, non-equilibrium microstructures such as bainite and martensite will form instead. The type of microstructures that form in a particular steel under non-equilibrium conditions depends largely on the cooling rate or degree of undercooling below the eutectoid temperature and the alloy chemistry of the

steel. Several non-equilibrium microstructures that can form in low carbon steels are described below.

Bainite

Bainitic microstructures can be divided into two distinct groups according to their morphology[11]. The type of bainite found in a final microstructure depends on the temperature at which the transformation takes place. Upper bainite generally forms between 550°C and 400°C whilst lower bainite forms between 400°C and 250°C. The overall appearance of both morphologies of bainite are similar in that they are both composed of elongated plates of ferrite which grow in groups known as sheaves nucleating at austenite grain boundaries. In upper bainite, the ferrite plates are separated by cementite films, which precipitate following the rejection of carbon into the remaining austenite as the ferrite plates grow. Carbon is rejected from the ferrite because the solubility of carbon in the bcc ferrite is significantly lower than in the fcc austenite.

Lower bainite also consists of ferrite plates but the key difference between upper and lower bainite is the nature of the carbides that form in the microstructure. Due to the lower transformation temperature, many of the carbon atoms in lower bainite do not have sufficient mobility to be rejected from the growing ferrite plates and instead precipitate within the plates themselves as well as between the plates as in upper bainite. However, because a lower fraction of the carbon is rejected into the austenite in lower bainite, the carbides that precipitate between the ferrite plates are much finer than those associated with upper bainite.

If the steel is continuously cooled rather than being held at an isothermal temperature within or cooled slowly through either the upper bainite or lower bainite temperature range, a third morphology of bainite can result. Granular bainite is relatively difficult to distinguish from the other two morphologies of bainite, since the mechanism by which it forms is the same[12]. However, because granular bainite forms gradually during cooling, the sheaves of bainitic ferrite that form can become relatively coarse and blocky. Granular bainite often lacks the carbides found in upper and lower bainite. Instead, the

carbon that is rejected from the bainitic ferrite stabilises the remaining austenite, so that the final microstructure contains some retained austenite and high carbon martensite in addition to the bainitic ferrite[12].

Acicular Ferrite

Acicular ferrite is composed of thin, interwoven lenticular plates. Bainite and acicular ferrite have essentially the same transformation mechanism, but whereas bainite nucleates at austenite grain boundaries and grows in the form of sheaves of parallel platelets, acicular ferrite plates nucleate intragranularly on non-metallic inclusions and radiate from these point nucleation sites producing a much more disorganised structure with adjacent platelets pointing in different directions.

The formation of acicular ferrite is encouraged by a large austenite grain size since under these conditions the number density of grain boundary nucleation sites is decreased relative to intragranular sites. The austenite grain surfaces can also be rendered ineffective as ferrite nucleation sites by the presence of inert grain boundary phases such as ferrite allotriomorphs, thus encouraging the formation of acicular ferrite in preference to bainite.

Martensite

Rapid quenching of austenite below a critical temperature often results in the formation of martensite via a diffusionless shearing process. Due to the high cooling rate, the carbon formerly in solid solution in the austenite remains in solution in the new phase, causing the lattice to become distorted. Martensite is therefore essentially a supersaturated solid solution of carbon in ferritic iron. The extent of the distortion depends on the amount of carbon trapped in the body centred tetragonal (BCT) lattice. The critical temperature for martensite formation is known as the martensite start temperature (M_s) with a complete transformation being achieved at the martensite finish temperature (M_f). The actual values of M_s and M_f are a function of the alloy content of the steel, with carbon having a particularly pronounced effect. Both M_s and M_f decrease sharply with increasing alloy content. In order to obtain a complete transformation the

rate of cooling prior to reaching M_s must be sufficient to suppress the higher temperature diffusion-controlled ferrite and pearlite reactions as well as the formation of other intermediate transformation products such as bainite and acicular ferrite. This critical cooling rate is also strongly dependent on the alloy chemistry of the steel, and will generally be lower the higher the concentration of alloying elements.

The general appearance of martensite in low carbon steels is of fine laths grouped together in 'packets' with low angle boundaries between each lath. Martensite provides the highest strength of any steel phase, however it is typically extremely hard and brittle in its as-formed condition. The high strength of martensite can be attributed to a combination of several possible strengthening mechanisms. It has been shown[23] that there is a strong relationship between the strength of martensite and its carbon content, since carbon additions increase the tetragonality of the body centred tetragonal unit cell. Other contributors to strength include a high dislocation density resulting from the shear transformation and the lath packet size. The maximum lath size is limited by the prior-austenite grain size, and a Hall-Petch type relationship between prior austenite grain size and strength has been found for several steel grades[23].

Fully martensitic steels are typically tempered post-quenching in order to improve toughness although a reduction in steel strength also occurs. Tempering reduces the level of residual stress present in the microstructure as a result of the shear transformation and leads to the precipitation of a fine dispersion of carbides from the α-iron matrix.

Retained austenite

Austenite (γ-iron) is the equilibrium face centred cubic form of iron which is usually only present in low carbon steel at temperatures above the eutectoid temperature of 723°C, as can be seen from figure 2.1[6]. Austenite can be retained in the microstructure at ambient temperatures through the addition of alloying elements which stabilise the austenite structure and suppress the transformation to ferrite. Such elements include carbon which, with a higher solubility in austenite than ferrite, favours the retention of austenite. Other examples of austenite stabilisers include manganese, nickel and nitrogen. Whilst silicon

acts as a ferrite stabiliser, it also inhibits the precipitation of cementite from austenite thus maintaining carbon in solution. Aluminium and phosphorus also inhibit cementite precipitation.

Austenite can also be retained in steel microstructures at ambient temperatures through quenching, provided that the M_f temperature of the steel is below ambient. Under these conditions a fraction of the austenite will not transform to martensite. Retained austenite is therefore frequently found in weld microstructures due to the rapid cooling rates generally associated with welding processes.

Retained austenite is thermodynamically unstable and will readily transform to martensite if subjected to mechanical deformation. This forms the basis of the TRIP effect which is discussed in greater detail in section 2.4.2.

2.2 Conventional high strength steels (HSS) for automotive applications

A selection of high strength steels already widely used in the automotive industry and the strengthening mechanisms through which they derive their enhanced properties are discussed below. Figure 2.3[8] illustrates the relationship between yield strength and elongation for a variety of conventional automotive strip steels as well as selection of advanced high strength steels (AHSS) which will be discussed in the following section.

2.2.1 Solid solution strengthened steels

The strength of steel can be increased by introducing solute atoms into the iron matrix. These solute atoms increase strength by distorting the iron lattice thereby impeding dislocation movement through the lattice during plastic deformation. Solute atoms can be divided into two distinct groups according to the positions they occupy in the parent lattice as illustrated in figure 2.4.

As the name suggests, interstitial solid solutions form when the solute atoms are small enough to occupy the interstices between the solvent atoms in the parent lattice. In simplest terms, steel is essentially an interstitial solid solution of carbon in iron. Other examples of elements that form interstitial solid solutions with iron include nitrogen and boron. The strain field associated with an interstitial atom can be minimised if the interstitial atom moves within the strain field of a dislocation. This leads to the formation of interstitial concentrations or 'atmospheres' in the vicinity of dislocations which has the effect of locking the dislocations in position, thus substantially increasing the stress necessary to cause dislocation movement[24].

Substitutional solid solutions form where solute atoms introduced into the parent lattice occupy lattice positions normally occupied by the solvent atoms. The parent lattice becomes distorted in the vicinity of the solute atoms due to the mismatch in atomic size between the solute and solvent atoms, however the crystal structure of the parent lattice remains unchanged. The degree of strengthening achieved by the addition of substitutional solute atoms is generally greater the larger this mismatch[25], however in order for a solute atom to enter into solution in a parent lattice, its diameter must be

within 15% of that of the solvent atoms in accordance with the Hume-Rothery rules. Examples of elements which can form a substitutional solid solution with iron include phosphorus, manganese, silicon, nickel and molybdenum. Phosphorus is widely used to strengthen low carbon strip steels primarily due to its low cost and limited impact on formability. The addition of phosphorus yields an increase in strength of approximately $10N/mm^2$ for every 0.01wt% P. Rephosphorised steels are commonly supplied to automotive manufacturers with yield strengths in the order of $220\text{-}260N/mm^2$[26].

2.2.2 High strength low alloy (HSLA) steels

Micro-alloyed HSLA steels owe their enhanced mechanical properties to the joint action of ferrite grain refinement and precipitation strengthening. This is achieved through the addition of small amounts of strong carbide or carbonitride forming elements such as niobium, vanadium and titanium. These alloying elements inhibit austenite grain growth during hot rolling thus producing a fine ferrite grain size in the final product. This increases strength in accordance with the Hall-Petch relationship [2.1]. In addition, the precipitation of fine carbide/carbonitride particles at the austenite-ferrite grain boundaries during cooling provides significant dispersion strengthening. The utilisation of these micro-alloying elements allows high strength levels to be achieved whilst maintaining very low carbon levels, thus making HSLA steels readily weldable.

Although HSLA steels with yield strengths in excess of $500N/mm^2$ are available, their application in vehicle construction tends to be limited to components with less complex shapes due to the inevitable loss of formability that occurs with increasing strength as illustrated in figure 2.3[8].

2.2.3 High strength interstitial-free (HSIF) steels

High strength interstitial free steels are typically based on ultra-low-carbon IF steels with additional phosphorus, manganese, silicon or boron to provide the required strength level. The removal of interstitial carbon and nitrogen from IF steels is traditionally achieved by microalloying with strong carbide and nitride-forming elements such as titanium, vanadium and/or niobium. However, advances in vacuum degassing techniques have

allowed the production of ultra-low carbon (<0.003%) IF steels, thereby lowering the amount of microalloying elements required whilst retaining excellent deep-drawing characteristics. The addition of solid solution strengthening elements such as manganese and phosphorus inevitably leads to a slight deterioration in *r* value, however HSIF steels still exhibit superior formability to HSLA steels with comparable tensile strengths.

2.2.4 Carbon manganese steels

Carbon manganese (C-Mn) steels generally have a two-phase microstructure consisting of a ferrite matrix containing a dispersion of pearlite particles. The enhanced properties of C-Mn steels can be attributed to a fine ferrite grain size, solid solution strengthening from the carbon and manganese additions and dispersion strengthening from the pearlite particles. Carbon Manganese steels typically exhibit tensile strengths of up to $450N/mm^2$, with the exact strength depending on the degree of ferrite grain refinement and the volume fraction and interlamellar spacing of the pearlite phase[18].

Further strength increases can be achieved by altering the morphology of the second phase constituent from pearlite to a harder transformation product of austenite such as martensite. The properties of such steels and the processing routes necessary for their production are discussed in the following section.

2.3 Advanced high strength steels (AHSS) for automotive applications

One of the most important advances in the world of automotive materials has been the development of advanced multiphase steels. Grades such as dual phase and TRIP exhibit higher strength/ductility ratios compared to conventional high strength steels which tend to suffer a loss of formability with increasing strength. Carefully controlled processing routes introduce dispersions of harder non-equilibrium phases into a comparatively soft ferritic matrix. The interaction between these various phases during subsequent deformation gives these grades their unique properties.

2.3.1 Dual phase steels

The microstructure of dual phase steels is comprised of a ductile ferrite matrix containing a dispersion of hard second phase particles, typically martensite. Dual phase steels are characterised by low yield to tensile strength ratios, continuous yielding behaviour and a high rate of work hardening. The combination of high strength and good formability make dual phase steels extremely attractive to automotive manufacturers seeking to down-gauge automotive components.

Dual phase grades suitable for automotive applications are generally produced through the continuous annealing of cold-rolled strip. Figure 2.5[20] shows a typical annealing cycle for the production of a dual phase microstructure. The strip is heated into the intercritical region of the iron – iron carbide phase diagram between the A_1 and A_3 temperatures (see figure 2.1). The strip is held at this temperature for a pre-set length of time during which recrystallisation of the highly deformed ferrite-pearlite microstructure produces a two phase structure of equiaxed ferrite grains and the required volume fraction of austenite. The amount of austenite formed during this stage of the annealing cycle is dependant on both the annealing temperature and the length of time for which the strip is held at this temperature. The face centred cubic (FCC) structure of austenite permits a greater amount of carbon to dissolve within its lattice compared to ferrite which has a body centred cubic (BCC) structure. Carbon is therefore readily rejected from the ferrite grains into neighbouring austenite grains, increasing the hardenability of the austenite and facilitating its transformation to martensite on quenching. Alloying

elements such as manganese, chromium and molybdenum are also added to increase hardenability. A schematic diagram of a typical dual phase microstructure can be seen in figure 2.6.

It has been shown that the strength of Dual Phase steels is linearly proportional to the volume fraction of martensite present in the ferrite matrix[28]. The low yield point of dual phase steels has been attributed to the generation of new mobile dislocations in the ferrite matrix as a result of the volume change associated with the transformation of austenite to martensite. As the steel deforms plastically, interactions between the increased number of dislocations and the finely dispersed martensite particles gives rise to a high strain-hardening rate.

2.3.2 Transformation induced plasticity steels

Transformation induced plasticity (TRIP) steels offer automotive manufacturers even greater formability and enhanced work hardening characteristics than dual phase grades of equivalent tensile strength. These properties are derived from their multi-phase ferrite/bainite/austenite microstructures, with the austenite phase persisting at ambient temperatures in a metastable state. The final microstructure may also contain a small volume fraction of martensite depending on the processing route. Generally, TRIP steels contain approximately 70% ferrite to ensure sufficient ductility. As with dual phase steels, TRIP steels exhibit a comparatively low yield stress. However as the steel undergoes plastic deformation, the retained austenite progressively transforms to martensite with increasing strain, generating new mobile dislocations within the ferrite. This allows TRIP steels to maintain a constant high strain hardening coefficient (n) even at high strain levels compared to dual phase steels where the strain hardening coefficient progressively diminishes with increasing strain, delaying the onset of necking. The additional forming capability of TRIP steels over dual phase steels affords the automotive engineer even more freedom in part design allowing optimisation of the structural performance of automobile components.

TRIP grades used in automotive applications are generally produced through the continuous annealing of cold-rolled strip. Figure 2.7[20] shows a typical annealing cycle for the production of a TRIP microstructure. As with the dual phase grades, the strip is initially heated into the intercritical region of the iron – iron carbide phase diagram between the A_1 and A_3 temperatures and held at a constant temperature for a predetermined length of time. Recrystallisation of the highly deformed ferrite-pearlite microstructure produces a two phase structure of equiaxed ferrite grains and the required volume fraction of austenite. The volume fraction of austenite aimed for in this stage is generally greater than that developed during the production of dual phase steels. In order for a quantity of austenite to persist in the final microstructure on cooling, the M_s of the austenite must be lowered below ambient temperatures. As described previously, during the intercritical annealing stage carbon is rejected from the ferrite into the austenite thereby lowering the M_s. However, this is not sufficient to suppress the M_s to temperatures below ambient and further carbon enrichment of the austenite is required to ensure its stability at ambient temperatures. This is achieved by holding the strip at the austempering temperature which is typically around 400°C. The cooling rate from the intercritical region must be high enough to suppress the transformation of the austenite to pearlite. At the austempering temperature, bainitic ferrite will begin to nucleate at the austenite grain boundaries and grow into the austenite grains. As the bainitic ferrite plates grow, carbon is rejected into the remaining austenite further lowering the M_s. Silicon and/or aluminium and phosphorus are added to TRIP steels to inhibit the precipitation of carbides between the bainitic ferrite laths, thereby maintaining the carbon in solution in the austenite phase. Manganese additions also have a stabilising effect on austenite.

The strip is held at the austempering temperature until the remaining austenite has become sufficiently enriched in carbon to suppress M_s to below ambient temperatures, upon which the strip is quenched producing a final microstructure of pro-eutectoid ferrite, bainitic ferrite and retained austenite. In practice, the final microstructure often contains a small volume fraction of martensite depending on the austempering temperature and hold time. A schematic diagram of a typical TRIP microstructure can be seen in figure

2.8. The volume fraction and distribution of the various phases in the TRIP microstructure strongly influences mechanical properties.

2.3.3 Complex phase steels

Complex phase steels consist of a very fine ferrite matrix containing a comparatively large volume fraction of hard second phase particles such as bainite or martensite, combined with a dispersion of fine precipitates. Complex phase steels contain many of the alloying elements found in TRIP steels and are produced via a similar processing route. They also contain small quantities of micro-alloying elements typically found in HSLA steels such as niobium, vanadium and titanium in order to refine the ferrite grain structure and generate the fine precipitates which provide additional dispersion strengthening. Complex phase steels can exhibit tensile strengths in excess of $1000N/mm^2$ whilst retaining a high degree of formability and providing high energy absorption[31], making them ideally suited for crash columns or side pillars.

2.3.4 Martensitic steels

Martensitic steels, as the name suggests, have a microstructure composed almost entirely of martensite. Figure 2.9 shows a typical annealing cycle for the production of a fully martensitic microstructure in cold rolled strip. The strip is heated above the A_3 temperature so that the microstructure becomes fully austenitic prior to being rapidly quenched, causing the austenite to transform almost entirely to martensite. In practice a small volume fraction of austenite is usually retained in the final microstructure. The cooling rate of the fully austenitic strip must be high enough to suppress the formation higher temperature transformation products such as pearlite or bainite. The strength of fully martensitic steel is strongly dependent on its carbon content[22] with elements such as manganese, silicon and chromium also providing solid solution strengthening. Martensitic steels can exhibit extremely high tensile strengths of up to $1500N/mm^2$ and typically require some form of post-quench tempering to improve ductility and relieve residual stresses in the material resulting from the martensite transformation. Due to their extremely high strength, low ductility and tendency for elastic spring back, the use of

martensitic steels in automobile construction is generally limited to applications that do not require a high degree of formability, such as side impact beams.

2.3.5 Hot formed boron steels

Boron steels offer similar tensile strengths to conventional martensitic steels, however the utilisation of a unique processing technique allows the production of complex component shapes not normally possible with steels exhibiting such high tensile strengths. Boron steels are supplied to automotive manufactures in a hot rolled, low strength condition. The high strength levels associated with boron steels are achieved via a hot forming process in which component blanks are heated to a normalising temperature above A_3 so that the microstructure becomes fully austenitic. The blanks are press formed while hot and quenched producing a fully martensitic microstructure in the formed component. Boron and manganese additions increase the hardenability of the steel and ensure that as much austenite as possible transforms to martensite during quenching. The principal disadvantage of this process is the increased cost associated with heat treating each component prior to forming. Boron steels were used extensively in the Volvo XC90 in components such as the rear bumper and side impact beams[33].

2.4 Novel automotive joining processes

There are several joining techniques currently available to automotive manufacturers for the construction of body-in-white structures. Where traditionally resistance spot welding was almost exclusively used, the desire to incorporate modern advanced high strength steels in automobile construction and the perceived difficulties in joining these materials using resistance welding has led some manufacturers to employ techniques such as laser beam welding and laser brazing. Laser welding in particular is finding applications where manufacturers wish to exploit the improved component rigidity offered by this continuous joining technique compared to a discrete joining process such as resistance spot welding or self piercing rivets. However, resistance spot welding still remains the dominant fabrication technique and has received heavy investment by the automotive sector and is therefore unlikely to be completely replaced by alternative joining techniques in the near future.

2.4.1 Laser beam welding

Laser beam welding is finding increasing applications in automobile manufacture, from the fabrication of tailor welded blanks to body-in-white construction. Laser welding is a joining process which produces melting and coalescence of two or more sheets using thermal energy generated from the coupling of a highly focused coherent light beam with the workpiece. Laser welding is generally an autogenous process i.e. no filler metal is added to the molten weld pool.

The focal spot is targeted on the joint surface, where the intense concentration of light energy is partially converted into thermal energy. The heat generation at the surface is so intense that a volume of the parent material is vaporised forming a 'keyhole' filled with metal vapour. The vapour absorbs the laser energy and conducts it to the sides of the keyhole, thus producing complete penetration with minimal melting of the parent material. In order to prevent the laser energy being absorbed above the metal surface by the ionised metal vapour emerging from the keyhole and also to prevent oxidation of the molten weld metal, a gas of low ionisation potential such as Helium or Argon is used to disperse the plasma above the sheet surface and shield the weld pool. Since the molten

weld bead is narrow and therefore of correspondingly low volume there is a minimal reservoir of heat energy that can be conducted into the surrounding material.

Overlap laser welding is most commonly used in the assembly of body-in-white structures. Unlike spot welding, which joins the parent materials at discreet locations, laser welding produces a continuous joint. Laser welded structures therefore benefit from improved fatigue resistance and increased torsional rigidity and stiffness. Another significant advantage of laser welding is the increased joint flexibility that it allows due to the fact that it is a non-contact process and only requires single sided access. However, due to the absence of the clamping effect offered by the welding electrodes, accurate jigging is required to obtain satisfactory part fit-up prior to laser welding.

Tailor welded blanks offer the automobile design engineer the ability to reduce the weight of the body-in-white structure by optimising the use of steel. Tailored blanks are composed of two or more sections of steel sheet with differing properties such as thickness, strength or coating type. These sections are laser butt welded together prior to stamping. This allows particular steel grades to be placed within a component precisely where their attributes are needed most. For example, in a part such as an inner door skin, thicker steel must be used in the region of the hinges due to the greater forces experienced at this location. Traditionally, this heavier gauge would have to be carried through the entire component. By utilising tailor welded blank technology, the remainder of the structure can be fabricated out of thinner strip thus reducing the overall weight of the component without compromising mechanical performance. The more efficient use of material through part consolidation also leads to a reduction in costs.

The principal concern for automotive manufacturers is the significant capital investment that a move towards laser processing would require. Laser welding equipment is currently expensive and the associated running costs and power requirements are also high. However, the specific advantages of laser welding are leading to an increase in its use within the automotive sector. Companies such as Volvo and BMW have been using laser welding for several years while others such as Nissan, Toyota and GM have begun

to utilise it as well. Volkswagen have invested heavily in laser welding equipment and this is reflected in the latest fifth-generation Golf which contains approximately 70 meters of laser welds[36].

2.4.2 Laser brazing

Brazing involves the joining of a metallic substrate with a suitable filler metal. The melting temperature of the filler metal is significantly lower than that of the components being joined which remain un-melted throughout the brazing process. The filler metal is melted in a closely fitting joint between the component parts and fills the joint by capillary action. In laser brazing, the energy required to heat the joint and melt the filler metal is supplied by a defocused laser beam. Copper and silver based alloys are used extensively for joining steel.

In automotive applications, the filler metal is generally introduced into the joint in wire form. Adequate atmospheric protection of the molten filler metal is essential as well as measures to ensure the joint is free from contaminants. Typical shielding gasses include argon and mixtures of hydrogen and nitrogen gas, which both prevent oxidation of the molten filler metal and enhance wetting of the components.

Laser brazing offers superior component fit up tolerance compared to laser welding, making it an attractive process for automobile production. The principal advantage offered by laser brazing over conventional welding processes when joining advanced high strength steels is the vastly reduced heat input into the parent material. Therefore the mechanical properties of the parent material remain largely unaltered by this process. The lower heat input also reduces problems associated with warping and distortion of formed components, which is an important consideration when joining thinner gauge materials. Laser brazing can also be readily applied to zinc alloy coated steels. During the laser brazing process, the zinc alloy coating enhances surface wetting of the components facilitating penetration of the filler metal into the joint thus increasing joint strength. The aesthetic appearance of laser brazed joints is generally very good and this therefore makes it suitable for exterior applications where good finish is essential. For

example, the exterior roof skin of the Audi TT sports coupe is attached to the rear quarter panel using laser brazing[35]. Volkswagen use laser brazing to attach the roof to body sides, the drain channel in the boot lid opening and the split skin panel of the boot lid of the fifth-generation Golf[36].

2.5 Resistance spot welding

Resistance spot welding is one of the oldest joining processes used in automobile manufacture and is still the predominant joining technique used today, with an average car containing approximately 4000 spot welds[44]. The principal advantages of resistance spot welding are the ease with which the process can be automated and the high production rates that can be achieved. Resistance spot welding is therefore ideally suited to high volume production environments such as automobile assembly lines. As a result automotive manufacturers have invested heavily in resistance spot welding equipment and therefore any potential automotive steel grade must be readily weldable using this process. For high strength grades, this may require modifications to established welding practices in order to achieve satisfactory weld formation and performance. However, with modern automotive production lines producing around 7 million spot welds per day[48], it is desirable that any modifications to weld schedules do not greatly increase the total time required for the formation of individual spot welds as this could significantly affect productivity.

2.5.1 The spot welding process

Resistance spot welding is a joining process in which faying surfaces of two or more sheets of a metallic material are melted and fused at a series of discreet points. The sheets are clamped together by a pair of electrodes which pass low voltage, high amperage current through the workpiece. Sufficient heat is generated by the weld current flowing against the resistance of the material between the electrodes that localised melting begins to occur at the point of greatest resistance i.e. at the sheet to sheet interface. The molten weld pool continues to grow until the current flow is terminated upon which the weld 'nugget' rapidly solidifies. The resistance spot welding process is represented schematically in figure 2.10. The amount of heat generated in the workpiece is dependant on the magnitude of the weld current, the length of time for which the current flows and the total resistance between the welding electrodes. This relationship is known as Joule's law, which in its simplest terms can be expressed by the equation shown overleaf:

$$H = K I^2 R t$$

Where:

H = heat energy (J)

K = constant

I = current (A),

R = resistance (Ω)

t = time (s)

The fact that the amount of heat generated is proportional to the square of the current means that a relatively small increase in weld current can lead to a large increase in the amount of material melted and the size of the resulting weld nugget. The traditional sequence of events that lead to the formation of a single spot weld is comprised of three main stages:

- **Squeeze**

The welding electrodes are closed on the sheets to be joined and apply a force of several kN. The use of a high electrode force provides good electrical contact between the sheets and the electrodes and ensures good part fit-up and joint accuracy. The squeeze time must be sufficient to allow the force applied by the electrodes to reach the pre-set level before current flow commences.

- **Weld**

Current is passed through the workpiece causing extremely localised heating at the sheet to sheet interface and in the bulk material which in turn leads to the formation of a molten weld nugget as described above. The size of the weld nugget and the rate at which it develops is determined by the rate of heat generation in the workpiece versus the rate of heat extraction into the water cooled electrodes and the bulk material. The length of time for which the current is applied should be sufficient for the weld nugget to grow to the required diameter. High weld currents and short weld times are frequently used in high

volume production environments such as automotive assembly lines to maximise productivity. However the time required for the development of a particular weld size can only be reduced to a certain extent by increasing the weld current. Beyond a certain current threshold, rapid and unstable growth of the weld pool can lead to expulsion of molten metal from the joint. This is known as 'splash' and should be avoided since the loss of material from the weld nugget leads to excessive electrode indentation and a corresponding deterioration in mechanical performance. As well as initially providing good electrical contact between the sheets, the pressure exerted by the electrodes helps to contain the molten nugget as it grows.

- **Hold**

The electrode force is maintained for a pre-set length of time after the termination of the weld current. Heat is rapidly drawn from the weld region into the water cooled electrodes thus ensuring rapid solidification and consolidation of the weld nugget before the electrodes are withdrawn. The length of time the water cooled electrodes are held in contact with the sheet can therefore greatly influence the cooling rate of the weld region. If the electrodes are withdrawn prematurely, elastic springback of the sheets can lead to the formation of voids in any regions of the weld nugget which have not yet completely solidified.

The duration of each stage is generally quoted in cycles, with one cycle being equal to 0.02 seconds for a 50Hz AC power supply. Depending on the steel being welded, the duration of each step can be altered along with other welding parameters such as weld current and electrode force in order to achieve satisfactory nugget formation and weld properties.

Figure 2.11 shows a schematic diagram of a section through a typical resistance spot weld. The weld nugget, heat affected zone and the notch at the periphery of the weld can be seen.

2.5.2 The resistance welding of advanced high strength steels – defining the problem

In order to maximise vehicle occupant safety in the event of a collision, there is an increasing demand for materials with high energy absorbing characteristics. For this reason, multiphase steels such as dual phase and TRIP are likely to become the materials of choice for the manufacture of vehicle impact structures. In terms of light-weighting, the principal advantage of utilising steels with enhanced strength and energy absorbing characteristics is that thinner gauge material can be used to fabricate vehicle components whilst maintaining a high level of crash performance.

Williams[52] considered that in order for any potential automotive grade to be considered interchangeable with existing products, it must satisfy the following requirements:

1. The new grade must be capable of being welded with existing equipment.

2. The static and dynamic properties of the welds must be at least equal to or better than those of welds in the steel being replaced.

3. It should be possible to test and assess welds using simple shop floor testing techniques.

The various weld failure modes resulting from destructive testing are shown in figure 2.12. Conventional high strength grades such as HSLA and HSIF steels have traditionally proved extremely weldable[73, 79, 85] due to their low alloy content and correspondingly low hardenability, leading to their widespread use in the automotive industry. However concerns over the performance of welds formed in advanced high strength steels are leading to reluctance on the part of automotive manufacturers in utilising these grades. Volvo for example have been unable to produce plug failures in their evaluation of TRIP steels and have therefore left them out of their materials catalogue for vehicle design[98,117].

A number of studies have been conducted in recent years into the resistance weldability of advanced high strength steels. A selection of the most relevant studies will now be discussed.

Ellwood[89] investigated the weldability of a 2.9mm TRIP grade with a tensile strength of 739N/mm^2. This grade contained 0.2% carbon, 1.45% manganese and 1.45% silicon in order to retain a volume fraction of austenite in the final microstructure. This resulted in a carbon equivalent of 0.47. Whist the weldability range of this grade was found to be acceptable the failure mode of the welds was considered to be brittle in nature and therefore unacceptable. Microhardness levels within the weld nugget were approximately 500HV. Welds formed in this grade also failed to meet the minimum shear strength requirements laid out in BS1140. It was concluded that the principal reason for the poor performance of welds formed in this grade was due to the excessively high carbon equivalent of the steel leading to the formation of hard and brittle welds.

Smith[91] investigated the weldability of a range of experimental dual phase and TRIP grades with nominal tensile strengths in the range of 700-800N/mm^2. It was discovered that the dual phase grades studied exhibited adequate weldability ranges in the order of 1kA. The cross tension failure mode was highlighted as a critical acceptance criterion for the automotive industry, with the dual phase grades failing in a ductile manner in the parent material. In contrast the growth curves of the TRIP grades exhibited a degree of instability with low current weld splash and wide scatter in weld diameters. None of the TRIP grades exhibited the required ductile failure mode on cross tension testing. Both the TRIP700 and TRIP800 grades exhibited either interfacial failure or small partial plugs. The poor performance of the TRIP steels studied was attributed to the high carbon and phosphorus contents of these grades, with phosphorus in particular leading to weakening of the interdendritic boundaries within the welds. Weld hardness levels were in excess of 500HV in each case.

In an earlier report[86], Smith also examined the weldability of a 1.8mm DP600 grade and a 2.0mm DP800 grade. It was discovered that where high electrode forces were used,

extremely good weldability ranges and plug sizes were achieved in both DP800 and DP600, however full plug failures only occurred at the top end of the weldability range i.e. at currents just below splash. At lower current levels failure modes consisted of interface and partial plug. The average shear strengths of the welds formed in the dual phase grades did not meet the minimum requirements laid out in BS1140, however it was considered that since the standard was not written with dual phase steels in mind, the minimum shear strengths should be used for guidance only. Weld hardness levels exceeding 400HV were recorded in weld nuggets formed in both grades which was suggested to indicate the presence of martensite, although no detailed metallographic information was presented.

Comparatively little work could be found on the resistance welding of steels with tensile strengths in excess of 800N/mm^2. However a study conducted by Shi and Westgate[96] sought to directly compare the weldability of a range of advanced high strength steels including dual phase, TRIP, complex phase and martensitic grades with tensile strengths ranging from 600-1200N/mm^2 and sheet thicknesses ranging from 0.8-2.0mm. It was discovered that acceptable weldability ranges could be achieved for all of the grades under investigation where the fused zone of the welds were measured, however the tendency of weld formed in the thicker grades to fail as partial plugs meant the weldability ranges based on plug diameter were comparatively small for these grades. Significant weld hardening was observed in the grades with tensile strengths up to 1000N/mm^2 with the TRIP steel exhibiting weld hardness levels of up to 580HV.

It can be seen from these studies that while the weldability of advanced high strength steels in terms of the current range over which acceptable weld diameters can be achieved is often acceptable, the principal concern from the point of view of automotive manufacturers is the tendency of welds formed in these grades to exhibit high hardness levels and fail in an interfacial manner when subjected to basic shop floor quality tests such as peel and chisel tests. This poor performance is generally attributed to the presence of martensite in the weld nuggets and heat affected zones, and appears to be a particular problem where TRIP steels are concerned. As described in the preceding

section, the chisel test remains firmly entrenched in plant practice due primarily to its simplicity and therefore the ability to pull full plug failures on chisel testing is likely to remain as one of the acceptance criteria for potential automotive grades in the immediate future. In addition, the general consensus within the automotive industry is that welds with hardness levels exceeding 450HV are considered likely to fail in a brittle manner in the event of an impact, potentially limiting the amount of energy absorbed by crash structures. Weld hardness levels exceeding 500HV, as was observed for several of the grades in the above studies, are unlikely to be acceptable to automotive manufacturers.

2.5.3 Enhancing the weldability of advanced high strength steels through the use of tailored welding parameters

Various studies have been conducted in recent years into the potential of tailored welding schedules for controlling the final properties of resistance welds formed in advanced high strength steels. The techniques employed in these studies can be grouped into two categories; those which aim to reduce the cooling rate of the weld region and thereby suppress or limit the martensite transformation and those designed to modify the properties of welds once they have fully hardened.

As described in section 2.1.2, in order for the martensite transformation to occur in a normalised weld, the austenite must be cooled below the martensite start temperature (M_s) at a rate sufficient to suppress diffusion controlled transformations. A reduction of the cooling rate of the weld region prior to reaching the martensite start temperature could potentially allow the formation of a volume fraction of higher temperature transformation products such as bainite or acicular ferrite. These microstructures typically exhibit significantly lower hardness than martensite and their presence in the weldment could potentially lead to improved mechanical properties. The cooling rate of the weld region can be reduced by passing additional current pulses through the workpiece after the weld has formed. However several authors[73, 89, 97] have commented that in order to reduce the cooling rate of the weld region sufficiently after weld formation to suppress the martensite transformation, a cooling time of several seconds

would be necessary, thus making the controlled cooling technique unsuitable for high volume production.

An alternative method for modifying the properties of resistance spot welds formed in advanced high strength steels is in-process tempering. As discussed previously, in its as-formed condition, martensite is typically very brittle. However it is possible to enhance the toughness of martensite by heating to a temperature in the range 150-700°C. Martensite is essentially a supersaturated solid solution of carbon in iron which, on heating, will readily reject carbon in the form of finely divided carbide phases. The loss of carbon from solid solution causes a reduction in the tetragonality of the martensite with a corresponding reduction in hardness. In resistance welding, this heating can be achieved via the introduction of a secondary current pulse into the welding schedule once the weld nugget has fully hardened, however the degree to which tempering can occur is likely to be limited by the extremely short cycle times associated with resistance welding.

A selection of the most relevant studies into the modification of weld properties through the use of tailored welding parameters will now be discussed.

Cretteur and Koruk[100] investigated the use of pre-heating and controlled cooling to enhance the cross tension strength of spot welds formed in a cold rolled, hot dip galvanised TRIP700 grade. Three parameters were investigated for the preheating phase; current, time and transition slope between pre-heat current and the welding current. Two weld times were tested; 250ms and 400ms, at currents sufficient to produce weld sizes in the range 6-7 mm. Several post heat times were investigated along with the influence of the transition slope between the welding current and post-heat current. It was discovered that in the pre-heating phase, the most important parameter was the up slope. It was also discovered that longer weld times with a lower current are favourable to short weld times and high current, and that the post heat current must be as high as possible without causing re-melting of the weld nugget. The optimal weld cycle was defined as three phases of 400 ms separated by transition slopes of 120 ms. For pre-heating, a current level of approximately 40-45% of the weld current was applied whereas for post heating,

a current just below the fusion limit was used (approximately 80% of the welding current). The hold time used was kept as short as possible in order to prevent excessive heat extraction through the welding electrodes and maintain the heat in the weld area. The optimised welding schedule produced an increase of 20-25% in cross tension strength over the basic single-pulse schedule, however no appreciable reduction in weld hardness was observed suggesting that the improvements in weld properties were due to geometrical factors i.e. blunting of the weld notch.

Simmie and Hipperson[99] saw the potential of post-weld tempering treatments for improving the properties of high strength steel welds as far back as 1944. Whilst the grades studied did not share the multiphase microstructures of modern advanced high strength steels, the chemical compositions were similar making the results of this study relevant to the present investigation. The authors sought to investigate the effect of the pause time between the welding and tempering pulses and the duration of the tempering pulse itself. The tempering current was held constant once the optimum level had been established. The tests used to establish the effect of the various tempering schedules employed included lap shear tests and 'U' tension tests. Significant reductions in weld hardness were observed for all of the high strength steels investigated, combined with improvements in lap shear and 'U' tension strength. Perhaps the most significant conclusion of this paper was that a minimum pause time was required between the primary welding pulse and the secondary tempering pulse in order to obtain appreciable reductions in weld hardness. It was suggested that the pause was necessary to allow the weld region to fully harden, however it was recognised that tempering should begin as soon as possible after this had occurred.

Anderson[112] investigated a variety of techniques for reducing the hardness of resistance welds formed in a 2.0mm DP800 grade including pulsing of the weld current, controlled cooling and post weld tempering. The unique feature of this study was that thermocouples were used in order to establish the effect of the various welding schedules on the cooling rate of the weld nuggets. Whilst the pulsed weld current and controlled cooling schedules both led to measured reductions in the cooling rate of the weld nugget

and heat affected zones, the reductions in weld hardness were limited suggesting that the cooling rate of the weld region had not been reduced sufficiently to inhibit the formation of martensite. The introduction of a post weld tempering pulse yielded slightly greater reductions in weld hardness. A single 2 cycle tempering pulse applied after a pause of 99 cycles resulted in a 7% decrease in average weld microhardness compared to a weld which had received no heat treatment. Unfortunately no detailed information was supplied on the effect of the selected schedules on weld microstructures or weld strength.

Smith[98] investigated the effect of controlled cooling and post weld heat treatment on the mechanical properties of a 1.0mm DP1000 grade. The controlled cooling pulse was performed at a current level approximately 50% of the primary welding current. This current is insufficient to cause further melting and therefore solidification begins. The controlled cooling schedule did not offer any appreciable reduction in weld hardness or increase in cross tension strength, however improvements in lap shear strength over the single pulse schedule were observed. The post weld heat treatment schedule yielded even greater improvements in lap shear strength of welds formed in DP1000 than the controlled cooling schedule. A 100% increase in lap shear strength was achieved compared to welds which had received no heat treatment. However as with the controlled cooling schedule, the cross tension strength was not greatly affected as a result of the post weld heat treatment.

Shi and Westgate[97] conducted a study into the effect of controlled cooling and in-process tempering on the hardness and static properties of resistance welds formed in 1.05mm TRIP700. The grade selected had a comparatively high carbon content of 0.31wt% along with 1.54wt% manganese and 0.29wt% silicon. This high alloy content lead to weld hardness levels of up to 600HV where basic single pulse schedules were used. The welds exhibited interfacial and partial plug failures in peel tests and low cross tension strength levels.

It was discovered that the cross tension and shear strength of welds could be improved by up to 30% with the introduction of pre-heating and controlled cooling, however little

reduction in weld hardness was observed. It was suggested that the increase in strength was due to an observed increase in weld size of approximately 10%. While there was an improvement in plug sizes where controlled cooling was used, full plug failures could not be achieved on peel testing. The absence of a significant reduction in weld hardness was explained with reference to the time-temperature-transformation (TTT) diagram for the TRIP700 grade which showed the incubation time for the bainite nose was longer than one minute. Therefore despite an increase in the weld cycle time of up to 40 cycles, the cooling curve of the resistance weld passes to the left of the bainite nose and no transformation of the austenite can occur before the martensite is formed.

The effect of in-process tempering was also studied. Weld hardness was significantly reduced from approximately 600HV to 400 HV whilst the cross tension strength was increased by up to a factor of four. The shear strength was also improved by approximately 25-30%. The weld failure mode on peel testing was transformed from brittle interface failures to full plug failures. However it was noted that the use of suitable parameters was critical in achieving the optimum results in terms of weld strength and fracture mode. For example, it was discovered that a minimum cool time of 20 cycles was necessary to allow the full transformation of austenite to martensite prior to the commencement of tempering. Below this critical cool time the weld fracture mode and weld hardness were similar to that of welds produced using the single pulse schedule.

It is clear from these studies that there is significant potential for the enhancement of weld properties through the utilisation of tailored welding parameters incorporating either controlled cooling or post-weld tempering. However little evidence could be found within the literature as to the exact mechanism by which these advanced weld schedules enhance the mechanical properties of welds formed in advanced high strength steels. A detailed examination of the influence of advanced weld schedules on the microstructural features of advanced high strength steel welds would therefore be beneficial.

3. AIMS OF STUDY

Based on the findings of the literature review, the specific objectives of this research programme were defined as follows:

1) Develop an understanding of the microstructural and mechanical properties of resistance spot welds formed in a range of advanced high strength steels using basic single pulse welding schedules typical of those currently used in an automobile production in comparison to low-alloy grades. Factors to be investigated should include:

   a) Weldability and weld failure mode

   b) Microhardness of weld nuggets and heat affected zones in comparison to the bulk parent material

   c) Microstructural characteristics of parent material, weld nugget and heat affected zones

   d) Lap shear and cross tension strength

2) Investigate the effects of basic modifications to welding parameters on the weldability and weld performance of any high strength grades that do not exhibit satisfactory performance when standard welding practices are used. Parameters that should be considered include:

   a) The effect of electrode force

   b) The effect of electrode tip diameter

   These parameters can be altered without lengthening the welding sequence and should be investigated before more complicated schedules are considered.

3) Investigate methods for modifying the final properties of resistance spot welds formed in AHSS grades using tailored weld parameters focusing on in-process tempering.

4) Investigate the effect of alloying between dissimilar steel combinations on the physical and mechanical properties of welds focusing on the joining of advanced high strength steel to grades with significantly lower alloy contents.

In summary, this study is intended to generate a deeper understanding of the complex relationships that exist between the physical and microstructural properties of welds and mechanical performance, thus facilitating the optimisation of the resistance spot welding process when applied to steel grades with specific mechanical properties derived from close control of alloy chemistry and microstructural constituents.

4. EXPERIMENTAL PROCEDURES

The following chapter describes the materials selected and the experimental techniques used during the course of this investigation.

4.1 Materials

A total of 6 advanced high strength steel grades were obtained from SSAB Tunnplåt and Sumitomo Metal Industries Ltd. These comprised three dual phase grades (DP600, DP800 and DP1000) and a martensitic grade (MS1400) from SSAB and two transformation induced plasticity grades (TRIP600 and TRIP800) from Sumitomo. In the preceding designations the prefix indicates the metallurgical properties of the grade and the numerical suffix indicates the nominal tensile strength of the grade in N/mm^2. A low carbon formable mild steel (LC) and a high strength interstitial free grade (IF260) were also obtained from Corus Strip Products to act as a reference for the high strength grades. The Corus grades are typical, both in terms of alloy content and mechanical properties, of those traditionally used in body-in-white construction. Unlike the high strength steels where the numerical suffix indicates the nominal tensile strength, with lower strength grades such as IF, the numerical suffix indicates the nominal yield stress of the material. The sheet thicknesses of the selected grades were as follows:

- LC - 1.15mm
- IF260 - 1.2mm
- TRIP600 - 1.0mm
- DP600 - 1.2mm
- TRIP800 - 1.2mm
- DP800 - 1.2mm
- DP1000 - 1.2mm
- MS1400 - 1.0mm

The variation in sheet thickness was kept as low as possible to limit its influence on the cooling conditions of the weld nuggets and also the effect of geometrical factors on mechanical performance.

The chemical composition of the selected grades was determined with the assistance of the BOS plant laboratory in the Corus Port Talbot Steelworks. The selection of these particular steel grades allowed the effect of increasing alloy content on the physical and mechanical properties of spot welds to be investigated. The Carbon Equivalent (CE) of the eight materials selected was calculated using the Ito-Bessyo equation[42];

$$CE = C + \frac{Si}{30} + \frac{(Mn + Cu + Cr)}{20} + \frac{Ni}{60} + \frac{Mo}{15} + \frac{V}{10} + 5B$$

and ranged from 0.045 to 0.307. The chemical compositions and carbon equivalents of the selected grades are detailed in table 4.1.

The LC grade had a carbon content of 0.03wt% and contained no specific alloying additions, therefore the carbon equivalent of this grade was 0.045. IF260 had a carbon content of just 0.0029wt%. As described in the literature review this ultra low carbon content is achieved via a combination of vacuum de-gassing and the addition of strong carbide forming elements such as niobium, vanadium and titanium. It can be seen from table 4.1 that this grade contains 0.0084wt% vanadium and 0.0647wt% titanium along with 1.008wt% manganese, 0.0532wt% phosphorus and 0.0007wt% boron which are added to provide solid solution strengthening. Therefore despite the extremely low carbon content the addition of specific alloying elements results in a carbon equivalent of 0.06.

It can be seen that the primary alloying elements added to the dual phase grades were carbon and manganese. The carbon contents ranged from 0.102wt% in DP600 to 0.143wt% in DP1000. The manganese contents ranged from 1.509wt% in DP800 to 1.538wt% in DP1000. The dual phase grades also contained additions of silicon ranging from 0.198wt% in DP600 to 0.55wt% in DP1000. MS1400 had a similar C-Mn-Si composition to the dual phase grades and contained 0.162wt% carbon, 1.63wt% manganese and 0.522wt% silicon.

As described in the literature review, the TRIP grades make use of austenite stabilisers such as carbon and manganese along with elements which suppress cementite precipitation such as silicon and aluminium to retain a volume fraction of austenite in the final microstructure. It can be seen that TRIP600 contains 0.083wt% carbon, 1.44wt% manganese, 1.35wt% silicon and 0.139wt% aluminium while TRIP800 contains 0.181wt% carbon, 1.33wt% manganese, 1.67wt% silicon and 0.137wt% aluminium.

The tensile properties of the selected steel grades were measured using a Zwick 1474 tensile testing machine and a 100kN load cell calibrated to UKAS standards. Testing was carried out in accordance with BS EN 10002-1:2001 using samples with an 80mm gauge length and overall dimensions of 20mm x 120mm. The crosshead speed used up to the 0.2% proof stress was 2.5mm/min and 50mm/min after this point. Four samples were tested for each grade, two parallel to the rolling direction of the sheet and two perpendicular to the rolling direction. The averages of the four tests carried out for each grade are presented in table 4.2. The tensile strengths (R_m) of the selected grades ranged from 313N/mm^2 to 1479N/mm^2 whilst the yield stresses (R_P) ranged from 209N/mm^2 to 1446N/mm^2 representing a wide range of material properties that could potentially be utilised in body-in-white applications.

4.2 Manufacture of welded samples

4.2.1 Welding equipment

All welding work undertaken during this investigation was carried out on an A-I A35036 spot welding machine which had a transformer rating of 50 kV·A. A photograph of this machine is shown in figure 4.1. The welder was connected to a 400v 50Hz alternating current (AC) power supply. The welding sequence was controlled with a British Federal Weldstar 2000 control system. This machine exhibits a typical pedestal configuration, with the lower electrode being fixed and the upper electrode driven vertically downwards by a pneumatic actuator. 16mm truncated cone Copper/Chromium/Zirconium electrodes were used for all welding trials. The diameter of the tips initially used was 5mm as specified in BS 1140:1993[41] for sheet thicknesses ranging from 1.0mm to 1.2mm. The electrode force was generated by an external compressed air supply and could be varied by altering the air pressure supplied to the actuator. The air pressure was adjusted with an inline Schrader valve with the maximum air pressure producing an electrode force of 6.5kN. The Weldstar controller triggers the pneumatic actuator via an electronic solenoid which allows the air supply to pressurise the actuator. Electrode force was measured with the aid of a Maltron 90061 force probe. The probe calculates the maximum force exerted by the electrodes via a load cell placed between the electrodes. The electrode force was set initially at 3.2kN prior to the commencement of welding and was checked frequently during the course of the welding trials to ensure that it had not deviated from the desired setting. This electrode force was chosen in accordance with BS1140:1993[41] which states that for high force, short time conditions, electrode force should be set to between 2.5 and 3.2kN for sheet thicknesses of 1.0mm to 1.2mm. Since high strength steels were being welded, the higher electrode force was used. The welding electrodes and transformer pack were cooled by a high pressure chilled water supply, the flow rate of which was set at 4 litres per minute. The welding sequence was programmed via a push-button keypad and digital display which was connected to the Weldstar control unit. The individual stages of the welding sequence (squeeze, weld, hold etc.) were measured in cycles, with 1 cycle equalling 0.02 seconds for a 50 Hz alternating current (AC) power supply. Each stage in the welding sequence could be programmed to last between 1 to 99 cycles (0.02 to 1.98 seconds). Alternatively a particular stage could be bypassed by

entering a value of 0. The secondary weld current level was controlled via two mechanisms. Coarse adjustments were made via the tap switches on the body of the welder. The tap settings determine the number of windings in the primary coil of the welding transformer and therefore the magnitude of the voltage and current in the secondary coil. The AI resistance welder used had 10 individual tap settings ranging from Low 5 to High 1. Fine adjustments in weld current were made by altering the phase shift between the voltage and current waveforms. The programmed weld sequence was initiated by a remote foot switch attached to the Weldstar controller. This allowed the operator to maintain a safe distance from the welding apparatus during the welding operation.

A Miyachi MM-315A current meter was used to determine the magnitude of the weld current passing through the work piece at a particular weld setting. The meter calculates the secondary root mean squared (RMS) current using a flexible toroid placed around the lower electrode, and displays the weld current in kA on a digital display upon cessation of the weld pulse. It was possible to measure several weld pulses with this current meter, provided that the pulses were discrete i.e. separated by a distinct pause in current flow. However due to the lack of a data logging facility it was necessary to monitor the current meter display throughout the welding operation in order to record the initial welding pulses. If the pauses or the individual current pulses are short in duration, accurate recording of the current pulses becomes difficult. The magnitude of the final current pulse remains on the display upon completion of the weld sequence.

Before any practical welding work could be conducted using new electrode tips, it was necessary to ensure that tips were properly aligned and conditioned by performing approximately fifty preliminary welds. When the electrodes are closed the interface between them must be as close to parallel as possible. Improperly aligned electrodes can lead to irregular indentation of the sheet surface and non-uniform heat generation in the weld region. Initial welds were examined to ensure uniform electrode indentation on both sheet surfaces and also that the oxidation of the sheet surface around the electrode indent was uniform. This process was repeated whenever it was necessary to replace the

electrode tips due to excessive deformation or growth. Figure 4.2 shows the surface appearance of a spot weld produced with electrodes that are not properly aligned. It can be seen that the indentation into the sheet is significantly deeper on one side and also that the surface oxidation is displaced to the region of greatest indentation. This indicates that heat generation in workpiece was not uniform. Figure 4.3 shows the surface appearance of a spot weld produced with electrodes that are properly aligned. It can be seen that the depth of indentation into the sheet surface is roughly equal around the diameter of the indent and that the surface oxidation of the sheet forms a circular 'halo' around the indent indicating uniform heat generation in the weld region.

4.2.2 Weld sample configurations

Three sample configurations were used during the course of this investigation. These are detailed in the following section as well as the methods used to fabricate them. The surface of the sheets was cleaned by dry wiping prior to welding to remove any solid contaminants.

Generating weld growth data

Welds were initially formed between pairs of coupons measuring 50mm x 50mm as specified in BS1140:1993[41], using a simple single-pulse welding schedule. The squeeze time, weld time, hold time and electrode force were kept constant during the production of each growth curve, whilst the weld current was gradually increased. For each steel grade, a series of welds were made at low current settings in order to determine the minimum weld current necessary to initiate fusion between the two coupons of a given steel grade. The weld current was then steadily increased by increasing the phase shift until a current level was reached where molten metal was consistently ejected from the weld nugget. This current level represents the 'splash limit' of that particular grade. The collection of spot welded coupons produced for each of the eight steel grades under investigation were subsequently forced apart using a tapered chisel causing the spot weld to fail. The chisel used had a notch machined into the cutting face to allow force to be applied either side of the spot weld and not directly to the weld itself. The diameter of the failed weld nugget was measured in accordance with the guidelines laid out in

BS1440:1993[41]. Knife-edged digital vernier callipers were used to measure weld diameter in two directions at 90° to each other, and the average weld diameter recorded. The failure mode of each weld was also recorded. Failure modes were defined as interface, full plug or an approximate percentage plug. The results were displayed on a plot of individual weld sizes versus the weld current necessary to form them, thus giving a visual representation of the rate of weld growth with increasing current as well as factors such as the current range over which welds of an acceptable diameter were produced. The lower limit of the current range was defined as the minimum weld current necessary to form a $3.5\sqrt{t}$ diameter weld (where t is the sheet thickness in mm). The upper limit of the current range was defined as the current level resulting in the onset of splash.

Lap shear and cross tension samples

Lap shear and cross tension samples were fabricated in accordance with the guidelines laid out in BS1140:1993[41]. The production of these samples was facilitated by a pair of jigs which allowed high accuracy and excellent repeatability between samples. Lap shear samples were fabricated from a pair of 105mm x 45mm coupons joined with a single $5\sqrt{t}$ spot weld with an overlap of 35mm giving an overall specimen length of 175mm. A typical lap shear sample is shown in figure 4.4.

Cross-tension samples were fabricated from a pair of 150mm x 50mm coupons also joined with a single $5\sqrt{t}$ spot weld formed directly at the centre point of the overlapping coupons. Four 15mm holes were drilled in each cross tension sample in order that they could be bolted into a jig which allowed the cross tension samples to be tested in the same tensile testing machine as the lap shear samples. A typical cross tension sample is shown in figure 4.5. Figure 4.6 shows a cross tension sample mounted into the testing jig.

4.3 Mechanical testing of welded components

4.3.1 Lap shear testing

A 50kN Dartec frame and a Zwick Roell K7500 digital controller were used to determine the maximum load (in kN) $5\sqrt{t}$ diameter spot welds could sustain in tensile shear. Lap shear specimens were placed into the tensile testing machine in a similar manner to standard tensile coupons. The grips were clamped onto a 40mm portion of each of the coupons, leaving an un-clamped length of 95mm as specified in BS1140:1993[41]. The samples were pulled until the weld had visibly failed and the maximum load sustained prior to failure recorded and a graph of load versus extension plotted. The manner in which the welds failed was also noted. Five lap shear samples were tested for each steel grade or combination of grades investigated in order to produce an average lap shear failure load. The crosshead speed was set at 5mm/minute.

4.3.2 Cross tension testing

As mentioned previously, it was necessary to mount the cross tension samples in a testing jig so that they could be loaded in tension normal to the direction of the sheet surface using a standard tensile testing machine. The same 50kN Dartec frame and Zwick Roell K7500 digital controller that was used to test the lap shear samples was used to test the cross tension samples with a crosshead speed of 5mm/minute. Again, five samples were tested for each condition and an average failure load calculated. Failure mode was also noted.

4.4 Material characterisation

In order to determine the effect of the resistance spot welding process on the parent metal microstructure and microhardness of the steels investigated, it was necessary to produce a series of mounted samples to allow microscopic examination and microhardness surveys to be carried out. This section details the various procedures used to prepare these samples. It was also necessary to prepare a series of interfacially failed welds for examination using the scanning electron microscope (SEM) in an attempt to establish the nature of the fracture mechanisms operating in each case.

4.4.1 Sample preparation

In order to examine interfacial fracture surfaces, weld coupons that had been chisel tested to failure were flattened out and cut into 15mm x 15mm squares incorporating the fractured spot weld. This was carried out with a Struers Discotom rotary cutting machine. This allowed the failed spot weld to be placed into the sample holder of a Jeol JSM-840 Scanning Electron Microscope (SEM) for surface analysis.

In addition to fracture analysis, the microstructure of the parent metal, weld nugget and heat affected zones (HAZ) also needed to be examined and classified. A selection of fractured and un-fractured $5\sqrt{t}$ welds were sectioned along the weld centre line using the Struers Discotom. The cut edges were sanded lightly to remove any burrs before the sectioned welds were mounted in resin. The sheets in the sample were prised apart slightly to allow good penetration of the resin into the notch at the periphery of the weld. This was intended to prevent the formation of pores which could lead to seepage in subsequent polishing operations.

4.4.2 Grinding, polishing and etching

The mounted weld cross sections were initially lightly ground on the underside and the edges rounded to remove any mould flash and limit the chance of injury in the subsequent grinding operations. The upper surface incorporating the sectioned spot weld was ground in four stages using increasingly finer grades of silicon carbide paper mounted on the rotating wheels of a pair of Struers Rotopol grinding machines. The

grades used comprised of 120 grit, 300 grit, 500 grit and 1000 grit paper. It was essential that the sample was ground completely flat and that any resin shrinkage around the mounted sample was eliminated during the first grinding stage. If any portion of the sample was unsupported by the resin it may become bevelled in subsequent grinding stages which would make it extremely difficult to resolve the sample surface using optical microscopy. The samples were rotated through 90° between each stage so that it could be easily seen when the grinding marks from the previous stage had been completely removed. The samples were then polished first with 6 micron and then 1 micron diamond suspension using a pair of Struers Labopol polishing machines. The surface of the polishing pad was lubricated with Struers DP blue alcohol based lubricant. The un-etched samples were examined under an optical microscope after polishing to 1 micron for evidence of cold cracking and porosity in the weldment and to ensure that all scratches had been removed from the surface prior to etching.

The polished samples were etched using 2% nital in order to reveal the grain structure of the parent metal, weld metal and heat affected zones. Etching times of between 5 and 10 seconds were used depending on the steel grade with each etching operation being timed using a stop watch. Samples were then re-examined under the optical microscope to ensure that they were sufficiently etched. Any samples whose microstructure had not been sufficiently revealed were re-etched for 2 seconds at a time in order that the microstructure could be clearly seen.

4.4.3 Microscopy

Three microscopes were used during the course of this investigation:

- The microstructure of the sectioned spot welds was examined using optical microscopy. A Polyvar optical microscope was used to produce macros of sectioned weld nuggets at x20 magnification and to produce micrographs of parent metal and weld microstructures at up to x500 magnification.

- A Jeol JSM-840A Scanning Electron Microscope (SEM) was used at magnifications of between x500 and x10000. It was used to examine etched welds and interfacial fracture surfaces of failed spot welds. A working distance of 15mm and an accelerating voltage set between 20k and 30k was used for all imaging. A Link ISIS energy dispersive x-ray (EDX) spectroscopy system, with a resolution of 62eV, was used to conduct point chemical analysis of precipitates observed in the etched weld cross-sections at a magnification of x10000.

- A Leica L100 optical microscope was also used to capture low magnification digital images of failed welds in lap shear and cross tension samples. A standard metric rule was used to provide a scale.

4.4.4 Microhardness testing

A Leco M-400-G2 microhardness machine was used to carry out all microhardness measurements on weld cross-sections. A load of 300g was applied for 5 seconds in each case. Measurements were taken in the bulk parent material in the bottom sheet through to the bulk parent metal in the top sheet completely traversing the weld nugget and heat affected zones, thus producing a hardness profile of the weld region. The indent spacing used ranged from 0.1mm to 0.5mm and depended on the level of detail required and the width of the microstructural regions under investigation.

5. RESULTS AND DISCUSSION

5.1 The resistance welding of advanced high strength steels using basic weld schedules

This section discusses the results of single pulse welding trials conducted on a low carbon mild steel (LC), an interstitial free steel (IF260), three dual phase steels (DP600, DP800 & DP1000), two transformation induced plasticity steels (TRIP600 & TRIP800) and a martensitic steel (MS1400). The aim of the initial trial was to compare the weldability of the selected advanced high strength steels to that of grades with significantly lower alloy contents such as LC and IF260 using a single pulse welding schedule typical of those currently used on automotive production lines. The effect of increasing weld current on weld growth is presented along with the lap shear and cross tension performance of welds with a diameter of $5\sqrt{t}$ (where t is the sheet thickness in mm) formed in each of the eight steel grades studied. In addition the microhardness of $5\sqrt{t}$ welds is discussed in relation to carbon equivalent (CE) along with a detailed microstructural examination of welds formed in each of the eight steel grades.

5.1.1 Weld growth characteristics and failure mode of welds produced using a single pulse weld schedule

The welding parameters used to generate the initial set of practical results were as follows:

- **Squeeze** - 35 cycles
- **Weld** - 10 cycles
- **Hold** - 5 cycles
- **Electrode Force** - 3.2 kN
- **Electrode tip diameter** - 5 mm

The weld time, electrode tip diameter and electrode force were chosen in accordance with the recommendations outlined in BS1140:1993[41] for un-coated steels being welded under high force, short time conditions. Since high strength steels were being welded, the highest recommended electrode force was chosen for a sheet thickness of 1.0mm to

1.2mm (3.2kN) whilst the weld time was set in between the recommended 8 to 12 cycles. The squeeze time of 35 cycles was intended to allow sufficient time for the electrode force to reach the preset level before the passage of weld current. The hold time of 5 cycles was intended to allow good consolidation of the weld nugget whilst limiting the cooling effect of the electrodes on the weld region. The total sequence time was 50 cycles or 1 second.

Weld growth curves generated for each of the eight grades under investigation using the weld parameters listed above are displayed in figures 5.1 to 5.8. Each point represents a single spot weld with the red points indicating splash welds.

In order to provide a suitable benchmark for assessing the weldability of the selected advanced high strength grades it was decided to conduct a weld growth trial on galvanneal-coated low carbon (LC) mild steel. This grade is typical of those traditionally used in body-in-white assemblies and would be considered readily weldable by automotive manufacturers. This grade had a carbon content of 0.03wt% and a carbon equivalent of 0.045 calculated using the Ito-Bessyo equation. The sheet thickness of this grade was 1.15mm. Figure 5.1 shows the relationship between weld current and weld diameter for welds formed in LC at an electrode force of 3.2kN. It can be seen that melting at the sheet to sheet interface and the formation of solid weld nuggets first began to occur at a weld current of approximately 7.7kA. As the weld current level was steadily increased the amount of heat energy generated in the workpiece between the electrodes and the volume of parent material melted also increased. This accounts for the increase in measured diameter of individual welds with increasing weld current. The weld current level at which weld splash first began to occur in this grade was 10.3kA. The current range over which weld diameters in excess of $3.5\sqrt{t}$ (where t = sheet thickness in mm) were achieved was approximately 1.9 kA. The current range over which weld diameters in excess of $5\sqrt{t}$ were achieved was approximately 1.1 kA. The maximum weld size achieved before the occurrence of splash was 6.98mm or $6.5\sqrt{t}$. The point at which full plugs were consistently obtained on chisel testing corresponded with a weld

diameter of approximately 3.75mm or 3.5√t. The current range over which full plugs were achieved was approximately 1.95kA.

In addition to the LC grade, it was decided to investigate the weldability of a galvanneal-coated interstitial free (IF260) grade. This grade was characterised by an extremely low carbon content of just 0.0029 wt%. However, the presence of specific alloying elements such as 1.005wt% manganese gives this grade a carbon equivalent of 0.06. The sheet thickness of this grade was 1.2mm. Figure 5.2 shows the relationship between weld current and weld diameter for welds formed in IF260 at an electrode force of 3.2kN. It can be seen that melting at the sheet to sheet interface and the formation of solid weld nuggets first began to occur in this grade at a weld current of approximately 6.4 kA. The diameter of individual welds increased steadily with increasing weld current up to 8.24 kA where weld splash began to occur. The current range over which weld diameters in excess of 3.5√t were achieved was approximately 1.43 kA. The current range over which weld diameters in excess of 5√t were achieved was approximately 0.7kA. The maximum weld size achieved before the occurrence of splash was 6.81mm or 6.2√t. The point at which full plugs were consistently obtained on chisel testing corresponded with a weld diameter of approximately 6mm or 5.5√t. The current range over which full plugs were achieved was approximately 0.44kA.

With a carbon content of 0.083wt% and a carbon equivalent of 0.204, TRIP600 had the lowest alloy content of the six AHSS grades studied and was supplied in the uncoated condition. The sheet thickness of this grade was 1.0mm. Figure 5.3 shows the relationship between weld current and weld diameter for this grade at an electrode force of 3.2kN. It can be seen that melting at the sheet to sheet interface and the formation of solid weld nuggets first began to occur at a weld current of approximately 5.25kA. The diameter of individual welds increased steadily with increasing weld current up to 7.46kA where weld splash first began to occur. The current range over which weld diameters in excess of 3.5√t were achieved was approximately 1.8kA. The current range over which weld diameters in excess of 5√t were achieved was approximately 0.9kA. The maximum weld size achieved before the occurrence of splash was 6.53mm or 6.5√t.

The point at which full plugs were consistently obtained on chisel testing corresponded with a weld diameter of approximately 4.1mm or $4.1\sqrt{t}$. The current range over which full plugs were achieved was approximately 1.46kA.

Figure 5.4 shows the relationship between weld current and weld diameter for 1.2mm uncoated DP600 sheet steel at an electrode force of 3.2kN. DP600 had a carbon content of 0.102wt% and a carbon equivalent of 0.215. It can be seen that melting at the sheet to sheet interface and the formation of solid weld nuggets first began to occur at a weld current of approximately 4.5kA. The diameter of individual welds increased steadily with increasing weld current up to a maximum of 7.84kA where weld splash first began to occur. The current range over which weld diameters in excess of $3.5\sqrt{t}$ were achieved was approximately 2.34kA. The current range over which weld diameters in excess of $5\sqrt{t}$ were achieved was approximately 1kA. The maximum weld size achieved before the occurrence of splash was 6.76mm or $6.2\sqrt{t}$. The point at which full plugs were consistently obtained on chisel testing corresponded with a weld diameter of approximately 5.54mm or $5.1\sqrt{t}$. The current range over which full plugs were achieved was approximately 1.02kA.

Figure 5.5 shows the relationship between weld current and weld diameter for 1.2mm uncoated DP800 sheet steel at an electrode force of 3.2kN. DP800 had a carbon content of 0.129wt% and a carbon equivalent of 0.217. It can be seen that melting at the sheet to sheet interface and the formation of solid weld nuggets first began to occur at a weld current of approximately 4.1kA. The diameter of individual welds increased steadily with increasing weld current up to a maximum of 7.32kA where weld splash first began to occur. The current range over which weld diameters in excess of $3.5\sqrt{t}$ were achieved was approximately 2.27 kA. The current range over which weld diameters in excess of $5\sqrt{t}$ were achieved was approximately 0.7kA. The maximum weld size achieved before the occurrence of splash was 6.48mm or $5.9\sqrt{t}$. The point at which full plugs were consistently obtained on chisel testing corresponded with a weld diameter of approximately 5.03mm or $4.6\sqrt{t}$. The current range over which full plugs were achieved was approximately 1.15kA.

Figure 5.6 shows the relationship between weld current and weld diameter for 1.2mm uncoated DP1000 sheet steel at an electrode force of 3.2kN. DP1000 had a carbon content of 0.143wt% and a carbon equivalent of 0.245. It can be seen that melting at the sheet to sheet interface and the formation of solid weld nuggets first began to occur at a weld current of approximately 3.9kA. The diameter of individual welds increased steadily with increasing weld current up to a maximum of 6.4kA where weld splash first began to occur. The current range over which weld diameters in excess of $3.5\sqrt{t}$ were achieved was approximately 1.4 kA, however it was not possible to consistently produce $5\sqrt{t}$ welds before the splash limit was reached. Whilst a maximum weld diameter of 5.66mm ($5.17\sqrt{t}$) was achieved, the current required to produce this weld corresponded roughly with the splash limit. Weld failure modes consisted entirely of interfacial and partial plug failures, however partial plug failures comprising approximately 90% plug were observed at current levels approaching the splash limit.

Figure 5.7 shows the relationship between weld current and weld diameter for 1.0mm uncoated MS1400 sheet steel at an electrode force of 3.2kN. MS1400 had a carbon content of 0.162wt% and a carbon equivalent of 0.266. It can be seen that melting at the sheet to sheet interface and the formation of solid weld nuggets first begins to occur at a weld current of approximately 3.1kA. The diameter of individual welds increased steadily with increasing weld current up to a maximum of 5.93kA where weld splash first began to occur. The current range over which weld diameters in excess of $3.5\sqrt{t}$ were achieved was approximately 1.8kA. However, it was not possible to produce $5\sqrt{t}$ welds before the onset of weld splash or obtain full plug failures. The maximum weld size achieved under these conditions was 4.97mm or $4.97\sqrt{t}$. Weld failure modes consisted entirely of interfacial and partial plug failures. Full plug failures were not observed.

Figure 5.8 shows the relationship between weld current and weld diameter for 1.2mm uncoated TRIP800 sheet steel at an electrode force of 3.2kN. TRIP800 had the highest alloy content of the six advanced high strength grades investigated with a carbon content of 0.181wt% and a carbon equivalent of 0.307. It can be seen that melting at the sheet to sheet interface and the formation of solid weld nuggets first began to occur at a weld

current of approximately 3.3kA. The diameter of individual welds increased steadily with increasing weld current up to a maximum of 5.76kA where weld splash first began to occur. The current range over which weld diameters in excess of $3.5\sqrt{t}$ were achieved was approximately 1.6 kA. However, as with MS1400, it was not possible to produce $5\sqrt{t}$ welds before the splash limit was reached. The maximum weld size achieved under these conditions was 5.37mm or $4.9\sqrt{t}$ with a weld current of 5.8kA, which is greater than the current level where weld splash first began to occur. Weld failure modes consisted entirely of interfacial and partial plug failures. Full plug failures were not observed.

Figure 5.9 shows the growth curves of all eight steels plotted on the same axes. As the Carbon Equivalent of the parent material increased the individual growth curves were displaced to lower current levels. The approximate current requirements to form $3.5\sqrt{t}$ diameter welds in each of the eight grades under investigation are listed in table 5.1 along with the carbon equivalent of each grade. It can be seen that generally as the carbon equivalent of the parent material increased, the current required to form a $3.5\sqrt{t}$ diameter weld decreased. It is thought that this was due to the increase in alloy content leading to a corresponding increase in the bulk resistivity of the material. According to Joule's law ($H = KI^2Rt$), an increase in the total resistance to current flow (R) will lead to a decrease in the weld current (I) necessary to generate the same amount of heat energy (H) during a fixed period of time (t), which in this case is 10 cycles or 0.2 seconds. However, it can be seen from table 5.1 that the current level required to form a $3.5\sqrt{t}$ weld in MS1400 was marginally lower than for TRIP800 despite TRIP800 having a higher carbon equivalent. This can be explained with reference to the difference in sheet thickness between MS1400 and TRIP800. A $3.5\sqrt{t}$ weld formed in 1.2mm TRIP800 has a greater diameter than a $3.5\sqrt{t}$ weld formed in 1.0mm MS1400 (3.83mm versus 3.5mm) and therefore requires a larger volume of material to be melted and a greater heat input. Extrapolating from figure 5.7, the weld current required to form a 3.83mm diameter weld in MS1400 was approximately 4.38kA compared to the 4.2kA required to form the same weld diameter in TRIP800. The presence of a galvanneal coating on the LC and IF260 grades is also likely to have contributed to the increased weld current requirements associated with these grades compared to the uncoated AHSS grades due to the reduction in the

contact resistance at the electrode/sheet and sheet/sheet interfaces caused by the zinc alloy coating.

By comparing the weld growth curves generated for LC, IF260, TRIP600, DP600 and DP800 (figures 5.1 to 5.5 respectively) it can be seen that the weldability of TRIP600, DP600 and DP800 compared favourably with that of LC and IF260, in terms of current range and weld failure mode, using welding parameters recommended in BS1140:1993[x] for uncoated low carbon steel. It was possible to produce welds with diameters well in excess of the preferred diameter of $5\sqrt{t}$ in TRIP600, DP600 and DP800 before the occurrence of weld splash. The current ranges over which weld diameters in excess of $3.5\sqrt{t}$ were obtained were greater for DP600 (2.34 kA), DP800 (2.27 kA) and TRIP600 (1.78 kA) than for IF260 (1.43 kA). All of these current ranges would be considered to offer adequate flexibility in a production environment. In addition full plug failures were observed from smaller weld diameters in TRIP600, DP600 and DP800 than in IF260. The current range over which full plug failures were achieved was greater than 1kA for TRIP600, DP600 and DP800.

These results indicate that TRIP600, DP600 and DP800 can be considered readily weldable and could potentially be integrated into body-in-white construction without any significant alterations to established plant practice. The total weld time of 50 cycles or 1 second is likely to be considered acceptable and the electrode force of 3.2kN well within the capacity of production line welding equipment.

It can be seen from figures 5.6, 5.7 and 5.8 that when using 5mm diameter electrode tips and an electrode force of 3.2kN, it was not possible to consistently achieve the preferred weld diameter of $5\sqrt{t}$ in DP1000, MS1400 or TRIP800 before the splash limit of these grades was reached. The failure modes exhibited by DP1000, MS1400 and TRIP800 spot welds consisted entirely of interfacial and partial plug failures. Full plug failures were not observed. On the basis of these initial results, automotive manufacturers would be reluctant to adopt these grades unless a method could be found to at least allow the

production of $5\sqrt{t}$ diameter welds at current levels well below the splash limit. The inability to pull full plug failures on chisel testing would also be of significant concern.

Since a weld size of $5\sqrt{t}$ is specified in BS1140:1993[41] for the production of lap shear and cross tension samples, a method had to be devised to displace the splash limit of DP1000, MS1400 and TRIP800 to higher current levels thus allowing the consistent production of $5\sqrt{t}$ welds without the risk of weld splash.

5.1.2 The effect of increasing electrode force on weld growth in DP1000, MS1400 and TRIP800

In order to address the issues described above, it was decided to investigate the effect of increasing the electrode force on the splash limit of DP1000, MS1400 and TRIP800. It was intended that a higher electrode force would provide more intimate contact between the sheets being joined and displace the splash limit of these materials to higher current levels thus allowing a greater maximum weld diameter to be achieved.

Figure 5.10 shows the relationship between weld current and weld diameter for DP1000 at an electrode force of 4kN. Increasing the electrode force from 3.2kN to 4kN had the effect of displacing the splash limit from 6.4 kA to 7.2 kA, allowing the production of a maximum weld diameter of 6.36mm or $5.8\sqrt{t}$. The current range over which weld diameters in excess of $3.5\sqrt{t}$ were achieved was approximately 2.15kA. The current range over which weld diameters in excess of $5\sqrt{t}$ were achieved was approximately 0.6kA. Weld failure modes consisted entirely of interfacial or partial plug failures, however as with the weld growth study conducted with an electrode force of 3.2kN, partial plug failures comprising approximately 90% plug were observed in DP1000 at current levels approaching the splash limit.

Figure 5.11 shows the relationship between weld current and weld diameter for MS1400 at an electrode force of 4kN. Increasing the electrode force from 3.2kN to 4kN had the effect of displacing the splash limit from 5.93kA to 6.7kA, allowing the production of a maximum weld diameter of 5.78mm or $5.78\sqrt{t}$. The current range over which weld

diameters in excess of $3.5\sqrt{t}$ were achieved was approximately 2.05kA. The current range over which weld diameters in excess of $5\sqrt{t}$ were achieved was approximately 0.8kA. Weld failure modes consisted entirely of interfacial and partial plug failures. Full plug failures were not observed.

Figure 5.12 shows the relationship between weld current and weld diameter for TRIP800 at an electrode force of 4kN. It can be seen that by increasing the electrode force from 3.2kN to 4kN the splash limit was increased from 5.76 kA to 6.1 kA. The current range over which weld diameters in excess of $3.5\sqrt{t}$ were achieved was approximately 1.3 kA. However, it was still not possible to obtain $5\sqrt{t}$ diameter welds before the occurrence of weld splash. The maximum weld diameter achieved before the onset of splash was 5.38mm or $4.9\sqrt{t}$. Weld failure modes consisted entirely of interfacial and partial plug failures. Full plug failures were not observed.

It was therefore decided to increase the electrode force to 5kN when joining TRIP800. Figure 5.13 shows the relationship between weld current and weld diameter for TRIP800 at an electrode force of 5kN. The further increase in electrode force successfully increased the splash limit to 6.6 kA, allowing the production of a maximum weld diameter of 5.74mm or $5.2\sqrt{t}$. The current range over which weld diameters in excess of $3.5\sqrt{t}$ were achieved was approximately 1.6 kA. The current range over which weld diameters in excess of $5\sqrt{t}$ were achieved was approximately 0.4kA. As in previous trials weld failure modes consisted entirely of interfacial and partial plug failures. Full plug failures were not observed.

Figure 5.14 illustrates the effect of increasing electrode force on the growth characteristics of welds formed in TRIP800. It can be seen that as well as increasing the maximum weld diameter that could be achieved during 10 cycles of current flow, increasing the electrode force also displaced the individual growth curves to higher current levels. The approximate weld current levels required to form a $3.5\sqrt{t}$ diameter weld in TRIP800 at 3.2kN, 4kN and 5kN are listed in table 5.2. Increasing the electrode force from 3.2kN to 5kN increased the approximate current required to form a $3.5\sqrt{t}$ weld

from 4.2kA to 5kA. It is thought that this was due to the higher electrode force improving electrical contact not only at the electrode/sheet interfaces but also at the sheet/sheet interface, leading to a corresponding reduction in contact resistance at these interfaces. According to joules law ($H = KI^2Rt$) any reduction in the total resistance to current flow (R) must be met with a proportional increase in weld current (I) in order that the same amount of heat energy (H) is generated during the period of time (t) for which the current flows which in each case was 10 cycles or 0.2 seconds. The more intimate contact between the water cooled electrodes and the sheet surfaces may also have lead to a greater rate of heat extraction from the weld region thus requiring a higher weld current in order to counteract this increased cooling effect.

Once the approximate welding conditions necessary to grow a $5\sqrt{t}$ weld in each of the eight steel grades under investigation had been established, lap shear and cross tension samples were fabricated using the methods described in section 4.2.3. Weld cross sections were also mounted in resin in preparation for microhardness measurements and microstructural examination using the methods described in section 4.4.

5.1.3 Lap shear performance of $5\sqrt{t}$ welds produced using a single pulse weld schedule

Five lap shear samples were tested for each steel grade investigated and an average failure load calculated. In each case the failure load was taken to be the maximum load sustained by each spot weld in kN prior to failure. The results of the lap shear tests are displayed in table 5.3 and summarised in table 5.4.

Figure 5.15 illustrates the relationship between parent metal strength and average lap shear failure load. The average lap shear failure load of $5\sqrt{t}$ welds increased approximately linearly with increasing parent metal strength up to DP1000 which had a tensile strength of $1048N/mm^2$. $5\sqrt{t}$ welds formed in MS1400 ($R_m = 1479N/mm^2$) on average sustained a lower shear load before failing than TRIP800, DP800 and DP1000. The thinner gauge of the MS1400 grade is thought to contribute to this reduction in lap

shear performance, since $5\sqrt{t}$ welds formed in the MS1400 grade have a smaller diameter than those formed in TRIP800, DP800 and DP1000.

BS1140:1993[41] provides an equation to calculate the minimum lap shear strength required for a particular weld diameter and sheet thickness:

$$P_s = 2.6t\ d\ P_{TS}$$

Where:

P_s = shear strength of the weld (N)

t = sheet thickness (mm)

d = weld diameter (mm)

P_{TS} = tensile strength of steel (N/mm^2)

The minimum lap shear strengths calculated for $5\sqrt{t}$ welds formed in the eight steels under investigation are displayed in table 5.4 along with the average lap shear strengths actually observed for each grade. The average shear strengths of welds formed in LC, IF260, TRIP600, DP600, TRIP800 and DP800 were all greater than the minimum shear strengths required by BS1140:1993[41]. However, the average shear strength of welds formed in DP1000 (17.68kN) was marginally lower than the minimum shear strength calculated by the above equation (17.91kN). It can also be seen from tables 5.3 and 5.4 that the minimum required shear strength calculated for the MS1400 grade, which takes into account the reduced sheet thickness and the reduced diameter of $5\sqrt{t}$ welds formed in this grade, was significantly higher than both the average and the maximum lap shear failure load sustained by this grade. This suggests that there is a critical parent metal UTS above which the lap shear strength of a weld becomes dependent more on the properties of the weld or heat affected zone than on the tensile strength of the parent material.

Whilst it is important to have an indication of the maximum shear load a $5\sqrt{t}$ weld formed in a particular grade can sustain, it provides no indication of failure mode of that spot weld or the energy absorbed by the joint prior to ultimate failure. It was therefore

decided to examine the failed lap shear samples and the load versus displacement curves obtained for each of the eight grades investigated.

Typical lap shear load versus displacement curves exhibited by each of the eight grades investigated are displayed in figures 5.16 to 5.23. The shape of the load versus displacement curves up to the point of initial weld failure was similar from grade to grade. The load sustained by each lap shear sample increased rapidly with increasing displacement until the weld began to fail. After this point, the load sustained by the lap shear samples fell as failure continued. The shape of the load versus displacement curves after the point of initial weld failure gave an indication of the failure modes operating in each case. It can be seen from figures 5.16 and 5.17 that lap shear failure in LC and IF260 was characterised by a large displacement after initial weld failure where the load sustained by the sample gradually fell. This indicates that the samples underwent significant deformation prior to ultimate failure. Typical lap shear load versus extension curves exhibited by TRIP600, DP600, TRIP800 and DP800 are shown in figures 5.18 to 5.21 respectively. It can be seen that load versus extension curves of these grades are similar in shape to those exhibited by LC and IF260 lap shear samples also indicating that the TRIP600, DP600, TRIP800 and DP800 lap shear samples also underwent significant deformation prior to ultimate failure.

Figure 5.22 shows a typical lap shear load versus displacement curve exhibited by DP1000. It can be seen that the shape of this curve is visually distinct from those obtained for the lower strength grades suggesting a change in failure mode. The load sustained by this sample fell from a maximum of 17.59kN to zero over approximately 2mm displacement, suggesting that deformation of the parent material after initial weld failure was more limited than in the lower tensile strength materials. Figure 5.23 shows a typical lap shear load versus displacement curve exhibited by MS1400. The welds in the MS1400 lap shear samples appeared to fail in a catastrophic manner since the load sustained by the lap shear samples rapidly fell to zero after fracture initiation.

Figures 5.24 to 5.32 show photographs of $5\sqrt{t}$ welds formed in the eight grades under investigation which have been loaded to failure in shear. The scale in each case is in millimetres.

Figure 5.24 shows the typical weld failure mode observed for $5\sqrt{t}$ welds formed in LC when loaded in shear. It can be seen that the weld was partially torn from both coupons in the lap shear sample (double plug failure) and rotated through approximately 180° so that the weld was folded back on itself. Failure occurred in the parent material. A tag of parent material was torn from one of the sheets in the joint. A similar lap shear failure mode was observed for welds formed in IF260, as can be seen from figure 5.25, thus explaining the similarities between the lap shear load versus displacement curves obtained for these grades.

Figure 5.26 shows the typical weld failure mode observed for $5\sqrt{t}$ welds formed in TRIP600 when loaded in shear. Unlike the LC and IF260 grades, lap shear failure consistently resulted in the weld being torn completely from only one of the coupons in the joint. The sheet from which the weld was torn underwent significant deformation prior to ultimate failure. As can be seen from figures 5.27, 5.28 and 5.29 respectively, $5\sqrt{t}$ welds formed in DP600, TRIP800 and DP800 exhibited similar failure mechanisms to welds formed in LC and IF260 when loaded in shear, in that the welds were partially torn from both sheets in the joint with failure occurring in the parent material. However failure in DP600, TRIP800 and DP800 did not result in a tag of parent material being torn from one of the coupons in the lap shear sample as was observed for LC and IF260. It was thought that this was due to the higher tensile strength and work hardening rate of the high strength grades leading to necking of the parent material behind the weld nugget as opposed to tearing. Figure 5.30 shows a side view of a TRIP800 spot weld captured during a lap shear test. The yellow arrow indicates the direction of travel of the upper sheet and the white arrow indicates the direction of travel of the lower sheet. The weld nugget can be clearly seen being torn from both sheets with failure occurring in the parent material.

Figure 5.31 shows the typical failure mode observed for $5\sqrt{t}$ welds formed in DP1000 when loaded in shear. Fracture appears to have initiated at the leading edge of the weld and propagated through the thickness of the sheet and around the periphery of the weld nugget, leaving a tab of parent material behind the weld nugget. The plastic deformation of this tab of material is thought to account for the load sustained by the sample after initial weld failure (see figure 5.22). A similar failure mechanism was observed for the MS1400 grade as can be seen from figure 5.32, however due to the shape of the load versus extension curve (figure 5.23) it is thought that fracture initiated at the notch in the same way as DP1000 but propagated completely through the sheet in a catastrophic manner with very little deformation of the parent material following fracture initiation. It can be seen from table 5.3 that one of the MS1400 lap shear samples failed in an interfacial manner suggesting low weld ductility.

It was decided to section a failed DP1000 lap shear sample along the weld centre line parallel to the direction of loading. An optical microscope was then used to examine the failed weld. It can be seen from the micrograph shown in figure 5.33 that failure appeared to have initiated at the notch tip at the edge of the solidified weld nugget and propagated at approximately 45° to the plane of the sheet surface through the heat affected zone immediately adjacent to the weld nugget. Figure 5.34 shows an SEM image of this fracture surface. The fracture surface was characterised by elongated open dimples (i.e. the dimples were not completely enclosed by a rim) indicating that failure occurred by shear rupture. The closed ends of the dimples pointed towards the notch tip again indicating that this was the fracture initiation point.

It is thought that the failure of DP1000 and MS1400 to meet the minimum lap shear strength required by BS1140:1993[41] was due to the fact that failure occurred in the HAZ in both cases and not the parent material as in the majority of the lower strength grades. Since the high strength exhibited by DP1000 and MS1400 is due to a high percentage of martensite in the parent microstructure, the physical and mechanical properties of the heat affected zones formed in these grades are likely to have been significantly altered by the thermal profiles generated during the welding process.

5.1.4 Cross tension performance of $5\sqrt{t}$ welds produced using a single pulse weld schedule

Five cross tension samples were tested for each steel grade investigated and an average failure load calculated. In each case the failure load was taken to be the maximum load sustained by each spot weld in kN prior to failure. The results of the cross tension tests are displayed in table 5.5. The average cross tension failure loads of $5\sqrt{t}$ welds formed in the eight grades studies are displayed in table 5.6 alongside the average lap shear failure loads. Figure 5.35 shows the relationship between average cross tension strength and the UTS of the material in which the welds were formed. Plotted on the same axes is the lap shear data obtained for each grade. It can be seen from table 5.6 and figure 5.35 that the average cross tension failure loads were consistently lower than the average lap shear failure loads and that parent metal UTS had a much less pronounced effect on cross tension strength than on lap shear strength. Therefore the difference between lap shear and cross tension strength increased with increasing parent material strength. For example, $5\sqrt{t}$ welds formed in LC on average sustained 8.17kN in shear and 6.85kN in tension compared to $5\sqrt{t}$ welds formed in MS1400 which sustained on average 15.05kN in shear and 4.22kN in tension. It can also be seen from table 5.6 that as the parent metal strength (R_m) increases, the ductility ratio generally decreased. However all of the grades exhibited a ductility ratio of 0.45 or higher with the exception of MS1400 which exhibited a ductility ratio of 0.27.

Typical cross tension load versus displacement curves exhibited by each of the eight grades investigated are displayed in figures 5.36 to 5.43. The overall shape of the load versus extension curves was similar from grade to grade, with the exception of MS1400. The curves are characterised by a large displacement where the coupons in the cross tension sample undergo significant deformation before the load is concentrated on the spot weld. The load sustained by the sample then increases rapidly up to a maximum at the fracture initiation point, upon which the load falls to zero as the weld continues to fail. Due to the high strength and resistance to deformation of the MS1400 grade (R_p/R_m = 0.98) the load was concentrated on the spot weld almost immediately which accounts for the approximately linear relationship between load and displacement prior to failure.

It can be seen from table 5.5 that in the majority of cases, failure of the cross tension samples resulted in the weld nugget being completely torn from one of the two sheets in the joint (plug failure). A typical cross tension plug failure can be seen in figure 5.44. However several of the welds formed in the dual phase grades were partially torn from both sheets when loaded in tension (double plug failure).

5.1.5 Microstructural characteristics of welds produced using single pulse weld schedule

Once the weldability and mechanical performance of $5\sqrt{t}$ welds had been established, a detailed microstructural examination was carried out on sectioned $5\sqrt{t}$ spot welds formed in each of the eight steel grades under investigation. The individual spot welds were mounted and etched using the methodology detailed in section 4.4. The welds were initially examined using an optical microscope. A low magnification macro was taken of each spot weld before a high magnification examination of the weld nugget, heat affected zones and parent material was conducted. Example micrographs can be found in figures 5.45 to 5.52.

Figures 5.45a to 5.45e show the microstructural features observed in a typical LC spot weld. LC had the lowest carbon equivalent of all the grades studied at 0.045. Figure 5.45a shows the general appearance of the weld formed in this grade. The weld nugget is approximately oval in shape and the thickness of the heat affected zone (HAZ) varies around the periphery of the weld nugget, being thinner at the top and bottom of the weld nugget in close proximity to the electrodes. The grain structure of the weld nugget is columnar in nature with the columnar grains in the central region of the weld nugget contained within the electrode area aligned perpendicular to the sheet surface. The grains at the edge of the weld nugget can be seen to rotate through approximately 90° until they are aligned roughly with the sheet to sheet interface. The solidification line coincides roughly with the original sheet to sheet interface. The indentation of the sheet surface caused by the electrodes is also clearly visible in this micrograph. The variations in microstructure traversing from the parent material to the weld nugget can be seen in figure 5.45b. The columnar nature of the weld structure and the rotation of these

columnar grains at the edge of the weld nugget described above can also be seen in greater detail in this micrograph. Figures 5.45c to 5.45e show the regions visible in figure 5.45b in greater detail. The parent microstructure of this grade which has not been affected by the heat generated during the welding process is shown in figure 5.45c. The microstructure is composed primarily of equiaxed ferrite grains. Figure 5.45d is typical of the microstructure found in the heat affected zone surrounding the weld nugget. The grains in this region are still roughly equiaxed, however the grain structure appears refined compared to that found in the parent metal with clusters of very small ferrite grains (typically less than 5μm) dispersed throughout the microstructure. Figure 5.45e shows a detailed micrograph the weld nugget microstructure. It is possible to distinguish an internal substructure of fine needles within the columnar prior austenite grains.

Figures 5.46a to 5.46e show the microstructural features observed in a typical IF260 spot weld. This grade also had a low carbon equivalent of 0.059 and an extremely low carbon content of just 0.0029wt%. Figure 5.46a shows the general appearance of the weld formed in this grade. It can be seen that as with the LC weld, the weld nugget is approximately oval in shape and that the thickness of the heat affected zone varies around the periphery of the weld nugget. The variations in microstructure traversing from the parent material to the weld nugget can be seen in figure 5.46b. The columnar structure within the weld is clearly visible, as is the heat affected zone surrounding the weld nugget. Figures 5.46c to 5.46e show the regions visible in figure 5.45b in greater detail. The base microstructure of IF260 can be seen in figure 5.46c. Like the LC grade, the IF260 parent metal is composed of roughly equiaxed ferrite grains. There does not appear to be any second phase constituents present in the microstructure. The heat affected zone microstructure is shown in figure 5.46d and is visually distinct from that formed in the LC grade. The microstructure in this region appears to be composed of blocky elongated grains of ferrite. The weld nugget microstructure is composed of a plate-like ferrite substructure contained within the columnar prior austenite grains as can be seen from figure 5.46e.

Figures 5.47a to 5.47g show the microstructural features observed in a typical TRIP600 spot weld. TRIP600 had the lowest carbon equivalent of the AHSS grades studied at 0.204. It can be seen from figure 5.47a that there is a significant difference in the general appearance of this spot weld compared to the welds formed in LC and IF260 (figures 5.45a and 5.46a respectively). However as with the low alloy grades, the weld nugget and heat affected zone are approximately oval in shape and the grain structure of the weld nugget appears columnar in nature. The significant differences in microstructure between the parent material and the weld region can be clearly seen in figure 5.47b. Two distinct microstructural regions are visible in the heat affected zone surrounding the weld nugget; a fine microstructure in the outer regions of the heat affected zone and a much coarser microstructure in close proximity to the columnar weld nugget. A sharp notch extends through the heat affected zone to the edge of the columnar weld nugget along the original sheet to sheet interface. Figures 5.47c to 5.47g show the regions visible in figure 5.47b in greater detail. The un-welded parent microstructure of this grade can be seen in figure 5.47c. Volume fraction analysis conducted on this grade[50] determined that the parent microstructure was composed of approximately 85% pro-eutectoid ferrite with the remainder of the microstructure being composed of bainite, martensite and retained austenite islands dispersed throughout the ferrite matrix. Figure 5.47d shows the transition from the parent material on the left hand side of the image to the heat affected zone on the right. It can be seen that the microstructure in the central region of the micrograph has essentially been transformed from a classical TRIP microstructure of ferrite-bainite-retained austenite to a dual phase ferrite-martensite microstructure. When traversing from the parent microstructure to the heat affected zone, the volume fraction of martensite at the ferrite grain boundaries increases steadily at the expense of the ferrite matrix until the microstructure is composed entirely of martensite. A detailed image of the outer heat affected zone is shown figure 5.47e. The microstructure in this region also appears to be composed of extremely fine martensite. However it was difficult to resolve the lath substructure using optical microscopy. Figure 5.47f shows a detailed micrograph of the inner heat affected zone in close proximity to the solidified weld nugget. The microstructure in this region is coarser than in the outer heat affected zone and the lath structure is more clearly visible. The laths appear to be grouped into packets of similar

orientation. Figure 5.47g shows the microstructure of the weld nugget. The weld is also composed of fine laths grouped into packets of similar orientation, however the laths in the weld nugget are much longer than those found in the inner heat affected zone.

Figures 5.48a to 5.48g show the microstructural features observed in a typical DP600 spot weld. Figure 5.48a shows the general appearance of the weld nugget formed in this grade. It can be seen by comparing with figure 5.47a that the weld formed in DP600 appears microstructurally similar to that formed in TRIP600. However the overall shape of the heat affected zone is approximately rectangular and can be seen to extend almost to the sheet surface at the extremities. The weld nugget itself is approximately oval in shape. The variations in microstructure traversing from the parent material to the weld nugget can be clearly seen in figure 5.48b. It can also be seen that as with the TRIP600 grade, there appears to be two distinct microstructural regions in the heat affected zone. The weld nugget extends almost to the edge of the heat affected zone producing a much blunter notch than that observed in the TRIP600 weld. Figures 5.48c to 5.48g show the regions visible in figure 5.48b in greater detail. The un-welded parent microstructure of this grade can be seen in figure 5.48c. Volume fraction analysis conducted on this grade[50] determined that the parent microstructure was composed of approximately 86% pro-eutectoid ferrite with the remainder of the microstructure being comprised of a dispersion of martensite islands. Figure 5.48d shows a detailed micrograph of the transition from the parent material on the left hand side of the image to the heat affected zone on the right. It can be seen that when traversing from the parent microstructure to the heat affected zone, the volume fraction of martensite at the ferrite grain boundaries steadily increases until the microstructure is composed entirely of fine martensite. The outer heat affected zone is shown figure 5.48e. The microstructure in this region also appears to be composed of extremely fine martensite, however as with the TRIP600 grade it was difficult to resolve the lath structure using the optical microscope. Figure 5.48f shows the inner heat affected zone in close proximity to the solidified weld nugget. The microstructure of this region is composed of fine laths groped into packets. Figure 5.48g shows the microstructure of the weld nugget. The weld nugget microstructure is

composed of long laths and is similar to that observed in the TRIP600 weld (figure 5.47g).

Figures 5.49a to 5.49g show the microstructural features observed in a typical DP800 spot weld. Figure 5.49a shows the general appearance of the weld nugget formed in this grade. The shape of the weld nugget and heat affected zone are similar to those observed in the DP600 weld. The variation in microstructure from the parent material to the weld nugget can be clearly seen in figure 5.49b. As with the DP600 weld, forging and deformation of the heat affected zone during weld formation produced a blunt notch. However, it can be seen that a much sharper notch runs through the heat affected zone to the edge of the solidified weld nugget along what would have been the original sheet to sheet interface. Figures 5.49c to 5.49g show the regions visible in figure 5.49b in greater detail. The un-welded parent microstructure of this grade can be seen in figure 5.49c. Volume fraction analysis conducted on this grade[50] determined that the parent microstructure was composed of approximately 73% pro-eutectoid ferrite with the remainder of the microstructure being comprised of a dispersion of martensite islands. However unlike the DP600 grade the martensite present in DP800 forms an almost continuous network around the ferrite grains. Figure 5.49d shows the transition from the parent material on the left hand side of the image to the heat affected zone on the right. It can be seen that as with TRIP600 and DP600, when traversing from the parent microstructure to the heat affected zone, the volume fraction of martensite at the grain boundaries steadily increases until the microstructure is composed entirely of fine martensite. The outer heat affected zone is shown figure 5.49e. The microstructure in this region again appears to be composed of extremely fine martensite. Figures 5.49f and 5.49g show the microstructures found in the inner heat affected zone and the weld nugget respectively. The microstructure of these regions is composed of laths grouped into packets of similar orientation with the laths in the weld nugget being longer than those present in the heat affected zone.

Figures 5.50a to 5.50g show the microstructural features observed in a typical DP1000 spot weld. Figure 5.48a shows the general appearance of the weld nugget formed in this

grade. The variation in microstructure from the parent material to the weld nugget can be clearly seen in figure 5.50b. A sharp notch extends through the heat affected zone to the periphery of the weld nugget. Figures 5.50c to 5.50g show the regions visible in figure 5.50b in greater detail. The un-welded parent microstructure of this grade can be seen in figure 5.49c. The microstructure is composed of a dispersion of pro-eutectoid ferrite grains surrounded by a continuous network of martensite representing a volume fraction of approximately 67%. Figure 5.50d shows the transition from the parent material on the left hand side of the image to the heat affected zone on the right. It can be seen that there is a band of material approximately at the centre of the micrograph in which there appears to have been coarsening of the ferrite grains in the microstructure. A detailed micrograph of the outer heat affected zone is shown figure 5.50e. The microstructure in this region appears to be composed of extremely fine martensite. Figures 5.50f and 5.50g show the microstructures found in the inner heat affected zone and the weld nugget respectively. The microstructure of these regions is composed of laths grouped into packets of similar orientation with the laths in the weld nugget being longer than those present in the heat affected zone.

Figures 5.51a to 5.51g show the microstructural features observed in a typical MS1400 spot weld. Figure 5.48a shows the general appearance of the weld nugget formed in this grade. The variation in microstructure from the parent material to the weld nugget can be clearly seen in figure 5.51b. A sharp notch extends through the heat affected zone to the periphery of the weld nugget. It can be seen that fracture of the weld nugget has initiated at the notch tip. Figures 5.47c to 5.51g show the regions visible in figure 5.51b in greater detail. The parent microstructure can be seen in figure 5.51c. Volume fraction analysis conducted on this grade[50] determined that the parent microstructure contained approximately 2% retained austenite with the remainder of the microstructure being composed of martensite. This was confirmed by XRD analysis. Figure 5.51d shows the transition from the parent material to the heat affected zone. In this micrograph the parent microstructure appears on the right hand side of the image whilst the heat affected zone microstructure appears on the left. Due to the high volume fraction of martensite in the parent microstructure, it is more difficult to distinguish between the parent

microstructure and the heat affected zone microstructure than in the lower strength dual phase grades. As was observed with the DP1000 grade, there is a band of material approximately at the centre of the micrograph in which there appears to have been ferrite grain growth making it microstructurally distinct from both the parent material and the outer heat affected zone which are both composed primarily of martensite. A detailed micrograph of the outer heat affected zone is shown figure 5.51e. The microstructure in this region appears to be composed of extremely fine martensite. Figure 5.51f shows the inner heat affected zone in close proximity to the solidified weld nugget. The microstructure of this region is composed of laths grouped into packets of similar orientation. It can be seen from figure 5.51g that the microstructure of the weld nugget is also composed of laths.

Figures 5.52a to 5.52g show the microstructural features observed in a typical TRIP800 spot weld. TRIP800 had the highest carbon equivalent of the AHSS grades studied at 0.307. Figure 5.48a shows the general appearance of the weld nugget formed in this grade. The variation in microstructure from the parent material to the weld nugget can be seen in figure 5.52b. It can be seen that as with the other AHSS grades, there are at least two distinct regions in the heat affected zone; a coarse inner heat affected zone in close proximity to the solidified weld nugget and a much finer outer heat affected zone. A sharp notch extends through the heat affected zone to the periphery of the weld nugget. Figures 5.52c to 5.52g show the regions visible in figure 5.52b in greater detail. The un-welded parent microstructure of this grade can be seen in figure 5.52c. Volume fraction analysis conducted on this grade[50] determined that the parent microstructure was composed of approximately 72% pro-eutectoid ferrite with the remainder of the microstructure being composed of bainite, martensite and retained austenite islands dispersed throughout the ferrite matrix. Figure 5.52d shows the transition from the parent material on the left hand side of the image to the heat affected zone on the right. As with the TRIP600 grade, the microstructure in this region has essentially been transformed from a ferrite-bainite-retained austenite microstructure to a dual phase ferrite-martensite microstructure with the volume fraction of martensite at the grain boundaries steadily increasing at the expense of ferrite when traversing from the parent microstructure to the

fully martensitic outer heat affected zone shown in figure 5.52e. The martensite in this region is extremely fine and difficult to resolve using the optical microscope. Figure 5.52f shows the inner heat affected zone in close proximity to the solidified weld nugget. The microstructure of this region is composed of laths grouped into packets of similar orientation. Figure 5.52g shows the microstructure of the weld nugget. As with the other AHSS grades studied, the weld nugget is composed of a lath substructure, with the laths grouped into packets of similar orientation as in the inner heat affected zone. However the laths found in the nugget are considerably longer than those found in the heat affected zone.

SEM examination of AHSS weld microstructures

It was decided to examine the AHSS weld cross sections using a Scanning Electron Microscope (SEM) in order to better resolve the microstructural features observed under the optical microscope, particularly the fine microstructures found in the heat affected zones. The SEM confirmed the lath-like morphology of the microstructures present in the weld nuggets and heat affected zones of welds formed in the selected advanced high strength steels. SEM images of microstructures found in the weld nugget and heat affected zone of the TRIP800 weld are shown in figures 5.53a to 5.53d.

Figure 5.53a shows an SEM image of the microstructure found in the outer heat affected zone of the TRIP800 weld (for a comparable optical micrograph see figure 5.52e). It can be seen that the microstructure in this region is composed of extremely fine laths. Figure 5.53b shows an SEM image of the weld nugget microstructure. The SEM clearly reveals the lath morphology of the weld nugget, confirming that the laths found in this region are significantly longer than those observed in the heat affected zone and are grouped into distinct 'packets' of laths sharing a similar orientation. These laths can be seen in greater detail in figure 5.53c.

It can also be seen from figures 5.53b and 5.53c that the SEM clearly revealed a dispersion of pores or voids in the etched surface of the sectioned weld. These pores were much less clearly visible when examining etched samples using the optical

microscope, however several pores can be seen in figure 5.47g. Further investigation revealed the presence of inclusions within the pores, as can be seen in figure 5.53d. Energy Dispersive X-Ray (EDX) point analysis was used to determine the chemical composition of a series of these inclusions. Figure 5.53e shows the EDX spectrum of the inclusion shown in figure 5.53d. The EDX spectrum indicates that the inclusion is a complex oxide of silicon, aluminium, iron and manganese. Porosity was observed in all of the AHSS grades studied. However it is thought that the porosity resulted from selective etching of the parent material around the inclusions by the 2% nital solution used since the pores were not visible when the polished samples were examined using the optical microscope prior to etching in accordance with the methodology described in section 4.4.2.

5.1.6 Microhardness of welds produced using a single pulse weld schedule

Microhardness surveys were conducted on the sectioned $5\sqrt{t}$ welds used in the preceding microstructural examinations. Measurements were taken in the parent material, heat affected zones and the weld nugget thus producing a microhardness profile of each weld. These microhardness profiles are shown in figures 5.54 to 5.61. The average weld hardness levels recorded in each of the eight grades under investigation are displayed in table 5.7 along with the carbon equivalent of each grade and average microhardness levels measured in the un-welded parent metal.

The microhardness profile of a $5\sqrt{t}$ weld formed in LC is shown in figure 5.54. The average microhardness of the parent metal was approximately $117HV_{0.3}$. Peak hardness levels were recorded in the weld nugget with hardness increasing to approximately $203HV_{0.3}$ while traversing from the parent material, through the HAZ and into the weld nugget.

The microhardness profile of a $5\sqrt{t}$ weld formed in IF260 is shown in figure 5.55. The average microhardness of the parent metal was approximately $133HV_{0.3}$. As with the LC grade, peak hardness levels were recorded in the weld nugget with hardness increasing to

approximately 233$HV_{0.3}$ while traversing from the parent material, through the HAZ and into the weld nugget.

The microhardness profile of a 5√t weld formed in TRIP600 is shown in figure 5.56. The hardness of the parent metal was approximately 205$HV_{0.3}$. Traversing from the parent metal into the solidified weld nugget, the measured microhardness levels rapidly increased to a maximum of 470$HV_{0.3}$ in the heat affected zone before decreasing to an average microhardness level of approximately 409$HV_{0.3}$ in the weld nugget.

The microhardness profile of a 5√t weld formed in DP600 is shown in figure 5.57. The hardness of the parent metal was approximately 204$HV_{0.3}$. The highest microhardness levels measured in the weld region occurred in the heat affected zones, as was observed for the TRIP600 grade. Traversing from the parent metal to the solidified weld nugget, the measured microhardness levels rapidly increased to a maximum of 467$HV_{0.3}$ in the heat affected zone before decreasing to an average microhardness level of approximately 424$HV_{0.3}$ in the weld nugget.

The microhardness profile of a 5√t weld formed in DP800 is shown in figure 5.58. The hardness of the parent metal was approximately 265$HV_{0.3}$. Again it can be seen that the highest microhardness levels measured in the DP800 weld region occurred in the heat affected zones. Traversing from the parent metal to the solidified weld nugget, the measured microhardness levels rapidly increased to a maximum of 510$HV_{0.3}$ in the heat affected zone before decreasing to an average microhardness level of approximately 449$HV_{0.3}$ in the weld nugget.

The microhardness profile of a 5√t weld formed in DP1000 is shown in figure 5.59. The hardness of the parent metal was approximately 359$HV_{0.3}$. As with TRIP600, DP600 and DP800 the highest microhardness levels measured in the DP1000 weld region occurred in the heat affected zones. However it can also be seen that while traversing from the parent metal to the heat affected zone, the measured microhardness levels initially dropped to a

minimum of $320HV_{0.3}$ before rapidly increasing to a maximum of $557HV_{0.3}$. The average microhardness of the weld nugget was approximately $499HV_{0.3}$.

The microhardness profile of a $5\sqrt{t}$ weld formed in MS1400 is shown in figure 5.60. The hardness of the parent metal was approximately $508HV_{0.3}$. It can be seen that the MS1400 weld exhibited a similar hardness profile to that of the DP1000 weld. As the heat affected zone was traversed, the hardness initially dropped to a minimum of $344HV_{0.3}$ before rapidly increasing to a maximum of $577HV_{0.3}$. The average microhardness of the weld nugget was approximately $514HV_{0.3}$.

The microhardness profile of a $5\sqrt{t}$ weld formed in TRIP800 is shown in figure 5.61. The hardness of the parent metal was approximately $239HV_{0.3}$. As with the other high strengths grades studied, the highest microhardness levels measured in the TRIP800 weld region occurred in the heat affected zones. Traversing from the parent metal to the solidified weld nugget, the measured microhardness levels increased rapidly to a maximum of $575HV_{0.3}$ in the heat affected zone before decreasing to an average microhardness level of approximately $527HV_{0.3}$ in the weld nugget.

The high hardness levels recorded in the weld nuggets and heat affected zones of welds formed in the six advanced high strength grades studied support the suggestion that these regions are composed of martensite as discussed in section 5.1.5. Whilst $5\sqrt{t}$ welds formed in TRIP600, DP600 and DP800 exhibited satisfactory performance in lap shear and cross tension and when subjected to the chisel test, the average weld microhardness levels recorded in these grades were all in excess of $400HV_{0.3}$ and up to $449HV_{0.3}$ in the case of DP800. $5\sqrt{t}$ welds formed in TRIP800 also exhibited satisfactory performance in lap shear and cross tension despite exhibiting an average weld microhardness level of approximately $527HV_{0.3}$. However the extremely high weld hardness levels measured in DP1000, TRIP800 and MS1400 are thought to account for the tendency of these welds to fail in a predominantly interfacial manner when subjected to the chisel test.

The percentage increase in hardness of the weld nugget compared to the parent material was also considered. These values are also shown in table 5.7. In all cases the hardness of the weld nugget was greater than that of the parent material. However the percentage increase in weld hardness over the parent metal hardness varied considerably from grade to grade. The increase in weld hardness in LC and IF260 was due to a transition from equiaxed ferrite in the parent material to lath ferrite in the weld nugget. In both cases the increase was approximately 75%. The percentage increases in hardness recorded for the TRIP grades was greater that 99% in both cases. This significant increase in hardness was due to the transition from a predominantly ferritic microstructure in the parent material to lath martensite in the weld nugget. It can be seen for the dual phase grades that as the strength of the parent material increased, the percentage increase in hardness of the weld nugget over the parent metal decreased. It is though that this was due to the increasing volume fraction of martensite in the parent microstructure at the expense of ferrite, which not only increases the tensile strength of the material but also its hardness. In the case of MS1400 there was only a 1.2% difference between the average hardness of the parent material and the weld nugget. As described previously, volume fraction analysis conducted on this grade[50] found that the microstructure was composed almost entirely of martensite, thus accounting for the similarity in hardness between the weld nugget and the parent material.

In order to relate the significant variations in Vickers microhardness recorded in the heat affected zones of the high strength grades to the microstructures present in those regions, it was decided to repeat a series of hardness measurement traversing the heat affected zones of the six advanced high strength grades studied and overlay this hardness data onto optical micrographs of the heat affected zones as shown in figures 5.62 to 5.67. The highest microhardness levels recorded in each high strength grade consistently coincided with the outer heat affected zone adjacent to the un-transformed parent material. As discussed in section 5.1.5, the microstructures in these regions appeared to be composed of martensite with an extremely fine lath packet size (see figures 5.47e, 5.48e, 5.49e, 5.50e, 5.51e and 5.52e).

Figure 5.68 shows the hardness profiles of the eight grades studied plotted on the same axes. The microhardness of the weld nuggets and heat affected zones increased with increasing carbon equivalent. Figure 5.69 shows the average microhardness of welds formed in each grade plotted against the corresponding carbon equivalent calculated using the Ito-Bessyo equation. It can be seen that there is an approximately linear relationship between carbon equivalent and weld microhardness. The regression line plotted through the points is described by the following equation:

$$\text{Weld microhardness} = 1307.5(CE) + 152.69$$

The correlation coefficient (R^2) is a measure of how well a regression line fits real data and can take a value of between 0 and 1, with 1 indicating a perfect fit. The R^2 value for this particular regression line is 0.9804.

5.1.7 SEM examination of interfacial fracture surfaces

As described in the literature review, an interfacial failure on chisel testing is generally considered unsatisfactory and thought to be indicative of low weld ductility. Due to the tendency of welds formed in advanced high strength steels such as TRIP800 and MS1400 to fail in a largely interfacial manner on chisel testing and the high weld microhardness levels recorded in these grades, it was decided to examine the fracture surfaces of interfacially failed welds formed in all eight of the steel grades investigated. A scanning electron microscope (SEM) was used to compare and contrast the fracture mechanisms operating in the AHSS welds with the fracture mechanisms operating in LC and IF260 welds, which exhibited significantly lower microhardness levels. SEM micrographs of interfacial fracture surfaces in failed welds formed in the eight steels under investigation are displayed in figures 5.70 to 5.77. It was expected that as the microhardness of the weld nuggets increased, there would be a transition from ductile failure to brittle fracture in the interfacial regions of failed welds. However it can be seen from figures 5.70 to 5.77 that all of the welds investigated exhibited evidence of both ductile failure and brittle fracture irrespective of the hardness levels measured within the welds.

Figure 5.70a shows evidence of dimple rupture in an interfacially failed LC spot weld. Dimple rupture occurs via the nucleation and growth of microvoids when a material is overloaded, in this case by the impact energy imparted on the weld during the chisel test. The voids tend to nucleate at particles within the parent material, either by fracture of the particles or as a result of decohesion of the parent material around the particle. As the strain in the material increases the microvoids grow and coalesce, eventually forming a continuous fracture surface. The fracture surface is characterised by numerous cuplike depressions which result from the coalescence of microvoids and can be considered to be indicative of ductile failure. Since LC had the lowest carbon equivalent and exhibited the lowest weld hardness levels of all the grades studied, it was expected that interfacial failure in this grade would occur in a ductile manner. However, as can be seen from figure 5.70b that there was also evidence of brittle trans-granular cleavage fracture operating on the same interfacial fracture surface. During trans-granular fracture, the crack front propagates through the grain structure along well defined crystallographic planes known as cleavage planes. Changes in crystal lattice orientation between individual grains and features such as dislocations and inclusions affect the fracture path of the propagating crack front producing a distinctive faceted fracture surface. Cleavage is a low energy fracture mechanism.

Due to its extremely low carbon content and correspondingly low carbon equivalent, it was also expected that any interfacial weld failures occurring in IF260 would have occurred in a ductile manner. Evidence of ductile dimple rupture can be seen in figure 5.71a. However, figure 5.71b shows evidence of brittle inter-granular fracture operating in the same fracture surface. Inter-granular fracture or decohesive rupture differs from trans-granular fracture in that the crack front propagates along the grain boundaries as opposed to cleaving through the grain structure and often occurs as a result of the fracture of weak grain boundary precipitate films which can form between the grains during solidification. Like inter-granular fracture, trans-granular fracture is a low-energy process.

Due to the significant increase in average weld hardness from LC and IF260 to the AHSS grades, it was expected that interfacial failure in the high strength grades would occur via a brittle low energy process. As can be seen from figures 5.72b, 5.73b, 5.74b, 5.75b, 5.76b and 5.77b, the interfacial fracture surfaces in the AHSS grades all showed evidence of trans-granular fracture. However, figures 5.72a, 5.73a, 5.74a, 5.75a, 5.76a and 5.77a show that regions of the same fracture surfaces also exhibited evidence of ductile dimple rupture despite average weld microhardness levels exceeding $400HV_{0.3}$ in the case of TRIP600, DP600, DP800 and DP1000 and $500HV_{0.3}$ in the case of MS1400 and TRIP800. Therefore the occurrence of interfacial or partial plug failures on chisel testing cannot be considered to be indicative of completely brittle fracture irrespective of weld hardness.

5.1.8 Summary

This section presented the first set of practical welding results. The weldability and weld growth characteristics of eight different steel grades were investigated using a basic single pulse weld schedule and parameters specified in BS1140:1993[41]. It was found that the weldability of TRIP600, DP600 and DP800 compared favourably with low carbon mild steel (LC) and IF260, both in terms of weld failure mode and the current range over which weld diameters in excess of $3.5\sqrt{t}$ were achieved. Full plug failures were observed in all of the above grades and $5\sqrt{t}$ diameter welds were achieved at current levels well below the splash limit of each grade. Higher electrode forces than those specified in BS1140:1993[41] were required to allow the formation of $5\sqrt{t}$ welds in DP1000, MS1400 and TRIP800. Full plug failures were not observed in these grades.

Microstructural examination revealed that the weld nuggets and heat affected zones in all six of the advanced high strength grades appeared to be composed of lath martensite, whilst welds formed in LC and IF260 appeared to be composed of a lath or plate-like morphology of ferrite. Three distinct zones could be distinguished within each AHSS weld; the columnar weld nugget, a coarse inner heat affected zone in close proximity to the solidified weld nugget and a fine outer heat affected zone. SEM examination of the

welds and heat affected zones formed in the AHSS grades confirmed the lath morphology of the microstructures in these regions.

Microhardness profiles of spot welds formed in the eight selected grades were also presented. It was discovered that the microhardness levels measured in the weld nuggets and heat affected zones increased as the alloy content and carbon equivalent of the parent material increased. It was also discovered that the highest microhardness levels recorded in the AHSS welds consistently coincided with the fine outer heat affected zones.

The lap shear and cross tension performance of TRIP600, DP600, DP800 and TRIP800 was found to be satisfactory despite weld microhardness levels in excess of $400HV_{0.3}$ in all cases and up to $541HV_{0.3}$ in the case of TRIP800. Whilst the DP1000 and MS1400 grades exhibited plug failures on lap shear testing the loads sustained before failure did not meet the level required by BS1140:1993[41] and in both cases failure occurred after limited deformation of the parent material. MS1400 exhibited poorer cross tension performance than LC.

SEM investigation of interfacial fracture surfaces revealed that in all of the grades studied, including LC and IF260, failure occurred via a combination of brittle fracture and ductile dimple rupture despite the vast differences in alloy chemistry, weld microhardness and weld microstructures observed between the advanced high strength steels and the lower strength grades.

5.2 The resistance welding of TRIP800 using a single pulse schedule and over-sized electrode tips

As discussed in section 5.1.2, when using 5mm diameter electrode tips and an electrode force of 5kN, the maximum weld diameter achieved in 1.2mm TRIP800 before the onset of splash was just $5.2\sqrt{t}$ (where t = sheet thickness in mm). It was also noted that welds formed in this grade tended to fail largely in the plane of the original sheet to sheet interface on chisel testing. It was therefore decided to substitute the 5mm diameter tips recommended in BS1140:1993[41] with 6mm and 7mm diameter tips in an attempt to increase the maximum achievable weld diameter in TRIP800 and to establish if there would be any performance benefits associated with an increase in weld diameter.

5.2.1 Weld growth characteristics and failure mode of welds formed in TRIP800 using 6mm and 7mm diameter electrode tips

In order that the weld growth data generated with 6mm and 7mm diameter electrodes was directly comparable with that generated using 5mm tips and a 3.2kN electrode force (see section 5.1.1) and that the pressure exerted by the electrodes on the sheet surfaces and the contact resistance at the electrode/sheet and sheet/sheet interfaces remained roughly constant for each electrode configuration, the electrode force was increased to 4.6 kN for the 6mm tips and 6.3 kN for the 7mm tips. The weld schedule used in the previous section was also kept constant;

- **Squeeze** - 35 cycles
- **Weld** - 10 cycles
- **Hold** - 5 cycles

The effects of increasing the electrode tip diameter on the growth characteristics and failure mode of welds formed in TRIP800 are displayed in figures 5.78 to 5.80.

Figure 5.78 shows the relationship between weld current and weld diameter for welds formed in 1.2mm uncoated TRIP800 sheet steel joined using electrodes with 6mm diameter tips and an electrode force of 4.6kN. It can be seen that melting at the sheet to sheet interface and the formation of solid weld nuggets first began to occur at a weld

current of approximately 3.89kA. The diameter of individual welds increased steadily with increasing weld current up to 8.59kA where weld splash first began to occur. The current range over which weld diameters in excess of $3.5\sqrt{t}$ were achieved was approximately 3.75kA. The current range over which weld diameters in excess of $5\sqrt{t}$ were achieved was approximately 2.2kA. The maximum weld size achieved before the occurrence of splash was 7.14mm or $6.5\sqrt{t}$. The point at which full plugs were consistently obtained on chisel testing corresponded with a weld diameter of approximately 6.9mm or $6.3\sqrt{t}$. The current range over which full plugs were achieved was approximately 0.5kA.

Figure 5.79 shows the relationship between weld current and weld diameter for welds formed in 1.2mm uncoated TRIP800 sheet steel joined using electrodes with 7mm diameter tips and an electrode force of 6.3kN. It can be seen that melting at the sheet to sheet interface and the formation of solid weld nuggets first began to occur at a weld current of approximately 5.25kA. The diameter of individual welds increased steadily with increasing weld current up to 7.46kA where weld splash first began to occur. The current range over which weld diameters in excess of $3.5\sqrt{t}$ were achieved was approximately 4.3kA. The current range over which weld diameters in excess of $5\sqrt{t}$ were achieved was approximately 2.85kA. The maximum weld size achieved before the occurrence of splash was 7.98mm or $7.3\sqrt{t}$. The point at which full plugs were consistently obtained on chisel testing corresponded with a weld diameter of approximately 6.85mm or $6.3\sqrt{t}$. The current range over which full plugs were achieved was approximately 1.31kA.

The use of 6mm and 7mm diameter tips offered significant increases in the current range over which acceptable weld diameters were achieved, where the minimum acceptable weld diameter remains $3.5\sqrt{t}$ as specified in BS1140:1993[41]. It can be seen that the weldability range increased from approximately 1.6kA with 5mm diameter electrode tips and an electrode force of 3.2kN to approximately 3.75kA with 6mm diameter tips and an electrode force of 4.6kN and approximately 4.3kA with 7mm diameter tips and an electrode force 6.3kN. This increase in weldability range was due to the greater electrode

tip diameter yielding an increase in the diameter to which welds could grow before splash began to occur. The maximum weld diameter achieved with 7mm diameter tips and an electrode force of 6.3kN was approximately 2.6mm greater than the maximum weld diameter achieved with 5mm diameter tips and an electrode force of 3.2kN. As mentioned previously, full plug failures were achieved at weld diameters greater than approximately $6.3\sqrt{t}$ for both electrode configurations. It was not possible to reach this weld diameter using 5mm tips and therefore full plug failures were not observed.

Figure 5.80 shows the weld growth curves produced with 6mm and 7mm diameter tips plotted on the same axes as the growth curve produced with 5mm diameter tips and an electrode force of 3.2kN. It can be seen that as well as significantly increasing the maximum weld diameter that could be achieved for a given weld time, increasing the electrode tip diameter also displaced the individual growth curves to higher current levels. The approximate weld currents required to form $3.5\sqrt{t}$ diameter welds in TRIP800 using 5mm, 6mm and 7mm diameter electrodes are listed in table 5.8. As the electrode tip diameter increased, the approximate current required to form a $3.5\sqrt{t}$ diameter weld in TRIP800 also increased. The increase in electrode surface area in contact with the sheet surfaces is thought to have increased the rate of heat extraction from the weld region into the electrodes and decreased the current density in the workpiece. Therefore higher current levels were required in order to generate sufficient heat in the workpiece to reach the required weld diameter of $3.5\sqrt{t}$.

5.2.2 Mechanical properties of welds formed in TRIP800 using 6mm and 7mm diameter electrode tips

A set of lap shear and cross tension samples were fabricated out of 1.2mm TRIP800 using 6mm and 7mm electrodes incorporating spot welds produced at current levels approaching the splash limit of each electrode configuration. The weld diameters investigated were $6.4\sqrt{t}$ and $7\sqrt{t}$ (produced using 6mm and 7mm diameter tips respectively). Five lap shear and cross tension samples were produced for each weld diameter and an average failure load calculated. In each case the failure load was taken to be the maximum load sustained by each spot weld in kN prior to failure.

It was also decided to investigate the effect of increasing electrode tip diameter on the lap shear and cross tension performance of $5\sqrt{t}$ welds. Since a $5\sqrt{t}$ diameter weld formed in 1.2mm TRIP800 would be completely contained within the electrode area of both 6mm and 7mm diameter tips, there could potentially have been an increase in the acuity of the notches formed at the periphery of the solidified weld nuggets. The presence of sharp notches at the edges of a weld could potentially have a deleterious effect on the lap shear and cross tension performance, particularly considering the high weld hardness levels previously recorded in TRIP800 (figure 5.61). Therefore five additional lap shear and cross tension samples incorporating $5\sqrt{t}$ welds were fabricated using both electrode configurations and an average failure load calculated.

Lap shear performance of $5\sqrt{t}$, $6.4\sqrt{t}$ and $7\sqrt{t}$ diameter welds

The lap shear strengths of samples incorporating $6.4\sqrt{t}$ and $7\sqrt{t}$ welds are displayed in table 5.9 and summarised in figure 5.81. It can be seen by comparing tables 5.9 and 5.3 that increasing the diameter of the welds in the lap shear samples lead to a significant increase in the load sustained by those welds prior to failure. $5\sqrt{t}$ diameter welds produced with 5mm diameter electrode tips sustained on average approximately 15.2kN prior to failure compared to $6.4\sqrt{t}$ diameter welds produced with 6mm diameter electrode tips which sustained on average approximately 18.4kN prior to failure and $7\sqrt{t}$ diameter welds produced with 7mm diameter electrode tips which sustained on average approximately 19.3kN prior to failure. There was no deterioration in the failure mode of the lap shear samples associated with the increase in weld diameter. Failure in each case resulted in the welds being pulled from one or both of the coupons in the lap shear sample with considerable tearing and deformation of the parent material.

The lap shear strengths of the $5\sqrt{t}$ welds formed using 6mm and 7mm diameter electrodes are also detailed in table 5.9 and summarised in figure 5.82. It can be seen from figure 5.82 that there was no reduction in average lap shear failure load of $5\sqrt{t}$ welds associated with the substitution of 5mm diameter tips with 6mm and 7mm diameter tips. As stated above $5\sqrt{t}$ welds formed using 5mm diameter tips sustained on average approximately 15.2kN prior to failure compared to $5\sqrt{t}$ diameter welds produced with 6mm diameter

electrode tips which sustained on average approximately 16.6kN prior to failure and 5√t diameter welds produced with 7mm diameter electrode tips which sustained on average approximately 17kN prior to failure. The failure modes of the 5√t welds formed using with 6mm electrodes compared favourably with those of 5√t welds formed with 5mm electrodes. In each case failure resulted in the weld being partially torn from both of the coupons in the joint. However, the 5√t welds formed with 7mm tips exhibited a mixture of double plug, plug and interface failures. This slight deterioration in failure mode could potentially be explained by an increase in notch acuity.

As discussed in section 5.1.2, BS1140:1993[41] provides an equation to calculate the minimum lap shear strength (P_S) of a spot weld of diameter d formed in a sheet of thickness t and tensile strength P_{TS}. The minimum lap shear strengths calculated for 6.4√t and 7√t diameter welds formed in 1.2mm TRIP800 are displayed in table 5.10 along with the average lap shear strengths actually observed. The average failure loads of lap shear samples incorporating 6.4√t and 7√t welds were greater than the minimum specified by BS1140:1993[41]. It can also be seen from table 5.10 that the average lap shear failure loads of 5√t welds formed using both 6mm and 7mm diameter tips were also greater than the minimum specified by BS1140:1993[41].

Cross tension performance of 5√t, 6.4√t and 7√t diameter welds

The cross tension strengths of the samples fabricated using 6mm and 7mm diameter electrodes are displayed in table 5.11 and summarised in figure 5.81. It can be seen from figure 5.81 that increasing the diameter of the welds in the cross tension samples lead to an increase in the load sustained by the welds prior to failure. 5√t diameter welds produced with 5mm diameter electrode tips sustained on average approximately 7kN prior to failure compared to 6.4√t diameter welds produced with 6mm diameter electrode tips which sustained on average approximately 8.8kN prior to failure and 7√t diameter welds produced with 7mm diameter electrode tips which sustained on average approximately 8.9kN prior to failure. It can be seen from table 5.11 that the 6.4√t welds exhibited plug and double plug failures whereas the 7√t welds exhibited a mixture of double plug, plug and partial plug failures.

The cross tension strengths of the $5\sqrt{t}$ welds formed using 6mm and 7mm diameter electrodes are also detailed in table 5.11 and summarised in figure 5.82. It can be seen from figure 5.82 that there was no reduction in average cross tension failure load of $5\sqrt{t}$ welds associated with the substitution of 5mm diameter tips with 6mm and 7mm diameter tips. As stated above $5\sqrt{t}$ welds formed using 5mm diameter tips sustained on average approximately 7kN prior to failure compared to $5\sqrt{t}$ diameter welds produced with 6mm diameter electrode tips which sustained on average approximately 7.7kN prior to failure and $5\sqrt{t}$ diameter welds produced with 7mm diameter electrode tips which sustained on average approximately 7.2kN prior to failure. It can be seen from tables 5.11 and 5.5 that $5\sqrt{t}$ diameter welds formed with 6mm tips tended to fail interfacially whereas the $5\sqrt{t}$ welds formed with 5mm tips exhibited plug failures. This could potentially be explained by an increase in notch acuity associated with the use of larger diameter electrode tips leading to an unfavourable stress state at the notch tip. However the $5\sqrt{t}$ welds formed with 7mm tips, which would be expected to suffer from the same problem, exhibited a mixture of plug and double plug failures.

5.2.3 Summary

This section evaluated the effect of using electrodes with tip diameters greater than the 5mm specified in BS1140:1993[41] for 1.2mm sheet steel on the weldability and weld strength of TRIP800. Significant increases in the maximum weld diameter possible before the occurrence of weld splash were observed when 5mm diameter tips were substituted for 6mm and 7mm diameter tips. Full plug failures were consistently achieved on chisel testing for weld diameters greater than approximately $6.3\sqrt{t}$.

The larger weld diameters achievable with the use of 6mm and 7mm diameter tips offered significant increases in the average lap shear loads compared to those sustained by $5\sqrt{t}$ welds formed with 5mm diameter electrodes. Increases in average cross tension failure loads were also observed for larger weld diameters. It was also noted that there was no deterioration in the lap shear or cross tension strength of $5\sqrt{t}$ welds produced using 6mm and 7mm electrodes compared to those produced with 5mm diameter tips.

5.3 The effect of post-weld heat treatment on the physical and mechanical properties of TRIP800, DP800 and DP1000 spot welds

This section discusses the results of attempts to influence the final properties of $5\sqrt{t}$ welds formed in the selected grades through the introduction of a discreet secondary current pulse into the basic single pulse weld schedules used in the preceding sections.

The weld parameters used in this section are summarised below:

- **Squeeze** - 35 cycles
- **Weld Pulse** - 10 cycles at current A
- **Pause** - 50 cycles
- **Secondary Pulse** - 50 cycles at current B
- **Electrode Force** - 5kN
- **Electrode tip diameter** - 5 mm

The secondary current pulse was intended to generate sufficient heat in the solidified weld nugget to temper the martensitic microstructures observed in the selected grades, thereby decreasing weld hardness and increasing weld toughness. The pause time between the primary weld pulse and the secondary tempering pulse was set at 50 cycles (1 second). This comparatively long pause was intended to ensure that transformation of the weld nugget and heat affected zones was complete before the secondary current was applied. The duration of the secondary current pulse was also set at 50 cycles to allow sufficient time for tempering to occur. It was decided that a further hold time after the passage of the secondary current would not be necessary since the weld had already solidified during the pause between the primary and second current pulses and would not be re-melted by the secondary pulse. The cooling effect of the electrodes on the weld region after the passage of the secondary current pulse was thereby eliminated, significantly reducing the cooling rate of the heat treated weld.

The initial post weld heat treatment trial was conducted on TRIP800. Once the approximate machine settings required to form a $5\sqrt{t}$ weld (Current A) had been established, the secondary current pulse was introduced to the weld schedule (Current B).

It was decided to initially pass a low secondary current through the solidified weld and then gradually increase the secondary current. The effect of increasing secondary current on weld hardness and microstructure was monitored by sectioning and mounting each successive weld using the methods described in section 4.4. The secondary phase shift was initially set at 25% compared to the 92% phase shift initially required to form the $5\sqrt{t}$ weld. These machine settings resulted in a primary weld current of approximately 6.6kA and a secondary current of 2.81kA. The secondary phase shift was gradually increased between successive welds until it was observed that a significant proportion of the weld nugget had apparently re-transformed to martensite at secondary phase shift of 45% (4.44kA secondary current). The above methodology was also applied to DP800 and DP1000. Once the current level necessary for the formation of a $5\sqrt{t}$ weld in each grade had been established, the secondary current pulse was introduced to the weld schedule and gradually increased between successive welds. As with TRIP800, it was observed that there was a critical current level at which a proportion of the weld nuggets in both grades appeared to re-transform to martensite. This critical current level was 4.98kA in the case of DP800 and 5.65kA in the case of DP1000.

5.3.1 Microhardness of $5\sqrt{t}$ welds subjected to secondary current pulse

Figure 5.83 illustrates the effect of increasing secondary current on the microhardness profiles of individual heat treated $5\sqrt{t}$ welds formed in TRIP800. Plotted on the same axes is the hardness profile of a $5\sqrt{t}$ weld which had received no heat treatment. As the secondary weld current increased from 2.81kA to 4.22kA the microhardness levels measured in the weld nuggets and heat affected zones steadily decreased, with the greatest reductions in hardness occurring in the central region of the weld nuggets. There was a significant reduction in weld microhardness as the secondary current increased from 3.74kA to 3.90kA, possibly signalling the occurrence of a phase transformation. As the secondary current level increased to 4.22kA, the microhardness levels measured in the individual weld nuggets continued to fall and the width of the softened region within the weld nuggets steadily increased.

In order to better visualise the effect of the 4.22kA secondary pulse, the microhardness profile of this weld was superimposed over the hardness profile of an un-treated TRIP800 weld as shown in figure 5.84. It can be seen that as well as yielding a reduction in weld microhardness from a peak of $541HV_{0.3}$ in the untreated weld to a minimum of $351HV_{0.3}$ in the central region of the heat treated weld, the 4.22kA secondary pulse also reduced the maximum microhardness levels recorded in the heat affected zones by approximately $90HV_{0.3}$. As described previously, a further increase in secondary current from 4.22kA to 4.44kA resulted in a significant change in weld appearance. The effect of this secondary current level on weld microhardness is also shown in figure 5.84. It can be seen that a significant proportion of this weld exhibited similar microhardness levels to the weld which had received no heat treatment, suggesting the presence of martensite. However, regions of the same weld nugget also exhibited similar hardness levels to those recorded in the weld nugget treated with the 4.22kA secondary pulse. The increase in secondary current from 4.22kA to 4.44kA also resulted in further reductions in the heat affected zone microhardness levels.

It was discovered that a 4.91kA secondary current pulse resulted in the greatest reductions in weld microhardness observed for the DP800 grade. Figure 5.85 shows the hardness profile of this weld plotted against the hardness profile of a DP800 weld which had received no heat treatment. It can be seen that as well as causing a reduction in weld microhardness from a peak of $458HV_{0.3}$ recorded in the untreated weld to a minimum of $288HV_{0.3}$ in the central region of the heat treated weld nugget, the 4.91kA secondary pulse also significantly reduced the microhardness levels recorded in the heat affected zones. As was observed with the TRIP800 grade, a further increase in secondary current resulted in a significant change in the visual appearance of the weld nugget. The hardness profile of the DP800 weld treated with a 4.98kA secondary pulse is also shown in figure 5.85. It can be seen that a significant proportion of this weld exhibited similar microhardness levels to the weld which had received no heat treatment again suggesting a partial re-transformation of the weld nugget to martensite. The increase in secondary current from 4.91kA to 4.98kA also resulted in further reductions in heat affected zone hardness levels.

It was discovered that a 5.21kA secondary current pulse resulted in the greatest reductions in weld microhardness observed for the DP1000 grade. Figure 5.86 shows the hardness profile of this weld plotted against the hardness profile of a DP1000 weld which had received no heat treatment. It can be seen that as well as causing a reduction in weld microhardness from a peak of $508HV_{0.3}$ recorded in the untreated weld to a minimum of $326HV_{0.3}$ in the central region of the heat treated weld nugget, the 5.21kA secondary pulse also reduced the maximum microhardness levels observed in the heat affected zones by $80\text{-}90HV_{0.3}$. The hardness profile of the DP1000 weld treated with a 5.65kA secondary pulse is also shown in figure 5.85. It can be seen that the region of the heat treated weld exhibiting similar microhardness levels to the untreated weld extended almost completely across the original weld nugget. It can also be seen that the microhardness levels measured in the heat affected zones were now comparable with those measured in the parent material.

5.3.2 Microstructural characteristics of $5\sqrt{t}$ welds subjected to secondary current pulse

Figures 5.87 to 5.95 illustrate the influence of increasing secondary current on the general appearance and microstructural characteristics of individual heat treated $5\sqrt{t}$ weld formed in TRIP800.

Figure 5.87a shows a macro of the TRIP800 weld treated with a 2.81kA secondary current pulse. This overall appearance of this weld is similar to the TRIP800 weld shown in figure 5.52a which had received no heat treatment. Figure 5.87b shows a detailed micrograph of the microstructure present at the approximate weld centre. The microstructure appears to be largely composed of lath martensite as in the weld which had received no heat treatment. However it can be seen that there is a dispersion of what appears to be carbide particles throughout the microstructure suggesting that tempering of the martensite had occurred.

Figure 5.88a shows a macro of the TRIP800 weld treated with a 3.25kA secondary current pulse. The overall appearance of this weld also resembled the TRIP800 weld

shown in figure 5.52a which had received no heat treatment. A detailed micrograph of the microstructure present at the approximate weld centre can be seen in figure 5.88b. The heat treatment appears to have resulted in the precipitation of what appears to be carbide particles from the martensite matrix as was observed for the 2.81kA secondary pulse. However there is also a dispersion of a light coloured phase visible throughout the microstructure which is thought to be ferrite.

Figure 5.89a shows a macro of the TRIP800 weld treated with a 3.74kA secondary current pulse. As with the welds treated with 2.81kA and 3.25kA secondary pulses, the general appearance of the weld treated with a 3.74kA secondary pulse does not appear to have been significantly altered as a result of the heat treatment. However it can be seen from the detailed micrograph shown in figure 5.89b that the microstructure at the approximate centre of the weld appears significantly different to the lath martensite observed in the untreated weld shown in figure 5.52g. The microstructural constituents are extremely fine and difficult to resolve using optical microscopy however it is possible to distinguish a substructure of laths or needles running through parts of the microstructure.

Figure 5.90a shows a macro of the TRIP800 weld treated with a 3.90kA secondary current pulse. It can be seen that there is a region approximately at the weld centre which has a paler appearance compared to the bulk of the weld nugget. This visually distinct region can be seen in greater detail in figure 5.90b which shows the edge of the heat treated weld nugget. Figure 5.90c shows a detailed micrograph taken from the approximate weld centre within the paler region visible in figure 5.90a. The lath substructure observed in the weld treated with the 3.74kA secondary pulse is much more clearly defined in this weld and extends throughout the area visible in the micrograph. Whilst the laths are still extremely fine, it can be seen that they are grouped into sheaves sharing a similar orientation.

Figure 5.91a shows a macro of the TRIP800 weld treated with a 4.05kA secondary pulse. The paler microstructure first observed in the weld treated with the 3.90kA secondary

current pulse now extends across a greater proportion of the weld nugget. This can be seen more clearly in figure 5.91b which shows the edge of the heat treated weld nugget. The new microstructure extends almost to the notch tip. Figure 5.91c shows a detailed micrograph of the microstructure present at the approximate weld centre. The microstructure in this region is visually similar to that observed at the centre of the weld treated with the 3.90kA secondary pulse (figure 5.90c) and appears to be composed of fine lath ferrite.

Figure 5.92a shows a macro the TRIP800 weld treated with a 4.22kA secondary current pulse. It can be seen that the new microstructure generated as a result of the secondary current pulse extends throughout the weld nugget and into the original heat affected zone produced by the primary welding pulse. Figure 5.92b shows the edge of the weld nugget and heat affected zone in greater detail. The transformed microstructure can be seen to extend well beyond the notch tip. A detailed micrograph of the microstructure present at the approximate weld centre can be seen in figure 5.92c. The microstructure appears to be composed largely of bainitic lath ferrite and is similar to those shown in figures 5.90c and 5.91c, however the lath substructure in this weld appears much coarser. It is possible to clearly distinguish individual ferrite laths as well as several prior austenite grain boundaries. The hardness of this microstructure is approximately $360HV_{0.3}$.

It can be seen by comparing figures 5.92a and 5.93 that when the secondary current level was increased from 4.22kA to 4.44kA, there was a significant change in the general appearance of the resulting weld nugget. Part of the weld nugget treated with a 4.44kA secondary pulse appears to have re-transformed to martensite on cooling instead of the bainitic ferrite observed in the weld nugget treated with a 4.22kA secondary pulse. As discussed in section 5.3.1, the microhardness levels recorded in this region of the weld were similar to those recorded in the TRIP800 weld which had not been subjected to any form of heat treatment, suggesting the presence of martensite. It was decided to conduct a detailed examination of the boundary between the two distinguishable microstructural regions within the heat treated weld nugget shown in figure 5.93. Figure 5.94 shows the area for investigation at a higher magnification. The numerals displayed on this image

indicate the locations of the microstructures displayed in figures 5.95a to 5.95e. It can be seen from these detailed micrographs that whilst traversing from position i to position v the microstructure gradually transforms from bainitic ferrite (figure 5.95a) to martensite (figure 5.95e). The microstructure shown in figure 5.95a closely resembles the microstructure found in the weld nugget treated with a 4.22kA secondary current pulse (figure 5.92c) whereas the microstructure shown in figure 5.95e more closely resembles the microstructure found in the heat affected zone of the TRIP800 weld nugget which had received no heat treatment (figure 5.52f). The microstructures shown in figures 5.95b to 5.95d contain a mixture of ferrite laths and martensite with the volume fraction of martensite increasing from position ii to position iv. Figure 5.96 illustrates the variation in Vickers microhardness traversing from the bainitic region of the weld shown on the left-hand side of the image to the martensitic region on the right. As the volume fraction of martensite in the microstructure increases at the expense of the lath ferrite (as illustrated in figures 5.95a to 5.95e) the microhardness of the material steadily increases.

Figure 5.97 shows a detailed micrograph of the microstructure found at the approximate centre of the DP800 weld treated with a 4.91kA secondary current pulse. As described in section 5.3.1, this secondary current level yielded the greatest reductions in weld nugget hardness observed for this grade. The microstructure in this weld appears to be composed largely of bainitic lath ferrite and is visually similar to the microstructure observed in the TRIP800 weld treated with a 4.22kA secondary current pulse (figure 5.92c). The hardness of this microstructure is approximately $300HV_{0.3}$.

Figure 5.98 shows a detailed micrograph of the microstructure found at the approximate centre of the DP1000 weld treated with a 5.21kA secondary current pulse. This secondary current level yielded the greatest reductions in weld nugget hardness observed for this grade. As in the heat treated DP800 weld nugget, the microstructure appears to be composed largely of bainitic lath ferrite. The hardness of this microstructure is approximately $330HV_{0.3}$. Figure 5.99 shows the microstructure visible in figure 5.98 at a higher magnification. The prior-austenite grain structure can be clearly seen. Sheaves of ferrite laths can be seen to extend across the prior-austenite grain visible at the

approximate centre of the micrograph. These laths appear to have nucleated at the prior austenite grain boundaries and are separated by a darker material which resembles martensite.

5.3.3 Mechanical properties of 5√t welds subjected to secondary current pulse

In order to establish the effect of the apparent transformation of the TRIP800, DP800 and DP1000 weld microstructure from lath martensite to bainitic ferrite on the mechanical properties of heat treated 5√t welds, it was decided to fabricate lap shear and cross tension samples using the approximate current settings which yielded the greatest reductions in weld hardness in each grade without a re-transformation to martensite. The secondary current level aimed for was 4.22kA in the case of TRIP800, 4.91kA in the case of DP800 and 5.21kA in the case of DP1000.

Lap shear performance

Five heat treated lap shear samples were tested for each of the three steel grades selected and an average failure load calculated. In each case the failure load was taken to be the maximum load sustained by each spot weld in kN prior to failure. The lap shear failure loads of the heat treated spot welds are summarised in table 5.12 along with the exact current conditions that formed each weld. Figure 5.100 shows the average lap shear strengths of the heat treated 5√t spot welds plotted against the average lap shear strengths of 5√t welds which had received no heat treatment. The heat treatment pulse had the effect of increasing the average lap shear failure load sustained by 5√t diameter welds formed in TRIP800 from 15.17kN to 16kN. However, the average failure load of DP800 fell from 16.19kN to 14.21kN and the average failure load of DP1000 fell from 17.68kN to 14.53kN.

Typical load versus displacement curves exhibited by heat treated TRIP800, DP800 and DP1000 lap shear samples are shown in figures 5.101, 5.102 and 5.103 respectively. It can be seen by comparing with figures 5.20, 5.21 and 5.22 that the initial loading of the heat treated spot welds occurred in a similar manner to welds that had received no heat

treatment. However, after weld failure had initiated the load sustained by the samples rapidly fell to zero suggesting that the welds had failed in a catastrophic manner.

Figures 5.104, 5.105 and 5.106 show photographs of the typical lap shear failure mode of heat treated welds formed in TRIP800, DP800 and DP1000 respectively. Failure in each case occurred through the weld nugget in the plane of the original sheet to sheet interface with little deformation of the parent material. As discussed in section 5.1.3, the DP800 and TRIP800 lap shear samples which received no post weld heat treatment all exhibited a double plug failure mechanism with failure occurring in the parent material. The majority of the as-welded DP1000 lap shear samples exhibited shear plug failure with fracture initiating at the notch tip and propagating through the heat affected zone.

Due to the deterioration in the lap shear failure mode described above, it was decided to examine the interfacial fracture surfaces shown in figures 5.104 to 5.106 using a scanning electron microscope (SEM). SEM images of these fracture surfaces are shown in figures 5.107 to 5.109 respectively. The elongated dimples visible in figure 5.107 indicate that fracture through the heat treated TRIP800 weld occurred via ductile shear rupture. The dimples observed on the interfacial fracture surface of the heat treated DP800 weld had a slightly more faceted appearance than those observed for the TRIP800 weld as can be seen from figure 5.108. However it is not thought that this was indicative of brittle failure. The interfacial fracture surface of the heat treated DP1000 weld is shown in figure 5.109. It can be seen that failure in this weld also occurred via ductile shear rupture.

Cross tension performance

The approximate weld current settings that were used to fabricate heat treated TRIP800, DP800 and DP1000 lap shear samples were also used to fabricate cross tension samples. Five cross tension samples were tested for each steel grade investigated and an average failure load calculated. In each case the failure load was taken to be the maximum load sustained by each spot weld in kN prior to failure. The cross tension failure loads of the heat treated spot welds are summarised in table 5.13 along with the current conditions

that formed each weld. Figure 5.110 shows the average cross tension strengths of the heat treated spot welds plotted against those of welds which had received no heat treatment. The introduction of a secondary current pulse into the weld schedule had the effect of increasing the average cross tension failure load sustained by $5\sqrt{t}$ diameter welds formed in DP800, TRIP800 and DP1000. For example, the average cross tension failure load of DP1000 increased from 7.95kN to 10.66kN. In the majority of cases failure resulted in the weld being torn from one of the coupons in the joint (plug failure).

Typical cross tension load versus displacement curves exhibited by heat treated TRIP800, DP800 and DP1000 spot welds are shown in figures 5.119, 5.120 and 5.121 respectively. It can be seen by comparing with figures 5.40, 5.41 and 5.42 that the overall shape of the load versus extension plots exhibited by the heat treated welds is similar to those exhibited by welds which had received no heat treatment suggesting that weld failure occurred via a similar mechanism.

5.3.4 Summary

This section considered the potential for controlling final weld properties through modifications to the basic single pulse welding schedule used throughout the preceding experiments, specifically through the introduction of a secondary current pulse into the weld schedule. It was discovered that in-process heat treatment could generate significant reductions in weld microhardness in TRIP800, DP800 and DP1000 and a transition in the failure mode of welds formed in TRIP800 and DP1000 from interfacial/partial plug failure on chisel testing to full plug failure.

Microstructural examination of heat treated TRIP800, DP800 and DP1000 welds revealed that as the secondary current level increased, there was a transition in the weld nugget microstructure from martensite to bainitic ferrite. Further increases in secondary current led to the re-formation of martensite in the weld nuggets of all three grades, however this corresponded with the greatest reductions in heat affected zone hardness levels.

It was discovered that when the machine settings which yielded the greatest reductions in weld hardness in TRIP800, DP800 and DP1000 were used to fabricate cross tension samples, higher average failure loads were sustained compared to the samples which had received no heat treatment suggesting an increase in weld ductility. However, when the same schedules were used to fabricate lap shear samples there was a transition in the lap shear failure mode from double plug failure in the case of DP800 and TRIP800 and shear plug failure in the case of DP1000 to interfacial failure in all three cases. Whilst the average lap shear failure load sustained by DP800 and DP1000 decreased as a result of the applied heat treatments, the average failure load sustained by the TRIP800 lap shear samples increased despite the deterioration in failure mode. SEM examination of the failed lap shear welds indicated that failure was occurring via shear rupture in each case. Typical lap shear load versus displacement curves exhibited by heat treated samples indicated that the welds were failing in a catastrophic manner with little deformation of the parent material. Further work would be beneficial to establish if adjustments to the current level and duration of the secondary pulse could yield improvements in lap shear performance.

5.4 The resistance spot welding of advanced high strength steels to low carbon formable mild steel

This section discusses the effects of joining selected advanced high strength grades to low carbon mild steel on the weld growth characteristics and the microstructural and mechanical properties of welds compared to joints where only one of the two component grades was present. The AHSS grades selected for this investigation were DP800, DP1000, MS1400 and TRIP800. The 1.15mm Corus low carbon formable strip steel used in this section was the same grade as that discussed in section 5.1 and was selected due to the fact that Corus have supplied this particular grade to automotive manufacturers. For brevity this grade will be referred to as LC henceforth. LC is typical, both in terms of sheet thickness and alloy content, of the formable grades from which body-in-white components such as the floor pan and boot floor are usually fabricated. Therefore it is likely that components that could potentially offer crash performance benefits when fabricated from advanced high strength steels, such as the gearbox tunnel and side pillars, would be joined to components fabricated from grades with significantly lower alloy contents. By joining a high strength grade to low carbon mild steel, the alloy composition of the resulting weld nugget should theoretically become an average of the compositions of the two parent grades, assuming that the weld nugget is formed from equal amounts of material from each sheet in the joint. It is therefore important to determine the effect of this weld nugget 'dilution' on weld hardness, strength and failure mode compared to joints in which only the high strength grade is present.

5.4.1 Growth characteristics and failure mode of welds formed between LC and DP800, DP1000, TRIP800 and MS1400

In order that the results of this weldability trial were directly comparable with those described in section 5.1.1, the same weld schedule, electrode force and electrode configuration were used. These parameters are summarised overleaf:

- **Squeeze** - 35 cycles
- **Weld** - 10 cycles
- **Hold** - 5 cycles
- **Electrode Force** - 3.2 kN
- **Electrode tip diameter** - 5 mm

Figure 5.114 shows the relationship between weld current and weld diameter for welds formed between 1.2mm DP800 and 1.15mm LC. It can be seen that melting at the sheet to sheet interface and the formation of solid weld nuggets first began to occur at a weld current of approximately 6.1kA. The diameter of individual welds increased steadily with increasing current up to a maximum of 8.92kA where weld splash first began to occur. The current range over which weld diameters in excess of $3.5\sqrt{t}$ were achieved was approximately 2.2kA. The current range over which weld diameters in excess of $5\sqrt{t}$ were achieved was approximately 1.2kA. The maximum weld size achieved before the occurrence of splash was 7.05mm or $6.5\sqrt{t}$. The point at which full plugs were consistently obtained on chisel testing corresponded with a weld diameter of approximately 2.65mm or $2.5\sqrt{t}$. In each case the plug was pulled from the LC sheet. The current range over which full plugs were achieved was approximately 2.7kA.

Figure 5.115 shows the relationship between weld current and weld diameter for welds formed between 1.2mm DP1000 and 1.15mm LC. It can be seen that melting at the sheet to sheet interface and the formation of solid weld nuggets first began to occur at a weld current of approximately 6kA. The diameter of individual welds increased steadily with increasing current up to a maximum of 8.97kA where weld splash first began to occur. The current range over which weld diameters in excess of $3.5\sqrt{t}$ were achieved was approximately 2.1kA. The current range over which weld diameters in excess of $5\sqrt{t}$ were achieved was approximately 1.1kA. The maximum weld size achieved before the occurrence of splash was 6.82mm or $6.3\sqrt{t}$. The point at which full plugs were consistently obtained on chisel testing corresponded with a weld diameter of approximately 2.86mm or $2.6\sqrt{t}$. In each case the plug was pulled from the LC sheet. The current range over which full plugs were achieved was approximately 2.72kA.

Figure 5.116 shows the relationship between weld current and weld diameter for welds formed between 1.0mm MS1400 and 1.15mm LC. It can be seen that melting at the sheet to sheet interface and the formation of solid weld nuggets first began to occur at a weld current of approximately 5.7kA. The diameter of individual welds increased steadily with increasing current up to a maximum of 8.7kA where weld splash first began to occur. The current range over which weld diameters in excess of $3.5\sqrt{t}$ were achieved was approximately 2.3kA. The current range over which weld diameters in excess of $5\sqrt{t}$ were achieved was approximately 1.4kA. The maximum weld size achieved before the occurrence of splash was 6.65mm or $6.4\sqrt{t}$. The point at which full plugs were consistently obtained on chisel testing corresponded with a weld diameter of approximately 2.61mm or $2.5\sqrt{t}$. In each case the plug was pulled from the LC sheet. The current range over which full plugs were achieved was approximately 2.81kA.

Figure 5.117 shows the relationship between weld current and weld diameter for welds formed between 1.2mm TRIP800 and 1.15mm LC. It can be seen that melting at the sheet to sheet interface and the formation of solid weld nuggets first began to occur at a weld current of approximately 5.6kA. The diameter of individual welds increased steadily with increasing current up to a maximum of 8.39kA where weld splash first began to occur. The current range over which weld diameters in excess of $3.5\sqrt{t}$ were achieved was approximately 2kA. The current range over which weld diameters in excess of $5\sqrt{t}$ were achieved was approximately 0.9kA. The maximum weld size achieved before the occurrence of splash was 6.5mm or $6\sqrt{t}$. The point at which full plugs were consistently obtained on chisel testing corresponded with a weld diameter of approximately 2.87mm or $2.7\sqrt{t}$. In each case the plug was pulled from the LC sheet. The current range over which full plugs were achieved was approximately 2.46kA.

By comparing figures 5.114 to 5.117 with figures 5.5 to 5.8 respectively it can be seen that maximum weld diameters achieved for each AHSS to LC combination before the occurrence of weld splash were greater than the maximum weld diameters achieved where the AHSS grades were welded to themselves. The weldability ranges of DP1000, MS1400 and TRIP800 were also significantly improved as a result of being joined to LC.

Full plug failures were achieved on chisel testing from weld diameters well below $3.5\sqrt{t}$ in each case. It is thought that this was due to the greater resistance to deformation of the AHSS component concentrating the impact energy imparted on the joint by the chisel in the LC component.

The approximate current requirements to form $3.5\sqrt{t}$ diameter welds between the four AHSS to LC combinations investigated are listed in table 5.14. It can be seen by comparing with table 5.1 that the current required to form a $3.5\sqrt{t}$ diameter weld in each AHSS to LC joint was significantly greater than that required to form the same weld diameter between two sheets of the high strength grade in question. It is thought that the substitution of one of the high strength sheets with LC lead to a reduction in the total resistance to current flow through the workpiece since LC had a significantly lower alloy content than all of the high strength grades (see table 4.1) and a correspondingly lower bulk resistivity. As described previously, according to joules law ($H = KI^2Rt$) any reduction in the total resistance to current flow (R) must be met with a proportional increase in weld current (I) in order that the same amount of heat energy (H) is generated (and material melted) during a fixed period of time, which in this case was 10 cycles or 0.2 seconds.

Once the approximate welding conditions necessary to form $5\sqrt{t}$ diameter welds in each of the AHSS to LC combinations had been established, lap shear and cross tension samples were fabricated using the methods described in section 4.2.3. Weld cross sections were also mounted in resin in preparation for microhardness measurements and microstructural examination using the methods described in section 4.4.

5.4.2 Lap shear performance of $5\sqrt{t}$ welds formed between LC and DP800, DP1000, MS1400 and TRIP800

Five lap shear samples were tested for each of the four AHSS to LC combinations investigated and an average failure load calculated. In each case the failure load was taken to be the maximum load sustained by each spot weld in kN prior to failure. The results of the lap shear tests are displayed in table 5.15 and summarised in figure 5.118.

It can be seen by comparing table 5.15 with table 5.3 that in each case the average failure loads of the AHSS to LC lap shear samples were significantly lower than those of samples fabricated from a pair of AHSS coupons. For example, the average failure load of the DP1000 lap shear samples was 17.68kN whereas the average failure load of the DP1000 to LC lap shear samples was 8.19kN. In each case failure initiated in the LC component of the lap shear samples and resulted in the weld being torn from LC coupon with minimal deformation of the high strength coupon. The average lap shear failure load of the AHSS to LC samples was similar to that of the samples fabricated from a pair of LC coupons, indicating that the strength of the joint was limited by the strength of the LC component.

5.4.3 Cross tension performance of $5\sqrt{t}$ welds formed between LC and DP800, DP1000, MS1400 and TRIP800

Five cross tension samples were tested for each of the four AHSS to LC combinations investigated and an average failure load calculated. In each case the failure load was taken to be the maximum load sustained by each spot weld in kN prior to failure. The results of the cross tension tests are displayed in table 5.16 and summarised in figure 5.119. It can be seen by comparing table 5.16 with table 5.5 that, with the exception of MS1400, the average failure loads of the AHSS to LC cross tension samples were lower than those of samples fabricated out of a pair of AHSS coupons. For example, the average failure load of the DP1000 cross tension samples was 7.95kN compared to the average failure load of the DP1000 to LC cross tension samples which was 6.25kN. The average failure load of the MS1400 to LC cross tension samples was 4.60kN whereas the average failure load of the MS1400 cross tension samples was 4.22kN. In all cases failure initiated in the LC component of the cross tension samples and resulted in the weld being torn from the LC sheet.

It can also be seen from figure 5.119 that with the exception of the DP800 to LC cross tension samples, the average failure load of the LC samples was marginally higher than that of the AHSS to LC samples i.e. the substitution of one of the LC coupons in the cross tension samples with an AHSS coupon led to a reduction in average failure load. For

example, the average failure load of the cross tension samples fabricated from a pair of LC coupons was 6.85kN compared to the average failure load of the TRIP800 to LC samples which was 6.50kN.

5.4.4 Microstructural characteristics of welds formed between LC and DP800, DP1000, MS1400 and TRIP800

Example micrographs from the weld nuggets and heat affected zones of $5\sqrt{t}$ welds formed in the four AHSS to LC combinations investigated can be seen in figures 5.120 to 5.123.

Figures 5.120a to 5.120d show the microstructural features observed in the DP800 to LC joint. Figure 5.120a shows a macro of the weld nugget. The difference in microstructural appearance between the DP800 parent material and the LC parent material can be clearly seen. The boundary between the weld nugget and the un-melted LC heat affected zone can also be clearly distinguished. The variations in microstructure from the parent metal in both sheets to the weld nugget are shown in figure 5.120b. The DP800 and LC heat affected zones do not appear to have been significantly affected as a result of being joined to a dissimilar grade. Figure 5.120c shows a detailed micrograph of the weld nugget microstructure. It can be seen that the weld nugget appears to be composed of lath martensite and bears a strong resemblance to the DP800 weld microstructure (figure 5.49g). Figure 5.120d shows a detailed micrograph of the boundary between the weld nugget and the LC heat affected zone and clearly illustrates the difference in microstructure between these two regions.

Figures 5.121a to 5.121d show the microstructural features observed in the DP1000 to LC joint. Figure 5.121a shows a macro of the weld nugget. The overall appearance of the weld is similar to that formed between DP800 and LC. The variations in microstructure from the parent metal in both sheets to the weld nugget can be seen in figure 5.121b. The DP1000 and LC heat affected zones do not appear to have been significantly affected as a result of being joined to a dissimilar grade. Figure 5.121c shows a detailed micrograph of the weld nugget microstructure. As with the DP800 to

LC joint, the microstructure of the weld nugget formed between DP1000 and LC appears to be composed of lath martensite. Figure 5.121d shows a detailed micrograph of the boundary between the weld nugget and the LC heat affected zone and illustrates the difference in microstructure between these two regions.

Figures 5.122a to 5.122d show the microstructural features observed in the MS1400 to LC joint. Figure 5.122a shows a macro of the weld nugget. The transition in microstructure from the parent metal in both sheets to the weld nugget can be seen in figure 5.122b. The MS1400 and LC heat affected zones do not appear to have been significantly affected as a result of being joined to a dissimilar grade. Figure 5.122c shows a detailed micrograph of the weld nugget microstructure. It can be seen that the weld nugget appears to be composed of lath martensite. Figure 5.122d shows a detailed micrograph of the boundary between the weld nugget and the LC heat affected zone and illustrates the difference in microstructure between these two regions.

Figures 5.123a to 5.123d show the microstructural features observed in the TRIP800 to LC joint. Figure 5.123a shows a macro of the weld nugget. The transition in microstructure from the parent metal in both sheets to the weld nugget can be seen in figure 5.123b. The TRIP800 and LC heat affected zones do not appear to have been significantly affected as a result of being joined to a dissimilar grade. Figure 5.123c shows a detailed micrograph of the weld nugget microstructure. As with the other AHSS to LC joints, the microstructure of the weld nugget formed between TRIP800 and LC appears to be composed of lath martensite. Figure 5.123d shows a detailed micrograph of the boundary between the weld nugget and the LC heat affected zone and illustrates the difference in microstructure between these two regions.

5.4.5 Microhardness of welds formed between LC and DP800, DP1000, MS1400 and TRIP800

The microhardness profiles of $5\sqrt{t}$ welds formed between the four AHSS to LC combinations investigated are shown in figures 5.124 to 5.127. Plotted on the same axes are the hardness profiles of a weld formed between two sheets of the AHSS grade in

question and a weld formed between two sheets of LC. The reductions in weld hardness associated with the replacement of an AHSS sheet with LC varied, however in each case the hardness of the weld nugget remained significantly higher than the hardness of the LC heat affected zone.

The average weld nugget microhardness levels measured in $5\sqrt{t}$ welds formed between the four AHSS to LC combinations investigated are shown in table 5.17. It can be seen by comparing tables 5.7 and 5.17 that the weld nugget formed between two sheets of DP800 had an average microhardness of approximately $449HV_{0.3}$ whereas the weld nugget formed between DP800 and LC had an average microhardness of approximately $425HV_{0.3}$ representing an approximate reduction of $24HV_{0.3}$ or 5%. Greater reductions in weld hardness were observed when DP1000, MS1400 and TRIP800 were joined to LC. The weld formed between two sheets of DP1000 exhibited an average microhardness of $499HV_{0.3}$ compared to the weld nugget formed between DP1000 and LC which exhibited an average microhardness of $450HV_{0.3}$ representing an approximate reduction of $49HV_{0.3}$ or 10%. The weld formed between two sheets of MS1400 exhibited an average microhardness of $514HV_{0.3}$ compared to the weld nugget formed between MS1400 and LC which exhibited an average microhardness of $440HV_{0.3}$ representing an approximate reduction of $74HV_{0.3}$ or 14%. The weld formed between two sheets of TRIP800 exhibited an average microhardness of $527HV_{0.3}$ compared to the weld nugget formed between TRIP800 and LC which exhibited an average microhardness of $457HV_{0.3}$ representing an approximate reduction of $70HV_{0.3}$ or 13%.

It can also be seen from figures 5.124 to 5.127 that there was a significant increase in the hardness of the LC heat affected zone in close proximity to the weld nugget in the four AHSS to LC joints compared to the heat affected zone in the LC joint. The maximum hardness of the LC heat affected zones in the AHSS to LC joints ranged from approximately $256HV_{0.3}$ in the DP800 to LC joint to $300HV_{0.3}$ in the TRIP800 to LC joint compared to approximately $180HV_{0.3}$ in the heat affected zones of the weld formed between two sheets of LC.

5.4.6 Summary

This section presented the effects of joining selected advanced high strength steel grades to low carbon (LC) formable mild steel on weld hardness, strength and failure mode. The weldability ranges of DP1000, MS1400 and TRIP800 were significantly improved as a result of being joined to LC. For each steel combination studied, full plug failures were achieved from weld diameters well below $3.5\sqrt{t}$. Alloying between the selected high strength grades and LC lead to reductions in weld hardness levels compared to joints in which only the AHSS component was present. The weld nuggets formed between the high strength grades and LC appeared to be composed of lath martensite. This observation was supported by microhardness measurements. The microstructure and microhardness of the heat affected zones in the high strength component did not appear to be significantly affected as a result of being welded to LC, however hardening of the LC heat affected zone immediately adjacent to the weld nugget suggests that carbon diffusion from the weld nugget into the un-melted LC heat affected zone had occurred.

The strengths exhibited by AHSS to LC lap shear samples were similar to those exhibited by LC lap shear samples and were significantly lower than those exhibited by corresponding AHSS lap shear samples. The average failure loads of the AHSS to LC cross tension samples were marginally lower than those sustained by the cross tension samples fabricated from a pair of LC coupons with the exception of the DP800 to LC samples. In each case failure occurred in the LC parent material without significant deformation of the high strength coupon, indicating that the lap shear and cross tension strength of dissimilar metal joints is limited by the lower strength component.

6. GENERAL DISCUSSION

Weight reduction of the body-in-white structure is increasingly necessary to improve vehicle fuel efficiency and thereby reduce CO_2 emissions. This goal must be achieved without compromising the strength of the body-in-white structure.

To this end steel manufacturers are continuing to develop advanced high strength grades such as dual phase and TRIP which not only exhibit high tensile strengths and excellent work hardening characteristics but also retain a comparable degree of formability to mild steel grades. The utilisation of such grades could yield significant benefits in terms of enhanced crash survivability for vehicle occupants and possible weight reduction of body-in-white structures by substituting for lower strength grades with greater sheet thicknesses. However, in order for automotive manufactures to take advantage of the potential benefits offered by advanced high strength steels it must be possible to integrate them into existing production facilities with minimal alterations to plant practice. A particular requirement is that they must be readily spot-weldable.

The complex alloy compositions of these advanced high strength grades coupled with the extremely high cooling rates associated with the resistance spot welding process have been shown to result in weld microstructures with properties differing greatly from the parent material. Of primary concern for automotive manufacturers is the potential for the formation of martensite in weld nuggets and heat affected zones, since its high hardness and low ductility are thought to result in poor weld performance.

The present work has been undertaken to determine the weldability of a range of commercially available advanced high strength steels using basic welding schedules typical of those used in production environments and to develop an understanding of the microstructural transformations that occur in these grades as a result of the resistance welding process.

A total of three dual phase steels were studied along with two TRIP steels and a martensitic grade. The selected grades represented a wide range of chemical

compositions and mechanical properties. In order to evaluate the effect of increasing carbon equivalent on weldability and weld performance and to provide a suitable benchmark, a low carbon formable strip steel and a high strength IF grade were also included in the investigation. The carbon equivalents of the selected grades, as calculated by the Ito-Bessyo equation[42], ranged from 0.045 to 0.307.

6.1 Properties of resistance welds formed in advanced high strength steels using basic welding schedules

The aim of the preliminary investigation was to assess the properties of resistance welds formed in a range of commercially available AHSS grades using a basic single-pulse weld schedule typical of those used in a production environment. By comparing the weldability of the selected advanced high strength steels with steels traditionally used in body-in-white construction, such as low carbon mild steel and high strength IF steel, it was possible to gain an indication as to the ease with which the advanced high strength grades could be integrated into body-in-white construction using established production techniques and acceptance criteria. A detailed microstructural examination of the weld nuggets and heat affected zones was also carried out in addition to microhardness surveys in order to assess the relationships between the physical and microstructural properties of AHSS spot welds and their mechanical performance and failure mode. The techniques used during the course of this investigation to assess weldability and weld quality included the chisel test, lap shear and cross tension tests and the production of weld growth curves for each of the selected grades. The results of these tests are discussed below.

6.1.1 Weldability

The initial welding conditions used for each grade were chosen in accordance with the guidelines laid out in BS1140:1993[41] for the joining of un-coated low carbon mild steel. The methods used in the production of weld growth curves are described in section 4.2.2.

Weld growth curves produced for each the eight grades under investigation are presented in figures 5.1 to 5.14. The weldability of DP600, TRIP600 and DP800 compared favourably with that of the low alloy grades, both in terms of weld failure mode and the current range over which weld diameters of $3.5\sqrt{t}$ (where t = sheet thickness in mm) or greater were achieved. This indicates that these grades are entirely weldable using parameters recommended for mild steel grades and could therefore be easily incorporated into vehicle design without any significant alterations to plant practice. However, it should be noted that full plug failures were not observed in these grades below a weld

size of $4\sqrt{t}$ and therefore it would be beneficial to increase the minimum weld size requirement from $3.5\sqrt{t}$ in order to increase the likelihood of full plug failures on chisel testing.

Full plug failures were achieved from smaller weld diameters in DP600, TRIP600 and DP800 than in IF260. It is thought that the tendency of the IF 260 spot welds to fail as partial plugs at weld diameters less than approximately $5.5\sqrt{t}$ (figure 5.2) was due to the comparatively high phosphorous content of this grade (0.0532 wt%). As described in the literature review, elements such as manganese and phosphorus are frequently added to IF steel to provide solid solution strengthening. The link between phosphorus and a tendency towards interfacial failure on chisel testing has been widely reported in welding literature[71, 73, 77, 91]. SEM examination of an interfacially failed IF260 weld revealed evidence of inter-granular fracture (figure 5.71b) which can be indicative of the presence of weak grain-boundary precipitates. It is thought that segregation of phosphorous to the columnar austenite grain boundaries during solidification provided a low energy fracture path through the weld nugget thus encouraging interfacial failure.

It was observed that there was a general decrease in maximum weld diameter that could be achieved with increasing alloy content of the parent material. Waddell[44] indicated that high alloy content and high bulk resistivity is generally accompanied by a reduction in thermal conductivity. It is thought that this had the effect of increasing not only the amount of heat energy generated in the AHSS grades at a particular current level compared to low alloy grades, but also decreasing the rate of heat conduction away from the weld area, thus increasing the rate of weld growth and the tendency for weld splash. As a result the preferred weld diameter of $5\sqrt{t}$ could not be achieved in DP1000, MS1400 and TRIP800 at an electrode force of 3.2kN, before the occurrence of weld splash. This problem was successfully overcome by increasing the electrode force levels used beyond those specified in BS1140:1993[41] when welding the above grades. In the case of TRIP800 an electrode force of 5kN was required to contain the growing weld nugget, representing an increase of 56% over the 3.2kN specified in BS1140:1993[41]. However, even at 5kN electrode force, the required diameter of $5\sqrt{t}$ was still only just achieved

before the splash limit of the material was reached. It was discovered that in the case of TRIP800, increasing the electrode force from 3.2kN to 5kN had the effect of increasing the current requirement to form equivalent weld sizes. It is thought that the increased electrode force improved the electrical contact at the sheet to sheet interface thereby reducing the contact resistance in this region, as discussed in section 5.1.2. The effect of electrode force on weld current requirements has been previously shown for HSLA[71] and rephosphorised[77] steel. Both papers indicate a shift to higher weld currents as electrode force is increased.

Due to the continued difficulty in obtaining the preferred weld diameter of $5\sqrt{t}$ in TRIP800, it was decided to investigate the potential of increasing the maximum achievable weld diameter through the use of electrodes with tip diameters greater than the 5mm recommended in BS1140:1993[41] for 1.2mm uncoated steel. The use of 6mm and 7mm diameter electrodes allowed the consistent production of $5\sqrt{t}$ welds in TRIP800 with a 10 cycle weld pulse at current levels well below the splash limit. The maximum weld diameters achieved were 7.14mm ($6.5\sqrt{t}$) using 6mm diameter tips and 7.98mm ($7.3\sqrt{t}$) using 7mm diameter tips. It was observed that for both electrode geometries that full plug failures were achieved on chisel testing for weld diameters greater than approximately $6.3\sqrt{t}$ suggesting that the ratio of sheet thickness to weld diameter had exceeded a critical value for this particular grade. It would therefore be beneficial for automotive manufacturers to use over-sized electrode tips and increase the preferred weld size from $5\sqrt{t}$ to $6.5 - 7\sqrt{t}$ when joining advanced high strength steels such as TRIP800 in order to ensure that these grades pass basic production line quality tests such as chisel and peel testing.

SEM investigation of interfacial fracture surfaces revealed that in all of the grades studied, including LC and IF260, failure occurred via a combination of brittle fracture and ductile dimple rupture despite the vast differences in alloy chemistry, weld microhardness and weld microstructures observed between the advanced high strength steels and the lower strength grades, suggesting that fracture surface appearance is not necessarily a good indicator of weld ductility. The SEM also revealed the presence of a

dispersion of intermetallic inclusions throughout the weld nuggets formed in the selected AHSS grades. It is thought likely that these inclusions acted as initiation sites for microvoid formation, either by fracturing or through decohesion from the matrix material, thus producing the distinctive ductile cup and cone fracture surfaces observed in these grades.

6.1.2 Mechanical properties

The lap shear failure mechanisms exhibited by TRIP600, DP600, DP800 and TRIP800 compared favourably with LC and IF260 in that full plug or double plug failures were observed in each case with failure occurring in the parent metal. Average lap shear failure loads were also higher than the minimum specified by BS1140:1993[41] in all cases. Therefore the lap shear performance of DP600, TRIP600, DP800 and TRIP800 can be considered acceptable. It was observed that as the tensile strength of the parent material increased, the lap shear strength of $5\sqrt{t}$ welds formed in those materials also increased up to a maximum parent metal tensile strength of $1048N/mm^2$ (DP1000). MS1400, which exhibited a tensile strength of $1479N/mm^2$, sustained a lower average lap shear load prior to failure than DP1000, DP800 or TRIP800. It was initially thought that this was due to the reduced sheet thickness of MS1400 (1.0mm vs. 1.2mm) and the correspondingly smaller diameter of $5\sqrt{t}$ welds formed in that grade. However, when the minimum shear strength required by BS1140:1993[41] was calculated, which took into account the reduced sheet thickness and weld diameter, it was discovered that the average lap shear strength of MS1400 was still significantly lower than expected. Despite sustaining the greatest lap shear load before failure of all of the grades studies, DP1000 also failed to meet the minimum shear strength required by BS1140:1993[41]. A transition in lap shear failure mode was observed from double plug failure as in the case of DP600, DP800 and TRIP800 to shear plug failure in the case of DP1000 and MS1400. It has been suggested by Shi & Westgate[96], who observed a similar trend in lap shear strength as parent metal strength increased, that the lower than expected lap shear performance of grades which contain a large volume fraction of martensite and tensile strengths in excess of $800N/mm^2$ is due to softening of the parent material in the heat affected zone. Whilst softening of the outermost heat affected zone was observed in both DP1000 and MS1400

in this investigation, it was discovered that in each case failure did not occur in this softened region and instead initiated at the sharp notch tip at the periphery of the weld nugget before propagating through the coarse inner heat affected zone in close proximity to the weld nugget (see figure 5.33) or as in the case of one of the MS1400 lap shear samples, through the weld nugget itself in the plane of the original sheet to sheet interface. Figure 6.1 illustrates the various stages of deformation that a lap shear sample undergoes prior to failure. It can be seen that the spot weld at the centre of the sample rotates as the lap shear test proceeds. It is thought that the transition in lap shear failure mode observed for DP1000 and MS1400 was due to the higher strength and resistance to deformation of the parent metal limiting the rotation of the weld nugget observed with the lower strength grades thus concentrating the load on the edge of the spot weld rather than on the parent material surrounding the spot weld. Therefore the lap shear strength exhibited by these grades becomes more dependent on the strength of the spot weld itself or the heat affected zone than on the strength of the parent material.

The cross tension strength was found to be significantly less dependent on parent material strength than lap shear strength. An increase in tensile strength of approximately 700N/mm^2 yielded an increase in average cross tension strength of just 1.1kN as can be seen from table 5.6. The average cross tension failure load of MS1400 was lower than that of the low carbon mild steel grade studied. This indicates that the enhanced mechanical properties offered by advanced high strength steels over conventional steel grades may be limited if the spot welds in an automotive assembly are loaded in tension as opposed to shear. Other work[52, 96] has also indicated that cross tension strength is largely independent of parent material strength.

6.1.2 Weld microstructures and microhardness

The microstructural characteristics of welds formed in the selected steel grades were presented in figures 5.45 to 5.52 and described in section 5.1.5. It was observed that the weld nuggets formed in all eight of the grades studied shared a common geometric appearance irrespective of the microstructural constituents found within the weld. The solidified nuggets were approximately oval in shape and were comprised of

microstructures that transformed from a coarse columnar prior-austenite grain structure. This is also illustrated in figure 5.75c which shows columnar dendrites growing into a void in an interfacially failed spot weld. The grains contained within the electrode area are aligned perpendicular to the original sheet to sheet interface whereas grains at the periphery of the weld tend to be aligned roughly with the sheet to sheet interface. During the solidification of a molten weld nugget, heat is rapidly conducted away from the weld region into the water cooled electrodes and the bulk material. The strong unidirectional cooling effect of the electrodes in close proximity to the solidifying weld nugget results in vertical growth of the columnar grains within the electrode area. However in welds that have a larger diameter than the electrode tip, the rate of heat conduction into the bulk material at the periphery of the weld is greater than into the electrodes resulting in lateral growth of the columnar grains in this region. This can be seen in figure 6.2. It is thought that the presence of these lateral dendrites at the periphery of the weld explain the tendency of welds exhibiting high hardness to initially fail in the plane of the original sheet to sheet interface along the prior-austenite grain boundaries between the lateral dendrites as opposed to failing in the parent material or heat affected zone. Den Uijl[73] proposed a three-step weld schedule in order to eliminate the disadvantageous dendrite structure described above. A primary welding pulse would form a weld nugget of the desired dimensions, followed by a secondary pulse designed to re-melt the edge of the weld nugget and destroy the lateral dendrite structure and also dissolve any phosphorus that may have precipitated at the prior-austenite grain boundaries during solidification. Finally a third current pulse would temper the phosphorus-bearing martensite formed by the secondary pulse to the desired hardness levels. Little information was given as to the duration of the individual pulses or the current levels used, however it was claimed that full plug failures could be achieved in two variants of a TRIP700 grade which had previously shown a tendency towards interface failure.

The cooling rates generated during the resistance welding process are extremely high due primarily to the presence of the water-cooled copper electrodes in close proximity to the solidifying weld nugget coupled with the extremely localised heating and comparatively small volume of material melted. Cooling rates in the order of 10,000°C/s have been

calculated for welds formed in strip with a thickness of around 1.0mm[90]. Therefore resistance spot welds can be expected to exhibit the maximum hardness possible for a particular alloy chemistry. The influence of different alloying elements on the hardenability of a particular steel alloy varies significantly. The relative contribution of each alloying element to overall hardenability can be expressed in a carbon equivalent equation. The Ito-Bessyo carbon equivalent equation[42] was used during the course of this investigation as it contains terms for the majority of alloying elements present in the selected steel grades and has been suggested as the most suitable equation for steels containing less than 0.18wt% carbon[94]. Carbon has a particularly pronounced effect on the hardenability of steel. The maximum solubility of carbon atoms is significantly higher in austenite than in ferrite since the interstitial sites which the carbon atoms occupy are larger in a face centred cubic structure than in a body centred cubic structure. Due to the comparatively high solubility of carbon in austenite, when a low carbon steel is normalised (during welding for example), all of the carbon present in the material is taken into solution in the austenite phase. Therefore as the carbon content of the steel increases, there is an increasing driving force for the microstructure to remain austenitic on cooling. If the austenite phase persists to a sufficiently low temperature on cooling, carbon atoms will have insufficient mobility to diffuse into the equilibrium phases of ferrite and pearlite and instead the non-equilibrium phase martensite is formed via diffusionless shearing of the austenite lattice trapping the carbon atoms in solution. Manganese also has a stabilising effect on the austenite phase while elements such as silicon and aluminium inhibit the precipitation of carbides from austenite thus maintaining carbon in solution, reducing the critical cooling rate for martensite formation. It can therefore be seen that as the cooling rate and the alloy content of the material increase, the likelihood of a non-diffusional transformation occurring also increases.

The weld nuggets formed in LC and IF260 (CE 0.045 and 0.059 respectively) appeared to be composed of a lath/plate-like morphology of ferrite. The carbon content of these grades is thought to be insufficient for a transformation to martensite, despite the extremely high cooling rates experienced by the weld region.

It was observed that that the microstructural characteristics of the AHSS welds were extremely similar from grade to grade despite the significant differences in alloy chemistry and the microstructural constituents of the un-welded parent materials. It was possible to distinguish four microstructural regions in each weld; a coarse columnar weld nugget, a coarse inner heat affected zone surrounding the weld nugget, a fine outer heat affected zone and a dual phase 'transition zone' between the fine outer heat affected zone and the unaffected parent material. The weld nuggets and heat affected zones formed in the AHSS grades appeared to be composed of lath martensite which is the morphology of martensite which typically forms in low carbon steel. The carbon content of the advanced high strength grades studied ranged from 0.083wt% to 0.181wt% whilst the carbon equivalents ranged from 0.204 to 0.307. Therefore a carbon equivalent of 0.204 as calculated by the Ito-Bessyo equation[42] was sufficient for a complete transformation of the weld nugget and heat affected zone to martensite in 1.0mm strip.

Gould et al[90] used two equations to calculate the critical cooling rate for martensite formation in a rage of steel types including mild, IF, dual phase and TRIP. Several of the grades had similar chemical compositions to the grades studied in the present research program. The most important conclusion of this work was that, with the exception of the IF steel, the critical cooling rates for martensite formation in the selected grades were significantly lower than the cooling rates calculated for the resistance welding process. In other words, resistance welds formed in all but the IF steel could be expected to be composed of martensite. Clearly the results of the present research program support this prediction.

The presence of martensite in the dual phase and martensitic steel welds is to be expected since the alloy chemistry of these grades is tailored to form martensite on quenching. The same is true of the TRIP grades since the austempering stage of the annealing cycle necessary for the production of the ferrite/bainite/retained austenite microstructure is absent from the thermal cycles generated by single pulse welding operations. Although the presence of martensite in the weldment is generally considered undesirable, it should be noted that the properties of martensite are strongly dependent on its carbon content[22].

As described in the literature review, martensite is essentially a super-saturated solid solution of carbon in ferritic iron. Increasing the carbon content of martensite increases the tetragonality of the BCT lattice which in turn increases the hardness and reduces the ductility of the martensite. Low carbon martensite however can often exhibit a reasonable degree of toughness[108]. The presence of martensite in a weld is therefore not necessarily an indicator that the weld will exhibit unsatisfactory performance in service, provided that the carbon content of the steel is comparatively low. This is illustrated by the acceptable failure modes observed when welds formed in TRIP600, DP600 and DP800 were subjected to the chisel test.

An indication of the maximum temperatures reached in the various regions of a resistance spot weld can be deduced from the final microstructures observed in each region. For example, the boundary between the columnar weld nugget and the equiaxed heat affected zone must by definition coincide with the melting point of steel, which is approximately 1530°C for most low carbon grades. In addition the boundary between the heat affected zone and the un-transformed parent material must coincide roughly with the A_1 temperature (723°C) while the point where the heat affected zone becomes fully martensitic must have exceeded the A_3 temperature prior to quenching. These isotherms are represented schematically in figure 6.3. It is also clear that the subsequent cooling rate of any austenite formed in the weld region during welding was sufficient for a complete transformation to martensite. This is supported by work presented by den Uijl[94] who used a SYSWELD model to predict weld and heat affected zone microstructures in TRIP steels. In practice it is extremely difficult to obtain real-time data on the peak temperatures and cooling rates for the different regions of a resistance spot weld[101, 107]. Attempts have been made[89, 112] to directly measure the temperature profiles generated in a material during resistance spot welding using a variety of techniques including thermocouples and thermal imaging cameras. However the temperature data obtained varied significantly between the various studies calling into question the reliability of the data.

As stated above, it can be inferred from microstructural constituents that the peak temperatures in the heat affected zone range from approximately 1530°C to 723°C and this is thought to account for the significant differences in martensite lath packet size observed between the inner and outer heat affected zones i.e. the higher temperatures reached in the inner heat affected zone result in coarsening of the prior austenite grain structure prior to quenching. In the outer region of the heat affected zone where the austenite grains are fine, the resulting high density of grain boundaries constitute obstacles against the formation of large martensite laths[92]. At the very edge of the visible heat affected zone where the peak temperatures reached lie in the intercritical region between the A_1 and A_3 temperatures, a dual phase ferrite-austenite microstructure develops during welding eliminating the parent microstructure. On quenching the austenite transforms to martensite thus producing a dual phase ferrite-martensite structure with the volume fraction of martensite increasing from the A_1 isotherm to the A_3 isotherm. This is illustrated by figure 6.4 which shows a micrograph of the dual phase 'intercritical zone' at the outermost extent of the visible heat affected zone of a typical AHSS spot weld. Superimposed on this micrograph are the approximate locations of the A_1 and A_3 isotherms, representing the maximum temperatures reached in this region during welding. The development of this dual phase structure at the periphery of the heat affected zone was also predicted by den Uijl[94] using SYSWELD.

Microhardness profiles of welds formed in the eight steels under investigation were presented in figures 5.54 to 5.61 and show a sensible trend. The microhardness levels measured in the weld nuggets formed in the selected steel grades increased with increasing alloy content of the parent material.

An equation was derived linking carbon equivalent with the average measured weld microhardness levels; Weld hardness = 1307.5(CE) + 152.69. Using this empirical equation, it is possible to predict the microhardness of a spot weld formed in a particular grade using the carbon equivalent of that grade calculated with the Ito-Bessyo equation[42]. It can be seen that the above equation does not take into account the effect of cooling rate on the final microstructure and microhardness, however this is unlikely to

be an issue with resistance welding since the extremely high cooling rates generated by this process are almost certain to yield the maximum hardness values possible for a particular steel chemistry.

It was discovered that weld nuggets and heat affected zones of welds formed in LC and IF260 exhibited higher microhardness levels than the parent material in both grades with peak hardness levels occurring in the weld nugget. This was due to the transition in microstructure from coarse equiaxed ferrite in the parent material to lath ferrite in the weld nugget.

The highest microhardness levels recorded in welds formed in the advanced high strength grades consistently coincided with the outer heat affected zone. This can be explained with reference to the extremely fine martensite present in this region. Refinement of the prior austenite grain size and consequently the martensite lath packet size has been shown[23] to increase mechanical strength and hardness of martensite. However the following mechanism is thought likely to contribute to the high hardness levels recorded in the outer heat affected zone. As described previously, the solubility of carbon in austenite is significantly higher than in ferrite since the interstitial sites which the carbon atoms occupy are larger in a face centred cubic lattice than in a body centred cubic lattice. As a result, carbon will readily diffuse from ferrite grains to occupy the interstices in neighbouring austenite grains in order to reduce the overall free energy of the system. At edge of the visible heat affected zone where the maximum temperatures reached lie in the intercritical region between A_1 and A_3, a two phase structure of ferrite and austenite is produced. This is shown schematically in figure 6.3. Carbon diffuses from the ferrite grains into the austenite grains thus increasing the carbon concentration of the austenite. Despite the high temperatures reached in the heat affected zone the short cycle times and the rapid cooling rates associated with the spot welding process limits the distance the carbon atoms can diffuse into the austenitic weld thus producing a carbon-rich layer in the outer heat affected zone. Therefore the martensite which forms from this carbon enriched austenite exhibits significantly higher hardness than that found in the rest of the weld region.

The hardness profiles of the welds formed in DP1000 and MS1400 where characterised by significant softening of the parent material in the outermost extent of the heat affected zone. Other researchers[96, 98] have also observed this phenomenon in steels with tensile strengths exceeding 800N/mm^2, attributing it to tempering of the large volume fraction of martensite present in the parent microstructure of such grades. Whilst there is likely to be a degree of tempering of the parent metal, it is though that ferrite grain growth in the intercritical region between the A_1 and A_3 isotherms (see figure 6.3) accounts primarily for the softening observed. This was supported by metallographic examination of the outer heat affected zone of welds formed in DP1000 (figure 5.50d) and MS1400 (5.51d).

6.2 The effect of in-process post-weld heat treatments on weld microstructure, microhardness and mechanical properties

Welds formed in TRIP800, DP800 and DP1000 were subjected to a range of post weld heat treatment pulses in order to modify the properties of the welds after they had cooled sufficiently to fully harden.

It was discovered that this technique yielded reductions in weld microhardness exceeding $150HV_{0.3}$ in all three grades as well as a transformation in weld failure mode on chisel testing from predominantly interfacial in the case of DP1000 and TRIP800 to full plug failure in all cases. Microstructural examination of the heat treated spot welds revealed that the greatest reductions in hardness coincided with a phase transformation within the weld nugget microstructure.

It has been suggested by den Uijl[73] that if any part of the weld nugget reached a sufficient temperature during heat treatment to become re-austenitised then these areas would subsequently re-transform to hard un-tempered martensite on cooling. However it was discovered in this work that when the post weld current level exceeded a critical value, a microstructure that was morphologically distinct from martensite was produced in all three grades. It is thought that the lower peak temperatures reached in the weld region during the secondary current pulse compared to the initial welding pulse and the rapid removal of the cooling effect of the electrodes after the heat treatment pulse resulted in a cooling rate that was insufficient for a complete transformation of austenite to martensite and instead resulted in the growth of a significant amount of bainitic ferrite before the M_s was reached. An additional factor which is thought likely to have reduced the cooling rate of the heat treated weld nugget is the reduction in the thermal gradient between the weld nugget and the bulk material caused by heat conduction into the bulk material during initial weld formation. The microstructure observed was consistent with granular bainite which forms when steel is continuously cooled as opposed to being held isothermally in either the upper or lower bainite region[12].

Micrographs of the microstructures developed in TRIP800, DP800 and DP1000 weld nuggets after post weld heat treatment can be seen in figures 5.92c, 5.97 and 5.98 respectively. All three microstructures are morphologically similar and contain a large volume fraction of bainitic ferrite plates. A high magnification micrograph of the heat treated microstructure found in DP1000 can be seen in figure 5.99. The prior austenite grain boundaries can be clearly distinguished in this micrograph along with bainitic ferrite plates which appear to have nucleated at the austenite grain boundaries. A darker phase can be seen to separate the bainitic ferrite plates and it is thought likely that this is martensite which transformed from the remaining austenite when the weld cooled below the M_S temperature. Again this is consistent with the description of continuously cooled granular bainite offered by Honeycombe and Bhadeshia[12].

As the secondary current level and the amount of heat generated in the solidified weld nugget increased, the area of the weld nugget transformed to bainitic ferrite also increased as illustrated by figures 5.90a, 5.91a and 5.92a which show heat treated TRIP800 weld nuggets. There was also a corresponding coarsening of the bainite plates as can be seen from figures 5.90c, 5.91c and 5.92c. Further increases in secondary current lead to the reappearance of martensite in the centre of welds formed in all three grades, as illustrated in figure 5.93. In order to establish the mechanism by which the martensite had re-formed, a detailed microstructural examination of the TRIP800 spot weld which had been treated with a 4.44kA secondary pulse was conducted. As illustrated by figures 5.95a to 5.95e there was a gradual transition from bainitic ferrite to martensite over a distance of approximately 1200μm. This was confirmed by microhardness measurements which showed a gradual increase in microhardness from the weld periphery to the weld centre with increasing volume fraction of martensite. It is thought that the re-transformation of as significant region of the heat treated welds to martensite beyond a critical current level was due to the following mechanism. As the secondary current level and peak temperature reached in the weld nugget increased, the temperature gradient between the centre of the re-austenitised weld and the bulk material became steeper leading to a corresponding increase in the cooling rate of this region. As the cooling rate increased from the periphery of the weld to the centre, the volume

fraction of bainitic ferrite that could form before the M_s temperature was reached steadily decreased. In the centre of the weld, the cooling rate was sufficient to suppress the formation of bainitic ferrite instead resulting in a complete transformation to martensite.

It was decided to utilise the secondary current levels which yielded the greatest reduction in weld hardness to fabricate lap shear and cross tension samples out of DP800, DP1000 and TRIP800 to investigate the effect on mechanical properties of the transformation of a significant proportion of the weld nuggets to bainitic ferrite. It was discovered that the post weld heat treatments yielded increases in the average cross tension failure loads sustained by $5\sqrt{t}$ welds in all three grades without any deterioration in failure mode. However the same weld schedules lead to a reduction in the average lap shear failure loads sustained by $5\sqrt{t}$ welds formed in DP800 and DP1000 and a transition in failure mode from double plug failure in the case of as-welded DP800 and TRIP800 and shear plug failure in the case of as-welded DP1000 to interfacial failure in all three cases. It is thought that the deterioration in lap shear failure mode was due to the crack front propagating along the well defined boundaries between the bainitic ferrite plates, possibly through weak grain boundary precipitates. The poor performance of the heat treated spot welds when loaded in shear calls in to question the usefulness of post weld heat treatments, particularly when the additional penalty in weld cycle time is considered.

These results are at odds with the results of post weld tempering trials conducted by Smith[98] and Westgate[97] who both discovered significant improvements in lap shear strength with post-weld tempering. This suggests that the tempering schedules used in the above examples did not result in the transformation of a large proportion of the weld nuggets to bainitic ferrite as was observed in this work. While there has been a significant amount of research conducted in the field of post weld heat treatments in recent years[97, 98, 100, 112], no published work could be found which included a detailed microstructural survey of the heat treated welds to offer and explanation for the changes in weld properties resulting from different post weld heat treatment schedules.

Microhardness measurements taken in the welds that had partially re-transformed to martensite (see figures 5.84, 5.85 and 5.86) revealed that despite the hardness levels of the martensitic regions often exceeding the hardness levels recorded in un-treated welds formed in the same grades, the greater heat generation in the weld region resulting from the higher secondary current levels lead to significant softening of the extremely hard heat affected zones formed during the primary weld pulse. It is thought that this structure of a hard martensitic core with a significantly softer bainitic heat affected zone could potentially address the poor lap shear performance of the fully bainitic welds produced with lower secondary current pulses, thus warranting further investigation.

Simmie and Hipperson[99] observed that a critical hold time was necessary before the commencement of the tempering pulse below which appreciable reductions in weld hardness could not be achieved. It was stated that the hold time between the primary and secondary pulses had to be sufficient to allow the complete transformation of the weld nugget to martensite prior to the commencement of heat treatment. For this reason a comparatively long hold time of 50 cycles or 1 second was selected for this research. Further experimentation would be beneficial to establish if this hold time can be reduced without limiting the efficacy of the secondary current pulse. It may also be possible to reduce the duration of the secondary current pulse if the aim of the heat treatment step is to produce a martensitic core with a bainitic heat affected zone as opposed to achieving maximum reductions in weld nugget hardness.

6.3 The effect of dissimilar steel combinations on weld properties and performance

The work described in the preceding sections was based on the premise that body-in-white components formed out of advanced high strength steel will be joined to other components formed out of the same grade. Whilst automotive manufacturers will undoubtedly want to know how a particular advanced high strength steel will perform when welded to itself, where high strength steels are currently used in body-in-white construction, they are far more likely to be joined to dissimilar grades, usually with significantly lower alloy contents[88]. For this reason it is important to establish the properties of welds formed between AHSS grades and lower strength steels. However with the proportion of high strength steels used in automotive structures continuing to rise, it is likely that advanced high strength steels will be increasingly joined to grades with the same or similar alloy chemistries and mechanical properties in the future.

The aim of this part of the investigation was to establish if there were any benefits in joining advanced high strength steels to a low carbon mild steel grade in terms of weldability, weld failure mode and weld properties. DP1000, MS1400 and TRIP800 were selected on the basis that they had previously exhibited less than satisfactory weldability and weld performance. DP800 was included in the study despite exhibiting excellent weldability when joined to itself due to the fact that microhardness levels exceeding $450HV_{0.3}$ had been recorded in weld nuggets formed in this grade. It was discovered that all of the selected advanced high strength grades could be readily welded to low carbon mild steel using basic single pulse weld schedules and an electrode force of 3.2kN. Weldability ranges in excess of 2kA were achieved in each case and full plug failures were observed from weld diameters as small as $2.5\sqrt{t}$.

It was thought that dilution of the alloy chemistry of the advanced high strength steel component of the dissimilar steel joint could potentially reduce the hardenability of the resulting weld nugget and increase the critical cooling rate for martensite formation. It was apparent from the metallographic examination however, that the dilution of the weld nuggets formed between the selected AHSS to LC combinations was insufficient to inhibit the formation of martensite (see figures 5.120 to 5.123). It is thought that this

accounted for the reductions in average weld hardness achieved ranging from as little as 5% in the case of DP800 to approximately 14% in the case of MS1400.

Weld failure invariably occurred in the LC sheet with limited deformation of the high strength component. Consequently the average lap shear and cross tension failure loads sustained by the AHSS to LC joints were comparable with those exhibited by lap shear and cross tension samples fabricated solely out of the LC grade. This could potentially limit the strength and energy absorbing benefits offered by components fabricated out of advanced high strength steels if they are subsequently joined to a grade with inferior mechanical properties.

It is thought that the hardening of the LC heat affected zone described in section 5.4.5 was due to carbon diffusion from the weld nugget into in the un-melted LC heat affected zone. Whilst the exact carbon content of the four AHSS to LC weld nuggets is not known the hardness levels recorded in the weld nuggets suggests that their carbon content was significantly higher that that of the LC parent material thus providing a driving force for the diffusion of carbon into the latter. Given that the peak temperature at the interface between the molten weld nugget and the heat affected zone must by definition correspond with the melting point of steel (~1530°C), it is thought that the rate of carbon diffusion from the weld nugget into the LC heat affected zone was sufficient to result in solid solution hardening of the heat affected zone.

Very little published work could be found relating to the joining of advanced high strength steels to dissimilar grades. Shi and Westgate[97] investigated the potential of weld carbon reduction by joining a TRIP grade to a dual phase grade with a lower tensile strength and carbon content. Whilst acceptable plug failures were achieved above a weld diameter of $4\sqrt{t}$, the reduction in weld hardness was limited. Lap shear and cross tension strengths were limited by the lower strength component as was observed in the present work.

Peterson[102] attempted to reduce weld hardness and brittleness in transformation hardened steels by introducing a low carbon steel interlayer into the joint. The initial study used two high strength grades with tensile strengths of 550N/mm^2 and 965N/mm^2 and showed that the fracture toughness of the welds formed in these grades could be significantly improved through the introduction of the low carbon interlayer without a significant loss in weld strength. Interface failures were eliminated with relatively small amounts of dilution.

6.4 Practical considerations relating to the implementation of recommended welding practices in a production environment

This research program has demonstrated several methods by which the automotive welding engineer can begin to address the perceived difficulties associated with the resistance welding of advanced high strength steels. However, the extent to which these methods could be implemented in a production environment would depend heavily on the welding equipment available.

It is widely accepted that higher electrode forces are required when welding advanced high strength steels to overcome their greater tendency for spring back[44]. However, it was discovered that in the case of certain advanced high strength grades, significant increases in electrode force over those recommended in BS1140:1993[41] were necessary to allow the production of the preferred weld diameter of $5\sqrt{t}$ before the splash limit was reached. In the case of the 1.2mm TRIP800 grade, it was necessary to increase the electrode force by 56% over that recommended in BS1140:1993[41] to 5kN in order to allow the production of $5\sqrt{t}$ diameter welds. Since the current research program was conducted using a large free-standing pedestal welder with an electrode force capacity of 6.5kN, a force of 5kN was well within the machines capabilities. However the conventional gun and servo welders found on automotive production lines may be unable to generate the electrode forces required. Where the electrode force required to prevent premature weld splash is beyond the capacity of the available welding equipment, it may be possible to reduce the electrode force requirement by using lower weld currents and extended weld times in order to allow the weld nugget to grow to the required diameter in a more controlled manner thus reducing the risk of weld splash. While any increase in weld time and the associated loss of productivity would likely prove un-popular with automotive manufacturers, the number of welds that would require an extended weld time is likely to represent a small proportion of the total number of welds in a complete body-in-white structure.

The larger weld diameters possible with 6mm and 7mm diameter electrode tips offered significant increases in lap shear strength and produced full plug failures on chisel

testing. In order that the pressure exerted by the electrodes on the steel surface remained constant for each electrode configuration, it was necessary to increase the electrode force from 3.2kN in the case of 5mm diameter electrode tips to 4.6kN in the case of the 6mm diameter tips and 6.3kN in the case of 7mm tips. As described above, an electrode force of 6.3kN is likely to be beyond the capacity of welding guns found on automotive production lines. However, an electrode force of 4.6kN is more realistically achievable. Further investigation would be beneficial in order to determine if weld diameters significantly greater than $5\sqrt{t}$ can still be achieved in advanced high strength steels such as TRIP800 at lower electrode forces when using electrodes with larger-than-specified tip diameters.

It was discovered that the incorporation of a secondary heat treatment current pulse after the initial weld pulse could yield significant reductions in weld hardness. However it was also discovered that the post heat treatment weld hardness levels were extremely sensitive to the secondary current level, with a difference of few hundred amps producing large variations in the microhardness profiles of the heat treated spot welds (see figures 5.83 and 5.84). This problem would be exacerbated by the inherent variability of the spot welding process in a high-volume production environment.

A contributing factor to the instability of production line weld current conditions is the variability in electrode tip geometry. The combination of high electrode forces, high cyclical temperatures and events such as weld splash leads to deformation of the electrode tips with increasing weld cycles[48, 49]. In addition, alloying between the copper electrodes and the zinc coatings frequently applied to automotive steels leads to a gradual increase in tip diameter with each weld made[44]. As the electrode tip diameter increases and the current density in the workpiece decreases, the diameter of the welds produced by a particular current setting will decrease. In a production environment, this can be controlled by gradually increasing the weld current to compensate for the electrode tip growth thus maintaining an acceptable weld diameter. However, when the current demands become too great the electrodes must be re-dressed with a mechanical cutting tool to restore their original geometrical configuration.

Another factor that can influence weld formation in a production environment is a phenomenon known as current shunting. When attempting to form a weld in close proximity to another solidified weld, a portion of the weld current can 'shunt' through adjacent welds since they represent a low resistance path for current flow. The effect of current shunting can be limited by maintaining a minimum distance or pitch between adjacent welds and by stepping up the current after the formation of the initial weld in an array. However in areas where spot welds are likely to be subjected to increased forces, such as in a suspension tower for example, it may be necessary to place spot welds within the minimum distance of each other.

Variations in current density caused by shunting and continuously varying electrode tip geometries ultimately leads to the production of a range of weld diameters in a completed body-in-white structure. BS1140:1993[41] specifies a preferred weld size of $5\sqrt{t}$ (where t is the sheet thickness in mm) and states that the weld diameter should not fall below 70% of this value i.e. the diameter of any given weld should be greater than or equal to $3.5\sqrt{t}$ in order to be considered acceptable. The present work has also demonstrated that it is possible to form welds with diameters significantly greater than $5\sqrt{t}$ in certain grades before the occurrence of weld splash. Weld splash itself results in significant variability in weld size since a large proportion of the weld material is ejected from the molten weld nugget.

The present research into post weld heat treatments was conducted on single $5\sqrt{t}$ welds formed between pairs of 50mm x 50mm coupons with careful scrutiny of both the primary and the secondary current levels to ensure close control of both weld diameter and the amount of heat generated in the solidified weld by the secondary pulse. However in a production environment such close control of weld size is not realistically achievable for the reasons described above. Before any post weld tempering operation could be successfully incorporated into production weld schedules, it would be essential to determine the effect of weld size on the efficacy of post weld heat treatments. A secondary current level which had proved effective in reducing the hardness of a $5\sqrt{t}$ weld is likely to have a significantly different effect on the properties of a $3.5\sqrt{t}$ weld for

example. It would also be beneficial to determine the effect of electrode geometry on the efficacy of post weld heat treatments since a change in electrode geometry is likely to influence the manner in which heat is generated in the solidified weld nugget. This is particularly important considering the array of different electrode geometries that are often used in a production environment.

The issues discussed above could potentially be resolved with the addition of dedicated welding stations to a production line. The present work has demonstrated that a minimum requirement of any dedicated equipment would be an electrode force capacity of at least 5kN. In addition, if post-weld heat treatments are to meet with any success in a production environment, the ability to precisely control and maintain weld current levels is essential.

7. CONCLUSIONS

The main conclusions of the present research programme are as follows:

- As the alloy content of the parent material increased, weld current requirements decreased and the weld growth curves were displaced to lower current levels.

- The weldability of TRIP600, DP600 and DP800 compared favourably with IF260 and low carbon mild steel using basic single pulse weld schedules. The preferred weld diameter of $5\sqrt{t}$ (where t = sheet thickness in mm) was achieved in all three grades at current levels well below the splash limit. This suggests that these grades could be integrated into automotive production without significant alterations to plant practice.

- Grades with higher alloy contents such as DP1000, MS1400 and TRIP800 required higher electrode forces to displace the splash limit to higher current levels and to allow the successful production of $5\sqrt{t}$ welds. Full plug failures were not observed in these grades where single pulse schedules were used.

- The average lap shear failure loads of welds formed in the selected grades generally increased with increasing parent metal strength.

- The lap shear performance of TRIP600, DP600, DP800 and TRIP800 was found to be acceptable, both in terms of weld failure mode and the load sustained before failure. Whilst plug failures were observed for DP1000 and MS1400 in lap shear, the maximum load sustained did not meet that required by BS1140:1993[41].

- The cross tension strength of welds formed in the selected grades appeared to be largely independent of parent metal strength. The average cross tension failure load of MS1400 was lower than that of low carbon mild steel.

- Microstructural examination of welds formed in the six AHSS grades studies revealed that the welds nuggets and heat affected zones were composed of lath martensite. Welds nuggets formed in low carbon mild steel and IF260 appeared to be composed of bainitic ferrite.

- Microhardness surveys of the welds revealed a positive correlation between weld nugget hardness and carbon equivalent. This relationship was described by the following equation;

$$\text{Weld hardness} = 1307.5(CE) + 152.69$$

- The highest microhardness levels recorded in the AHSS welds consistently coincided with the fine outer heat affected zones observed in each grade.

- Evidence of brittle and ductile failure was observed in the fracture surfaces of interfacially failed welds formed in all of the steel grades studied irrespective of weld hardness or microstructural constituents. For example, regions of ductile failure were observed in interfacially failed TRIP800 spot welds despite an average weld hardness of $527HV_{0.3}$.

- The use of welding electrodes with 6mm and 7mm diameter tips allowed the production of welds with diameters significantly greater than the preferred $5\sqrt{t}$ in TRIP800. An increase in weld diameter from $5\sqrt{t}$ to $7\sqrt{t}$ yielded significant improvements in lap shear strength. Full plug failures were also observed on chisel testing at weld diameters greater than approximately $6.3\sqrt{t}$.

- The introduction of a secondary heat treatment pulse into the basic welding schedule used in the preceding experiments yielded significant reductions in the microhardness levels of $5\sqrt{t}$ welds formed in TRIP800, DP800 and DP1000. Reductions in excess of $150HV_{0.3}$ were achieved in all three grades with a corresponding transition form partial plug failure to full plug failure on chisel testing.

- The greatest reductions in weld hardness corresponded with the transformation of the weld nuggets from martensite to a microstructure largely composed of bainitic ferrite, indicating that regions of the weld nuggets had become re-austenitised during the heat treatment pulse.

- Post weld heat treatments that offered the greatest reductions in weld and heat affected zone hardness in TRIP800, DP800 and DP1000 also yielded significant improvements in cross tension strength. However the same treatments caused a transition in lap shear failure mode from plug to interfacial failure in each case and a reduction in the lap shear strength of DP800 and DP1000 spot welds.

- Further increases in the secondary current level eventually lead to the reappearance of martensite in heat treated TRIP800, DP800 and DP1000 welds with an associated increase in microhardness. However, hardness levels measured in the heat affected zones continued to decrease.

- Joining DP800, DP1000, MS1400 and TRIP800 to low carbon mild steel yielded modest reductions in weld microhardness levels and significant improvements in weldability and weld failure mode compared to joints in which only the high strength component was present. Lap shear and cross tension strengths were limited by the mild steel component in each case.

8. RECOMMENDATIONS FOR FURTHER WORK

The results of the present research programme have highlighted a number of areas that require further investigation. In particular the following areas are considered important for future consideration.

Further work in the area of in-process post weld heat treatments is required to establish if modifications to parameters such as the duration of the pause between the primary and secondary current pulses and the duration and magnitude of the secondary current pulse could yield further improvements in weld quality and performance. It would also be beneficial to determine the effect of other variables such as weld size and sheet thickness on the efficacy of post weld heat treatments. There is scope for the development of a dynamic feedback control system which could accurately control the amount of heat generated in the solidified weld by the secondary current pulse by monitoring the dynamic resistance between the welding electrodes. The utilisation of finite element modelling software such as SYSWELD in conjunction with thermal profile monitoring (using thermocouples for example) would assist in the evaluation and development of advanced weld schedules.

It has become apparent that there is a need to develop a more robust weld testing methodology than the chisel test which is almost exclusively used throughout the automotive industry in order to determine weld quality. This testing methodology should more closely approximate in-service loading conditions that welds formed in advanced high strength steels are likely to be subjected to and would ideally include impact and fatigue testing of complete vehicle components. This would allow the effect of advanced welding schedules such as post-weld heat treatments on the energy absorbing characteristics of entire body-in-white structures and the crash survivability of vehicle occupants to be established to far greater degree of accuracy. Further development of non-destructive testing techniques such as ultrasonic testing could potentially offer an alternative to the chisel test for weld quality determination on the production line.

The present research was carried out on commercially available advanced high strength steels which had complex chemical compositions and relied on a variety of strengthening mechanisms to derive their enhanced properties. Further research into the effect of individual alloying elements on weld properties by utilising experimental alloys would allow welding engineers to contribute to the alloy composition design of potential automotive grades.

9. REFERENCES

1. N. Stern, 'The economics of climate change', Cambridge University Press, 2007. Also available at http://www.hm-treasury.gov.uk/independent_reviews/stern_review_economics_climate_change /stern_review_report.cfm
2. M. Jeanneau and P. Pichant, 'The trends of steel products in the European automotive industry', La Revue de Métallurgy-CIT, November 2000, pp1399-1408.
3. European New Car Testing Programme, Assessment Protocol and Biomechanical limits, Version 4.0, January 2003.
4. New Car Assessment Programme online. Last accessed March 2007 at URL: http://www.euroncap.com/content/test_procedures/introduction.php
5. J. Fenton, 'Handbook of automotive body construction and design analysis', Professional Engineering Publishing Limited, 1998, ISBN 1 86058 073 4.
6. Online, Last accessed February 2007 at URL: http://www.sv.vt.edu/classes/MSE2094_NoteBook/96ClassProj/examples/kimcon.html
7. 'Welding and Coating Metallurgy', October 1999, pp13. Last accessed March 2007 at URL http://www.castolin.com/wCastolin_com/pdf/publications/welding_coatings .pdf
8. ULSAB-AVC Online. Last accessed February 2007 at URL, http://www.ulsab-avc.org/image_library
9. D.T. Llewellyn, 'Steels: metallurgy and applications', 3rd edition, Butterworth-Heinemann Ltd, 1998, ISBN 0 7506 3757 9, pp8.
10. R.W.K Honeycombe and H.K.D.H Bhadeshia, 'Steels: Microstructure and properties', 2nd Edition, Butterworth-Heinemann, 1995, ISBN 0 340 58946 9, pp53.
11. R.W.K Honeycombe and H.K.D.H Bhadeshia, 'Steels: Microstructure and properties', 2nd Edition, Butterworth-Heinemann, 1995, ISBN 0 340 58946 9, pp115.
12. R.W.K Honeycombe and H.K.D.H Bhadeshia, 'Steels: Microstructure and properties', 2nd Edition, Butterworth-Heinemann, 1995, ISBN 0 340 58946 9, pp130.
13. J.W. Edington and F.G. Wilson 'The automobile, fuel economy and the drive for lightweight materials', Automotive Technology International, November 1994.

14. K. Kishida, 'High strength steel sheets for light weight vehicle', Nippon Steel Technical Report No. 81, January 2000.
15. R. Terakado, 'Strategies for expanding the use of high-strength steel sheets for automobiles', Nippon Steel Corporation, IISI-31 Vienna, PROMCO Panel Discussion: 'Steel and the Automobile – Assessing the Playing Field'.
16. E. Walker and K. Lowe, 'Ultra light auto bodies constructed from steel', Automotive Materials, December 1995, pp585-587.
17. J.P. Schaffer, A. Saxena, S.D. Antolovich, T.H. Sanders, Jr. and S.B. Warner, 'The science and design of engineering materials', 2nd Edition, McGraw-Hill, 1999, ISBN 0-265-24766-8, pp305-319.
18. P.J. Evans, L.K. Crawford and A. Jones, 'High strength C-Mn steels for automotive applications', Iron and Steelmaking, Vol. 24 No. 5, 1997, pp361-367.
19. B. Engl et al, 'Recent experience with the application of TRIP and other advanced multiphase steels', SAE Technical Paper No. 982408, 1998.
20. P. Jacques, 'On the physics and mechanics of phase transformations in TRIP-assisted multiphase steels', Thesis doctorate. UCL, FSA, Unité PCIM, 1998.
21. D.P. Koistinen and R.E. Marburger, 'A general equation prescribing the extent of the austenite-martensite transformation in pure iron-carbon alloys and plain carbon steels', Acta Metallurgica, vol.7, 1959, pp50-60.
22. M. Cohen, 'The strengthening of steel', Howe Memorial Lecture, Trans. AIME **224**, 638, 1962.
23. R.W.K Honeycombe and H.K.D.H Bhadeshia, 'Steels: Microstructure and properties', 2nd Edition, Butterworth-Heinemann, 1995, ISBN 0 340 58946 9, pp107-113.
24. R.W.K Honeycombe and H.K.D.H Bhadeshia, 'Steels: Microstructure and properties', 2nd Edition, Butterworth-Heinemann, 1995, ISBN 0 340 58946 9, pp18.
25. R.W.K Honeycombe and H.K.D.H Bhadeshia, 'Steels: Microstructure and properties', 2nd Edition, Butterworth-Heinemann, 1995, ISBN 0 340 58946 9, pp23.
26. D.T. Llewellyn, 'Steels: metallurgy and applications', 3rd edition, Butterworth-Heinemann Ltd, 1998, ISBN 0 7506 3757 9, pp28.

27. B. Carlsson, J. Larsson and T. Nilsson, 'Dual phase steels for autobody design, forming and welding aspects', SSAB Technical Note, SSAB Tunnplåt, Borlänge, Sweden.
28. 'Dual phase and TRIP steels', Niobium Information Leaflet No. 15/97, Comphanhia Brasileira de Metalurgia e Minerção.
29. H. Hayashi, 'Forming technology and sheet materials for weight reduction of automobile', 19th IDDRG Biennial Congress, Eger, 10-14 June 1996, pp13-31.
30. ULSAB-AVC (Advanced Vehicle Concepts), Technical Transfer Dispatch #6, ULSAB-AVC Body Structure Materials, May 2001, Appendix III, pp5. Last accessed online February 2007 at URL: http://www.worldautosteel.org/ulsab-avc/download/ TTD6.pdf
31. J-O. Sperle and K. Olsson, 'High strength automotive sheet steels for weight reduction and safety applications', SSAB Technical Paper, SSAB Tunnplåt, Borlänge, Sweden.
32. T. Tröster and W. Rostek, 'Advanced Hot Forming', in proceedings from 'New Development in Sheet Metal Forming Technology Conference', Stuttgart, Germany, 2004, pp. 49-63.
33. L.-E. Svensson and J.K. Larsson, 'Welding and joining of high performance car bodies', Steel World 2002, Vol. 7, pp21-26.
34. J.K. Larsson, 'Laser welding, structural adhesive bonding, for body-in-white assembly. Competing or complementary joining methods?', The Fabricator, May 2007.
35. J.K. Larsson, 'Laser Welding as a Competitive Joining Method in Body-in-White Assembly – An Automotive State-of-the-Art Report With Complementary Future Challenges', in proceedings from '10th Nordic Laser Manufacturing Processes Conference', Piteå, August 2005.
36. J.K. Larsson and N. Palmquist, 'Extensive Laser Processing on the New Volvo C70 Convertible', in proceedings from 'Automotive Laser Applications Workshop', Plymouth, Michigan, March 2006.
37. P.D. Marchal, 'Laser welding of high strength steels', Corus Technical Report, IJTC/PPA/AUT/JON/K/R8282/2004/A, September 2004.

38. C. Bratt, 'Laser processing of automotive steel grades – review of WTC knowledge', Chorus Technical Report, WL/AA/TN/C650350/2/00/D, December 2000.
39. C. Goos, L. Liemburg and E.J. de Wit, 'Local post heat treatment of laser welds', Corus Technical Report, IJTC/AUT/JON/KR/08282/2004/A, December 2004.
40. J. Bakels, T van der Veldt, 'Literature study of brazing technology and costs', Corus Technical Report, IJTC/AUT-JON/C/R/6503/2002/A, September 2002.
41. 'Resistance spot welding of uncoated and coated low carbon steel', British Standard, BS1140:1993.
42. D.T. Llewellyn, 'Steels: metallurgy and applications', 3rd edition, Butterworth-Heinemann Ltd, 1998, ISBN 0 7506 3757 9, pp189.
43. 'Recommended practices for test methods for evaluating the resistance spot welding behaviour of automotive sheet steel materials', American National Standard, ANSI/AWS/SAE/D8.9-97.
44. W. Waddell, 'Resistance spot welding of uncoated and coated mild and high strength steel – review of WTC knowledge', Corus Technical Report, WL/AA/TN/C650340/1/2001/R.
45. T.B. Jones, 'A review of impact testing techniques for assessing spot weld quality', British Steel Technical Report, WL/FP/1018/78/A, February 1978.
46. M.J. Karagoulis, 'A nuts and bolts approach to the control of resistance spot welding', Welding Journal, July 1994, pp27-31.
47. N.T. Williams and T.B. Jones, 'Factors governing the selection of spot weld size and fracture mode in low carbon mild steel', British Steel Technical Report, WL/FP/1094/79/C, May 1979.
48. N.T. Williams and J.D. Parker, 'Review of resistance spot welding of steel sheets. Part I – Modelling and control of weld nugget formation', International Materials Reviews, Volume 49, Number 2, April 2004, pp45-75.
49. N.T. Williams and J.D. Parker, 'Review of resistance spot welding of steel sheets. Part II – Factors influencing electrode life', International Materials Reviews, Volume 49, Number 2, April 2004, pp77-108.

50. S. Oliver, 'Development and dynamic performance of high strength and advanced high strength strip steels', EngD thesis, Swansea University, 2007.
51. P.L. Harrison, 'Literature review on weldability of hot rolled high strength steels', Corus Technical Report, STC/TRA SIN/CKR/08357/2003/A, July 2003.
52. N.T. Williams, 'Practical considerations relating to the use of high strength steels for resistance welding applications', British Steel Technical Report, WL/FP/1226/82/C, March 1982.
53. M.W. Kolder and A.W.M. Bosman, 'Influence of the welding equipment on the weldability lobe of a HSLA steel', Doc IIW-III-796-84.
54. T. vd Velt, T. Moolevliet, T. Kolder and S. Smith, 'Investigation on the joining characteristics of high strength steels using spot welding', Corus Technical Paper No. 106185, January 2002.
55. D.J. VandenBossche, 'Ultimate strength and failure mode of spot welds in high strength steel', SAE Technical Paper No. 770214, 1977.
56. C. Lewis and W. Waddell, 'Resistance spot weldability of hot rolled high strength steels used in automotive components', British Steel Technical Report, WL/PE/PP/3421/8/97/D, February 1997.
57. T. Herai and Y. Takahashi, 'Resistance spot welding of high strength steel sheets', Nippon Steel Technical Report, IIW Doc. III-612-79, July 1979.
58. R.M. Rivett, 'Welding of high strength steels for vehicle parts: part 1 – resistance welding', TWI Research Report No. 5534/10/83.
59. R.M. Rivett, 'Assessment of resistance spot welds in low carbon and high strength steel sheet – Part 1: Static properties', TWI Research Report No. 193/1982.
60. R.M. Rivett, 'Assessment of resistance spot welds in low carbon and high strength steel sheet – Part 2: Impact and fatigue', TWI Research Report No. 212/1982
61. R.M. Rivett, M.G. Murch, S.A. Westgate and M.N. Watson, 'Welding of high strength steel sheet – a literature review', TWI Final Contract Report No. 5534/9/83, September 1983.
62. R.C. Lavery and N.T. Williams, 'Resistance spot welding of high tensile steel in the hot rolled condition', British Steel Technical Report, No. 230/D, February 1971.

63. N.T. Williams, 'Resistance spot welding of low-carbon and high strength low-alloy (HSLA) steels', E.C.S.C. Sponsored Research Project, Technical Report No. 1, January 1980.
64. N.T. Williams, 'Resistance spot welding of low-carbon and high strength low-alloy (HSLA) steels', E.C.S.C. Sponsored Research Project, Technical Report No. 2, July 1980.
65. N.T. Williams, 'Resistance spot welding of low-carbon and high strength low-alloy (HSLA) steels', E.C.S.C. Sponsored Research Project, Technical Report No. 3, January 1981.
66. N.T. Williams, 'Resistance spot welding of low-carbon and high strength low-alloy (HSLA) steels', E.C.S.C. Sponsored Research Project, Technical Report No. 4, July 1981.
67. N.T. Williams, 'Resistance spot welding of low-carbon and high strength low-alloy (HSLA) steels', E.C.S.C. Sponsored Research Project, Technical Report No. 5, January 1982.
68. J. Defourny and A. Bragard, 'Chemistry of the high strength steel sheets for automotive industry and the criteria to define the resistance spot weldability', Revue de la Soudre 1, 1984, pp17-24.
69. T.B. Jones and N.T. Williams, 'Factors which influence the type of failure in resistance spot welds in unalloyed and high strength steels', British Steel Technical Report, June 1981.
70. J.E. Gould, 'Mechanisms of hold time sensitivity behaviour in resistance spot welds in high strength steel sheet', in proceedings from 'Joining High Strength Steel for Automotive Applications Seminar', Troy, Michigan, February 1999.
71. J.E. Gould and D. Workman, 'Fracture morphologies of resistance spot welds exhibiting hold time sensitivity behavior', EWI Research Report 2, Edison Welding Institute, Columbus, Ohio.
72. M. Marya and K. Wang, 'Tensile-shear forces and fracture modes in single and multiple weld specimens in dual-phase steels', Journal of Manufacturing Science and Engineering, February 2006, Volume 128, pp287-298.

73. N. den Uijl and S. Smith, 'Resistance spot welding of advanced high strength steels for the automotive industry', in proceedings from '4th International Seminar on Advances in Resistance Welding', Wels, Austria, November 2006.
74. V. Cuddy, 'Manufacturing guidelines when using ultra high strength steels in automotive applications', E.C.S.C. sponsored research project, Final Report, January 2004.
75. T.B. Jones and N.T. Williams, 'Spot and projection welding of high strength steels', British Steel Technical Report, WL/FP/1156/80/C, November 1980.
76. C. Lewis and W. Waddell, 'Resistance spot welding of CMn 300 grade steel', British Steel Technical Note, WL/PA/TN/5413/1/94/R, June 1994.
77. T.B. Jones, 'The weldability of rephosphorised, high strength and dual phase steels', British Steel Technical Report.
78. D.W. Dickinson and T.V. Natale, 'Observations of factors which influence the spot weldability of high strength steels', SAE Technical Paper Series, No. 810353, 1981.
79. J.W. Mitchell and U.I. Chang, 'Resistance spot welding of microalloyed steels for automotive applications', in proceedings from 'Microalloying '75 Conference', Washington D.C., October 1975, pp599-609.
80. J.M. Sawhill Jnr. and S.T. Furr, 'Spot weldability tests for high strength steels', SAE Technical Paper Series, No. 810352, 1981.
81. T. Nishi, T. Saito, A. Yamada, Y. Takahashi, 'Evaluation of spot weldability of high strength sheet steels for automobile use', Nippon Steel Technical Report, December 1982, (20), pp37-44.
82. J-O Sperle, 'Fatigue strength of spot welded high strength steel sheet', IIW Doc. III-WG12-30-85.
83. K. Tanuma and T. Hashimoto, 'Static fracture appearance of spot welded joints of cold rolled carbon steel sheets', Trans. Nat. Research Inst. For metals, 1979, 21, (4), pp32-37.
84. H. Kitagawa, 'Report on spot welding conditions of high strength steel sheets', IIW Doc. II-808-85.
85. A. Blarasin and M. Castagna, 'Mechanical properties of spot welded HSLA steel sheets for automotive applications', Fiat Research Centre, Orbassano.

86. S. Smith, 'Weldability assessment of SSAB dual phase steels', British Steel Technical Note, WL/PE/TA4/A02/2/99/R, September 1999.
87. B. Pollard and R.H. Goodenow, 'Spot weldability of dual phase steel', SAE Technical Paper Series, No. 790006, 1979.
88. R.J. Holliday, 'Welding DP steels', Rover Technical Report, January 1999.
89. R. Ellwood, 'Resistance spot weldability of hot rolled TRIP steel', British Steel Technical Note, WL/PE/TN/3323/6/97/D, September 1997.
90. J.E. Gould, S.P. Khurana and T. Li, 'Predictions of microstructures when welding automotive advanced high-strength steels', Welding Journal, May 2006, pp111-116.
91. S. Smith, 'The resistance weldability of CSPIJ AHSS production trial materials, DP800 and TRIP800 production trial – 2006', Corus Technical Report No. 121368, July 2006.
92. M. Maraya and X.Q. Gayden, 'Development of requirements for resistance spot welding dual-phase (DP600) steels. Part 1 – The causes of interfacial fracture', Welding Journal, November 2005, pp172-182.
93. M. Maraya and X.Q. Gayden, 'Development of requirements for resistance spot welding dual-phase (DP600) steels. Part 2: Statistical analyses and process maps', Welding Journal, December 2005, pp197-204.
94. N. den Uijl, 'Modelling the influence of resistance spot welding on material properties', Corus Technical Report, 121162, June 2006.
95. P.S. Wei and C.Y. Ho, 'Axisymmetric nugget growth during resistance spot welding', Journal of Heat Transfer, 1990, **112**, pp309-316.
96. S.G. Shi and S. Westgate, 'Resistance spot welding of high strength steel sheet (600-1200N/mm^2)', TWI Research Report No. 767/2003, April 2003.
97. S.G. Shi and S. Westgate, 'Techniques for improving the resistance weldability of TRIP steel using resistance spot welding', TWI Research Report No. 13198.02/03/1176.2, October 2003.
98. S. Smith, 'Optimising the spot welding performance of AHSS by the use of tailored welding parameters', Corus Technical Report No. 113056, November 2004.
99. W.S. Simmie and A.J. Hipperson, 'Spot welding high tensile steels with automatic post heat treatment', Sheet Metal Industries, September 1944, pp1609-1619.

100. L. Cretteur and A. Lhasan Koruk, 'Improvement of weldability of TRIP steels by use of in-situ pre- and post-heat treatments', in proceedings from '55th Annual Assembly of International Institute of Welding', Doc. III-1218-02, June 2002.
101. N. den Uijl, 'Post weld heat treatment of advanced high strength steel for automotive joining', Corus Technical Report.
102. W. Peterson, 'Dilution of weld metal to eliminate interfacial fractures of spot welds in high and ultra high strength steels', in proceedings from 'ICAWT '97 conference', Columbus, Ohio, September 1997, pp331-346.
103. M. Gleave and J. Mundy, 'Investigation on the joining characteristics of dual phase steel to HSLA steel for wheel manufacture', Corus Technical Note, WL/AA/TN/835711/1/01/D, July 2001.
104. S.G. Shi and S. Westgate, 'Better and better....resistance spot weldability progress made in car, truck and bus applications', TWI Technical Bulletin.
105. A. Matsuzuki and H.K.D.H Bhadeshia, 'Effect of austenite grain size and bainite morphology on overall kinetics of bainite transformation in steels', Materials Science and Technology, May 1999, **15**, pp518-522.
106. K. Chilvers and N.T. Williams, 'The design of an analogue / digital data acquisition system for recording resistance seam welding parameters', British Steel Technical Report WL/FP/1348/85/D, January 1985.
107. S. Westgate, private communication.
108. V. Jerath, private communication.
109. R. Holliday, 'Mechanisms of electrode growth during spot welding of coated steel', EngD Thesis, Swansea University, 1996.
110. L. Gavard, 'A model for the optimisation of multiphase steels weldability (automotive applications)', Corus Technical Paper, December 2005.
111. G.E. Pellissier, 'Effects of microstructure on the fracture toughness of ultra high strength steels', Engineering Fracture Mechanics, 1968, **1**, pp55-75.
112. C.M. Anderson, 'The weldability of high and ultra high strength steel', EngD thesis, Swansea University, 2003.
113. N.D. Beynon, 'Relationship between metallurgical properties and crash performance of automotive structures', EngD Thesis, Swansea University, 2005.

114. S.J. Hambling, 'Fatigue performance of welded connectors / components using high strength strip steels', EngD thesis, Swansea University, 2004.
115. D.G. Chucas, 'Fatigue of spot welded high strength steel sheets', EngD Thesis, Swansea University, 2002.
116. N. Harlin, T.B. Jones and J.D. Parker, 'Weld growth mechanisms in two and three thickness joints', Science and Technology of Welding & Joining, February 2002, **7** (1), pp35-41.
117. L.E. Svensson, R. Johansson and M. Mlmer, 'Possibilities to improve fracture behaviour in resistance spot welds of EHSS and UHSS by process modifications', Volvo Truck Corporation.
118. H.K.D.H. Bhadeshia, 'Bainite in steels', 2nd Edition, Institute of Materials, 2001, ISBN 1 86125 112 2 (H).
119. D.A. Porter and K.E. Easterling, 'Phase transformations in metals and alloys', 2nd Edition, Chapman & Hall, 1992, ISBN 0 7487 5741 4.
120. ASM Handbook Volume 9, 'Metallography and Microstructures', ASM international, 1995.
121. ASM Handbook Volume 12, 'Fractography', ASM international, 1995.
122. ASM Handbook Volume 6, 'Welding, soldering and brazing', ASM international, 1995.

Table 4.1 Chemical composition of selected steel grades (wt%)

	C	Mn	Si	Al(tot)	S	P	Cu	Cr	Ni	Mo	V	B	Ti	Nb	CE*
LC	0.03	0.169	0.01	0.04	0.009	0.007	0.009	0.012	0.016	0.001	0.001	0.0002	0.005	0.001	**0.0448**
IF260	0.0029	1.008	0.0077	0.0443	0.0064	0.0532	0.0225	0.0169	0.0123	0.0015	0.0084	0.0007	0.0647	0.001	**0.0599**
DP600	0.102	1.53	0.198	0.0408	0.002	0.0117	0.007	0.423	0.0374	0.006	0.006	0.0003	0.0031	0.0018	**0.2153**
DP800	0.129	1.509	0.24	0.032	0.0025	0.0079	0.017	0.028	0.049	0.0037	0.0043	0.0001	0.0025	0.0178	**0.2167**
DP1000	0.143	1.538	0.55	0.04	0.001	0.0112	0.014	0.041	0.0426	0.0161	0.0073	0.0002	0.005	0.019	**0.2445**
MS1400	0.162	1.63	0.522	0.042	0.001	0.0072	0.0163	0.032	0.042	0.0076	0.004	0.0002	0.0025	0.0188	**0.2659**
TRIP600	0.083	1.441	1.35	0.139	0.0011	0.0083	0.016	0.0248	0.0172	0.001	0.002	0.0002	0.015	0.001	**0.2036**
TRIP800	0.181	1.33	1.67	0.137	0.001	0.0088	0.026	0.026	0.02	0.001	0.0026	0.0001	0.0129	0.001	**0.3069**

*Calculated using the Ito-Bessyo equation[42]

Table 4.2 Mechanical properties of selected steel grades

Steel Grade	R_p (N/mm^2)	R_m (N/mm^2)	R_P/R_m	Total Elongation (%)
LC	209	313	0.67	39.8
IF260	233	390	0.60	33.2
TRIP600	402*	623	0.65	29.6
DP600	399*	635	0.63	25.9
TRIP800	476*	788	0.60	30
DP800	513*	806	0.64	16.2
DP1000	854*	1048	0.82	8.3
MS1400	1446	1479	0.98	5.9

*0.2% proof stress

Table 5.1 Approximate weld current required to form $3.5\sqrt{t}$ diameter welds in selected steel grades

Steel Grade	Carbon Equivalent	Electrode tip diameter (mm)	Electrode force (kN)	Weld time (cycles)	Weld Current (kA)
LC	0.045	5	3.2	10	8.4
IF260	0.060	5	3.2	10	6.8
TRIP600	0.204	5	3.2	10	5.7
DP600	0.215	5	3.2	10	5.5
DP800	0.217	5	3.2	10	5.1
DP1000	0.245	5	3.2	10	4.9
MS1400	0.266	5	3.2	10	4.1
TRIP800	0.307	5	3.2	10	4.2

Table 5.2 Effect of electrode force on approximate current required to form $3.5\sqrt{t}$ diameter weld in 1.2mm TRIP800

Electrode Force (kN)	Electrode tip diameter (mm)	Weld Time (cycles)	Weld current (kA)
3.2	5	10	4.2
4	5	10	4.85
5	5	10	5

Table 5.3 Summary of lap shear performance of $5\sqrt{t}$ welds formed in selected steel grades

Grade	Weld current (kA)	Failure Load (kN)	Failure mode
LC	9.1	8.29	double plug
	9.09	8.32	double plug
	9.07	8.08	double plug
	9.12	8.09	double plug
	9.17	8.09	double plug
		Av = 8.174	
IF260	7.78	8.47	double plug
	7.72	8.25	double plug
	7.74	8.35	double plug
	7.85	8.32	double plug
	7.76	8.38	double plug
		Av = 8.354	
TRIP600	6.63	11.79	plug
	6.66	11.55	plug
	6.56	11.46	plug
	6.53	11.66	plug
	6.61	11.62	plug
		Av = 11.616	
DP600	6.95	13.71	double plug
	6.98	13.70	double plug
	6.98	13.78	double plug
	7.00	13.75	double plug
	6.98	13.78	double plug
		Av = 13.744	
DP800	6.64	16.37	double plug
	6.68	16.16	double plug
	6.60	15.92	double plug
	6.55	15.92	double plug
	6.66	16.56	double plug
		Av = 16.186	
TRIP800	6.56	15.09	double plug
	6.53	15.21	double plug
	6.56	15.15	double plug
	6.57	15.26	double plug
	6.55	15.13	double plug
		Av = 15.168	
DP1000	6.50	17.49	double plug
	6.55	17.76	shear plug
	6.59	17.59	shear plug
	7.09	17.68	shear plug
	7.08	17.90	shear plug
		Av = 17.684	

Table 5.3 continued

Grade	Weld current (kA)	Failure Load (kN)	Failure mode
MS1400	6.31	15.19	shear plug
	6.06	15.46	shear plug
	6.37	14.84	interface
	6.38	14.88	shear plug
	6.29	14.90	shear plug
		Av = 15.054	

Table 5.4 Minimum shear strengths required by BS1140:1993[41] compared to average shear strengths achieved

Steel Grade	Sheet Thickness (mm)	R_m (N/mm^2)	Min. shear strength (kN)	Av. shear strength (kN)
LC	1.15	313	5.018	8.174
IF260	1.2	390	6.665	8.354
TRIP600	1.0	623	8.099	11.616
DP600	1.2	635	10.852	13.744
TRIP800	1.2	788	13.466	15.168
DP800	1.2	806	13.774	16.186
DP1000	1.2	1048	17.909	17.684
MS1400	1.0	1479	19.227	15.054

Table 5.5 Summary of cross tension performance of $5\sqrt{t}$ welds formed in selected steel grades

Grade	Weld current (kA)	Failure Load (kN)	Failure mode
LC	9.11	7.08	plug
	9.12	6.47	plug
	9.12	6.96	plug
	9.08	6.93	plug
	9.09	6.80	plug
		Av = 6.848	
IF260	7.75	6.22	plug
	7.72	6.34	plug
	7.80	6.48	plug
	7.82	6.32	plug
	7.80	6.30	plug
		Av = 6.332	
TRIP600	6.59	7.10	plug
	6.63	6.01	plug
	6.63	6.48	plug
	6.59	6.75	plug
	6.55	6.26	plug
		Av = 6.52	
DP600	6.99	7.07	double plug
	6.99	7.67	double plug
	7.00	7.51	plug
	6.99	7.64	plug
	6.98	7.43	plug
		Av = 7.464	
DP800	6.66	7.72	double plug
	6.66	8.01	plug
	6.65	7.76	plug
	6.64	7.29	plug
	6.67	7.31	plug
		Av = 7.618	
TRIP800	6.50	6.91	plug
	6.52	6.62	plug
	6.53	7.25	plug
	6.45	7.37	plug
	6.44	6.81	plug
		Av = 6.992	
DP1000	6.54	7.59	plug
	6.58	7.82	plug
	6.67	8.15	double plug
	6.62	7.82	plug
	6.69	8.37	plug
		Av = 7.95	

Table 5.5 continued

Grade	Weld current (kA)	Failure Load (kN)	Failure mode
MS1400	5.95	4.02	plug
	5.97	4.09	double plug
	5.99	4.54	plug
	6.03	4.02	plug
	6.08	4.45	plug
		Av = 4.224	

Table 5.6 Comparison of lap shear and cross tension performance of $5\sqrt{t}$ welds formed in selected steel grades

Steel Grade	Thickness (mm)	R_m (N/mm^2)	lap shear strength (kN)	cross tension strength (kN)	Difference (kN)	Ductility Ratio
LC	1.15	313	8.174	6.848	1.326	0.84
IF260	1.2	390	8.354	6.332	2.022	0.76
TRIP600	1.0	623	11.616	6.52	5.096	0.56
DP600	1.2	635	13.744	7.464	6.28	0.54
TRIP800	1.2	788	15.168	6.992	8.176	0.46
DP800	1.2	806	16.186	7.618	8.568	0.47
DP1000	1.2	1048	17.684	7.95	9.374	0.45
MS1400	1.0	1479	15.054	4.224	10.83	0.28

Table 5.7 Average weld microhardness levels observed in relation to carbon equivalent

Steel Grade	Carbon Equivalent	Av. Parent metal hardness ($Hv_{0.3}$)	Av. Weld hardness ($Hv_{0.3}$)	% increase in hardness
LC	0.045	117	203.1	73.6
IF260	0.060	132.8	233.1	75.5
TRIP600	0.204	204.7	408.5	99.6
DP600	0.215	203.8	423.8	108.0
DP800	0.217	265.3	449.2	69.3
DP1000	0.245	358.5	498.9	39.2
MS1400	0.266	508.3	514.3	1.2
TRIP800	0.307	238.6	526.5	120.7

Table 5.8 Effect of electrode tip diameter on approximate current required to form $3.5\sqrt{t}$ diameter welds in 1.2mm TRIP800

Electrode tip diameter (mm)	Electrode Force (kN)	Weld Time (cycles)	Weld current (kA)
5	3.2	10	4.2
6	4.6	10	4.8
7	6.3	10	5.8

Table 5.9 Summary of lap shear performance of TRIP800 samples fabricated using 6mm and 7mm diameter electrode tips

Electrode / weld diameter	Weld current (kA)	Failure Load (kN)	Failure mode
6mm / $5\sqrt{t}$	6.30	16.66	double plug
	6.37	16.47	double plug
	6.40	16.62	double plug
	6.47	16.31	double plug
	6.42	16.71	double plug
		Av = 16.554	
6mm / $6.4\sqrt{t}$	8.03	18.40	double plug
	8.13	18.58	double plug
	8.35	18.49	plug
	8.38	18.60	plug
	7.97	18.12	double plug
		Av = 18.438	
7mm / $5\sqrt{t}$	7.37	17.19	interface
	7.39	16.73	double plug
	7.38	16.95	interface
	7.38	16.33	double plug
	7.37	17.71	plug
		Av = 16.982	
7mm / $7\sqrt{t}$	9.59	19.46	double plug
	9.60	19.78	double plug
	9.66	19.21	double plug
	9.56	19.26	plug
	9.68	18.96	plug
		Av = 19.334	

Table 5.10 Minimum shear strengths required by BS1140:1993[41] compared to average shear strengths measured for TRIP800 samples fabricated using 6mm and 7mm diameter electrode tips

Electrode tip diameter / weld diameter	Min. req. shear strength (kN)	Av. shear strength (kN)
6mm / $5\sqrt{t}$	13.466	16.554
6mm / $6.4\sqrt{t}$	17.237	18.438
7mm / $5\sqrt{t}$	13.466	16.982
7mm / $7\sqrt{t}$	18.853	19.334

Table 5.11 Summary of cross tension results from 1.2mm TRIP800 samples fabricated using 6mm and 7mm diameter electrode tips

Electrode / weld diameter	Weld current (kA)	Failure Load (kN)	Failure mode
6mm / $5\sqrt{t}$	6.34	7.86	interface
	6.40	7.96	plug
	6.34	8.02	interface
	6.33	7.42	interface
	6.32	7.20	interface
		Av = 7.692	
6mm / $6.4\sqrt{t}$	7.78	8.68	double plug
	7.90	8.53	double plug
	8.13	9.26	plug
	8.07	8.64	plug
	7.89	8.93	plug
		Av = 8.808	
7mm / $5\sqrt{t}$	7.32	7.45	plug
	7.37	7.35	plug
	7.32	7.41	double plug
	7.36	7.10	plug
	7.32	6.50	plug
		Av = 7.162	
7mm / $7\sqrt{t}$	9.41	9.12	double plug
	9.65	8.84	partial plug
	9.56	9.14	plug
	9.45	8.65	partial plug
	9.55	8.71	double plug
		Av = 8.892	

Table 5.12 Summary of lap shear results for heat treated $5\sqrt{t}$ welds formed in DP800, DP1000 and TRIP800

Grade	Current A (kA)	Current B (kA)	Failure load (kN)	Failure mode
DP800	7.25	4.78	15.09	interface
	7.23	4.80	14.28	interface
	7.54	4.89	14.37	interface
	7.46	4.92	13.52	interface
	7.47	4.92	13.78	interface
			Av = 14.208	
TRIP800	6.71	4.22	15.60	interface
	6.82	4.24	15.64	interface
	6.87	4.24	16.59	interface
	6.83	4.23	16.53	interface
	6.79	4.18	15.65	interface
			Av = 16.002	
DP1000	7.05	5.09	14.18	interface
	7.14	5.20	14.45	interface
	7.12	5.17	14.09	interface
	7.15	5.23	15.17	interface
	7.16	5.22	14.76	interface
			Av = 14.53	

Table 5.13 Summary of cross tension results for heat treated $5\sqrt{t}$ welds formed in DP800, DP1000 and TRIP800

Grade	Current A (kA)	Current B (kA)	Failure load (kN)	Failure mode
DP800	7.51	4.94	8.76	double plug
	7.54	4.89	9.18	plug
	7.53	4.89	8.51	plug
	7.54	4.84	8.78	plug
	7.58	4.90	9.53	plug
			Av = 8.952	
TRIP800	6.75	4.17	9.37	plug
	6.81	4.14	9.56	plug
	6.83	4.21	9.89	plug
	6.85	4.24	9.03	plug
	6.82	4.14	9.00	plug
			Av = 9.37	
DP1000	7.08	5.18	10.83	plug
	7.07	5.19	10.49	plug
	7.06	5.11	10.82	plug
	7.07	5.13	10.48	plug
	7.07	5.20	10.67	plug
			Av = 10.658	

Table 5.14 Approximate weld current required to form $3.5\sqrt{t}$ diameter welds between the selected AHSS to LC combinations

Grade Combination	Electrode tip diameter (mm)	Electrode force (kN)	Weld time (cycles)	Weld Current (kA)
DP800-LC	5	3.2	10	6.7
DP1000-LC	5	3.2	10	6.8
MS1400-LC	5	3.2	10	6.3
TRIP800-LC	5	3.2	10	6.4

Table 5.15 Summary of lap shear results of $5\sqrt{t}$ welds formed between the selected AHSS to LC combinations

Grade Combination	Weld current (kA)	Failure Load (kN)	Failure mode
DP800 - LC	8.36	8.70	plug
	8.40	8.49	plug
	8.36	8.50	plug
	8.34	8.46	plug
	8.42	8.54	plug
		Av = 8.538	
TRIP800 - LC	7.57	8.02	plug
	7.50	8.19	plug
	7.60	8.03	plug
	7.57	8.05	plug
	7.53	8.15	plug
		Av = 8.088	
DP1000 - LC	7.69	8.21	plug
	7.64	8.30	plug
	7.72	8.16	plug
	7.58	8.15	plug
	7.61	8.13	plug
		Av = 8.19	
MS1400 - LC	7.34	7.91	plug
	7.29	7.82	plug
	7.27	7.91	plug
	7.33	7.91	plug
	7.38	7.96	plug
		Av = 7.902	

Table 5.16 Summary of cross tension results for $5\sqrt{t}$ welds formed between the selected AHSS to LC combinations

Grade Combination	Weld current (kA)	Failure Load (kN)	Failure mode
DP800 - LC	8.27	7.16	plug
	8.29	7.37	plug
	8.28	7.00	plug
	8.27	6.64	plug
	8.36	6.86	plug
		Av = 7.006	
TRIP800 - LC	7.50	6.59	plug
	7.54	6.47	plug
	7.59	6.33	plug
	7.58	6.53	plug
	7.57	6.56	plug
		Av = 6.496	
DP1000 - LC	7.34	6.31	plug
	7.59	6.24	plug
	7.67	6.15	plug
	7.69	6.26	plug
	7.69	6.30	plug
		Av = 6.252	
MS1400 - LC	7.50	4.30	plug
	7.43	4.91	plug
	7.44	4.77	plug
	7.46	4.62	plug
	7.51	4.42	plug
		Av = 4.604	

Table 5.17 Average weld microhardness levels measured in the weld nuggets formed between the selected AHSS to LC combinations and the percentage reduction in hardness compared to a joint in which only the AHSS component is present

Steel Combination	Average measured weld microhardness ($HV_{0.3}$)	% Reduction
DP800 – LC	425	5
DP1000 – LC	450	10
MS1400 – LC	440	14
TRIP800 – LC	457	13

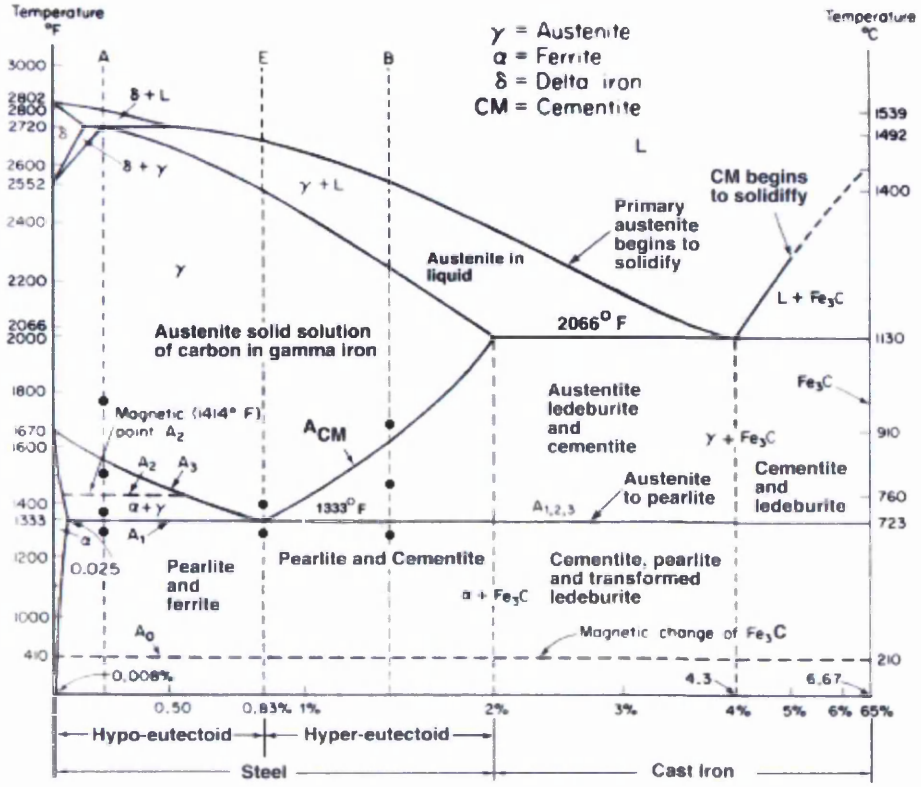

Figure 2.1 Iron – iron carbide equilibrium phase diagram[6]

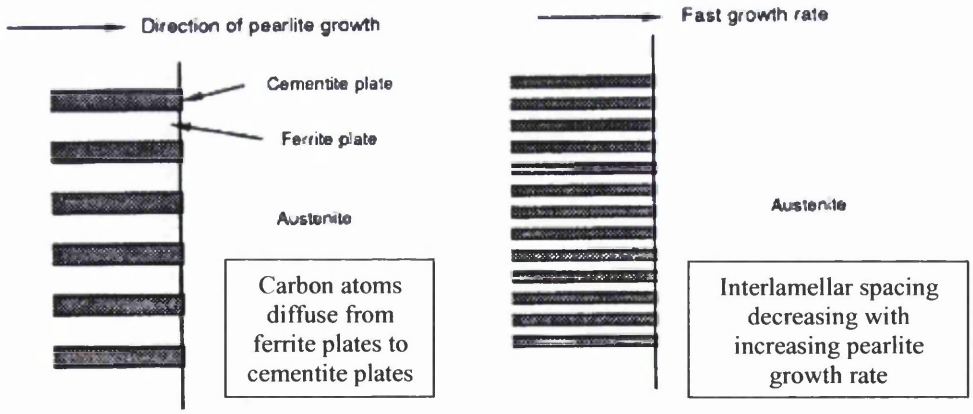

Figure 2.2 Schematic diagram illustrating the effect of growth rate on the interlamellar spacing of pearlite[7]

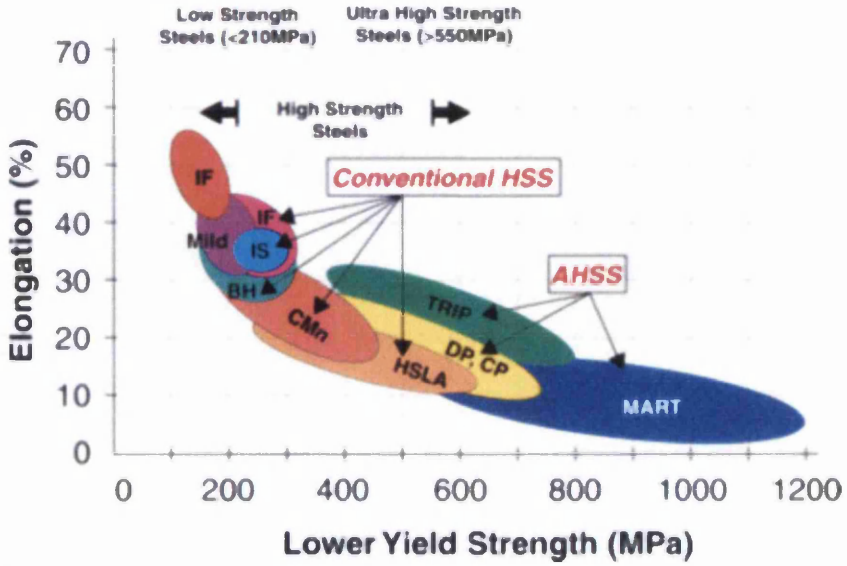

Figure 2.3 Relationship between yield strength and elongation for a range of automotive strip steel grades[8]

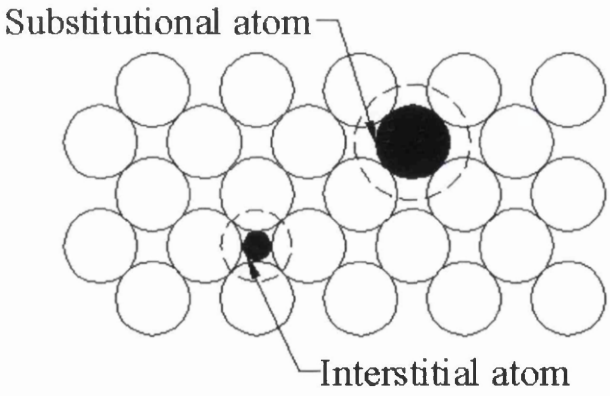

Figure 2.4 Schematic diagram illustrating the positions that solute atoms can occupy in the parent lattice

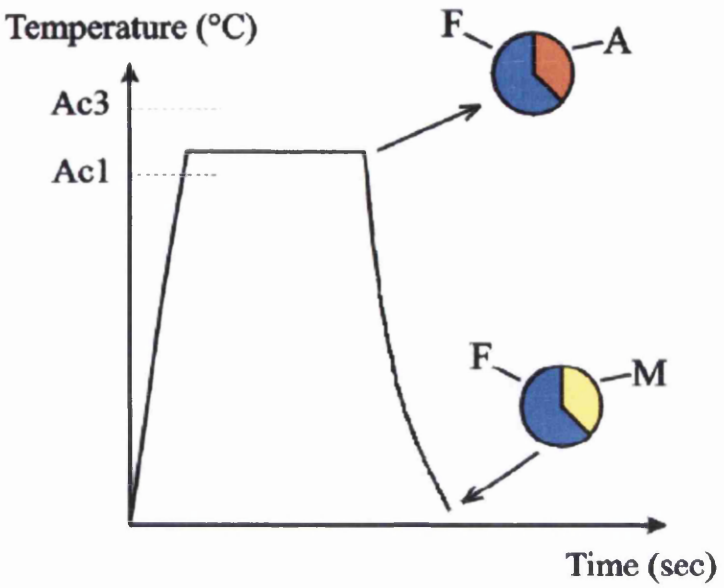

Figure 2.5 Schematic diagram of a typical annealing cycle for the production of a dual phase microstructure in cold rolled strip[20] (F = Ferrite, A = Austenite, M = Martensite)

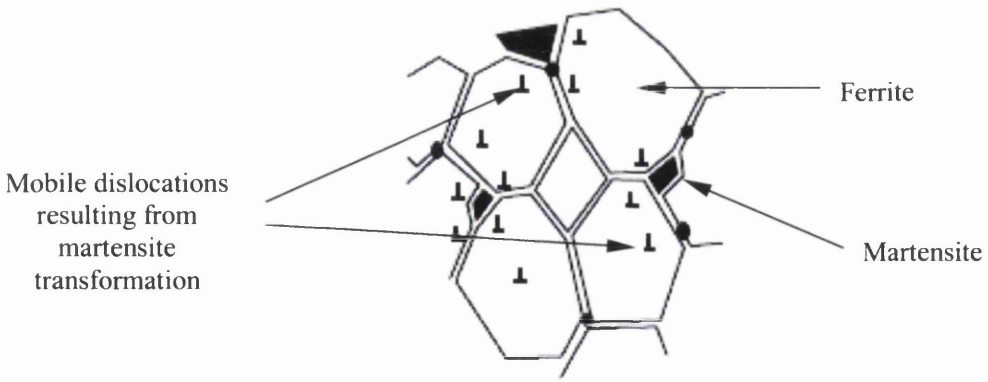

Figure 2.6 Schematic diagram of a typical dual phase microstructure

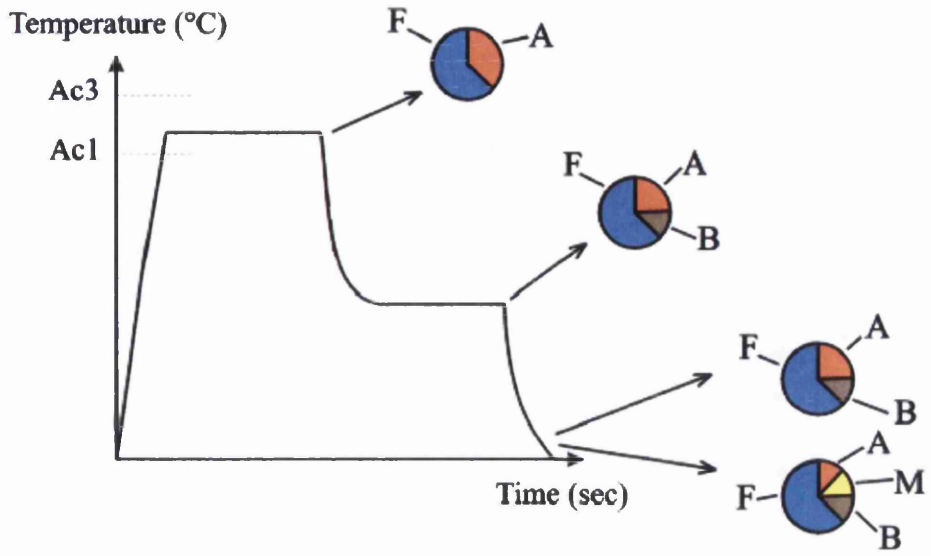

Figure 2.7 Schematic diagram of a typical annealing cycle for the production of a TRIP microstructure in cold rolled strip[20] (F = Ferrite, A = Austenite, B = Bainite, M = Martensite)

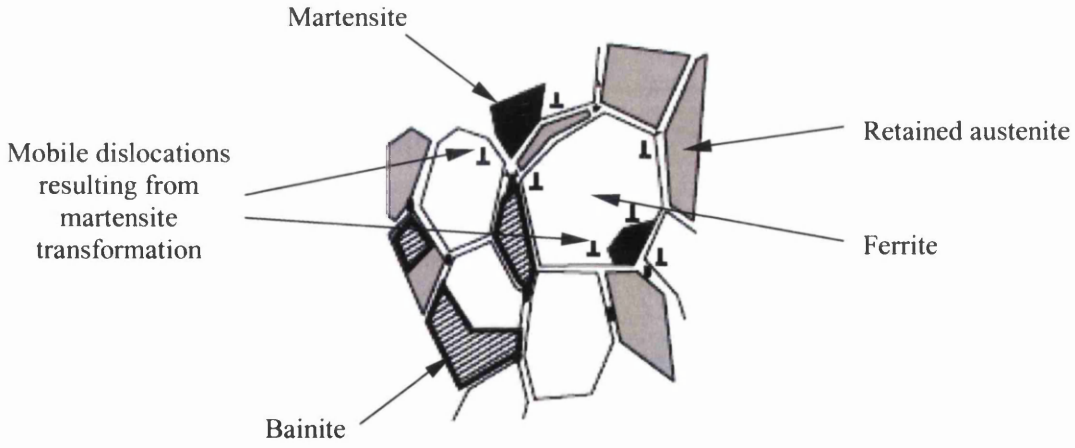

Figure 2.8 Schematic diagram of a typical TRIP microstructure

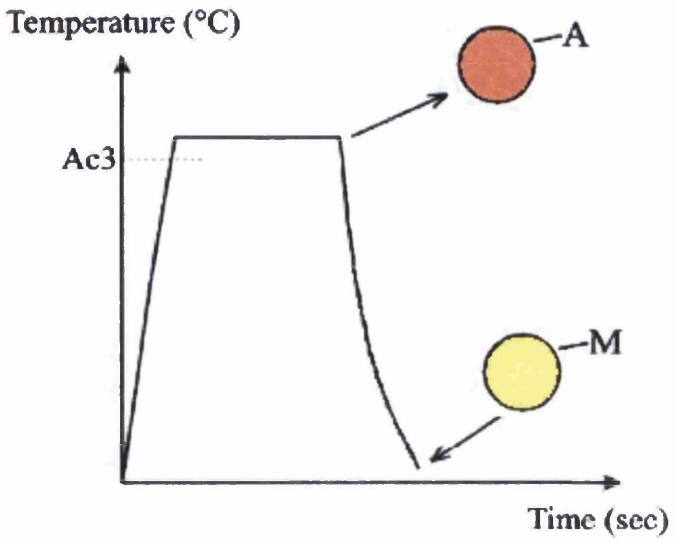

Figure 2.9 Schematic diagram of a typical annealing cycle for the production of a fully martensitic microstructure in cold rolled strip (A = Austenite, M = Martensite)

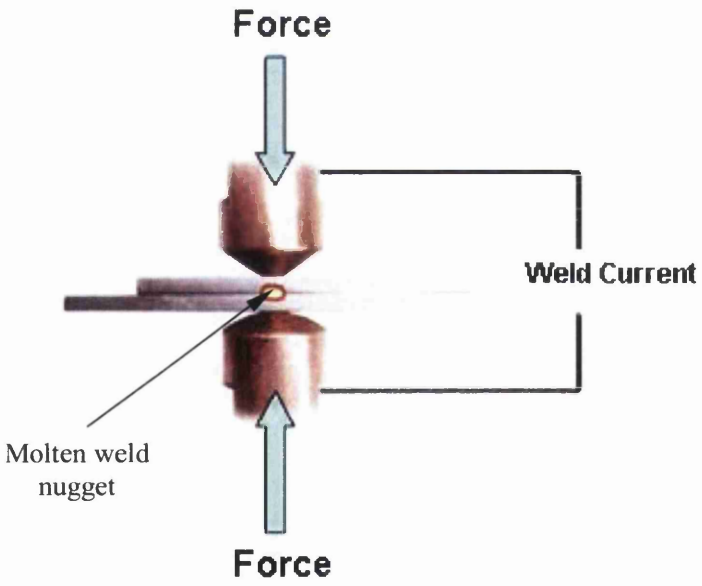

Figure 2.10 Schematic diagram of the resistance spot welding process

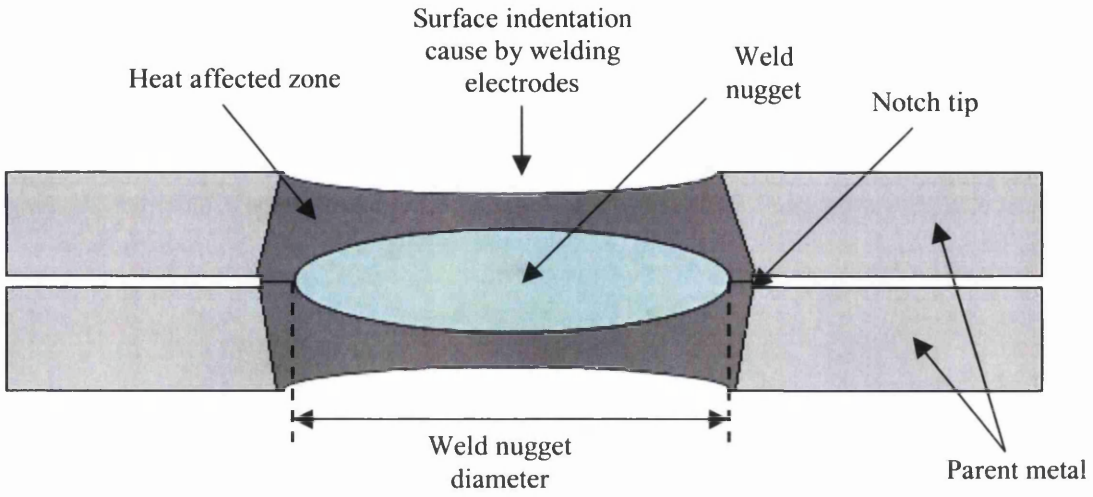

Figure 2.11 Schematic diagram of a resistance spot weld

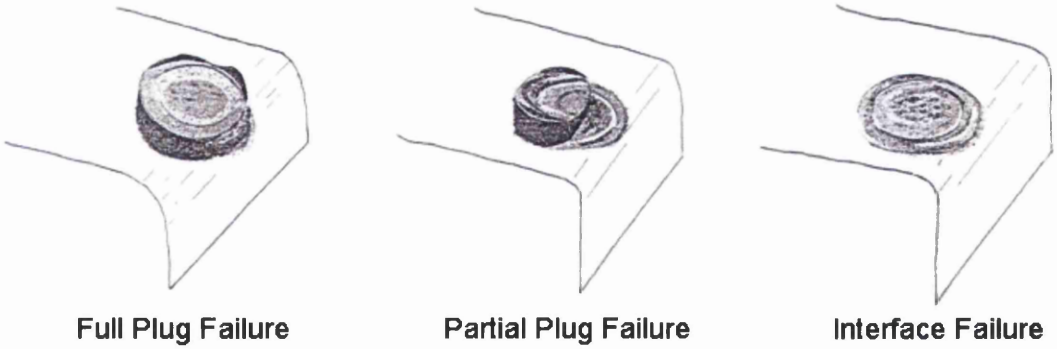

Figure 2.12 Various weld failure modes resulting from destructive testing[68]

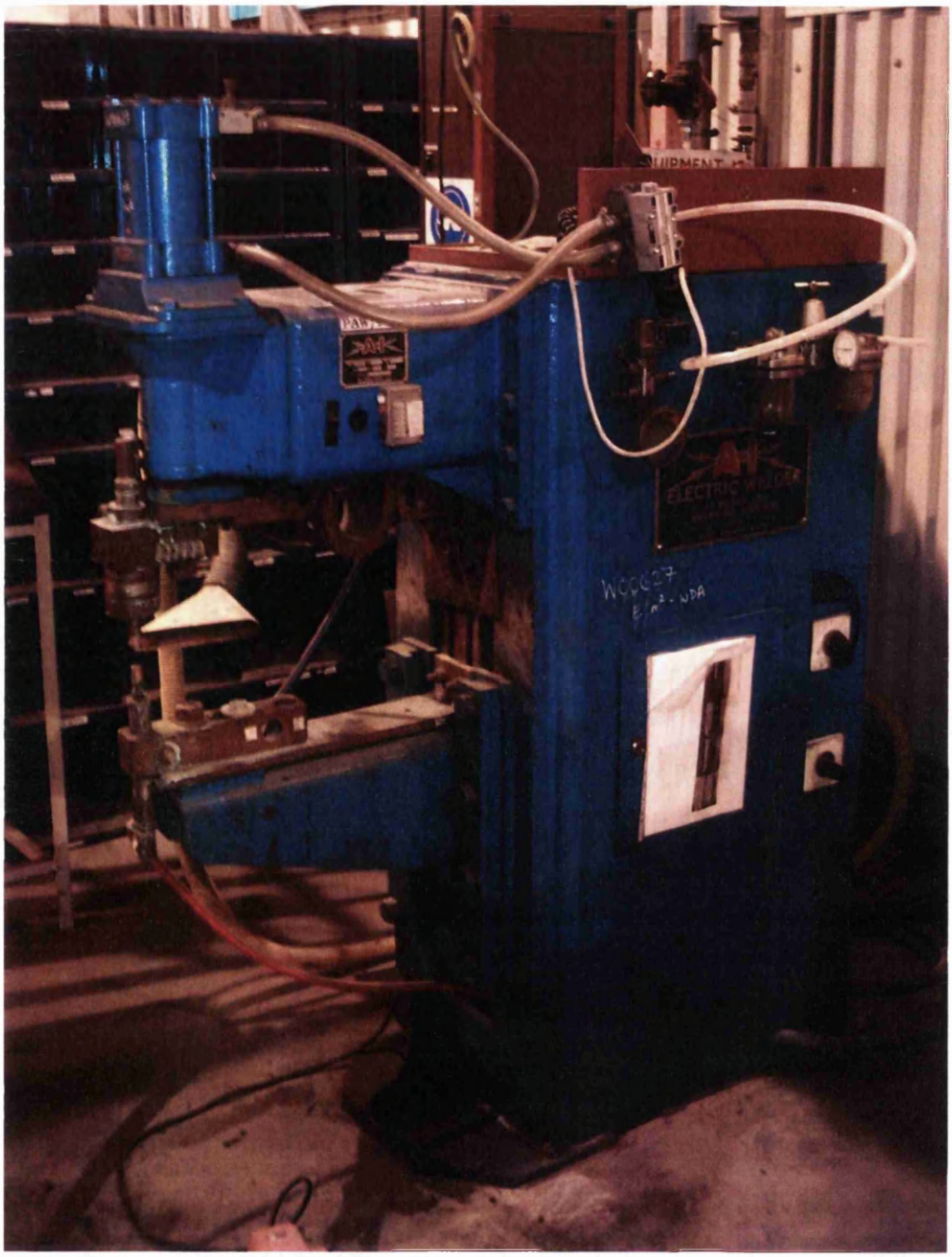

Figure 4.1 Photograph of the 50 kV·A AI pedestal resistance spot welder used during the course of this investigation

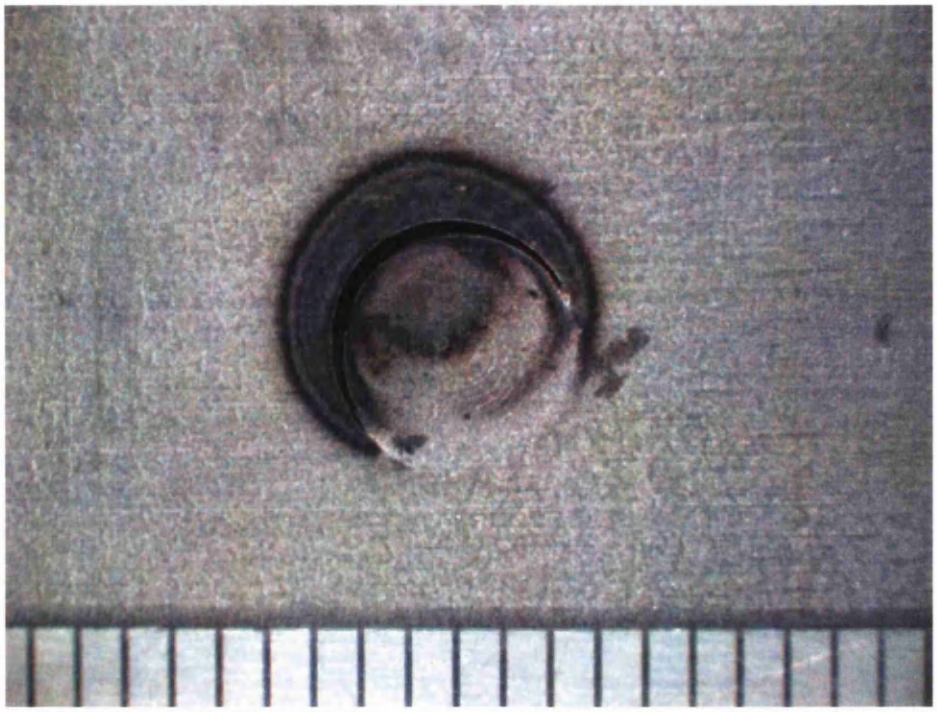

Figure 4.2 Photograph of the surface appearance of spot weld produced with misaligned electrode tips (Scale is in mm)

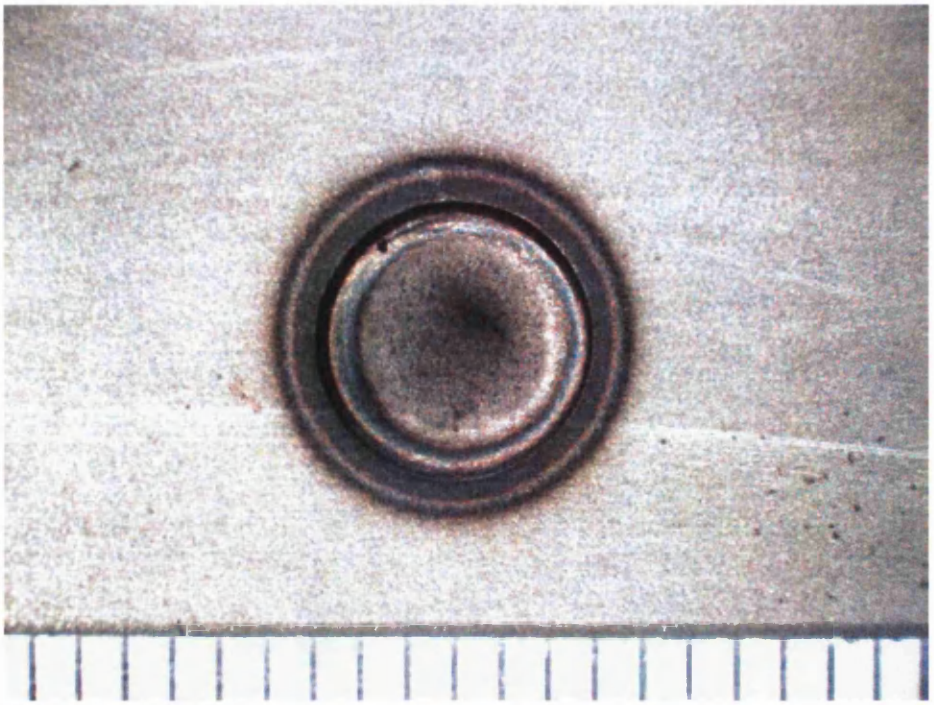

Figure 4.3 Photograph of the surface appearance of a spot weld produced with properly aligned electrode tips (Scale is in mm)

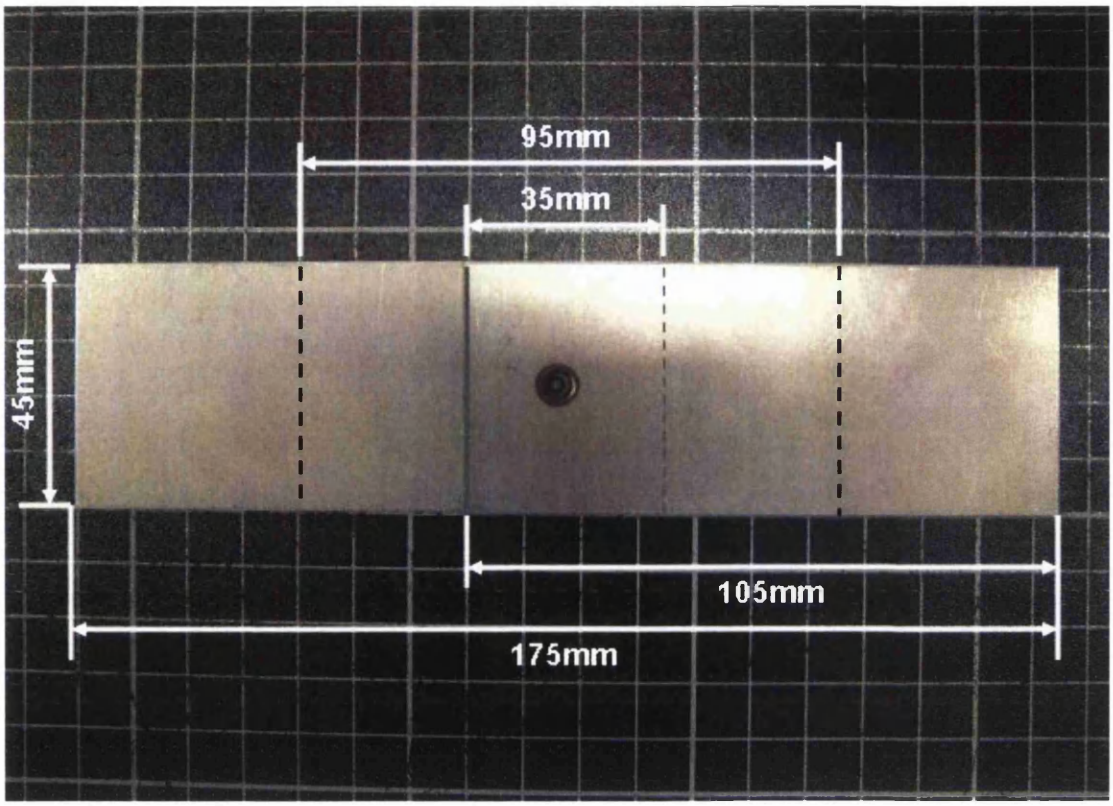

Figure 4.4 Dimensions of a lap shear sample fabricated in accordance with the guidelines laid out in BS1140:1993[41]

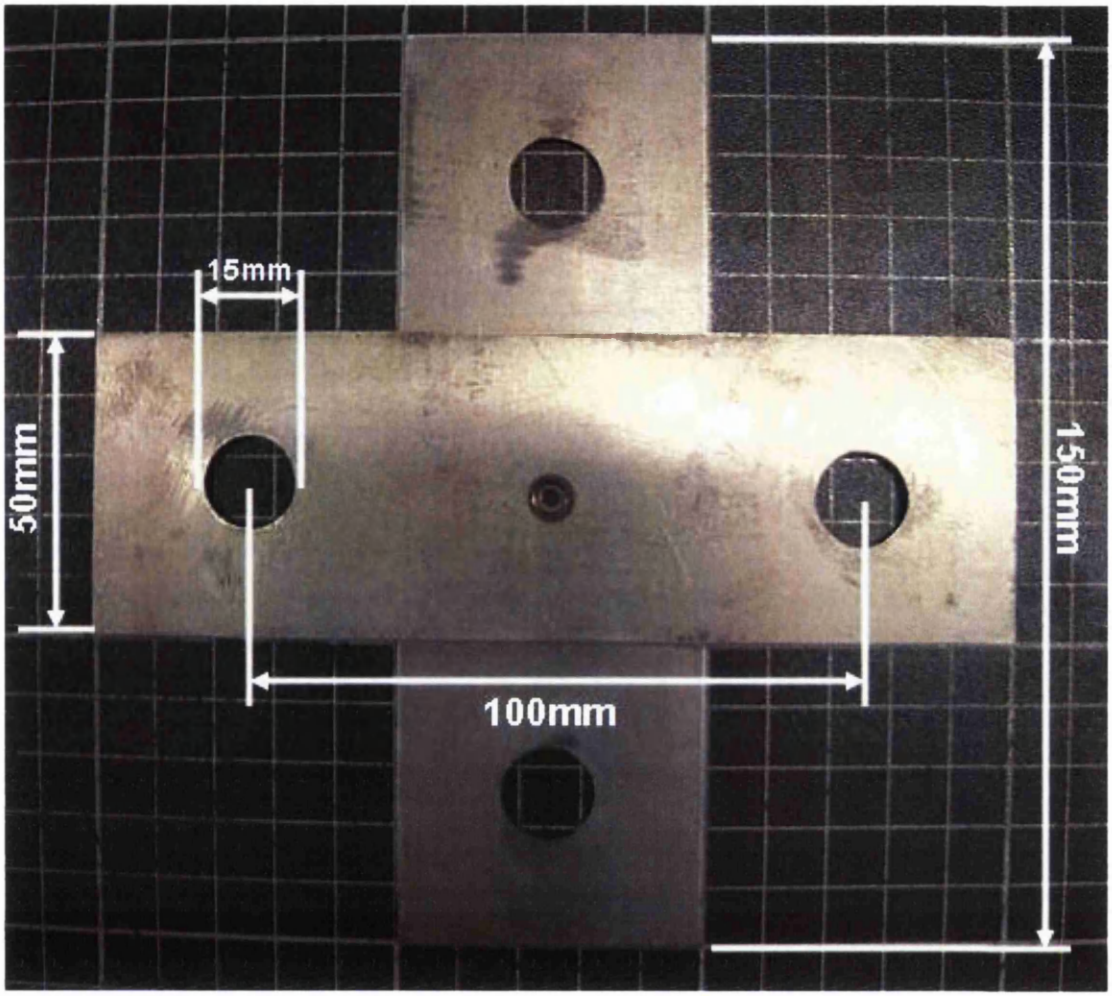

Figure 4.5 Dimensions of a cross tension sample fabricated in accordance with the guidelines laid out in BS1140:1993[41]

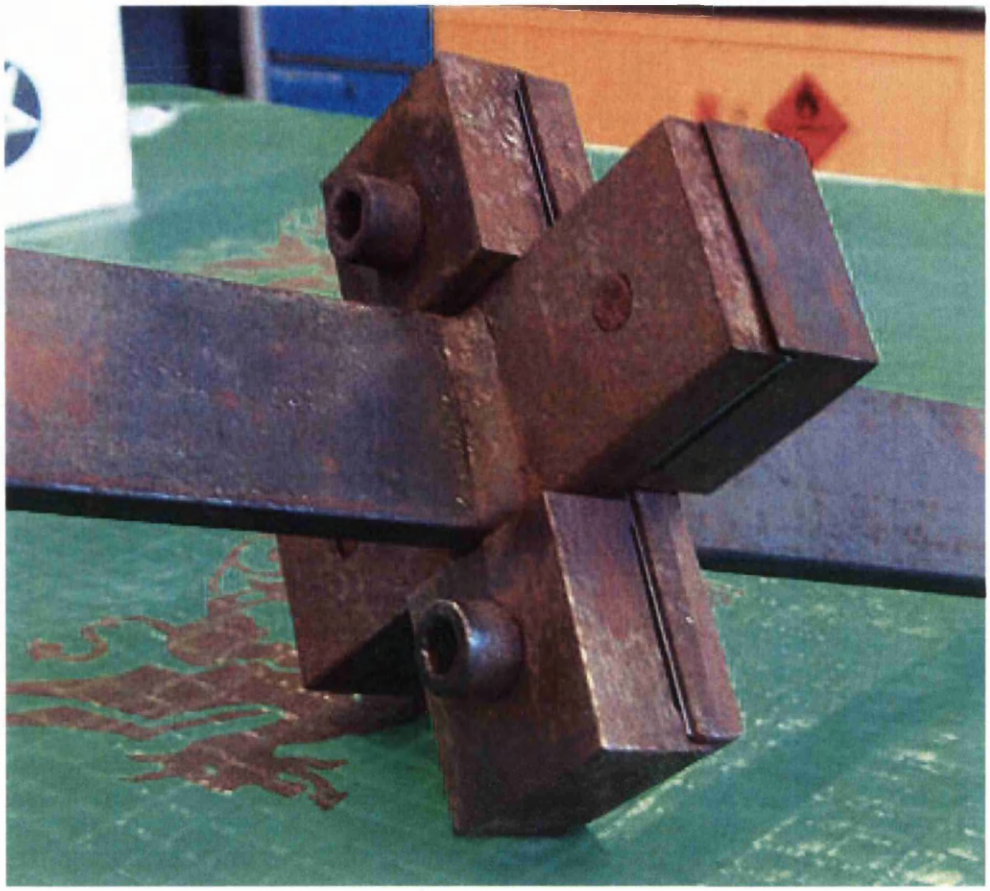

Figure 4.6 Photograph of cross tension sample mounted in tensile testing jig

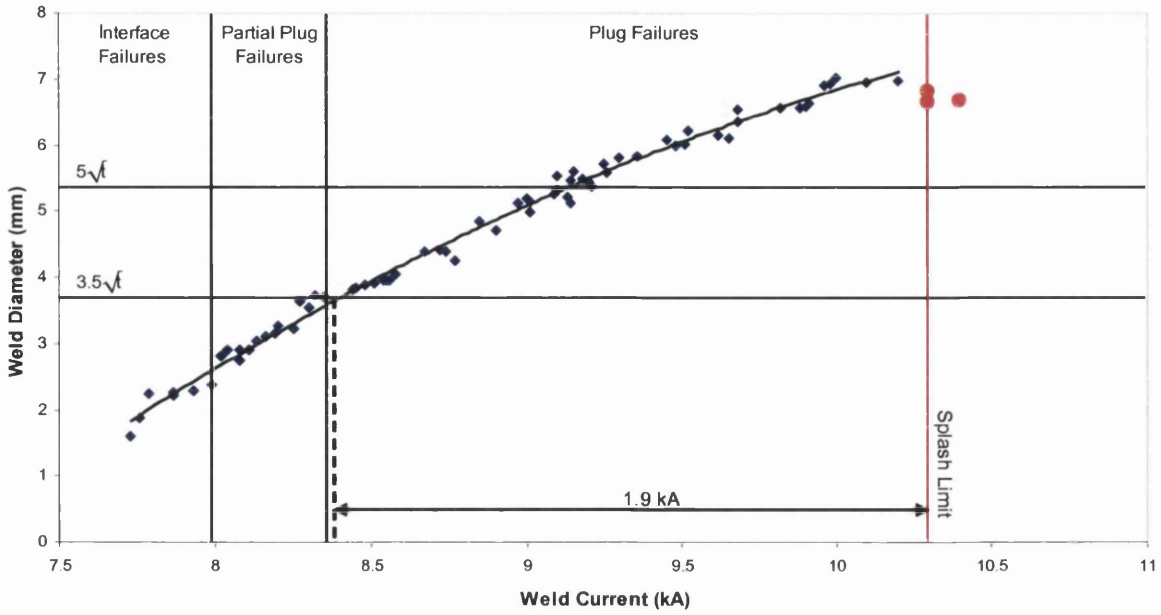

Figure 5.1 Relationship between weld current and weld diameter for 1.15mm low carbon (LC) mild steel (3.2kN electrode force)

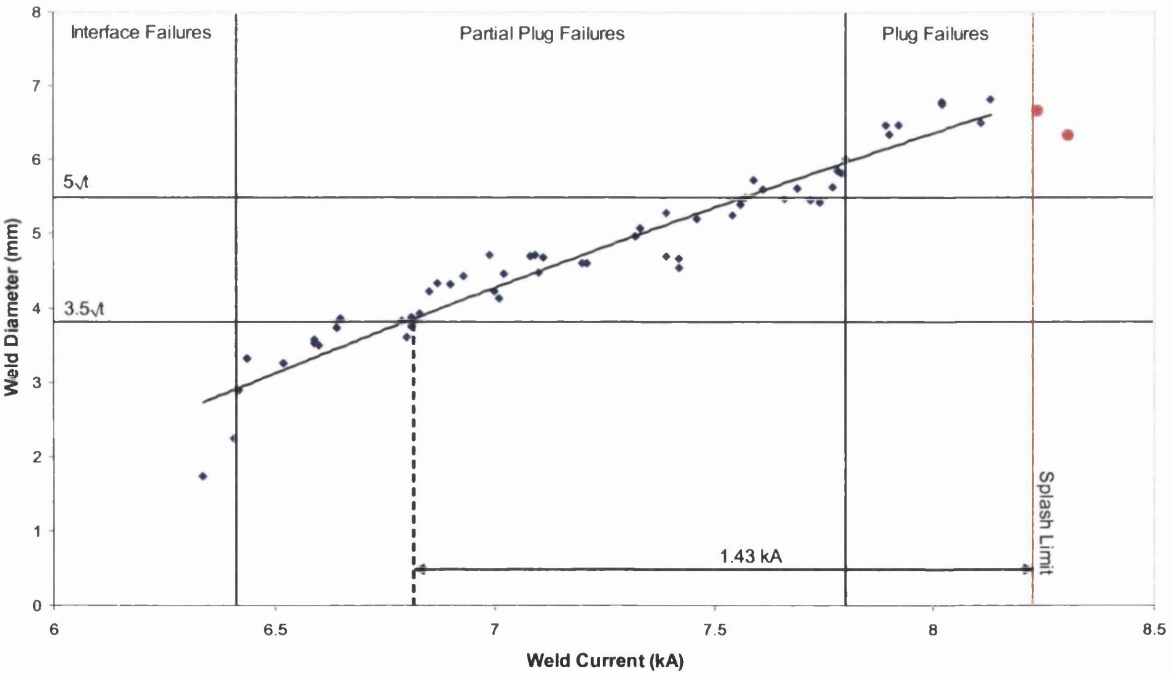

Figure 5.2 Relationship between weld current and weld diameter for 1.2mm IF260 (3.2kN electrode force)

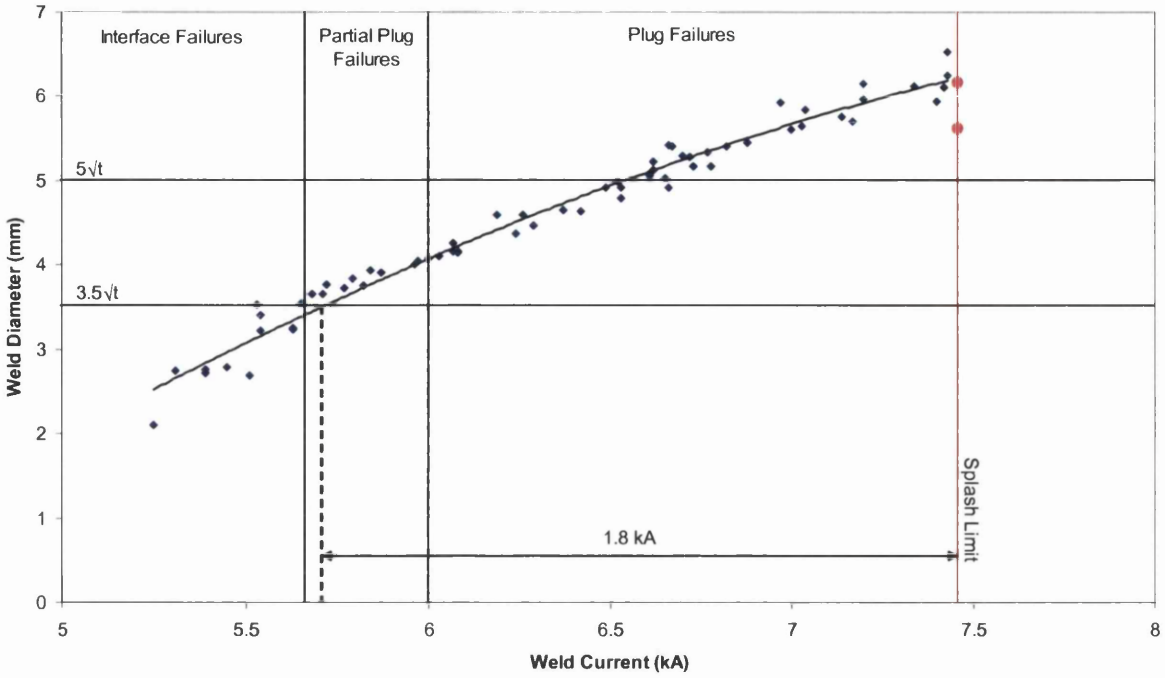

Figure 5.3 Relationship between weld current and weld diameter for 1.0mm TRIP600 (3.2kN electrode force)

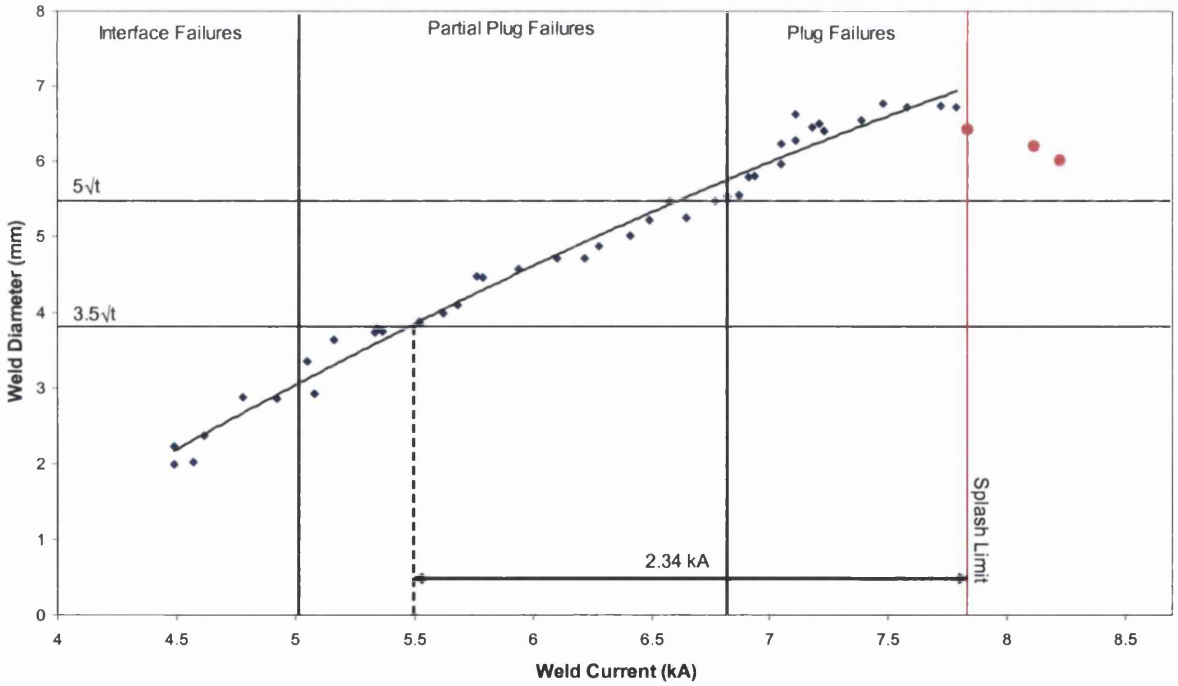

Figure 5.4 Relationship between weld current and weld diameter for 1.2mm DP600 (3.2kN electrode force)

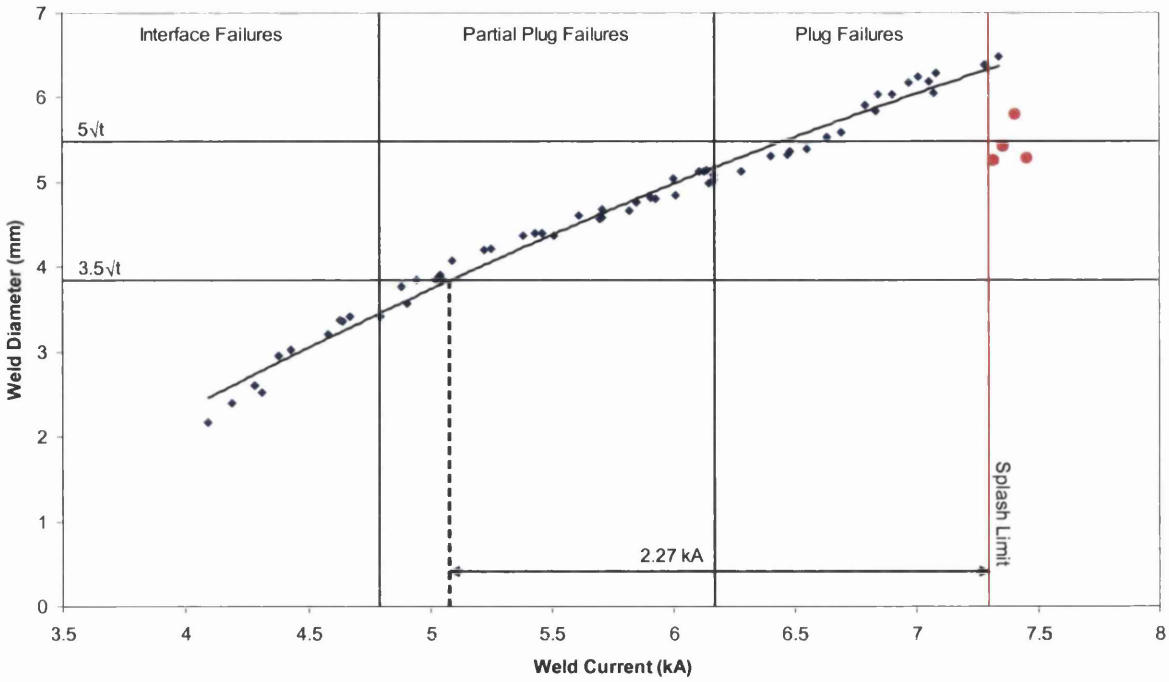

Figure 5.5 Relationship between weld current and weld diameter for 1.2mm DP800 (3.2kN electrode force)

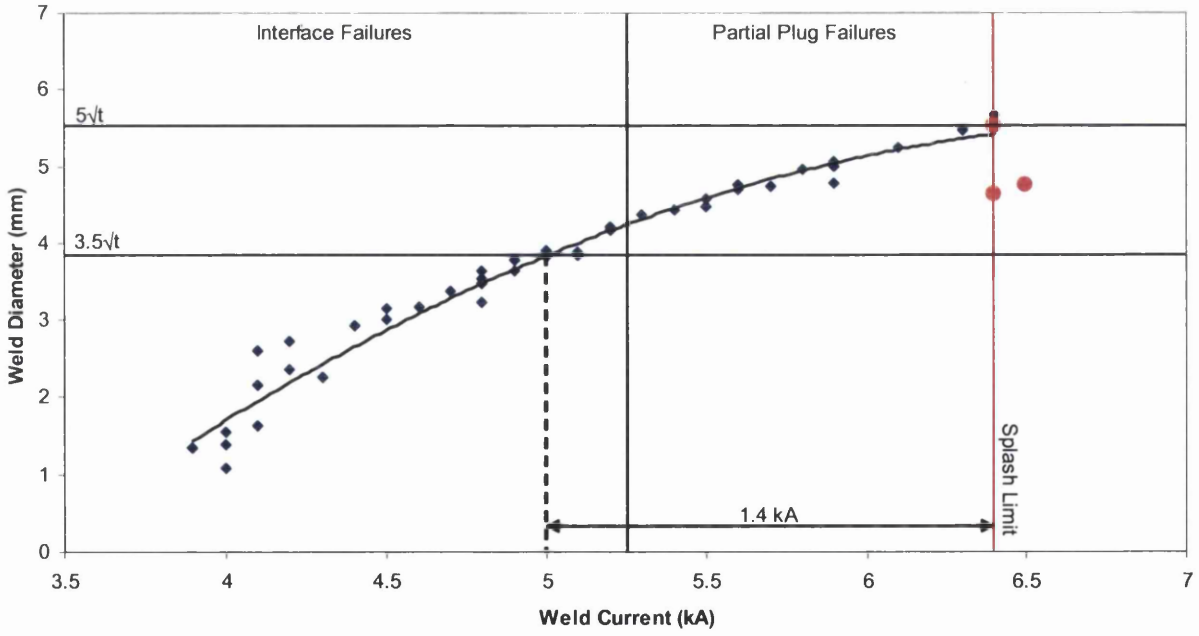

Figure 5.6 Relationship between weld current and weld diameter for 1.2mm DP1000 (3.2kN electrode force)

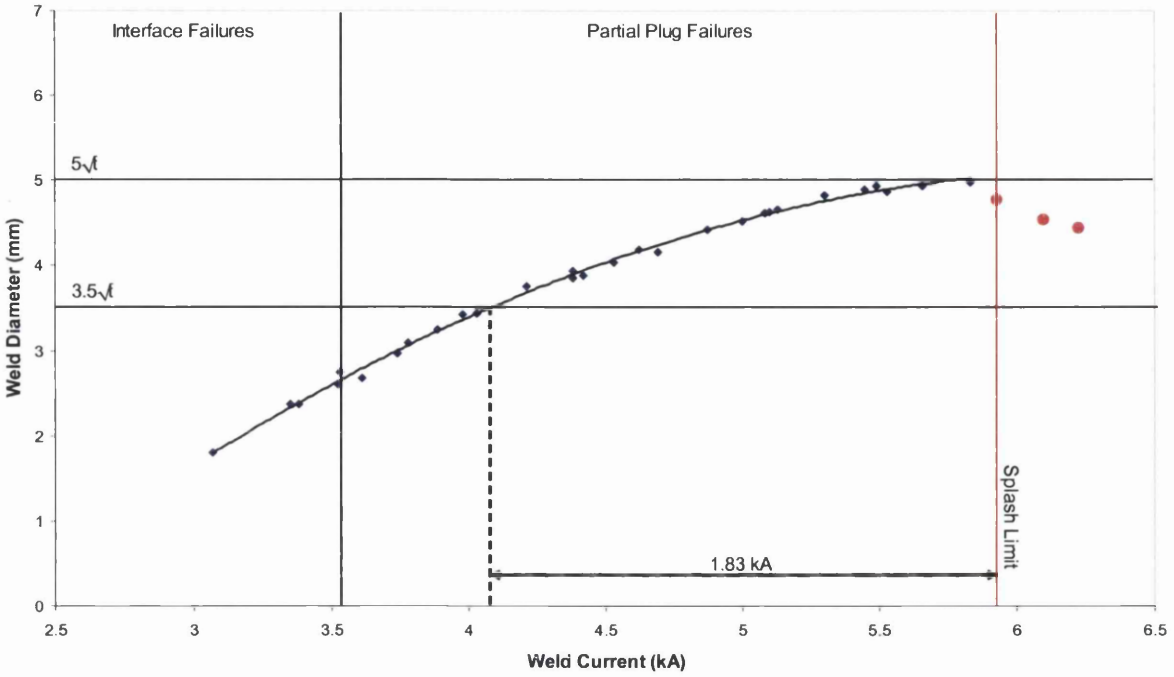

Figure 5.7 Relationship between weld current and weld diameter for 1.0mm MS1400 (3.2kN electrode force)

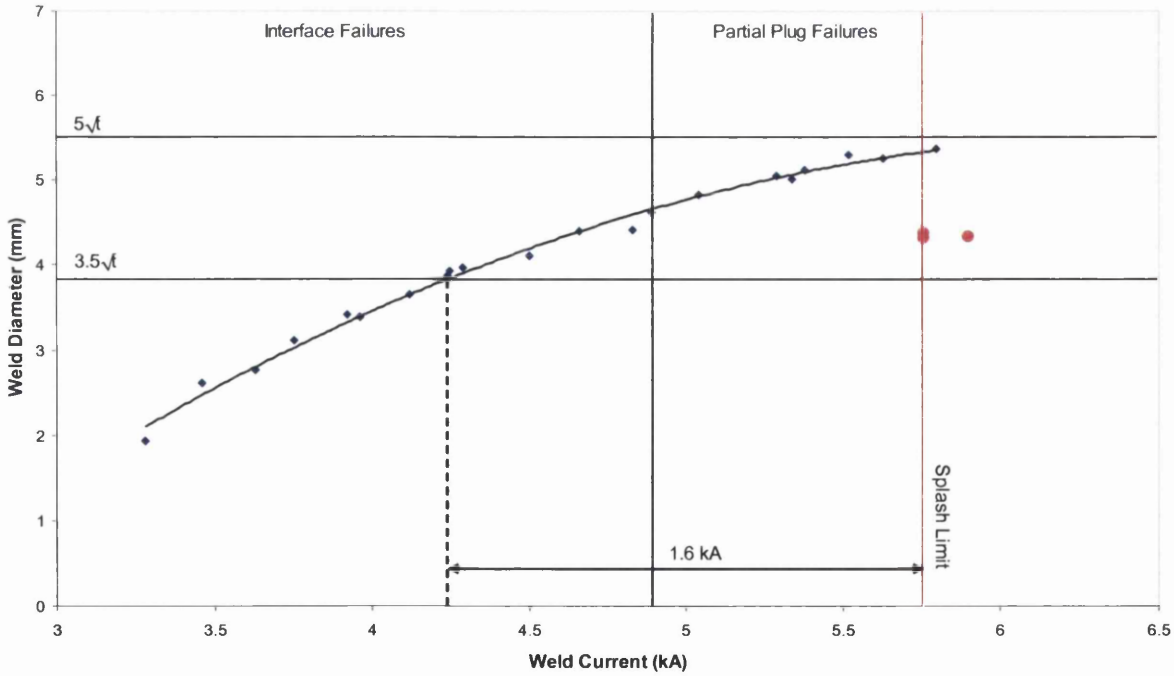

Figure 5.8 Relationship between weld current and weld diameter for 1.2mm TRIP800 (3.2kN electrode force)

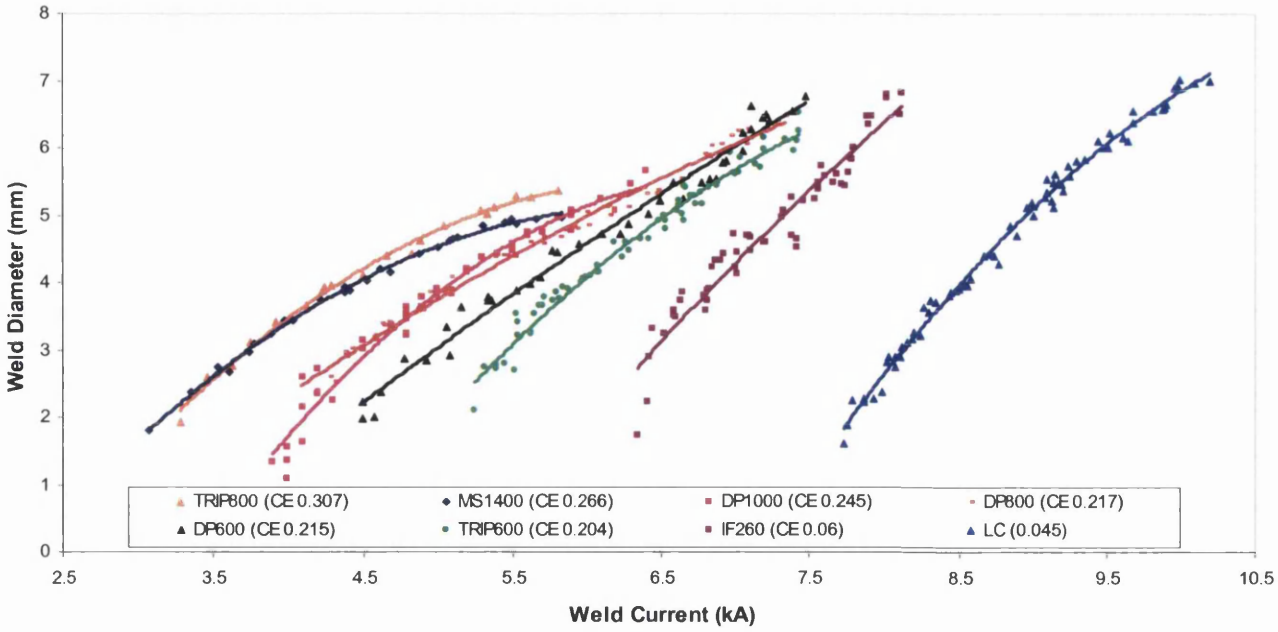

Figure 5.9 Effect of carbon equivalent (CE) on weld growth (3.2kN electrode force)

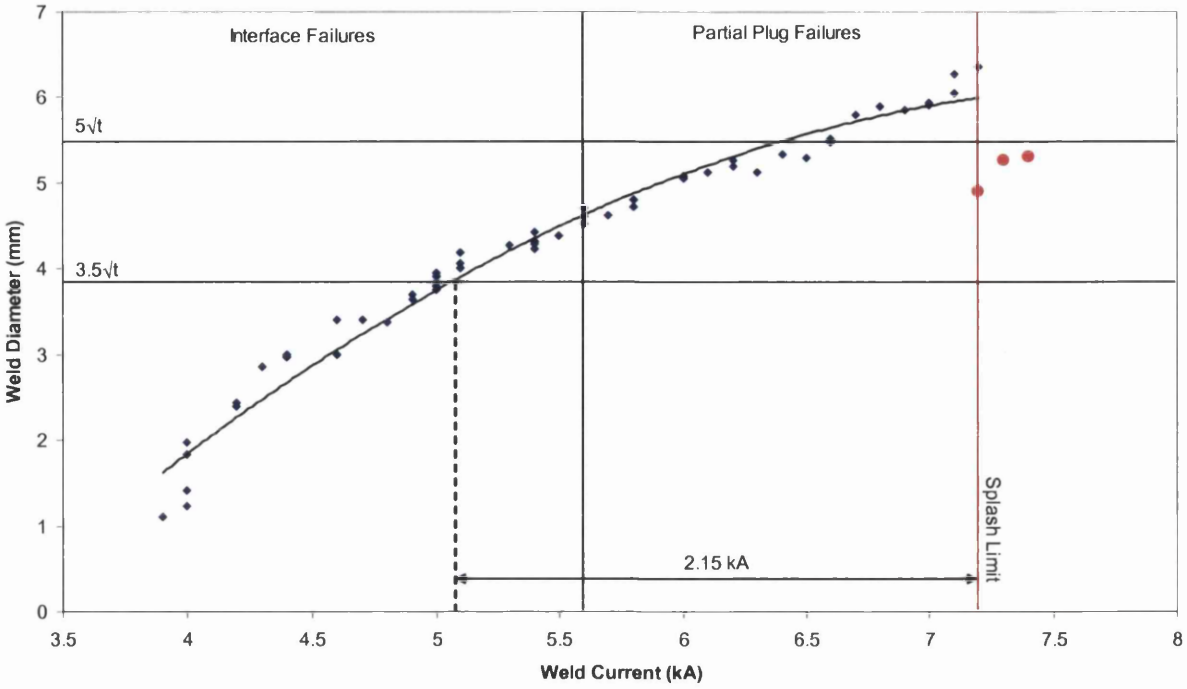

Figure 5.10 Relationship between weld current and weld diameter for 1.2mm DP1000 (4.0kN electrode force)

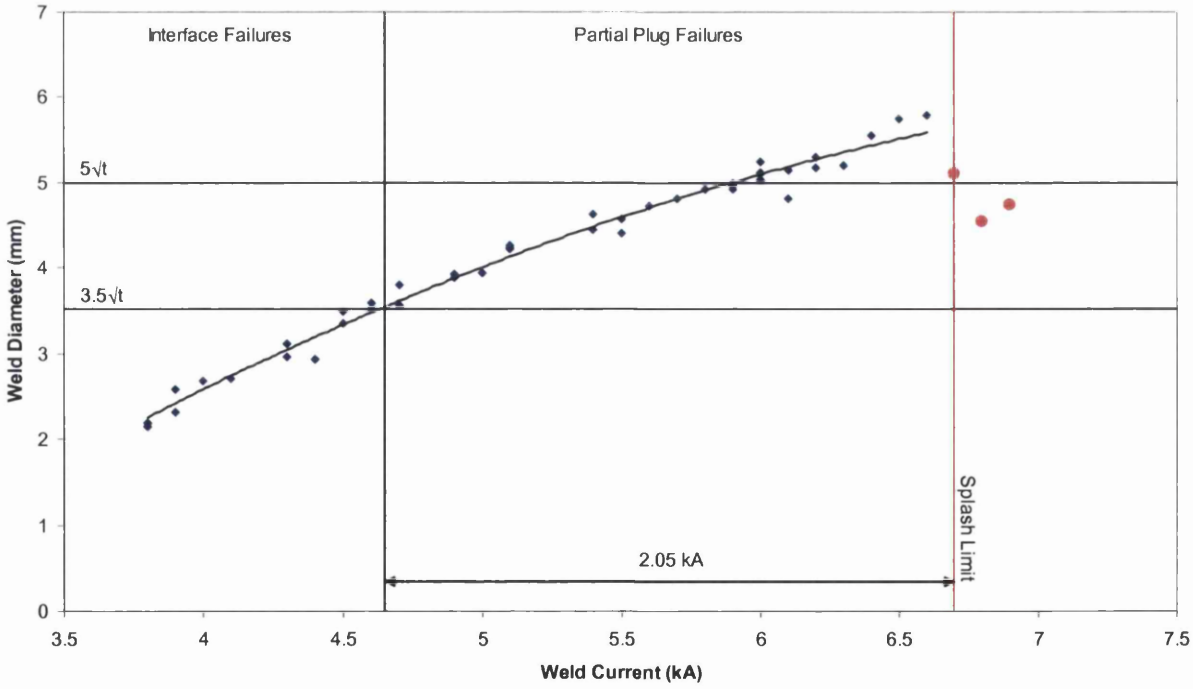

Figure 5.11 Relationship between weld current and weld diameter for 1.0mm MS1400 (4.0kN electrode force)

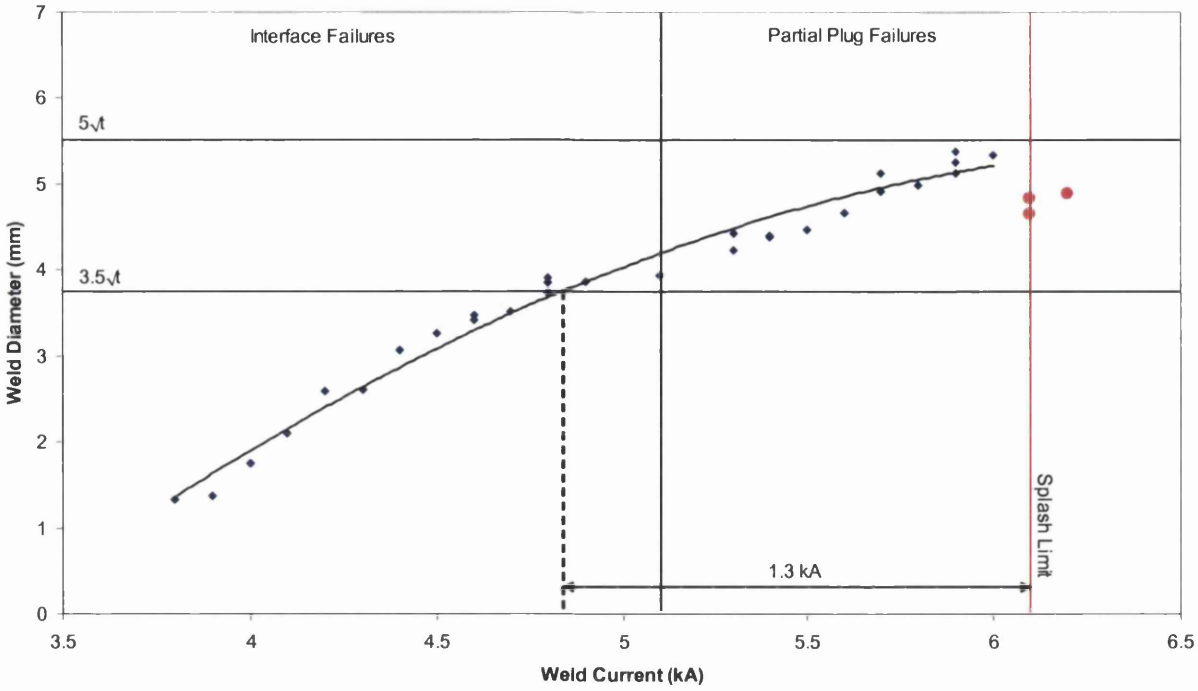

Figure 5.12 Relationship between weld current and weld diameter for 1.2mm TRIP800 (4.0kN electrode force)

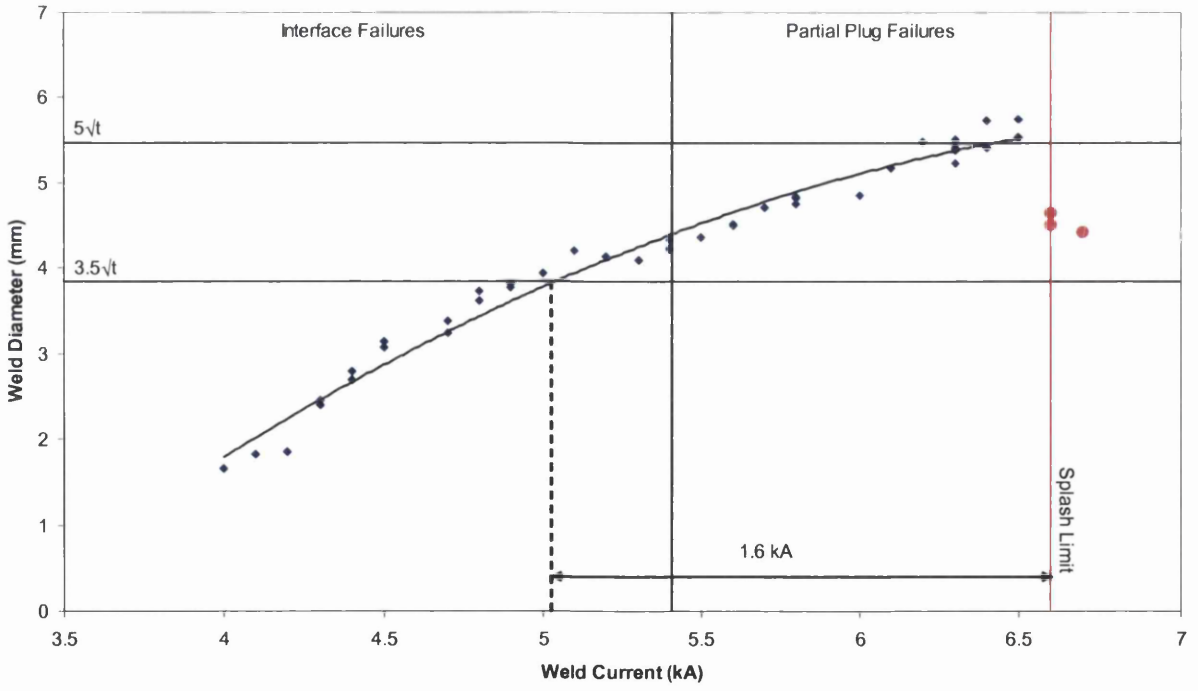

Figure 5.13 Relationship between weld current and weld diameter for 1.2mm TRIP800 (5.0kN electrode force)

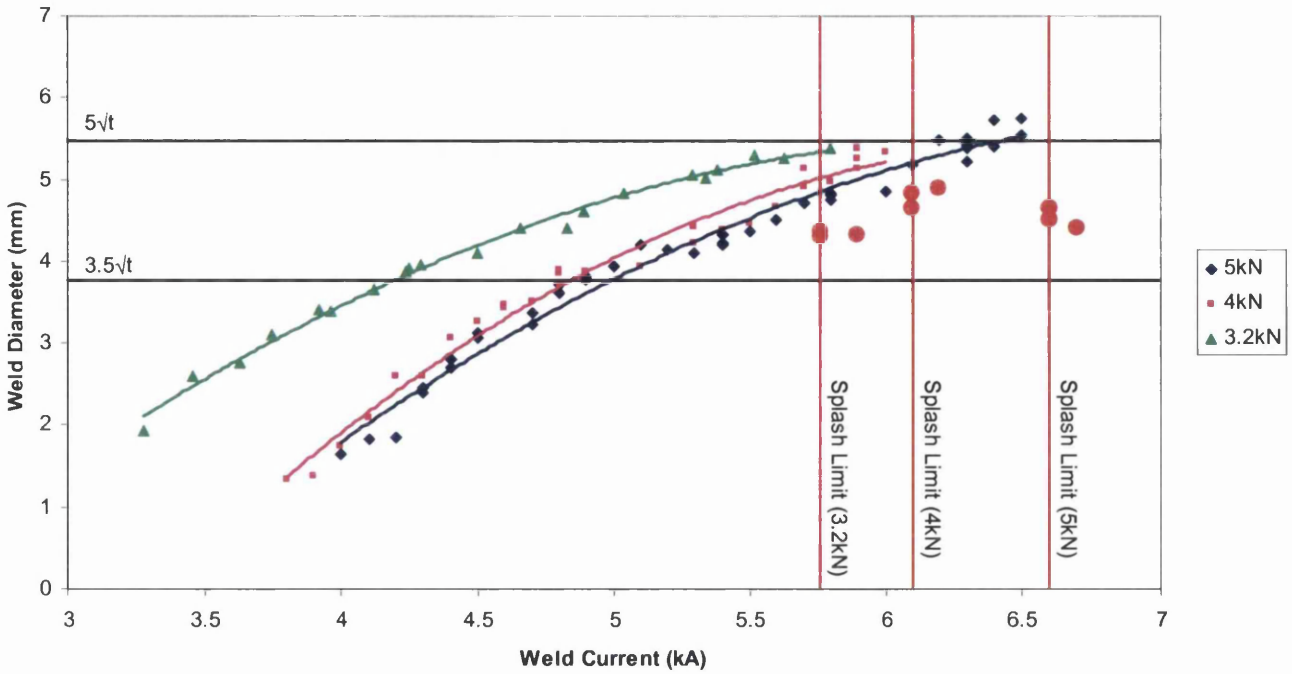

Figure 5.14 Effect of electrode force on weld growth in 1.2mm TRIP800

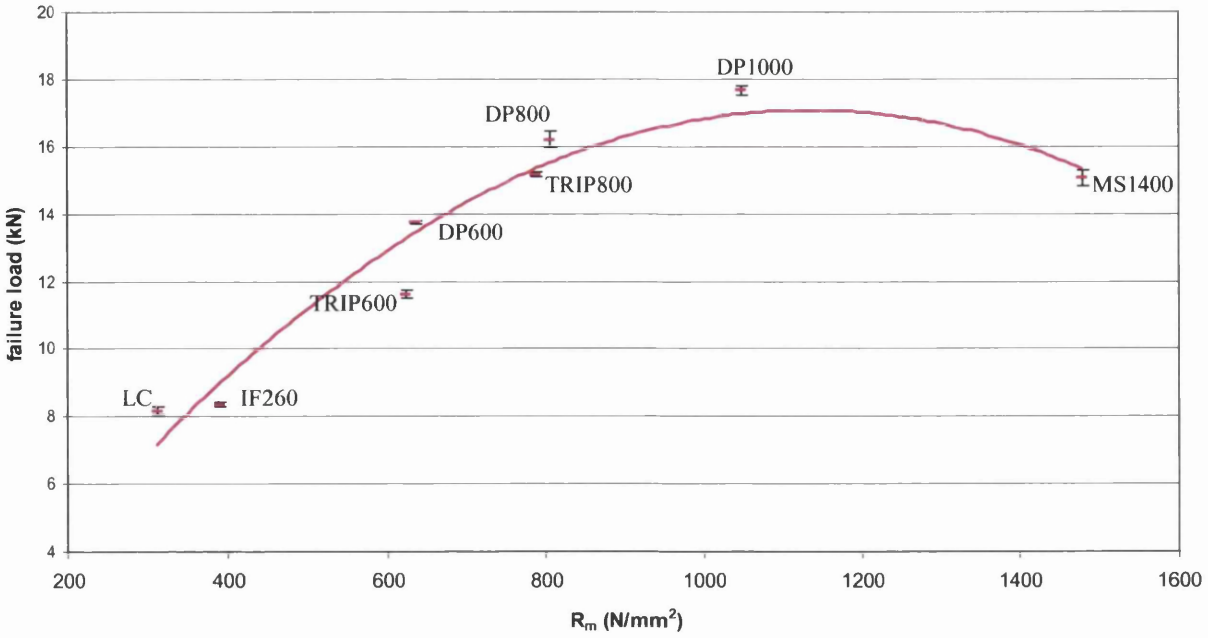

Figure 5.15 Graph illustrating the relationship between parent metal strength and average lap shear failure load of $5\sqrt{t}$ welds. Error bars indicate one standard deviation from the mean

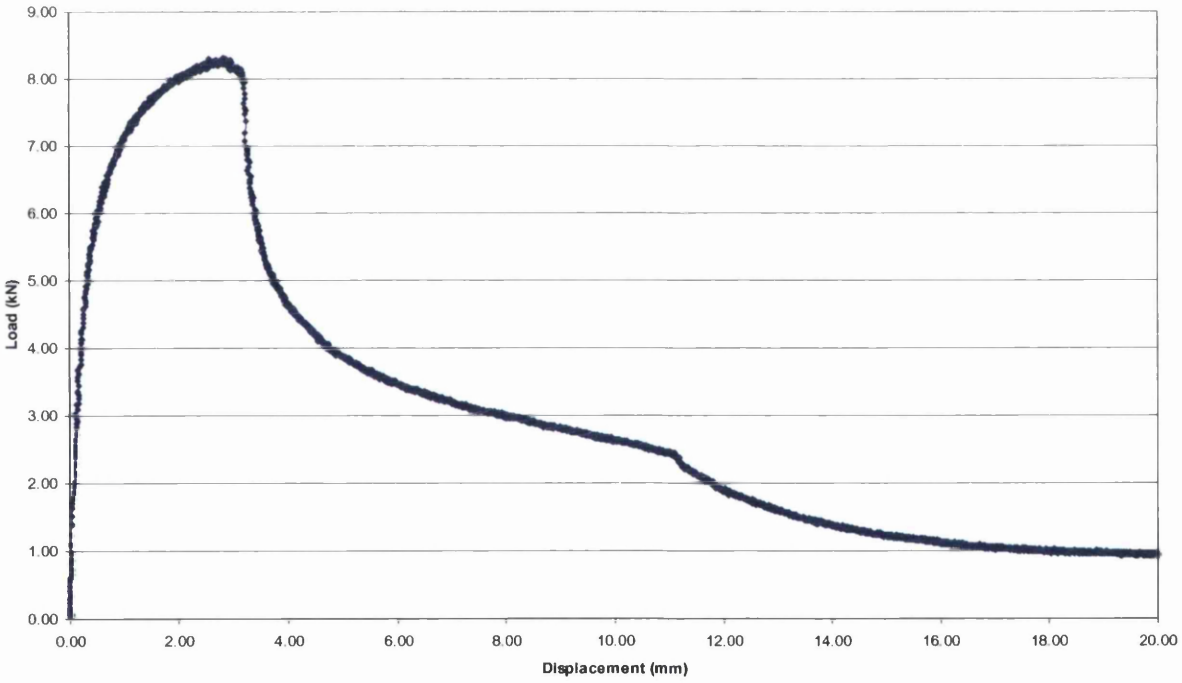

Figure 5.16 Typical lap shear load vs. displacement curve exhibited by $5\sqrt{t}$ welds formed in 1.15mm LC

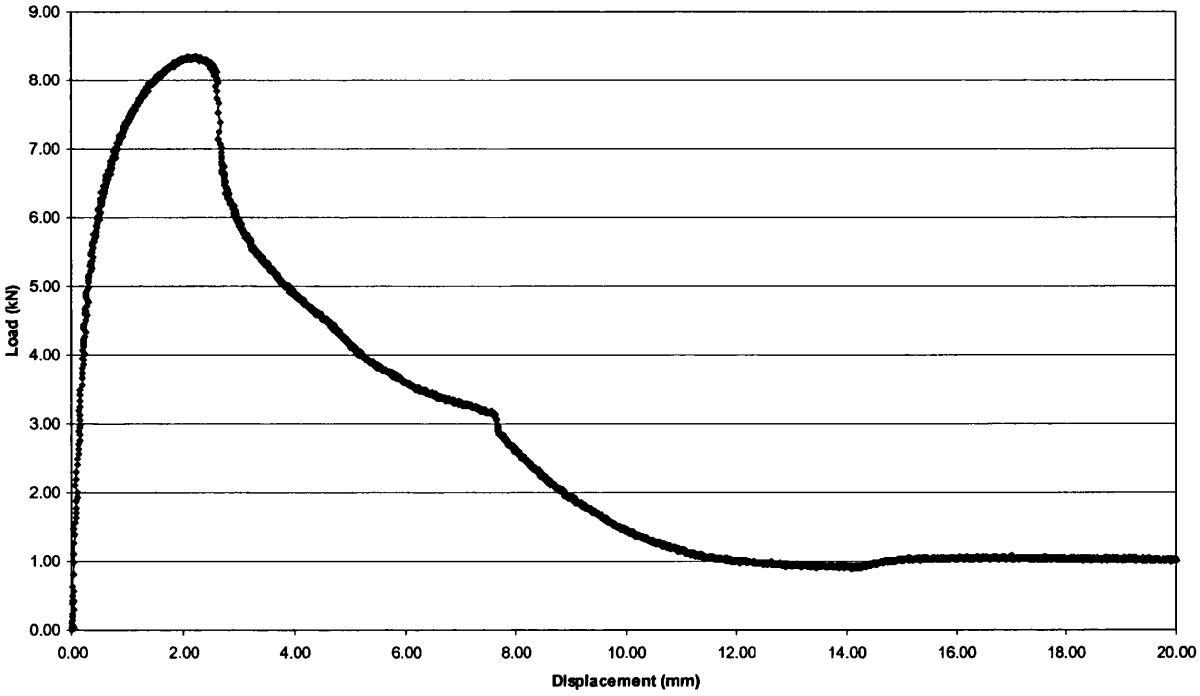

Figure 5.17 Typical lap shear load vs. displacement curve exhibited by $5\sqrt{t}$ welds formed in 1.2mm IF260

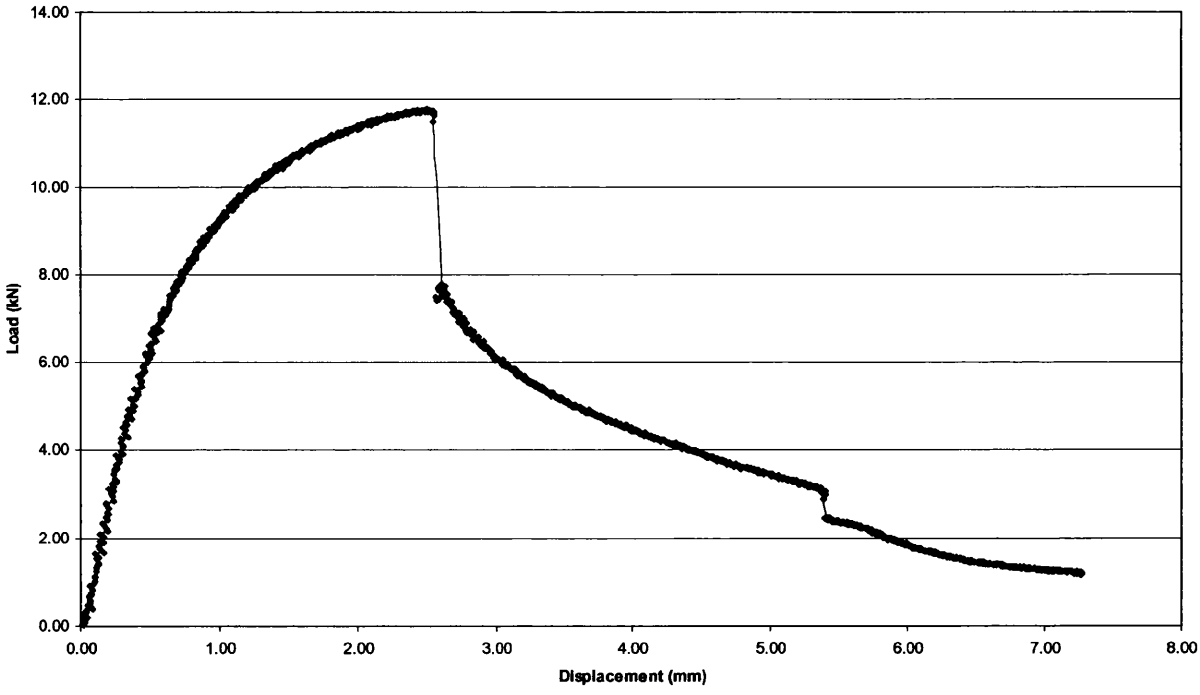

Figure 5.18 Typical lap shear load vs. displacement curve exhibited by $5\sqrt{t}$ welds formed in 1.0mm TRIP600

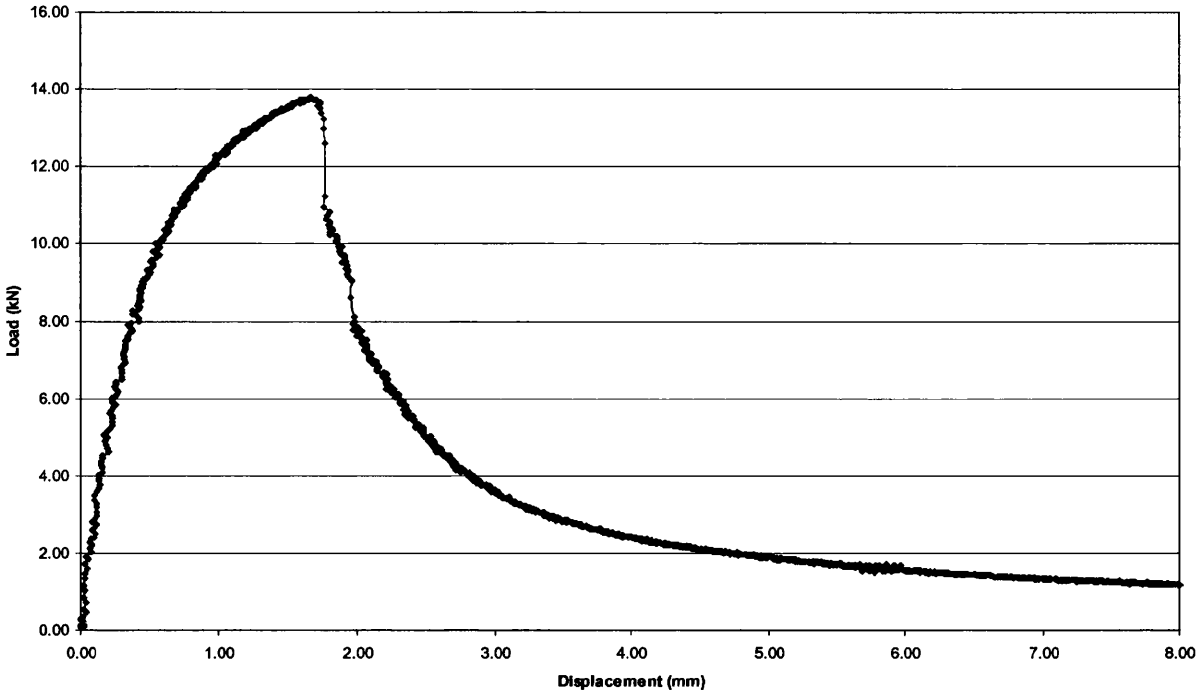

Figure 5.19 Typical lap shear load vs. displacement curve exhibited by $5\sqrt{t}$ welds formed in 1.2mm DP600

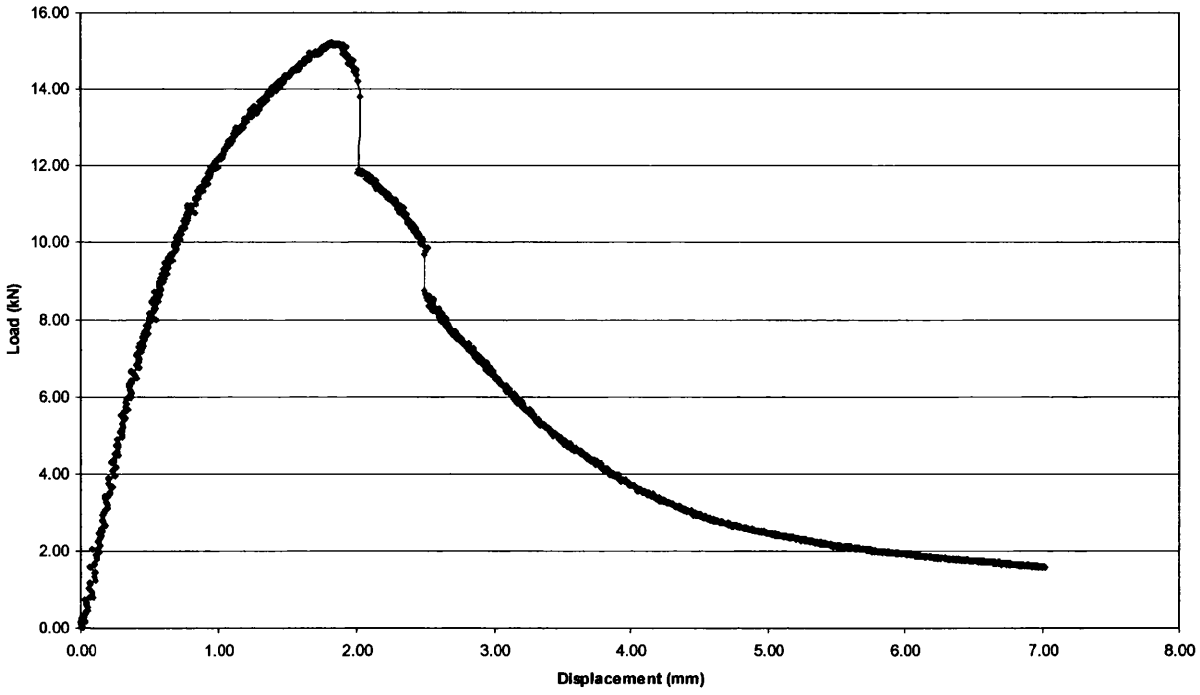

Figure 5.20 Typical lap shear load vs. displacement curve exhibited by $5\sqrt{t}$ welds formed in 1.2mm TRIP800

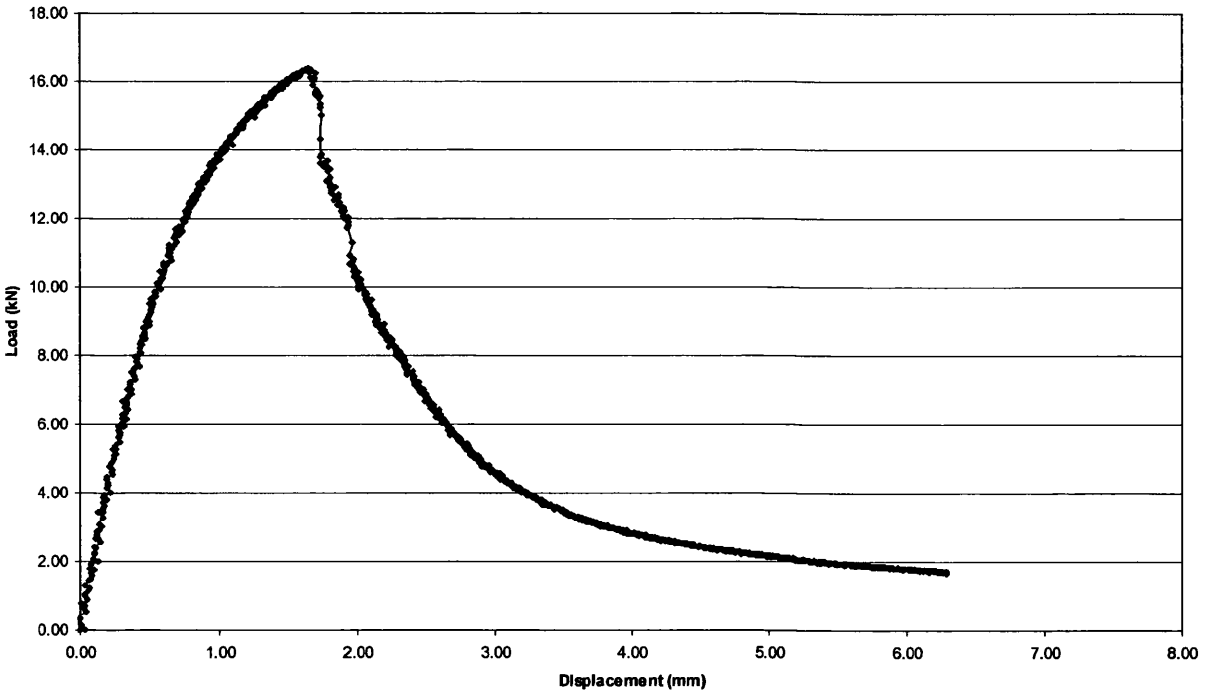

Figure 5.21 Typical lap shear load vs. displacement curve exhibited by $5\sqrt{t}$ welds formed in 1.2mm DP800

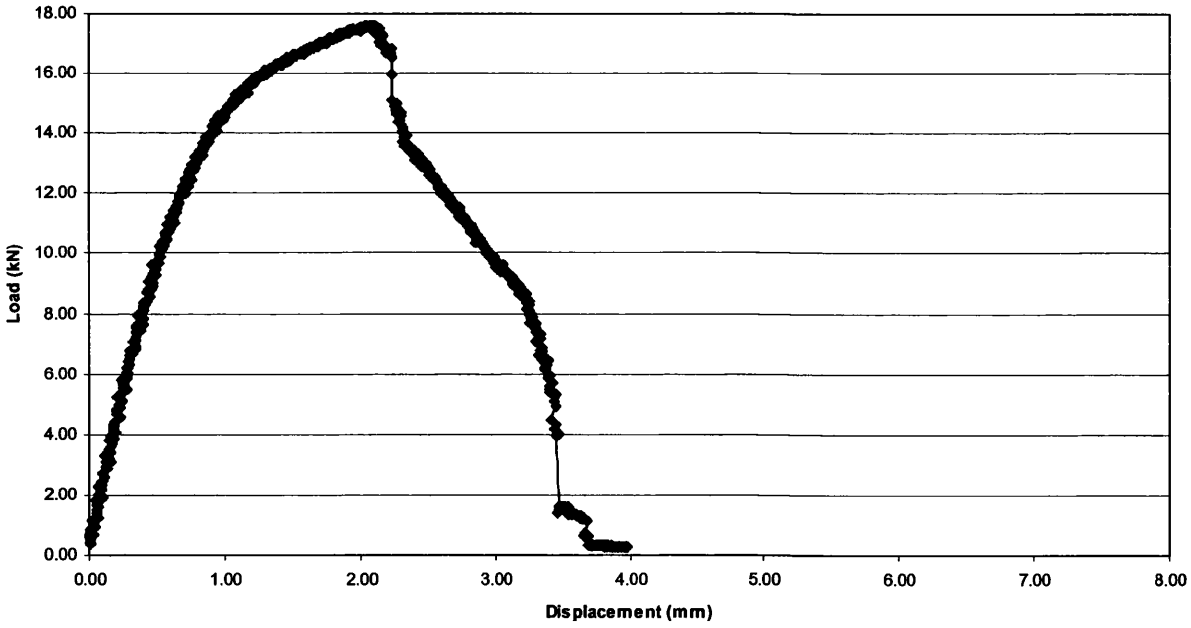

Figure 5.22 Typical lap shear load vs. displacement curve exhibited by $5\sqrt{t}$ welds formed in 1.2mm DP1000

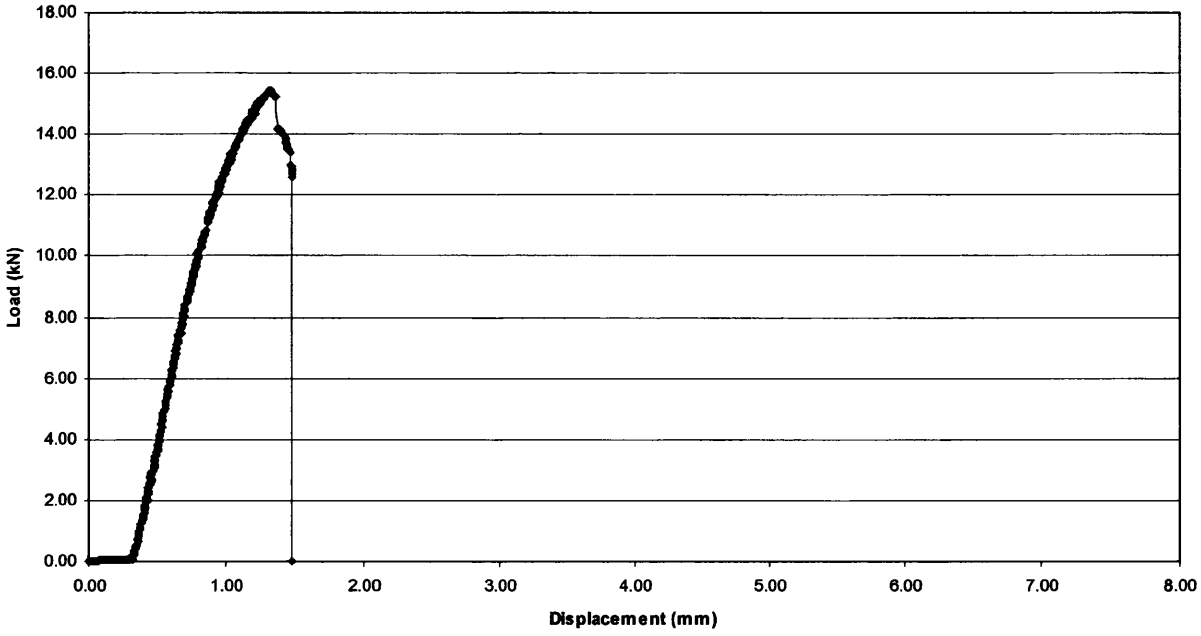

Figure 5.23 Typical lap shear load vs. displacement curve exhibited by $5\sqrt{t}$ welds formed in 1.0mm MS1400

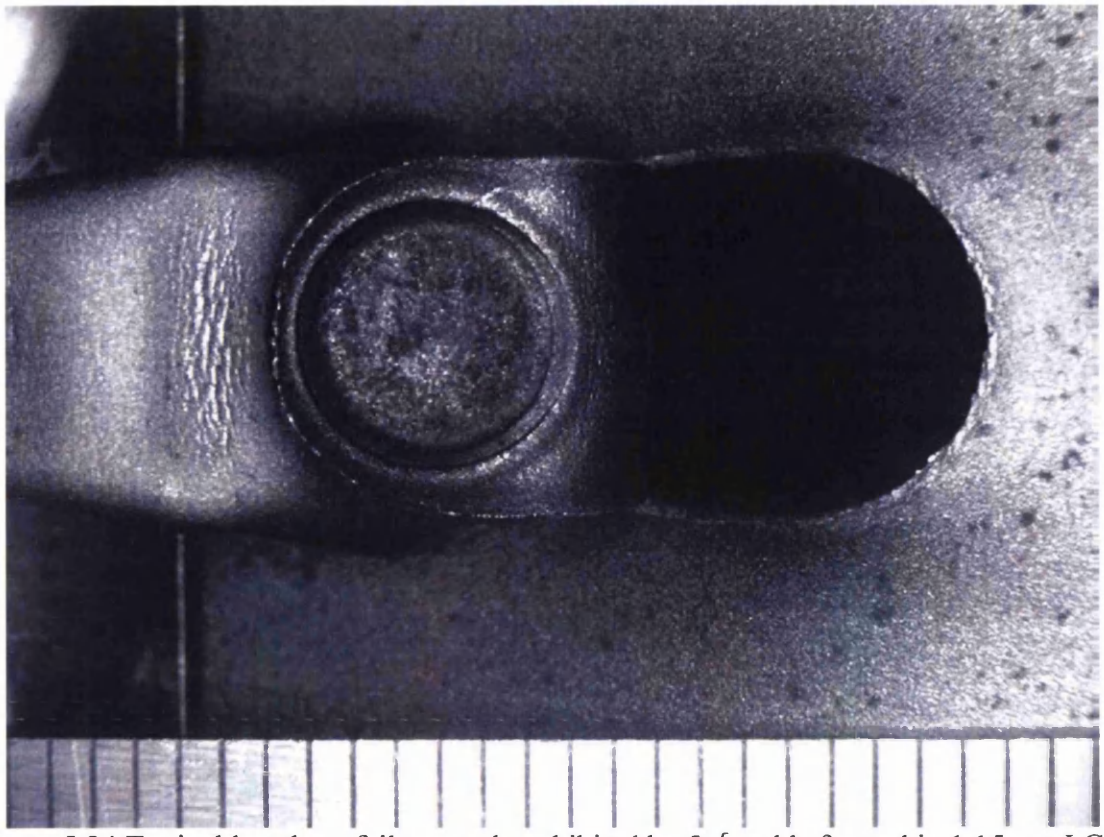

Figure 5.24 Typical lap shear failure mode exhibited by $5\sqrt{t}$ welds formed in 1.15mm LC (Scale is in mm)

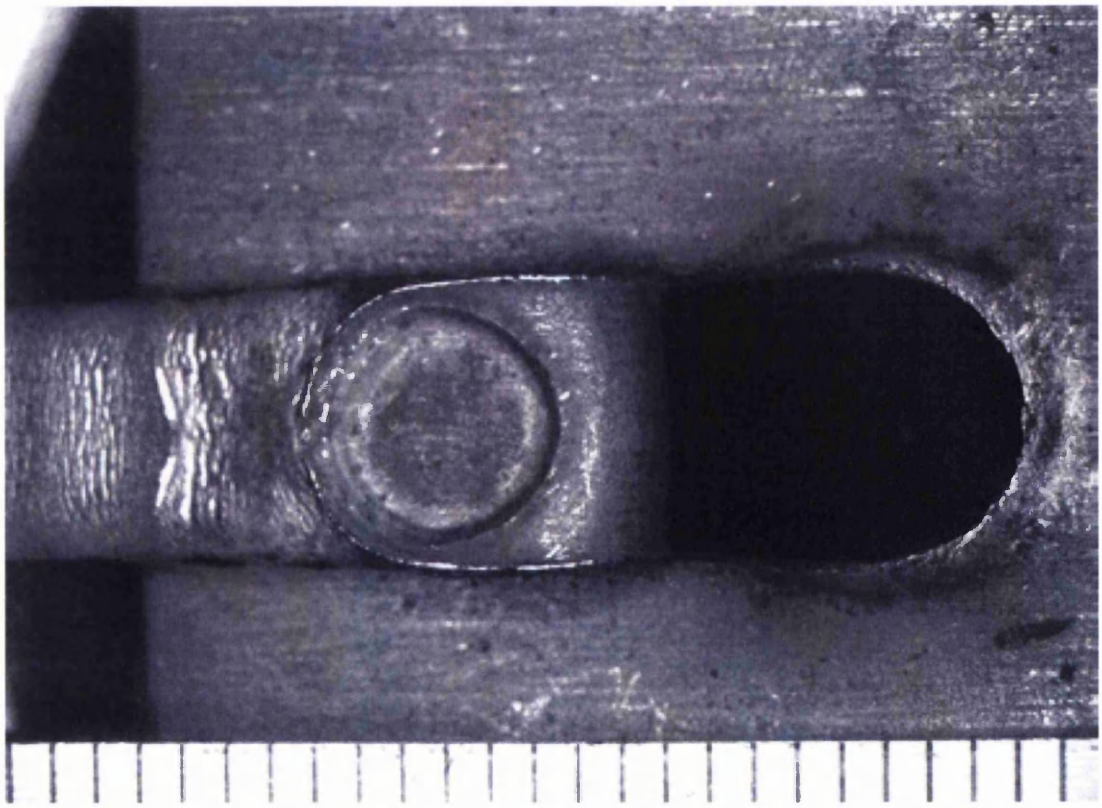

Figure 5.25 Typical lap shear failure mode exhibited by $5\sqrt{t}$ welds formed in 1.2mm IF260 (Scale is in mm)

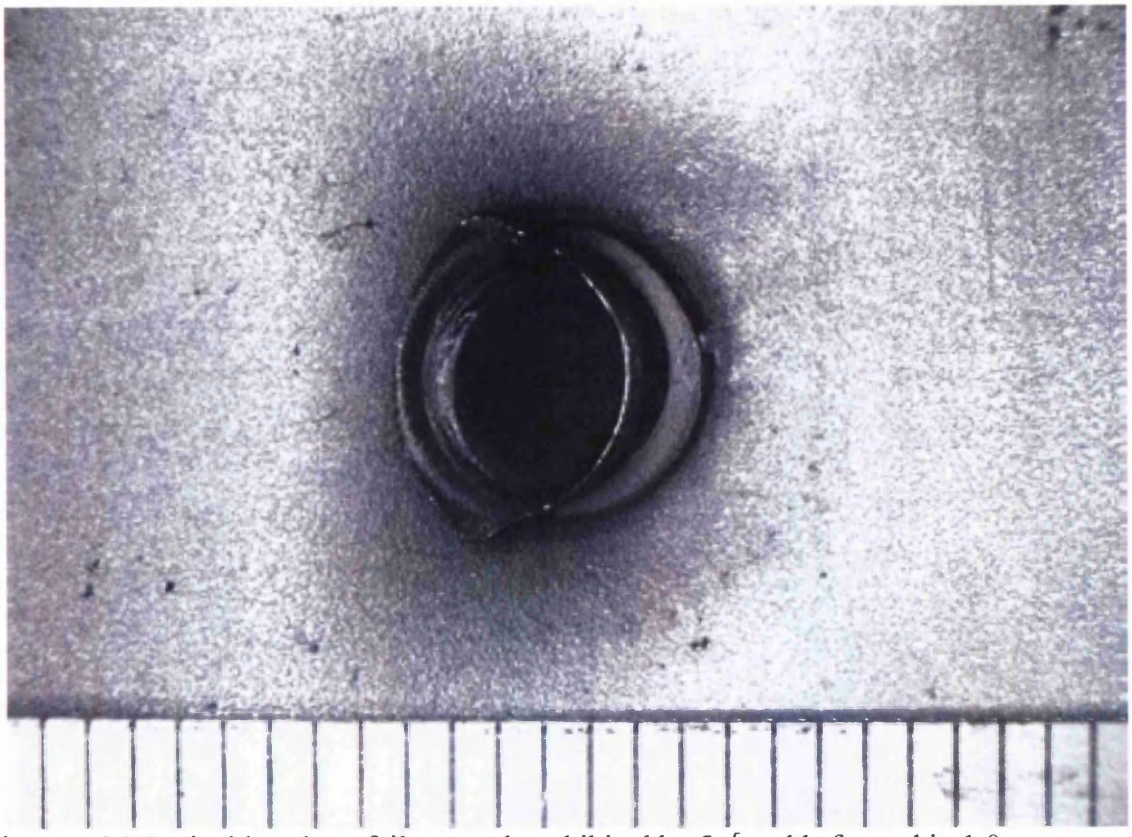

Figure 5.26 Typical lap shear failure mode exhibited by $5\sqrt{t}$ welds formed in 1.0mm TRIP600 (Scale is in mm)

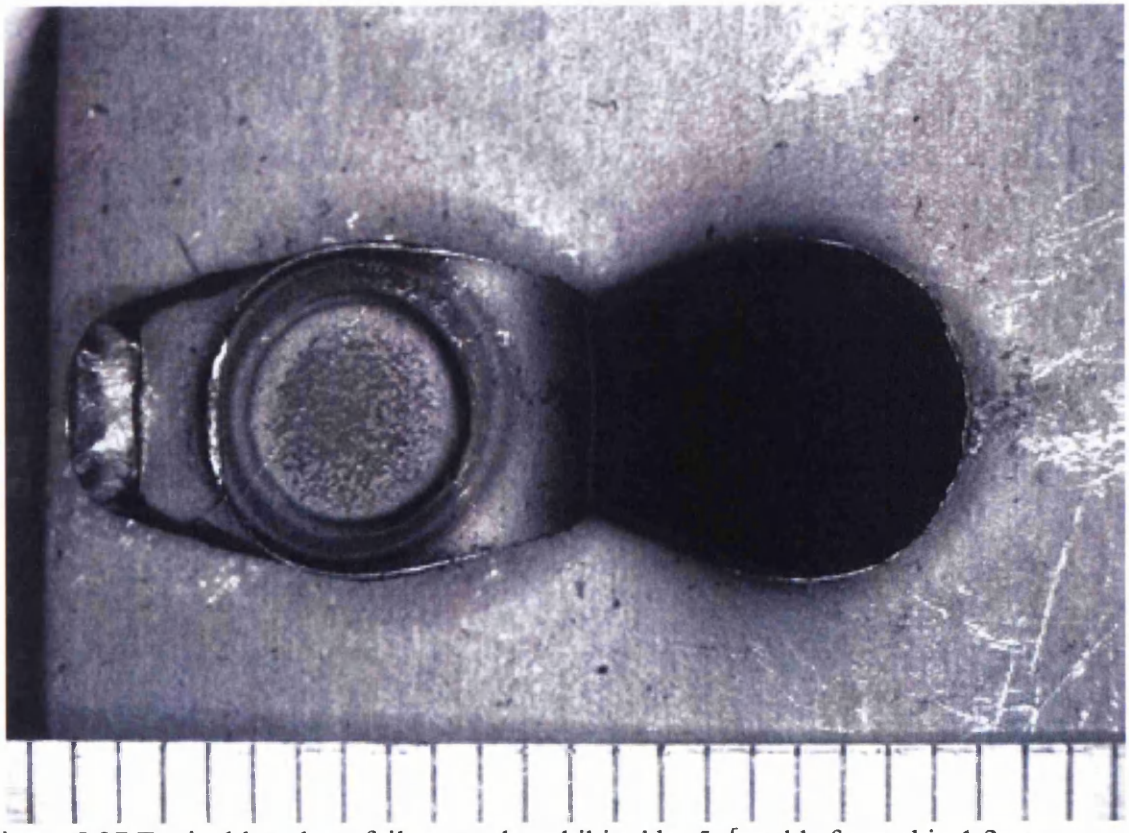

Figure 5.27 Typical lap shear failure mode exhibited by $5\sqrt{t}$ welds formed in 1.2mm DP600 (Scale is in mm)

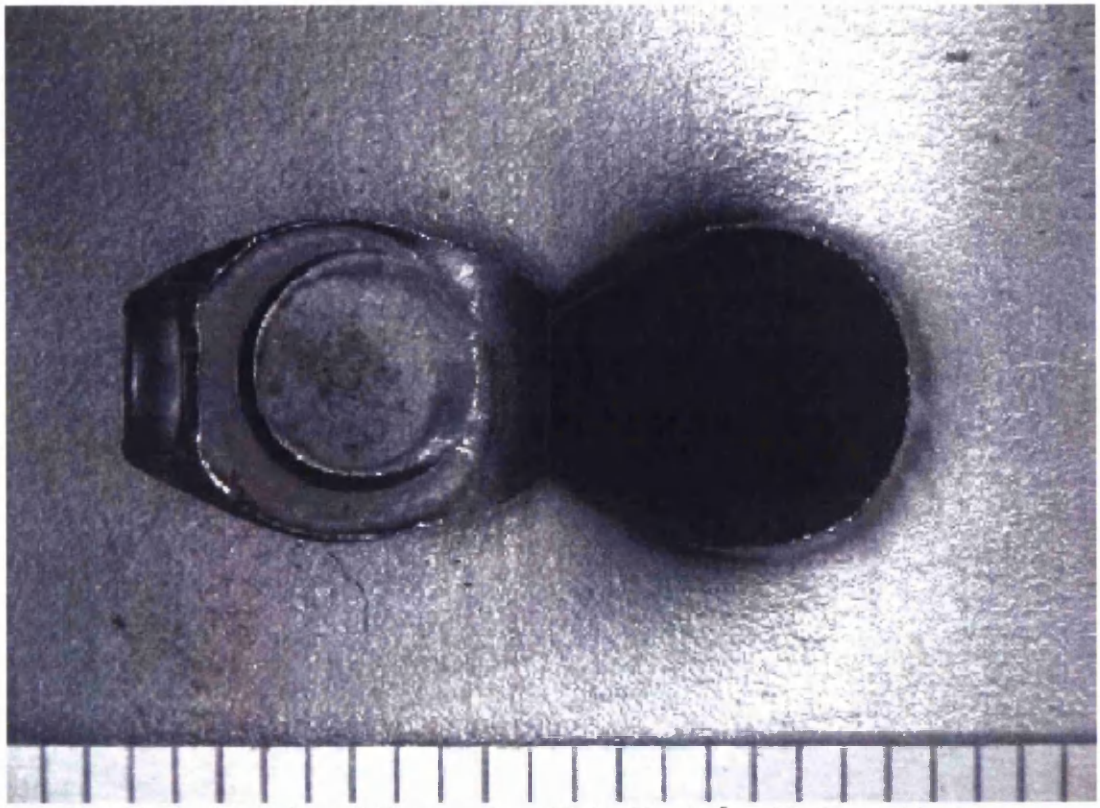

Figure 5.28 Typical lap shear failure mode exhibited by $5\sqrt{t}$ welds formed in 1.2mm TRIP800 (Scale is in mm)

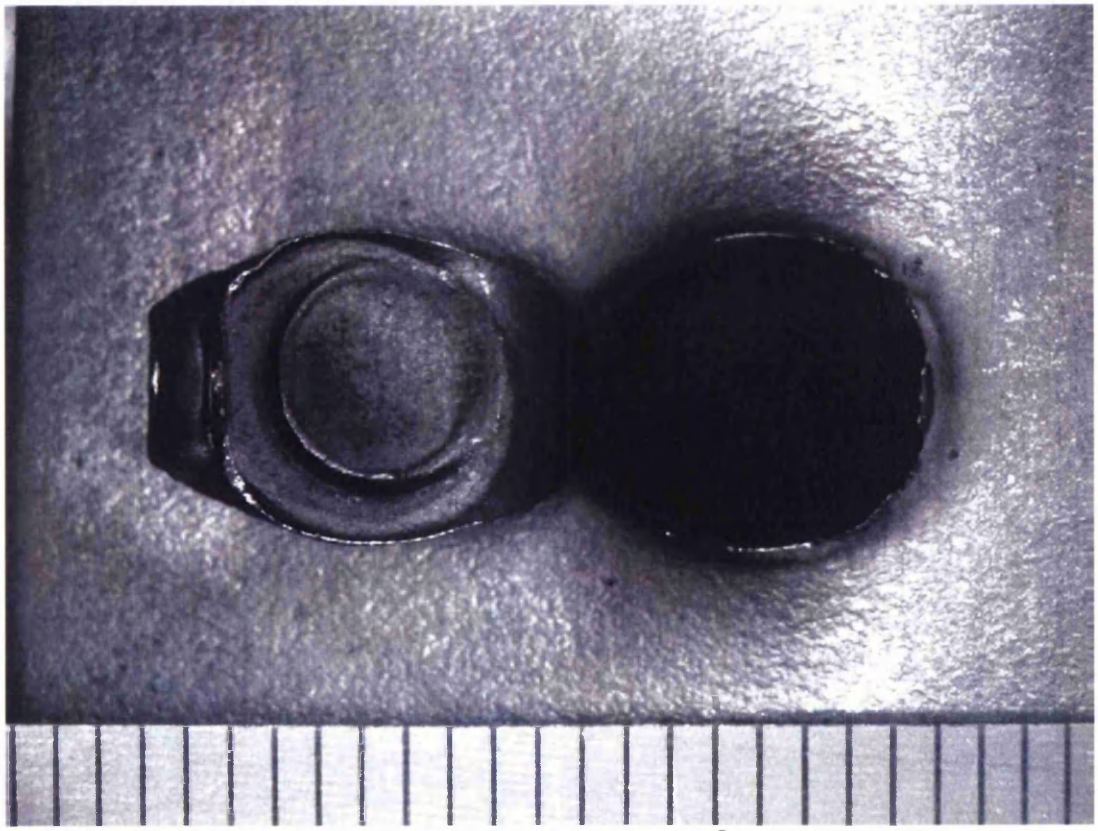

Figure 5.29 Typical lap shear failure mode exhibited by $5\sqrt{t}$ welds formed in 1.2mm DP800 (Scale is in mm)

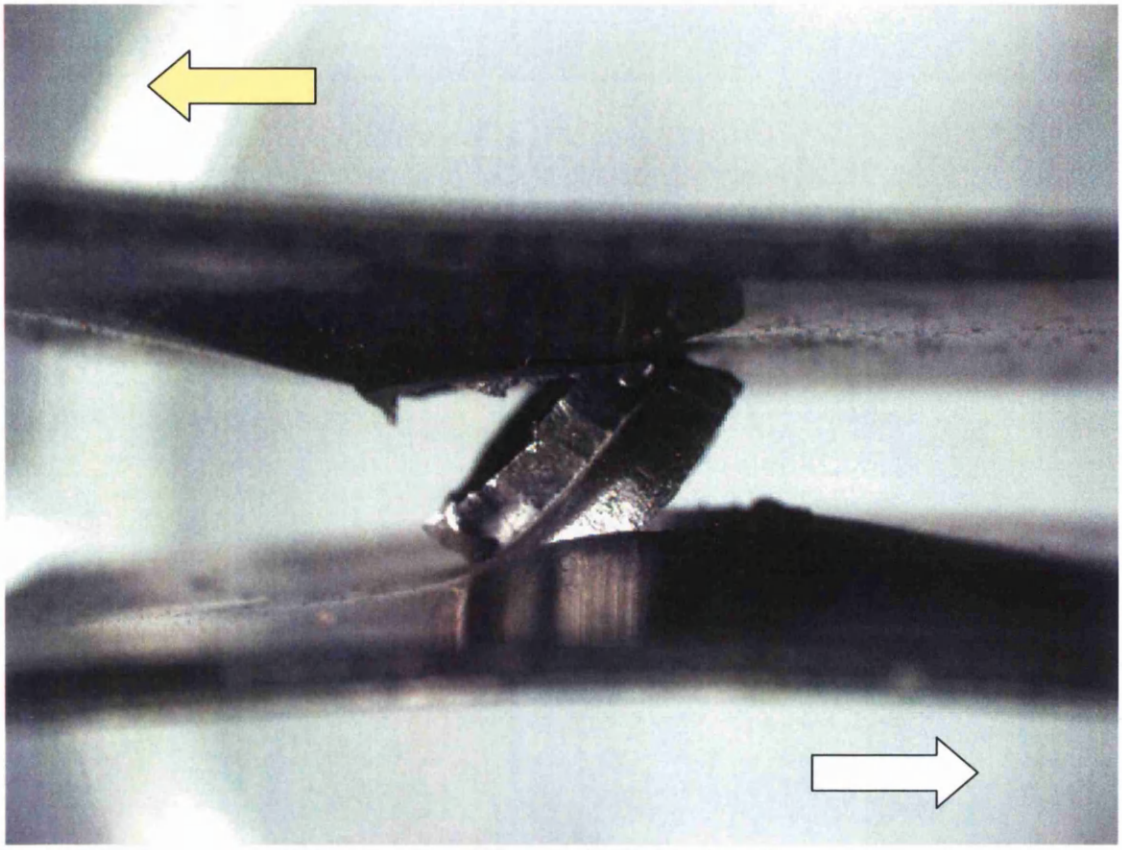

Figure 5.30 Side view of double plug failure in TRIP800 lap shear sample. Arrows indicate the loading direction of the sheets

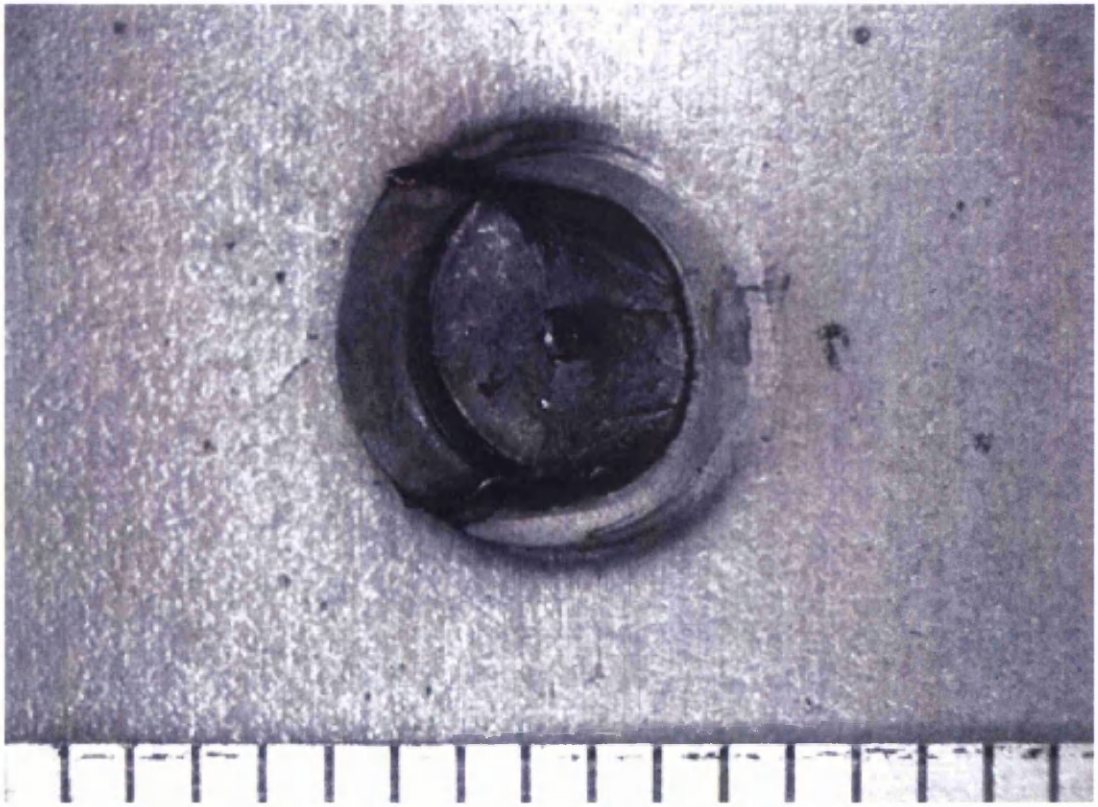

Figure 5.31 Typical lap shear failure mode exhibited by $5\sqrt{t}$ welds formed in 1.2mm DP1000 (Scale is in mm)

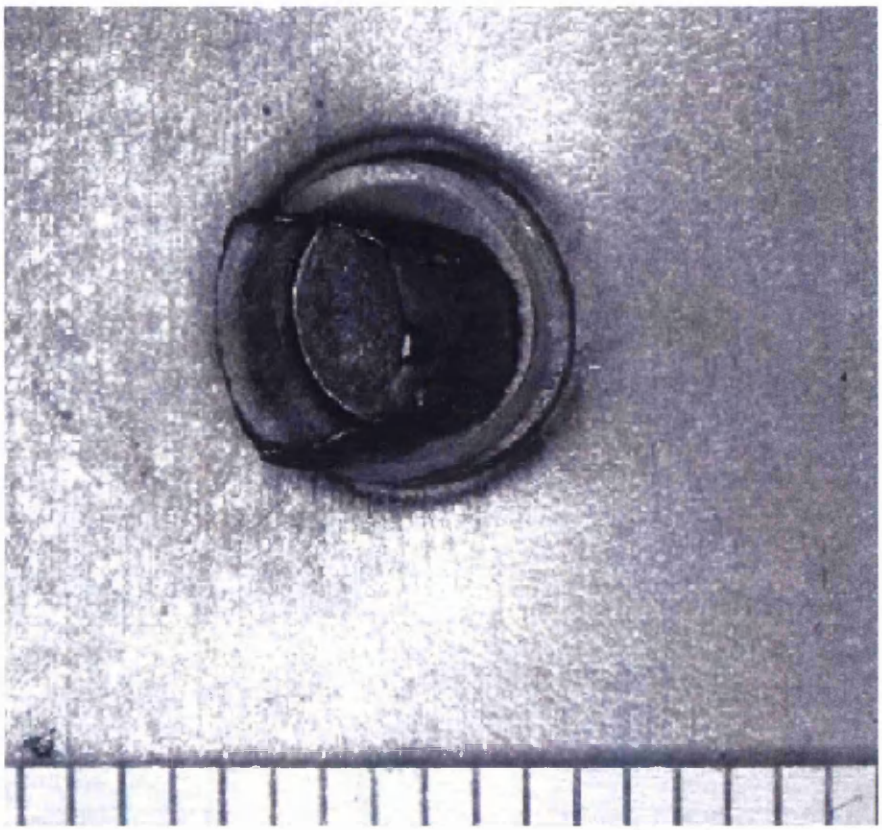

Figure 5.32 Typical lap shear failure mode exhibited by $5\sqrt{t}$ welds formed in 1.0mm MS1400 (Scale is in mm)

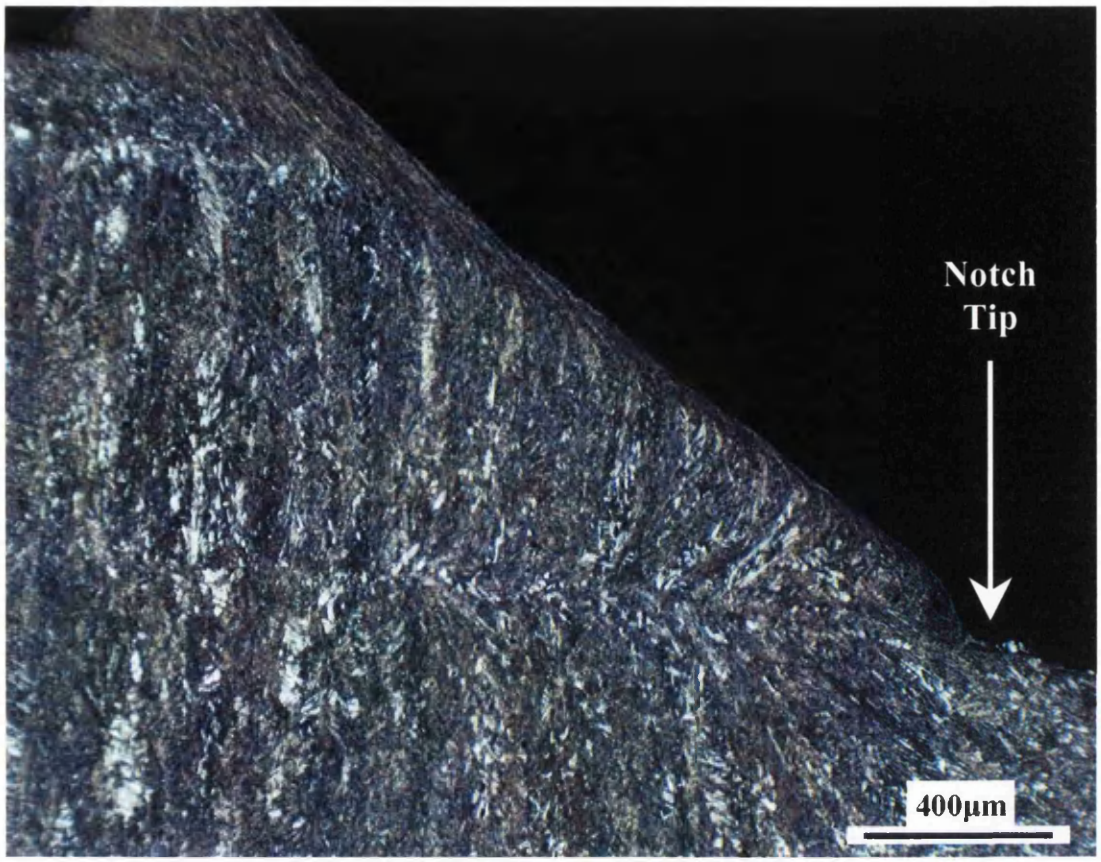

Figure 5.33 Cross-section of failed DP1000 weld nugget (lap shear)

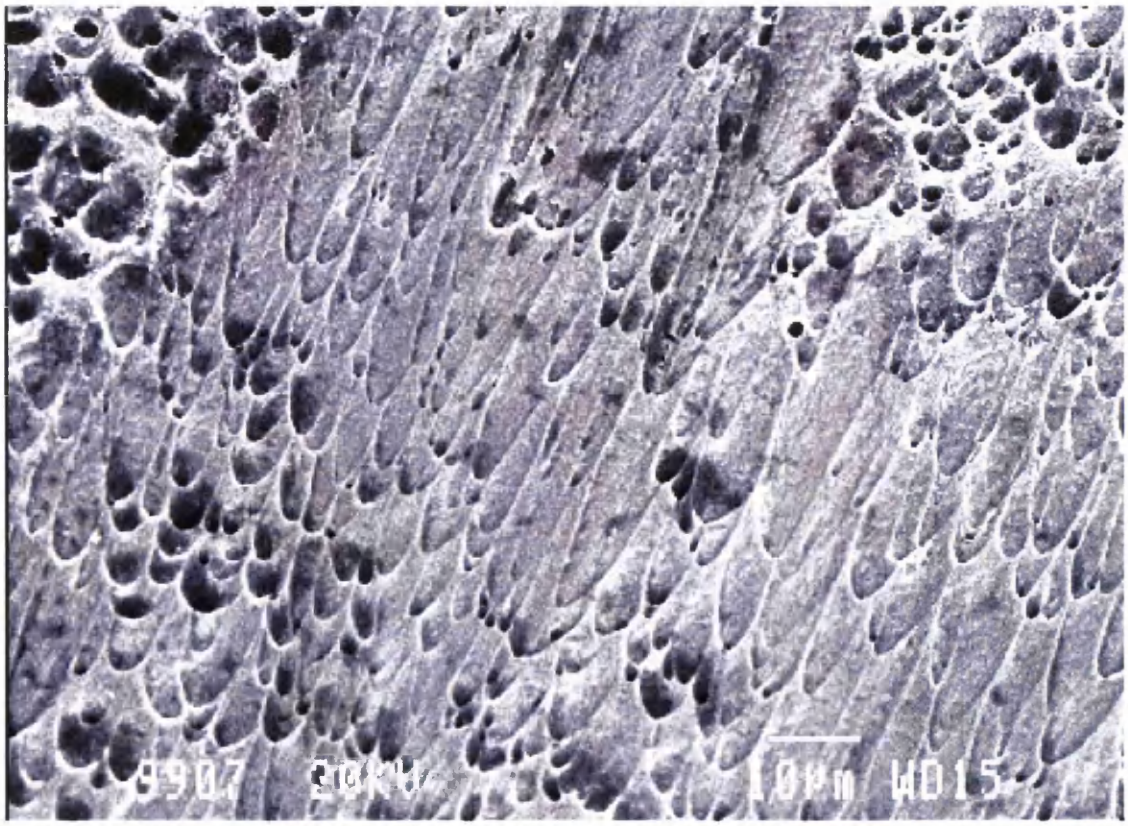
Figure 5.34 SEM image of shear fracture surface from DP1000 lap shear sample

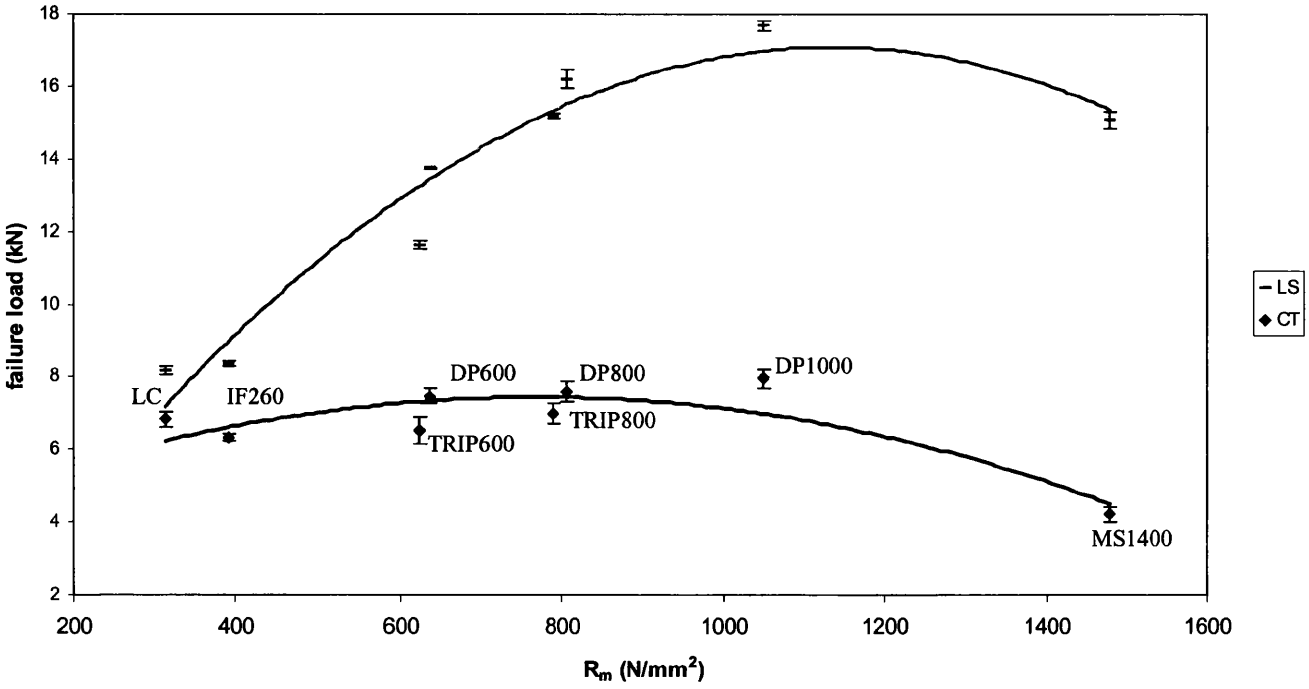

Figure 5.35 Graph illustrating the relationship between parent metal strength and average lap shear (LS) and cross tension (CT) failure load of $5\sqrt{t}$ welds. Error bars indicate one standard deviation from the mean

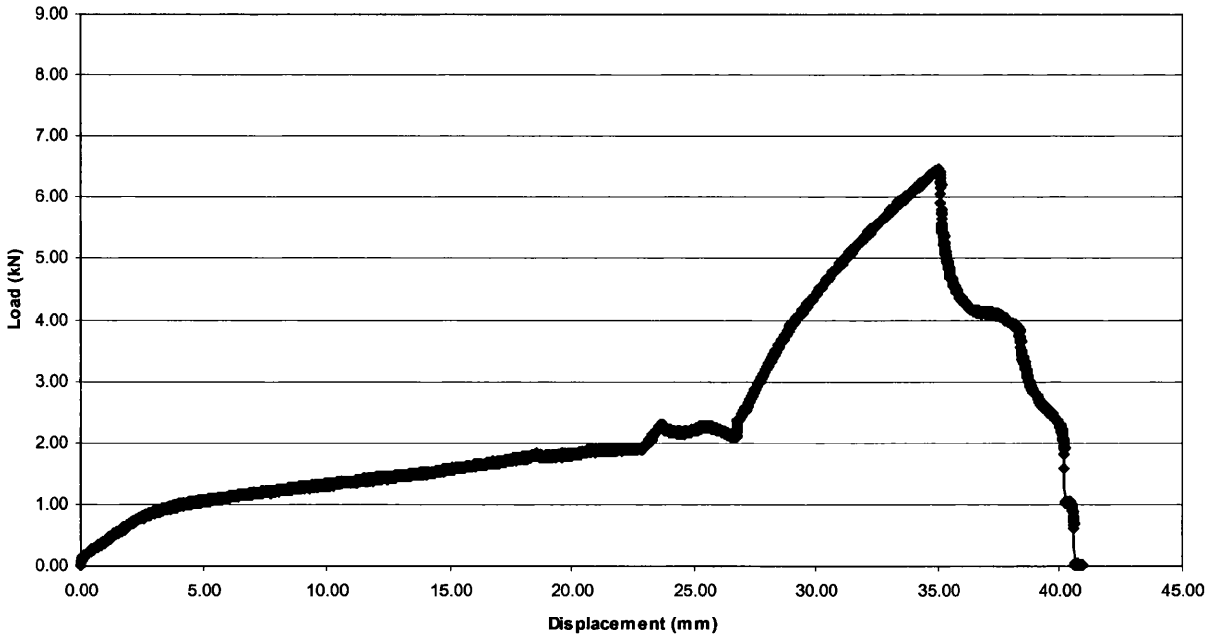

Figure 5.36 Typical cross tension load vs. displacement curve exhibited by $5\sqrt{t}$ welds formed in 1.15mm LC

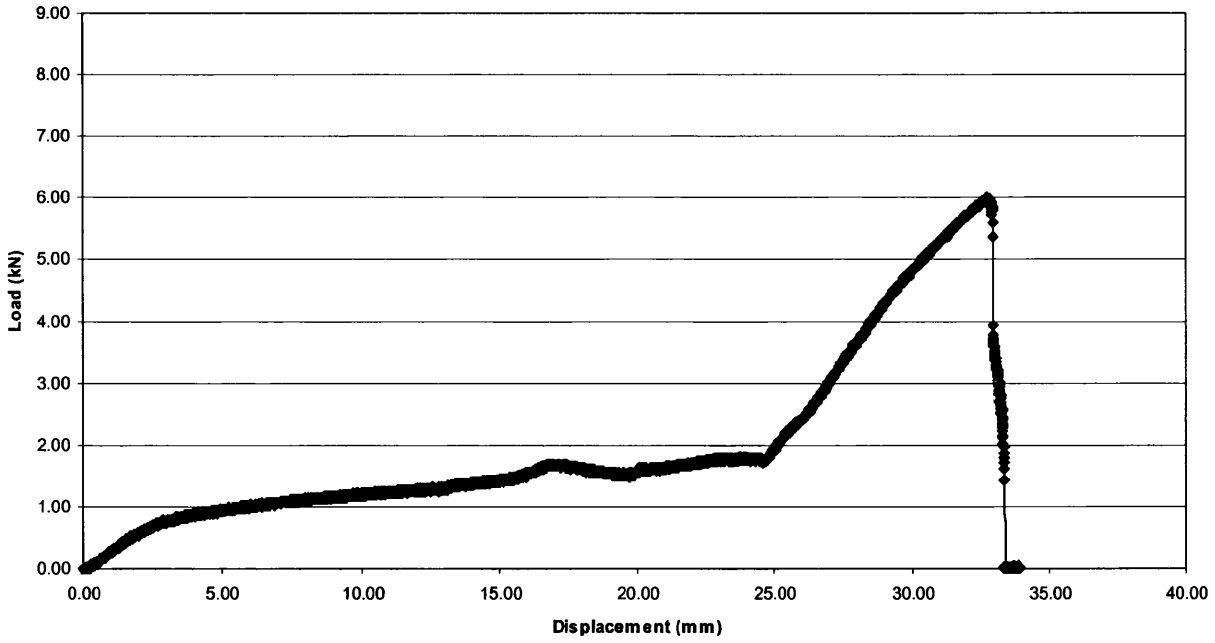

Figure 5.37 Typical cross tension load vs. displacement curve exhibited by $5\sqrt{t}$ welds formed in 1.2mm IF260

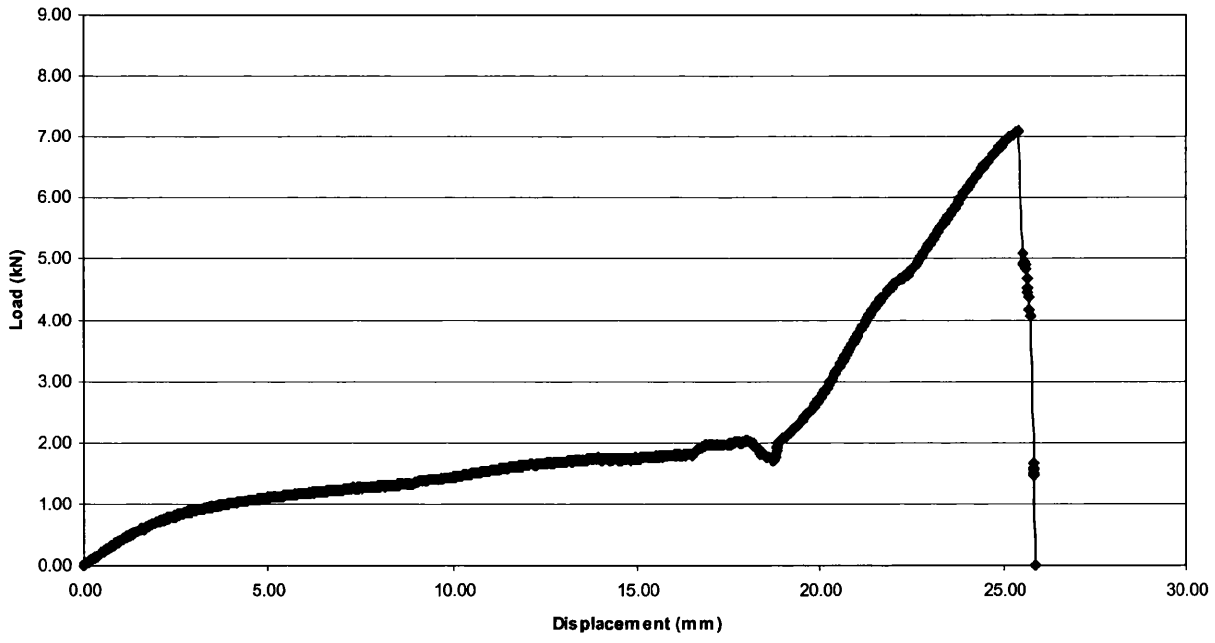

Figure 5.38 Typical cross tension load vs. displacement curve exhibited by $5\sqrt{t}$ welds formed in 1.0mm TRIP600

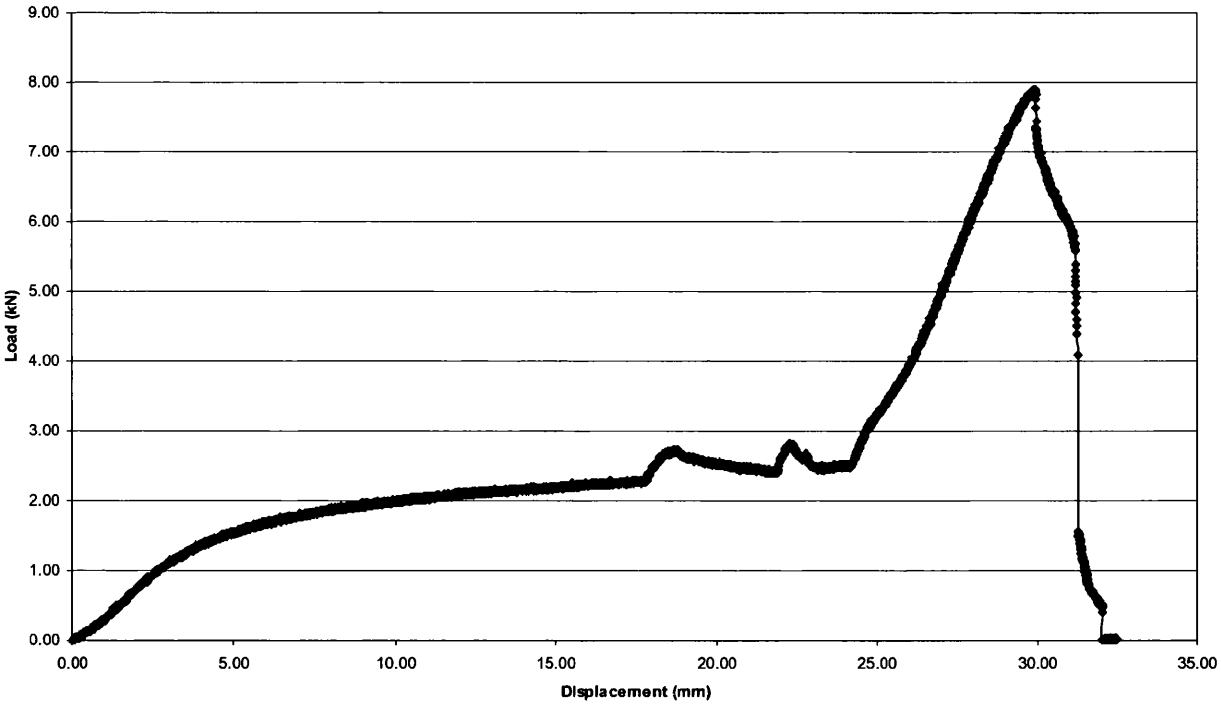

Figure 5.39 Typical cross tension load vs. displacement curve exhibited by $5\sqrt{t}$ welds formed in 1.2mm DP600

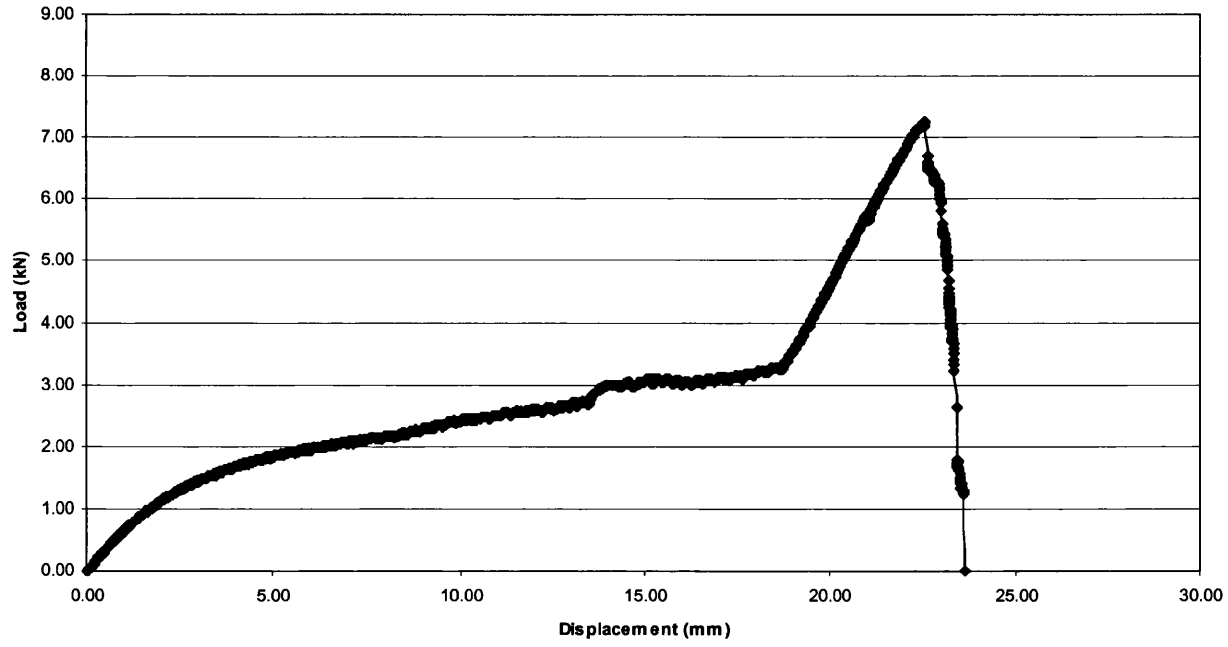

Figure 5.40 Typical cross tension load vs. displacement curve exhibited by $5\sqrt{t}$ welds formed in 1.2mm TRIP800

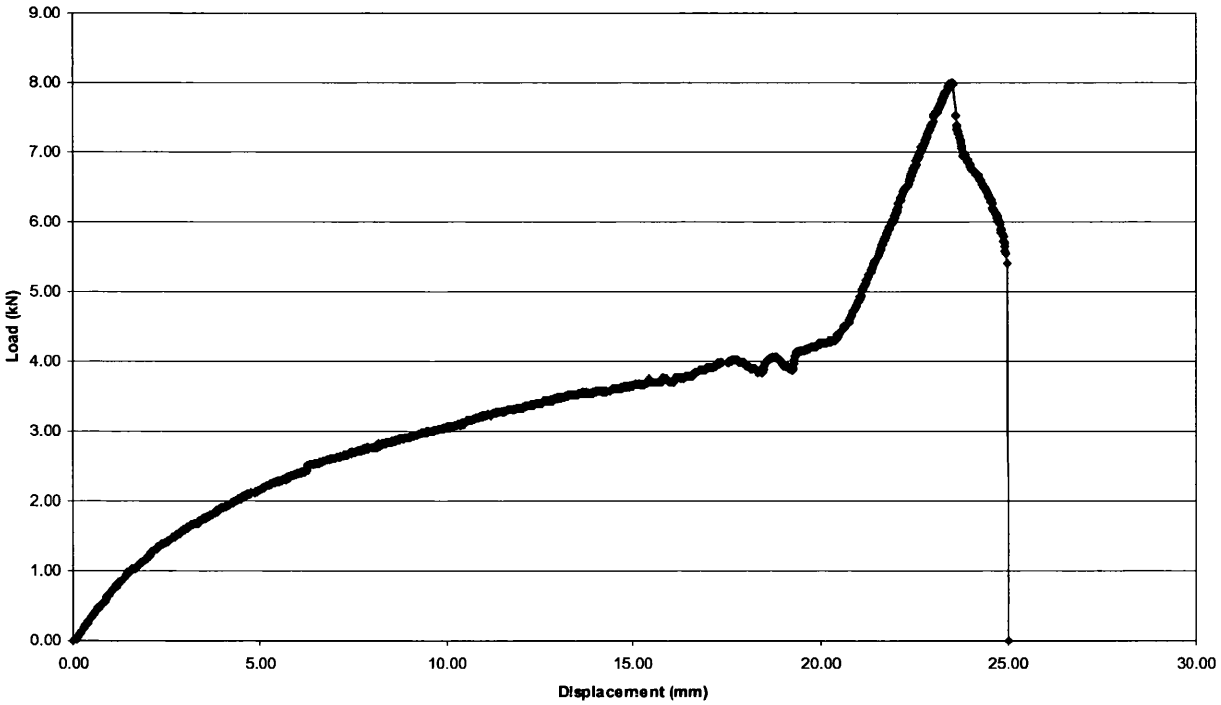

Figure 5.41 Typical cross tension load vs. displacement curve exhibited by $5\sqrt{t}$ welds formed in 1.2mm DP800

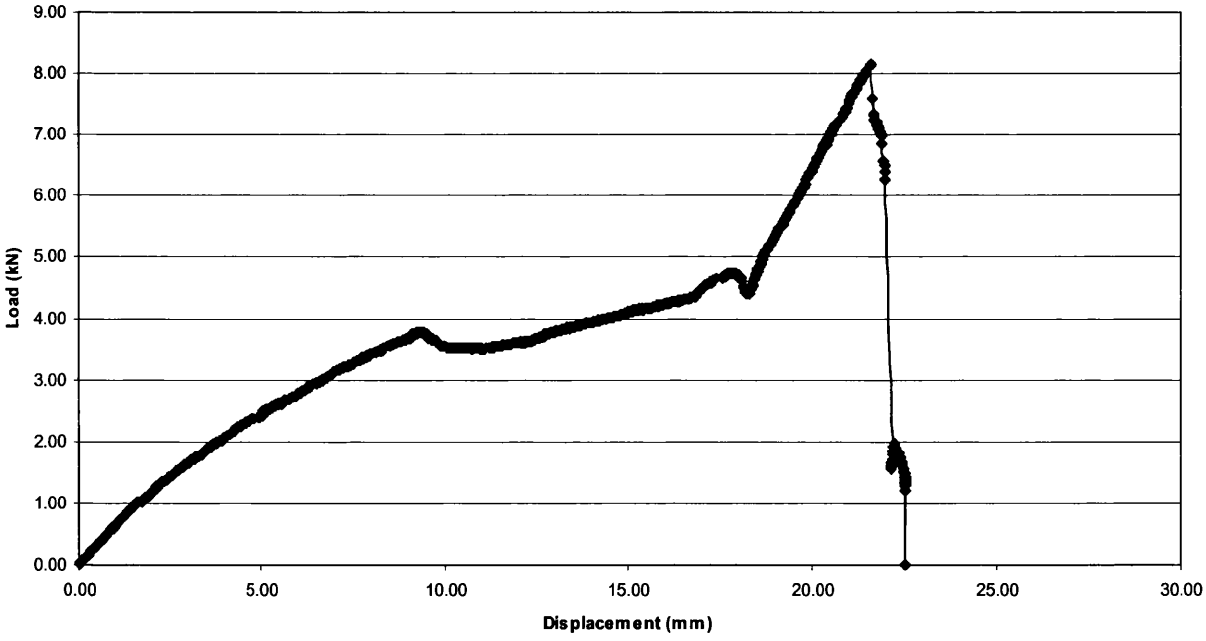

Figure 5.42 Typical cross tension load vs. displacement curve exhibited by $5\sqrt{t}$ welds formed in 1.2mm DP1000

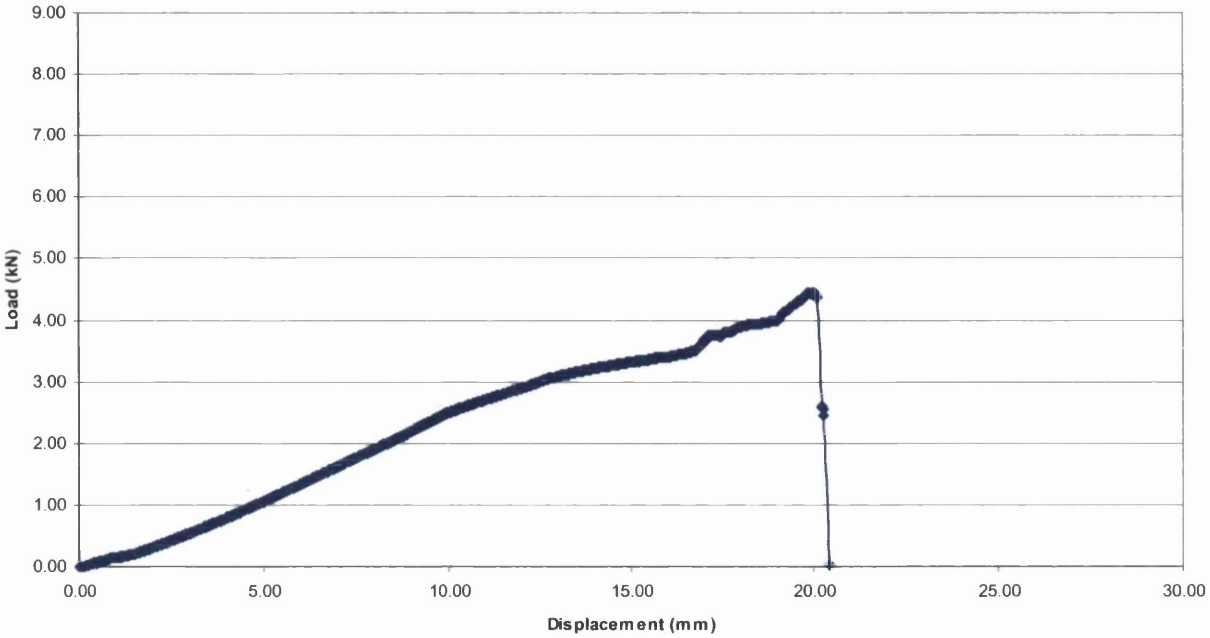

Figure 5.43 Typical cross tension load vs. displacement curve exhibited by $5\sqrt{t}$ welds formed in 1.0mm MS1400

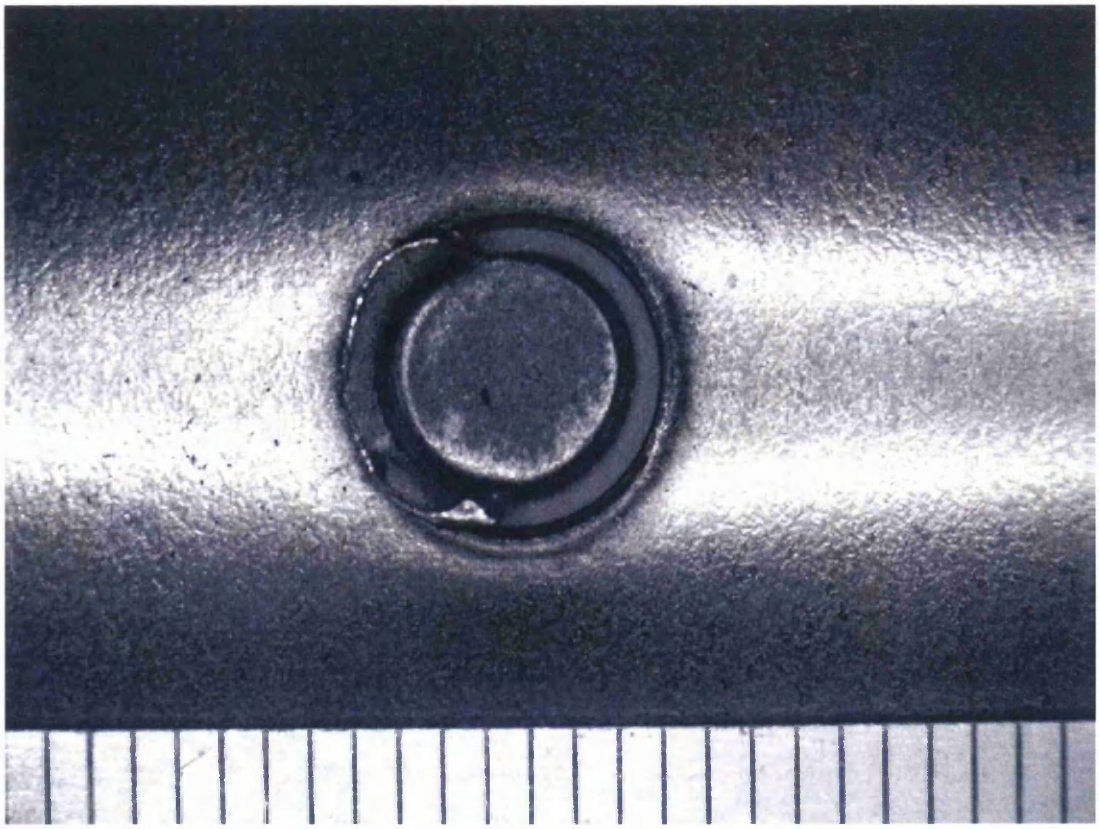

Figure 5.44 Typical cross tension plug failure (Scale is in mm)

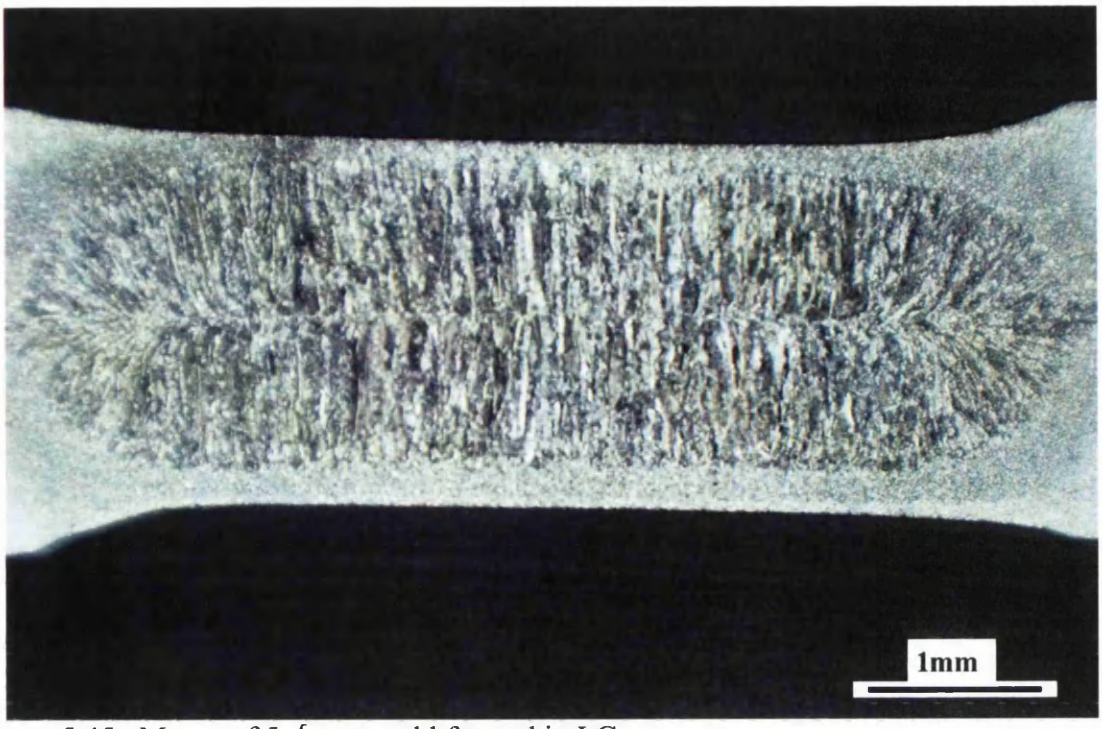

Figure 5.45a Macro of 5√t spot weld formed in LC

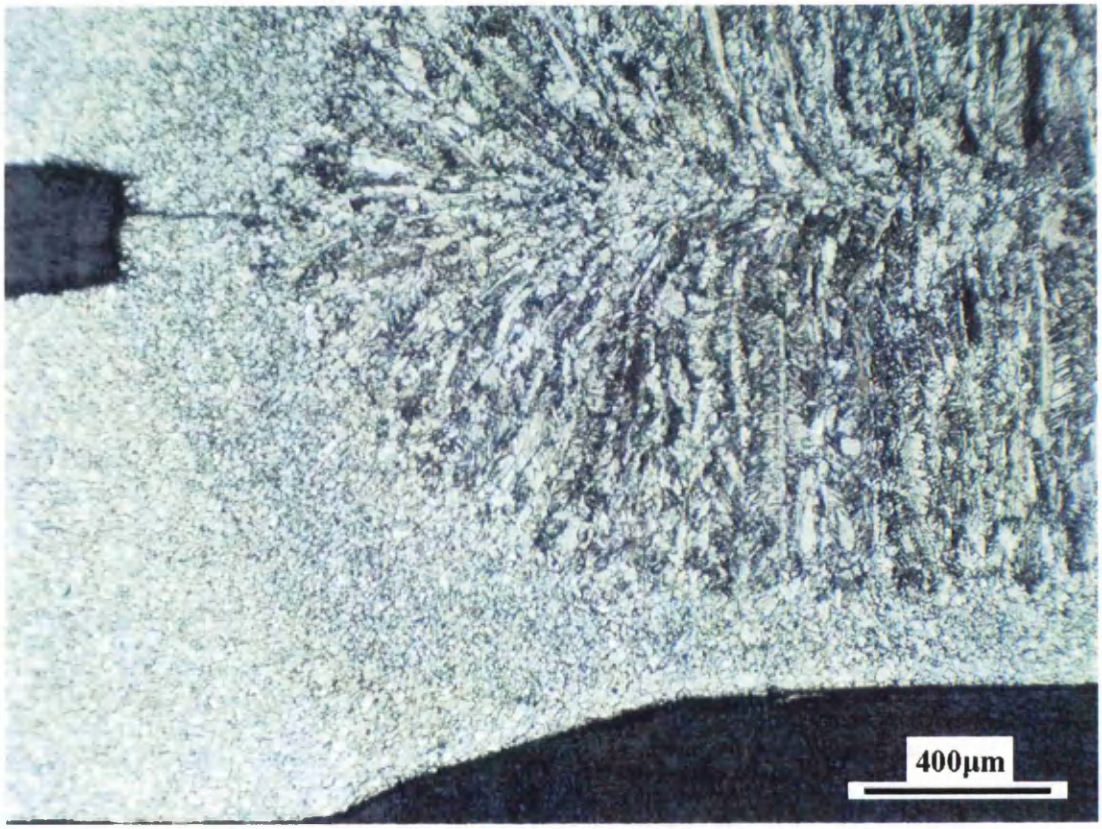

Figure 5.45b Micrograph illustrating the variation in microstructure from parent metal to weld nugget in LC weld

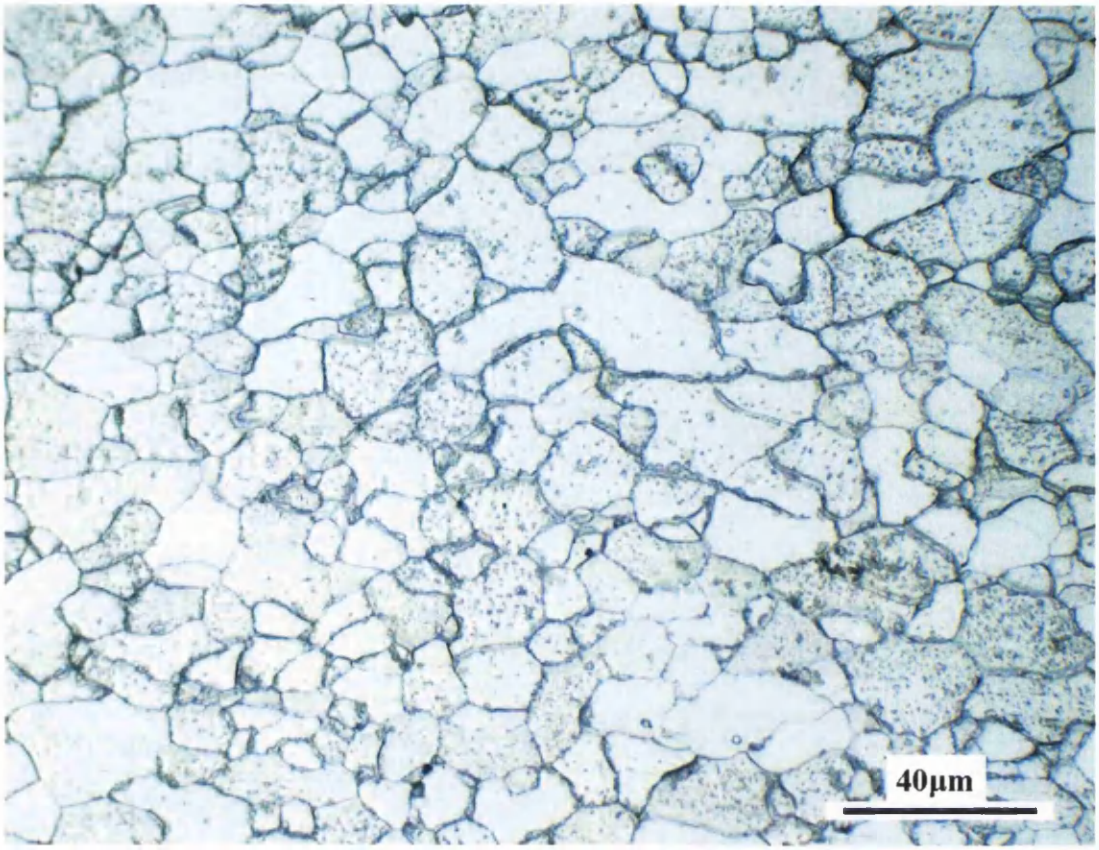

Figure 5.45c Micrograph of LC parent microstructure

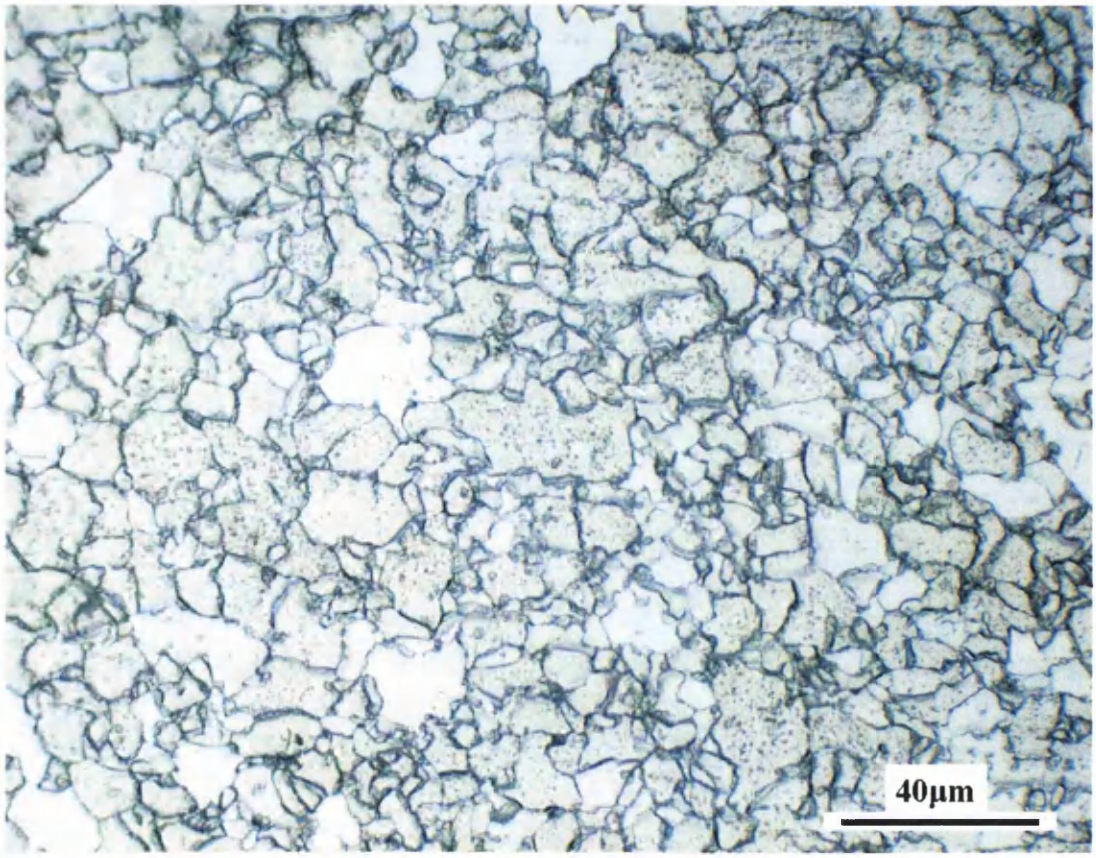

Figure 5.45d Micrograph showing heat affected zone microstructure in LC

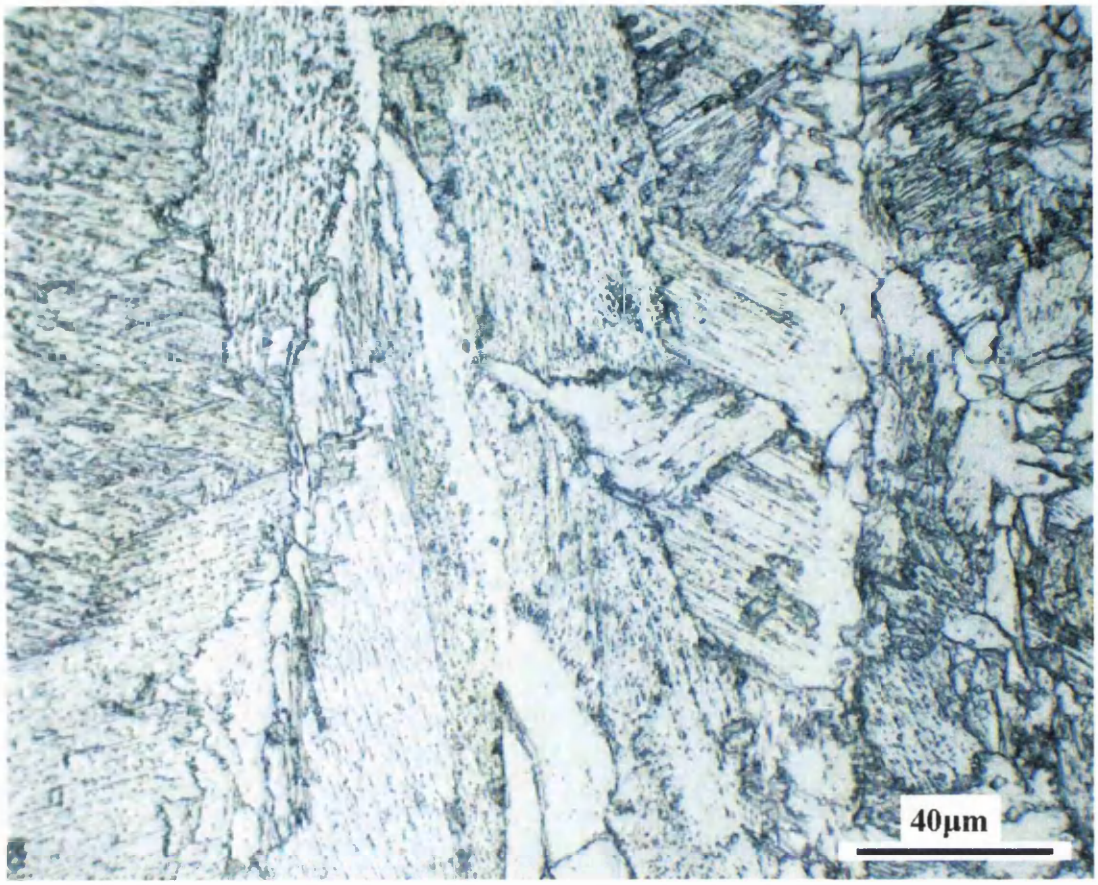

Figure 5.45e Micrograph showing weld nugget microstructure in LC

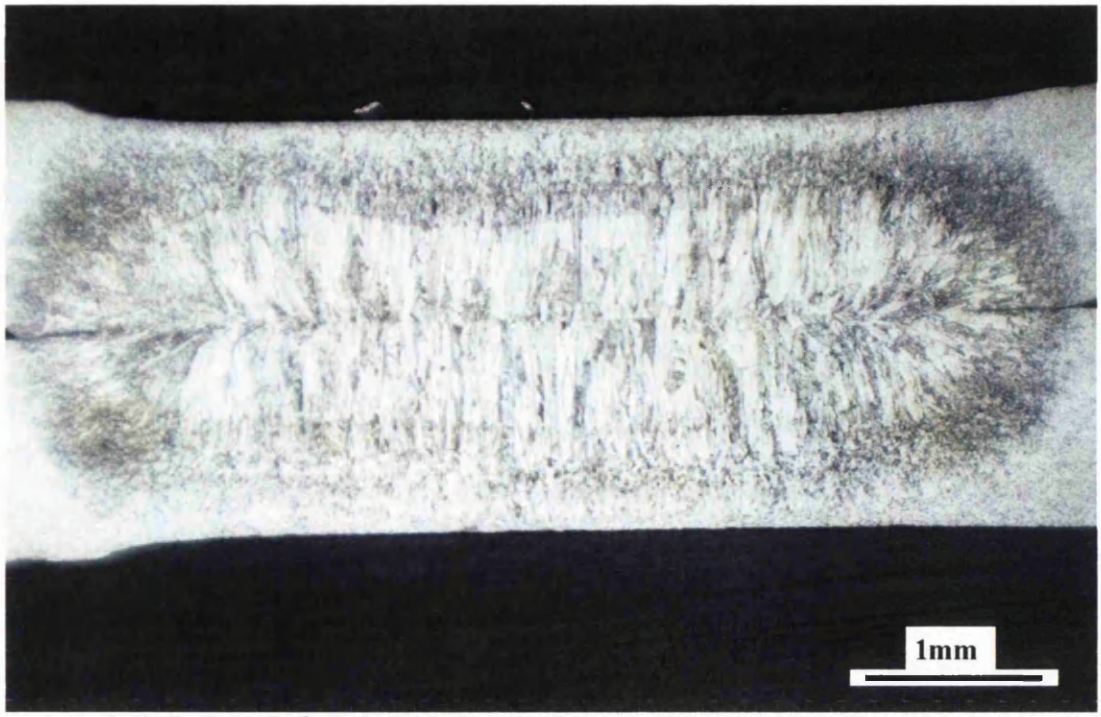

Figure 5.46a Macro of $5\sqrt{t}$ spot weld formed in 1.2mm IF260

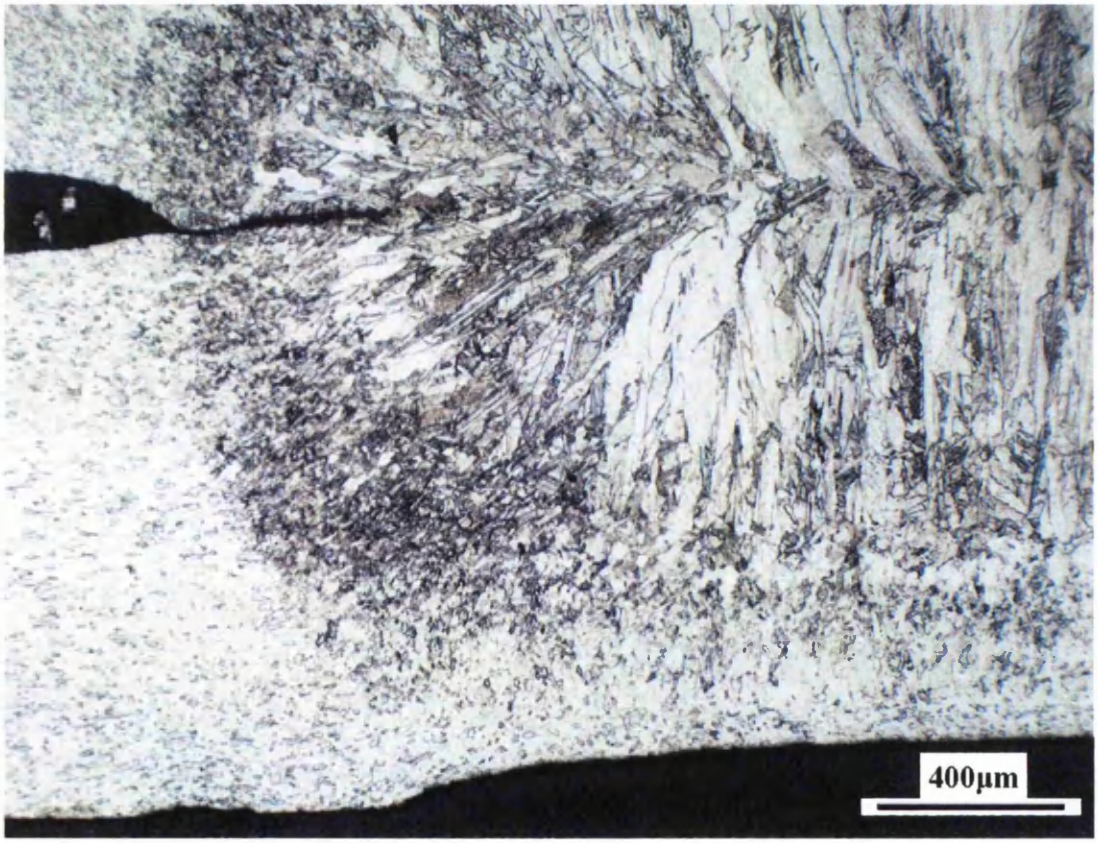

Figure 5.46b Micrograph illustrating the variation in microstructure from parent metal to weld nugget in IF260 weld

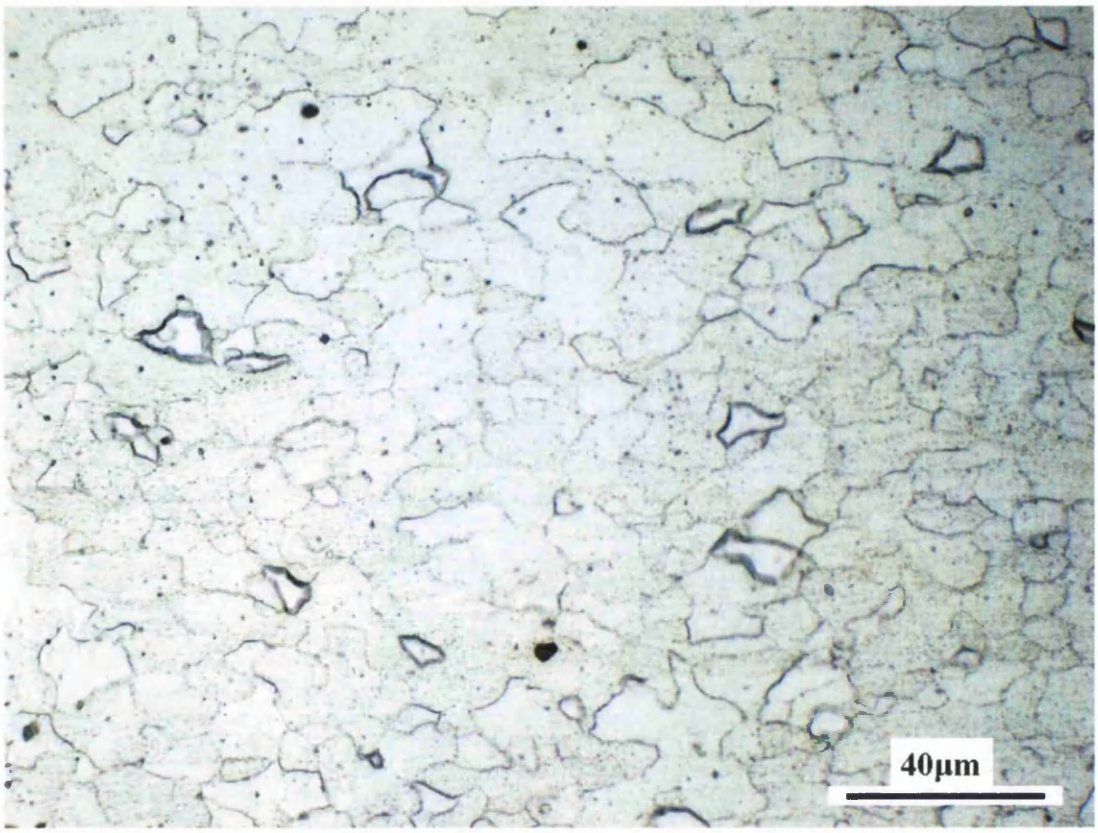

Figure 5.46c Micrograph of IF260 parent microstructure

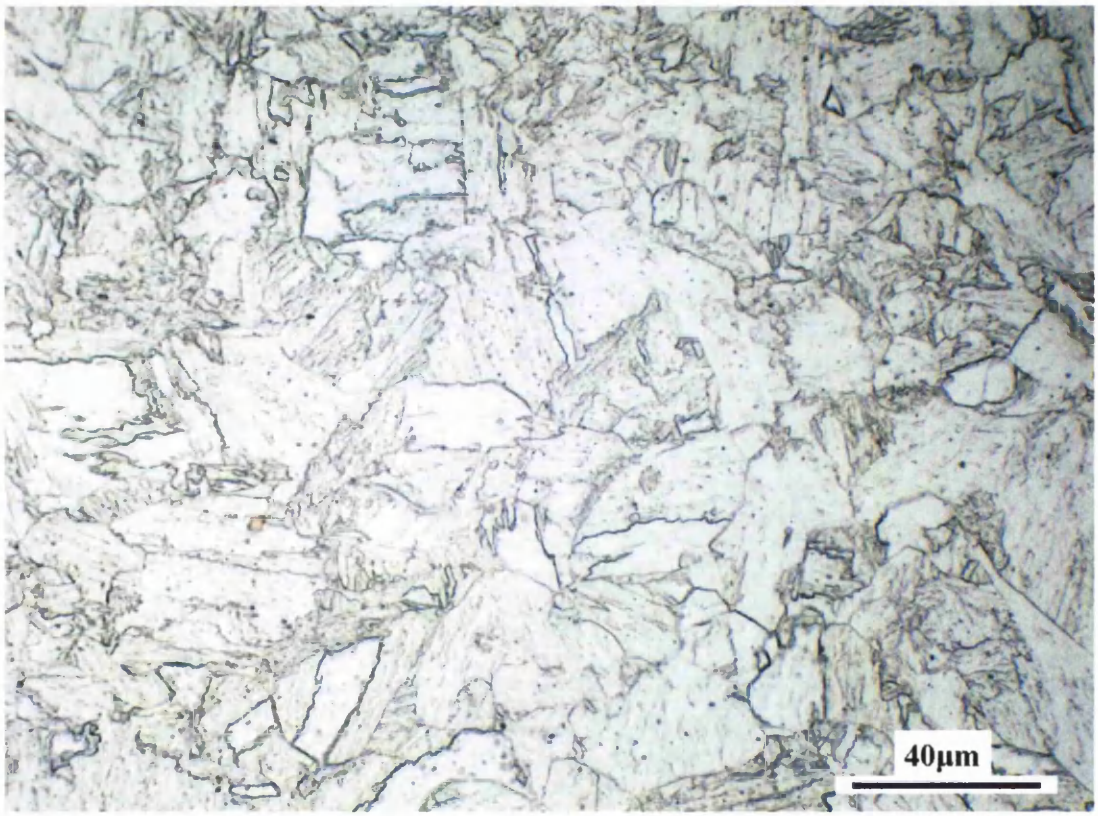

Figure 5.46d Micrograph showing microstructure of the heat affected zone in IF260

Figure 5.46e Micrograph showing weld nugget microstructure in IF260

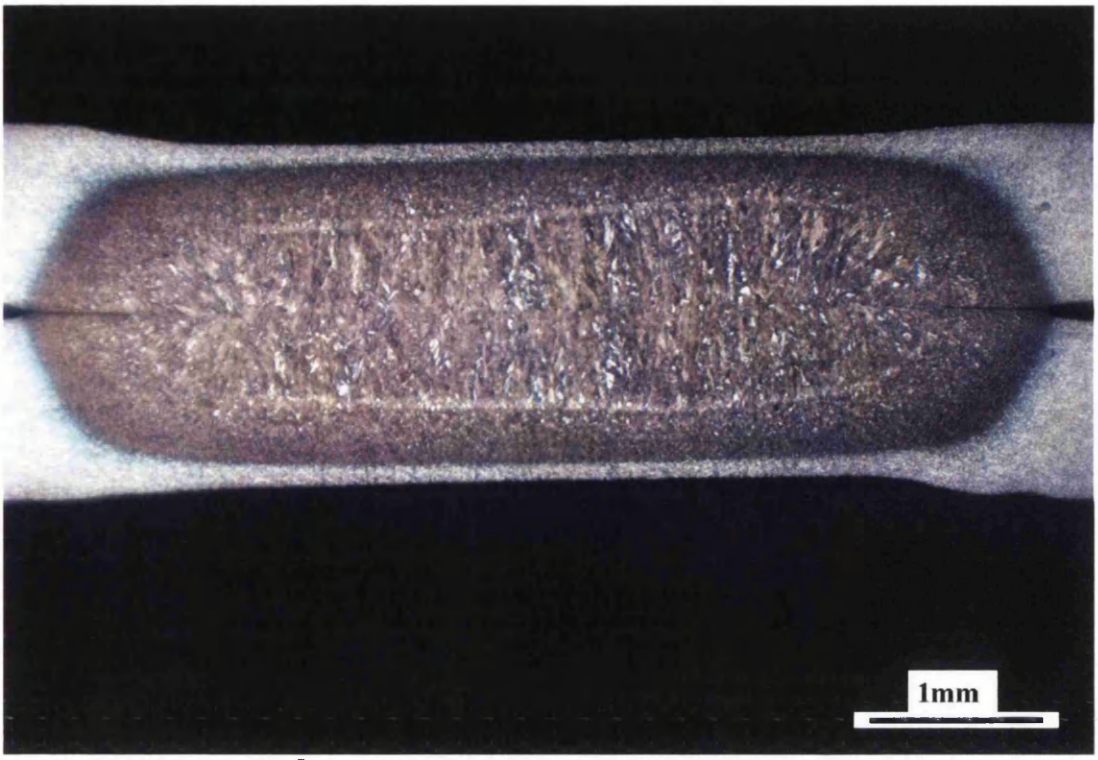

Figure 5.47a Macro of 5√t spot weld formed in 1.0mm TRIP600

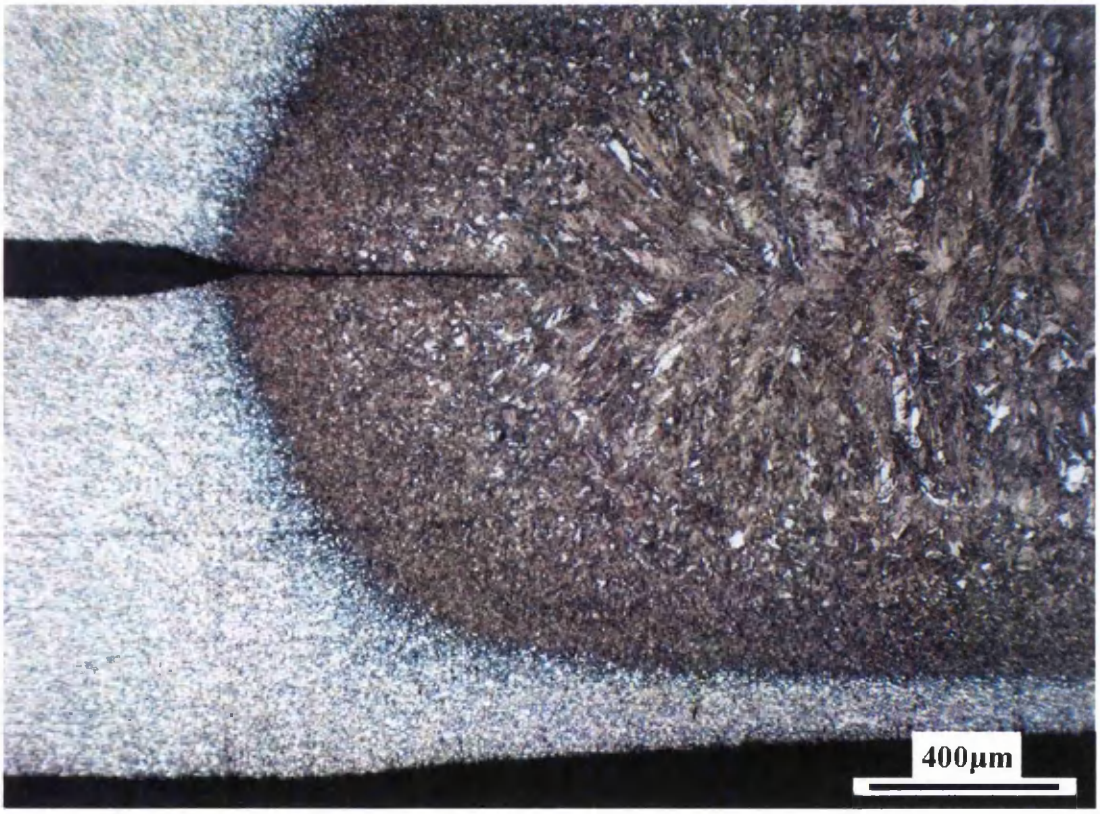

Figure 5.47b Micrograph illustrating the variation in microstructure from parent metal to weld nugget in TRIP600 weld

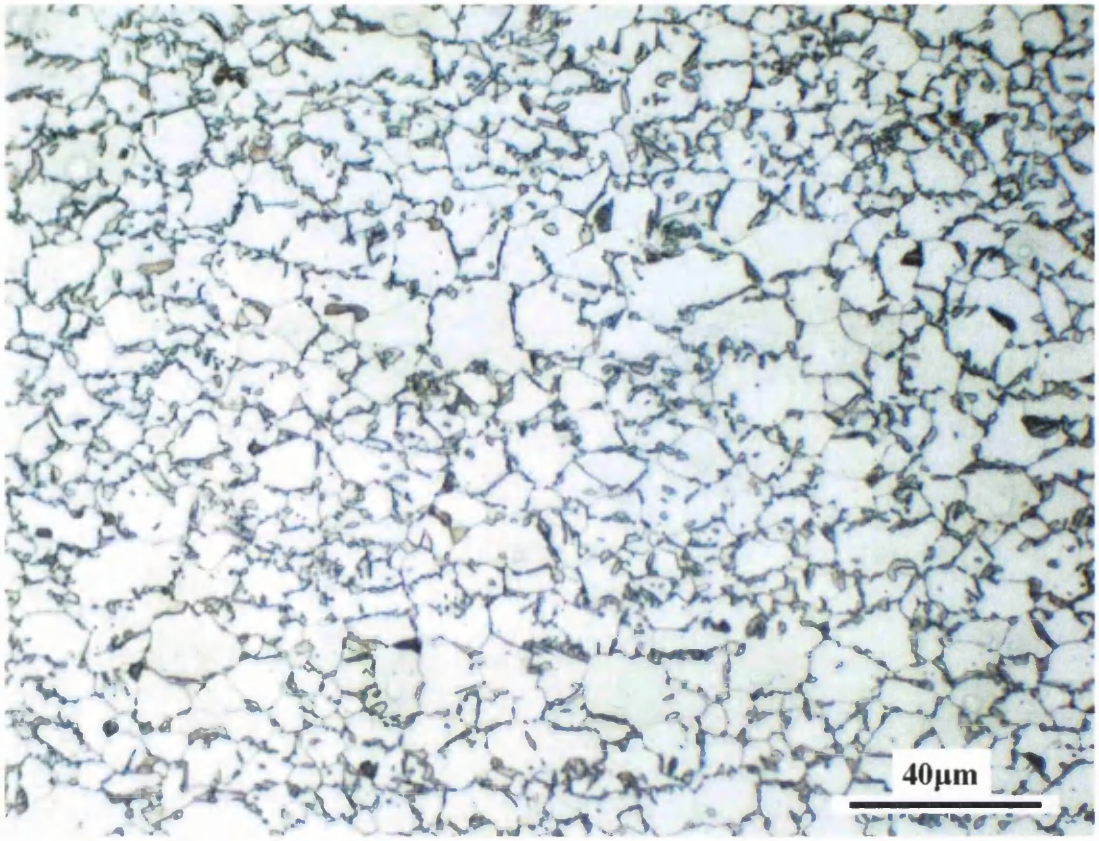

Figure 5.47c Micrograph of TRIP600 parent microstructure

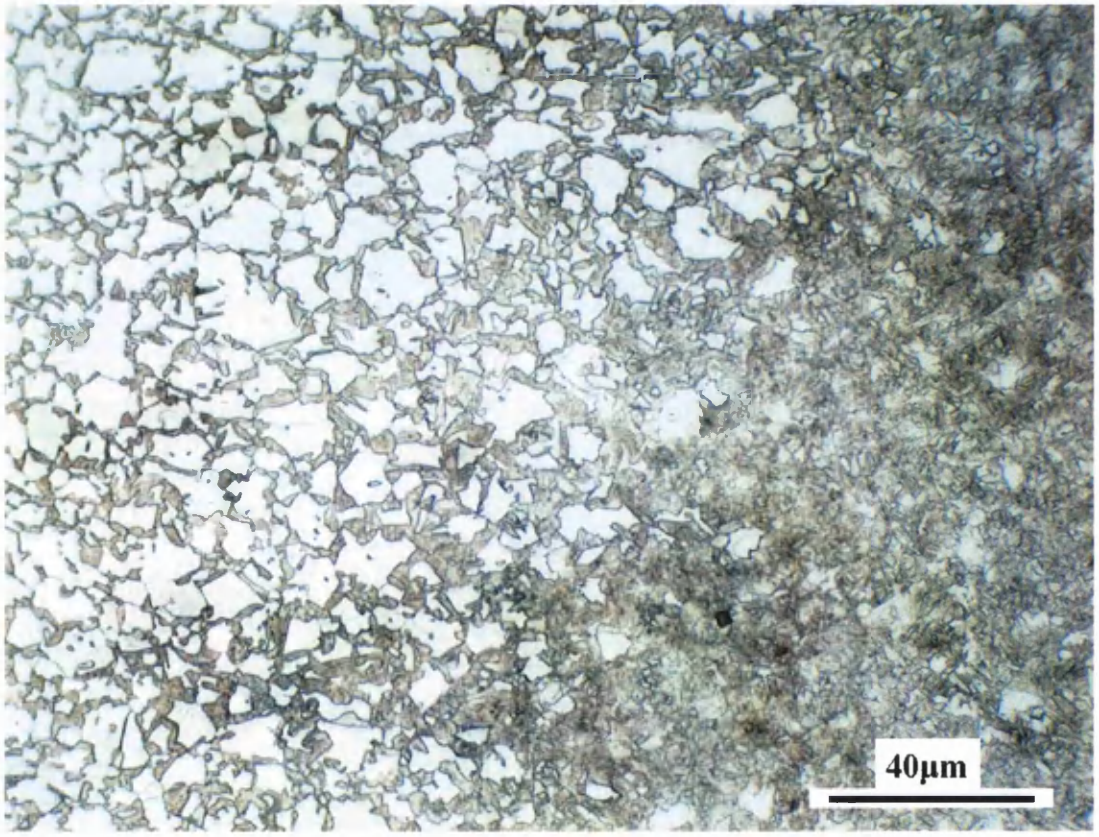

Figure 5.47d Micrograph showing transition from parent material microstructure to heat affected zone microstructure in TRIP600

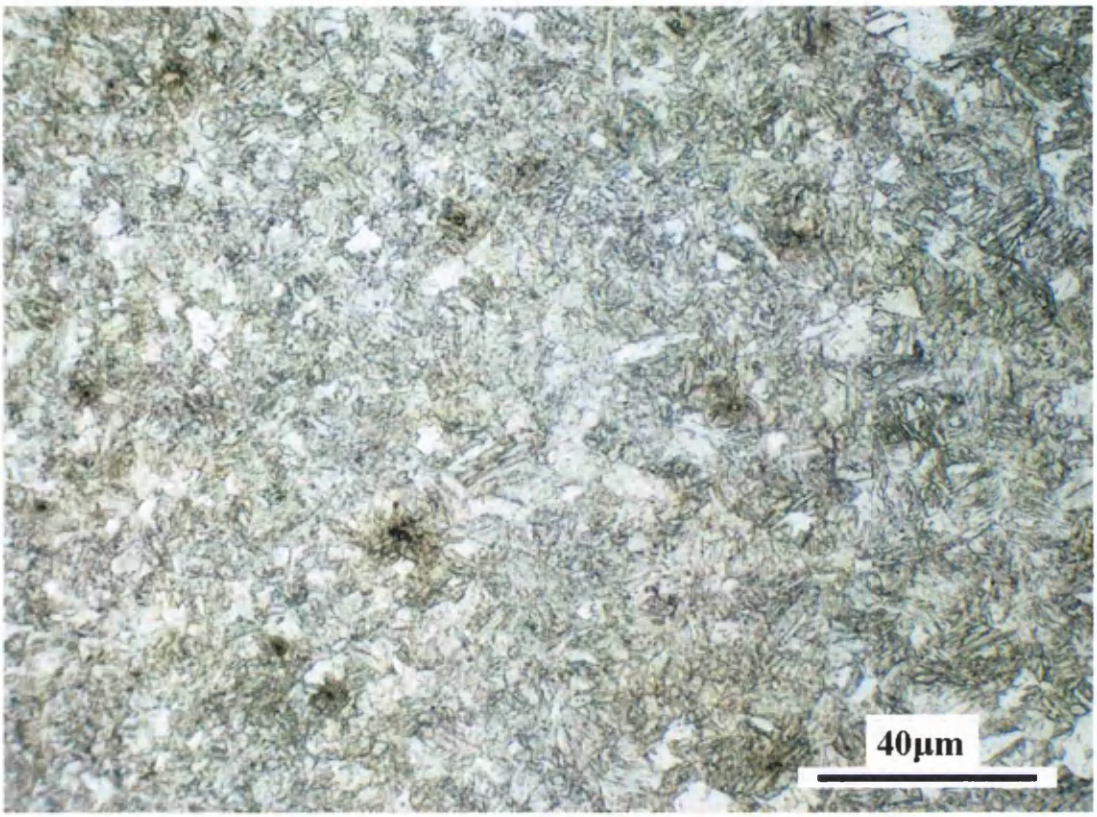

Figure 5.47e Micrograph showing microstructure of the outer heat affected zone in TRIP600

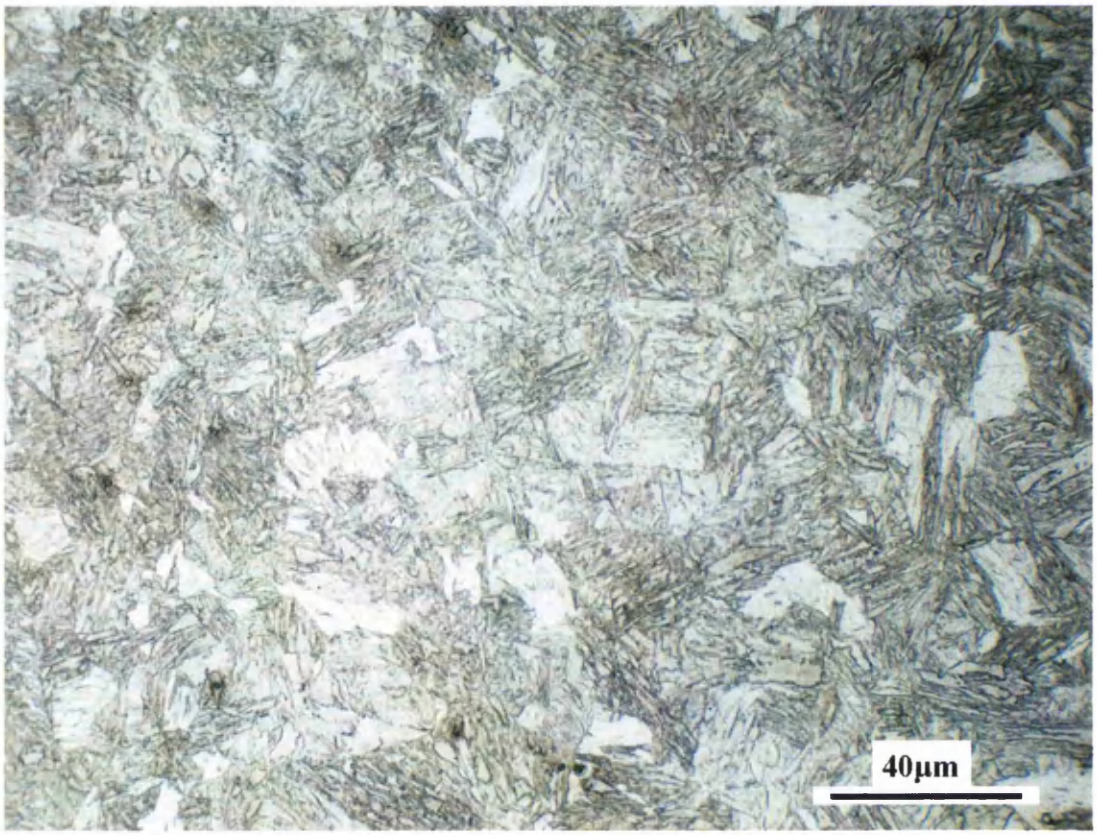

Figure 5.47f Micrograph showing microstructure of the inner heat affected zone in TRIP600

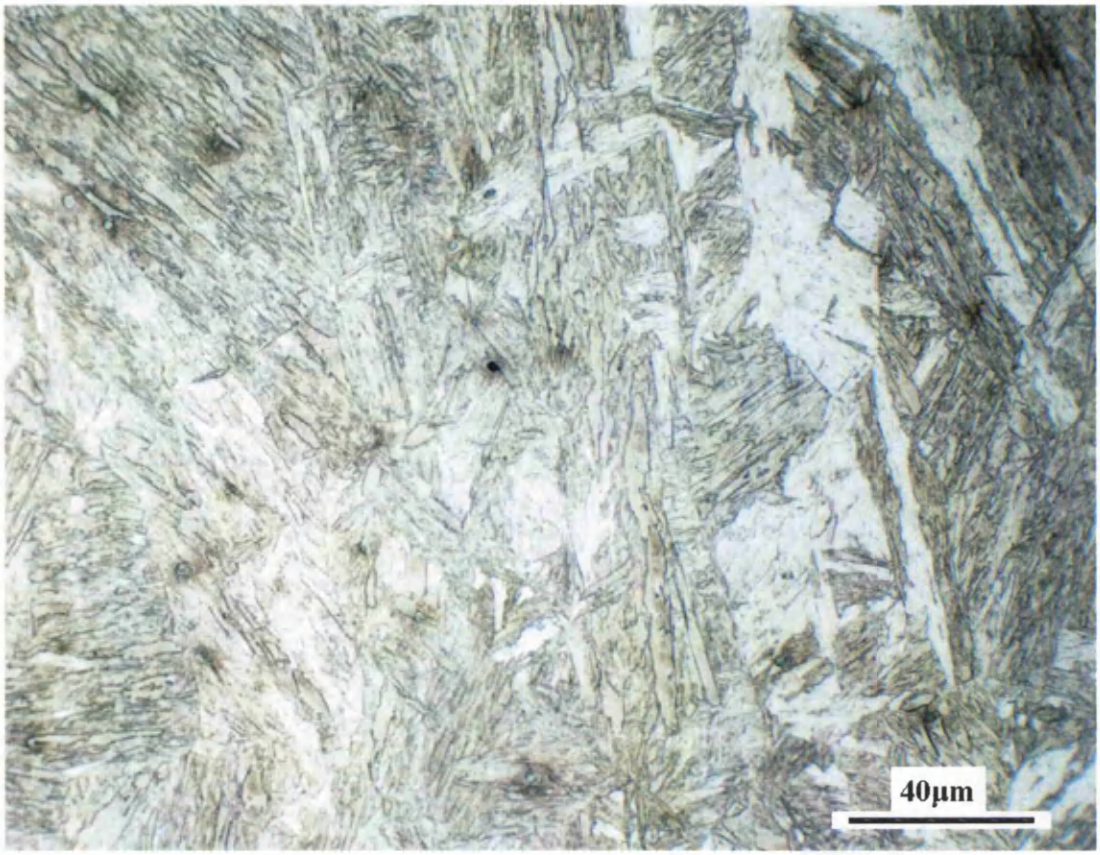

Figure 5.47g Micrograph showing weld nugget microstructure in TRIP600

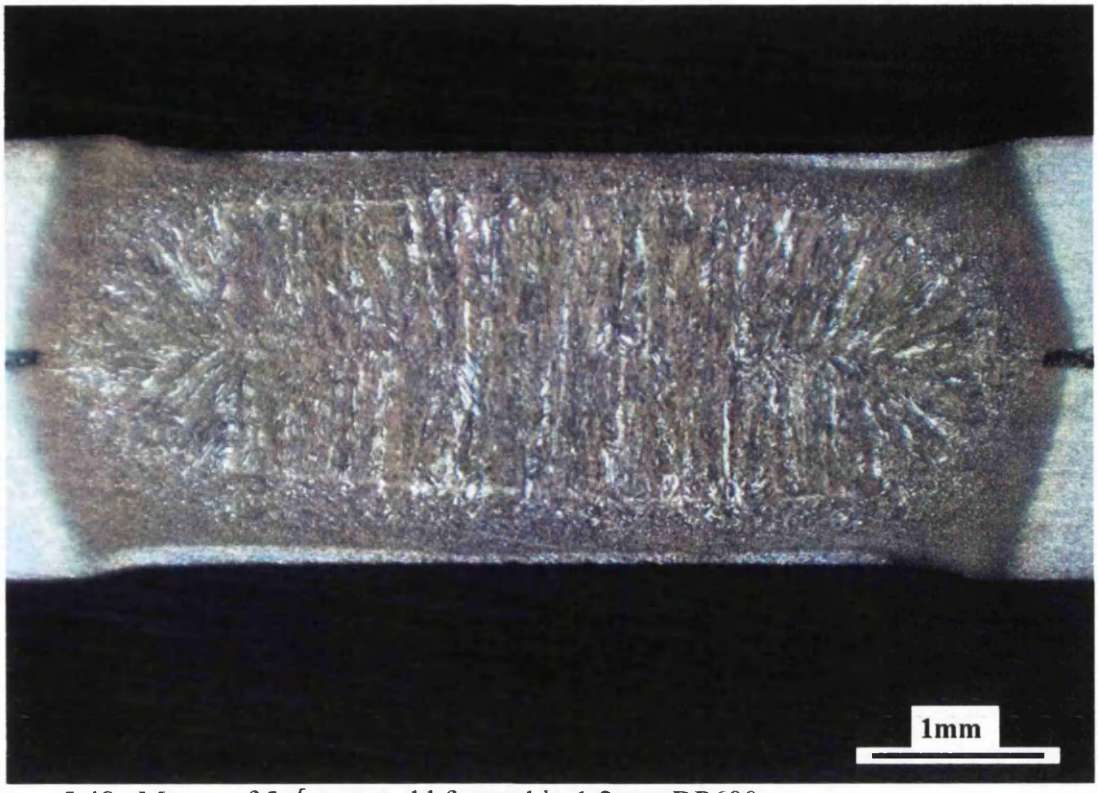

Figure 5.48a Macro of $5\sqrt{t}$ spot weld formed in 1.2mm DP600

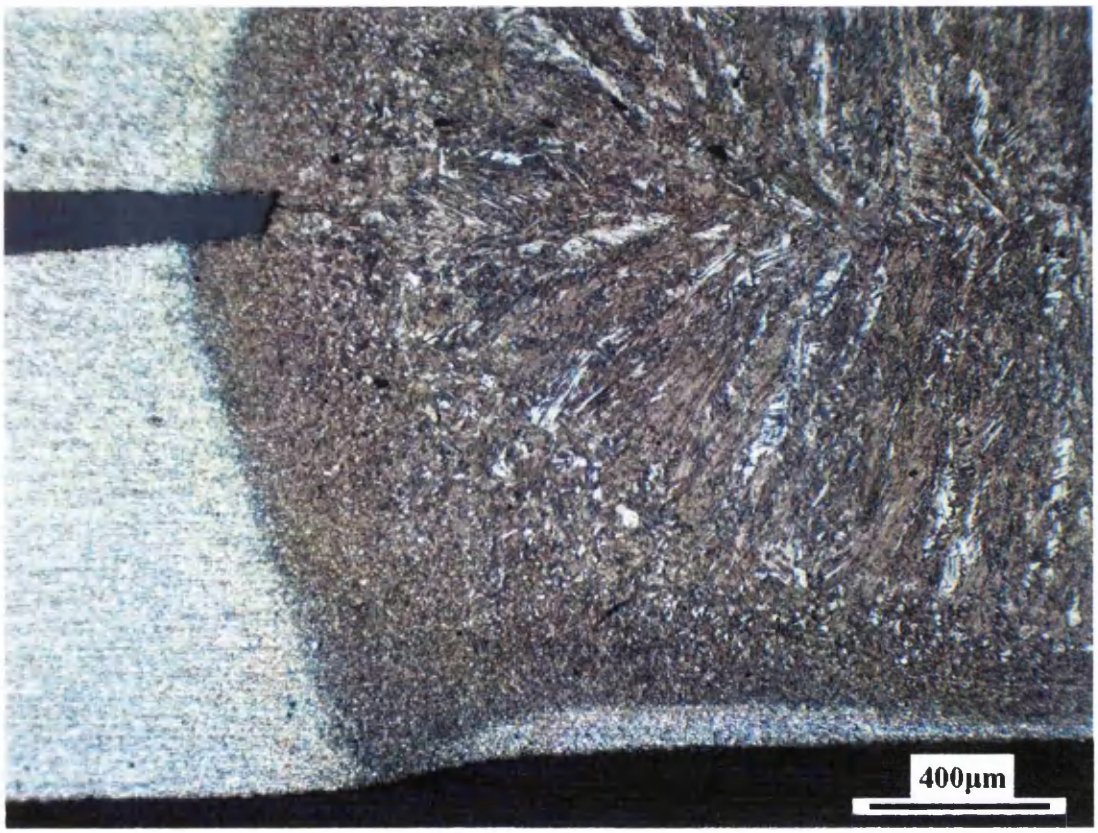

Figure 5.48b Micrograph illustrating the variation in microstructure from parent metal to weld nugget in DP600 weld

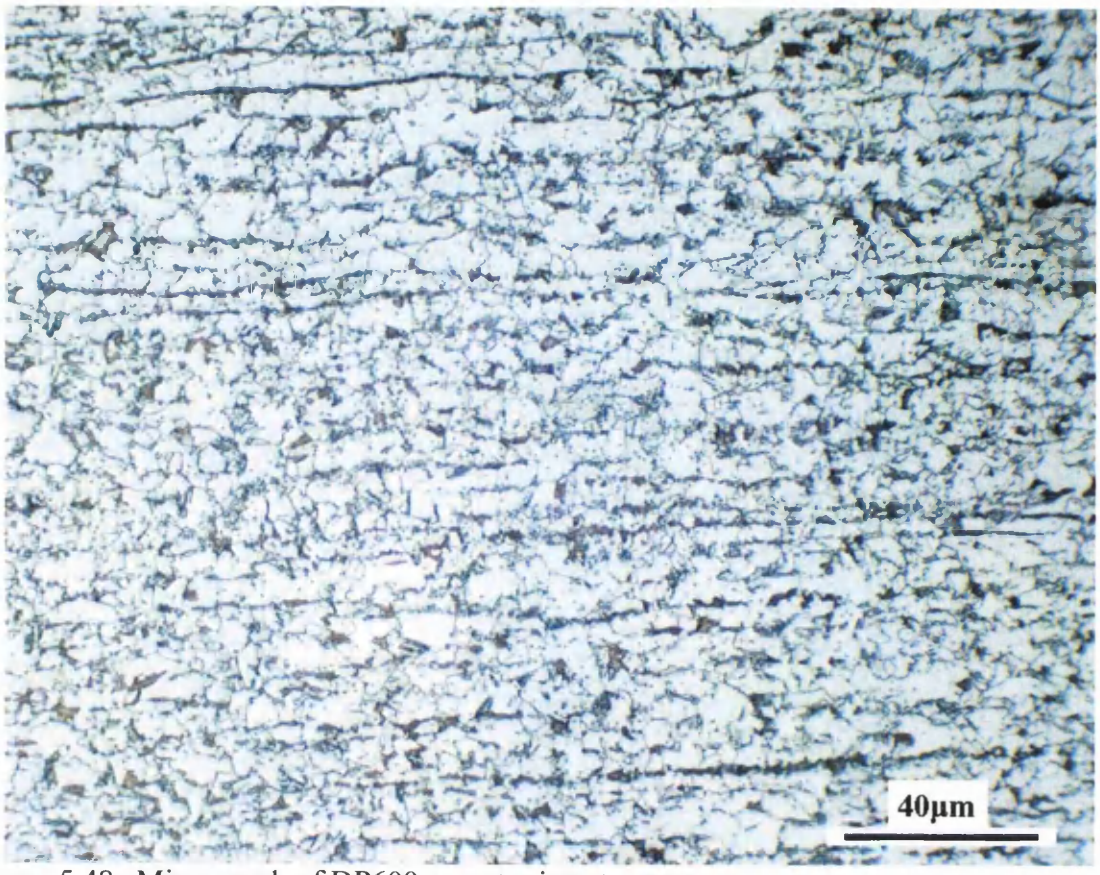

Figure 5.48c Micrograph of DP600 parent microstructure

Figure 5.48d Micrograph showing transition from parent material microstructure to heat affected zone microstructure in DP600

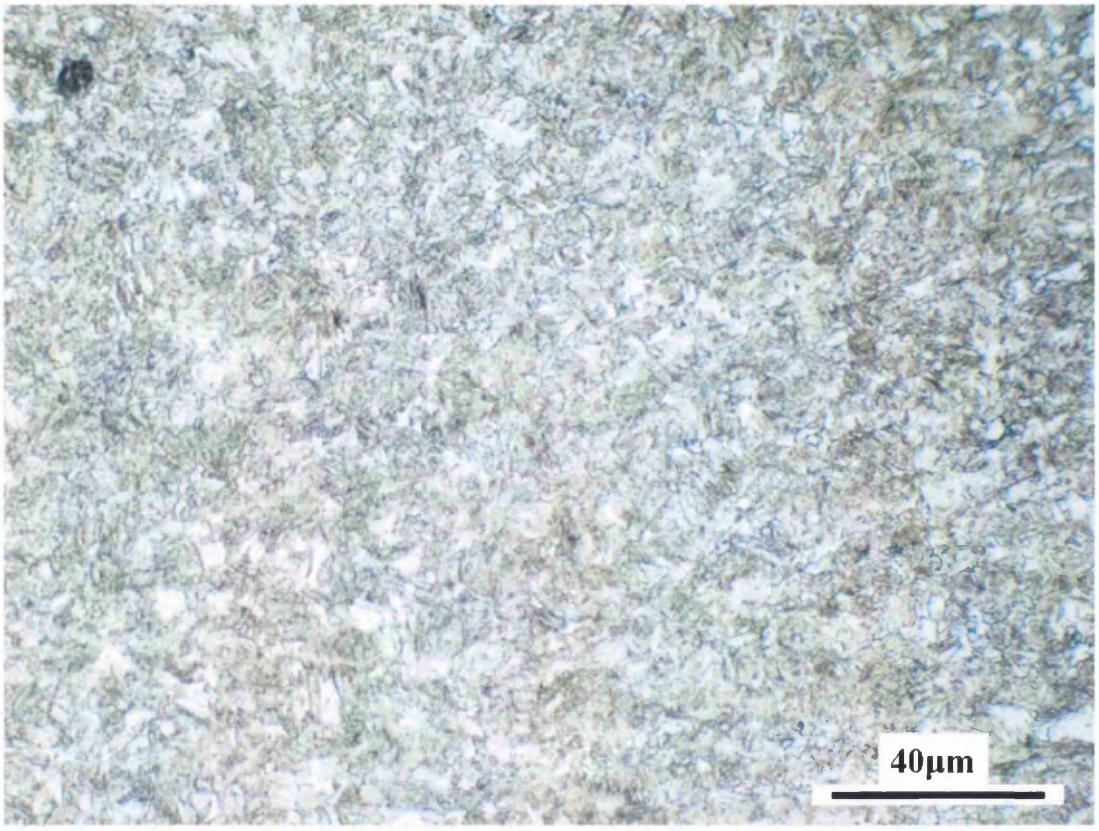

Figure 5.48e Micrograph showing microstructure of the outer heat affected zone in DP600

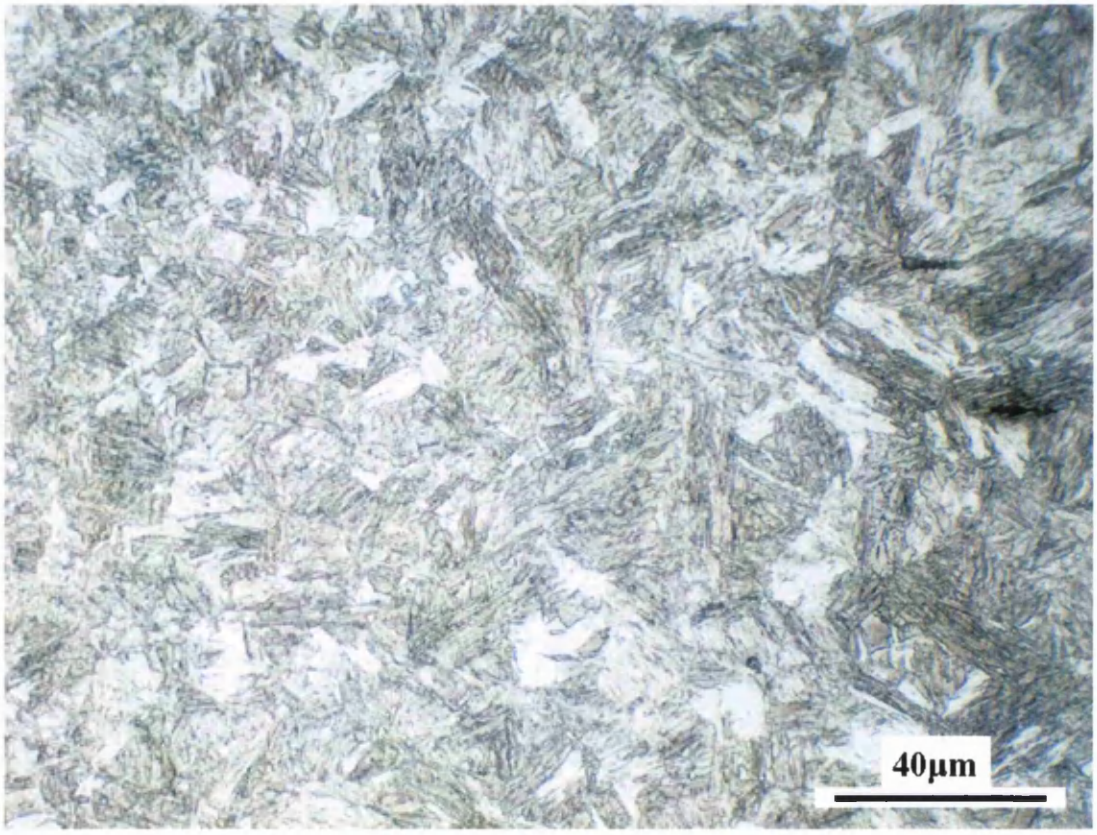

Figure 5.48f Micrograph showing microstructure of the inner heat affected zone in DP600

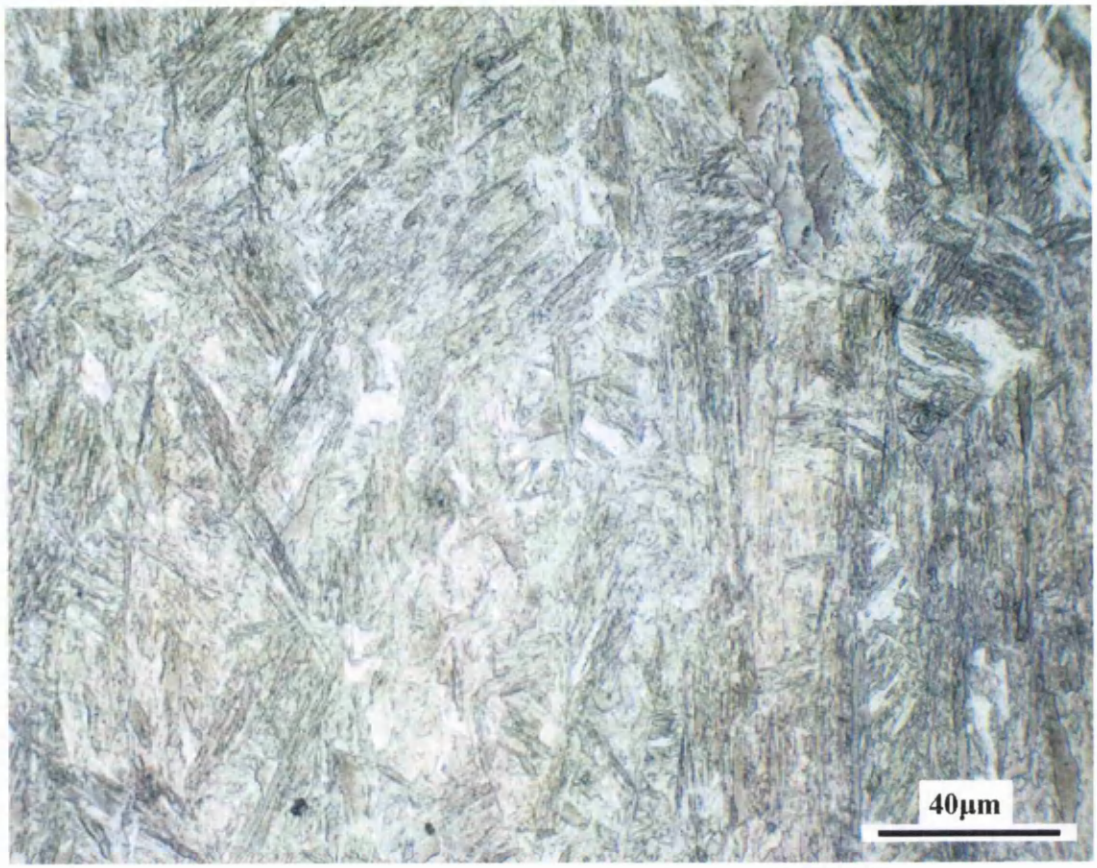

Figure 5.48g Micrograph showing weld nugget microstructure in DP600

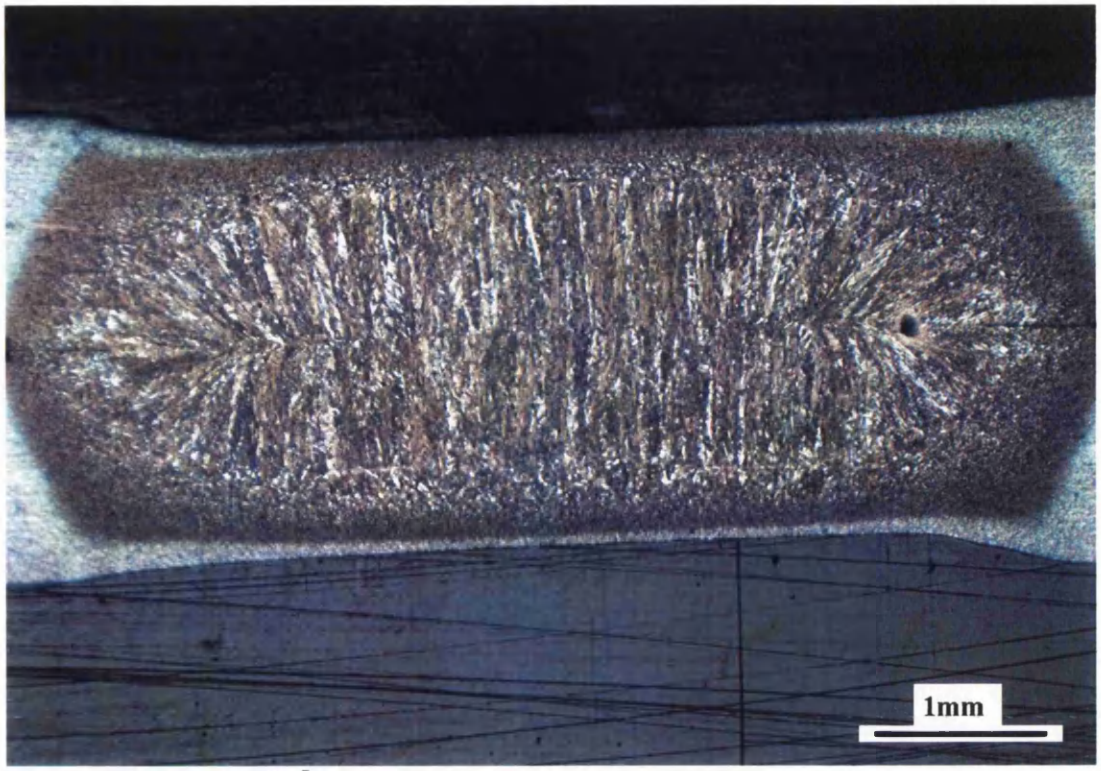

Figure 5.49a Macro of $5\sqrt{t}$ spot weld formed in 1.2mm DP800

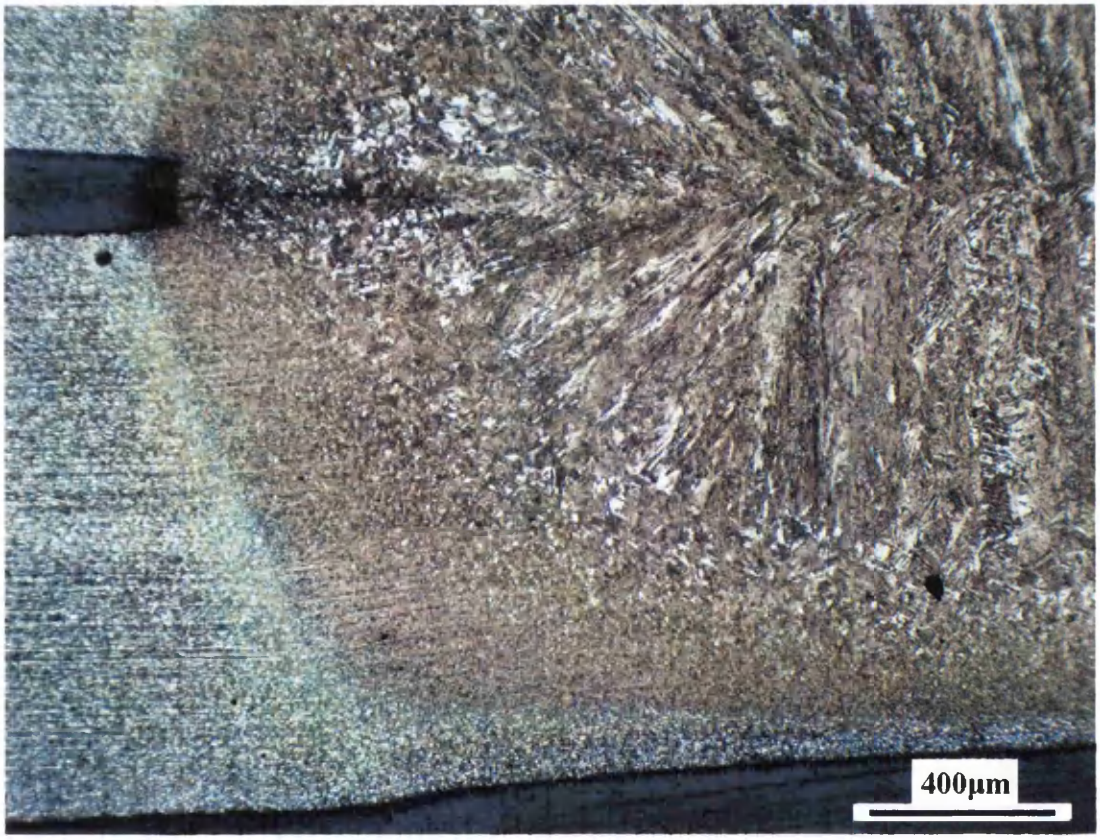

Figure 5.49b Micrograph illustrating the variation in microstructure from parent metal to weld nugget in DP800 weld

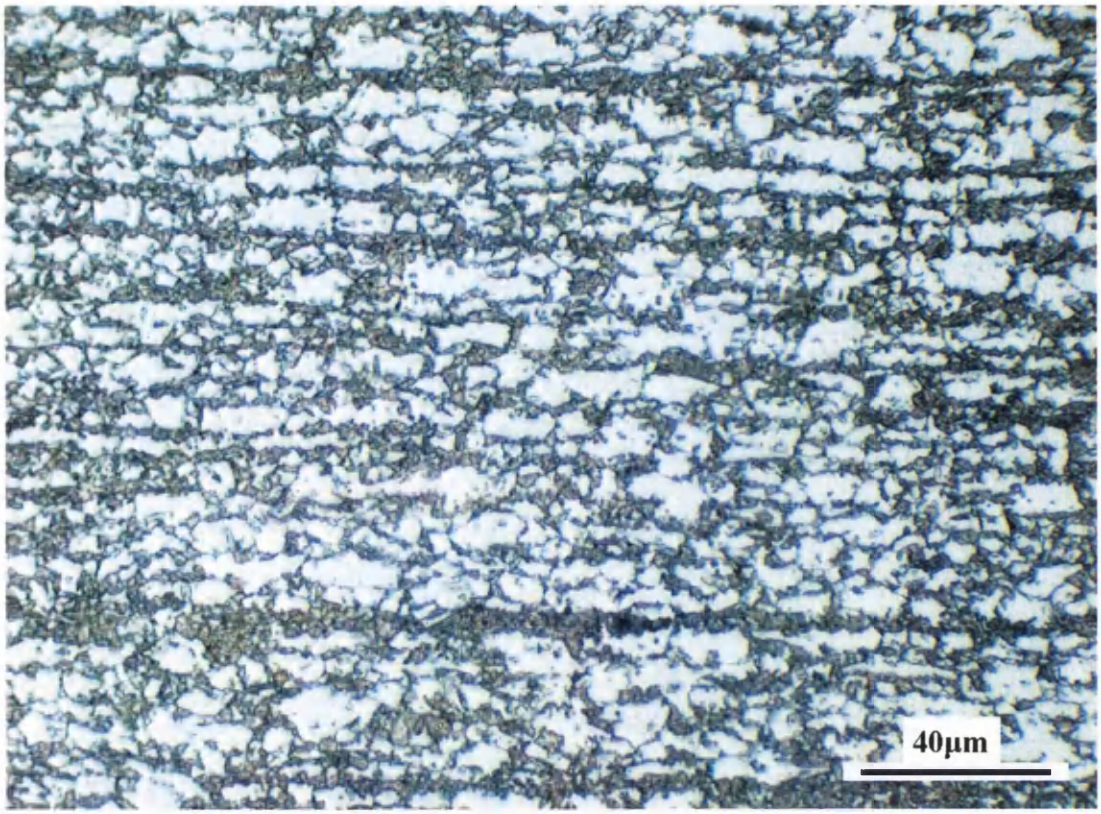

Figure 5.49c Micrograph of DP800 parent microstructure

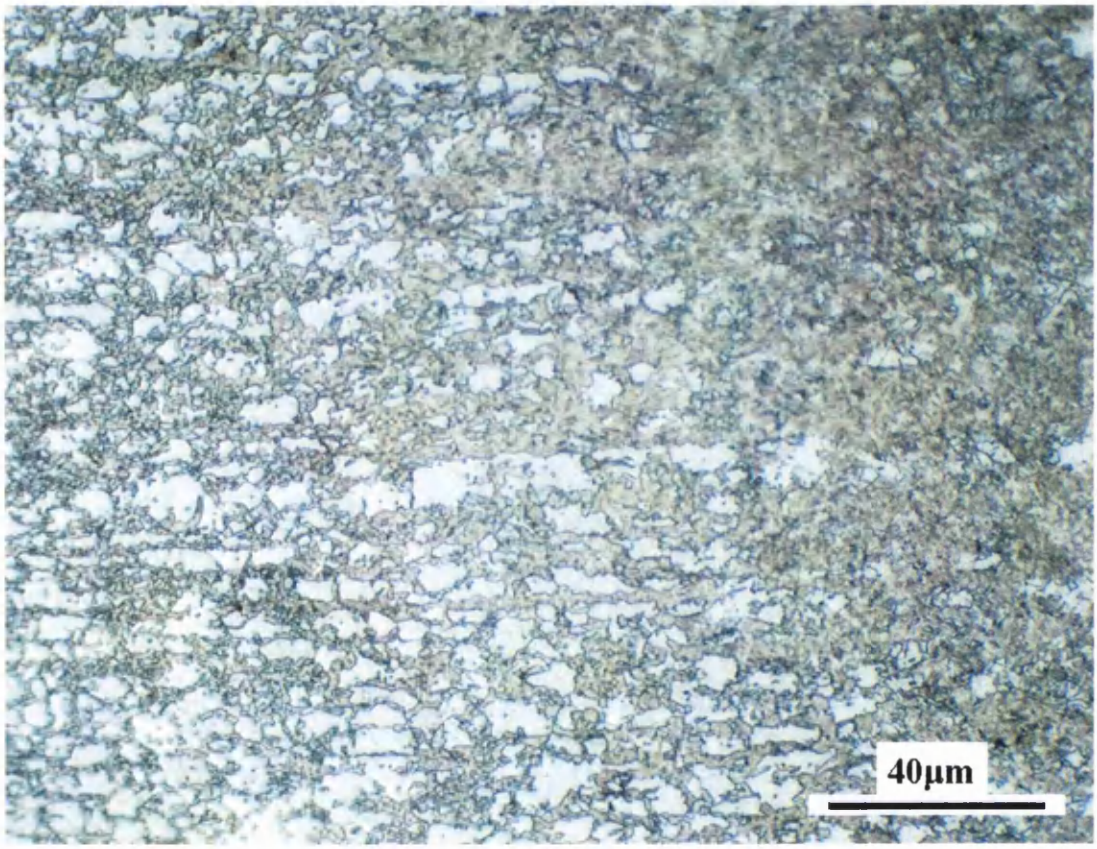

Figure 5.49d Micrograph showing transition from parent material microstructure to heat affected zone microstructure in DP800

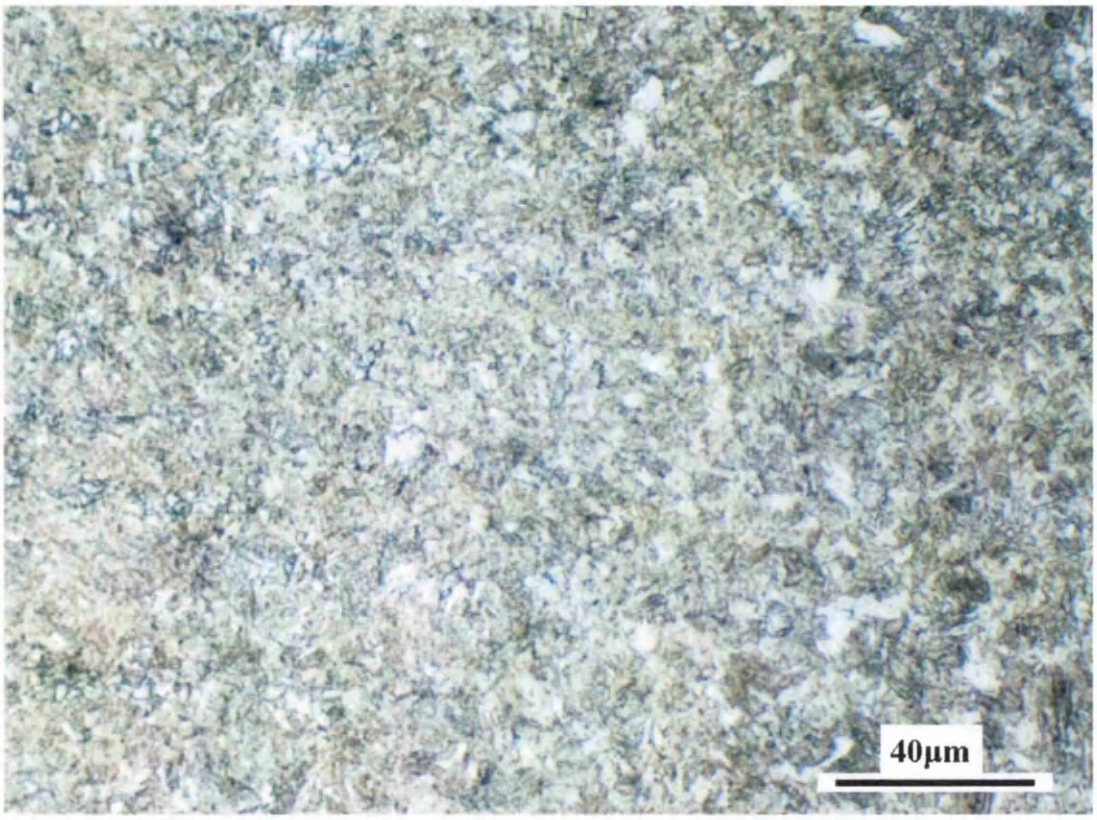

Figure 5.49e Micrograph showing microstructure of the outer heat affected zone in DP800

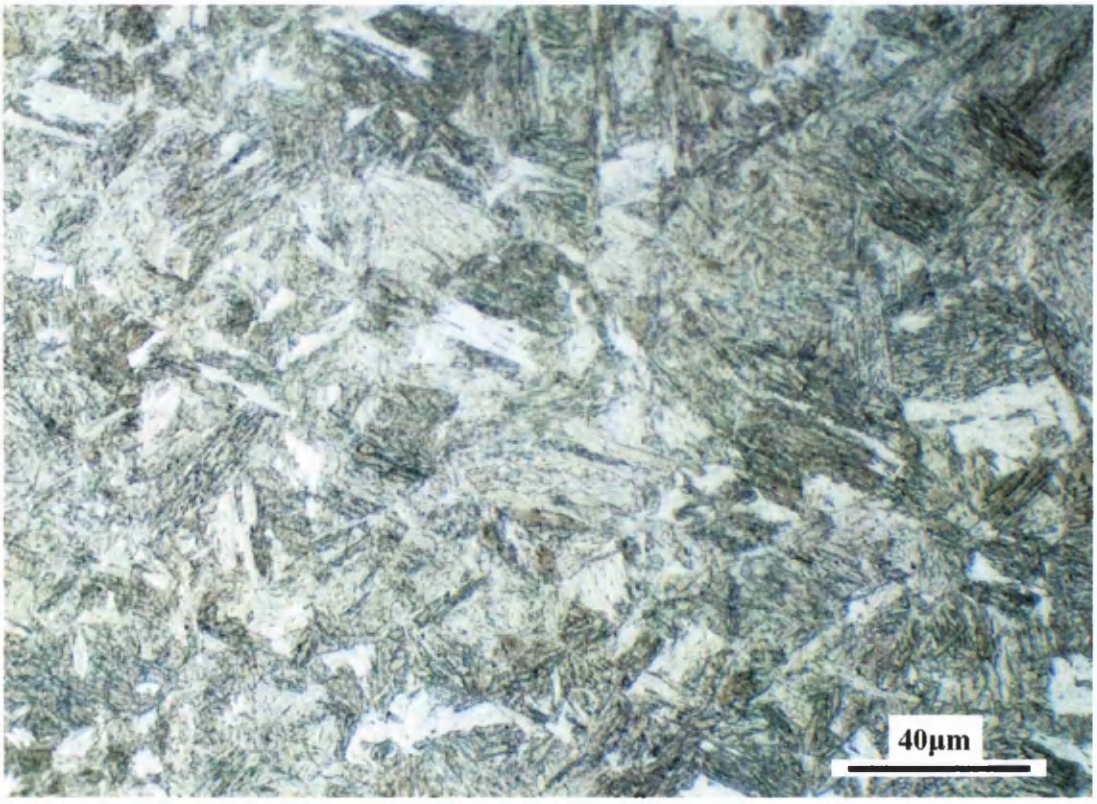

Figure 5.49f Micrograph showing microstructure of the inner heat affected zone in DP800

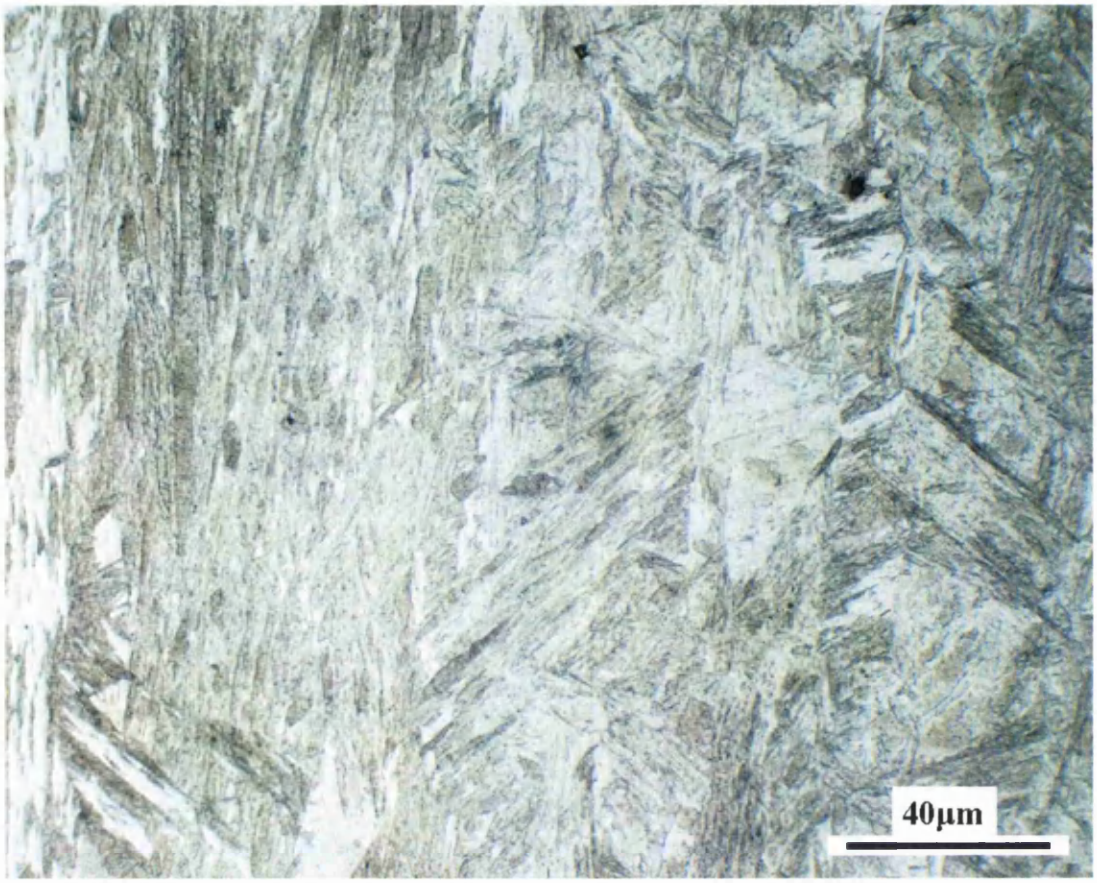

Figure 5.49g Micrograph showing weld nugget microstructure in DP800

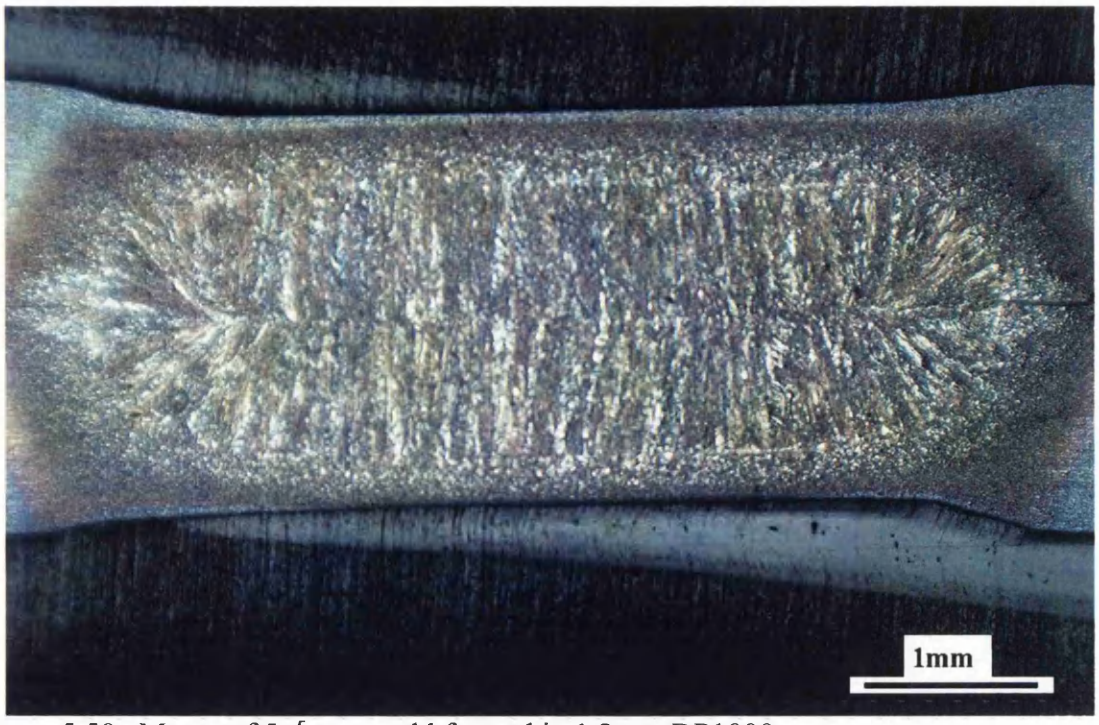

Figure 5.50a Macro of $5\sqrt{t}$ spot weld formed in 1.2mm DP1000

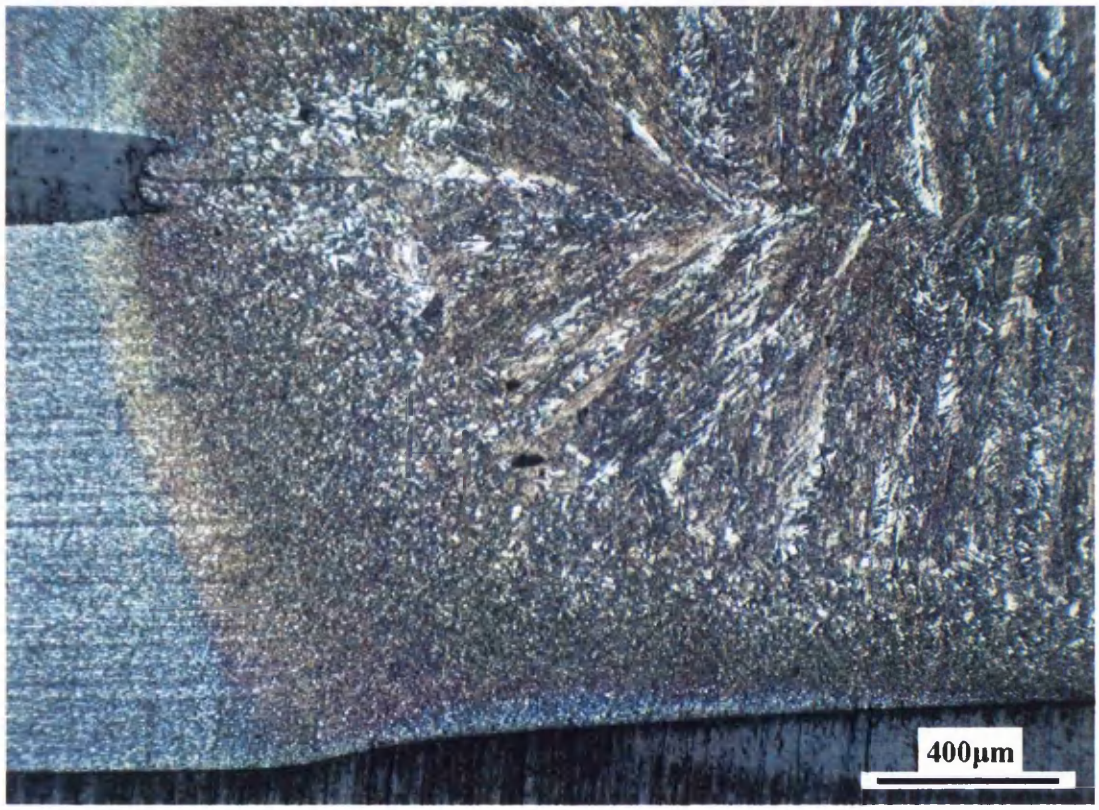

Figure 5.50b Micrograph illustrating the variation in microstructure from parent metal to weld nugget in DP1000 weld

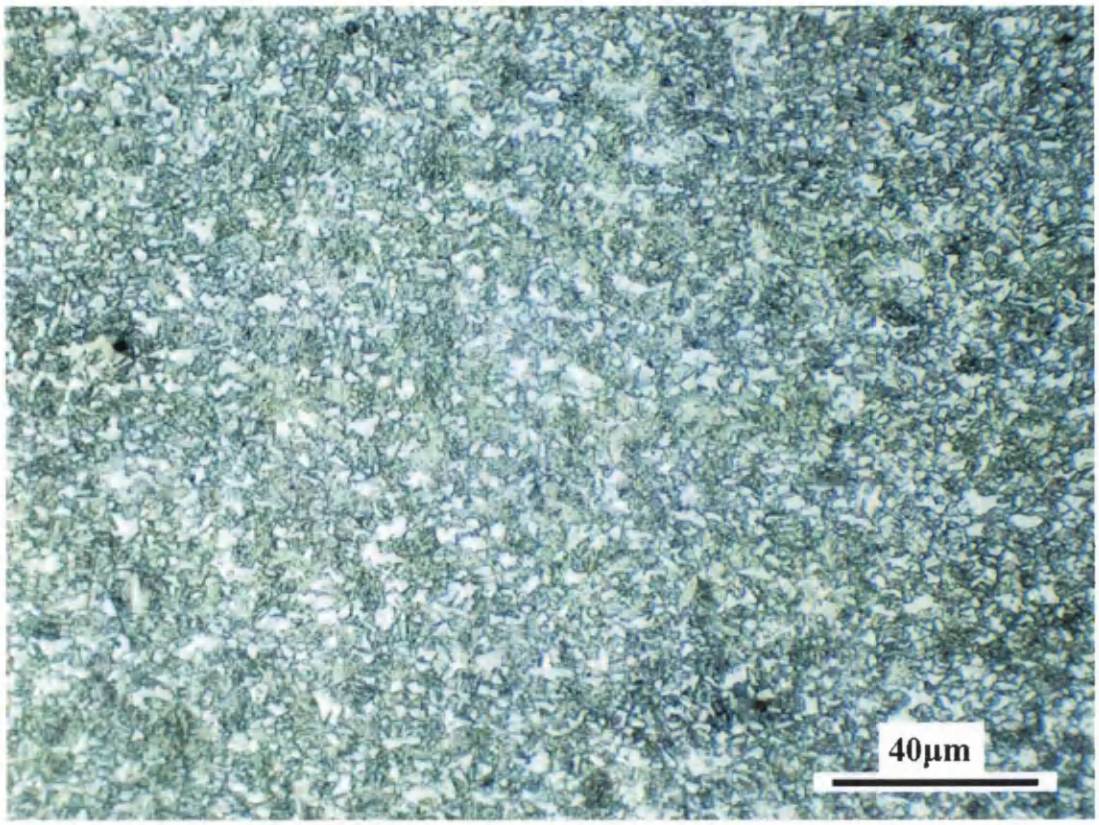

Figure 5.50c Micrograph of DP1000 parent microstructure

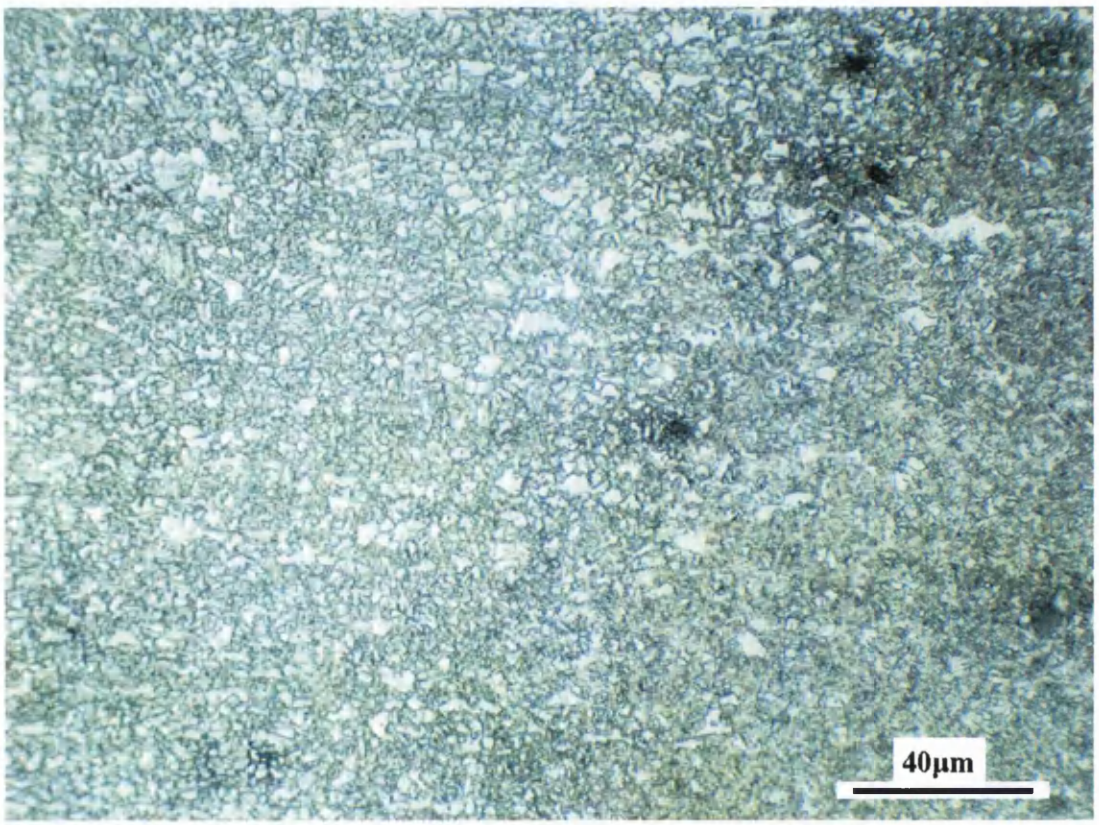

Figure 5.50d Micrograph showing transition from parent material microstructure to heat affected zone microstructure in DP1000. Parent microstructure appears on left-hand side of image

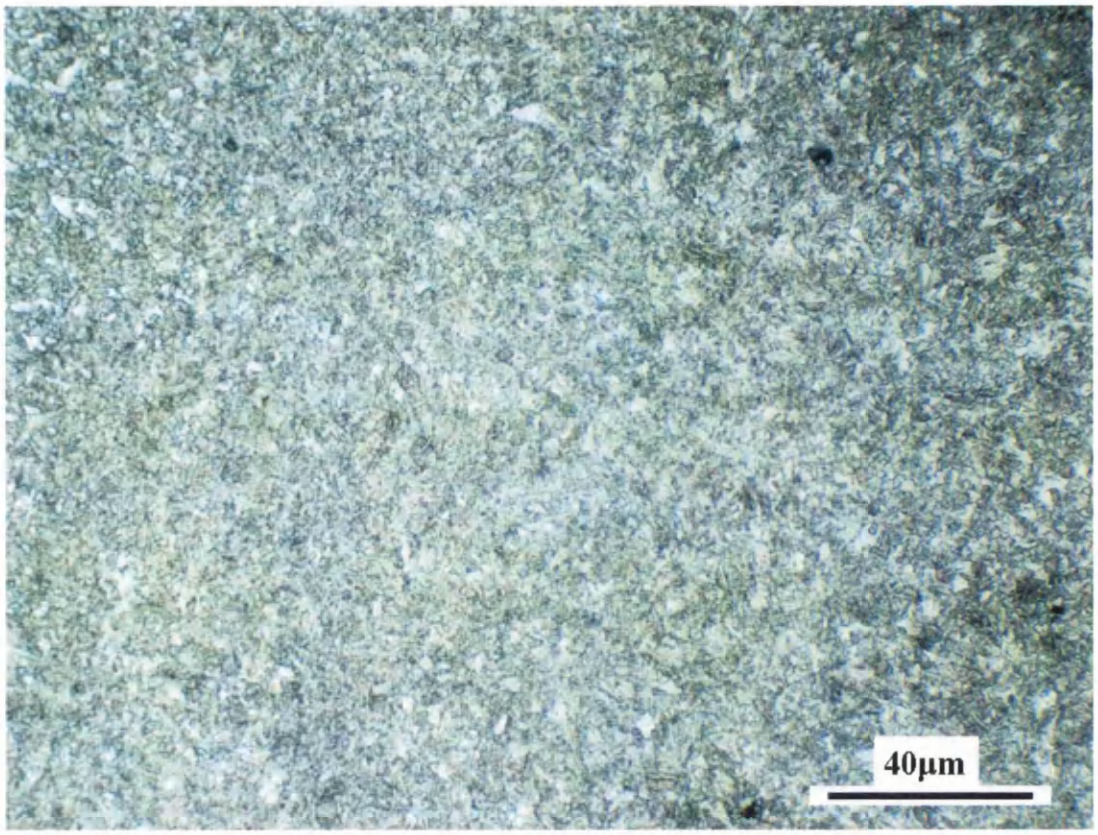

Figure 5.50e Micrograph showing microstructure of the outer heat affected zone in DP1000

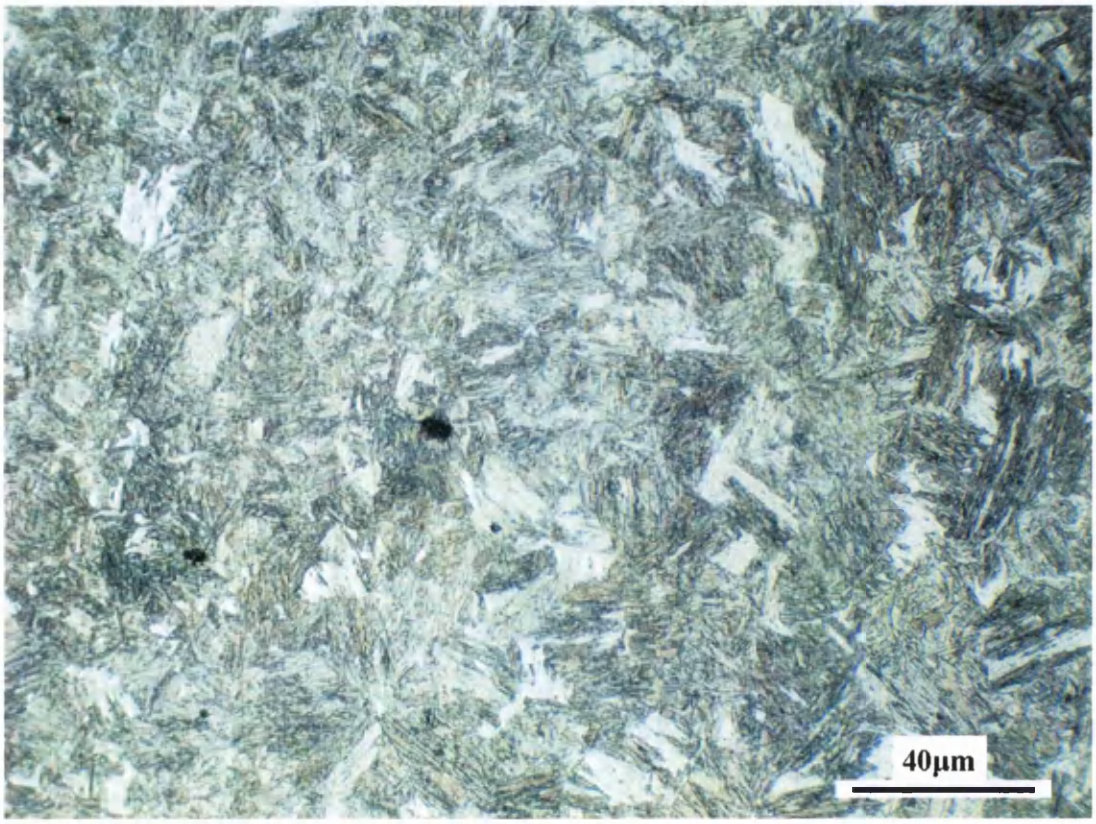

Figure 5.50f Micrograph showing microstructure of the inner heat affected zone in DP1000

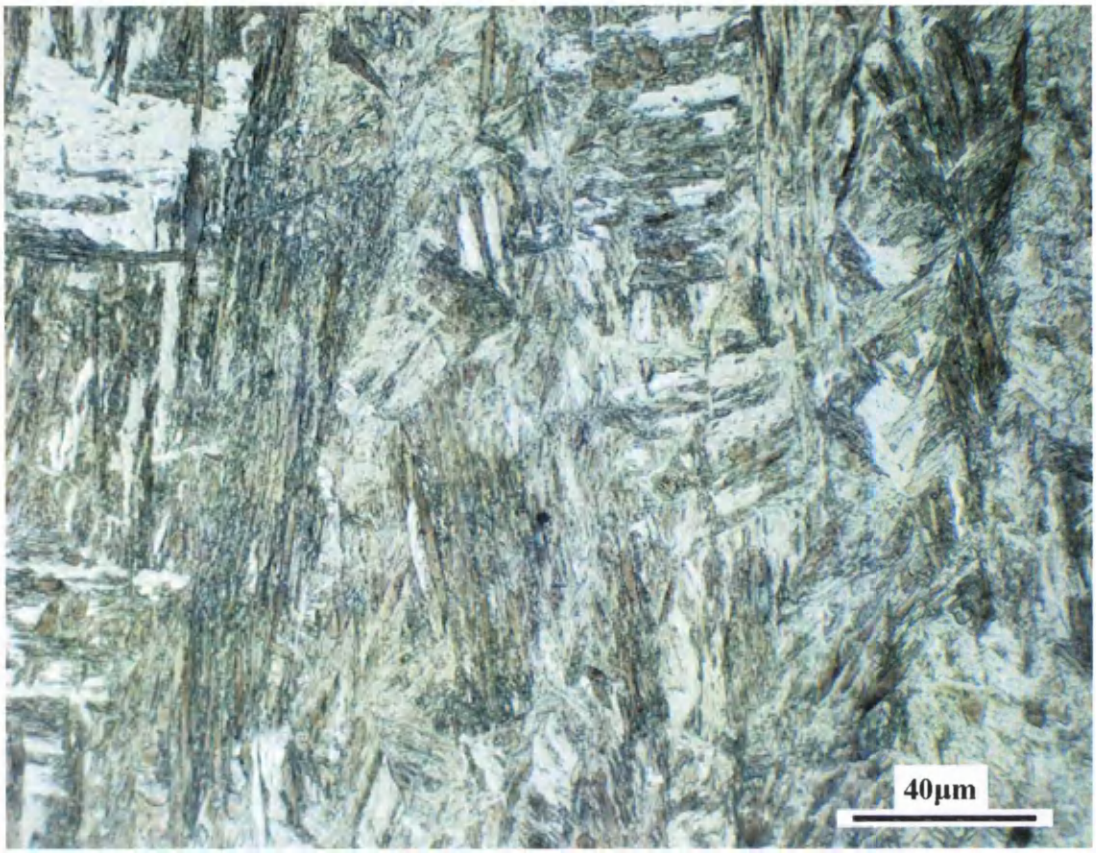

Figure 5.50g Micrograph showing weld nugget microstructure in DP1000

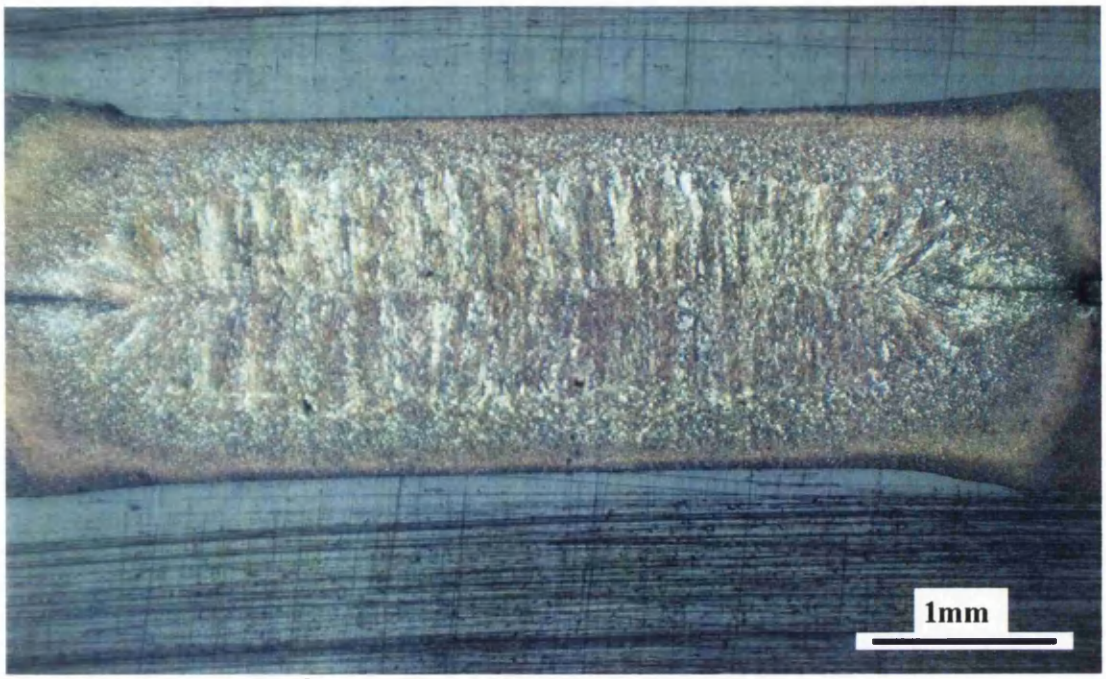

Figure 5.51a Macro of $5\sqrt{t}$ spot weld formed in 1.0mm MS1400

Figure 5.51b Micrograph illustrating the variation in microstructure from parent metal to weld nugget in MS1400 weld

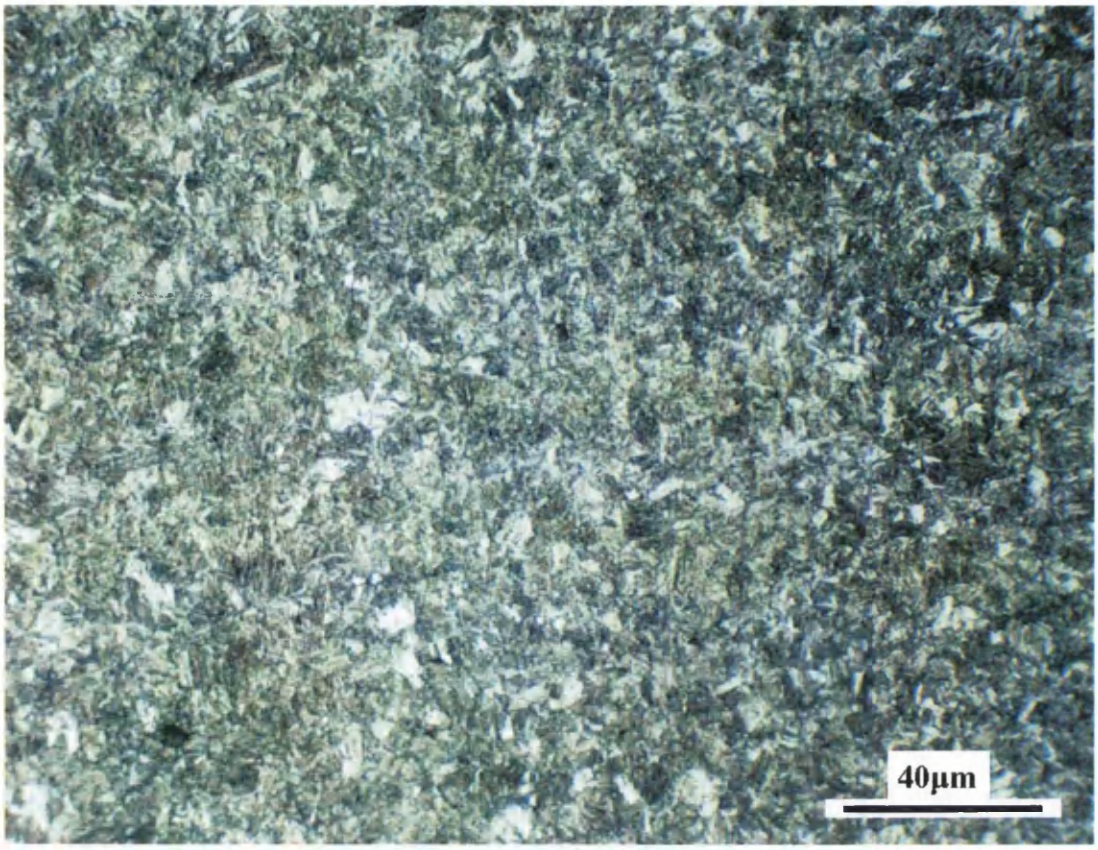

Figure 5.51c Micrograph of MS1400 parent microstructure

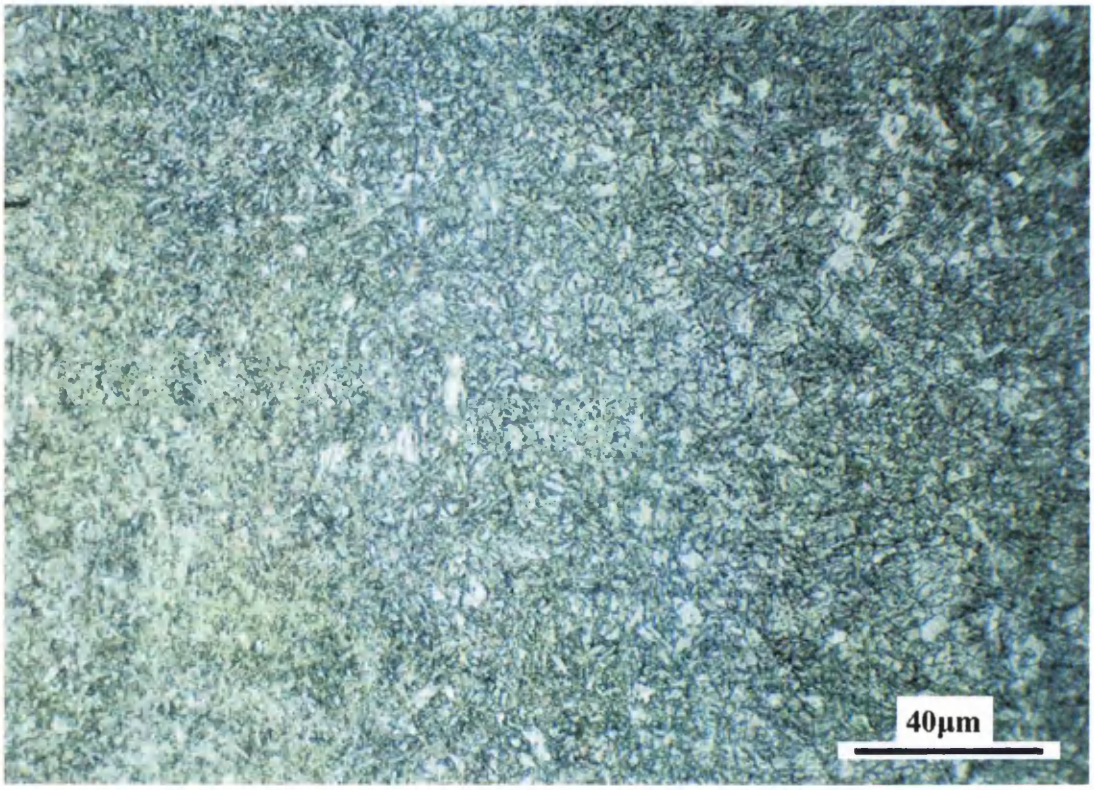

Figure 5.51d Micrograph showing transition from parent material microstructure to heat affected zone microstructure in MS1400. Parent microstructure appears on right-hand side of image

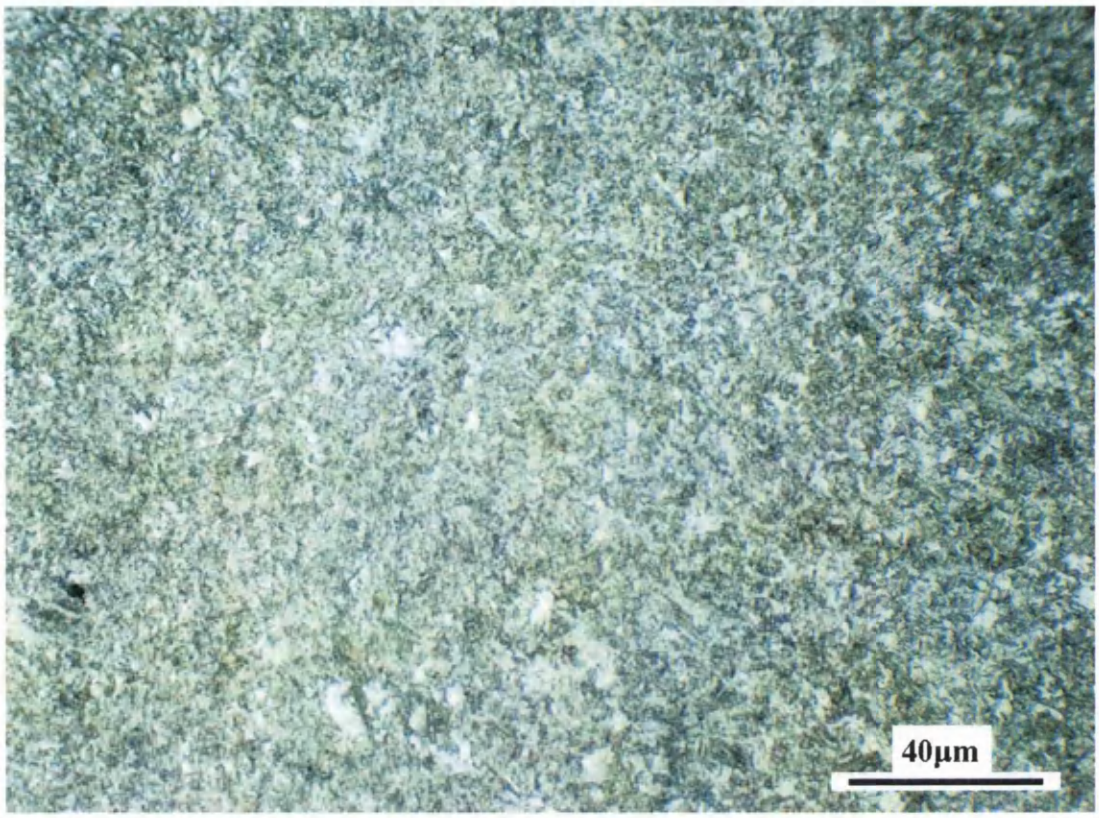

Figure 5.51e Micrograph showing microstructure of the outer heat affected zone in MS1400

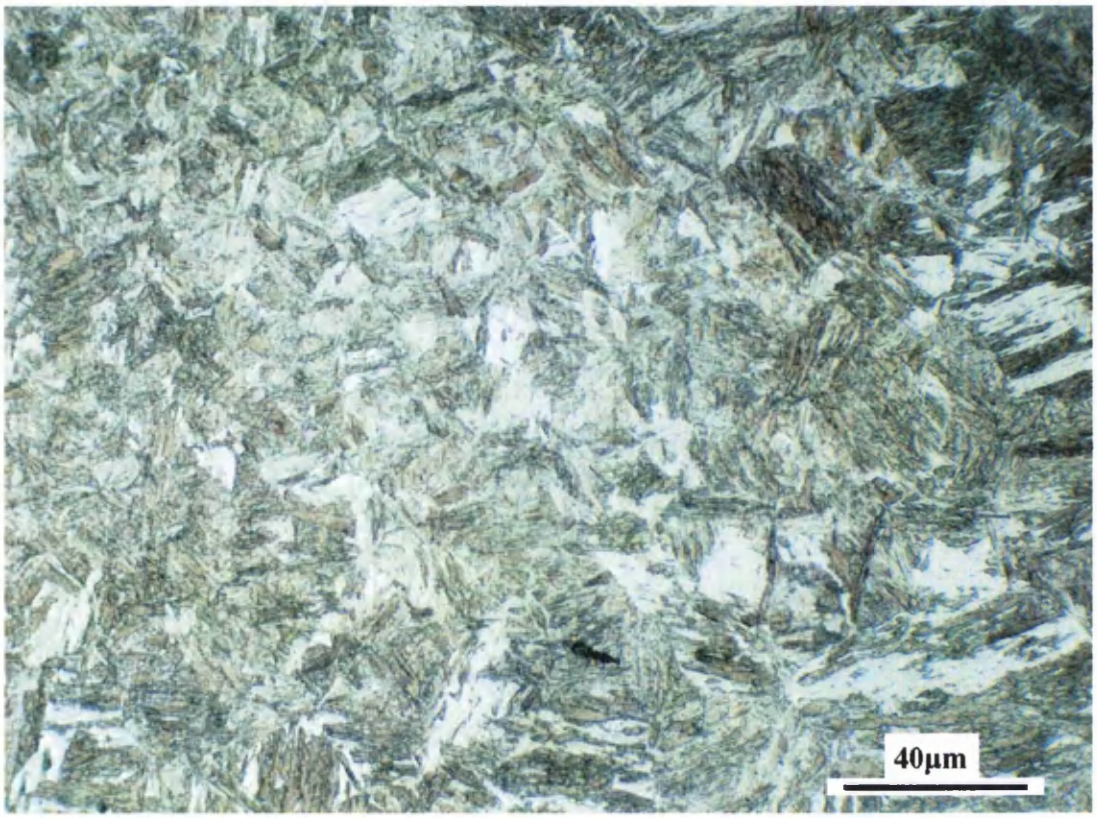

Figure 5.51f Micrograph showing microstructure of the inner heat affected zone in MS1400

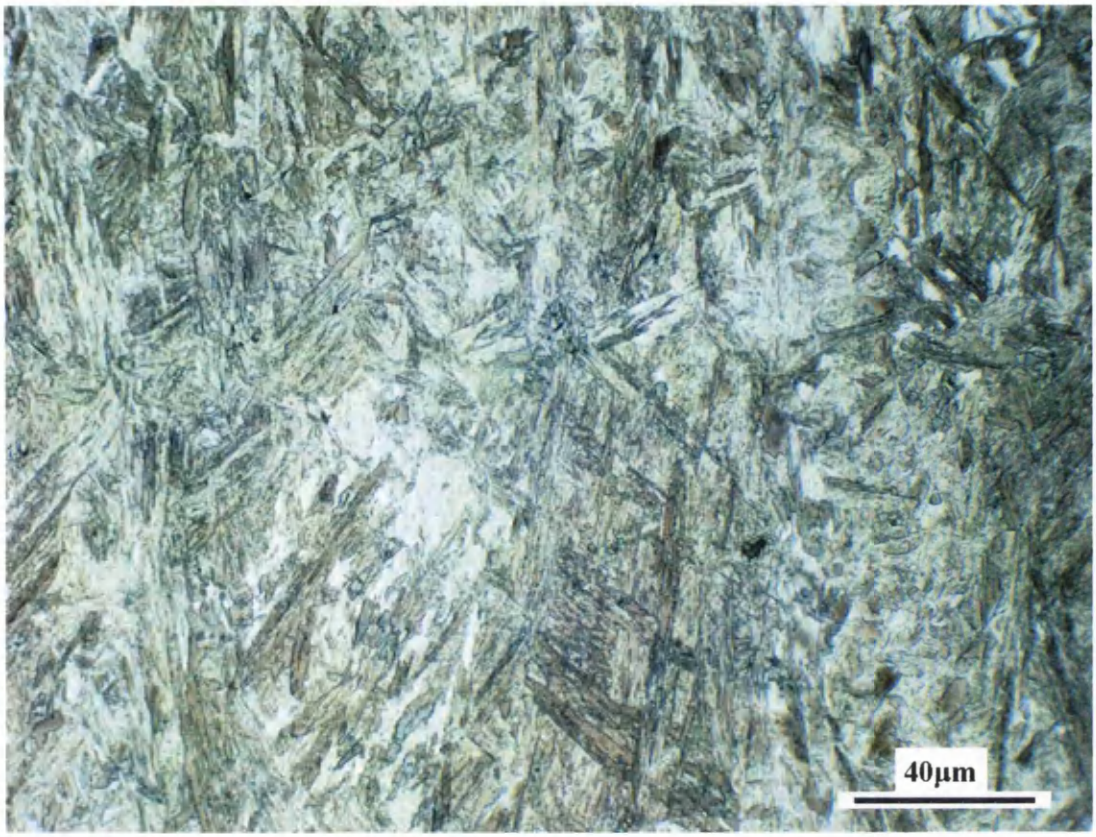

Figure 5.51g Micrograph showing weld nugget microstructure in MS1400

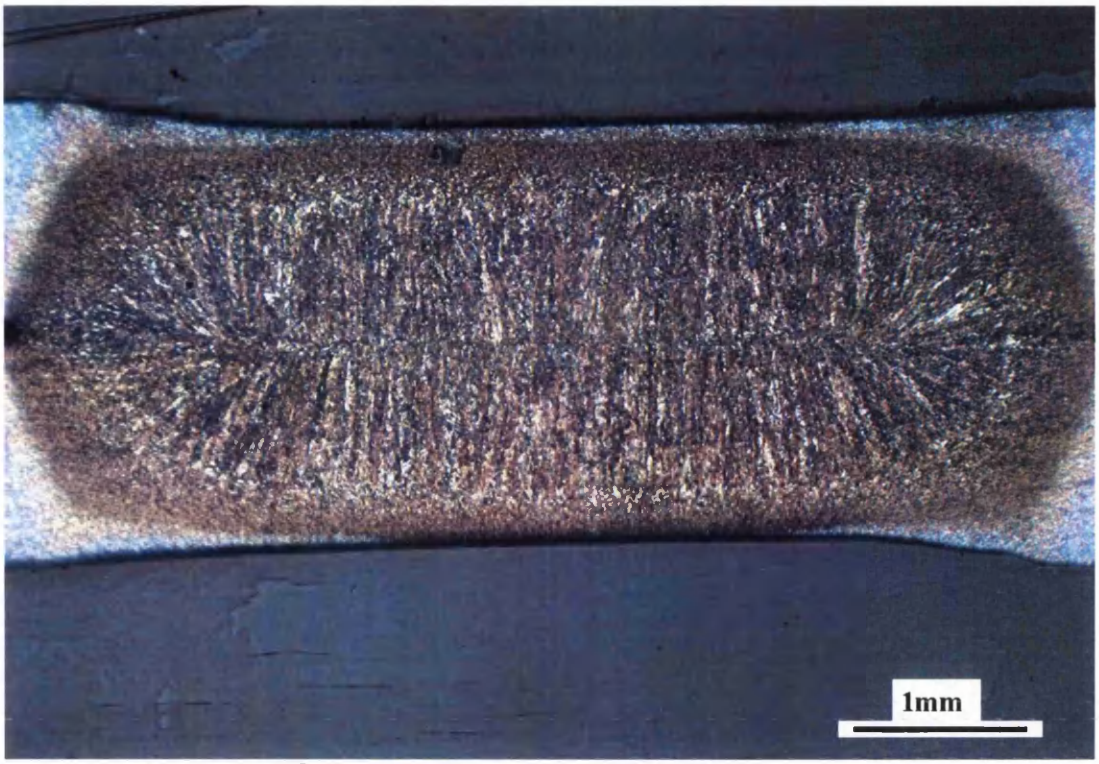

Figure 5.52a Macro of 5√t spot weld formed in 1.2mm TRIP800

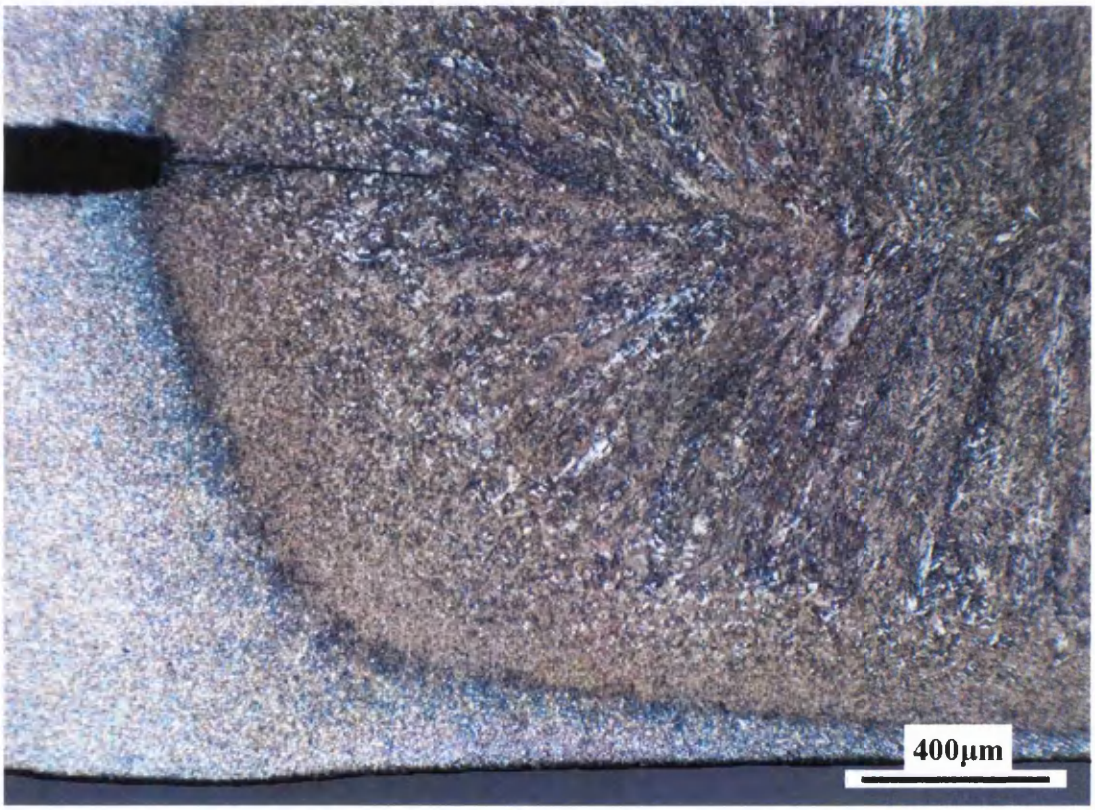

Figure 5.52b Micrograph illustrating the variation in microstructure from parent metal to weld nugget in TRIP800 weld

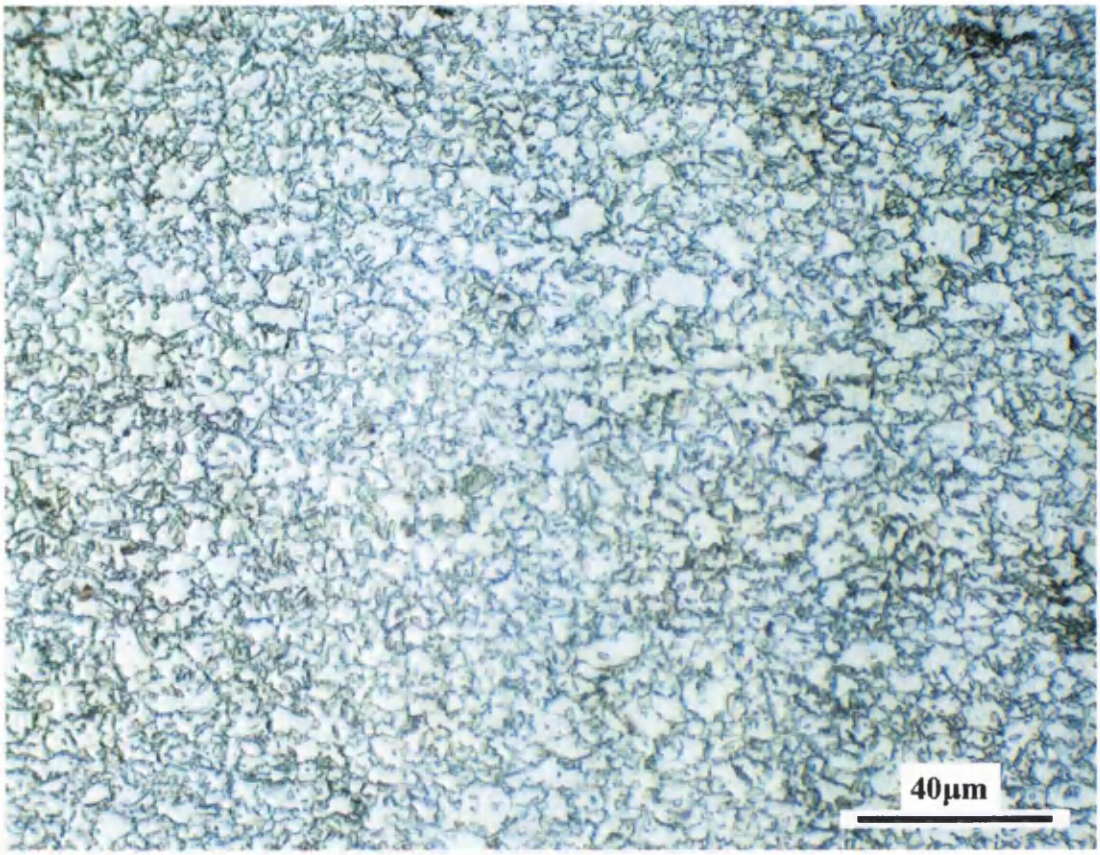

Figure 5.52c Micrograph of TRIP800 parent microstructure

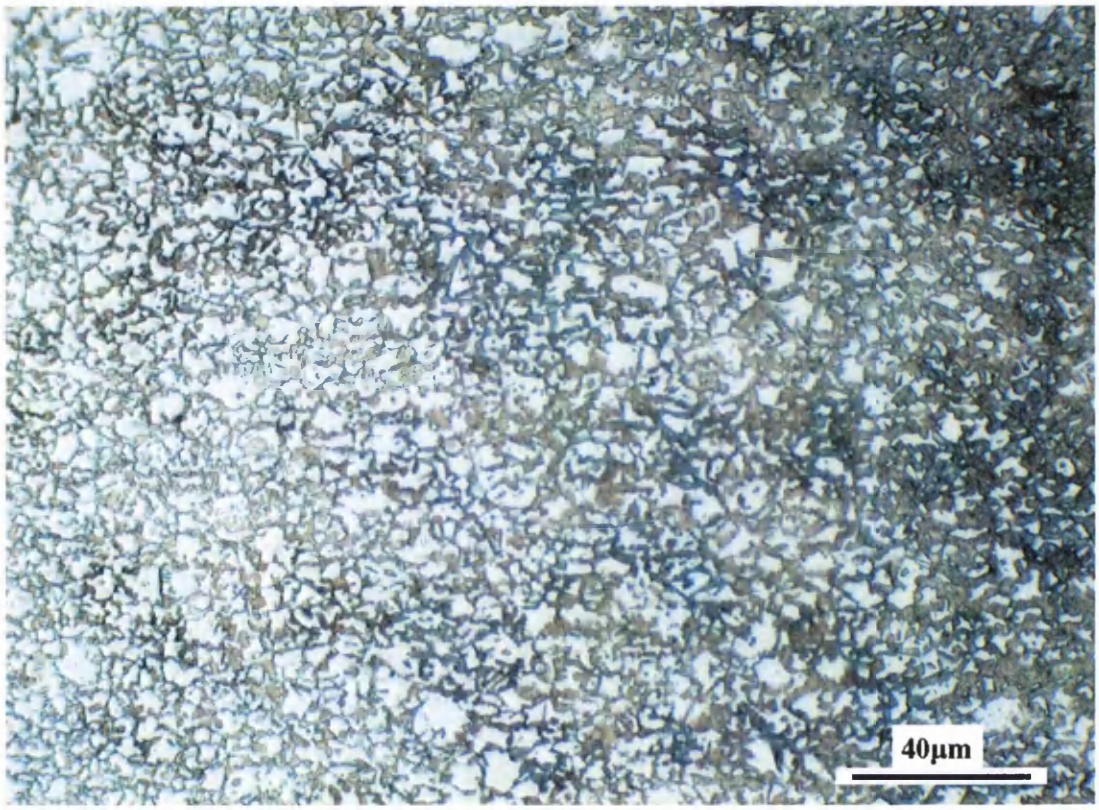

Figure 5.52d Micrograph showing transition from parent material microstructure to heat affected zone microstructure in TRIP800

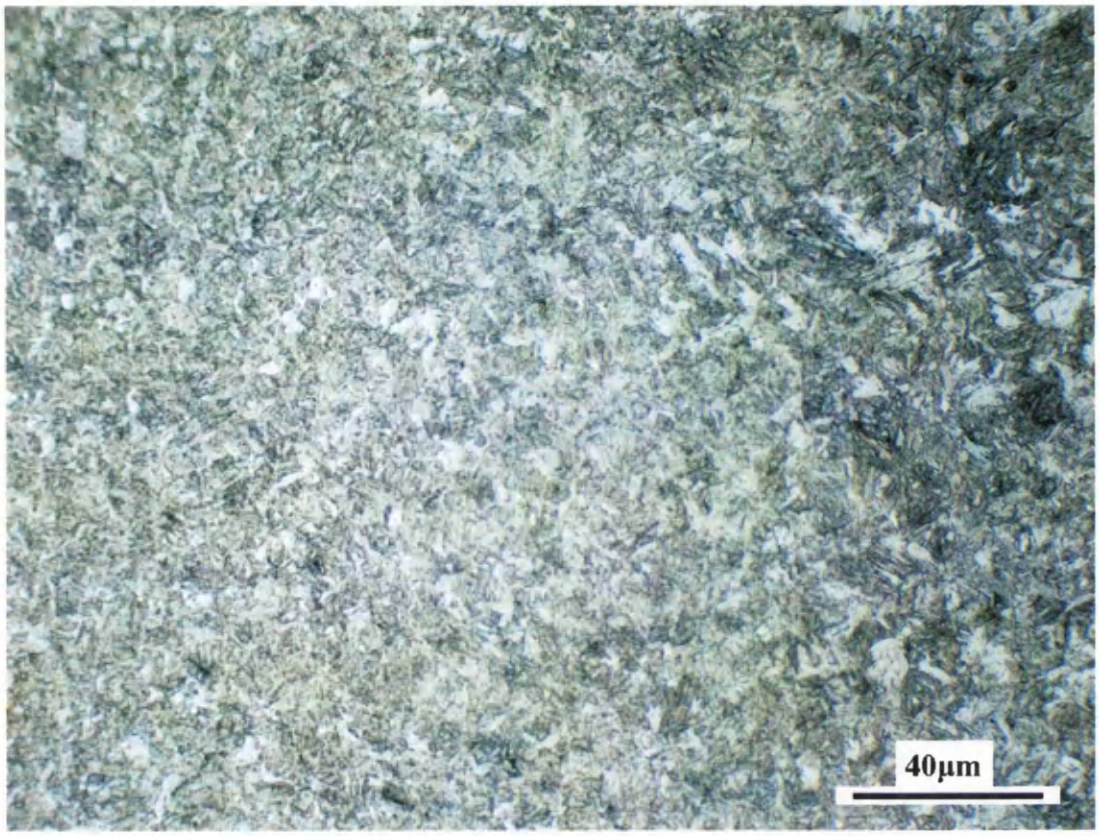

Figure 5.52e Micrograph showing microstructure of the outer heat affected zone in TRIP800

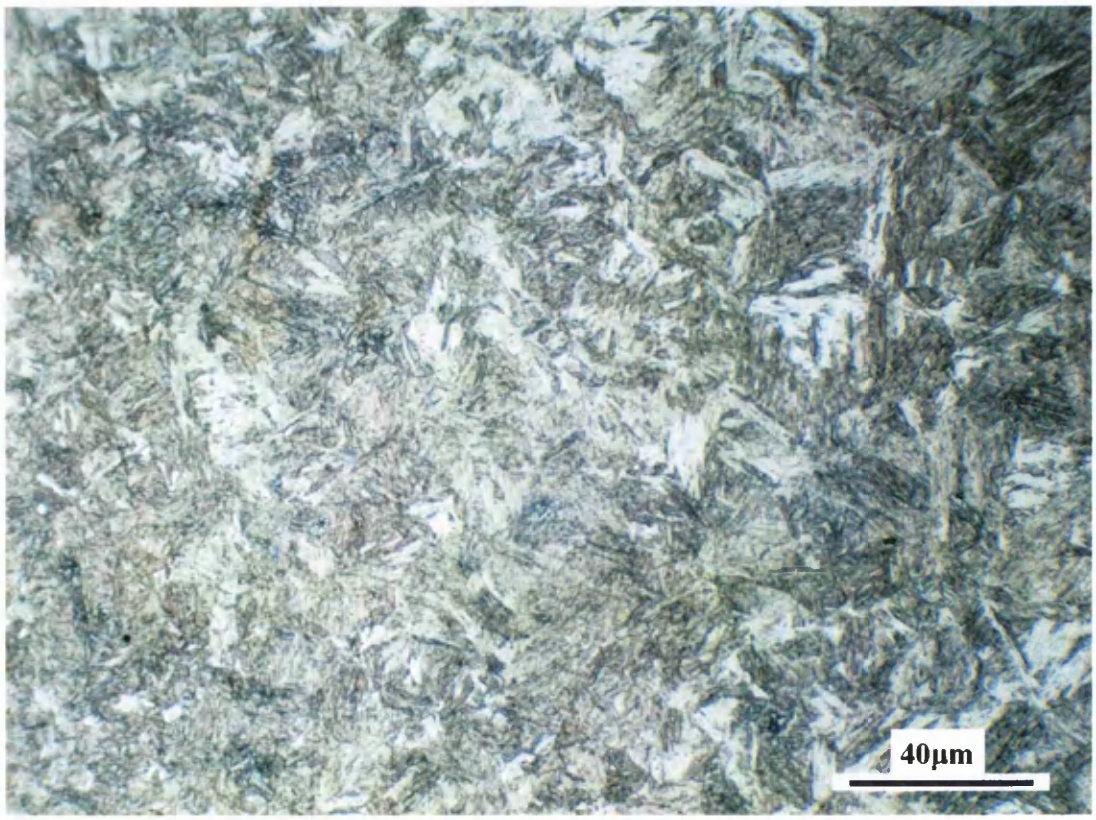

Figure 5.52f Micrograph showing microstructure of the inner heat affected zone in TRIP800

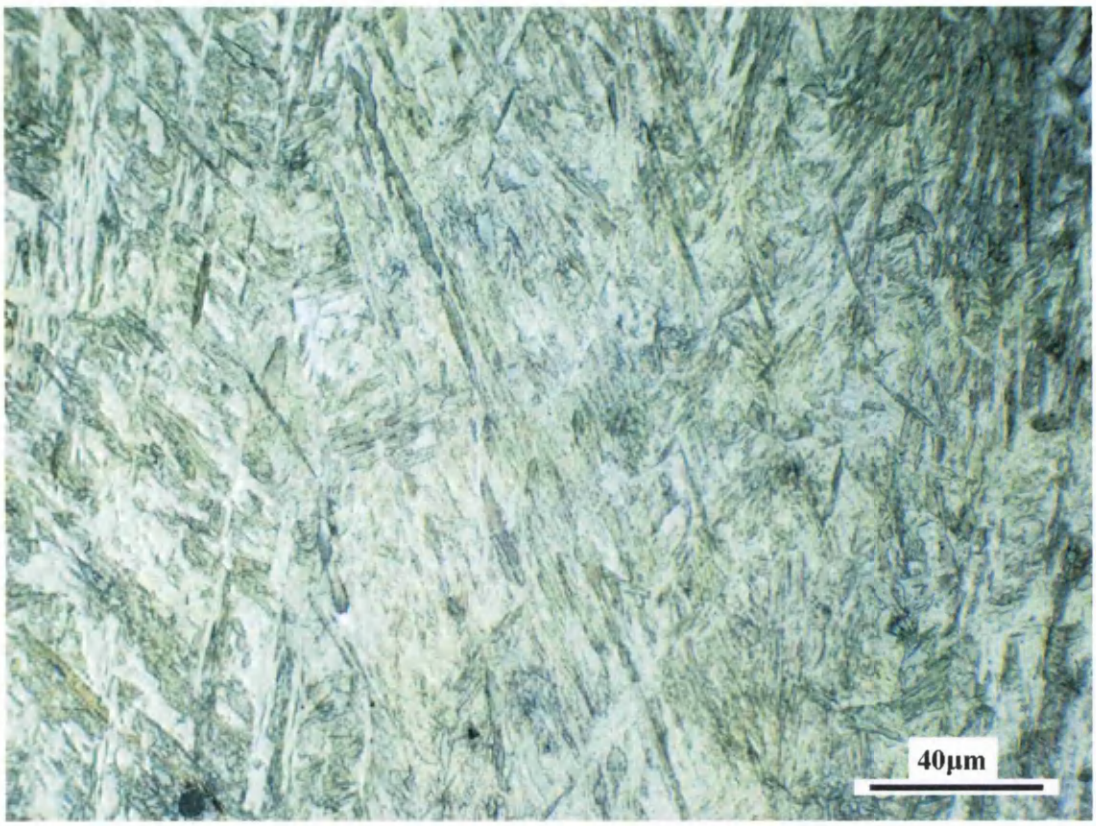

Figure 5.52g Micrograph showing weld nugget microstructure in TRIP800

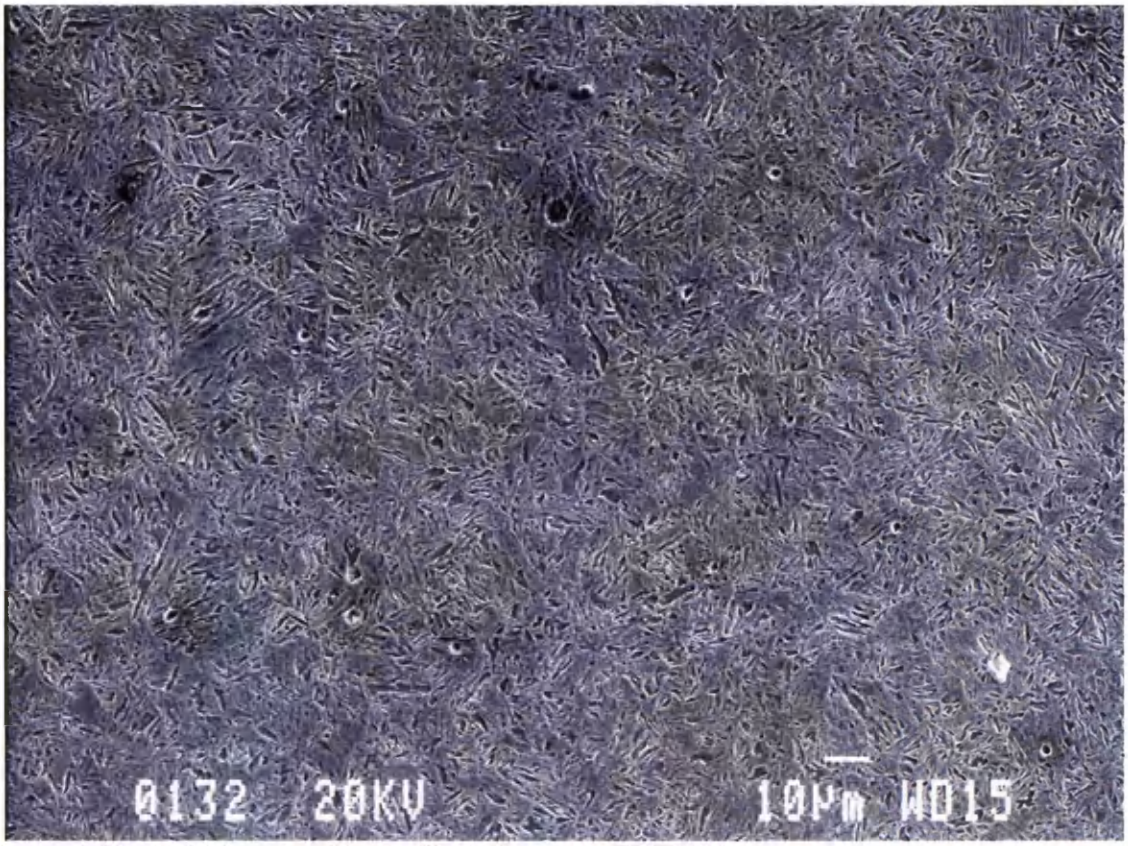

Figure 5.53a SEM image of heat affected zone in TRIP800

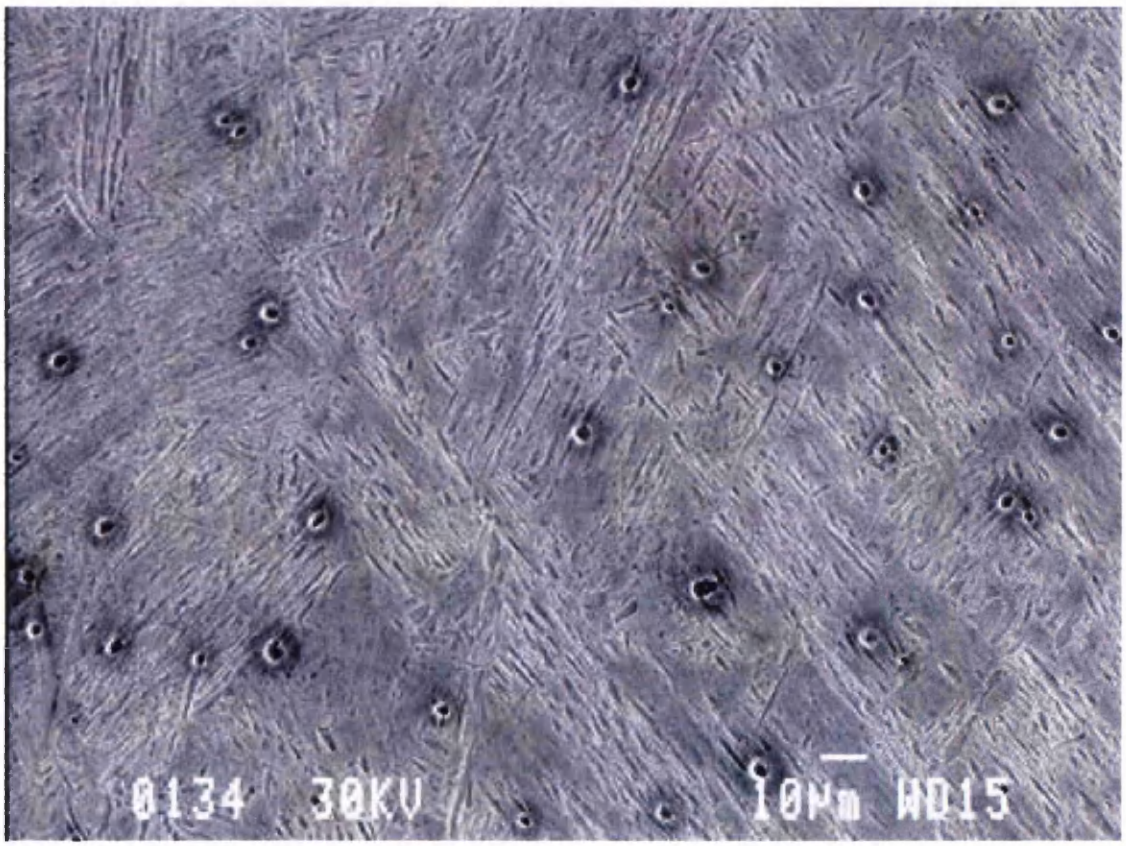

Figure 5.53b SEM image of weld nugget microstructure in TRIP800

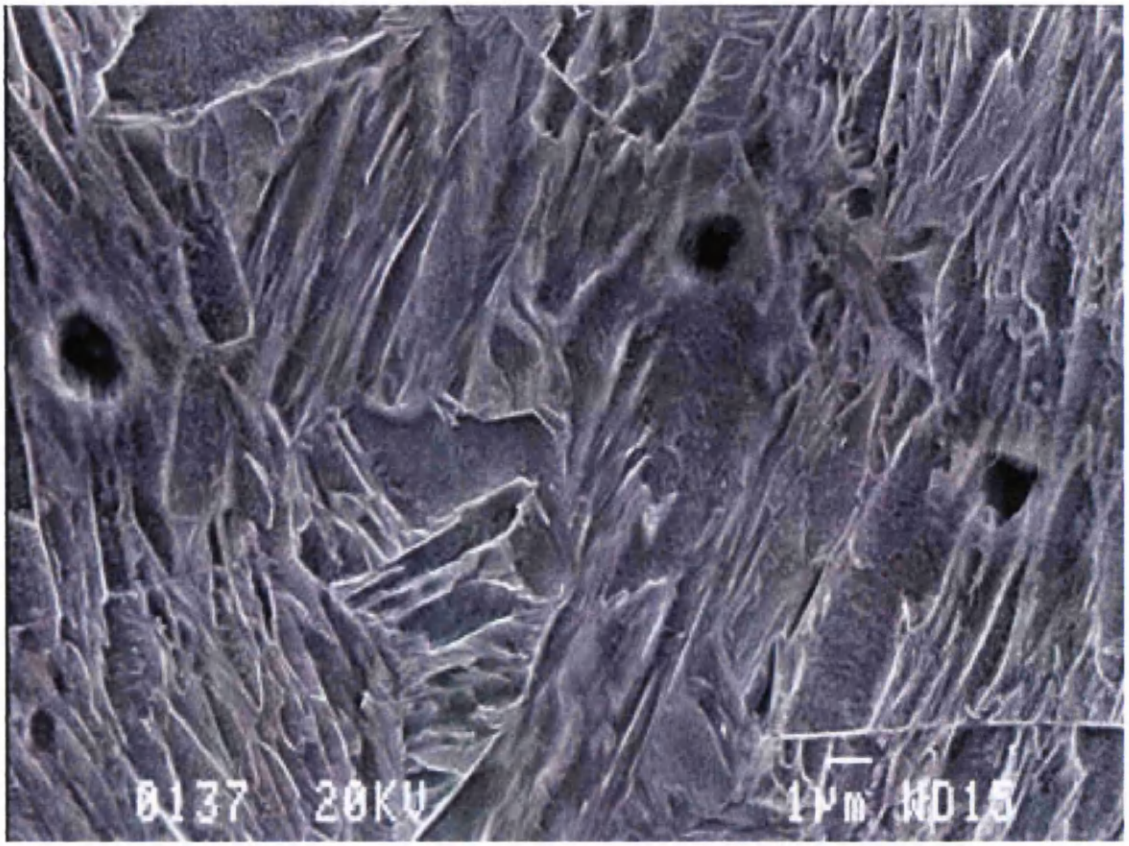

Figure 5.53c Detailed SEM image of weld nugget microstructure in TRIP800

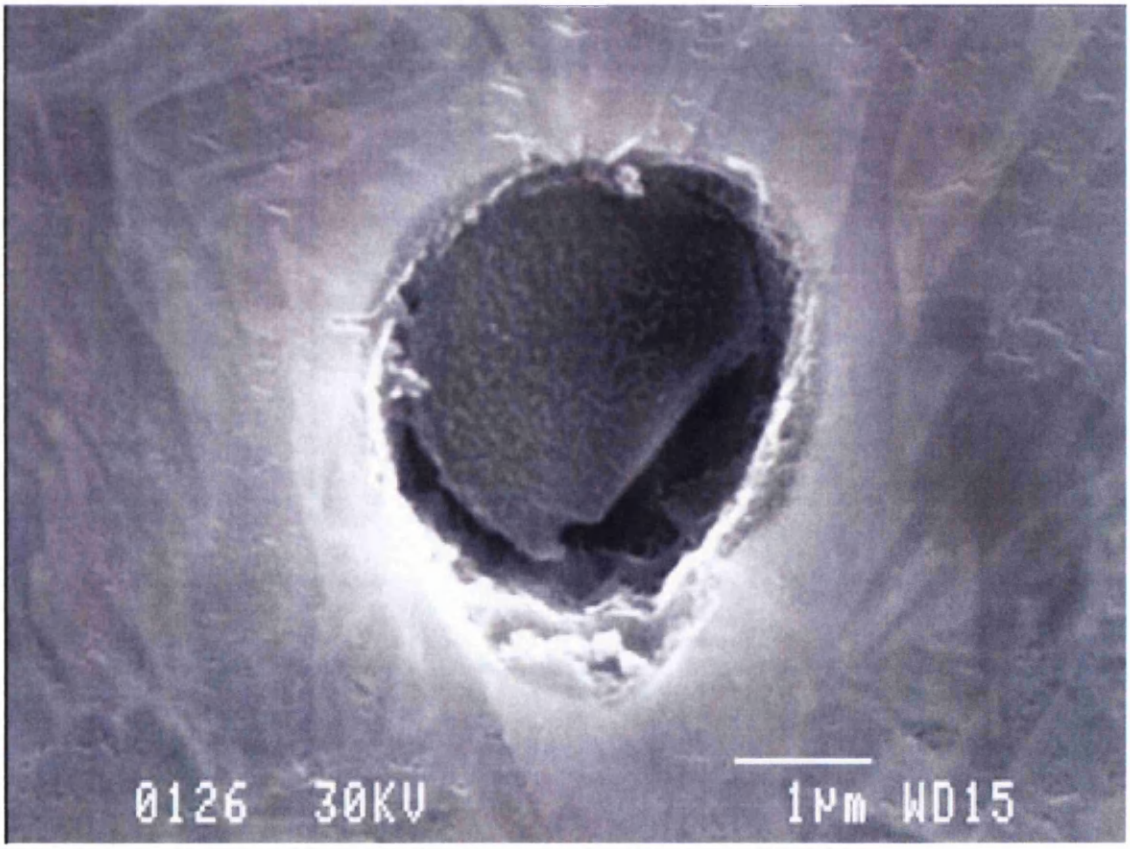

Figure 5.53d High magnification SEM image of inclusion in TRIP800

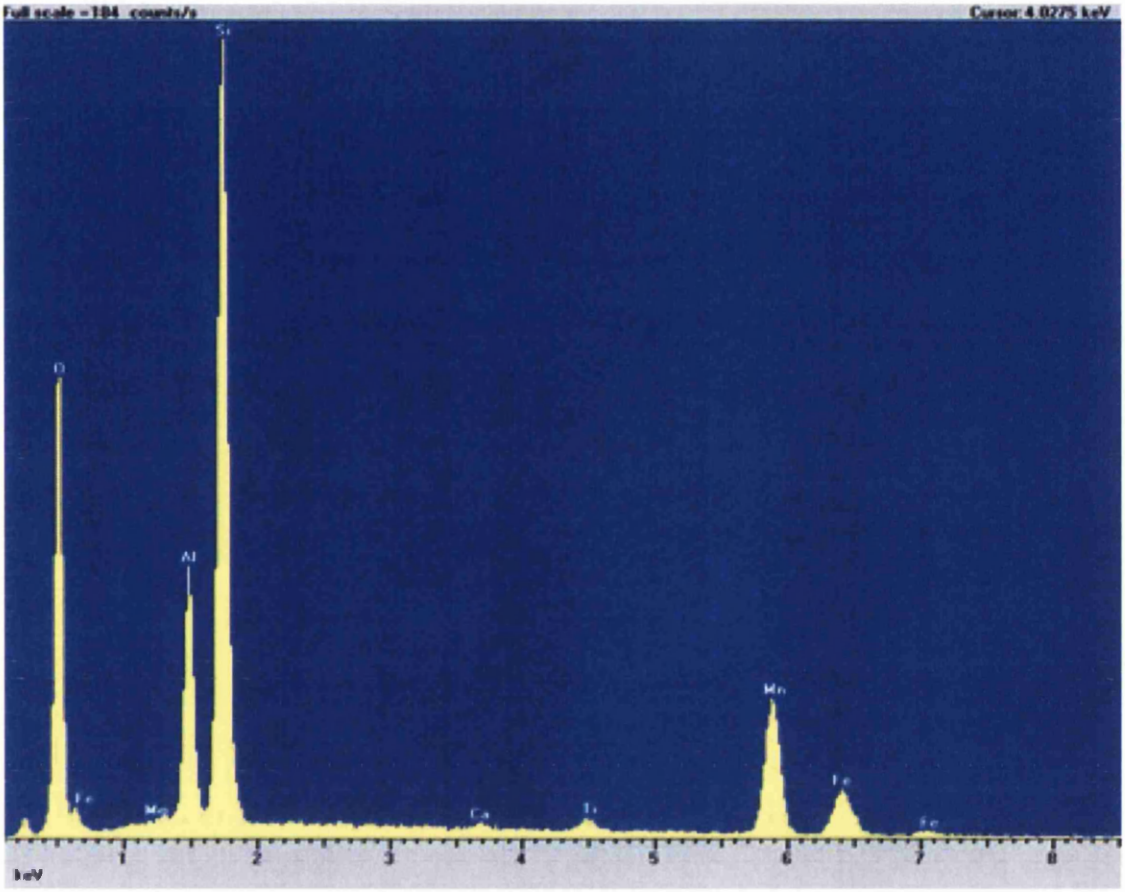

Figure 5.53e EDX spectrum of inclusion shown in figure 5.53d

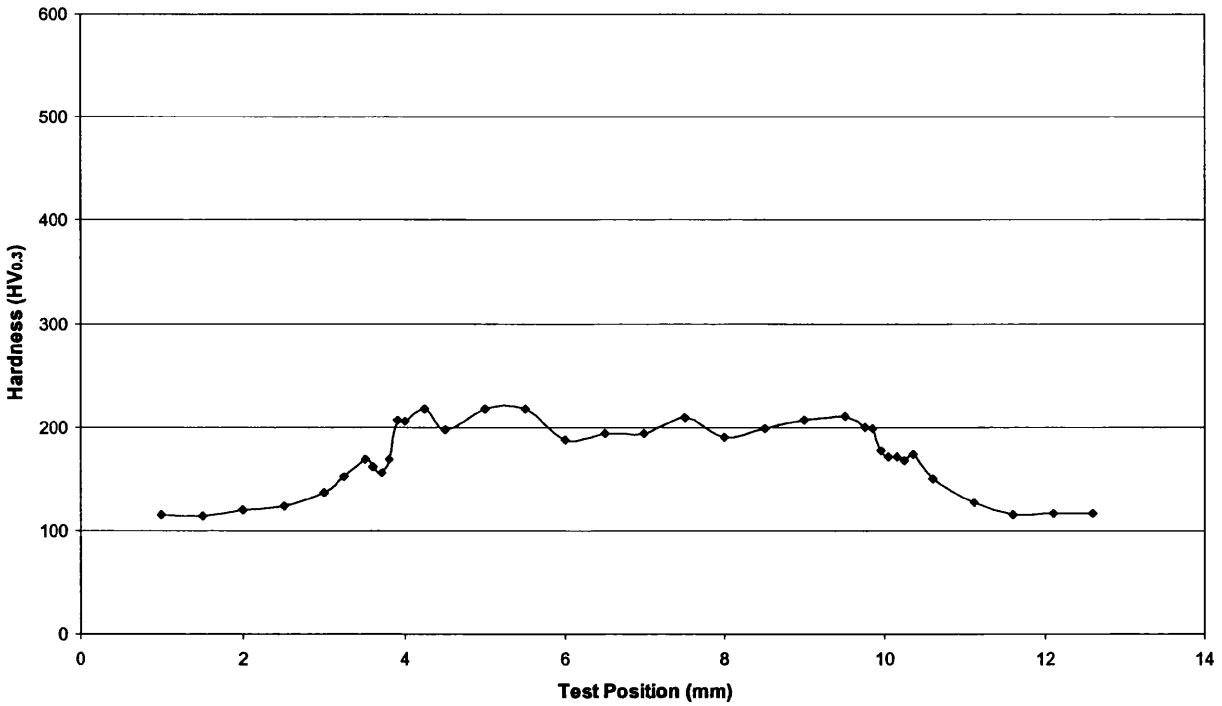

Figure 5.54 Vickers microhardness profile across a $5\sqrt{t}$ weld formed in 1.15mm LC

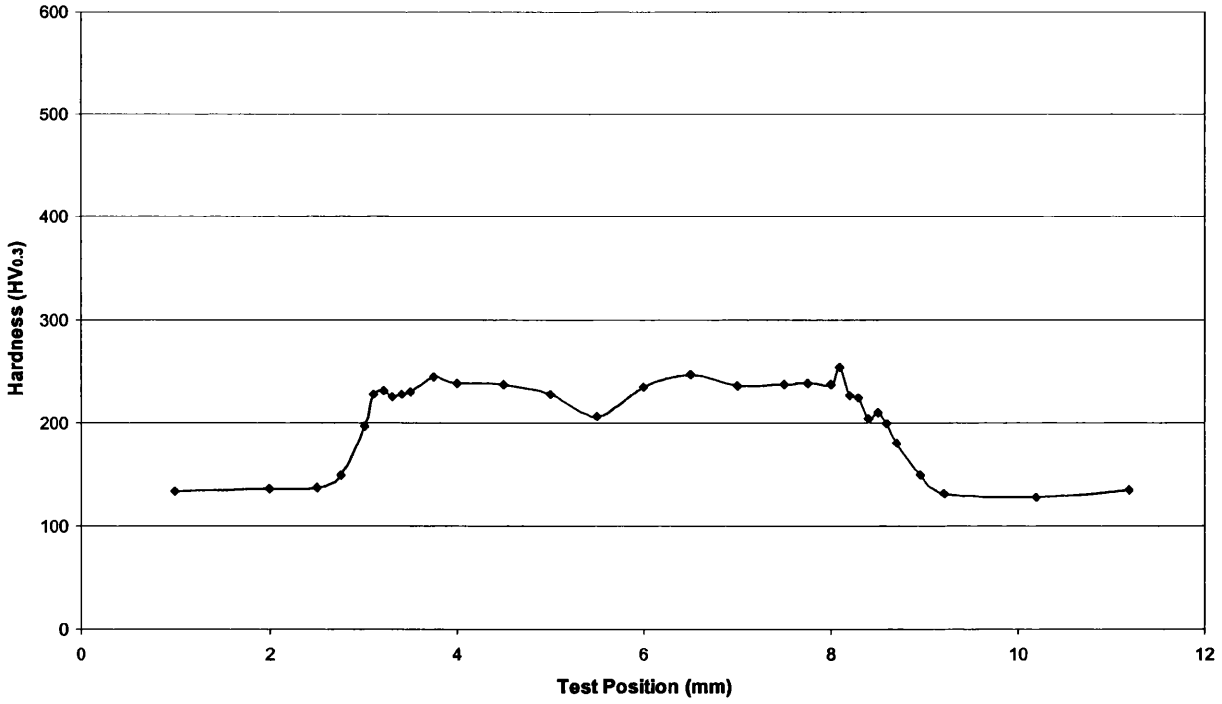

Figure 5.55 Vickers microhardness profile across a $5\sqrt{t}$ weld formed in 1.2mm IF260

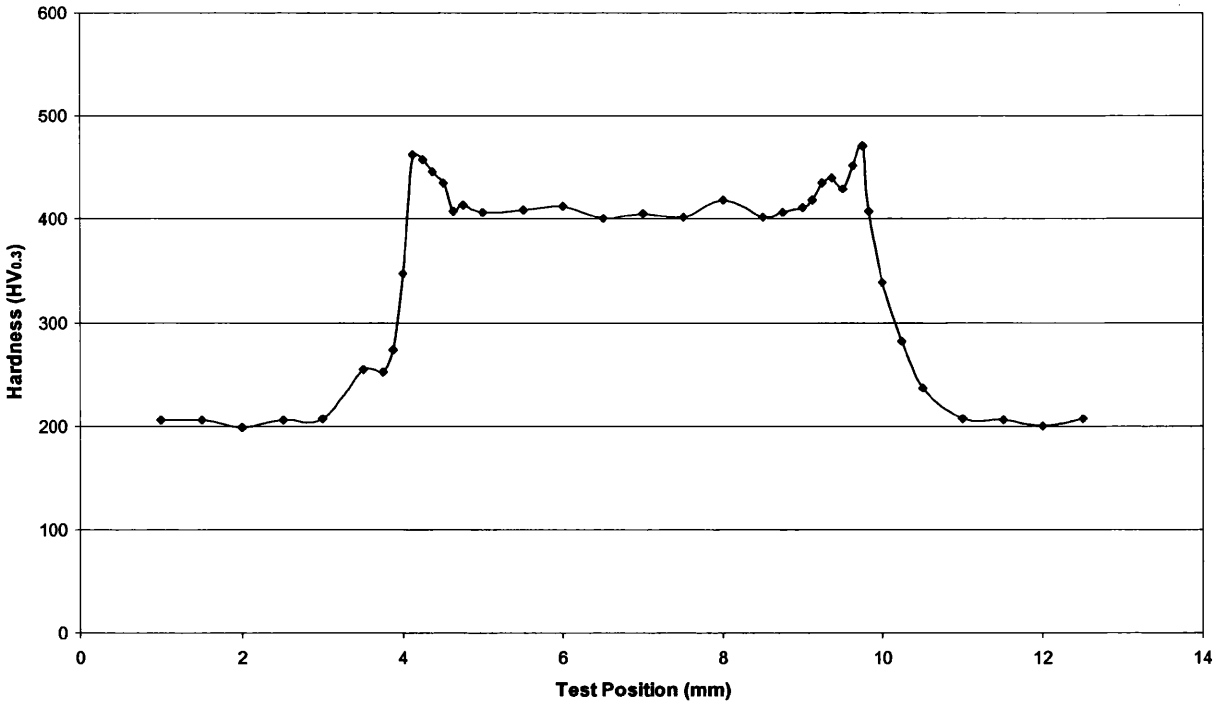

Figure 5.56 Vickers microhardness profile across a $5\sqrt{t}$ weld formed in 1.0mm TRIP600

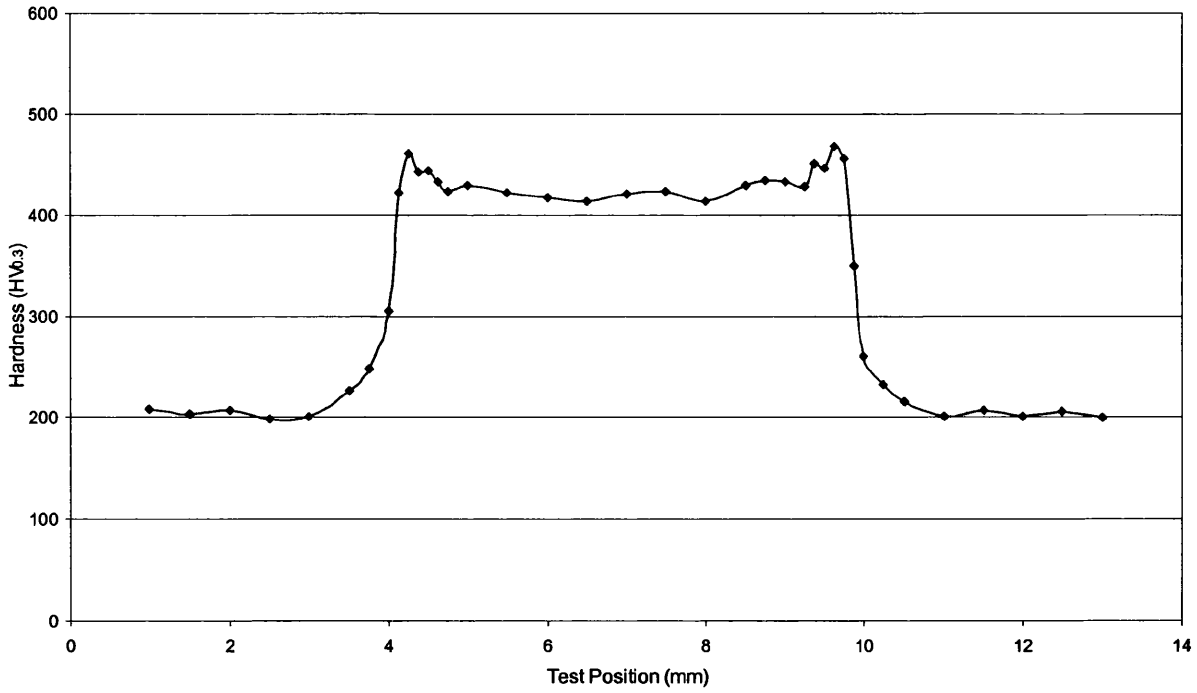

Figure 5.57 Vickers microhardness profile across a $5\sqrt{t}$ weld formed in 1.2mm DP600

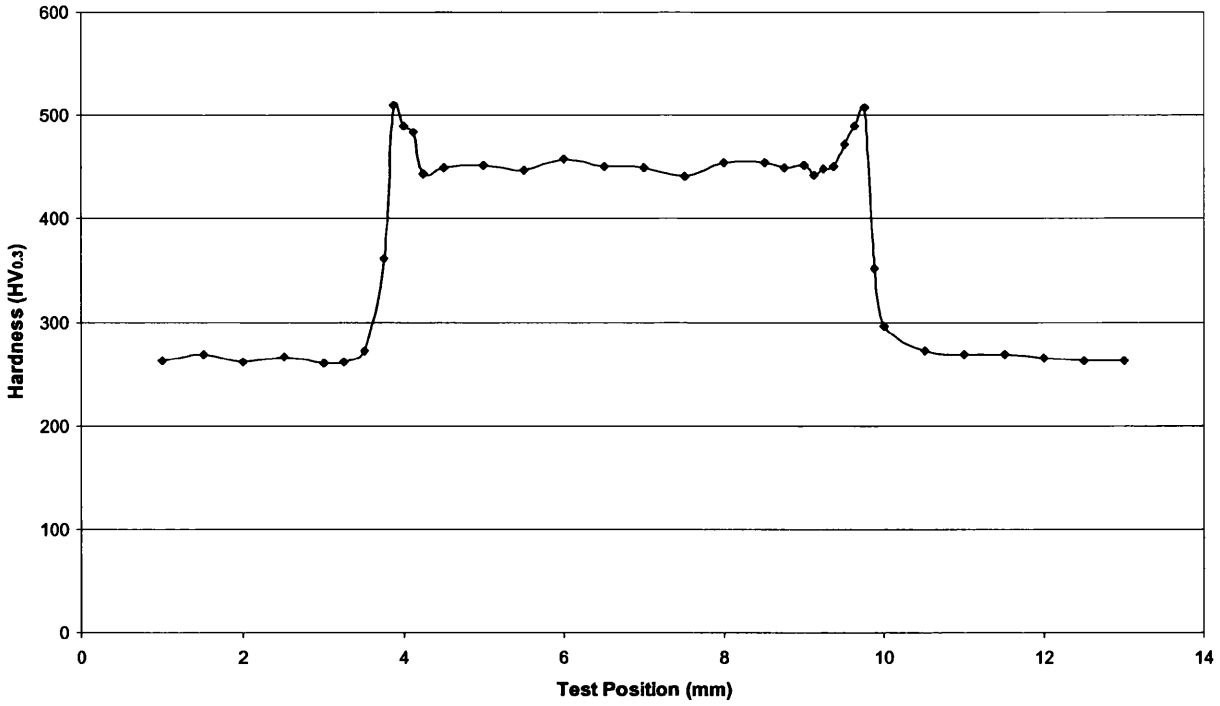

Figure 5.58 Vickers microhardness profile across a $5\sqrt{t}$ weld formed in 1.2mm DP800

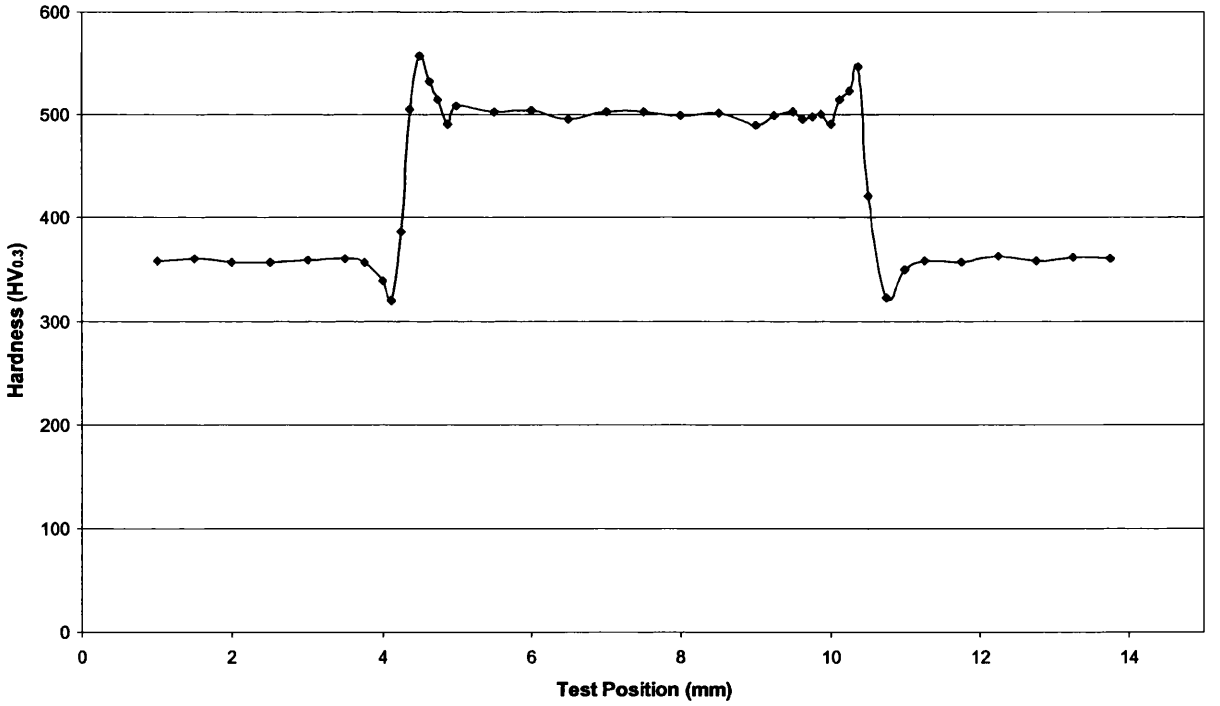

Figure 5.59 Vickers microhardness profile across a $5\sqrt{t}$ weld formed in 1.2mm DP1000

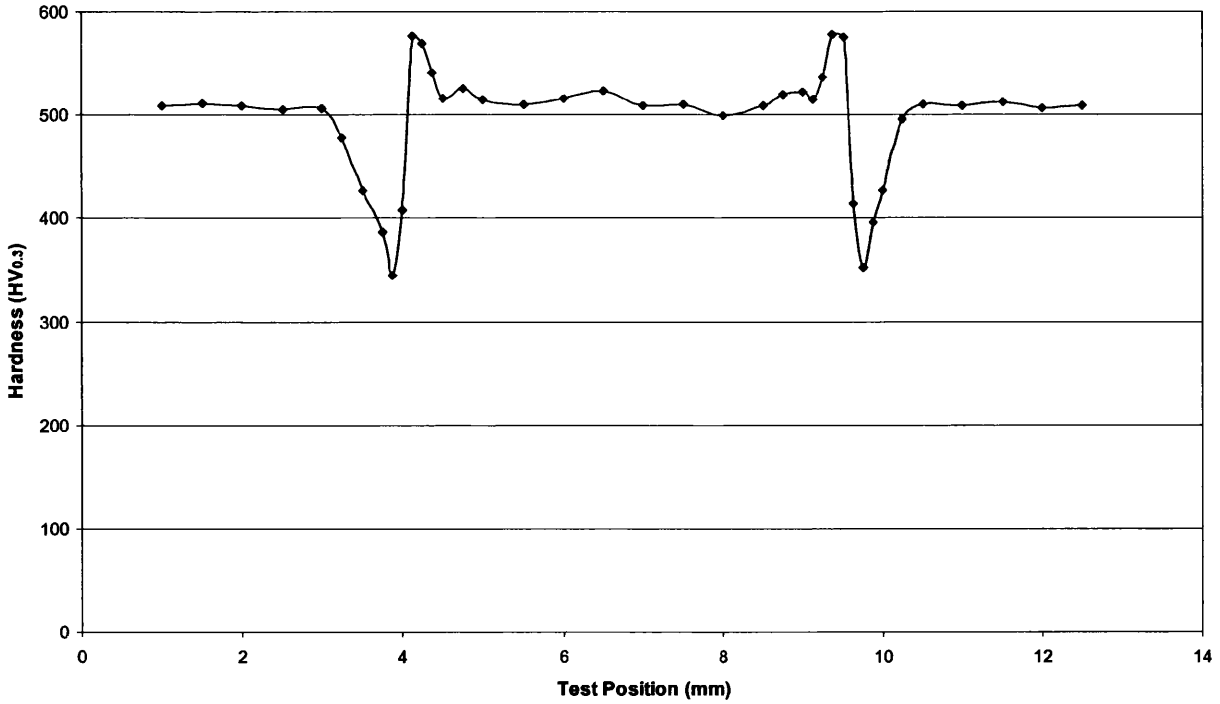

Figure 5.60 Vickers microhardness profile across a $5\sqrt{t}$ weld formed in 1.0mm MS1400

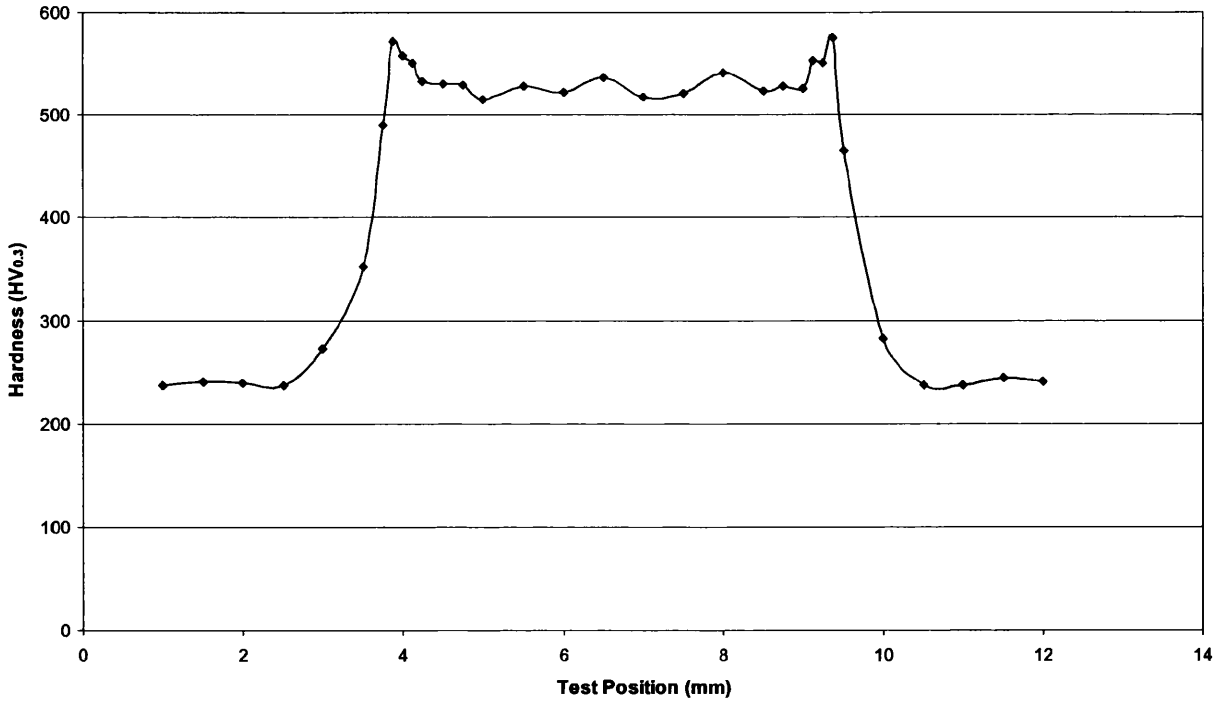

Figure 5.61 Vickers microhardness profile across a $5\sqrt{t}$ weld formed in 1.2mm TRIP800

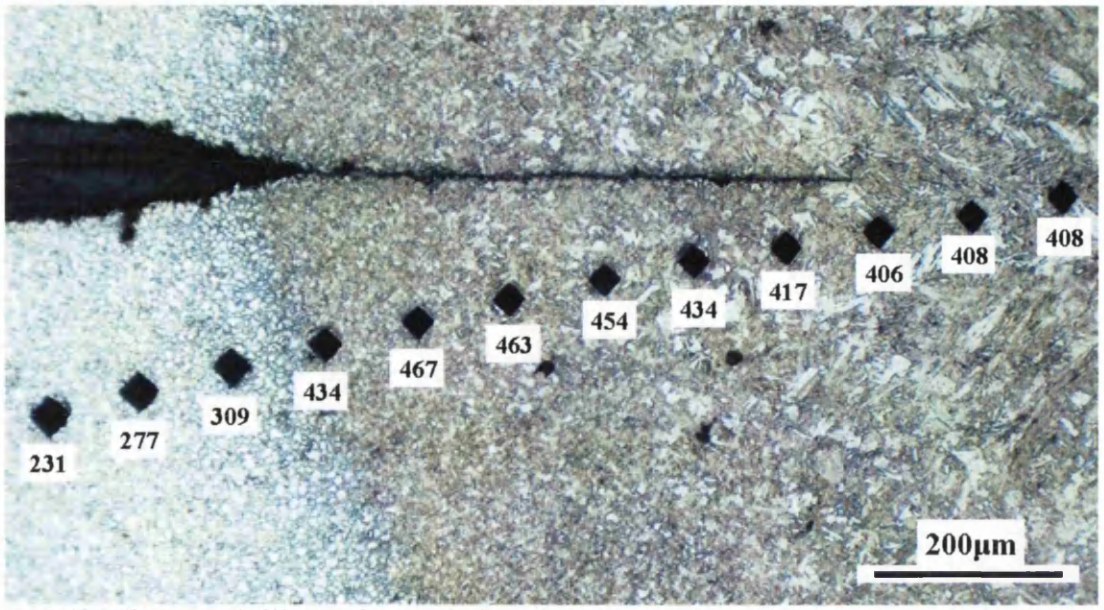

Figure 5.62 Micrograph illustrating variations in microhardness ($HV_{0.3}$) through the heat affected zone of a TRIP600 spot weld

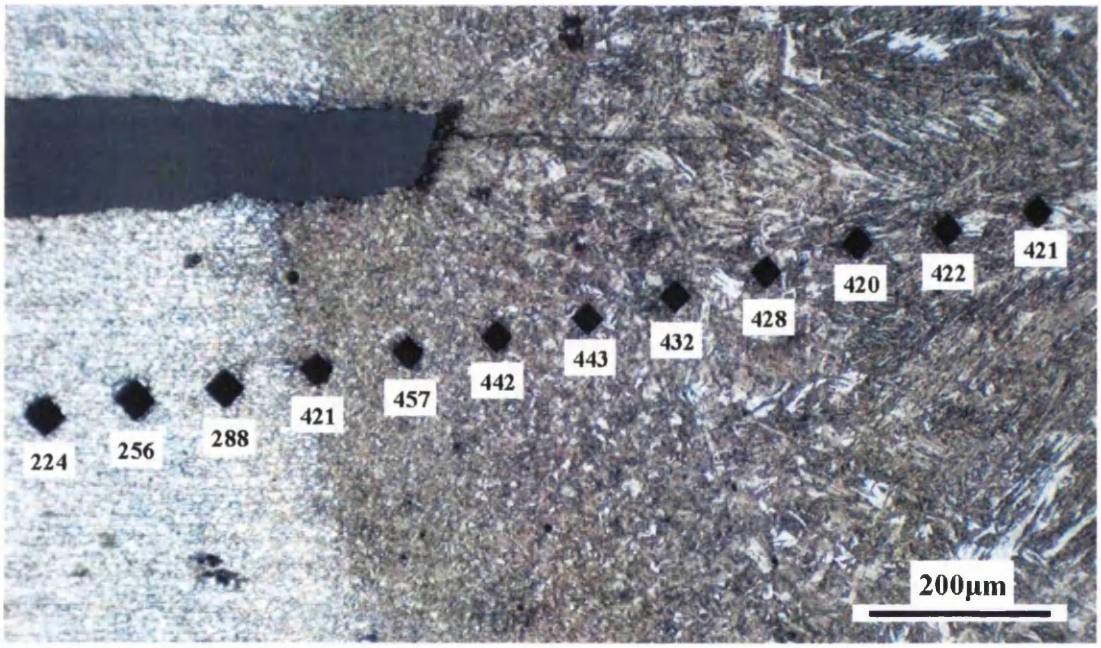

Figure 5.63 Micrograph illustrating variations in microhardness ($HV_{0.3}$) through the heat affected zone of a DP600 spot weld

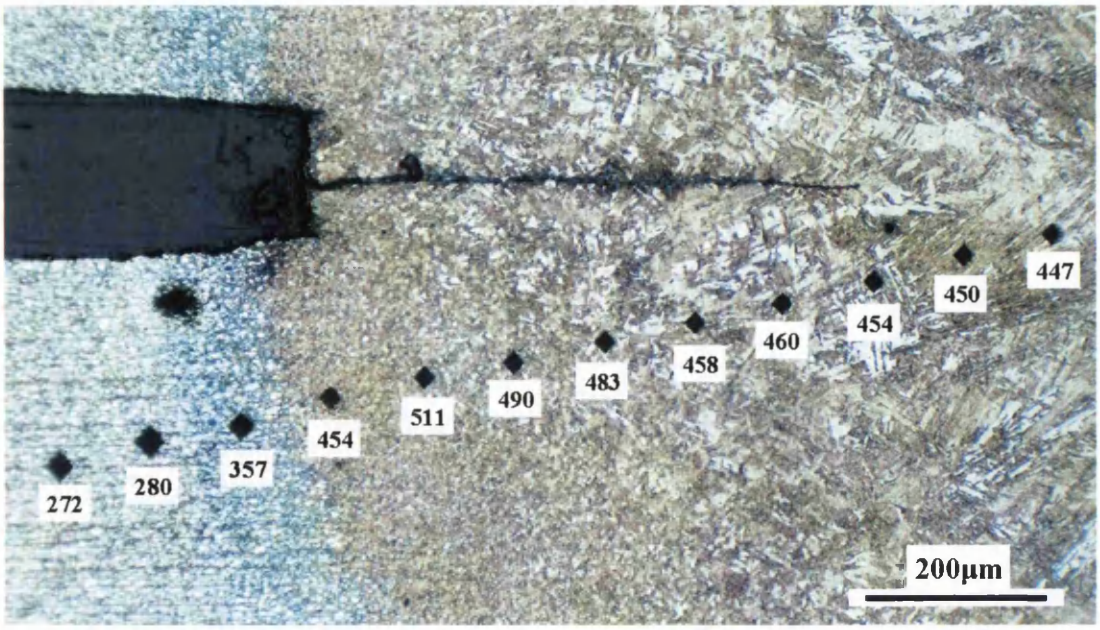

Figure 5.64 Micrograph illustrating variations in microhardness ($HV_{0.3}$) through the heat affected zone of a DP800 spot weld

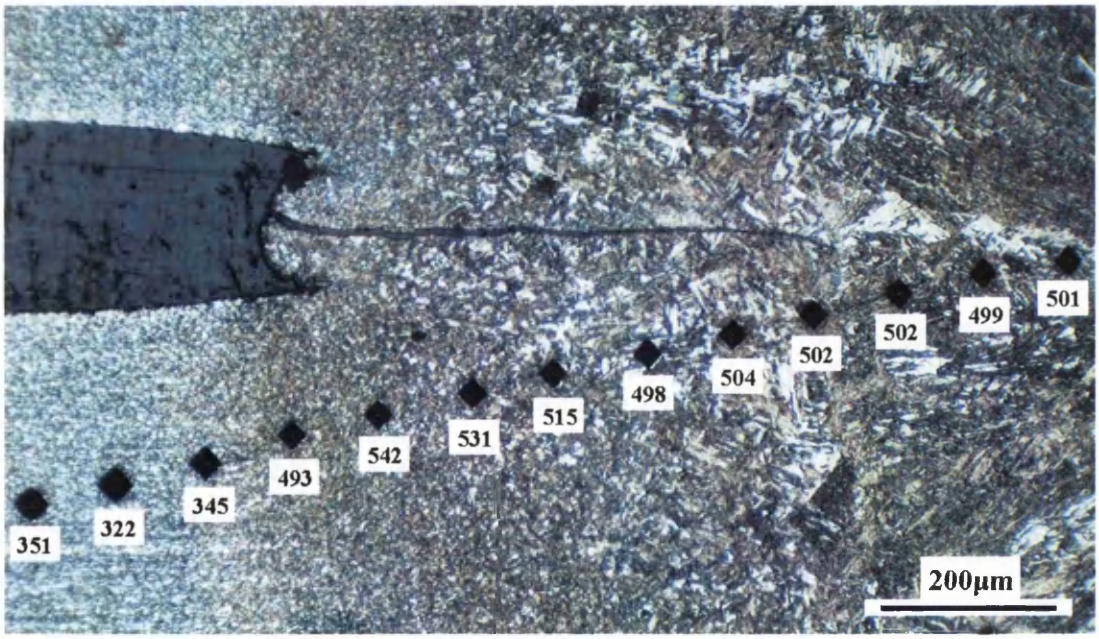

Figure 5.65 Micrograph illustrating variations in microhardness ($HV_{0.3}$) through the heat affected zone of a DP1000 spot weld

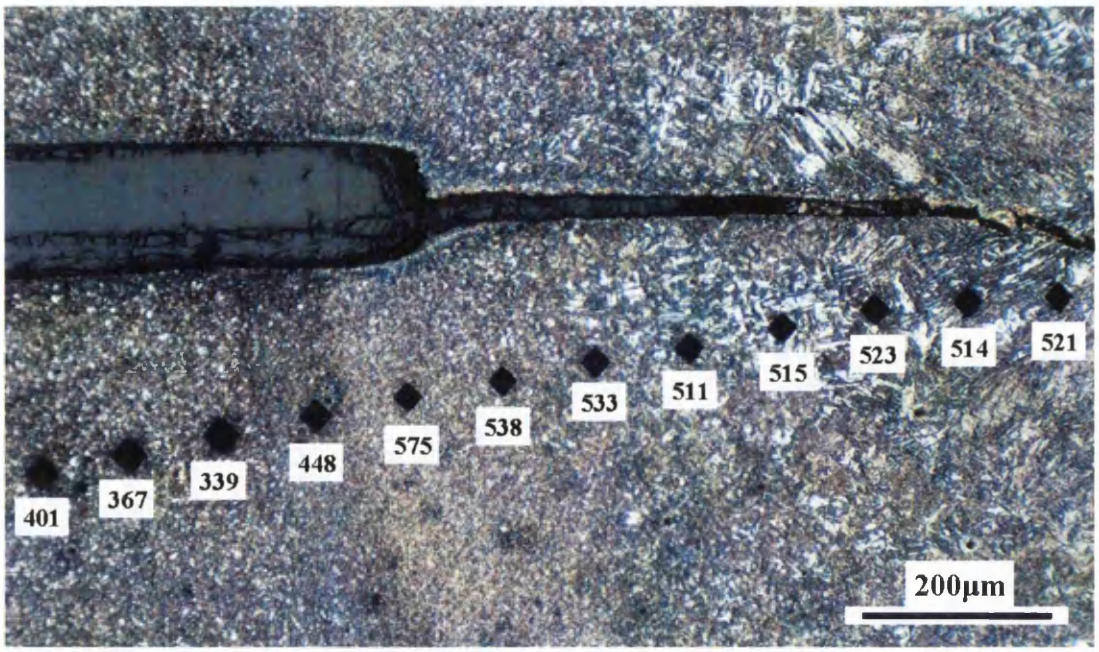

Figure 5.66 Micrograph illustrating variations in microhardness ($HV_{0.3}$) through the heat affected zone of a MS1400 spot weld

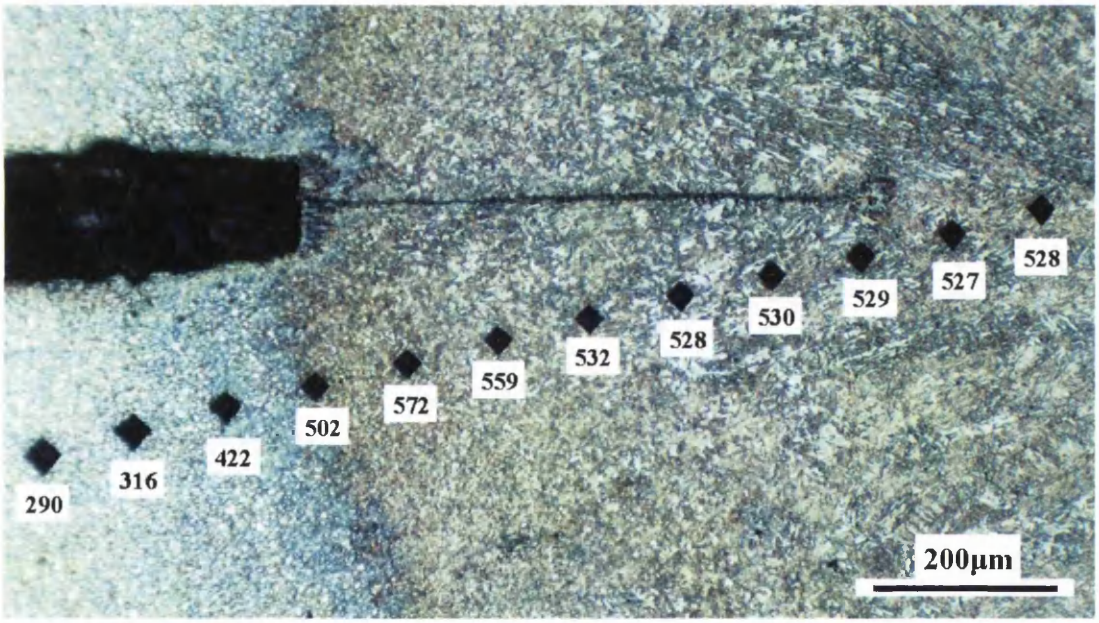

Figure 5.67 Micrograph illustrating variations in microhardness ($HV_{0.3}$) through the heat affected zone of a TRIP800 spot weld

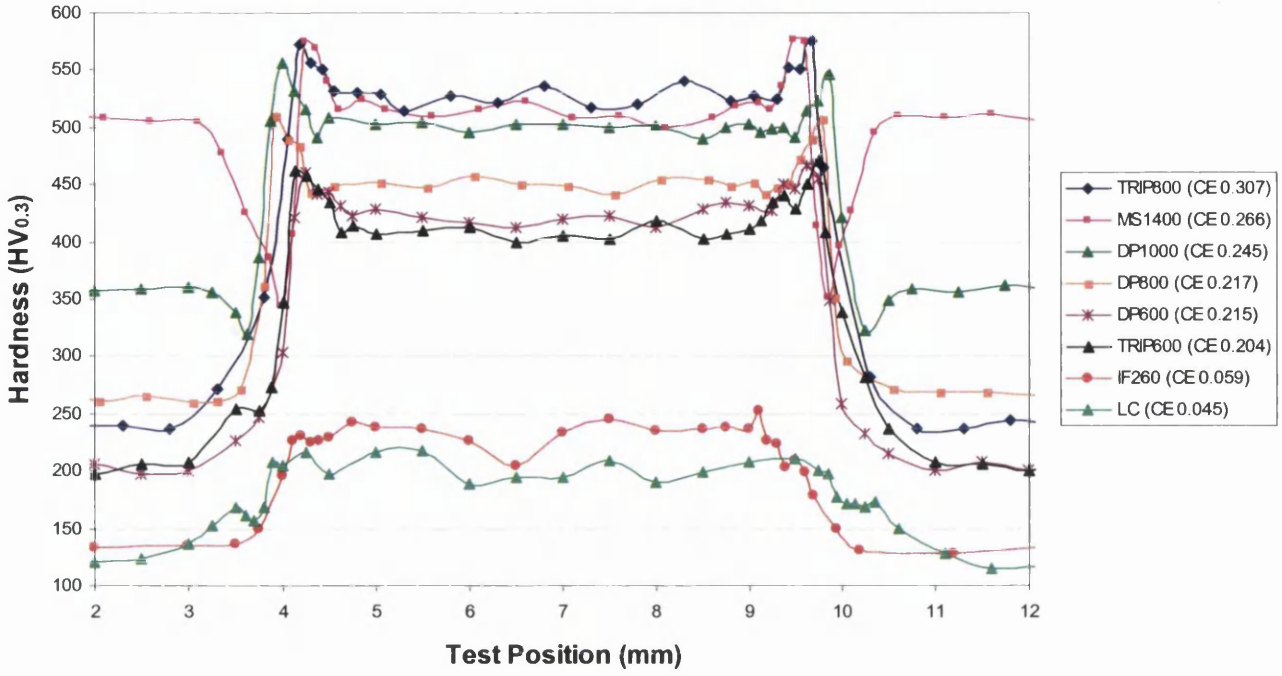

Figure 5.68 Microhardness profiles across $5\sqrt{t}$ welds formed in all eight steels investigated illustrating effect of increasing carbon equivalent on weld microhardness

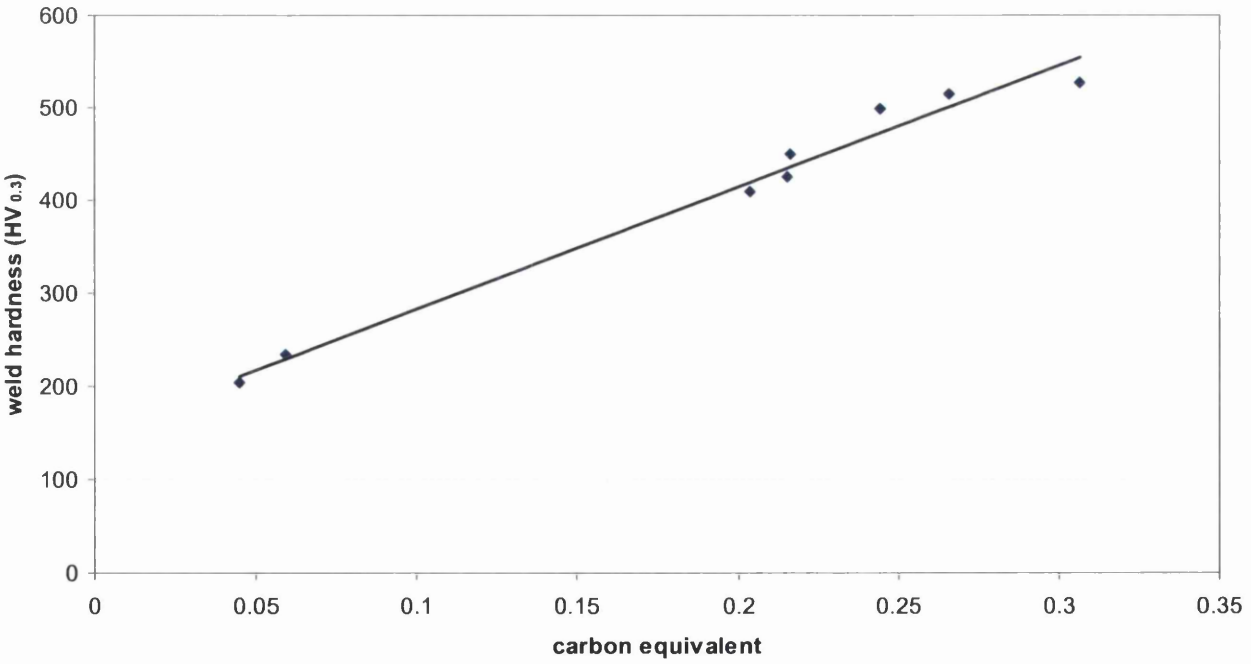

Figure 5.69 Graph illustrating the relationship between carbon equivalent and average weld nugget microhardness

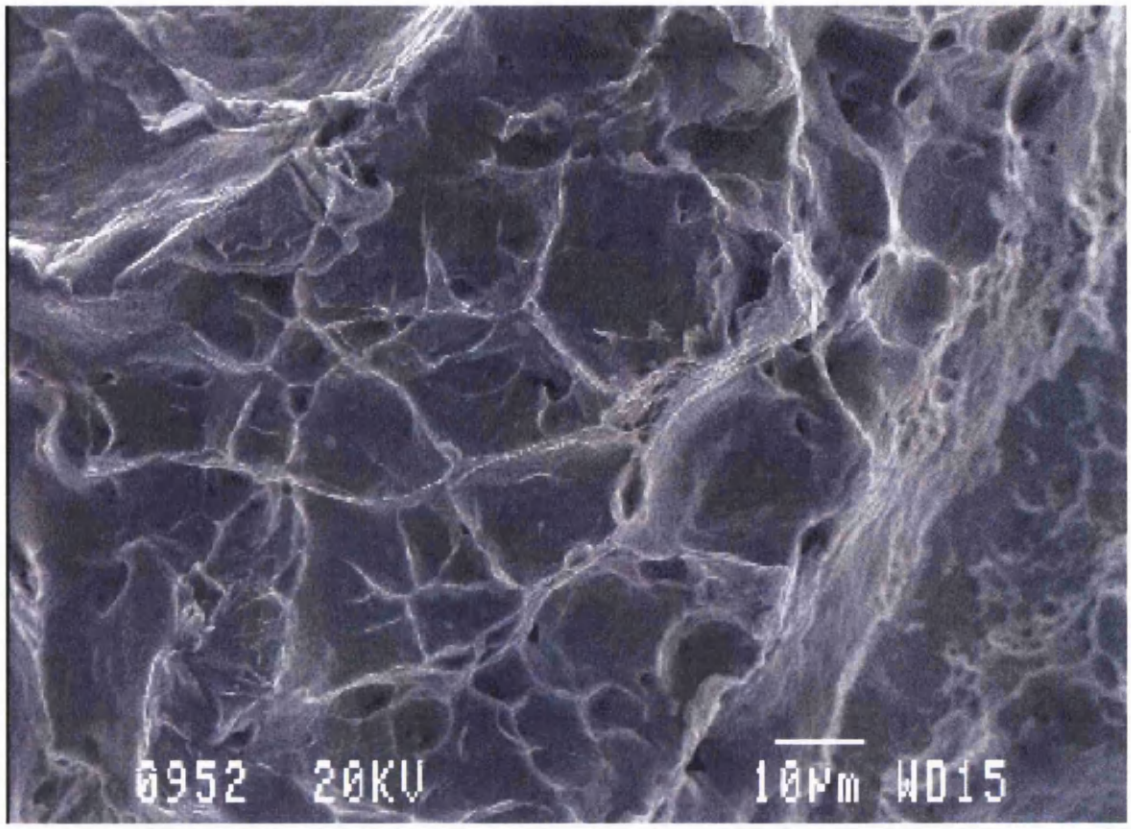

Figure 5.70a SEM image of dimple rupture occurring in an interfacially failed LC spot weld

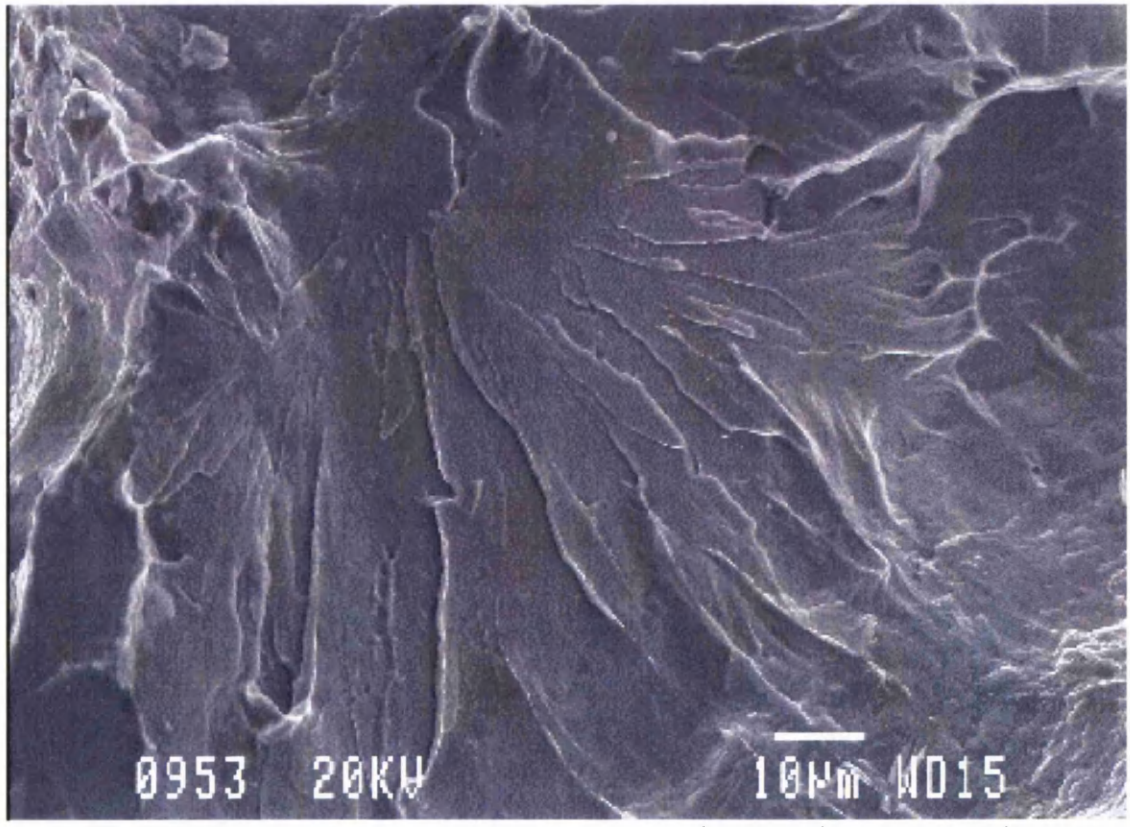

Figure 5.70b SEM image of trans-granular fracture occurring in an interfacially failed LC spot weld

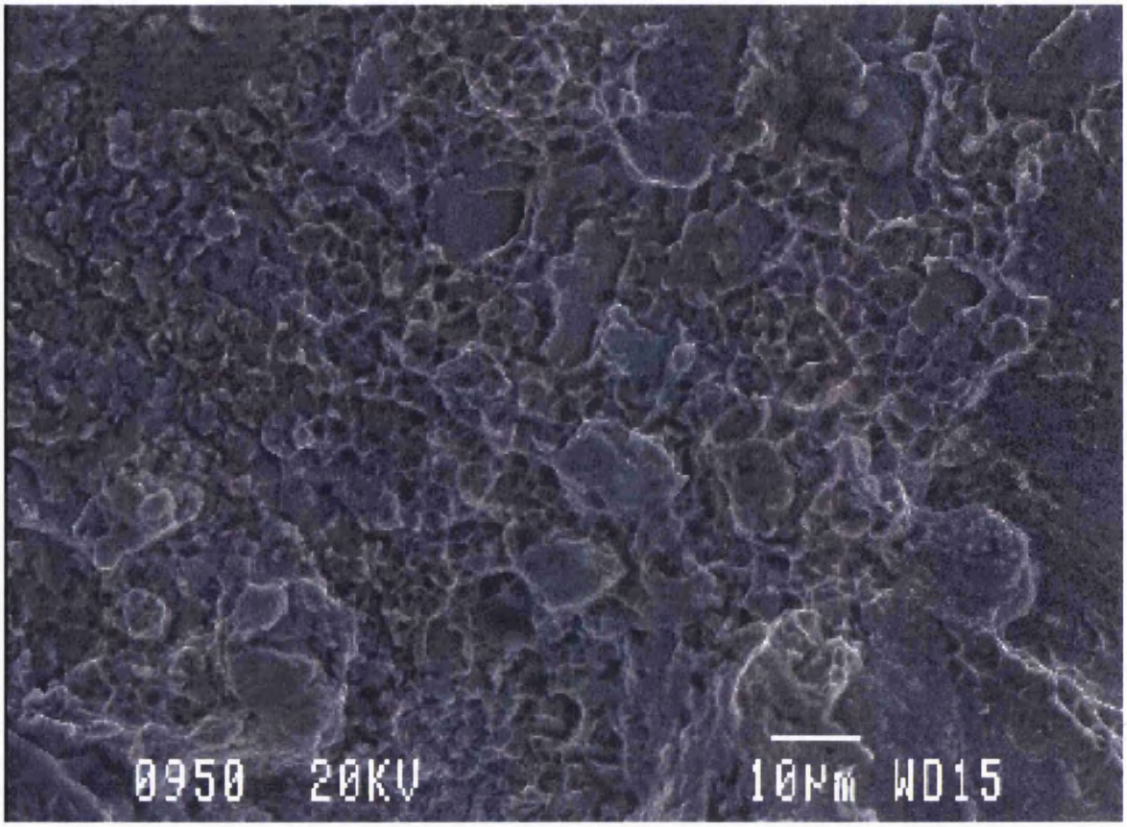

Figure 5.71a SEM image of dimple rupture occurring in an interfacially failed IF260 spot weld

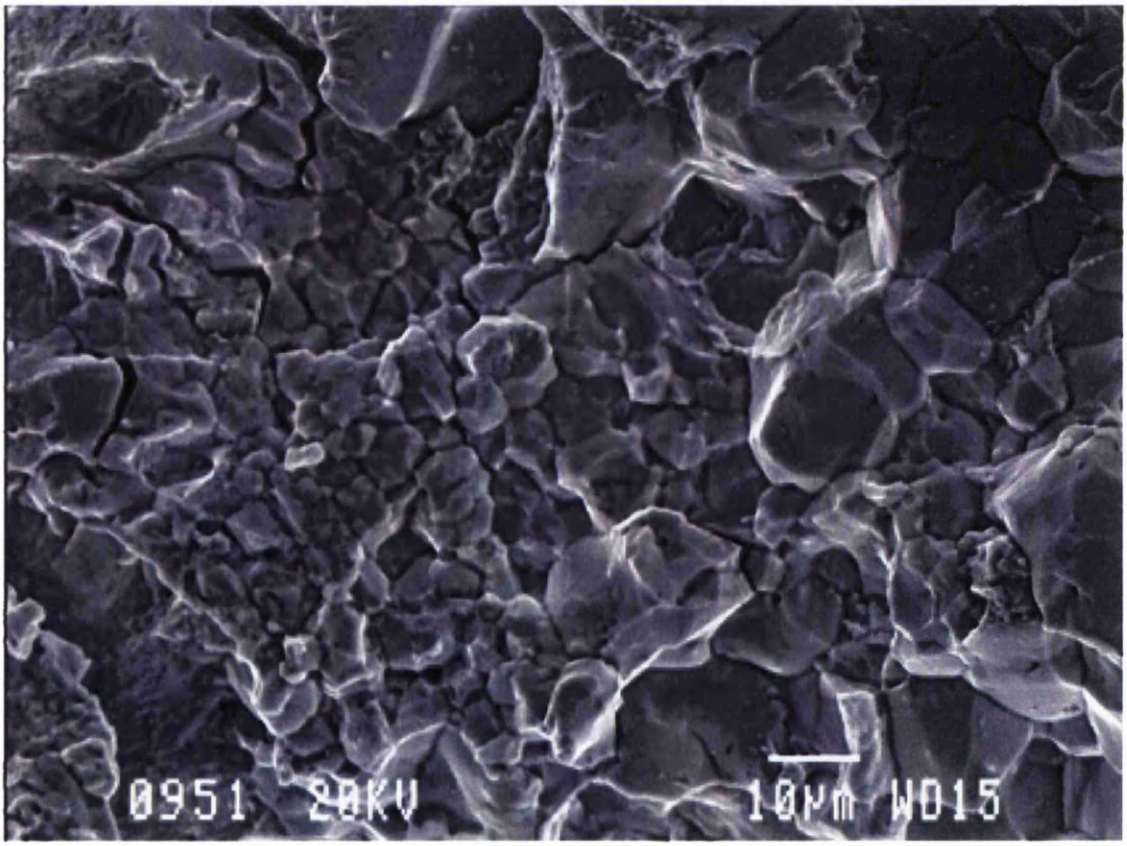

Figure 5.71b SEM image of inter-granular fracture occurring in an interfacially failed IF260 spot weld

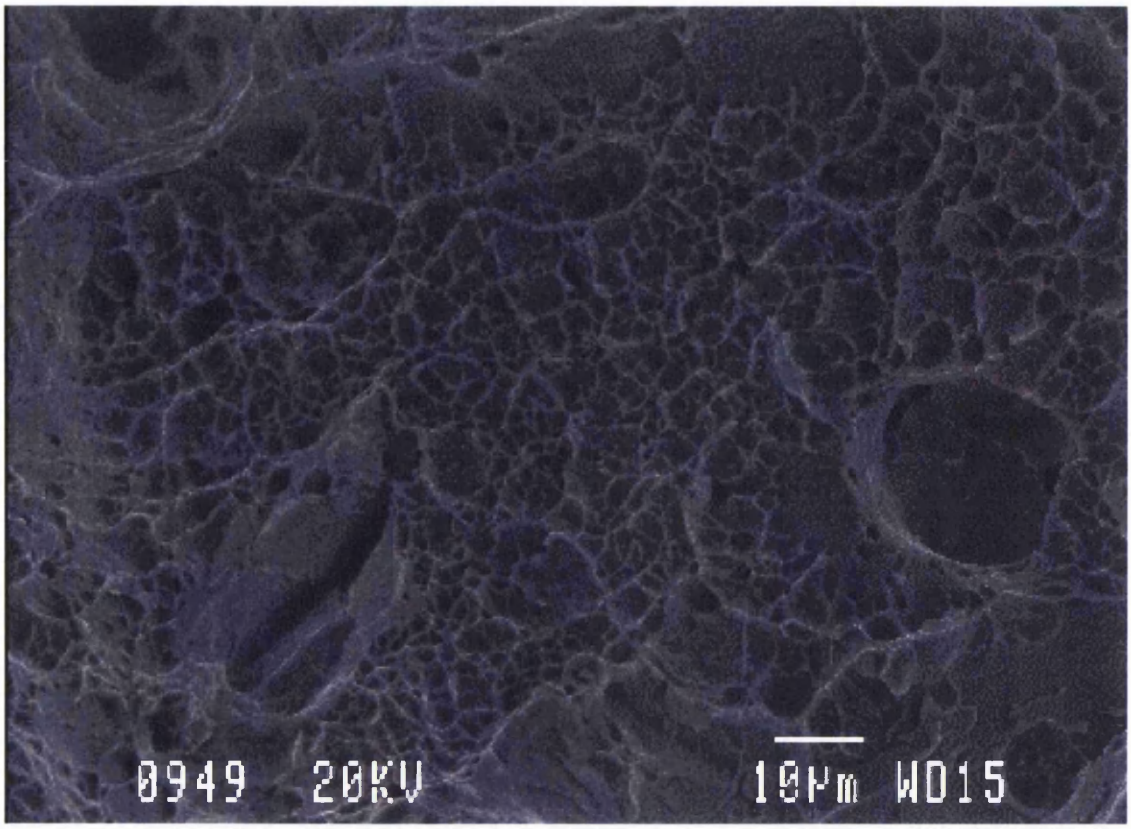

Figure 5.72a SEM image of dimple rupture occurring in an interfacially failed TRIP600 spot weld

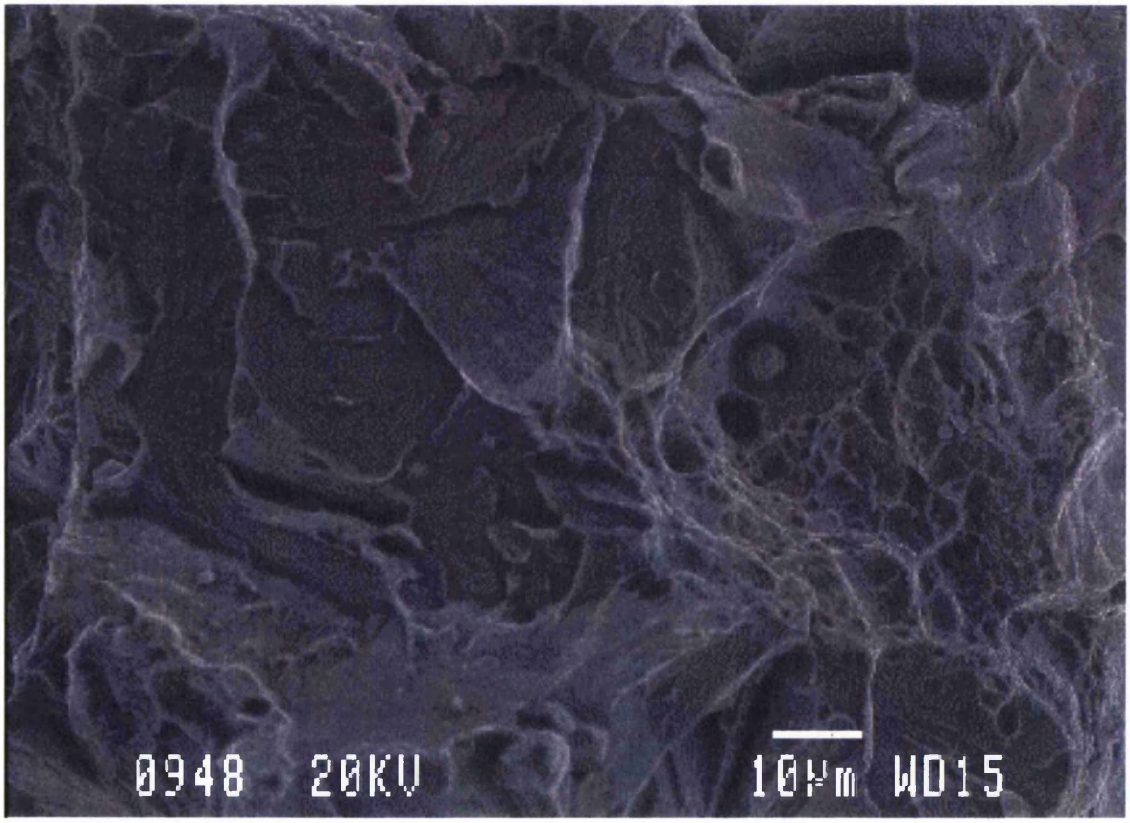

Figure 5.72b SEM image of dimple rupture and trans-granular fracture occurring in an interfacially failed TRIP600 spot weld

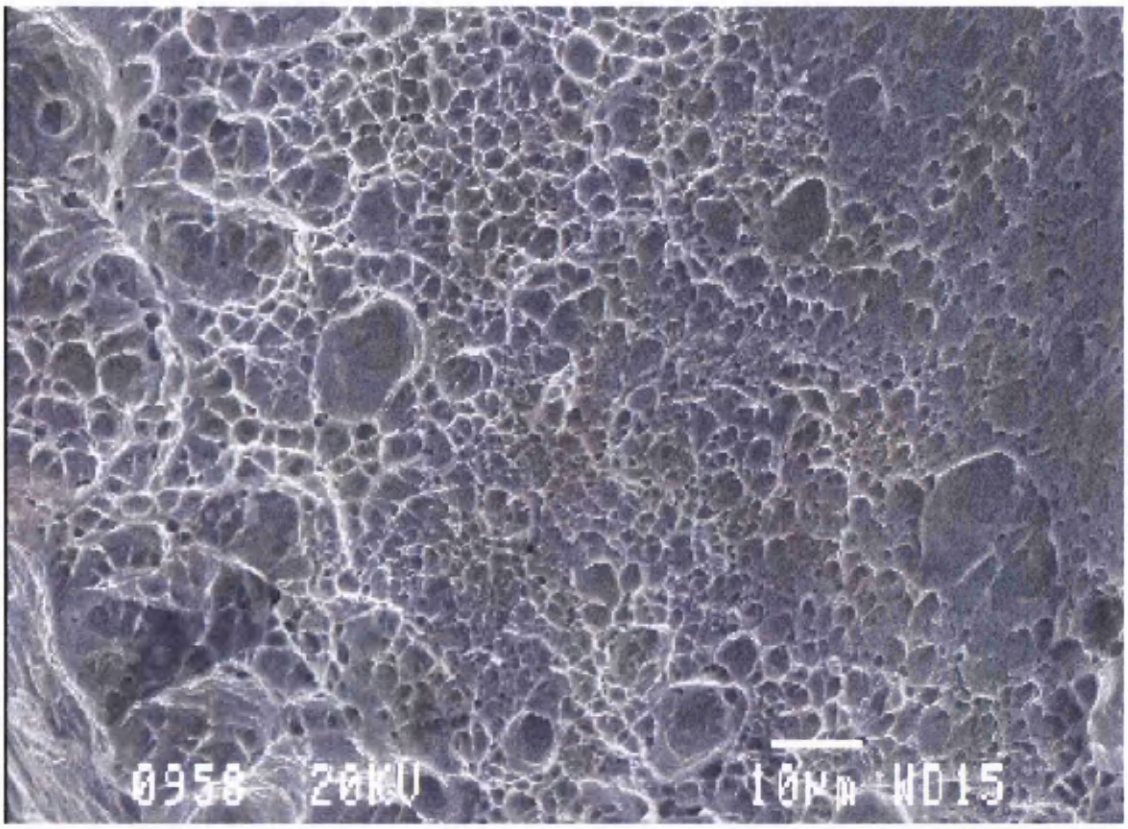

Figure 5.73a SEM image of dimple rupture occurring in an interfacially failed DP600 spot weld

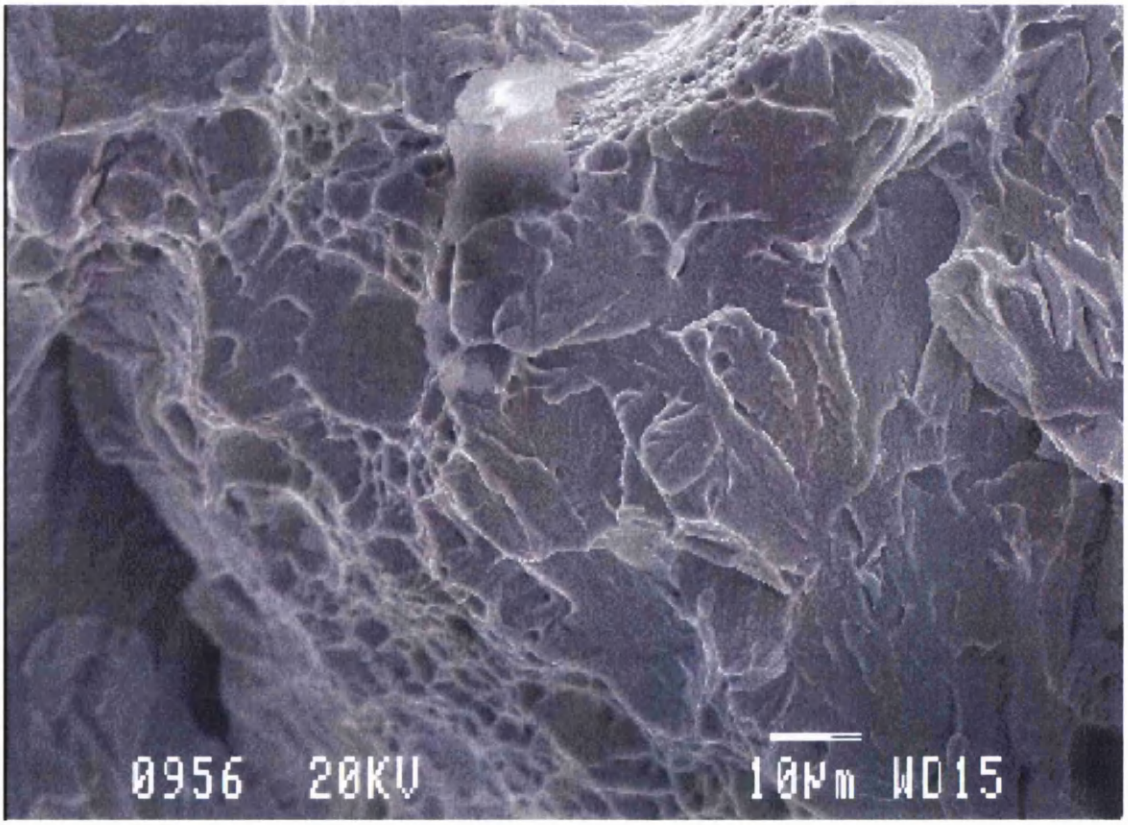

Figure 5.73b SEM image of dimple rupture and trans-granular fracture occurring in an interfacially failed DP600 spot weld

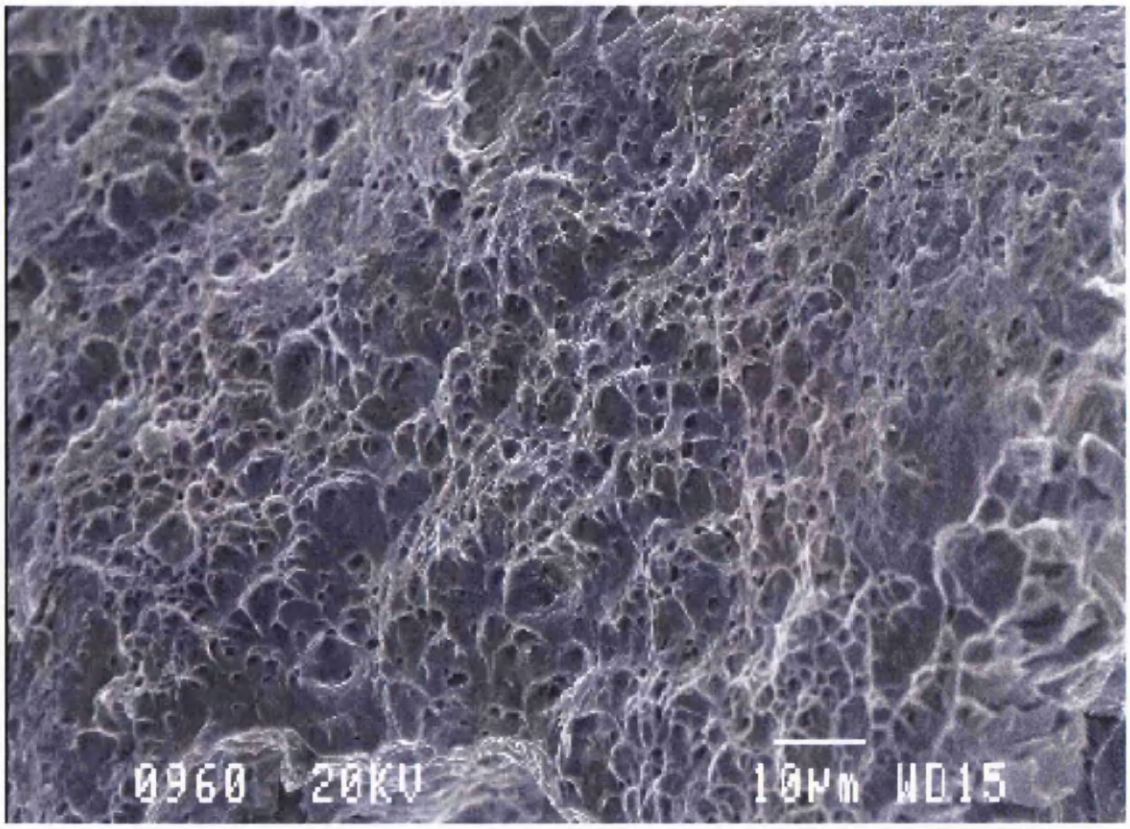

Figure 5.74a SEM image of dimple rupture occurring in an interfacially failed DP800 spot weld

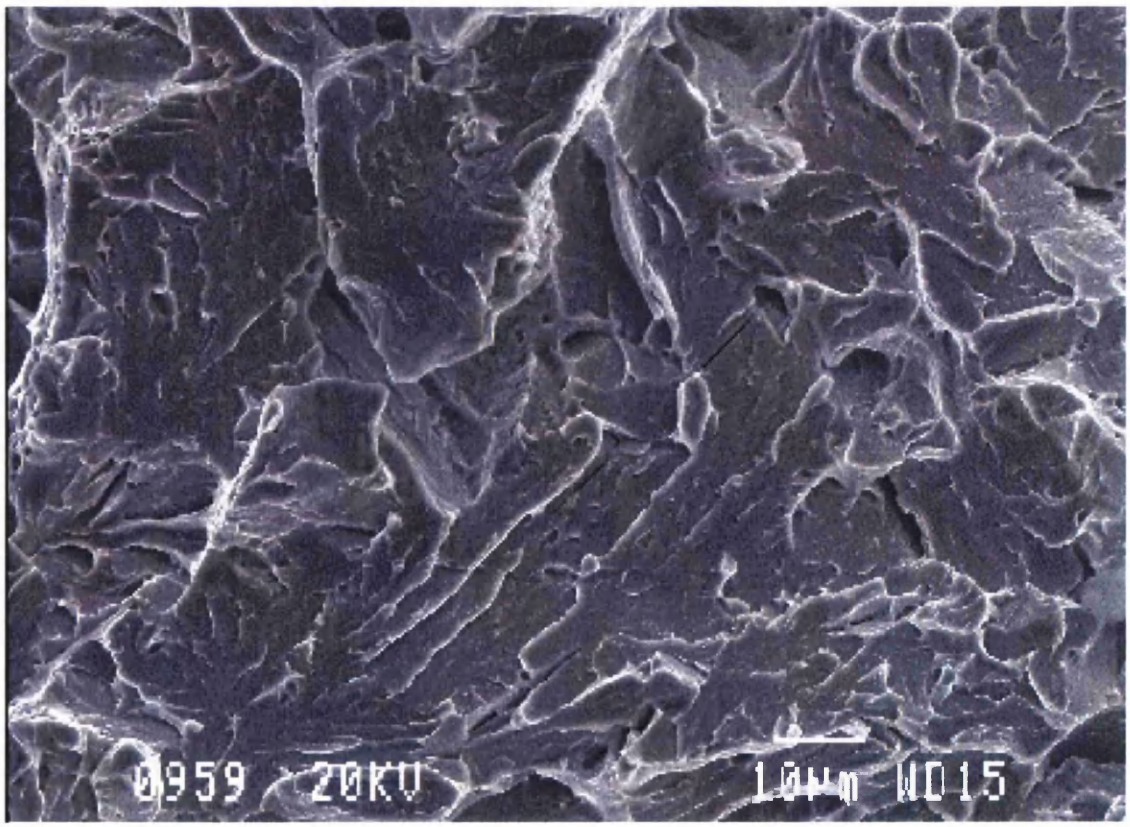

Figure 5.74b SEM image of trans-granular fracture occurring in an interfacially failed DP800 spot weld

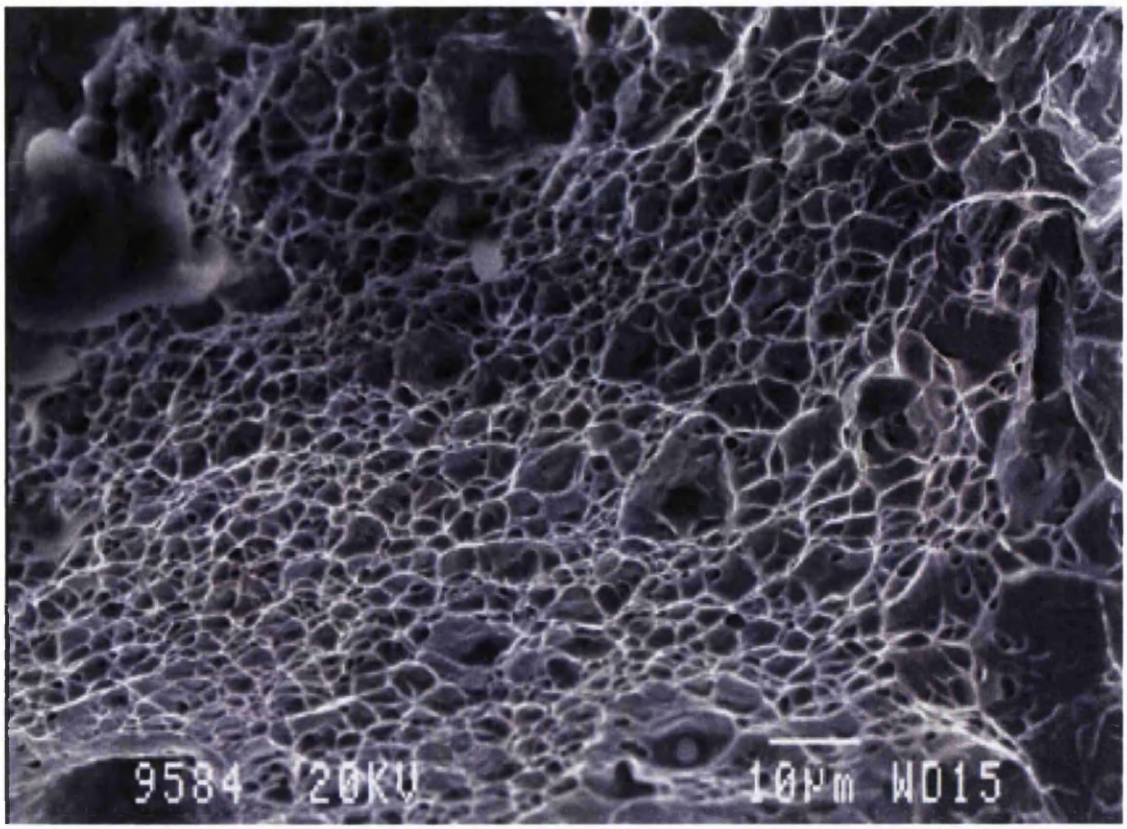

Figure 5.75a SEM image of dimple rupture occurring in an interfacially failed DP1000 spot weld

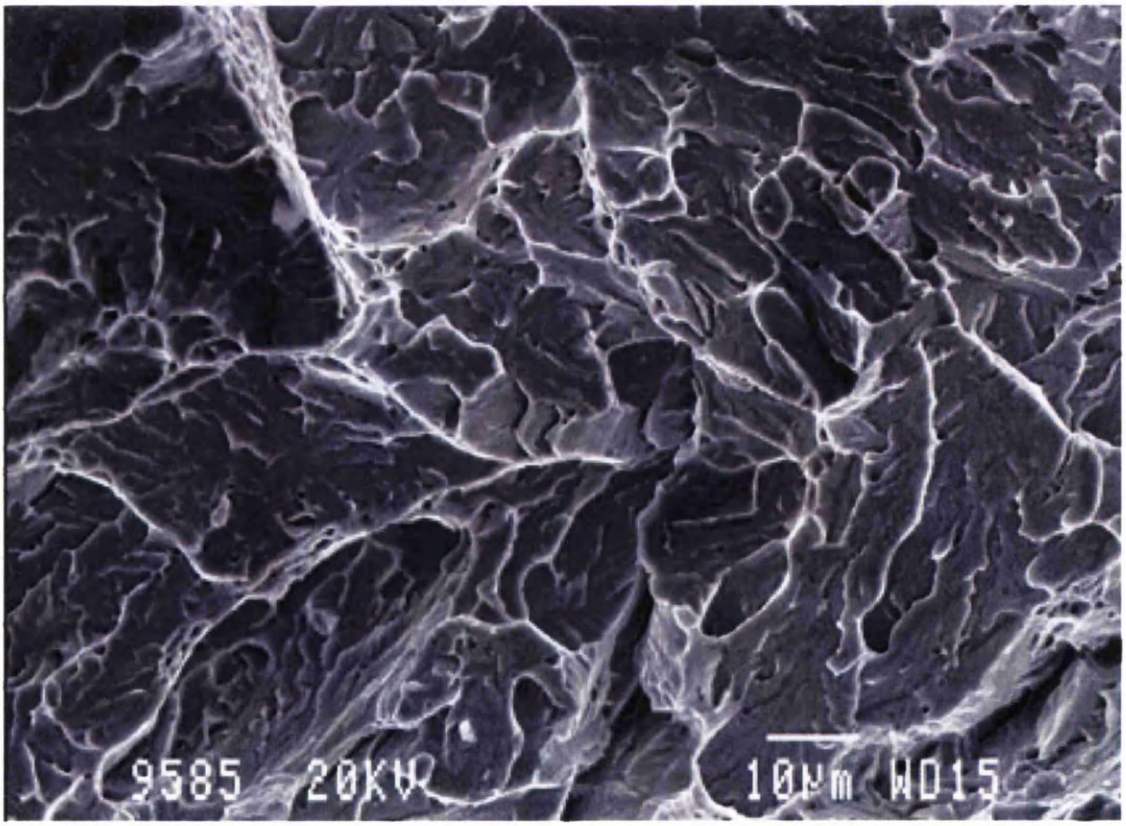

Figure 5.75b SEM image of trans-granular fracture occurring in an interfacially failed DP1000 spot weld

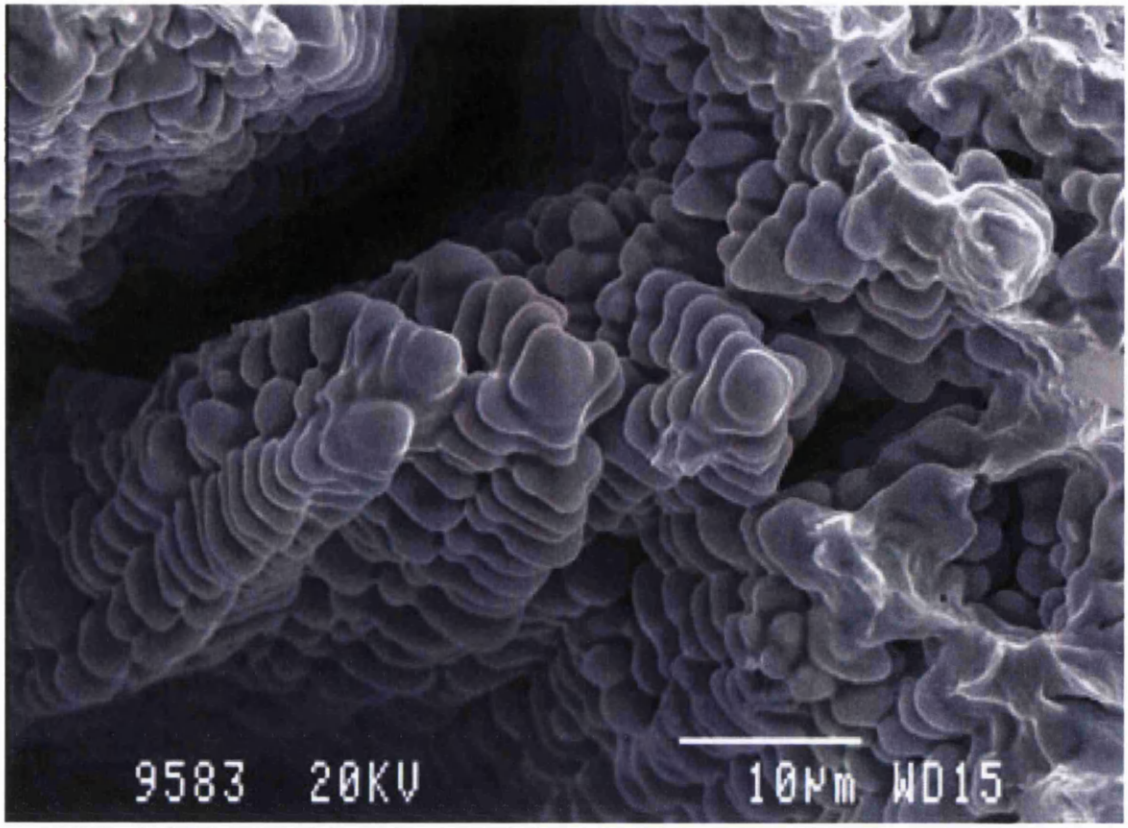

Figure 5.75c SEM image of dendrite growth into a void in an interfacially failed DP1000 spot weld

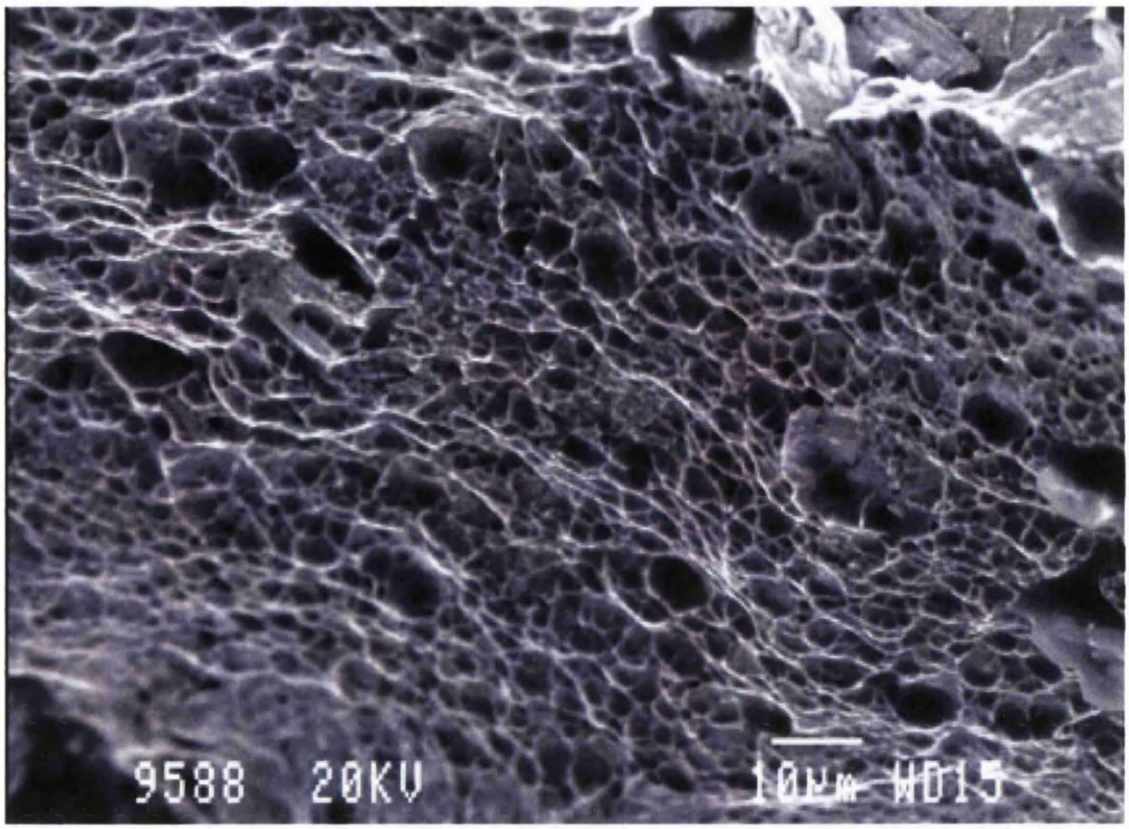

Figure 5.76a SEM image of dimple rupture occurring in an interfacially failed MS1400 spot weld

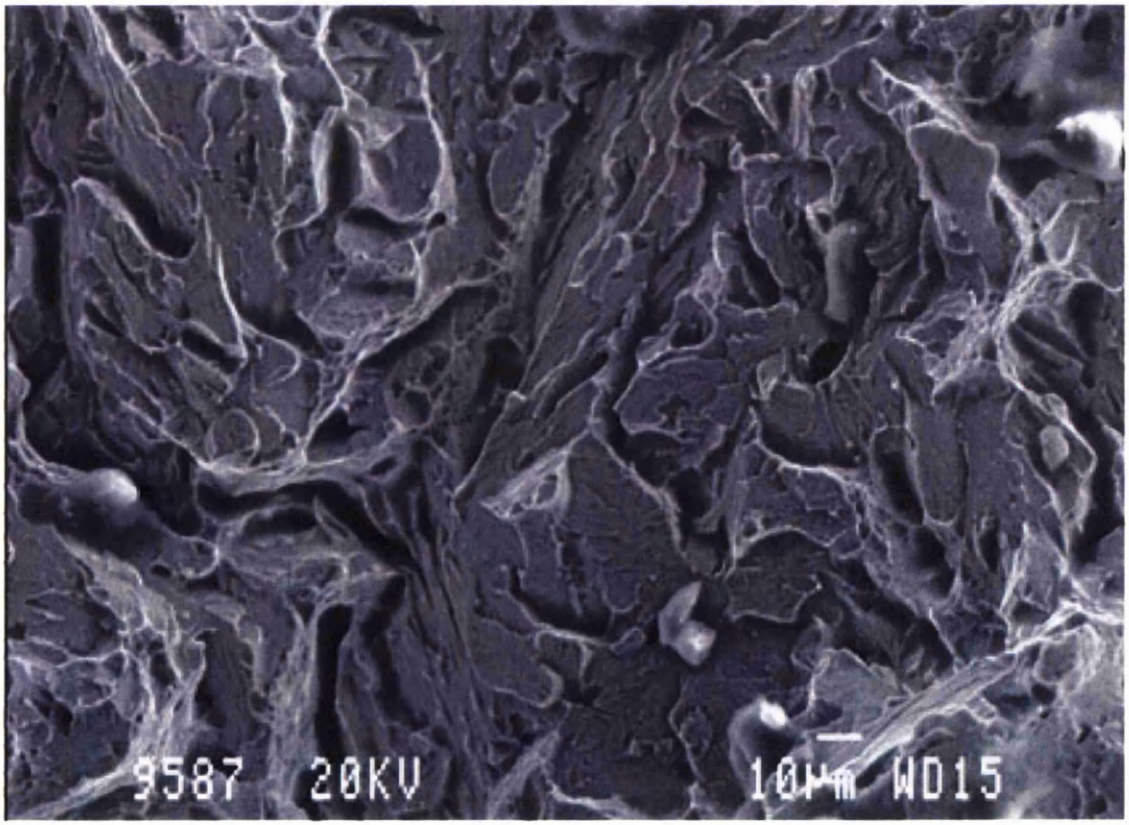

Figure 5.76b SEM image of trans-granular fracture occurring in an interfacially failed MS1400 spot weld

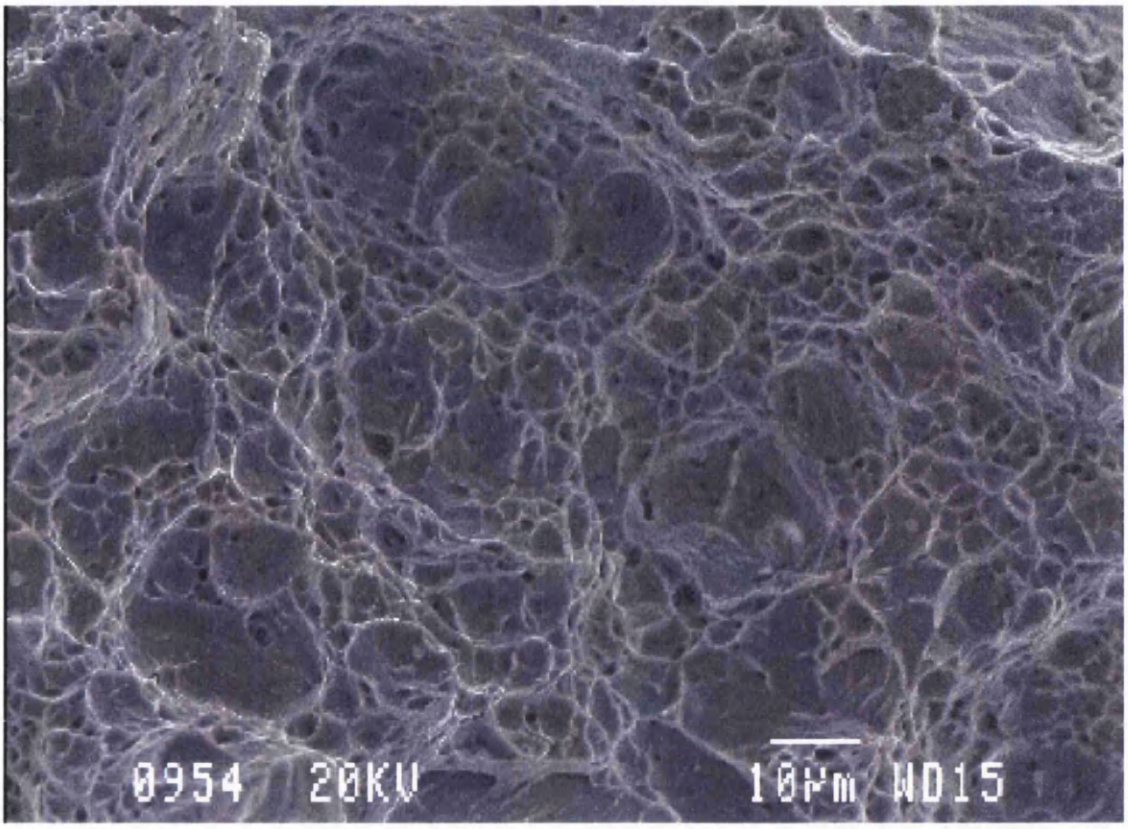

Figure 5.77a SEM image of dimple rupture occurring in an interfacially failed TRIP800 spot weld

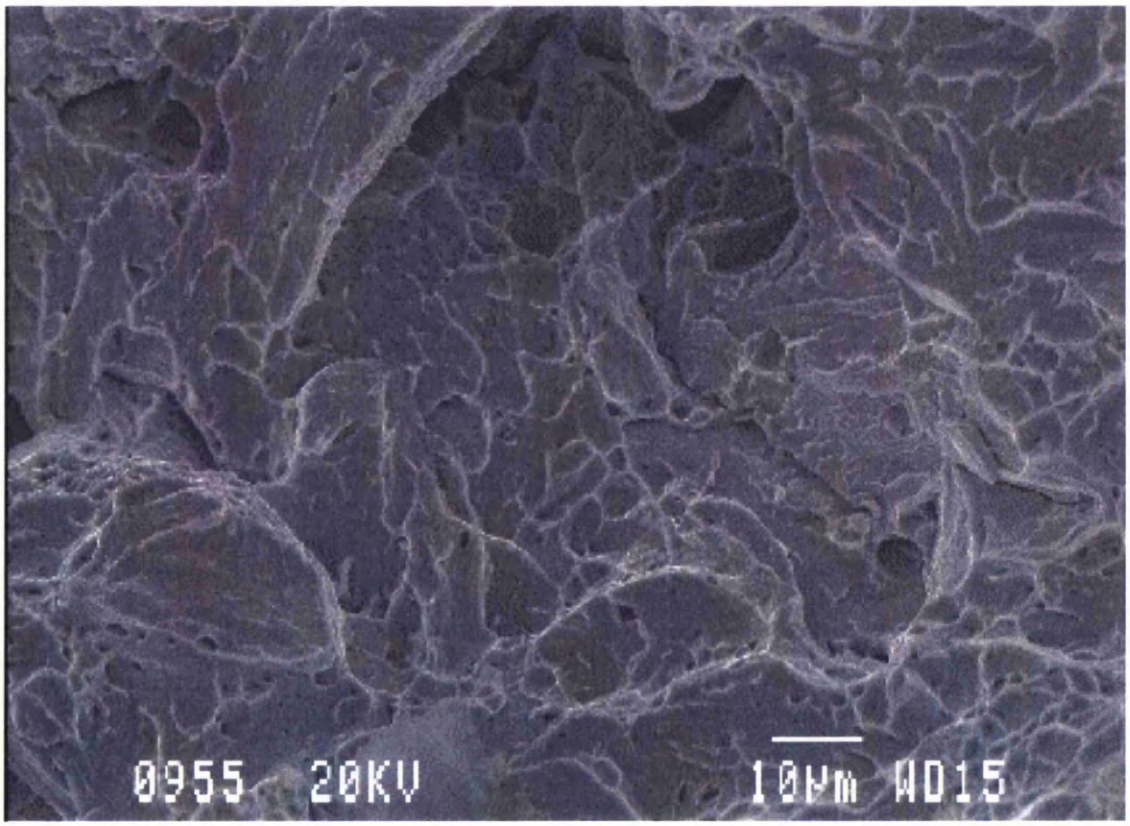

Figure 5.77b SEM image of trans-granular fracture occurring in an interfacially failed TRIP800 spot weld

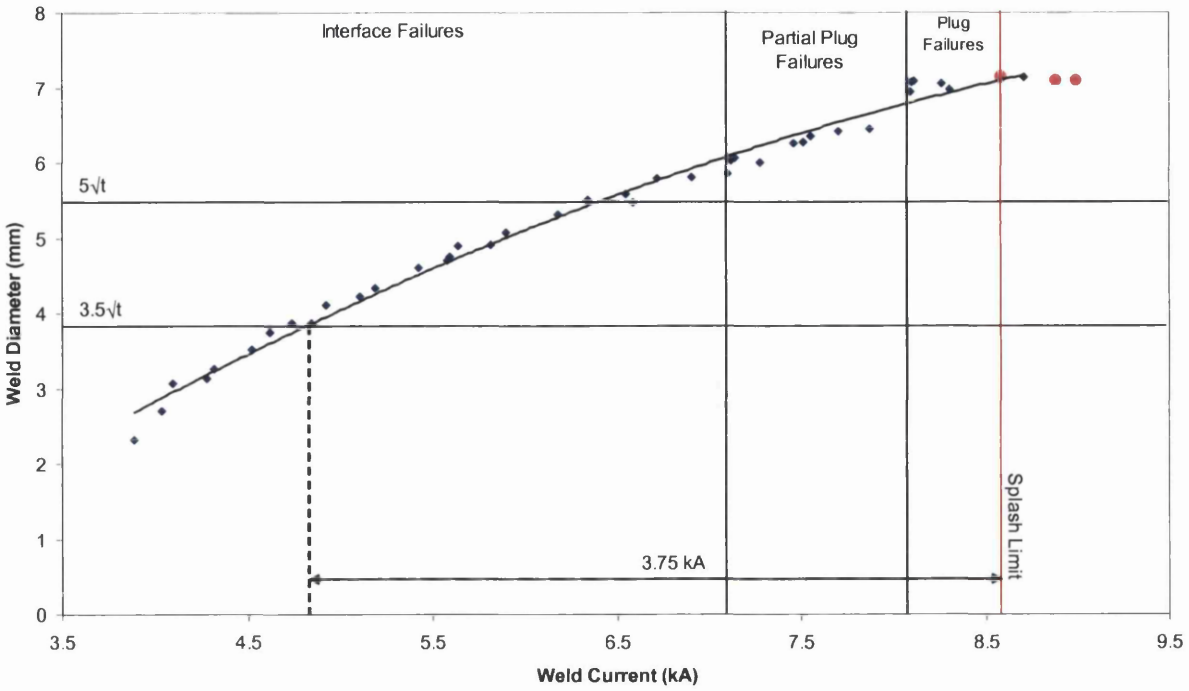

Figure 5.78 Relationship between weld current and weld diameter for 1.2mm TRIP800 (6.0mm diameter electrode tips, 4.6kN electrode force)

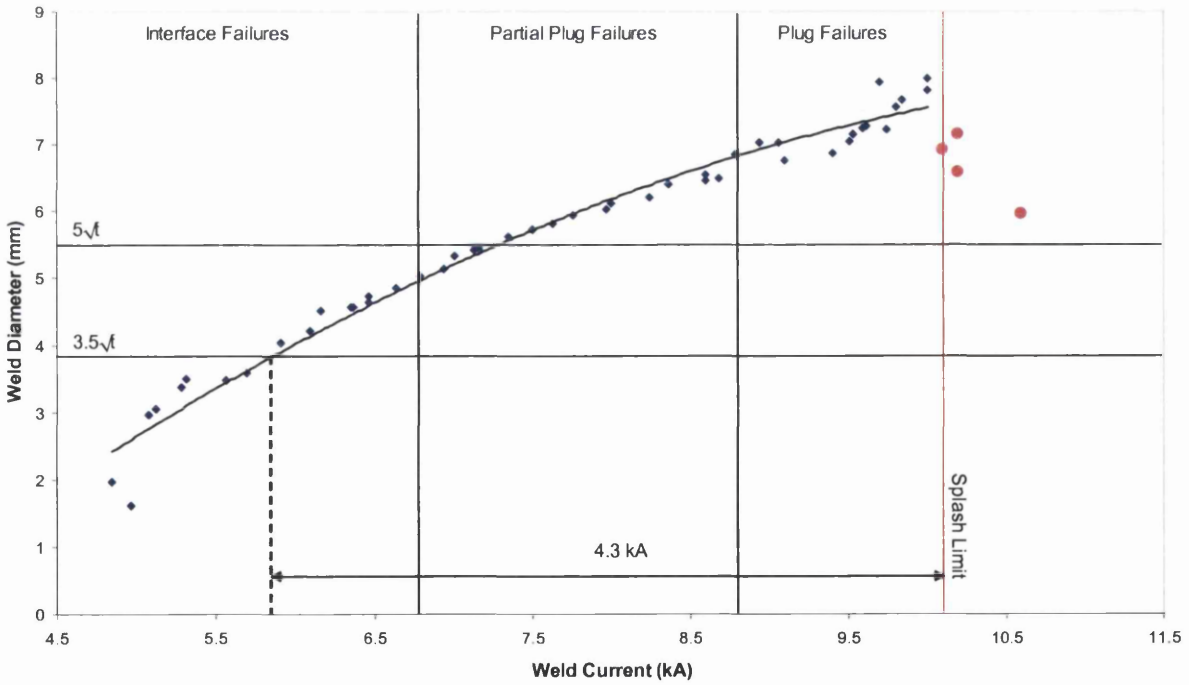

Figure 5.79 Relationship between weld current and weld diameter for 1.2mm TRIP800 (7.0mm diameter electrode tips, 6.3kN electrode force)

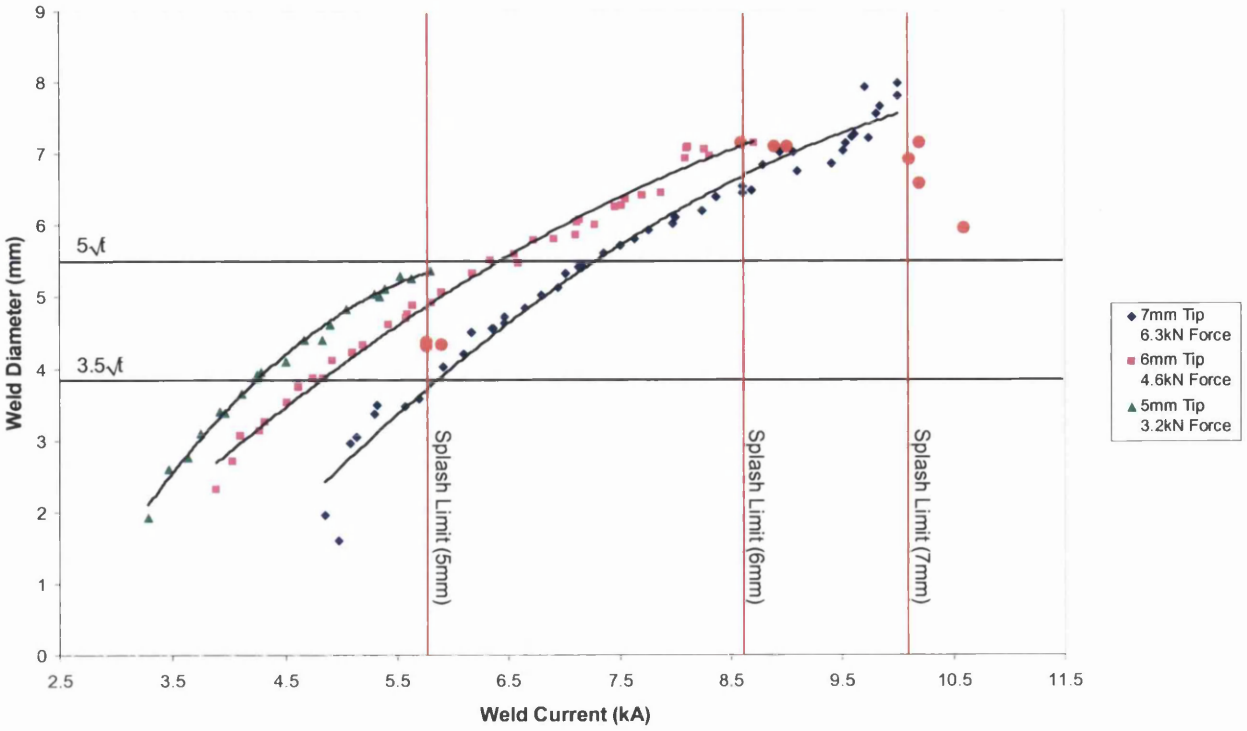

Figure 5.80 Effect of electrode tip diameter on weld growth in 1.2mm TRIP800

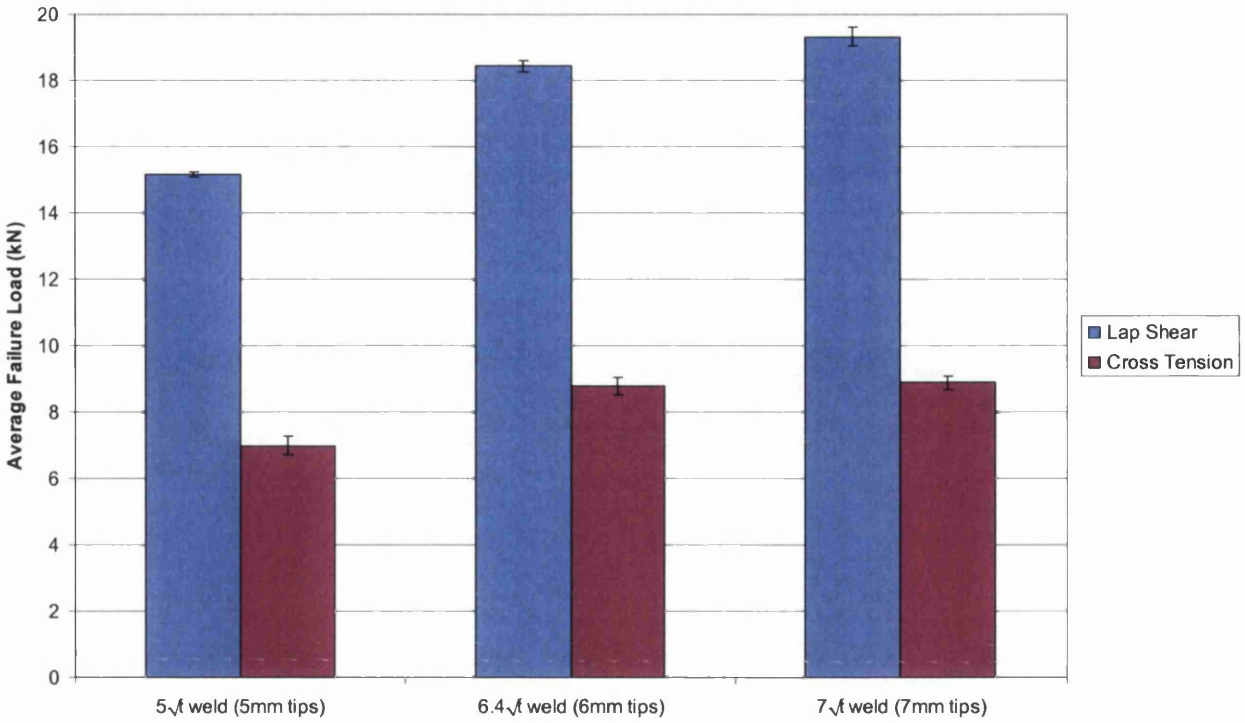

Figure 5.81 Effect of weld diameter on average lap shear and cross tension failure load of welds formed in 1.2mm TRIP800. Error bars indicate one standard deviation from the mean

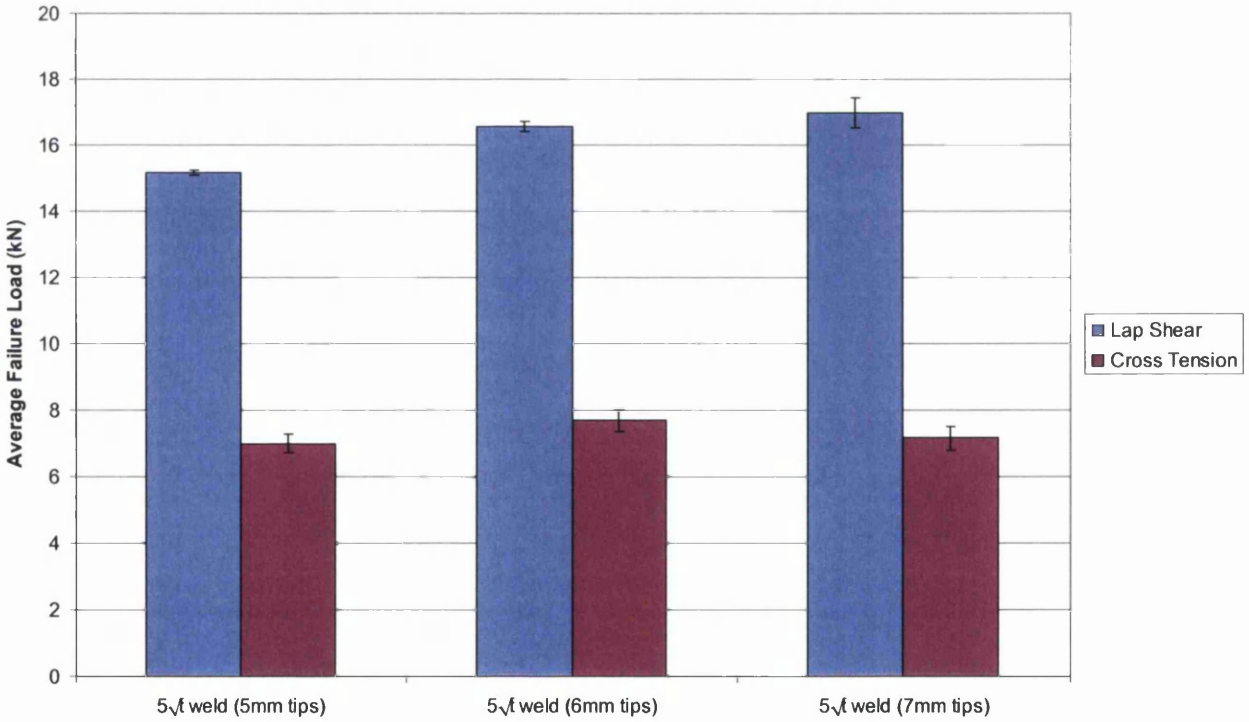

Figure 5.82 Effect of electrode tip diameter on the average lap shear and cross tension failure loads of 5√t welds formed in 1.2mm TRIP800. Error bars indicate one standard deviation from the mean

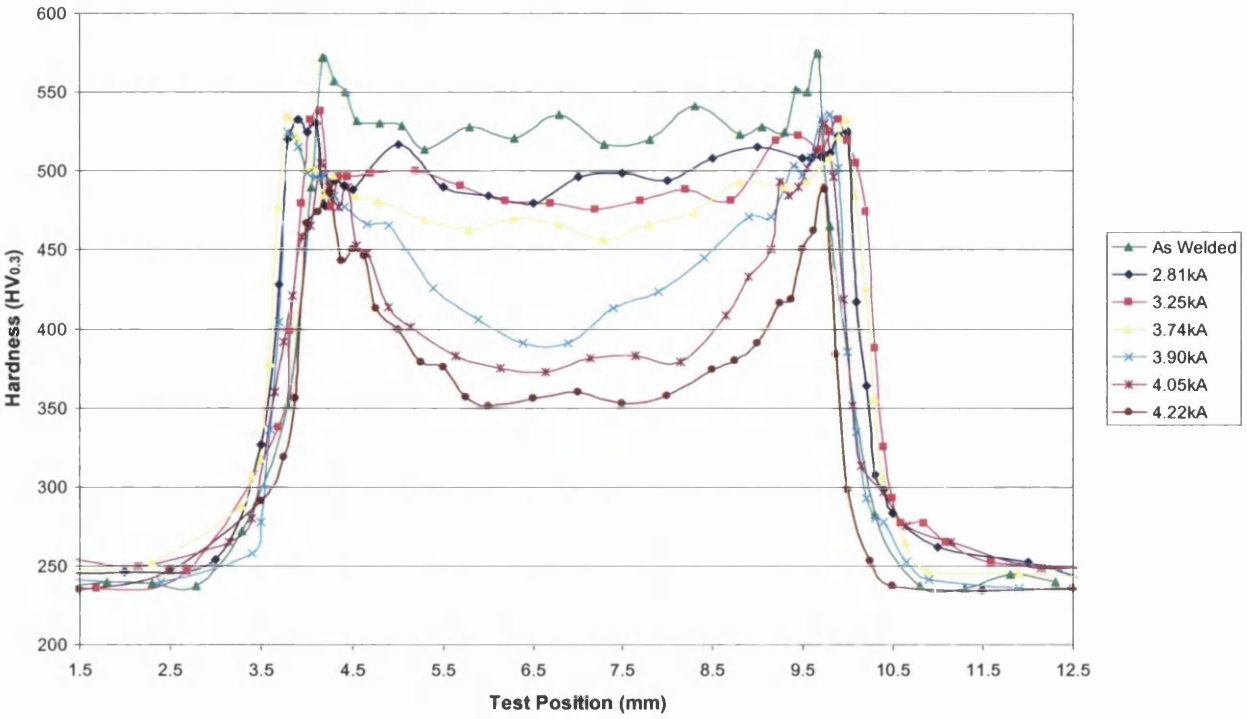

Figure 5.83 Effect of increasing secondary current on the Vickers microhardness of heat treated $5\sqrt{t}$ spot welds formed in TRIP800

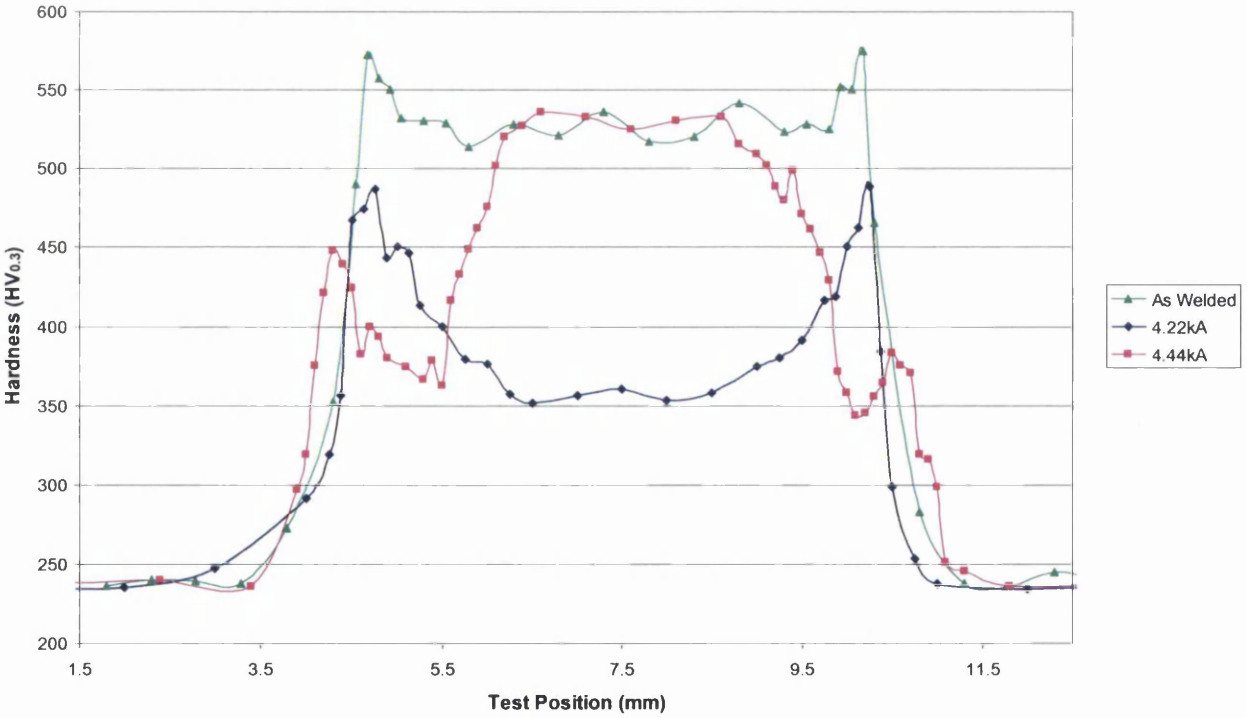

Figure 5.84 Vickers microhardness profiles of an untreated TRIP800 spot weld and TRIP800 spot welds treated with 4.22kA and 4.44kA secondary current pulses

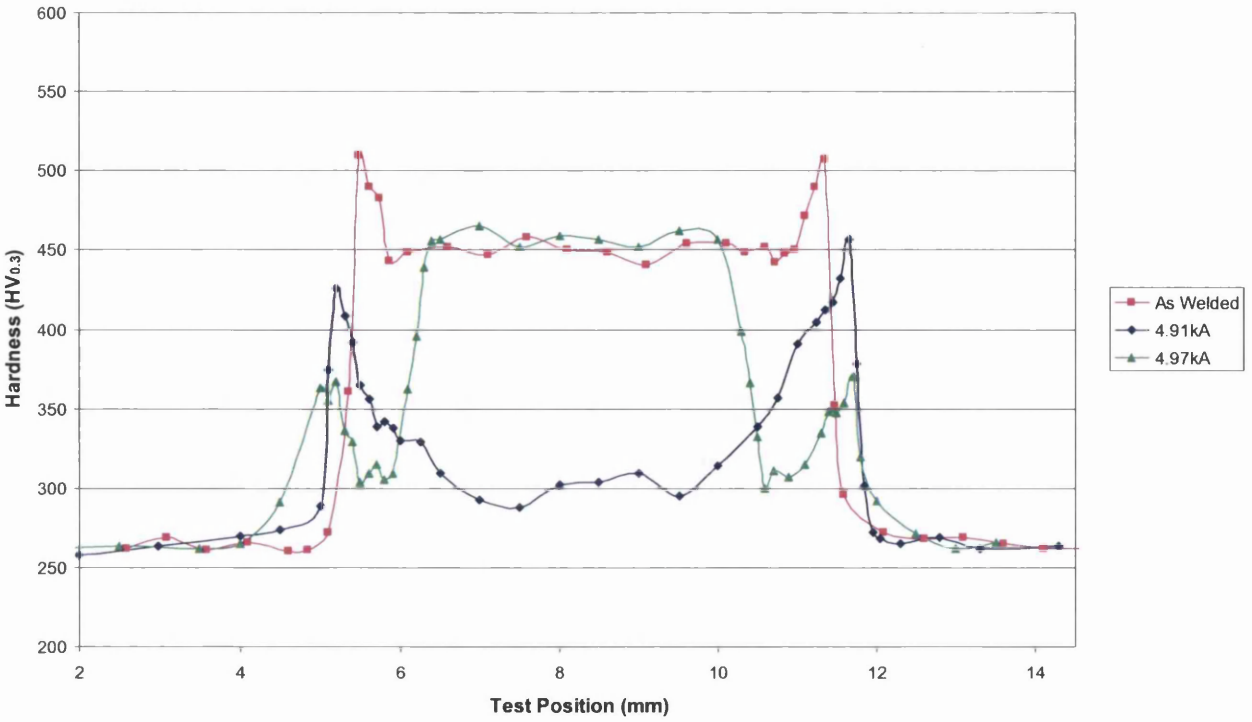

Figure 5.85 Vickers microhardness profiles of an untreated DP800 spot weld and D800 spot welds treated with 4.91kA and 4.97kA secondary current pulses

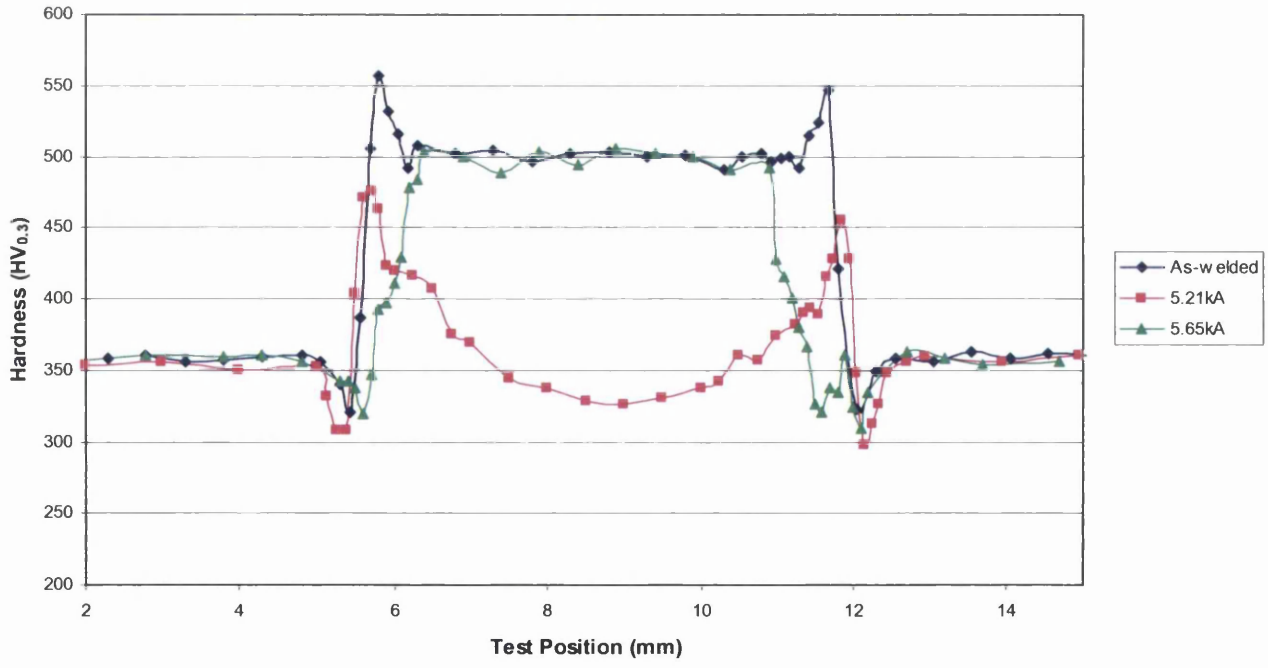

Figure 5.86 Vickers microhardness profiles of an untreated DP1000 spot weld and D1000 spot welds treated with 5.21kA and 5.65kA secondary current pulses

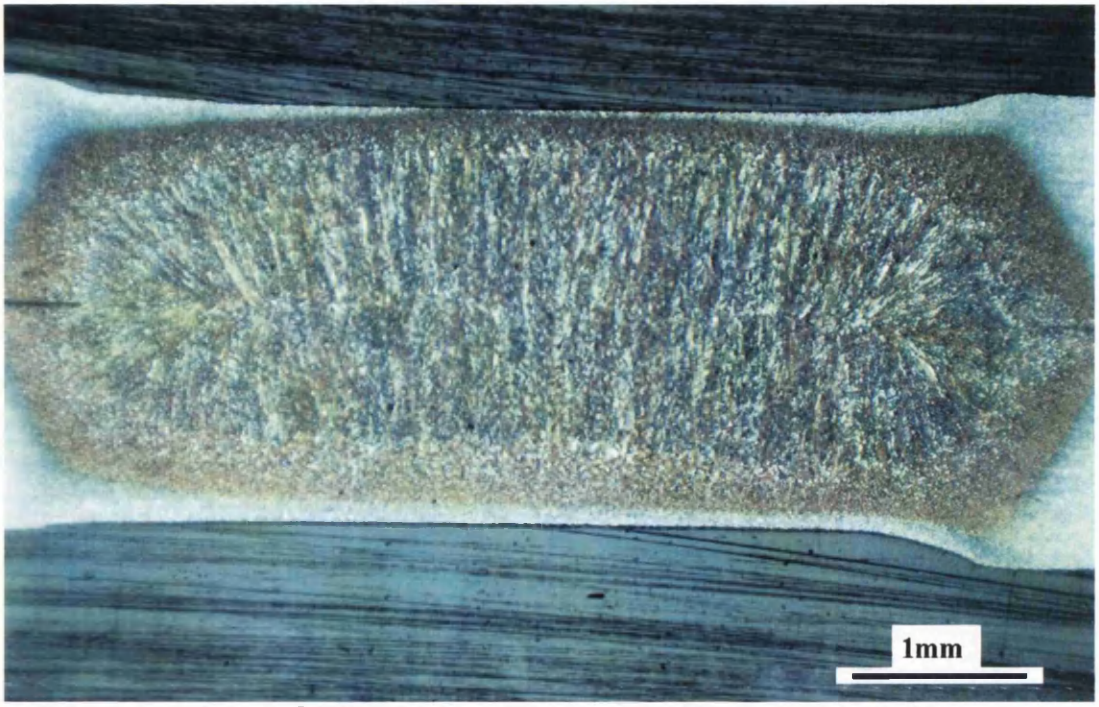

Figure 5.87a Macro of a 5√t TRIP800 spot weld treated with a 2.81kA secondary current pulse

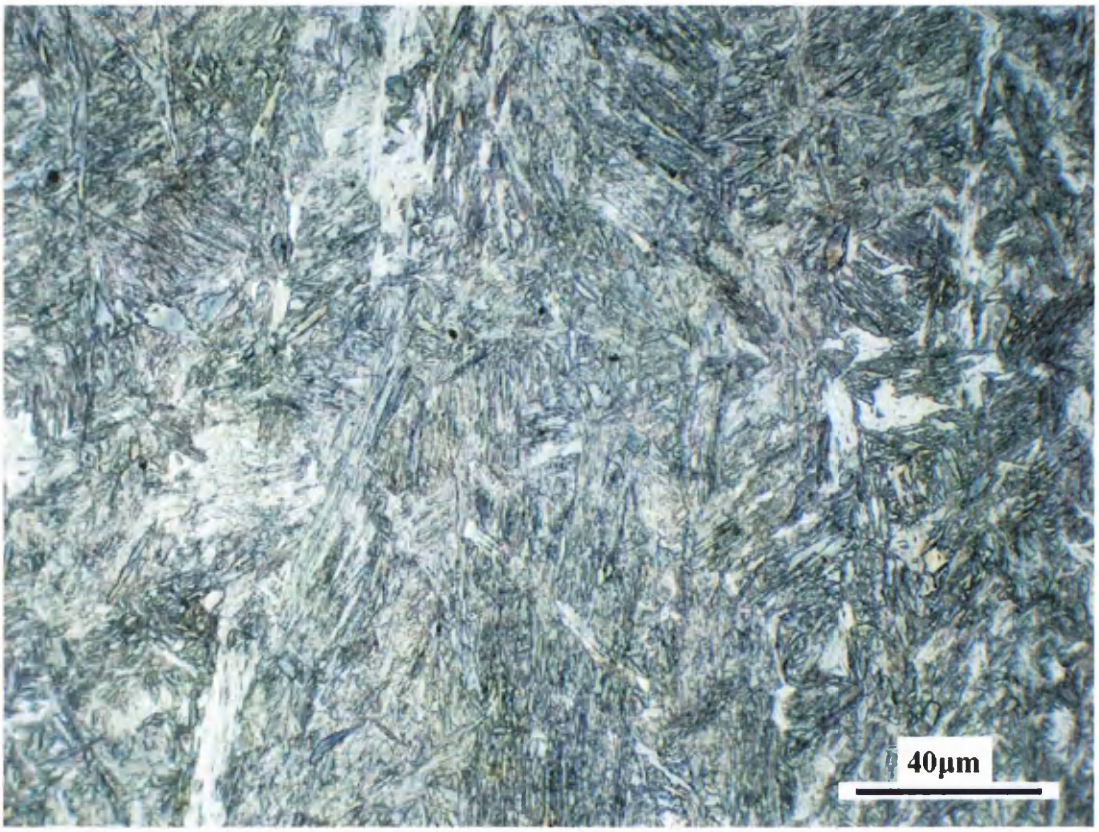

Figure 5.87b Micrograph showing microstructure in TRIP800 weld nugget treated with a 2.81kA secondary current pulse

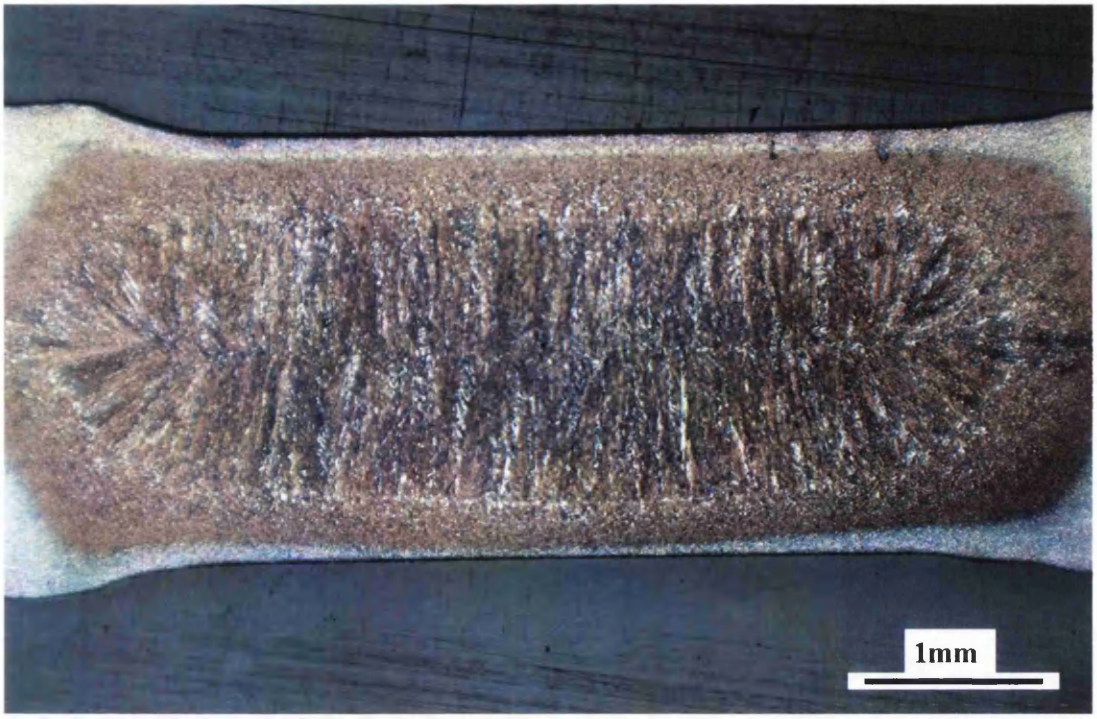

Figure 5.88a Macro of a $5\sqrt{t}$ TRIP800 spot weld treated with a 3.25kA secondary current pulse

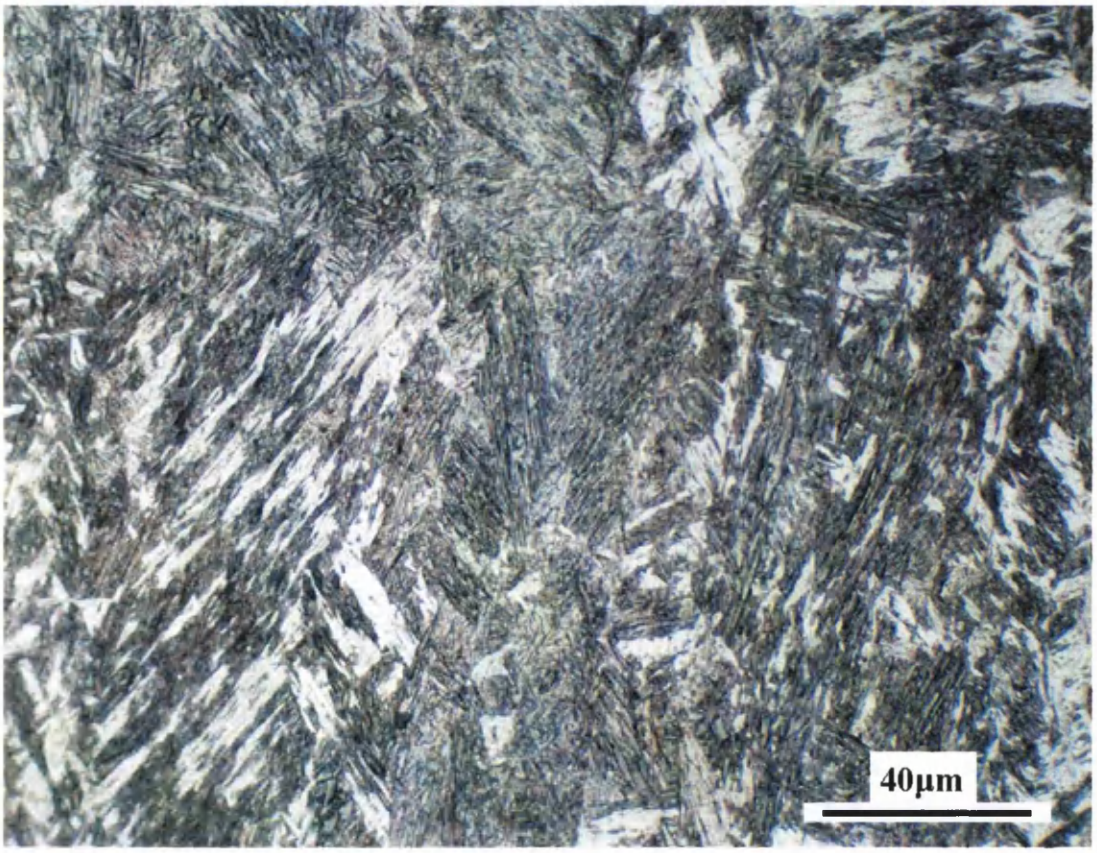

Figure 5.88b Micrograph showing microstructure in TRIP800 weld nugget treated with a 3.25kA secondary current pulse

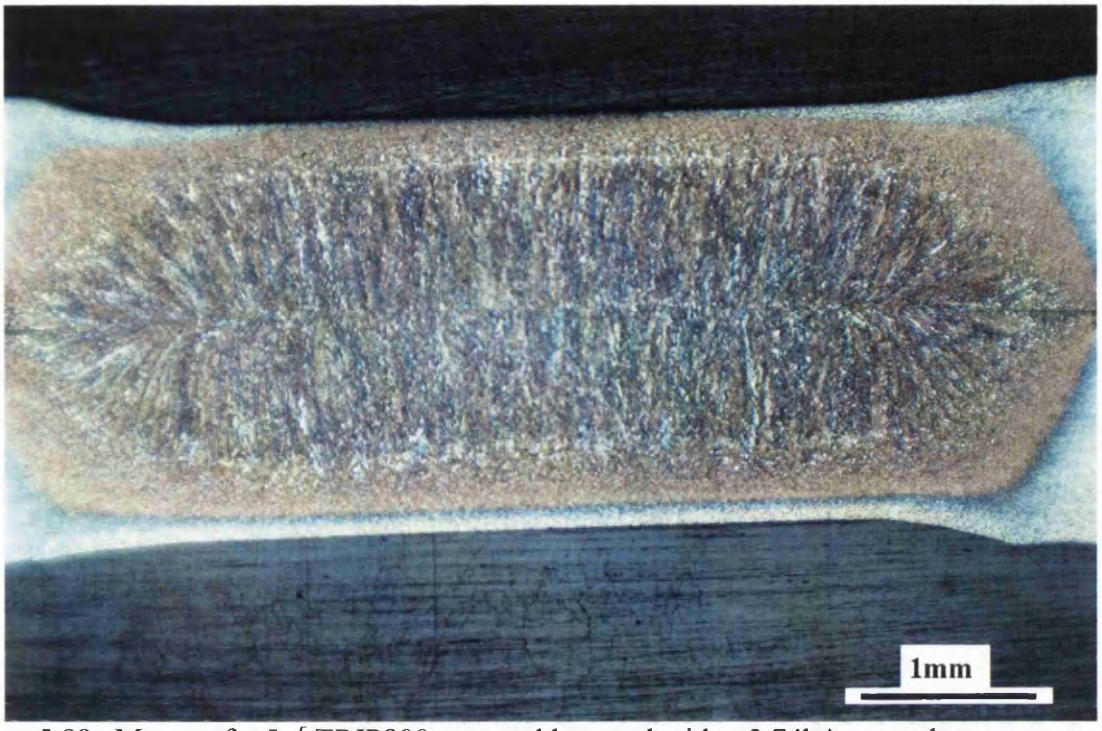

Figure 5.89a Macro of a 5√t TRIP800 spot weld treated with a 3.74kA secondary current pulse

Figure 5.89b Micrograph showing microstructure in TRIP800 weld nugget treated with a 3.74kA secondary current pulse

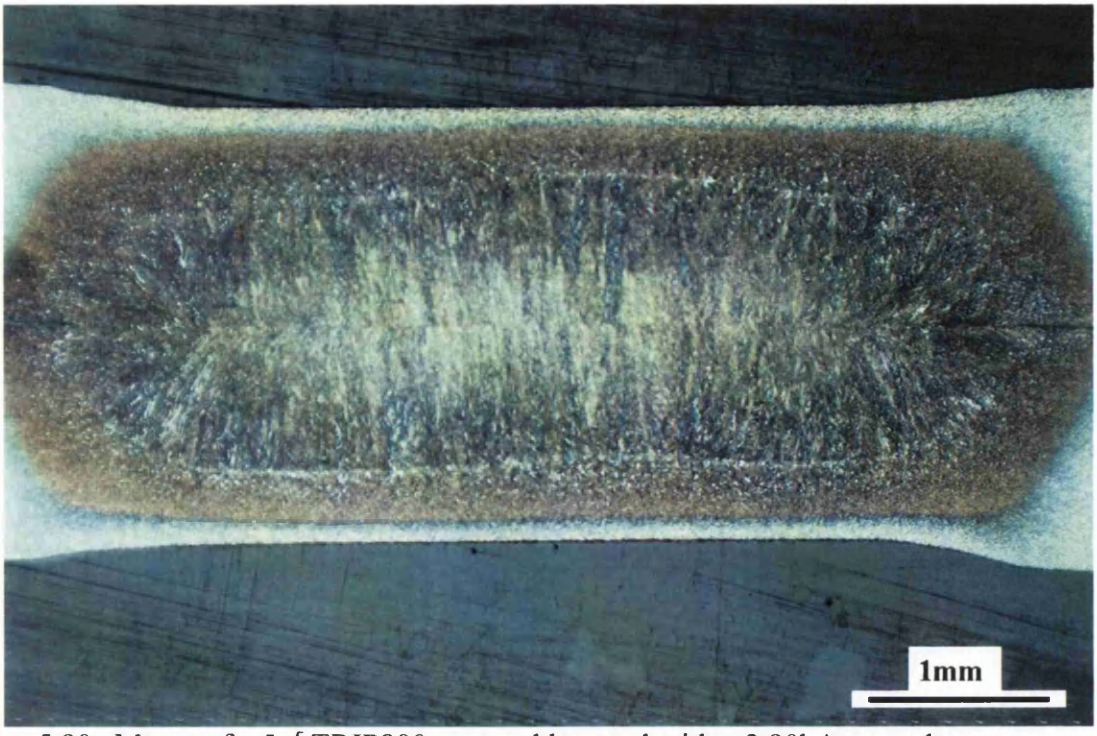

Figure 5.90a Macro of a 5√t TRIP800 spot weld treated with a 3.90kA secondary current pulse

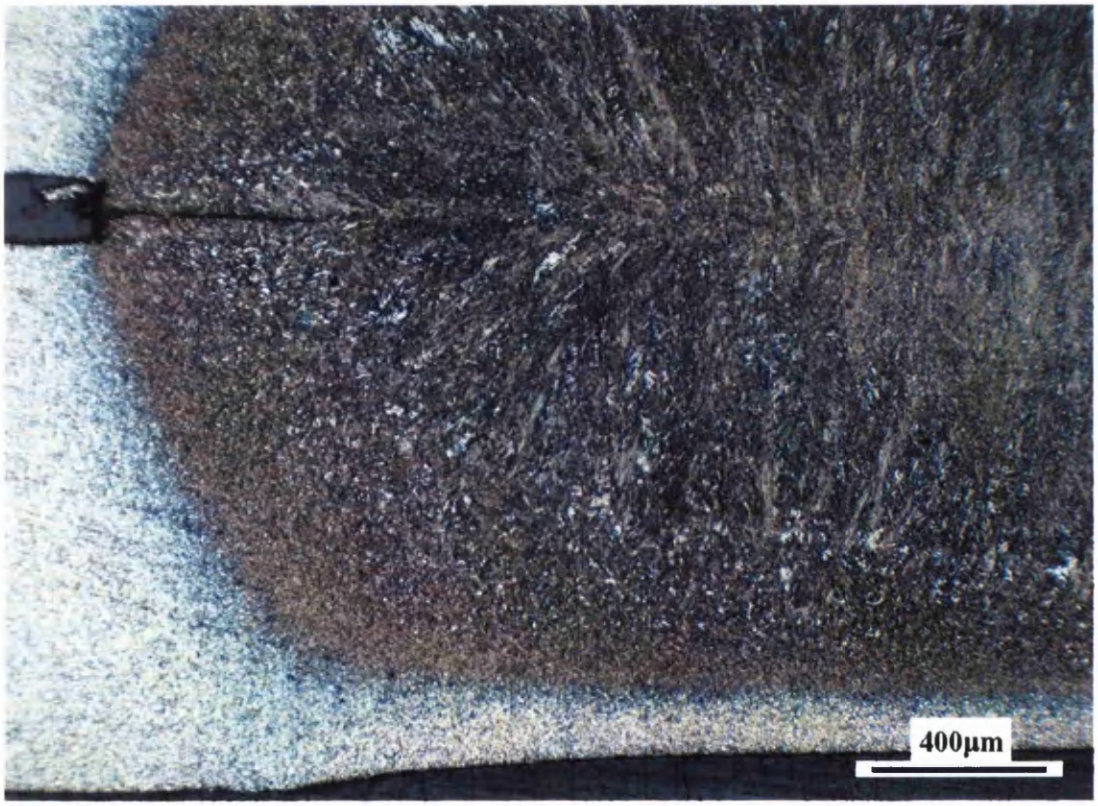

Figure 5.90b Micrograph illustrating the variation in microstructure from parent metal to weld nugget in TRIP800 spot weld treated with a 3.90kA secondary current pulse

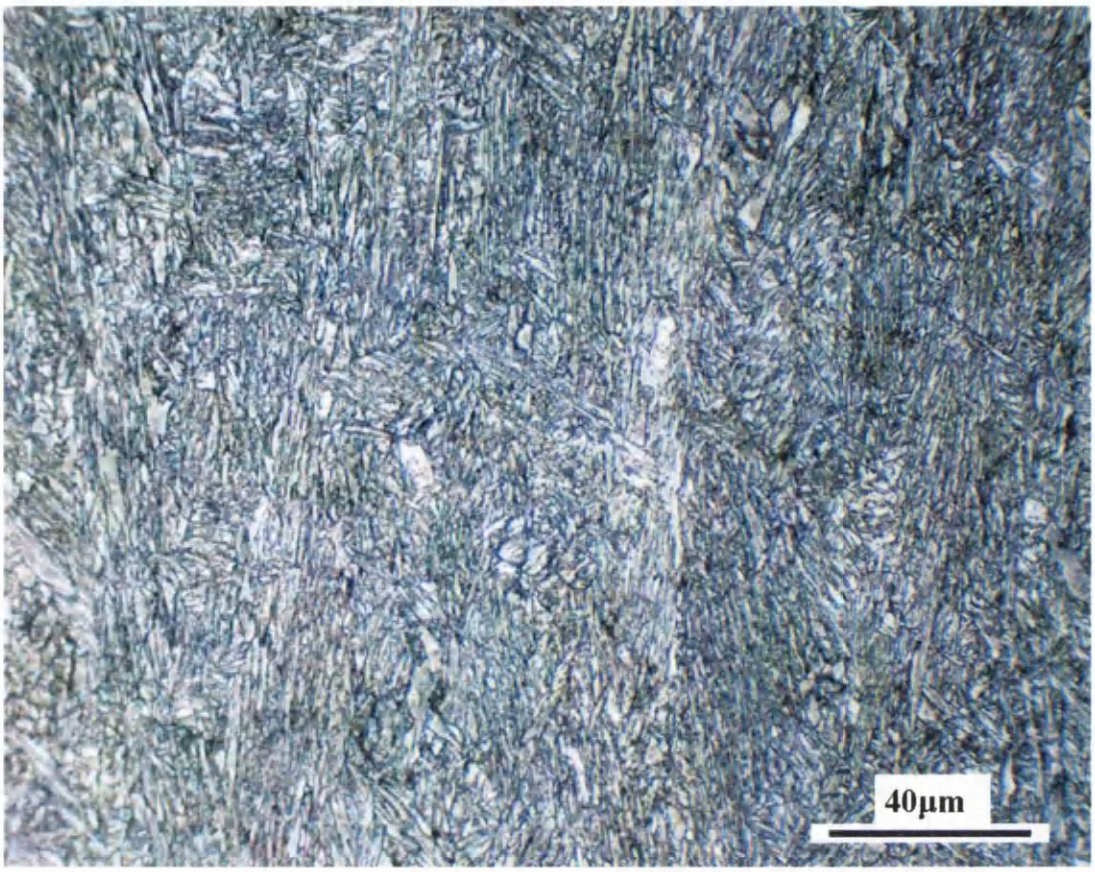

Figure 5.90c Micrograph showing microstructure in TRIP800 weld nugget treated with a 3.90kA secondary current pulse

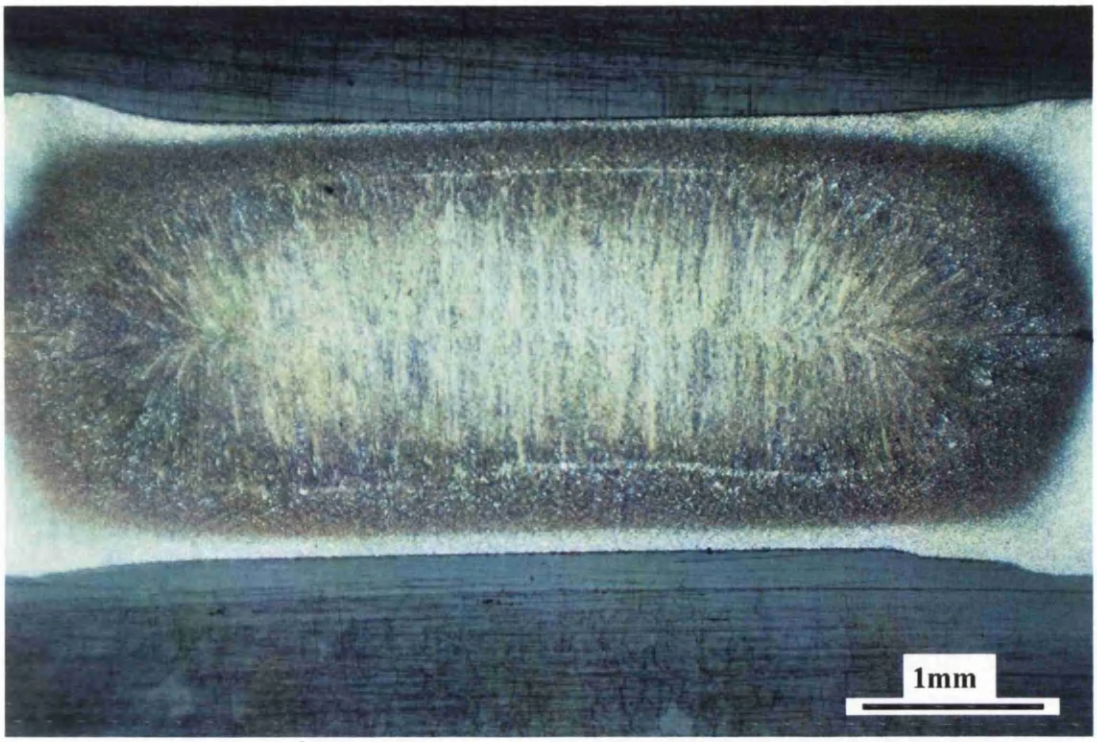

Figure 5.91a Macro of a 5√t TRIP800 spot weld treated with a 4.05kA secondary current pulse

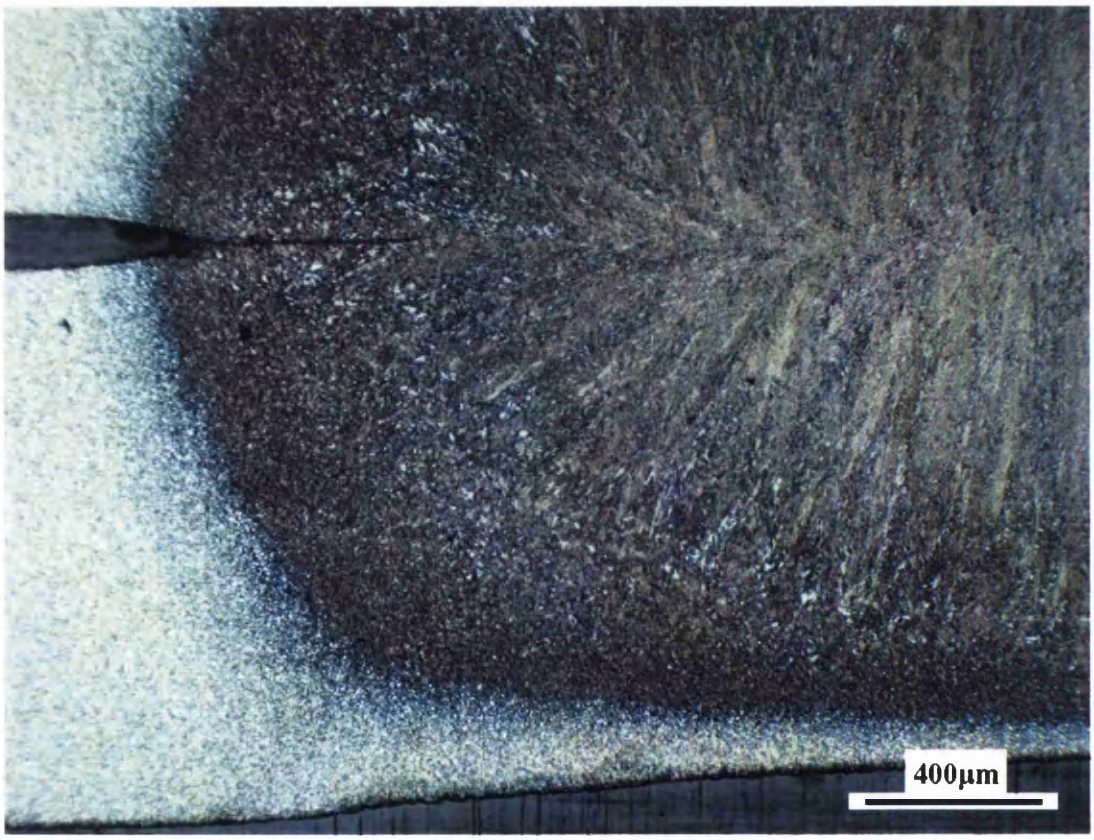

Figure 5.91b Micrograph illustrating the variation in microstructure from parent metal to weld nugget in TRIP800 spot weld treated with a 4.05kA secondary current pulse

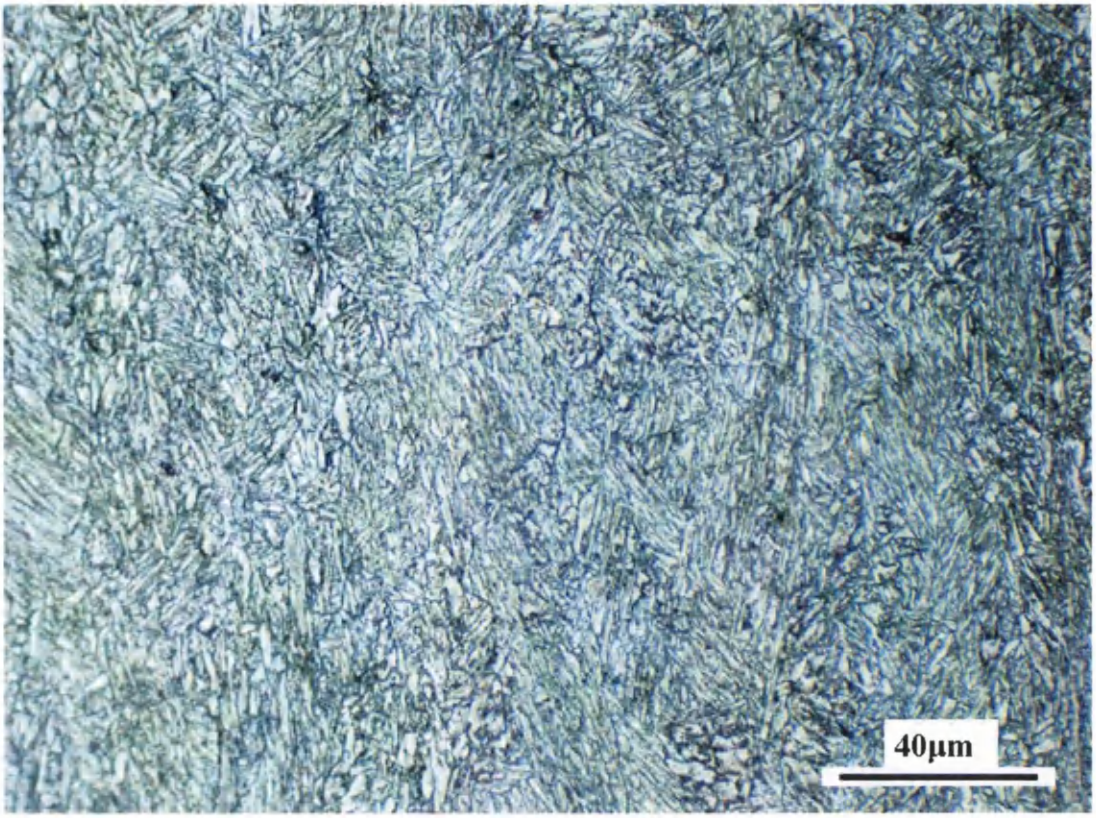

Figure 5.91c Micrograph showing microstructure in TRIP800 weld nugget treated with a 4.05kA secondary current pulse

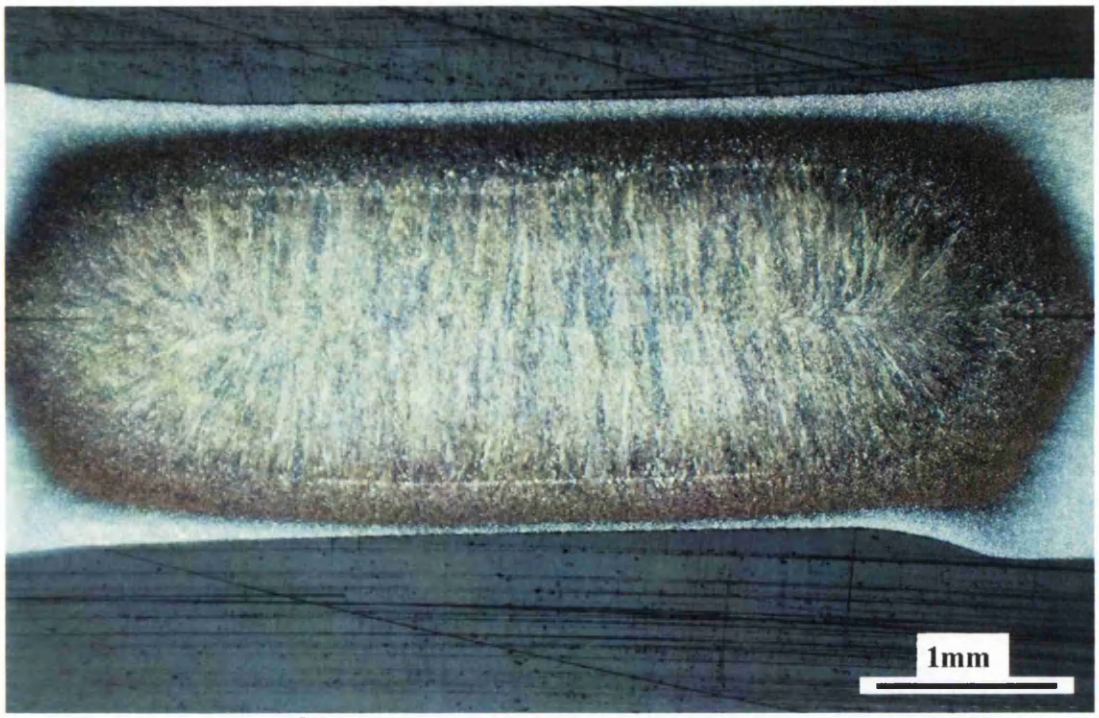

Figure 5.92a Macro of a 5√t TRIP800 spot weld treated with a 4.22kA secondary current pulse

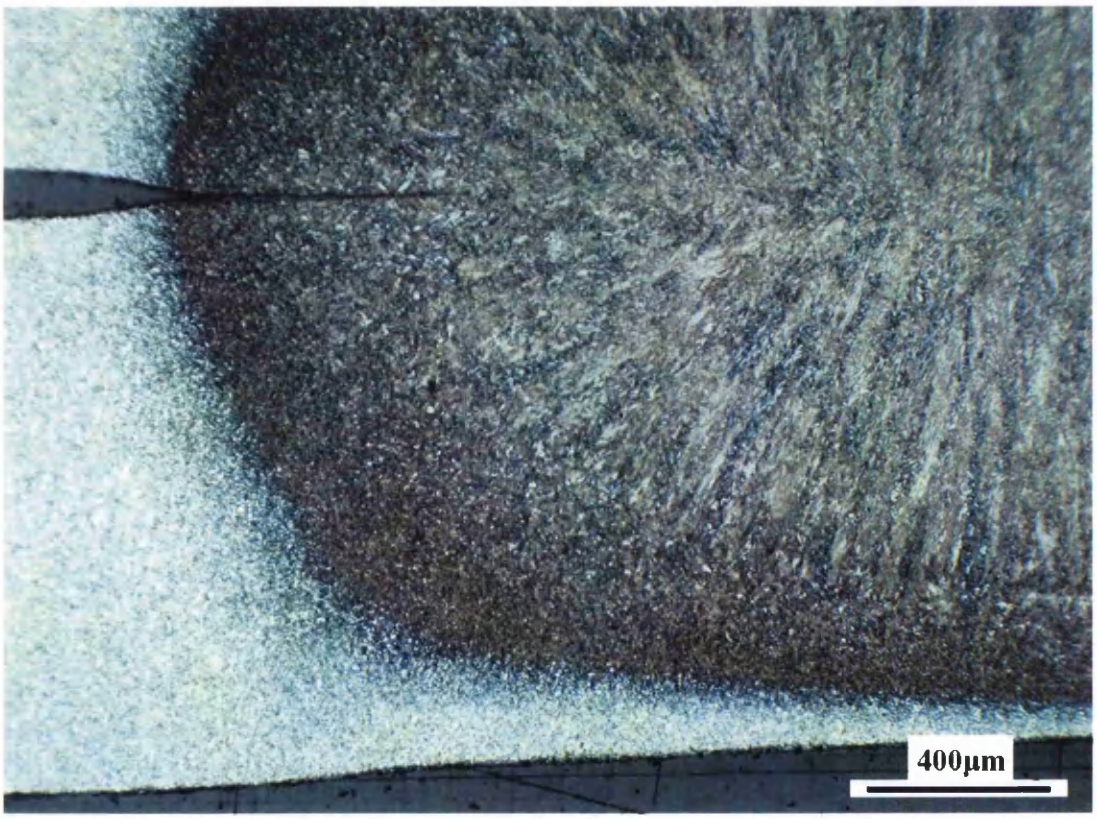

Figure 5.92b Micrograph illustrating the variation in microstructure from parent metal to weld nugget in TRIP800 spot weld treated with a 4.22kA secondary current pulse

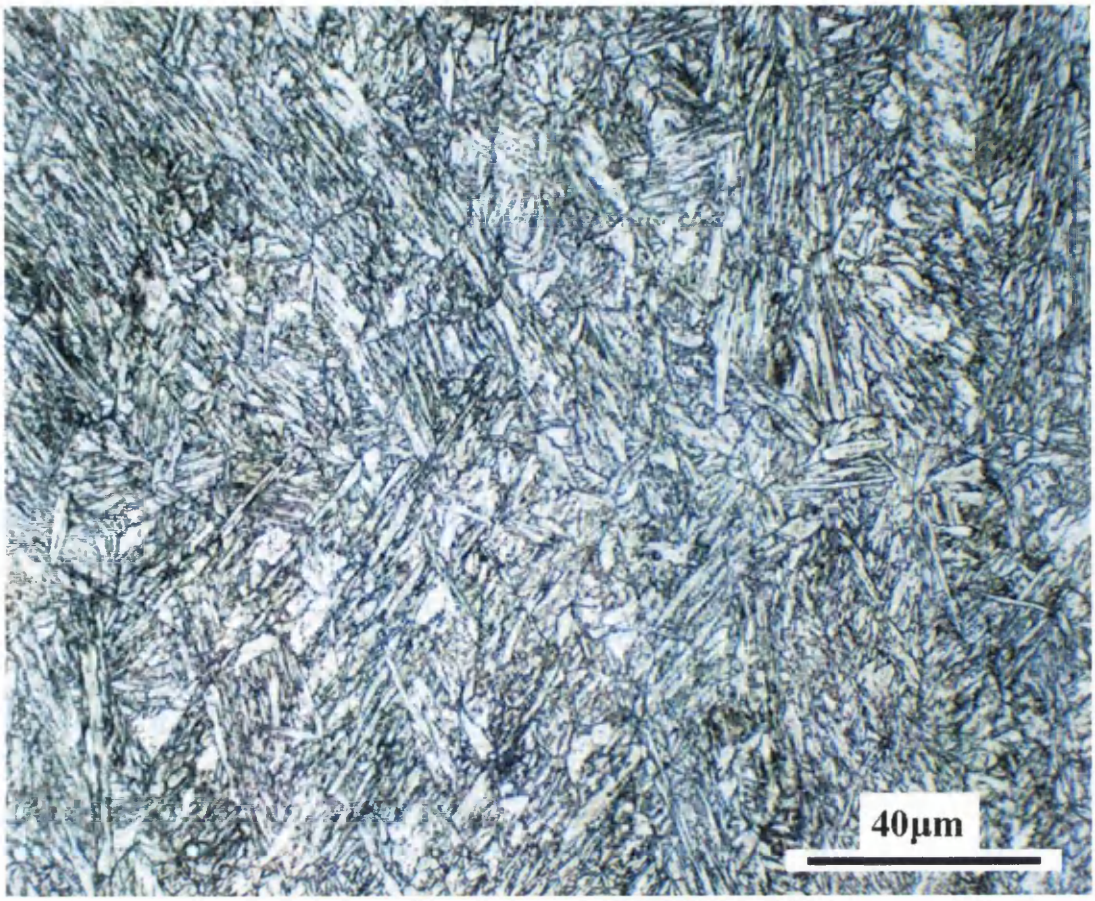

Figure 5.92c Micrograph showing microstructure in TRIP800 weld nugget treated with a 4.22kA secondary current pulse

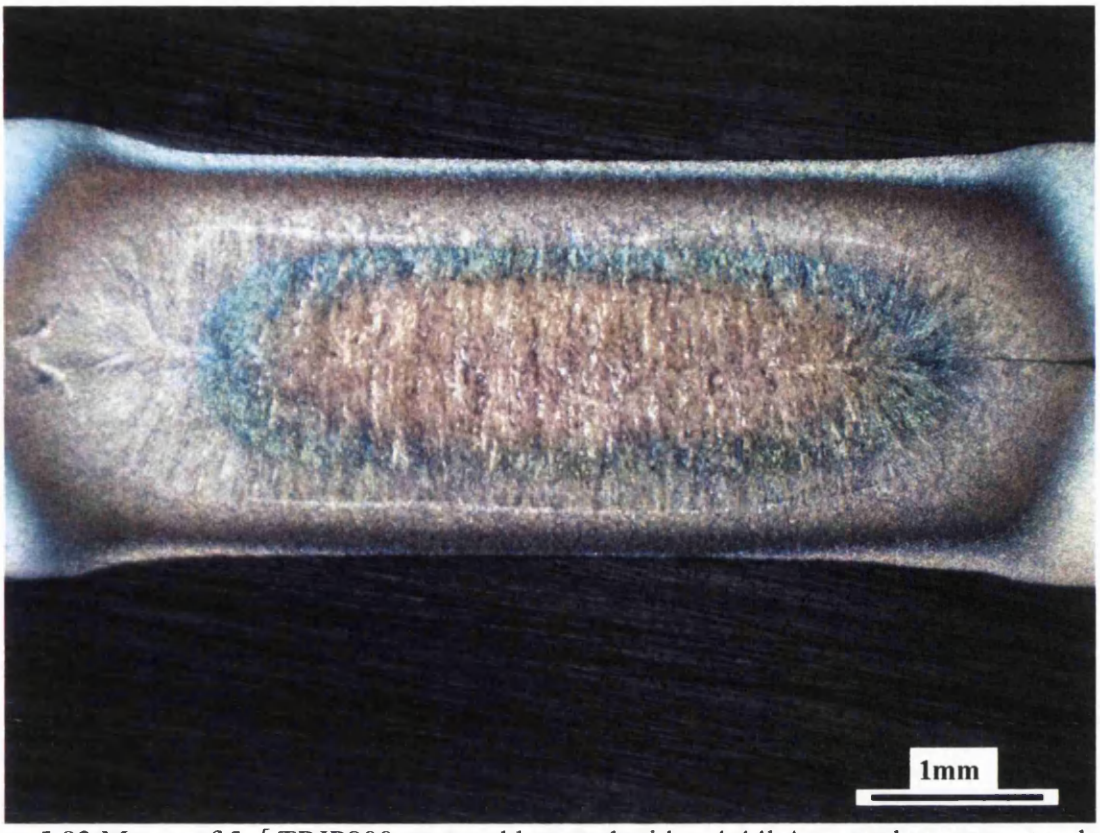

Figure 5.93 Macro of 5√f TRIP800 spot weld treated with a 4.44kA secondary current pulse

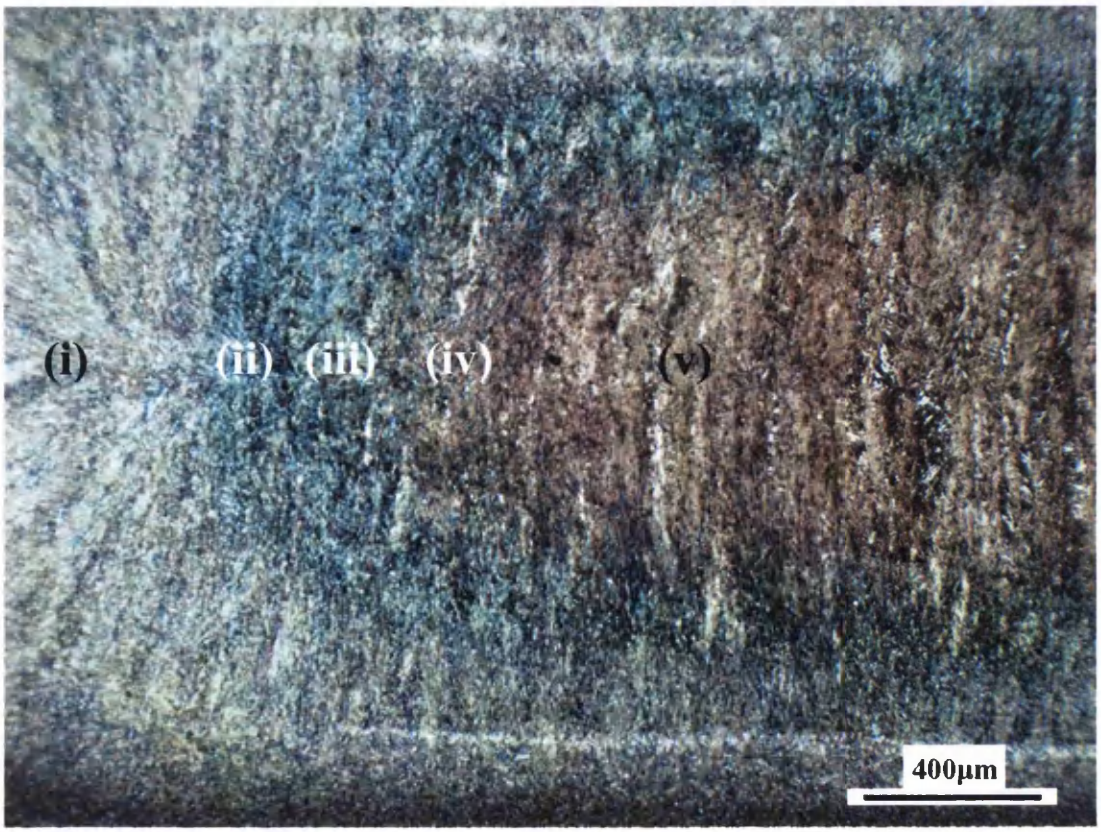

Figure 5.94 Micrograph illustrating variations in microstructure in TRIP800 weld nugget treated with a 4.44kA secondary current pulse

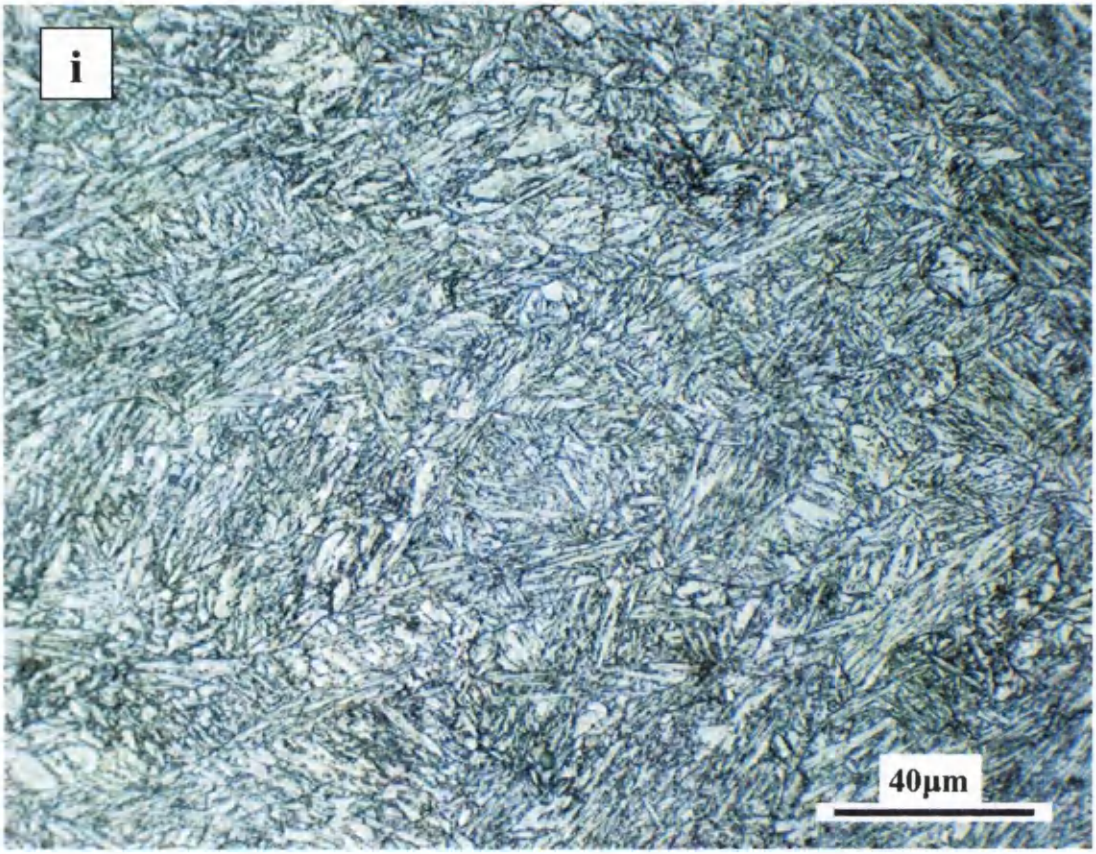

Figure 5.95a Micrograph showing microstructure of weld at position (i) in figure 5.94

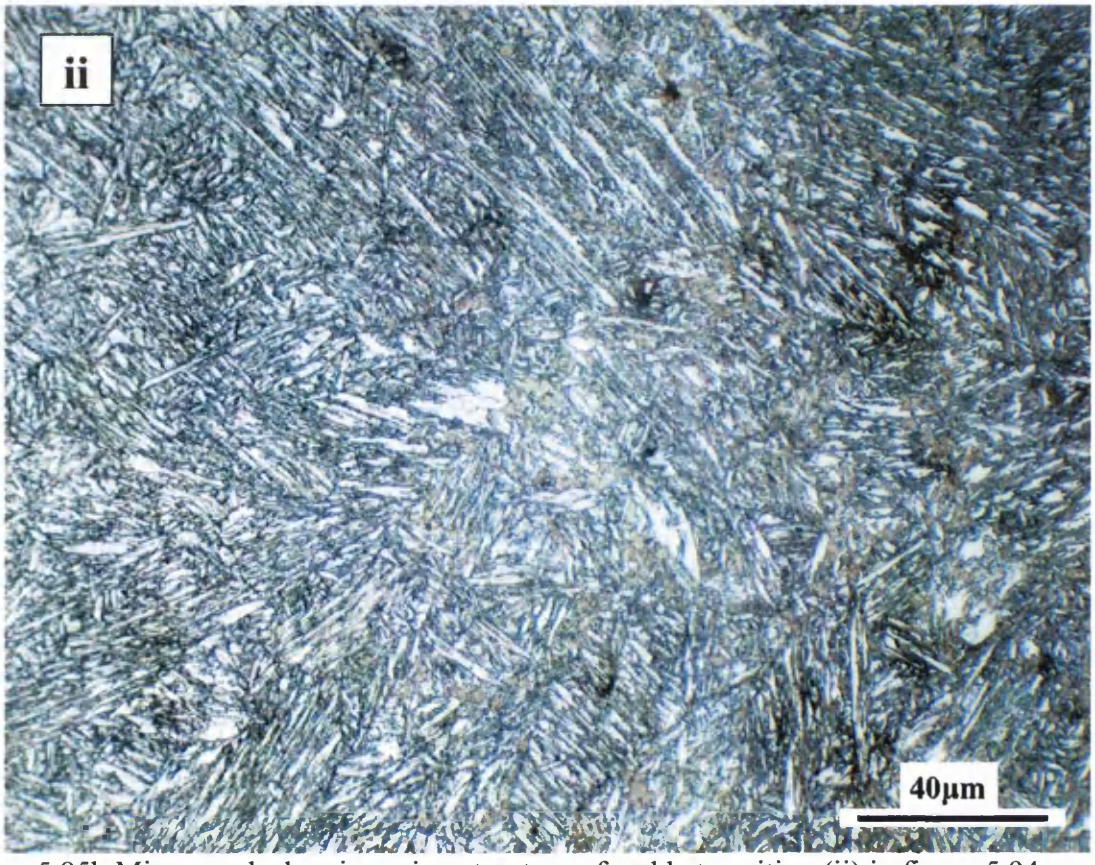

Figure 5.95b Micrograph showing microstructure of weld at position (ii) in figure 5.94

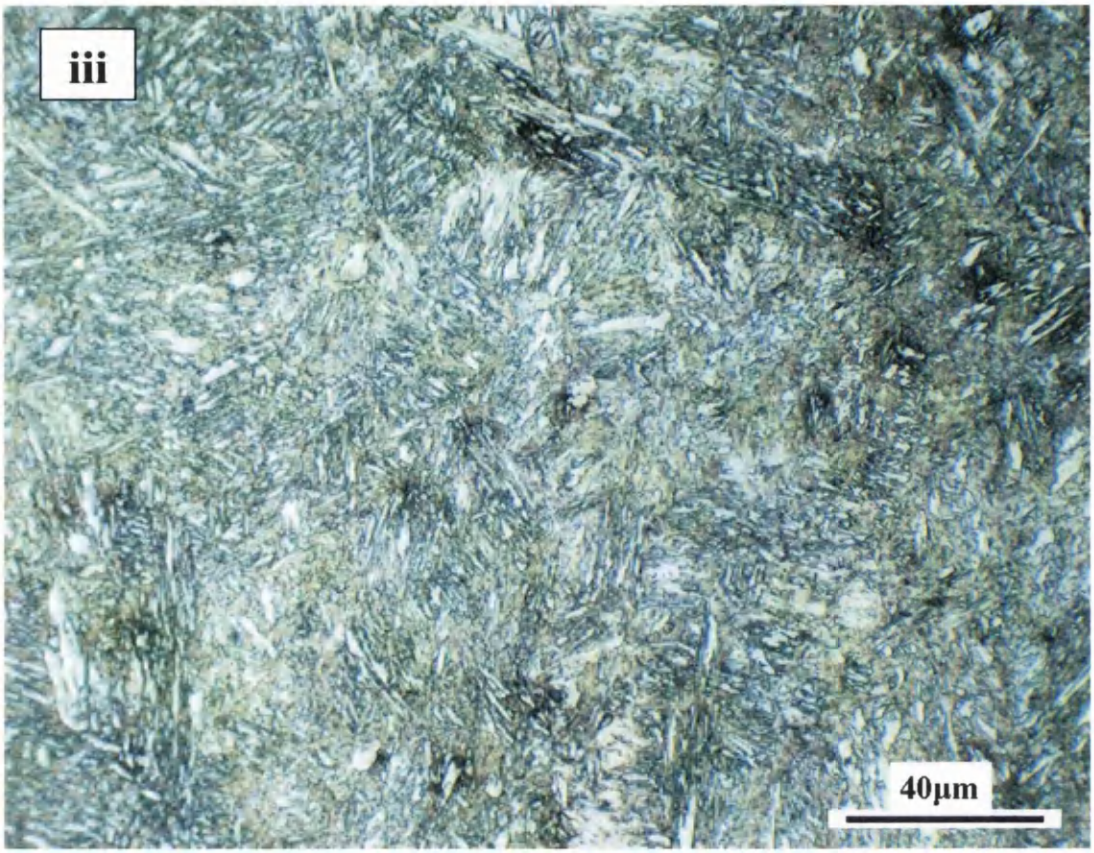

Figure 5.95c Micrograph showing microstructure of weld at position (iii) in figure 5.94

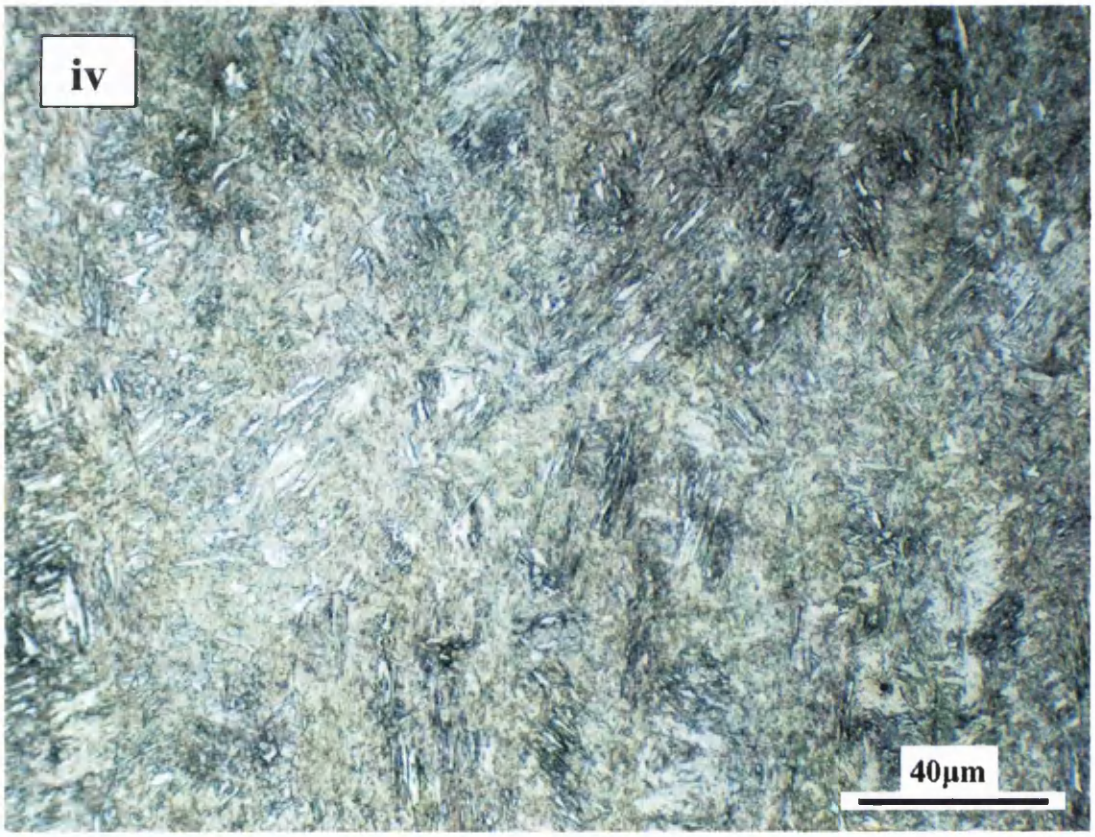

Figure 5.95d Micrograph showing microstructure of weld at position (iv) in figure 5.94

Figure 5.95e Micrograph showing microstructure of weld at position (v) in figure 5.94

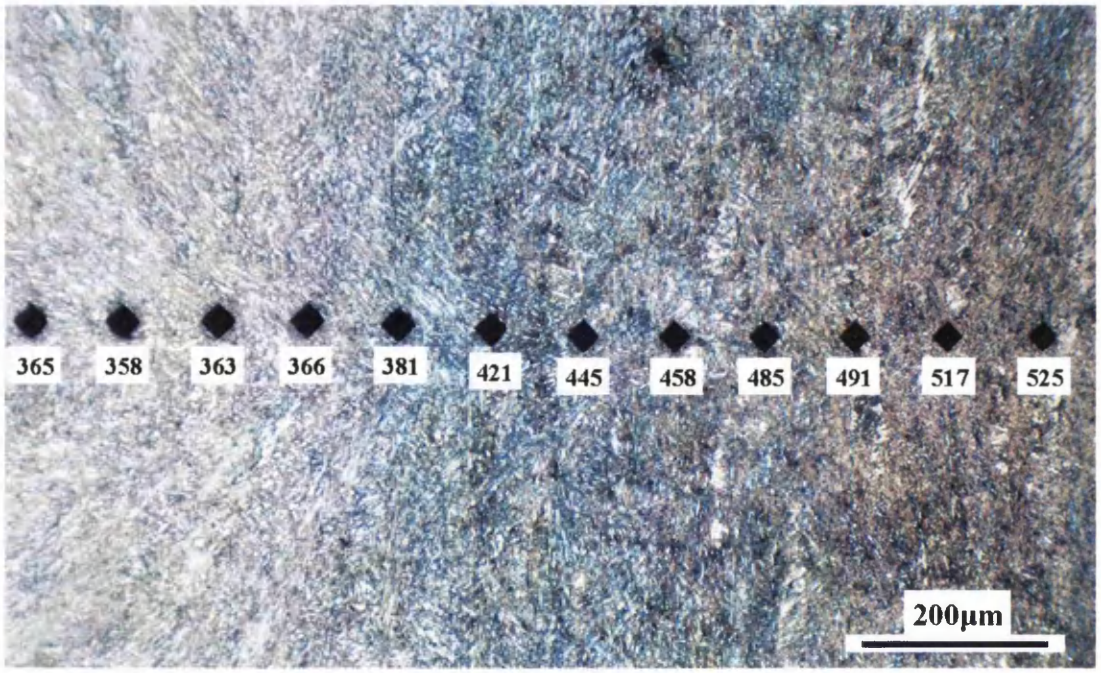

Figure 5.96 Micrograph illustrating variations in microhardness ($HV_{0.3}$) traversing the microstructures observed within the TRIP800 weld nugget treated with a 4.44kA secondary current pulse

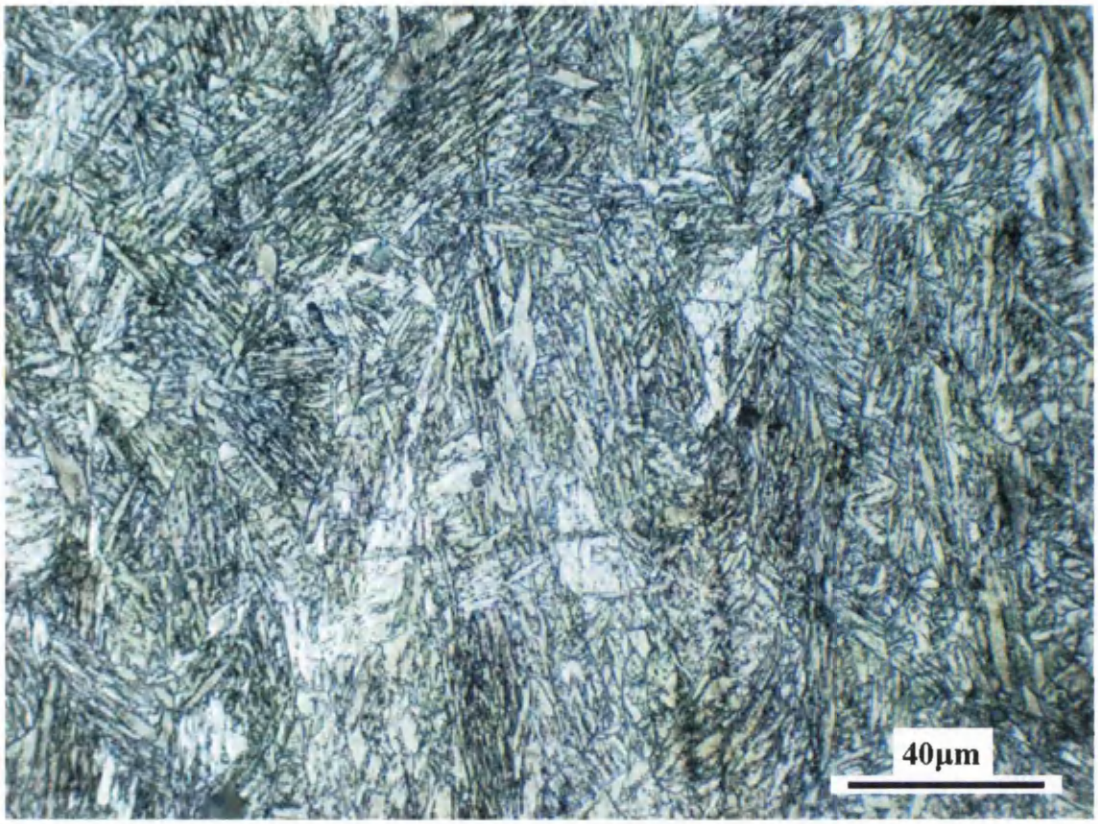

Figure 5.97 Micrograph showing microstructure in DP800 weld nugget treated with a 4.91kA secondary current pulse

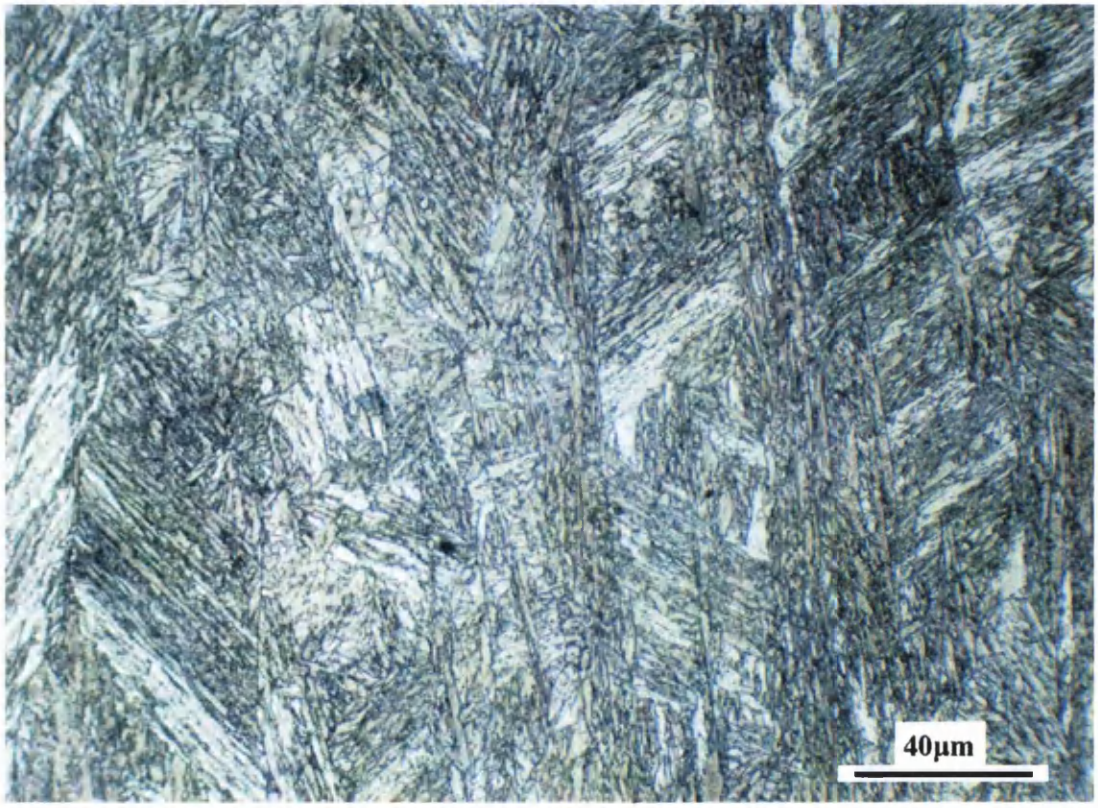

Figure 5.98 Micrograph showing microstructure in DP1000 weld nugget treated with a 5.21kA secondary current pulse

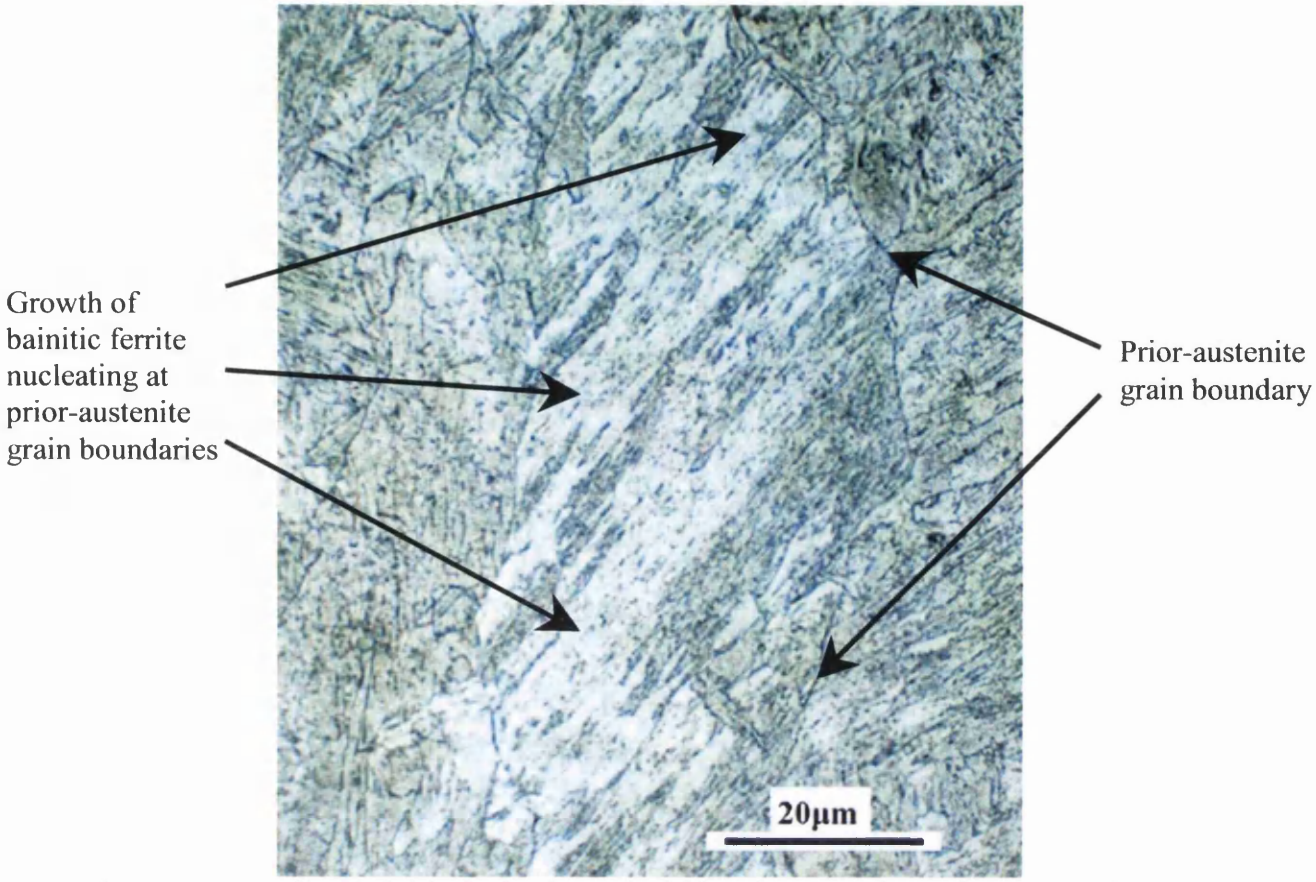

Figure 5.99 Detail of bainitic ferrite formed within prior austenite grain structure in DP1000 weld nugget treated with 5.21kA secondary current pulse

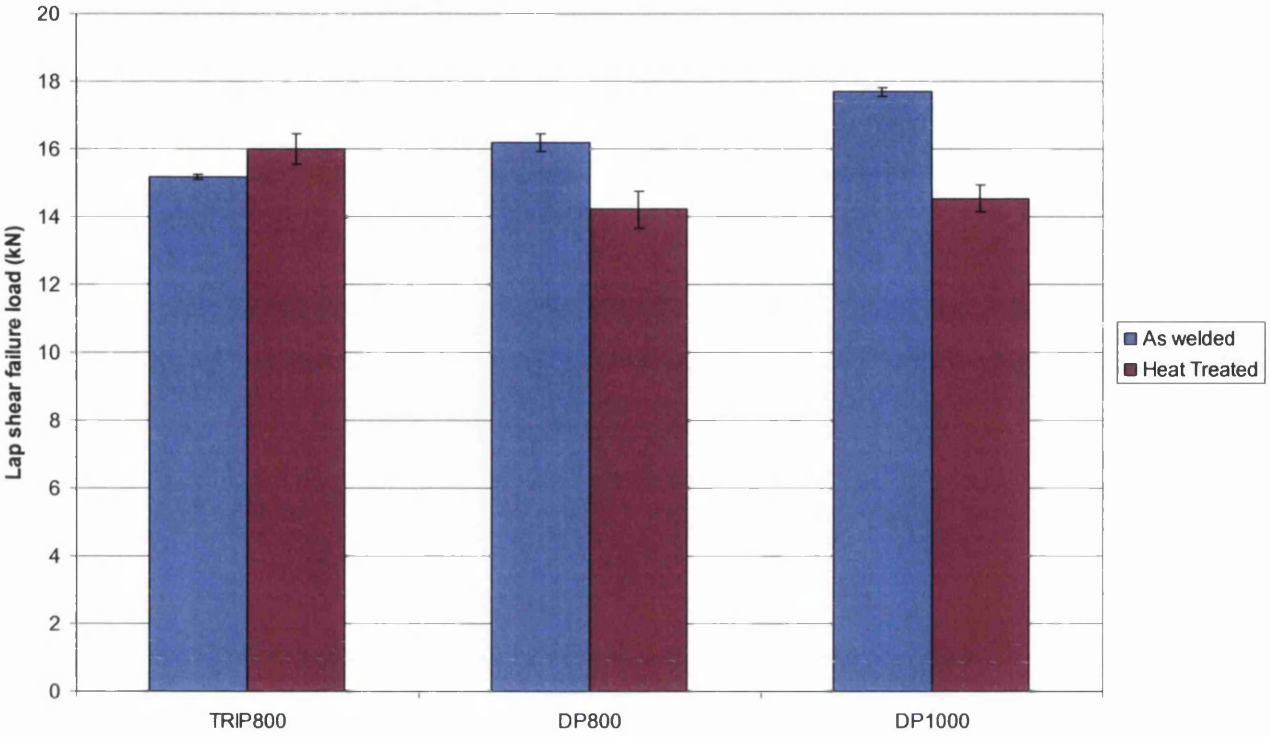

Figure 5.100 Effect of optimum heat treatments on average lap shear failure load sustained by 5√t welds formed in TRIP800, DP800 and DP1000. Error bars indicate one standard deviation from the mean

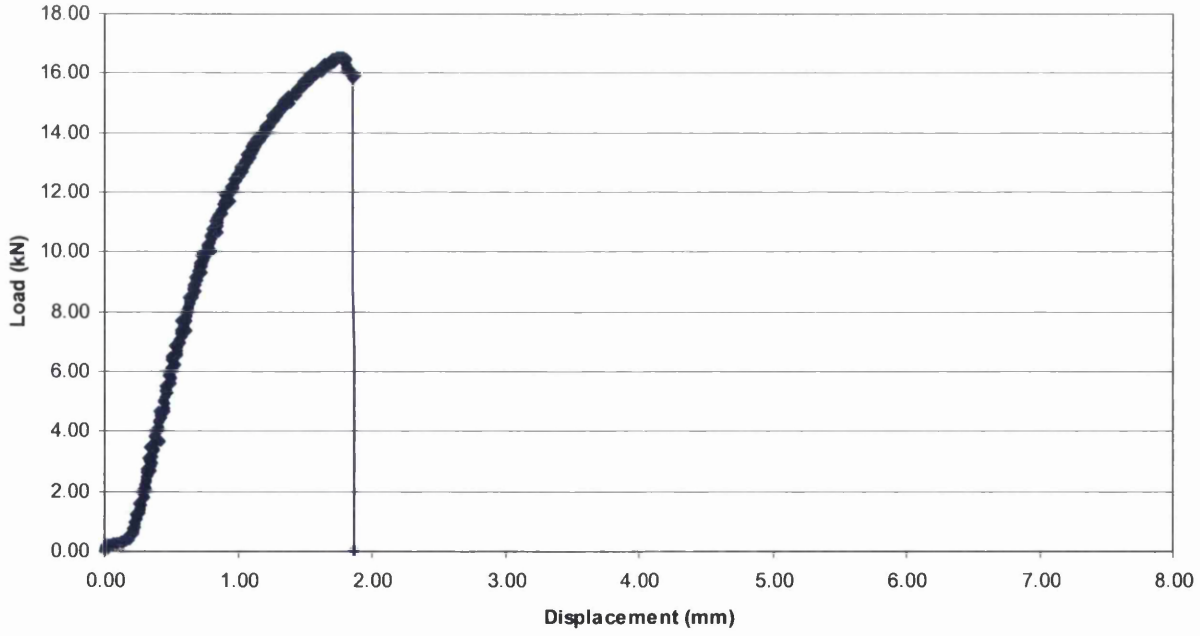

Figure 5.101 Typical lap shear load vs. displacement curve exhibited by heat treated 5√t welds formed in 1.2mm TRIP800

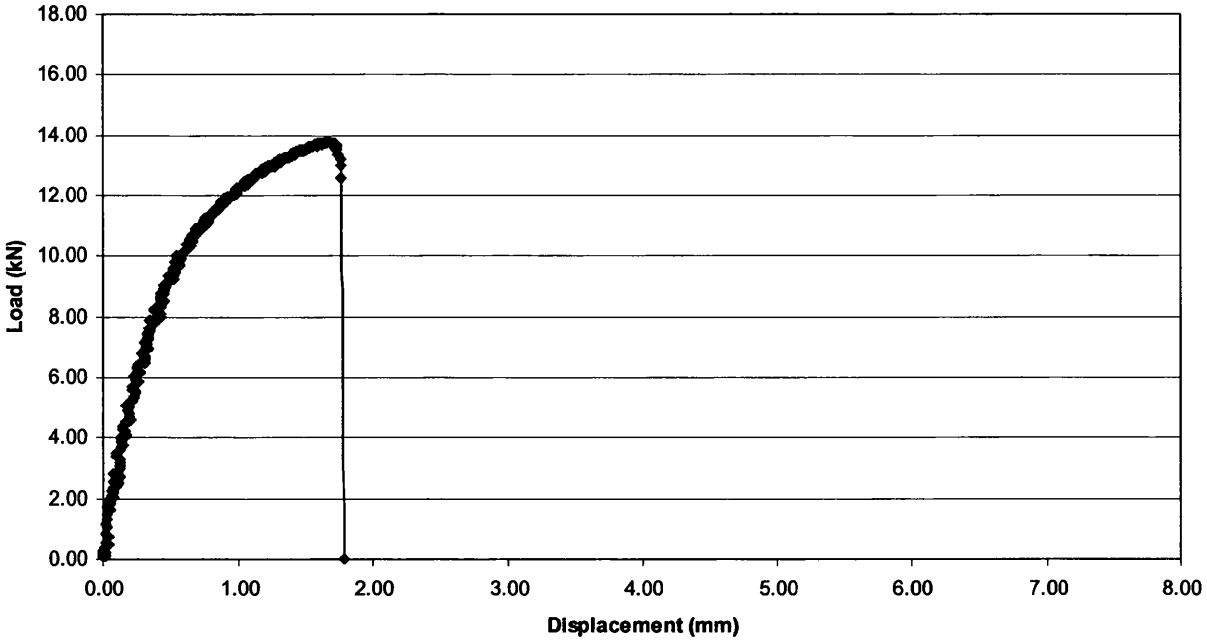

Figure 5.102 Typical lap shear load vs. displacement curve exhibited by heat treated $5\sqrt{t}$ welds formed in 1.2mm DP800

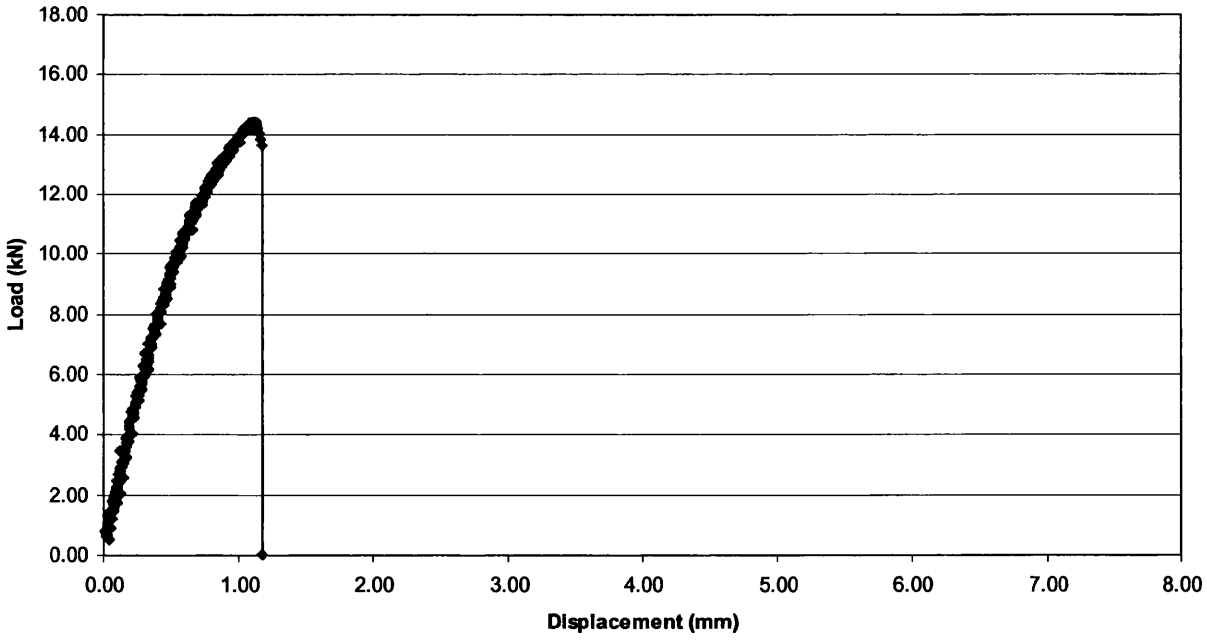

Figure 5.103 Typical lap shear load vs. displacement curve exhibited by heat treated $5\sqrt{t}$ welds formed in 1.2mm DP1000

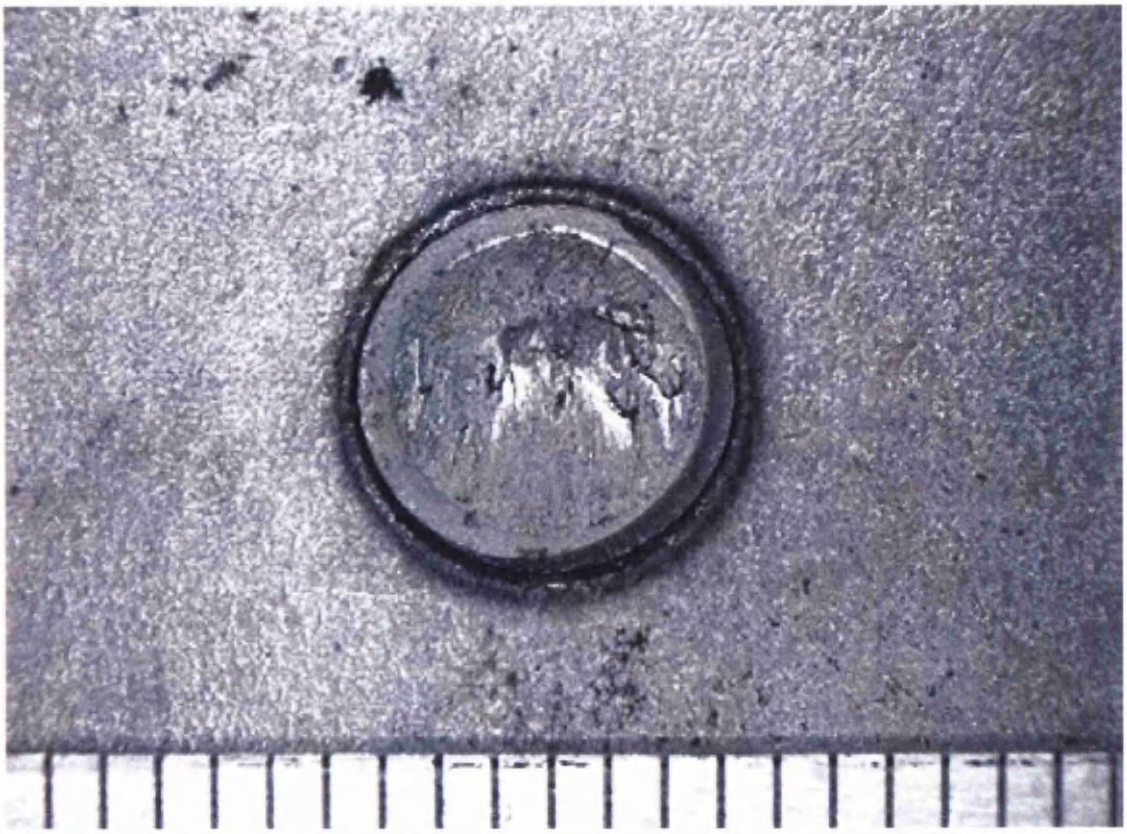

Figure 5.104 Typical lap shear failure mode exhibited by heat treated TRIP800 spot welds (Scale is in mm)

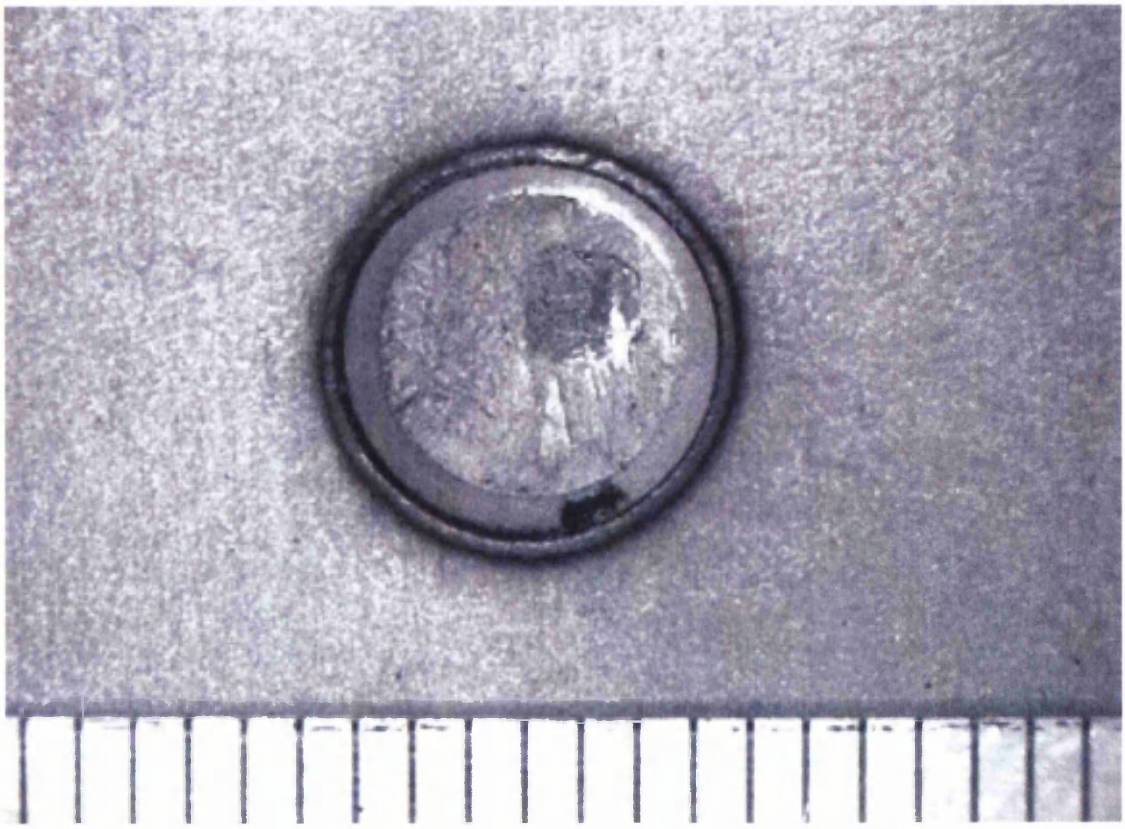

Figure 5.105 Typical lap shear failure mode exhibited by heat treated DP800 spot welds (Scale is in mm)

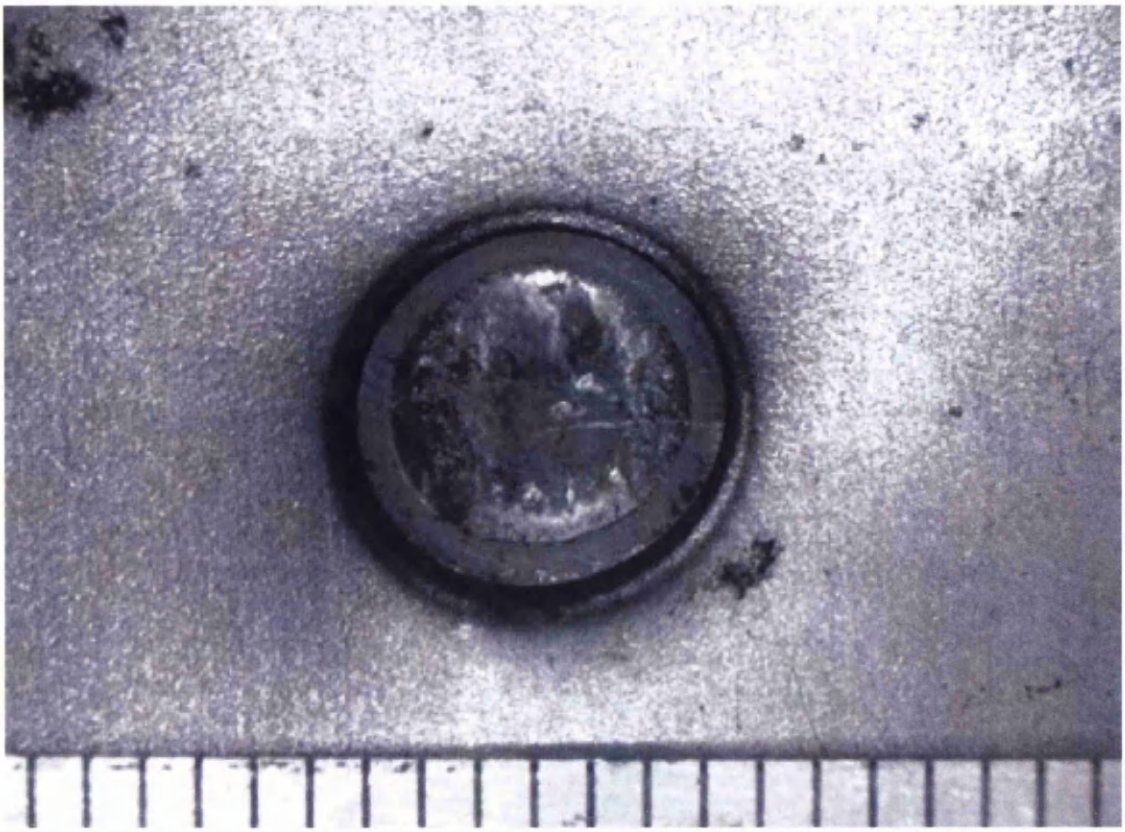

Figure 5.106 Typical lap shear failure mode exhibited by heat treated DP1000 spot welds (Scale is in mm)

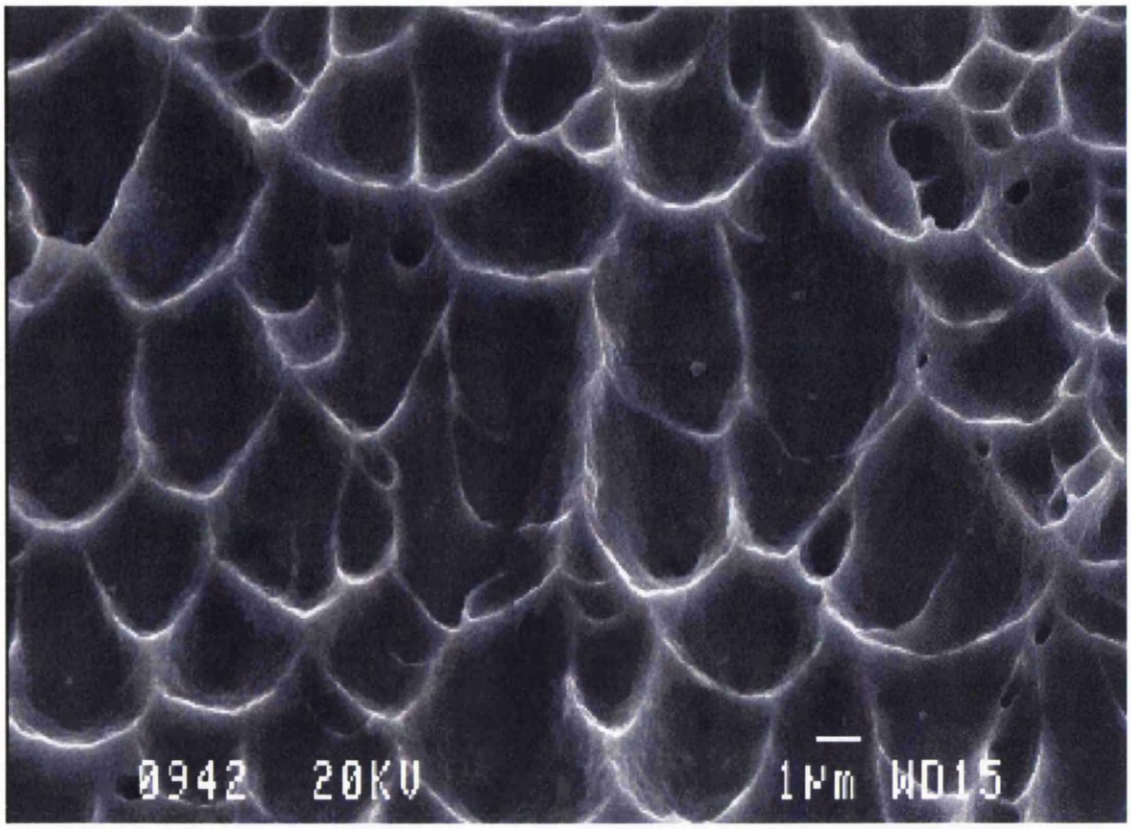

Figure 5.107 SEM image of interfacial fracture surface in heat treated TRIP800 lap shear sample

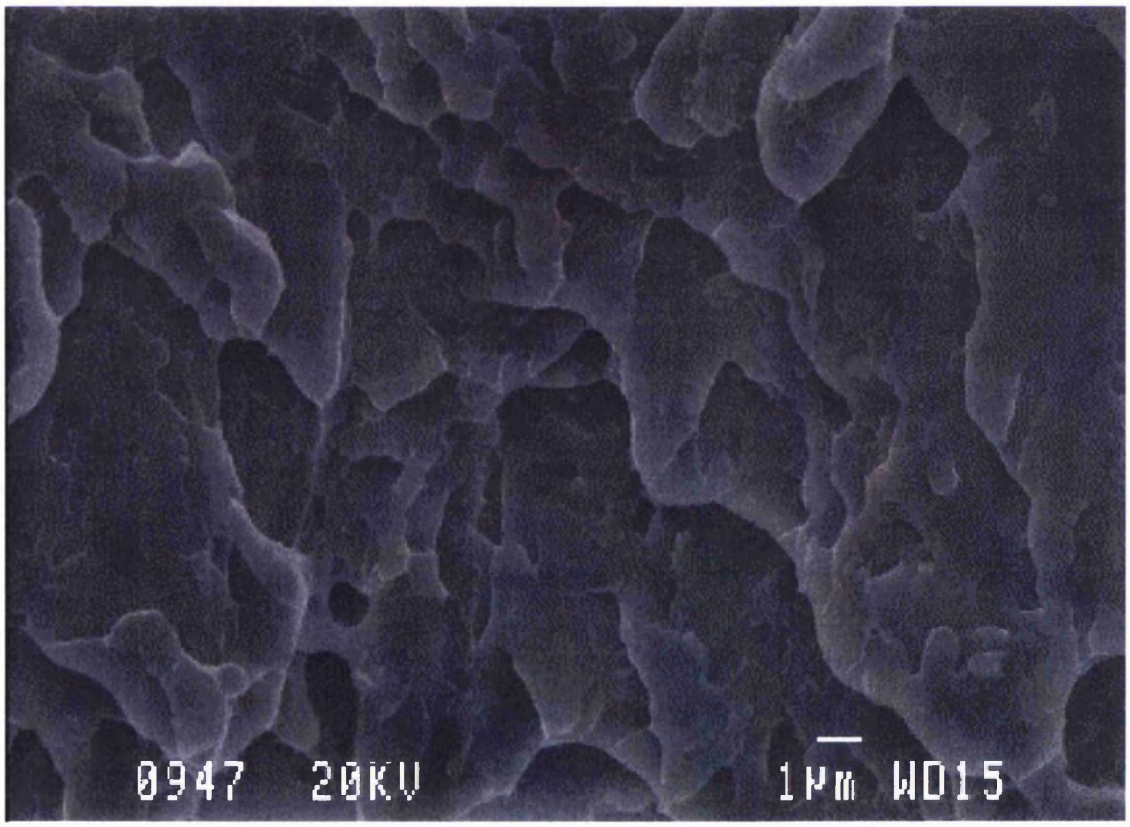

Figure 5.108 SEM image of interfacial fracture surface in heat treated DP800 lap shear sample

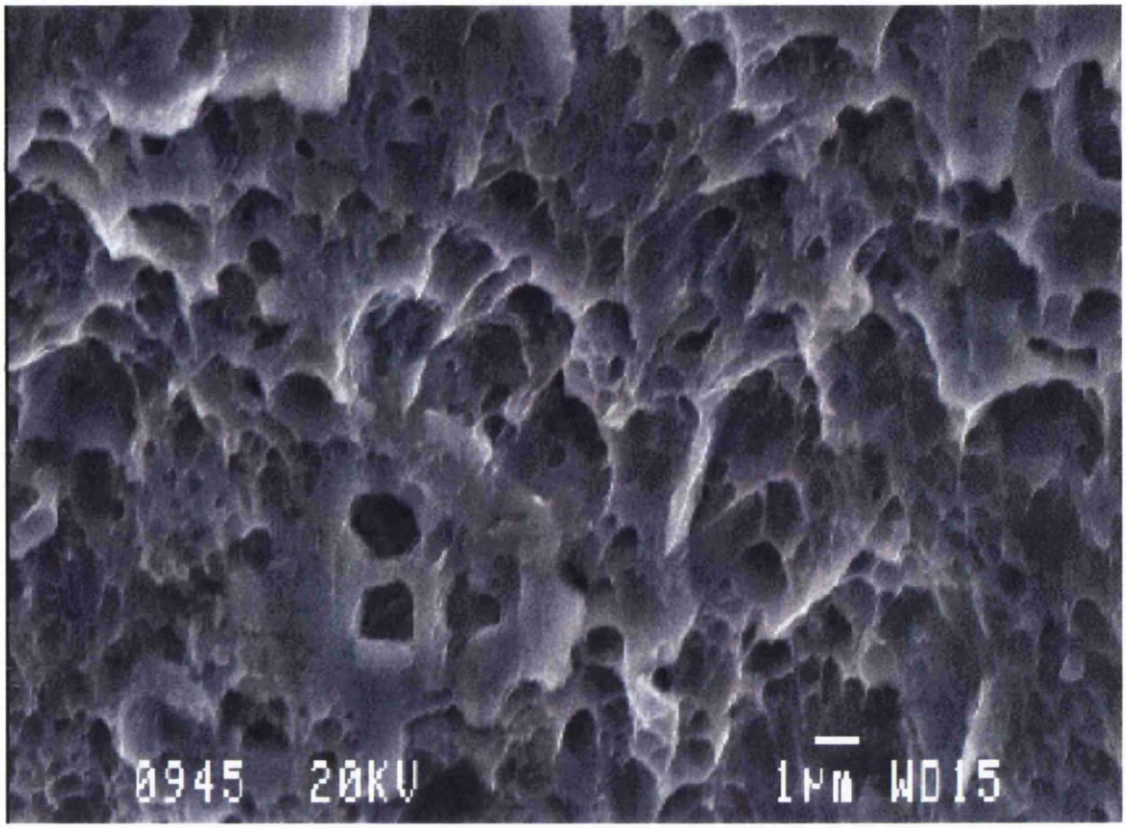

Figure 5.109 SEM image of interfacial fracture surface in heat treated DP1000 lap shear sample

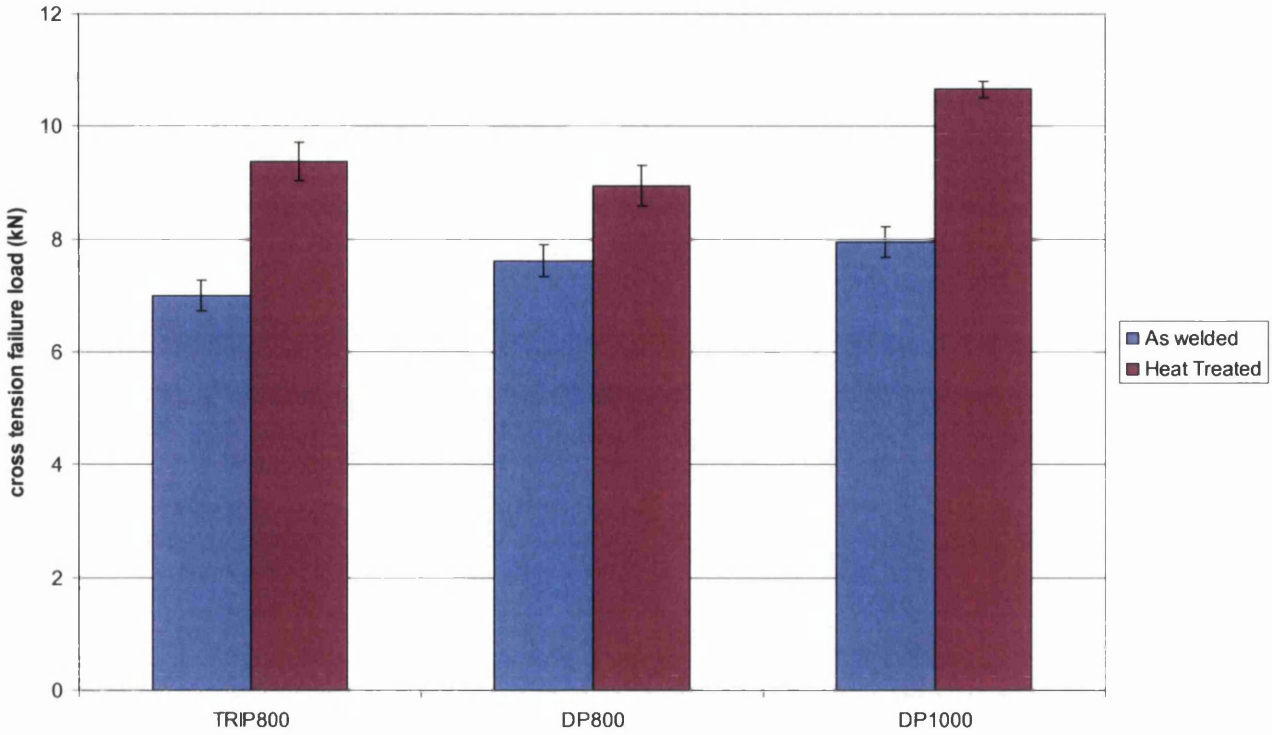

Figure 5.110 Effect of optimum heat treatments on average cross tension failure loads sustained by $5\sqrt{t}$ welds formed in TRIP800, DP800 and DP1000. Error bars indicate one standard deviation from the mean

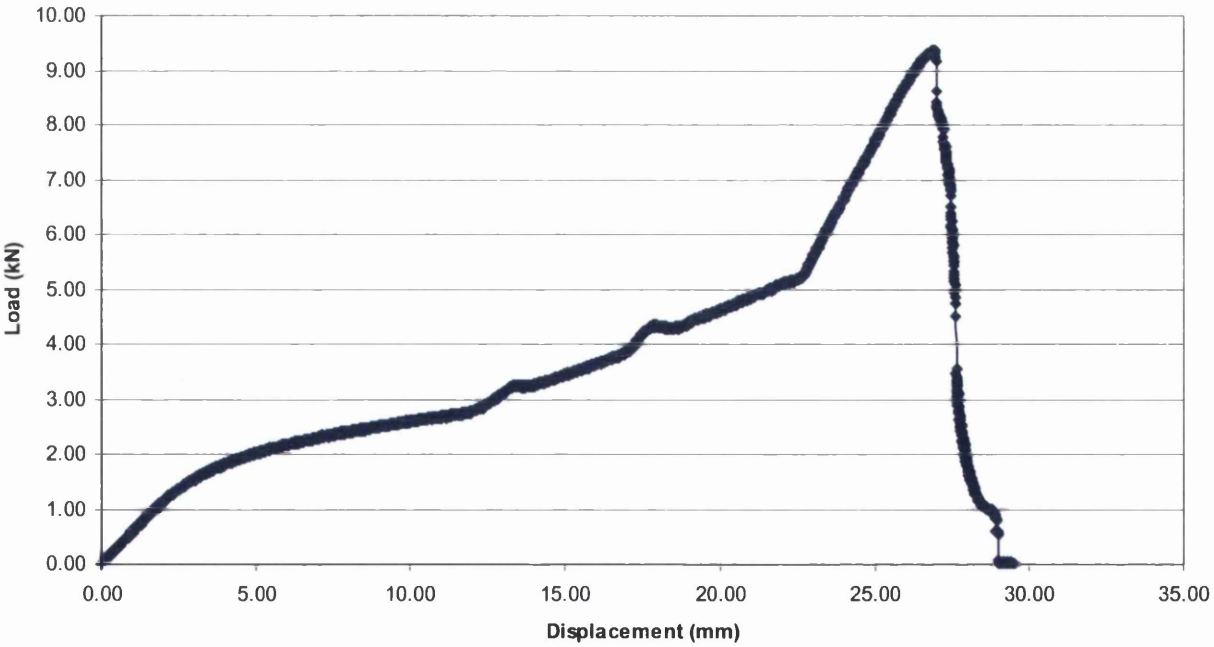

Figure 5.111 Typical cross tension load vs. displacement curve exhibited by heat treated $5\sqrt{t}$ welds formed in 1.2mm TRIP800

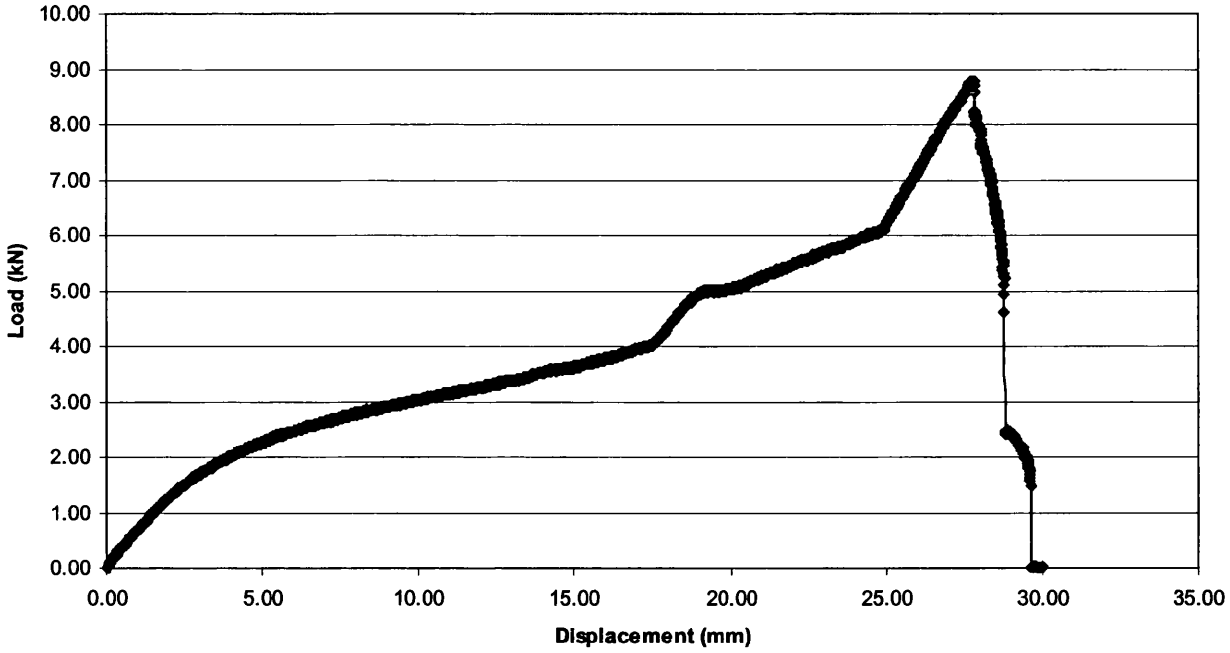

Figure 5.112 Typical cross tension load vs. displacement curve exhibited by heat treated $5\sqrt{t}$ welds formed in 1.2mm DP800

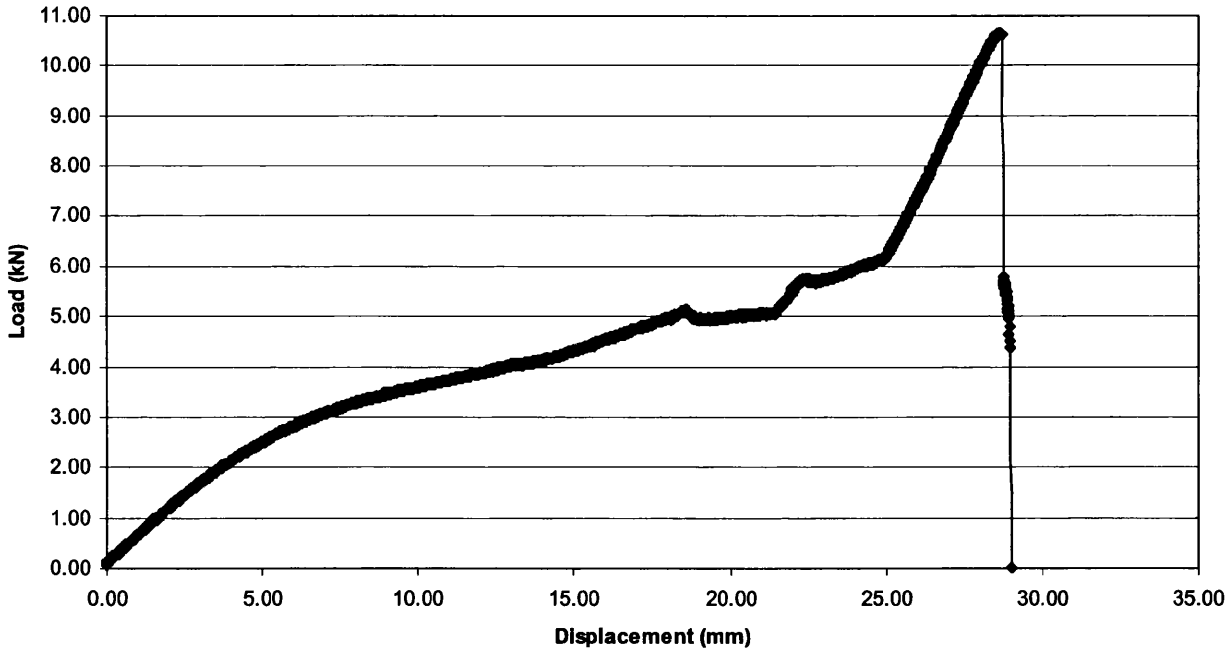

Figure 5.113 Typical cross tension load vs. displacement curve exhibited by heat treated $5\sqrt{t}$ welds formed in 1.2mm DP1000

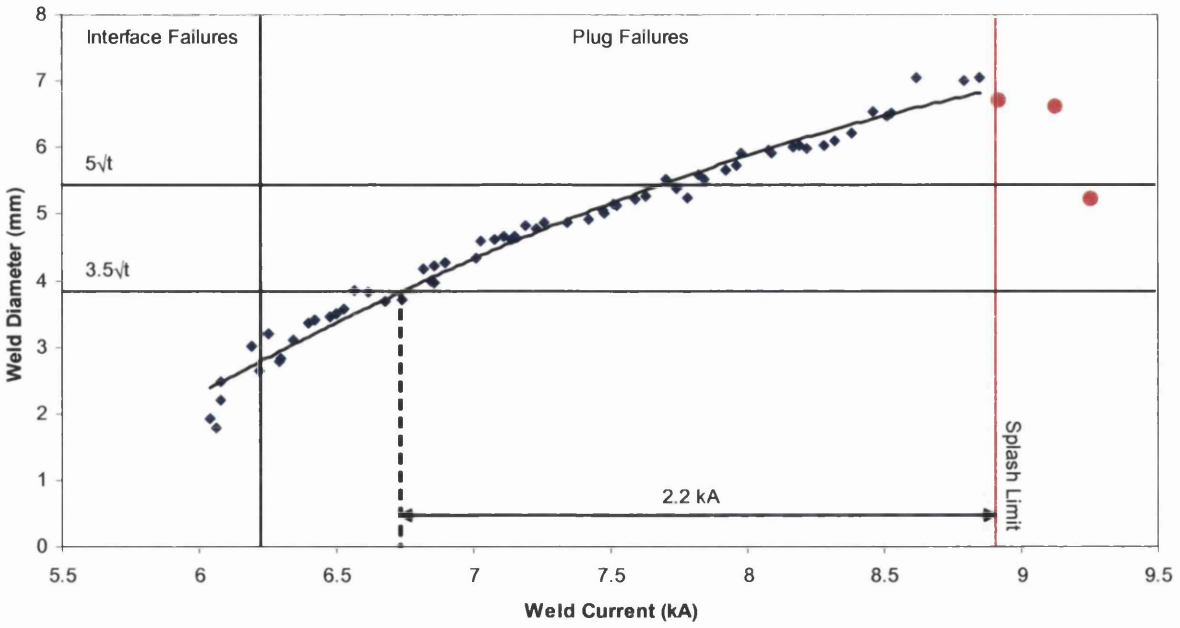

Figure 5.114 Relationship between weld current and weld diameter for 1.2mm DP800 to 1.15mm LC joint (3.2kN electrode force)

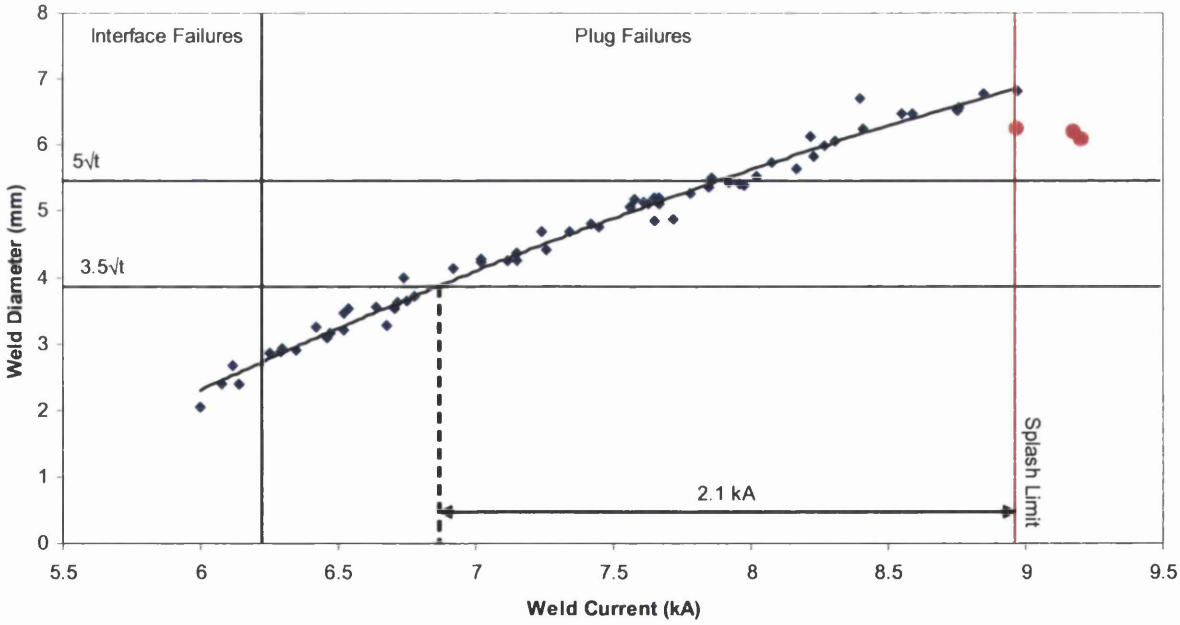

Figure 5.115 Relationship between weld current and weld diameter for 1.2mm DP1000 to 1.15mm LC joint (3.2kN electrode force)

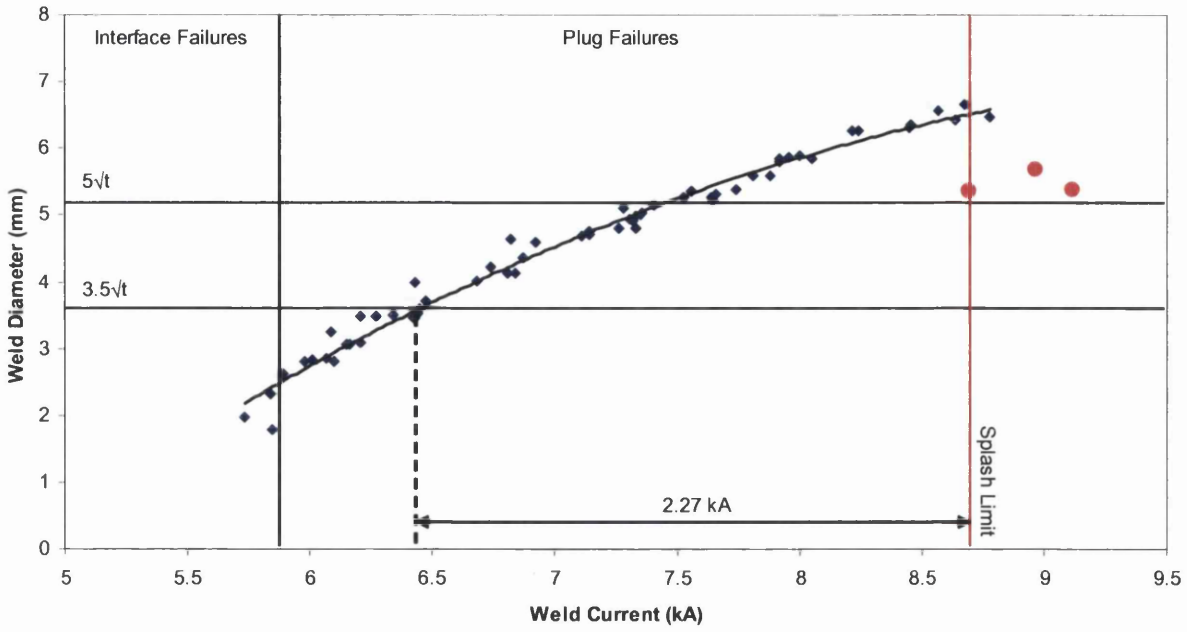

Figure 5.116 Relationship between weld current and weld diameter for 1.0mm MS1400 to 1.15mm LC joint (3.2kN electrode force)

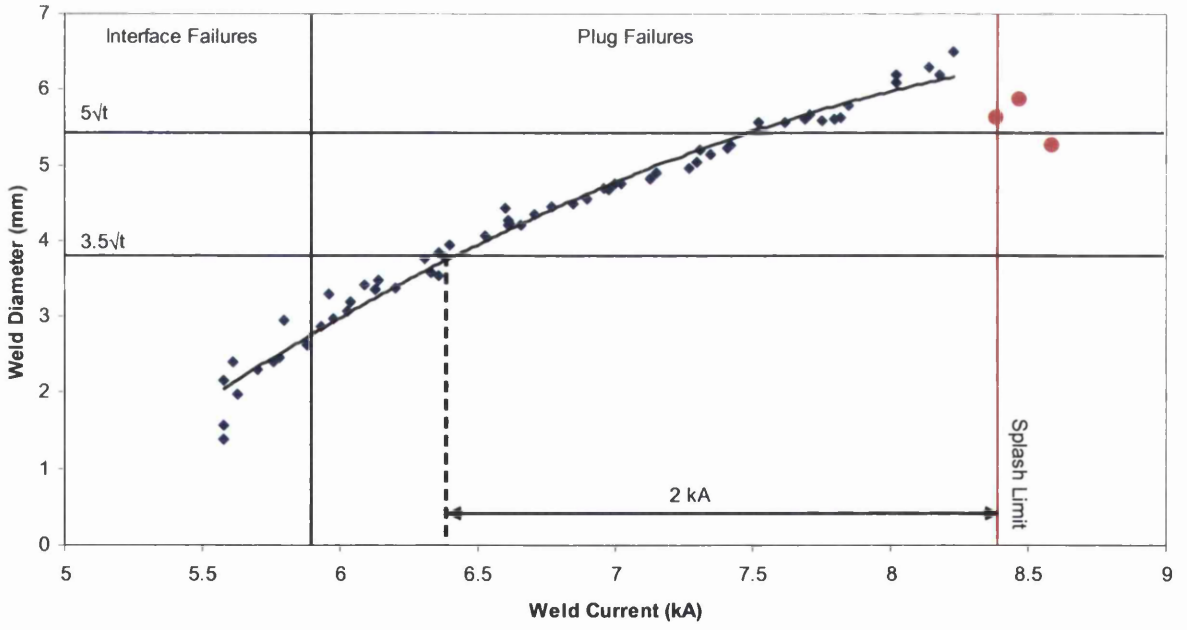

Figure 5.117 Relationship between weld current and weld diameter for 1.2mm TRIP800 to 1.15mm LC joint (3.2kN electrode force)

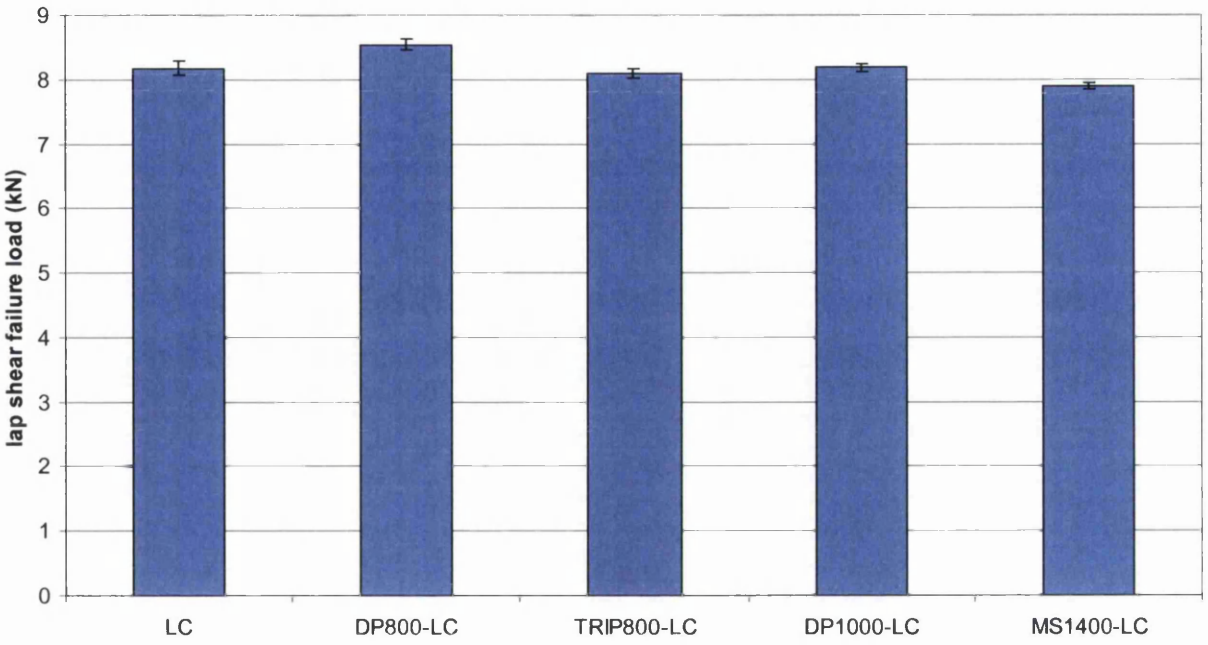

Figure 5.118 Summary of average lap shear failure loads sustained by $5\sqrt{t}$ welds formed in low carbon (LC) mild steel and between selected advanced high strength steels and LC. Error bars indicate one standard deviation from the mean

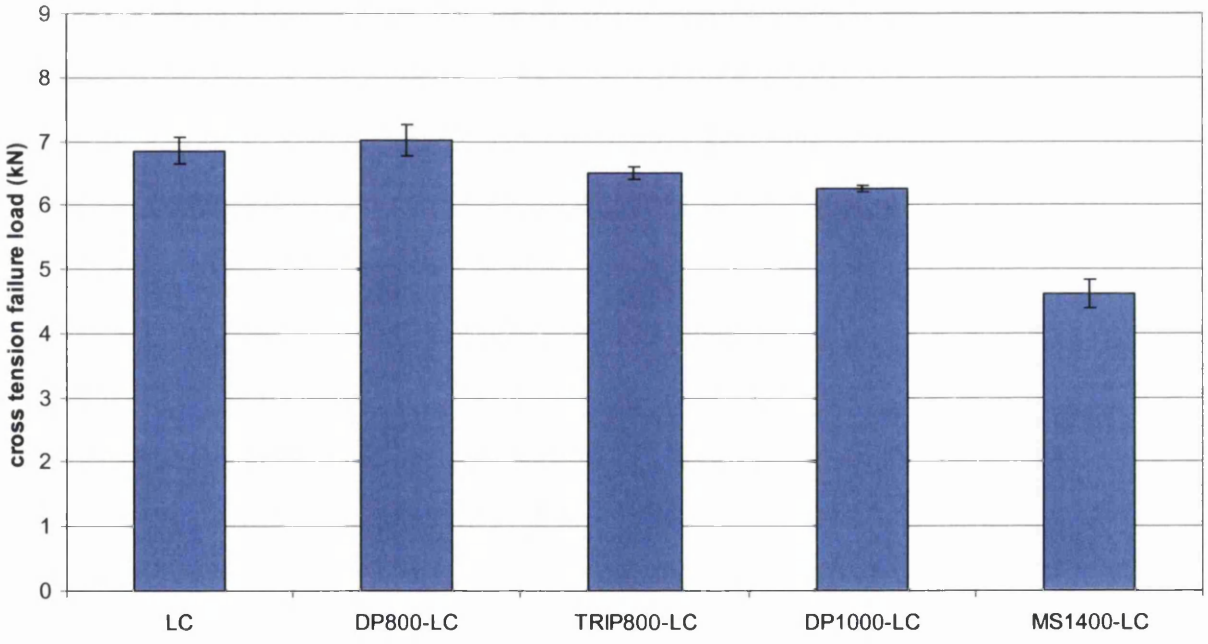

Figure 5.119 Summary of average cross tension failure loads sustained by $5\sqrt{t}$ welds formed in low carbon (LC) mild steel and between selected advanced high strength steels and LC. Error bars indicate one standard deviation from the mean

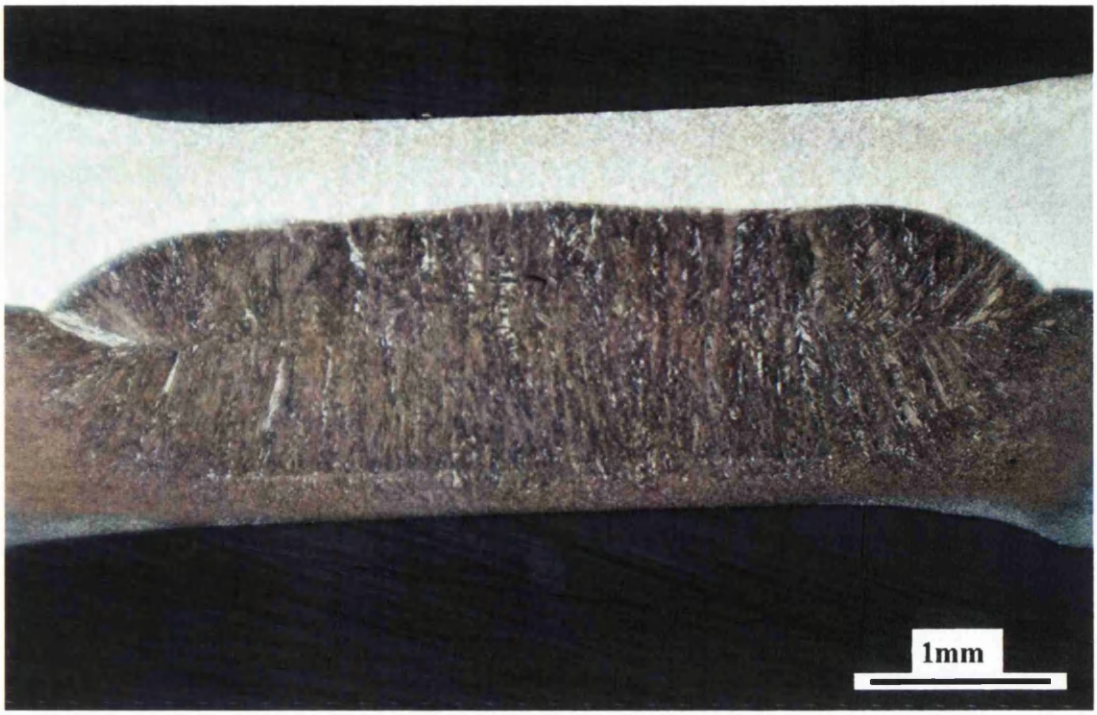

Figure 5.120a Macro of weld nugget formed between DP800 and LC

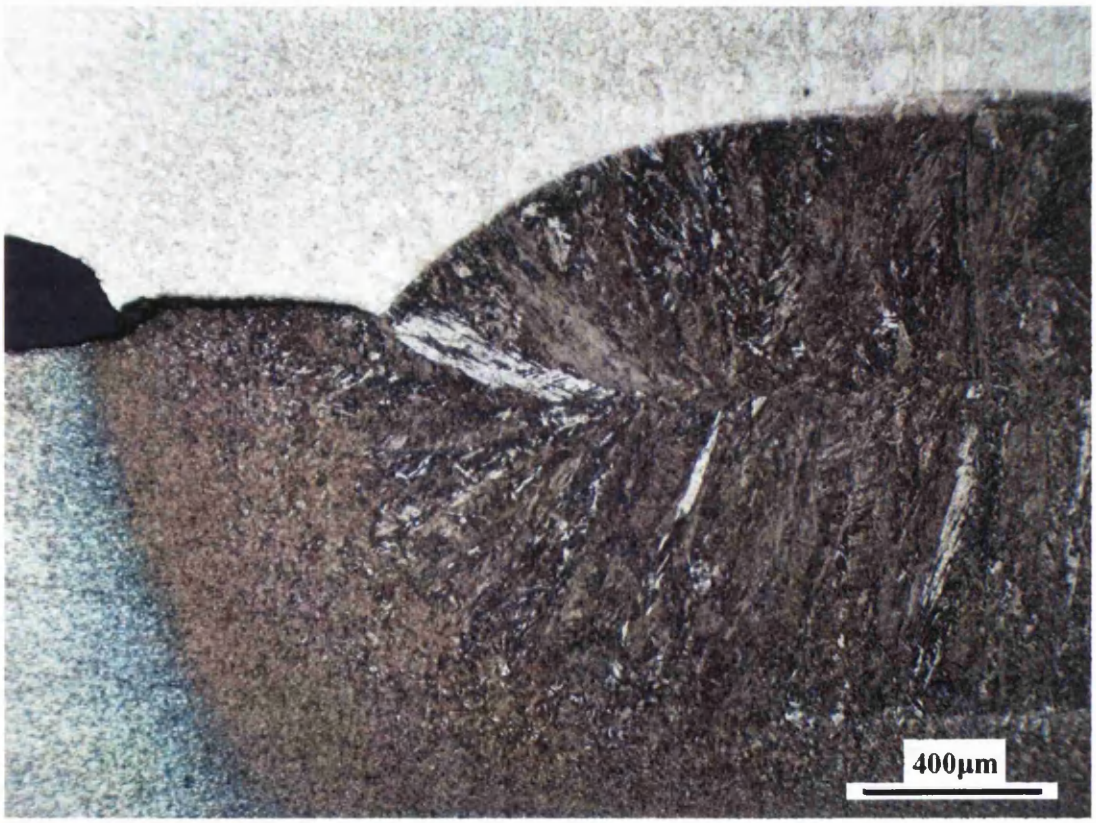

Figure 5.120b Micrograph illustrating the variation in microstructure from parent metal to weld nugget in DP800 to LC joint

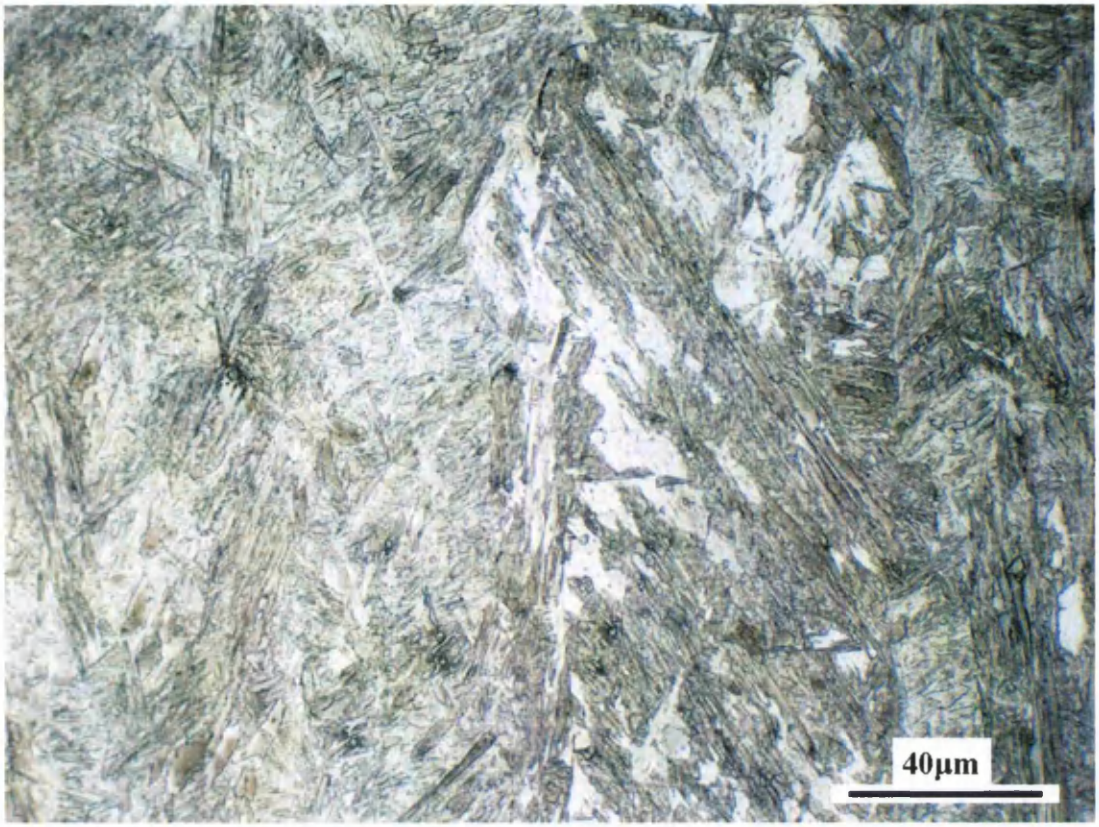

Figure 5.120c Micrograph showing microstructure of weld nugget formed between DP800 and LC

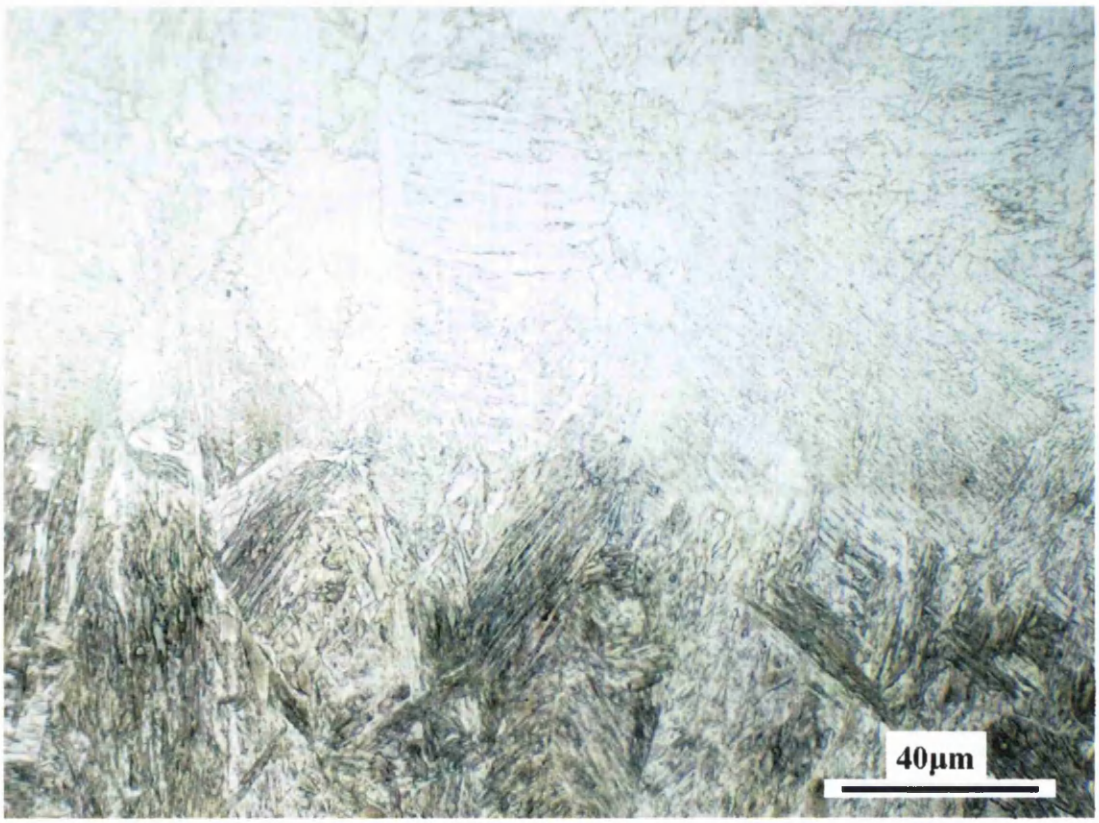

Figure 5.120d Micrograph showing transition in microstructure from weld nugget to LC heat affected zone in DP800 to LC joint

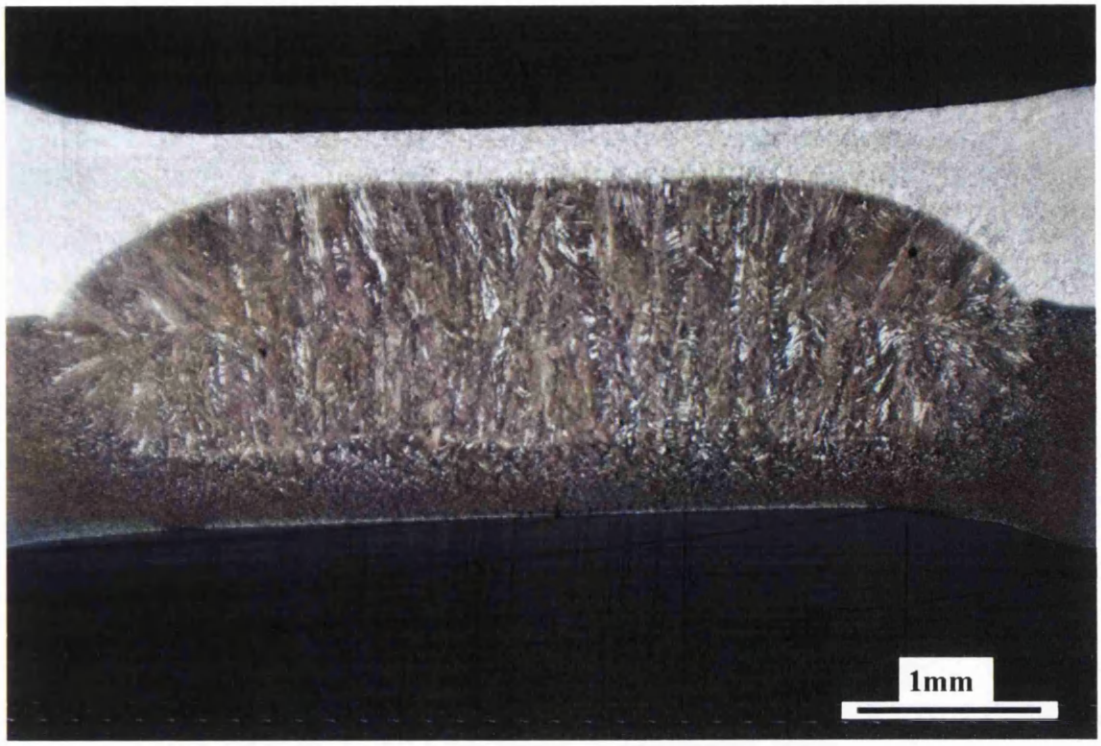

Figure 5.121a Macro of weld nugget formed between DP1000 and LC

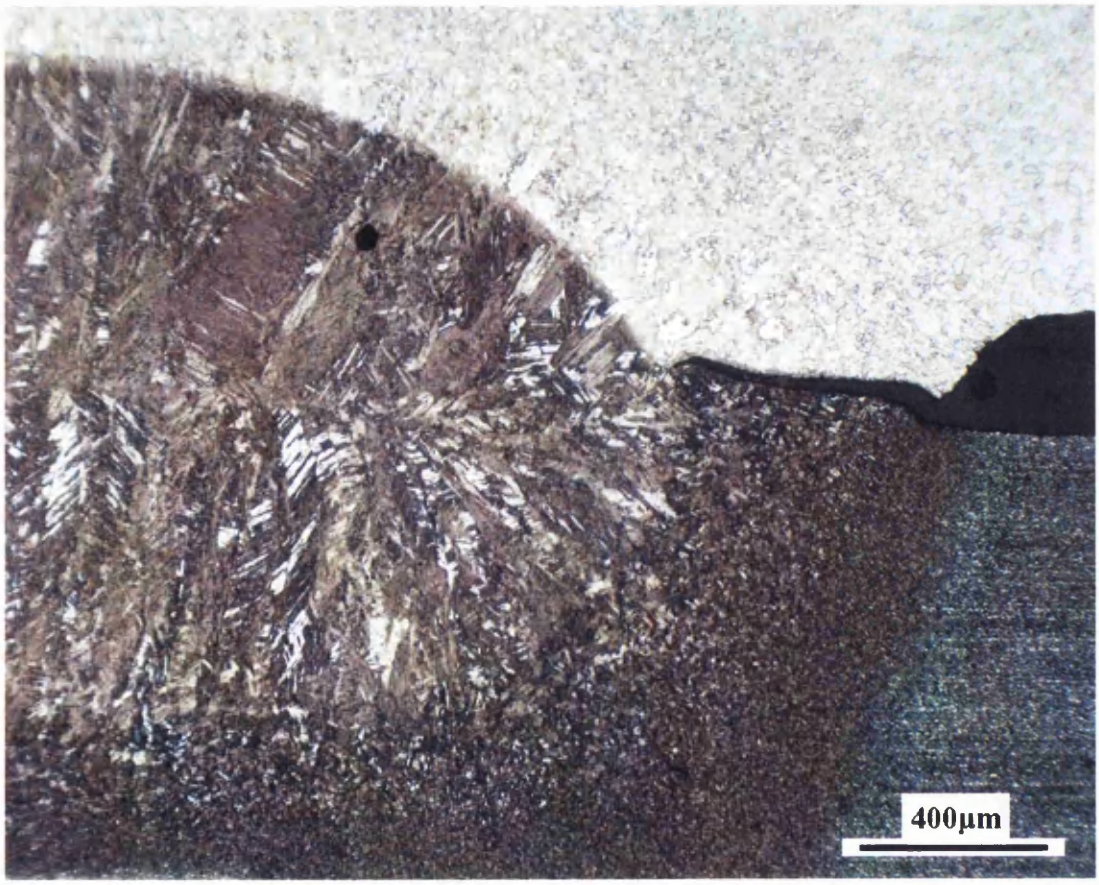

Figure 5.121b Micrograph illustrating the variation in microstructure from parent metal to weld nugget in DP1000 to LC joint

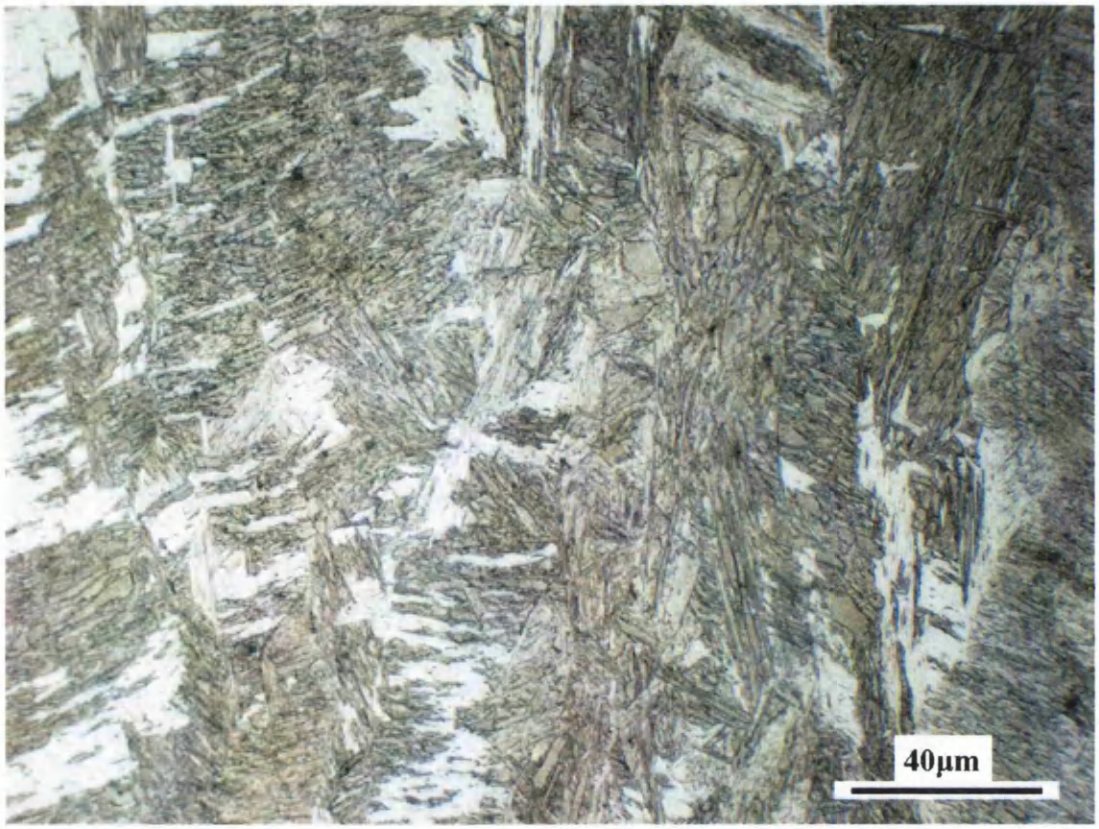

Figure 5.121c Micrograph showing microstructure of weld nugget formed between DP1000 and LC

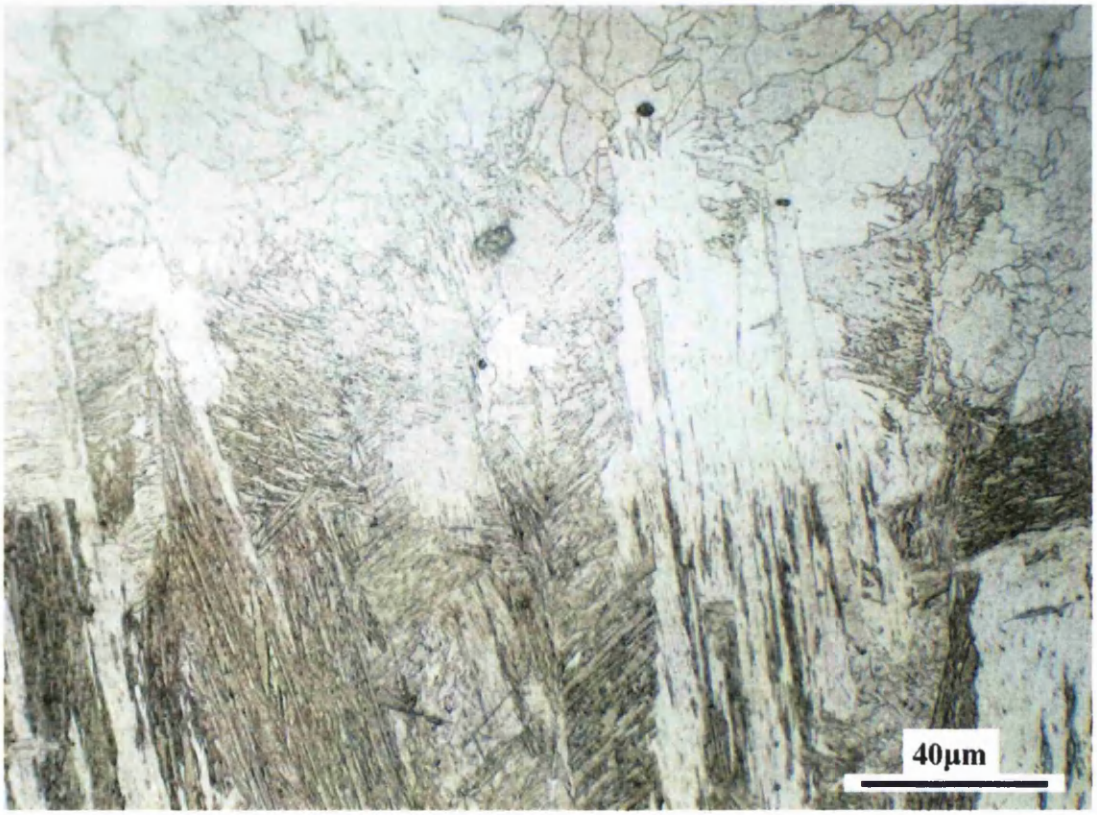

Figure 5.121d Micrograph showing transition in microstructure from weld nugget to LC heat affected zone in DP1000 to LC joint

Figure 5.122a Macro of weld nugget formed between MS1400 and LC

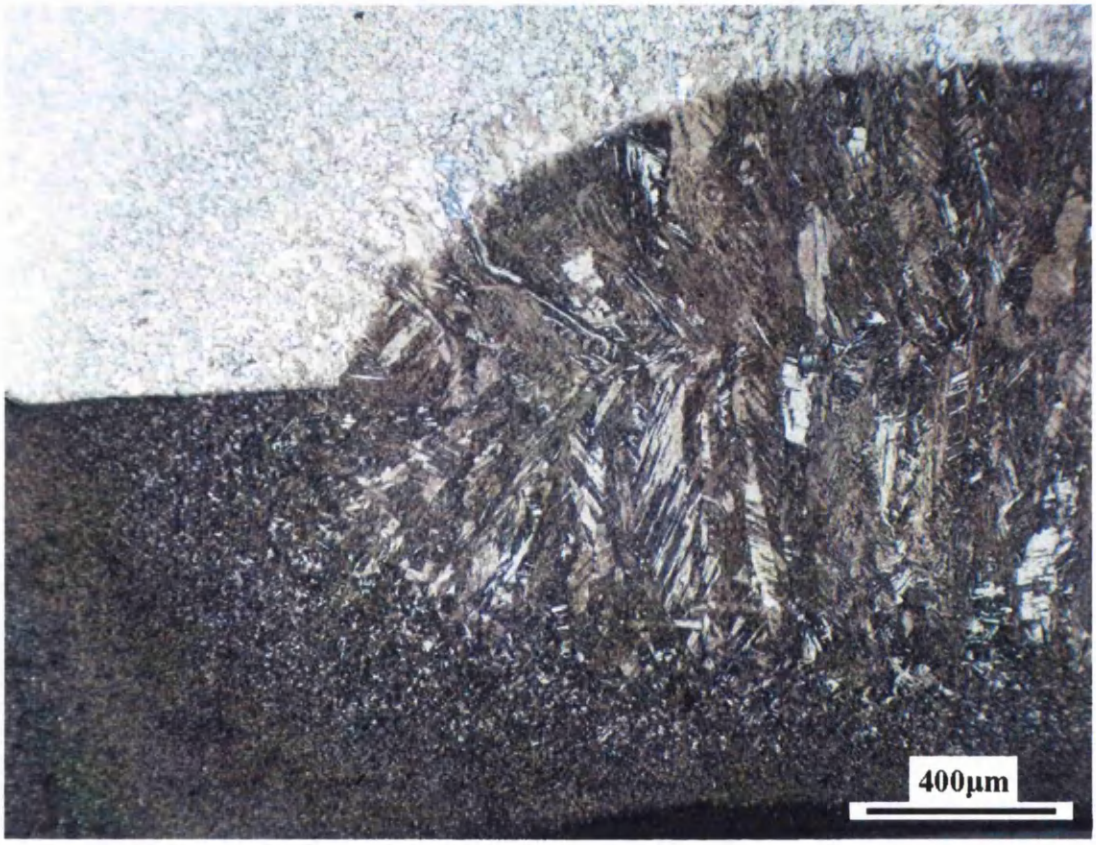

Figure 5.122b Micrograph illustrating the variation in microstructure from parent metal to weld nugget in MS1400 to LC joint

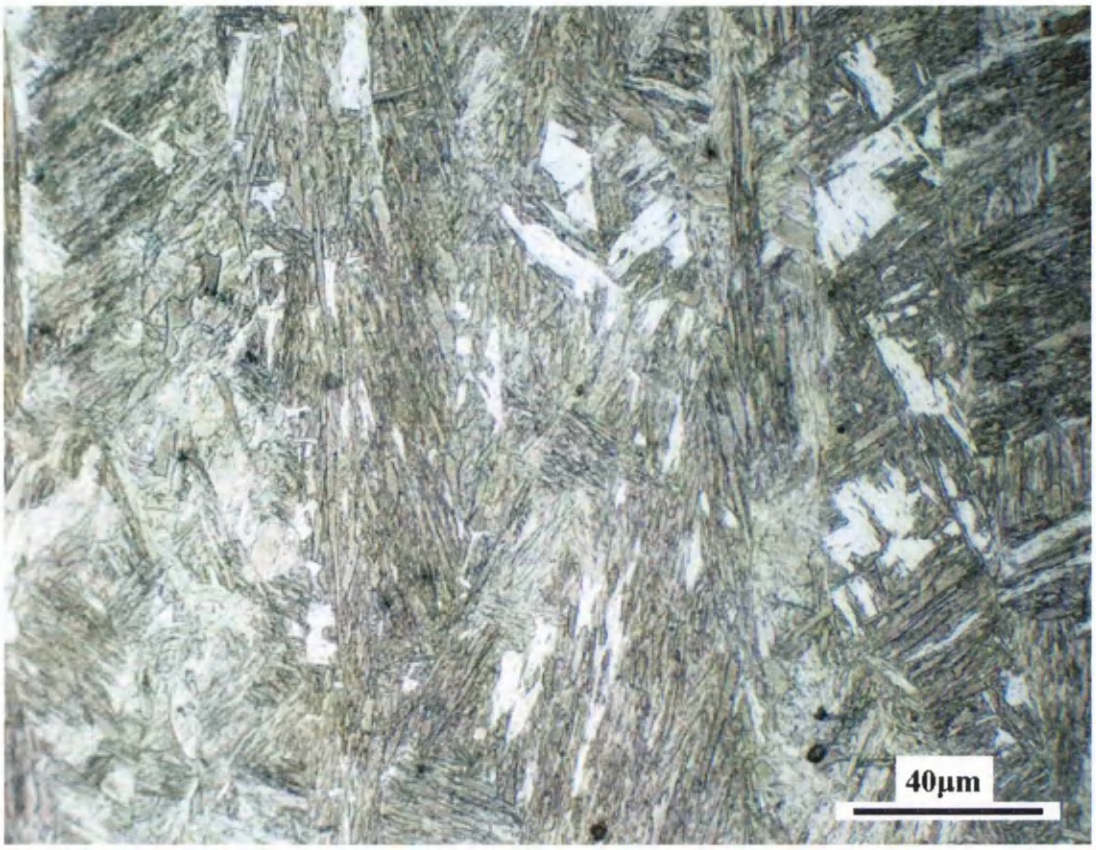

Figure 5.122c Micrograph showing microstructure of weld nugget formed between MS1400 and LC

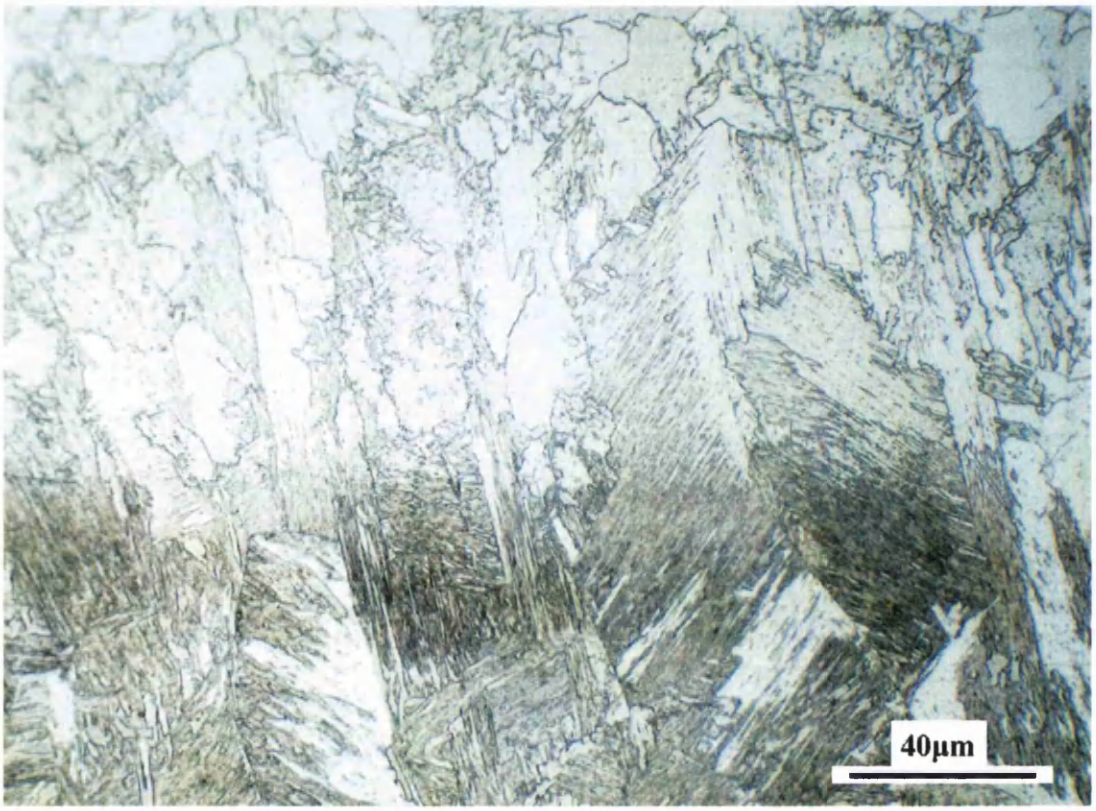

Figure 5.122d Micrograph showing transition in microstructure from weld nugget to LC heat affected zone in MS1400 to LC joint

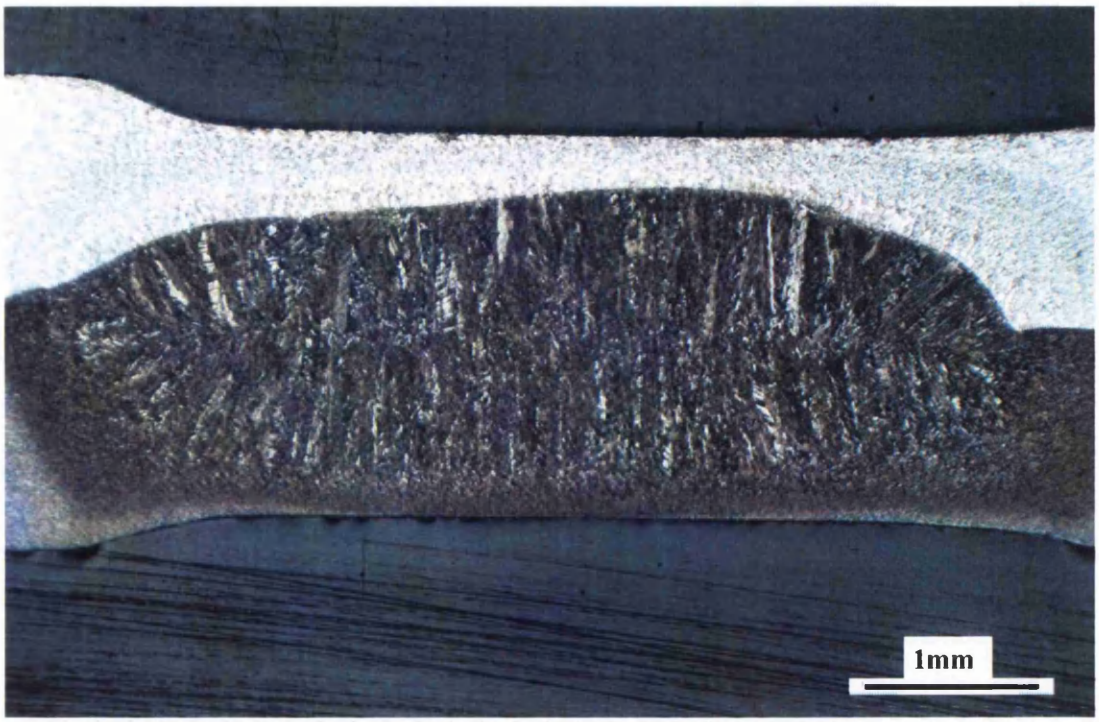

Figure 5.123a Macro of weld nugget formed between TRIP800 and LC

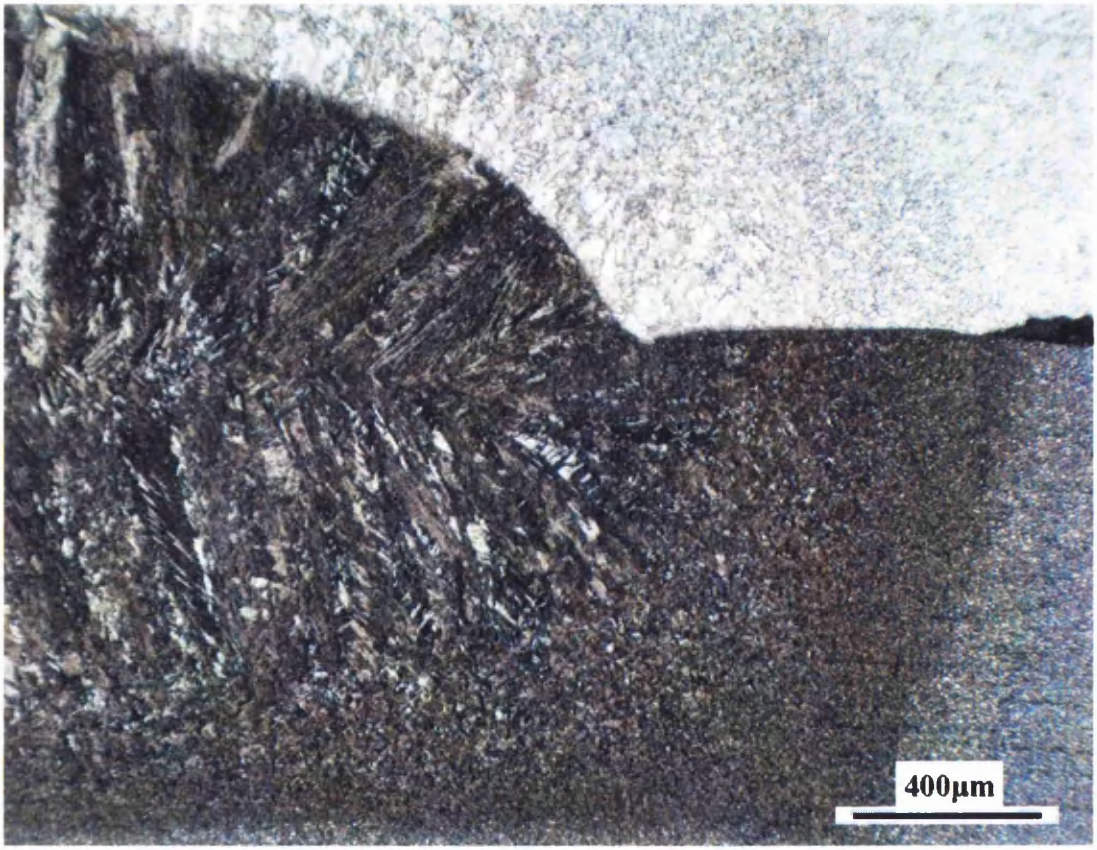

Figure 5.123b Micrograph illustrating the variation in microstructure from parent metal to weld nugget in TRIP800 to LC joint

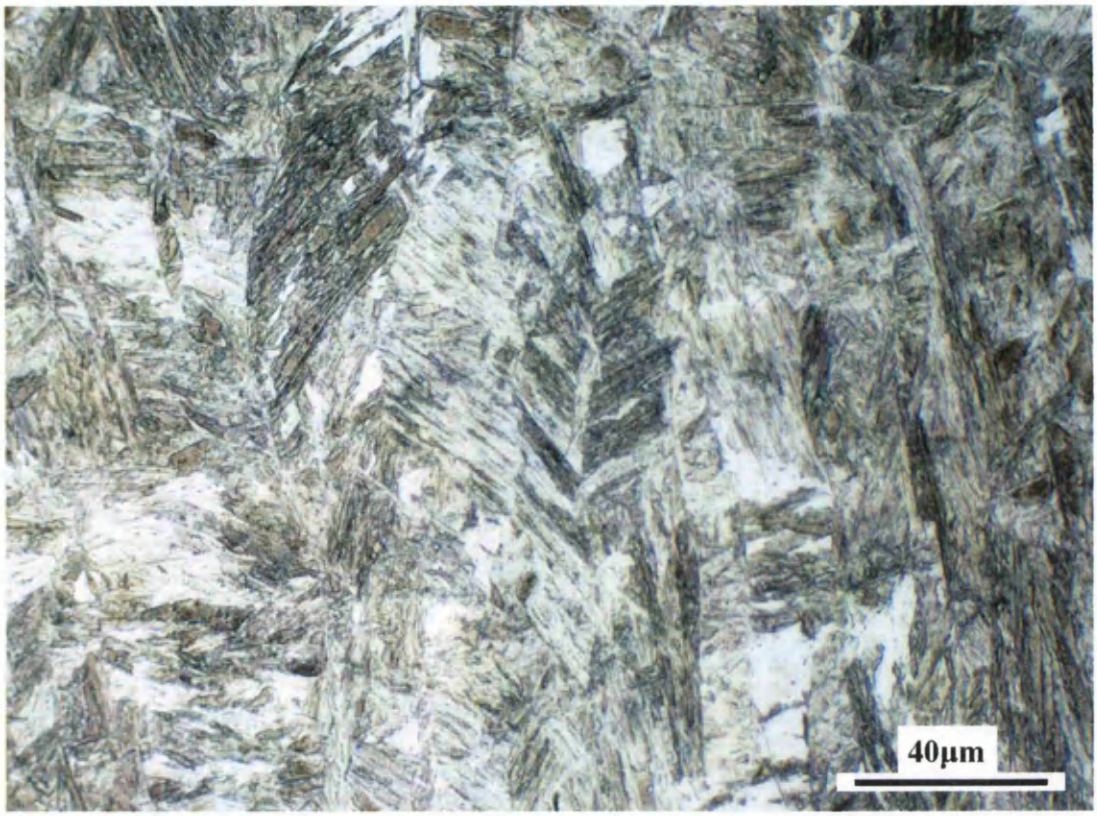

Figure 5.123c Micrograph showing microstructure of weld nugget formed between TRIP800 and LC

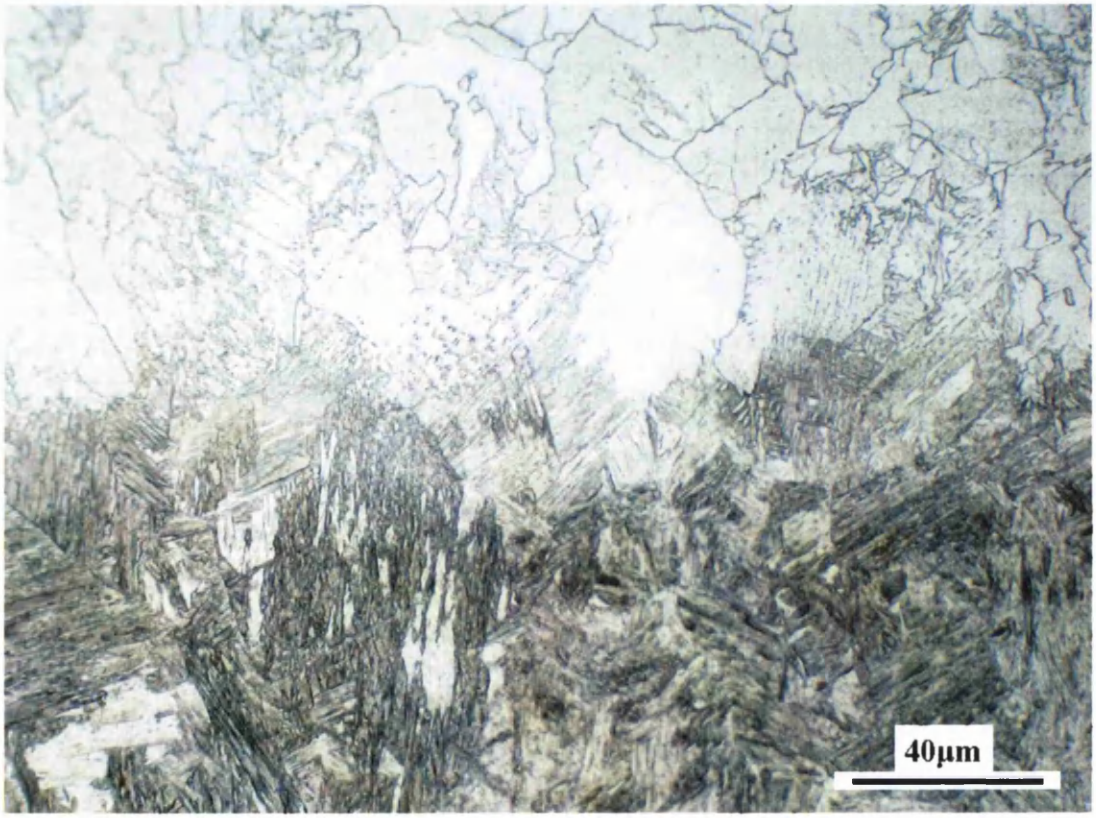

Figure 5.123d Micrograph showing transition in microstructure from weld nugget to LC heat affected zone in TRIP800 to LC joint

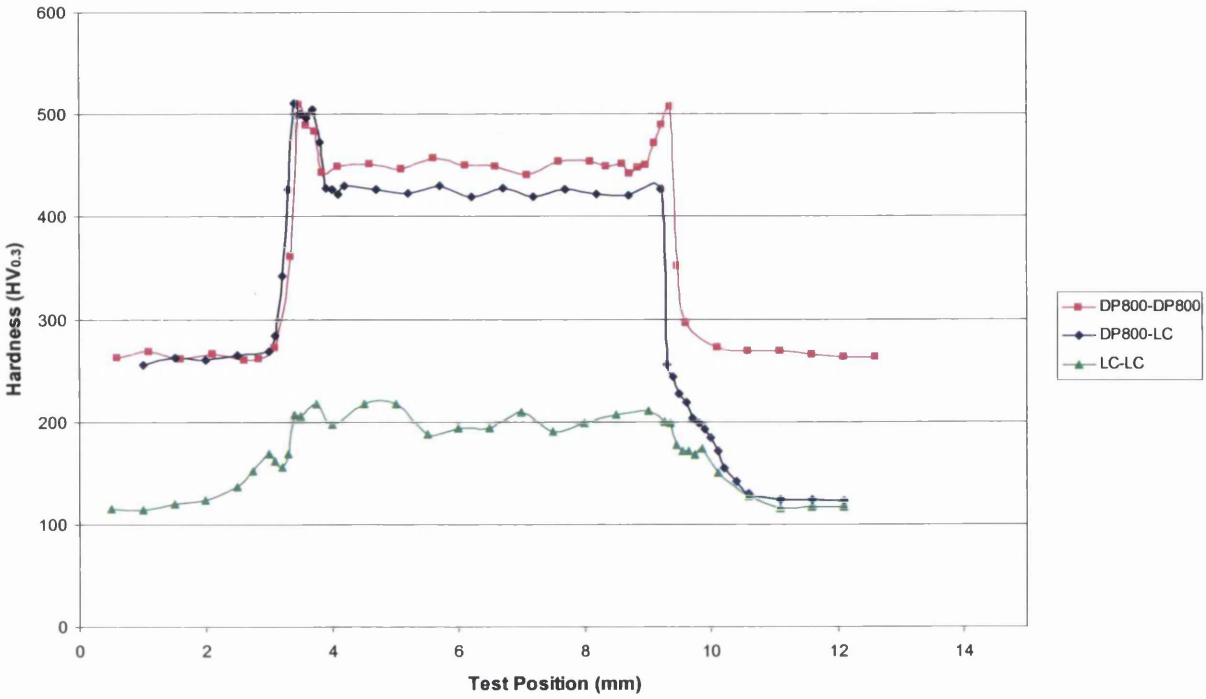

Figure 5.124 Comparison of microhardness profiles across a DP800 weld, a DP800 to LC weld and a LC weld

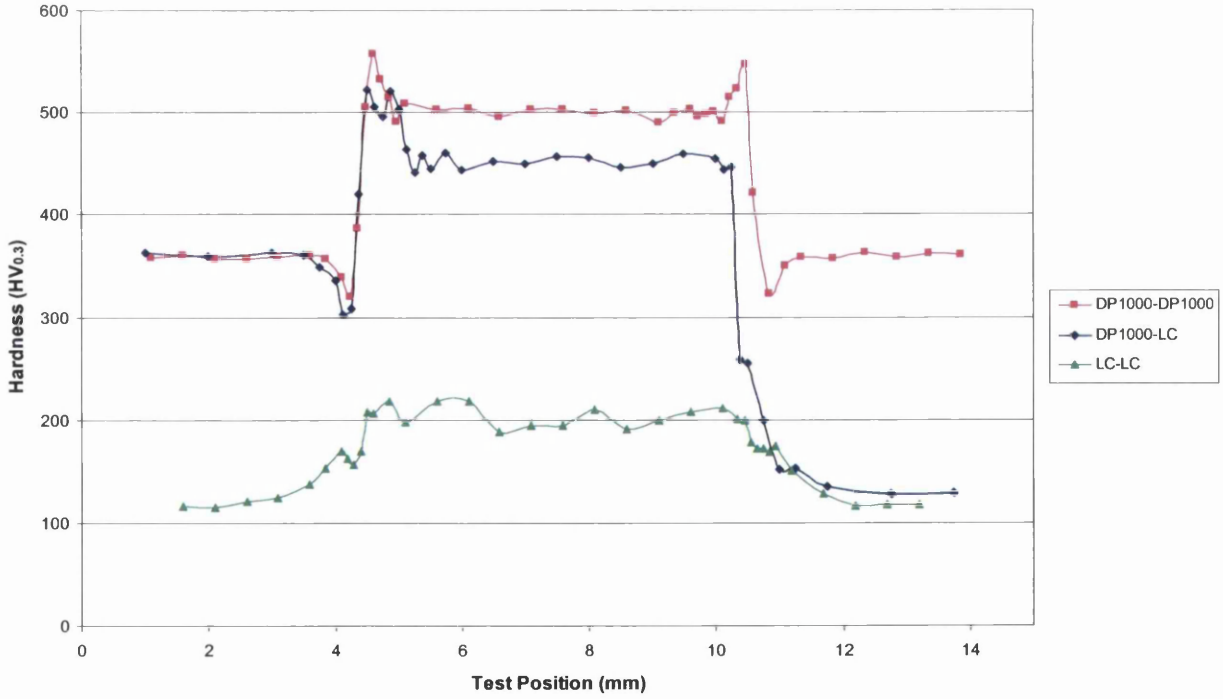

Figure 5.125 Comparison of microhardness profiles across a DP1000 weld, a DP1000 to LC weld and a LC weld

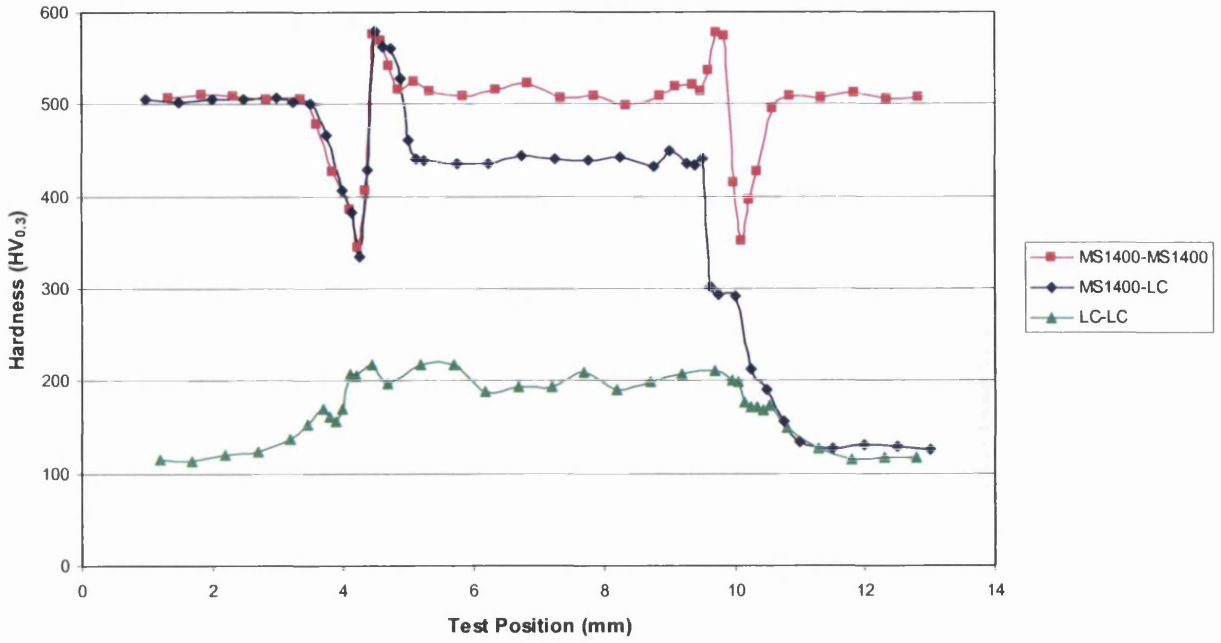

Figure 5.126 Comparison of microhardness profiles across a MS1400 weld, a MS1400 to LC weld and a LC weld

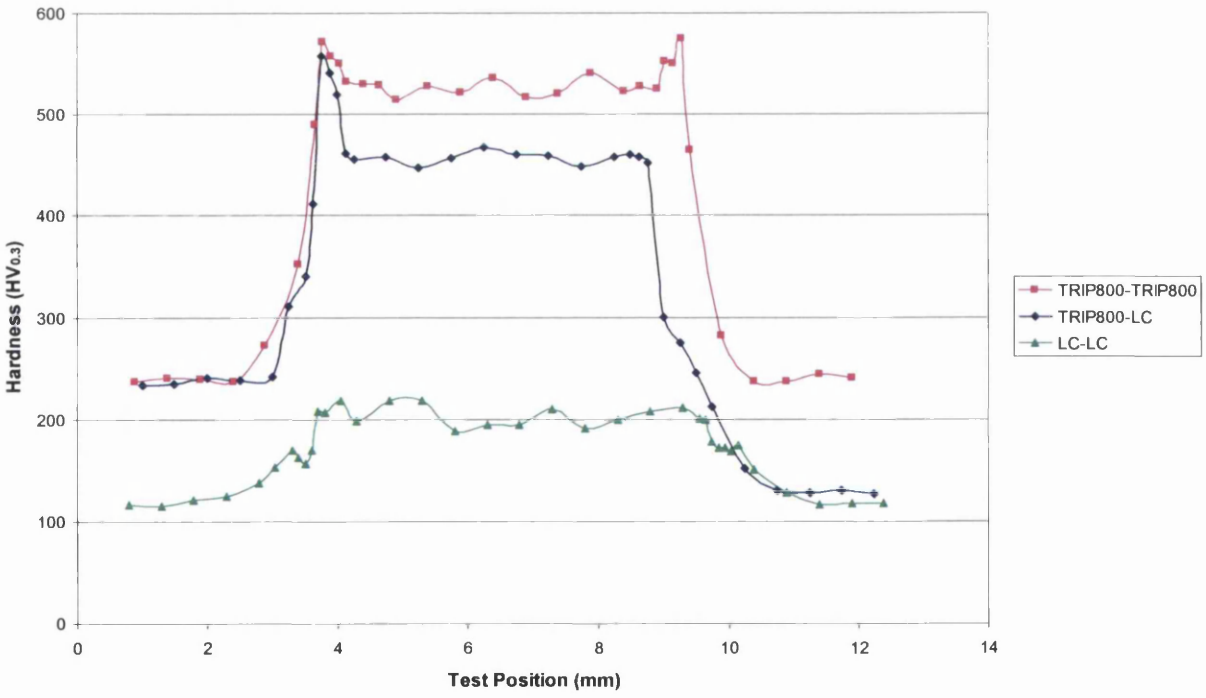

Figure 5.127 Comparison of microhardness profiles across a TRIP800 weld, a TRIP800 to LC weld and a LC weld

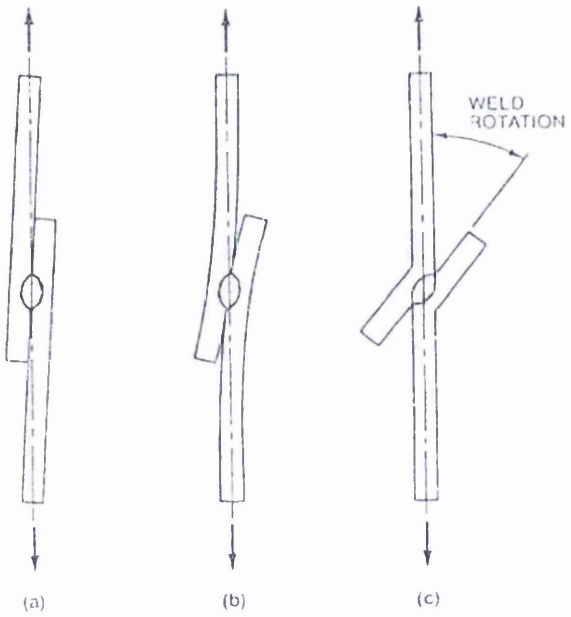

Figure 6.1 Schematic diagram illustrating the successive stages of distortion due to shear loading of lap joint[55]

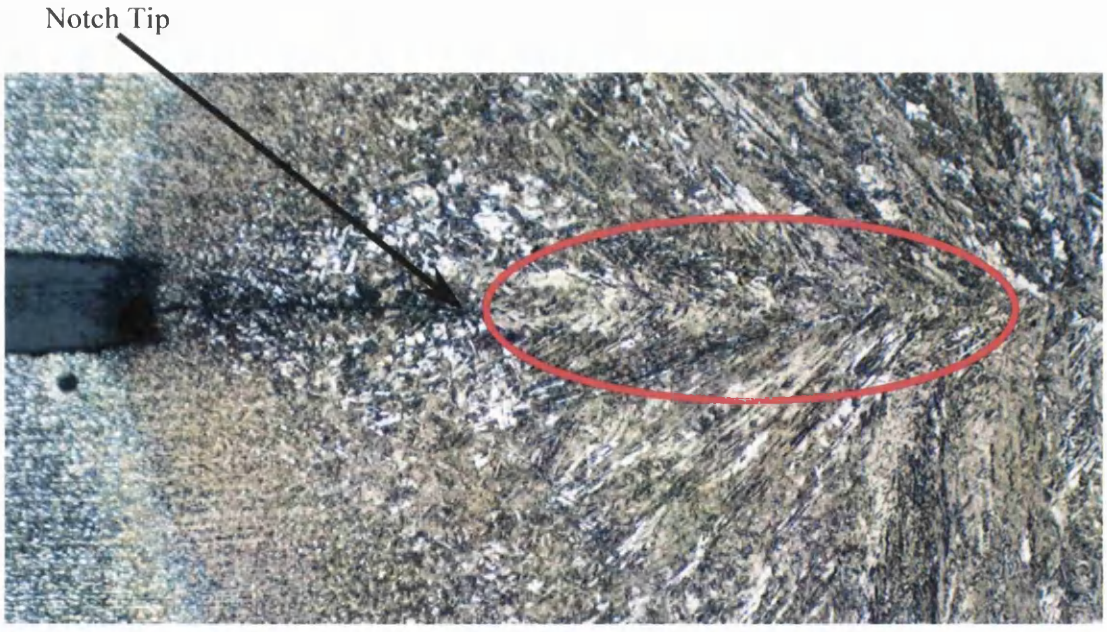

Figure 6.2 Micrograph showing lateral dendrites at the periphery of an advanced high strength steel spot weld

DURING WELDING

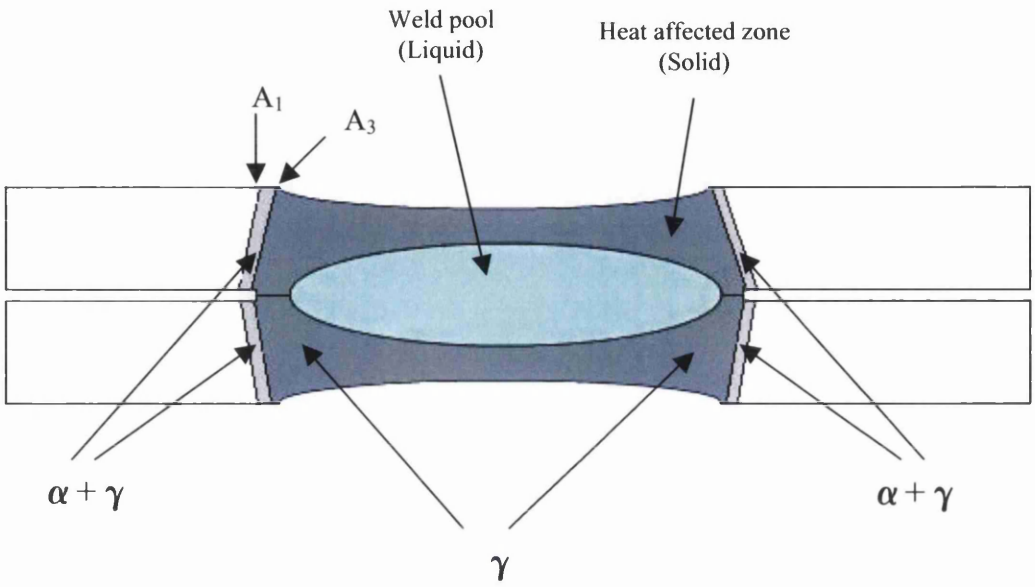

POST QUENCH

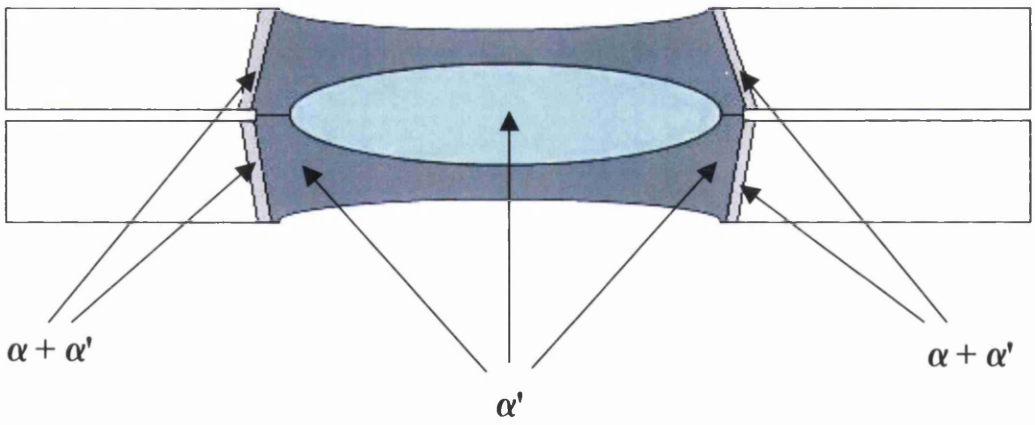

Figure 6.3 Schematic diagram of microstructures developed in the weld nugget and heat affected zone of AHSS spot welds during welding and after quenching (α = Ferrite, γ = Austenite, α' = Martensite)

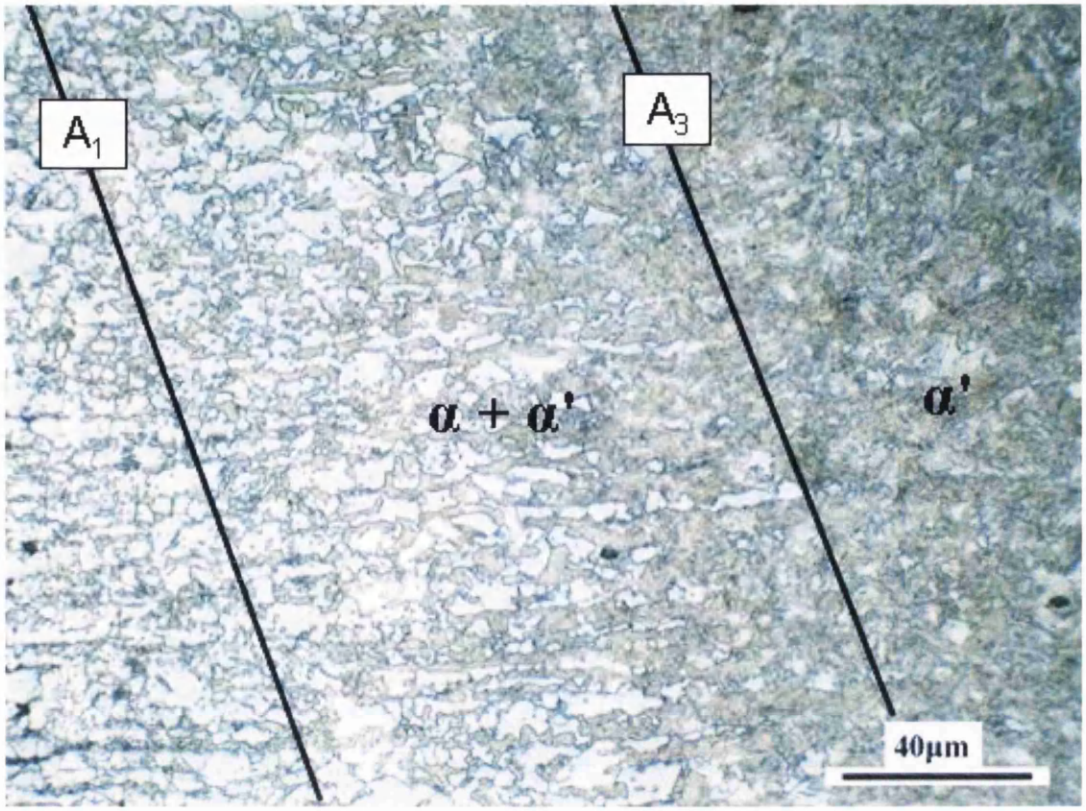

Figure 6.4 Micrograph showing the outer 'intercritical' region of the heat affected zone. (α = Ferrite, α' = Martensite)